WILDLAND FIRE

EDITED BY: Michael John Gollner, Xinyan Huang, Jason John Sharples and Melanie C. Rochoux

PUBLISHED IN: Frontiers in Mechanical Engineering

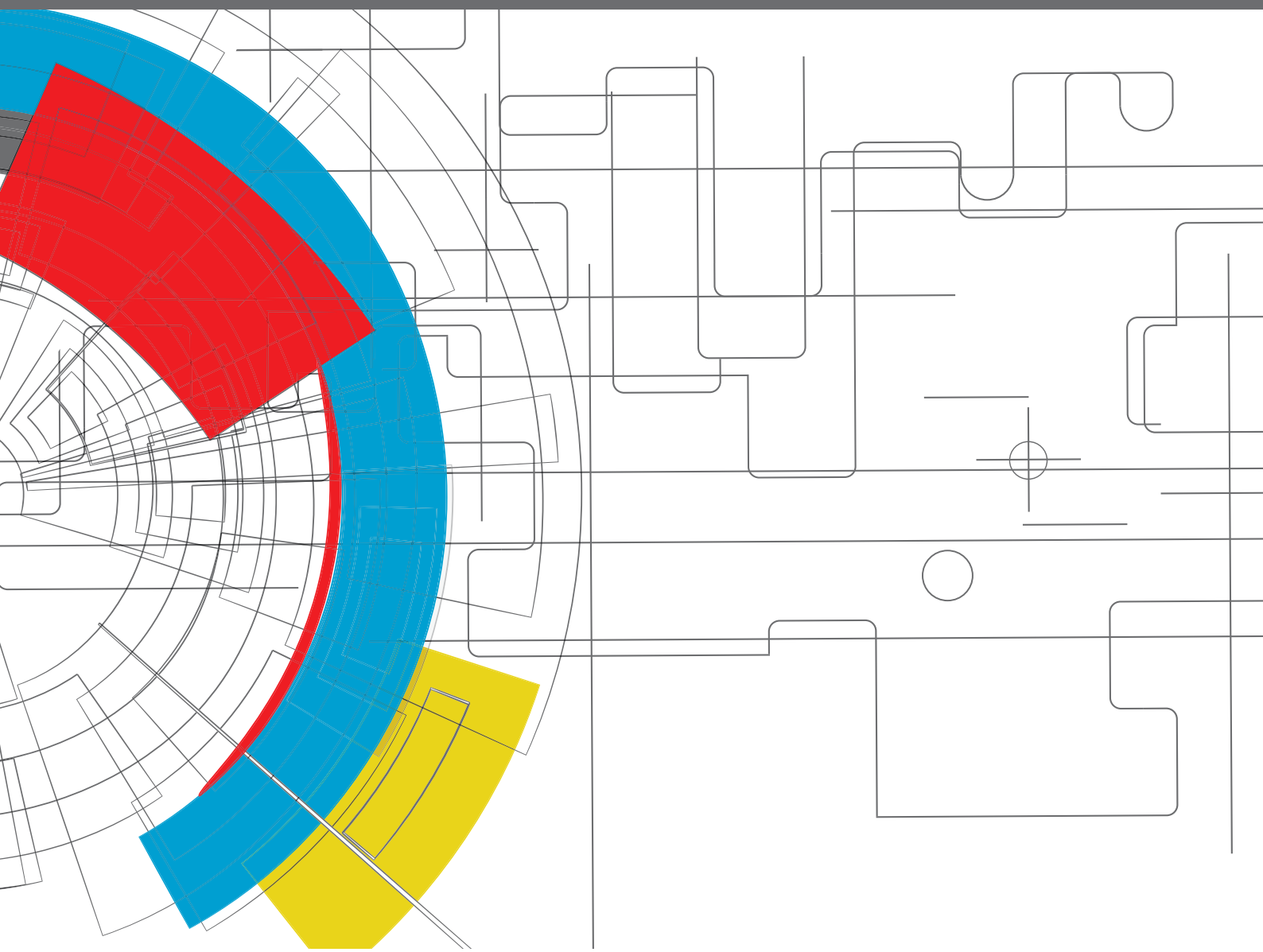

frontiers Research Topics

ISSN 1664-8714
ISBN 978-2-88963-966-3
DOI 10.3389/978-2-88963-966-3

About Frontiers

Frontiers is more than just an open-access publisher of scholarly articles: it is a pioneering approach to the world of academia, radically improving the way scholarly research is managed. The grand vision of Frontiers is a world where all people have an equal opportunity to seek, share and generate knowledge. Frontiers provides immediate and permanent online open access to all its publications, but this alone is not enough to realize our grand goals.

Frontiers Journal Series

The Frontiers Journal Series is a multi-tier and interdisciplinary set of open-access, online journals, promising a paradigm shift from the current review, selection and dissemination processes in academic publishing. All Frontiers journals are driven by researchers for researchers; therefore, they constitute a service to the scholarly community. At the same time, the Frontiers Journal Series operates on a revolutionary invention, the tiered publishing system, initially addressing specific communities of scholars, and gradually climbing up to broader public understanding, thus serving the interests of the lay society, too.

Dedication to Quality

Each Frontiers article is a landmark of the highest quality, thanks to genuinely collaborative interactions between authors and review editors, who include some of the world's best academicians. Research must be certified by peers before entering a stream of knowledge that may eventually reach the public - and shape society; therefore, Frontiers only applies the most rigorous and unbiased reviews.
Frontiers revolutionizes research publishing by freely delivering the most outstanding research, evaluated with no bias from both the academic and social point of view. By applying the most advanced information technologies, Frontiers is catapulting scholarly publishing into a new generation.

What are Frontiers Research Topics?

Frontiers Research Topics are very popular trademarks of the Frontiers Journals Series: they are collections of at least ten articles, all centered on a particular subject. With their unique mix of varied contributions from Original Research to Review Articles, Frontiers Research Topics unify the most influential researchers, the latest key findings and historical advances in a hot research area! Find out more on how to host your own Frontiers Research Topic or contribute to one as an author by contacting the Frontiers Editorial Office: researchtopics@frontiersin.org

WILDLAND FIRE

Topic Editors:
Michael John Gollner, University of Maryland, College Park, United States
Xinyan Huang, Hong Kong Polytechnic University, Hong Kong
Jason John Sharples, University of New South Wales Canberra, Australia
Melanie C. Rochoux, Centre Europeen De Recherche Et De Formation Avancee En Calcul Scientifique, France

Citation: Gollner, M. J., Huang, X., Sharples, J. J., Rochoux, M. C., eds. (2020). Wildland Fire. Lausanne: Frontiers Media SA. doi: 10.3389/978-2-88963-966-3

Table of Contents

frontiers in Mechanical Engineering

ORIGINAL RESEARCH
published: 26 February 2019
doi: 10.3389/fmech.2019.00005

Modeling Wind Direction Distributions Using a Diagnostic Model in the Context of Probabilistic Fire Spread Prediction

Rachael Quill[1], Jason J. Sharples[2,3], Natalie S. Wagenbrenner[4], Leesa A. Sidhu[2] and Jason M. Forthofer[4]*

[1] ARC Centre of Excellence for Mathematical and Statistical Frontiers, School of Mathematics, University of Adelaide, Adelaide, SA, Australia, [2] School of Science, UNSW Canberra, Canberra, ACT, Australia, [3] Bushfire and Natural Hazards Cooperative Research Centre, Melbourne, VIC, Australia, [4] Missoula Fire Sciences Laboratory, US Forest Service, Missoula, MT, United States

OPEN ACCESS

Edited by:
Guillermo Rein, Imperial College London, United Kingdom

Reviewed by:
Wei Tang, National Institute of Standards and Technology (NIST), United States
Xinyan Huang, Hong Kong Polytechnic University, Hong Kong
Wolfram Jahn, Pontificia Universidad Católica de Chile, Chile

***Correspondence:**
Rachael Quill
rachael.quill@adelaide.edu.au

Specialty section:
This article was submitted to Thermal and Mass Transport, a section of the journal Frontiers in Mechanical Engineering

Received: *23 November 2018*
Accepted: *04 February 2019*
Published: *26 February 2019*

Citation:
Quill R, Sharples JJ, Wagenbrenner NS, Sidhu LA and Forthofer JM (2019) Modeling Wind Direction Distributions Using a Diagnostic Model in the Context of Probabilistic Fire Spread Prediction. Front. Mech. Eng. 5:5. doi: 10.3389/fmech.2019.00005

With emerging research on the dynamics of extreme fire behavior, it is increasingly important for wind models, used in operational fire prediction, to accurately capture areas of complex flow across rugged terrain. Additionally, the emergence of ensemble and stochastic modeling frameworks has led to the discussion of uncertainty in fire prediction. To capture the uncertainty of modeled fire outputs, it is necessary to recast uncertain inputs in probabilistic terms. WindNinja is the diagnostic wind model currently being applied within a number of operational fire prediction frameworks across the world. For computational efficiency, allowing for real-time or faster than real-time prediction, the physical equations governing wind flow across a complex terrain are often simplified. The model has a number of well documented limitations, for instance, it is known to perform poorly on leeward slopes. First, this study is aimed at understanding these limitations in a probabilistic context, by comparing individual deterministic predictions to observed distributions of wind direction. Secondly, a novel application of the deterministic WindNinja model is presented in this study which is shown to enable prediction of wind direction distributions that capture some of the variability of complex wind flow. Recasting wind fields in terms of probability distributions enables a better understanding of variability across the landscape, and provides the probabilistic information required to capture uncertainty through ensemble or stochastic fire modeling. The comparisons detailed in this study indicate the potential for WindNinja to predict multi-modal wind direction distributions that represent complex wind behaviors, including re-circulation regions on leeward slopes. However, the limitations of using deterministic models within probabilistic frameworks are also highlighted. To enhance fire prediction and to better understand uncertainty, it is recommended that statistical approaches also be developed to complement existing physics-based deterministic wind models.

Keywords: complex terrain, deterministic, ensemble models, probability distributions, uncertainty, von Mises, wind modeling, WindNinja

1. INTRODUCTION

The accurate prediction of wind fields across all types of terrain is fundamental to capturing the range of possible spreading patterns a fire can exhibit. Operational wind and fire spread models are typically deterministic; a single collection of input variables gives rise to a single and fixed prediction value. However, wind fields and fire spread are driven by a range of processes which can experience variations at multiple scales, some of which cannot be fully captured within operationally constrained models. This gives rise to uncertainty in predicted fire behaviors. To address this uncertainty, probabilistic modeling techniques have emerged in the field of fire prediction.

Newly developed fire modeling frameworks allow for the prediction of fire perimeters and characteristics with associated probabilities, resulting in scenarios being analyzed in the context of risk and likelihood. Cruz (2010) noted that ensemble predictions would extend the interpretation of predicted outcomes, not necessarily improving individual prediction accuracy but providing more information to model end users. Even in early fire modeling research, Kourtz (1972) indicated potential improvements in the reliability of predictions by using such techniques. More recently, it was demonstrated that the ensemble-based decision support tool, FireDST, was able to produce a probabilistic prediction that adequately covered the actual extent of an observed fire, as such implying that it is plausible to view the actual fire as a realization of the ensemble distribution. This approach allowed for the provision of detailed probabilistic information about exposure and potential losses (French et al., 2013). Such information could be scrutinized by emergency service managers to analyze the variety of potential outcomes and impacts from a single event.

To construct probabilistic predictions, frameworks such as SABRE (Twomey and Sturgess, 2016) and FireDST (French et al., 2013, 2014) developed in Australia, and FSPro (Finney et al., 2011) developing in the US, have considered such ensemble-based probabilistic approaches to fire modeling through variations of the input parameters using pre-determined distribution structures. Probabilistic prediction of terrain-modified wind fields is therefore vital to the accurate and informative modeling of fire spread as a key model input but also as a tool for identifying the varying likelihood of important fire behaviors, which can arise as a consequence of complex wind-terrain interaction (e.g., Sharples et al., 2012). The information gleaned from probabilistic wind models can also help identify parts of the landscape where three-way interactions between the wind, the terrain and a fire can dominate fire propagation; these are instances where coupled fire-atmosphere models may be required to overcome the limitations of traditional surface-based fire spread models.

However, the distribution structures used in current operational fire prediction, such as the Uniform, Gaussian or point distributions, may not be most representative of the true variability of factors driving surface fire behavior. In the context of fire spread prediction, wind fields have been considered in probabilistic terms in only a limited number of studies (e.g., Sharples et al., 2010). In contrast, the wind energy and environmental sciences sectors have contributed analyses that consistently show the variability of wind speed and direction to be more complex, exhibiting features such as skewness, multi-modality and non-stationarity (e.g., Carta et al., 2008a,b; Erdem and Shi, 2011; Alegría et al., 2016; Lagona and Picone, 2016). In addition, Quill (2017) highlighted that the structure of wind direction distributions can vary considerably through space.

For effective modeling of bushfire spread across complex landscapes, input variables need to be modeled at all relevant scales. Mesoscale Numerical Weather Prediction (NWP) systems provide accurate real-time weather predictions over a range of appropriate spatio-temporal scales but, with horizontal resolutions from 3km up to 12km, these models do not resolve winds at sufficient scales to capture detailed topographic effects that can influence surface fire behavior. In particular, Wagenbrenner et al. (2016) highlighted the limited ability of broad-scale weather prediction to capture the variability of wind fields across complex terrain and indicated the need for downscaling models to better predict meteorological variables at finer resolutions.

WindNinja is the primary down-scaling wind model for bushfire prediction across numerous countries, including Australia, Greece, Canada and the United States (Forthofer et al., 2014a). In particular, WindNinja is operationally applied within the Phoenix Rapidfire model utilized across Eastern Australia (Tolhurst et al., 2008), as well as within FARSITE, Behave and FlamMap, among others, which are routinely used across the US[1]. WindNinja was originally developed due to a lack of operational down-scaling wind models available or widely used for bush-fire prediction (Forthofer, 2007) and, due to its success, few alternatives have been developed. As a deterministic diagnostic model, WindNinja is generally preferred for operations, as opposed to prognostic approaches using full computational fluid dynamics (CFD) models, due to the computational constraints on producing useful, fine-scale wind model outputs in real or near-real time (Forthofer et al., 2014b). It has also been shown that full physical wind models can be highly sensitive to input data such as surface roughness or boundary layer conditions over complex terrain, where these details are often not available in operational contexts (Lopes, 2003). However, due to the simplification of physical equations needed to obtain this computational efficiency, WindNinja is known to have significant limitations.

A number of evaluation studies throughout the development of the WindNinja software have compared the mass-consistent model to wind observations taken over complex terrain (Forthofer et al., 2014b; Butler et al., 2015; Wagenbrenner et al., 2016), as well as comparing fire spread prediction driven by the WindNinja model to those driven by a full CFD wind model (Forthofer et al., 2014a). Each of these studies has highlighted the greatest limitations of the model on leeward slopes where the complex nature of the flow field, including separation, can cause unsteady flow. It was noted by Wagenbrenner et al. (2016)

[1]https://www.firelab.org/project/windninja

that they were in fact to be expected since the version WindNinja 2.5.2 was designed to account for only mass-conservation across the landscape and did not take into consideration momentum conservation which causes features such as re-circulation on leeward slopes. Some of these issues were resolved by the addition of a momentum solver in later versions of the model (to be published), yet it is expected to have similar limitations on leeward slopes as seen by Forthofer et al. (2014b).

The limitations of models such as WindNinja are well documented and well understood. Forthofer et al. (2014b) warned that users should be aware of model limitations and interpret results cautiously where appropriate. The potential consequences of not capturing particular wind features in the context of fire modeling are significant, with characteristics such as flow separation on leeward slopes linked to extreme fire behaviors (Sharples et al., 2012; Simpson et al., 2013). However, the known limitations of deterministic wind field predictions have yet to be rigorously characterized for the purposes of quantifying error propagation or uncertainty in operational fire modeling.

In an investigation into the uncertainty of fire spread predictions, Cruz and Alexander (2013) suggested that, across the current global suite of fire models, percentage errors in the rates of spread predictions range from 20% up to 40%. The authors went as far as to say that "one could argue that perhaps the only certainty about wild-land fire behavior prediction is that it is extremely unlikely that a prediction will match the observed fire behavior characteristics" (Cruz and Alexander, 2013, p. 20). The main sources of uncertainty in fire rates of spread prediction have been cited as a lack of model applicability, internal model inaccuracy and input data errors (Albini, 1976; Alexander and Cruz, 2013). Operational settings have also been suggested to increase potential errors, particularly for data inputs, with greater uncertainty in weather forecasts and fuel variability (Cruz and Alexander, 2013).

There is currently limited literature quantifying uncertainty in operational fire prediction frameworks. Cruz (2010) noted that gaps in dealing with uncertainty exist in both literature and operations, and commented, for example, that the lack of confidence intervals for deterministic predictions leaves the onus of uncertainty estimation solely with the decision makers. Sensitivity analyses are one way to better understand the propagation of errors through a modeling framework and their impacts on final predicted outputs. One analysis of Phoenix Rapidfire, used in the Australian environment, was conducted by Penman et al. (2013) and concluded that fire weather (as characterized by the McArthur Forest Fire Danger Index) had the greatest influence on fire behavior, over suppression efforts and fuel treatments. The Forest Fire Danger Index (FFDI) is a function of temperature, relative humidity, wind speed, fuel moisture and fuel availability (Noble et al., 1980) and is classified into five categories. Penman et al. (2013) considered the sensitivity of fire outcomes in terms of these five categories, finding that increased FFDI led to reduced probability of containment, increased fire size and increased distance traveled by the fire. However, as far as the authors are aware, no detailed analysis of the influence of individual input parameters, such as wind speed, has been conducted. Although beyond the scope of this study, this research looks to drive toward such analysis.

The focus of this research is to consider wind direction, conditioned on wind speed, as an input variable to fire prediction. Clear links have been shown between wind speed and fire behavior through the traditional fire spread prediction models using tools such as the FFDI with broad-scale wind direction assumed to be the key driver of fire spread direction (Noble et al., 1980). Yet new research into extreme fires suggests that terrain-level wind direction can have significant impacts on fire behavior, including the generation of vorticity-driven lateral spread which can see fire propagate in directions perpendicular to the prevailing wind (Simpson et al., 2013). However, such behaviors are yet to be captured in traditional fire models.

Leading from the emergence of work in fire modeling, to better understand bushfire prediction uncertainty with the use of ensemble or stochastic modeling, this research reframes wind prediction in probabilistic terms. The study then aims to understand the capacity of the operational deterministic wind model WindNinja to capture terrain-level variability of wind fields. A novel application of the existing model is taken to predict the distribution of wind directions observed over complex terrain. By recasting wind fields in terms of probability distributions, the limitations of current modeling techniques can be quantified. Accurately modeled probability distributions of wind characteristics can feed directly into the ensemble-based fire modeling frameworks that are currently operational in Australia but require further uncertainty analysis. While this analysis remains beyond the scope of the present study, it is an important area of further research in the field and will help facilitate more informed decision making.

The remaining sections are organized as follows. Section 2 details the data collected and analyzed for this research, including the framing of wind direction distributions. Section 3 outlines the deterministic wind model WindNinja, using both mass-consistent and mass-and-momentum consistent solvers, as well as detailing the novel application of the model to predict wind direction distributions. Section 4 describes the comparison of wind model outputs with observed wind direction distributions, followed by a discussion of the results in section 5. Finally, section 6 concludes the study.

2. OBSERVED DATA

2.1. Case Study Region

Wind observations were taken across Flea Creek Valley (FCV) in the Brindabella National Park, approximately 40 km west of Canberra, Australia (**Figure 1**) (Quill and Sharples, 2018). The terrain across the broader region can be classified as rugged (McRae and Sharples, 2013), with elevation across the study area ranging from 767 m up to 1,077 m. The study area is dominated by Eucalyptus forest, with canopies up to approximately 15 m. The valley was heavily affected by fire in 2003, when atypical fire spread was observed in the region (McRae, 2004; Sharples et al., 2010).

The Bureau of Meteorology (BoM) have permanent automatic weather stations situated at Mount Ginini (approximately

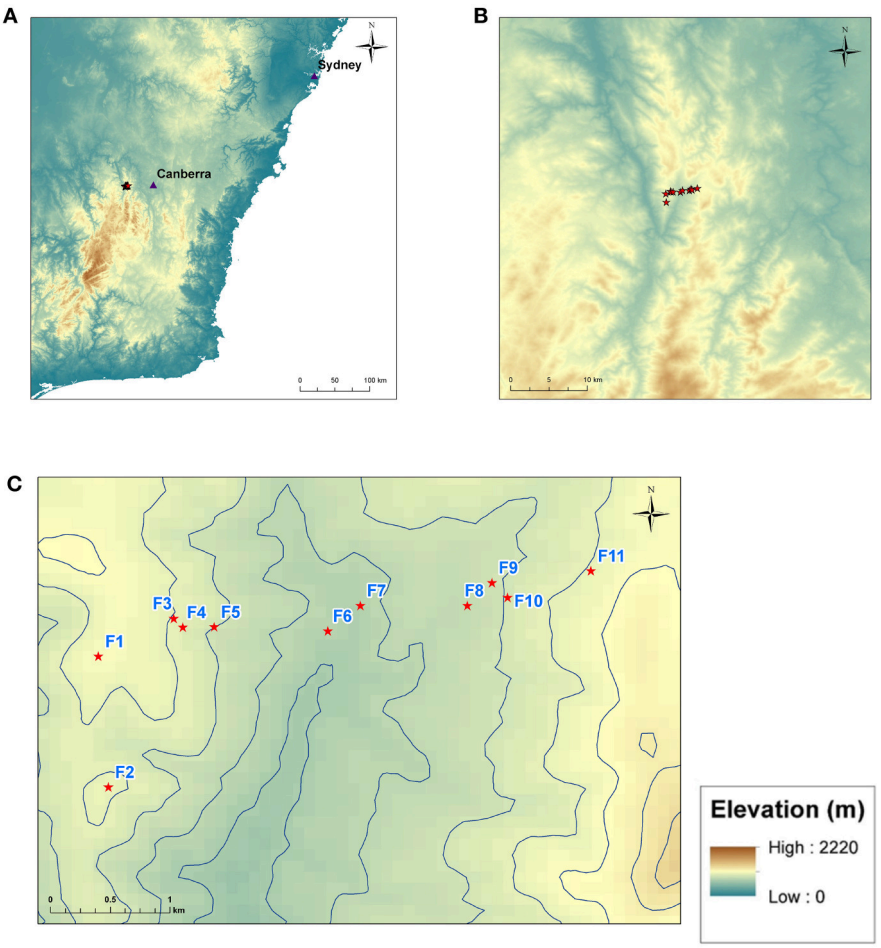

FIGURE 1 | Maps showing the locations of weather station sites. **(A)** Shows south-eastern Australia, **(B)** shows the broad topography surrounding the study region, and **(C)** shows the location of the eleven weather stations F1–F11 across Flea Creek Valley.

20 km south) and Canberra Airport (approximately 40 km east) which reflect the broad scale meteorology experienced across the region. The synoptic patterns in the region are dominated by high-pressure weather systems which produce west-northwesterly (WNW) winds during the summer and westerly winds throughout the winter. Flea Creek Valley runs approximately North-South through the Brindabella Ranges, and so is aligned approximately perpendicularly to the dominant WNW prevailing wind direction.

Eleven Davis® Vantage Pro 2 portable automatic weather stations with Weatherlink® data loggers connected to Raspberry Pi® microcomputers were used to collect data across Flea Creek Valley. The stations were set approximately 300–500 m apart along a 3–4 km East-West transect of the valley. The locations of the stations (F1 to F11) are indicated in **Figure 1**, and **Table 1** outlines the vegetation and topographic details of each site. Topography was obtained through ArcGIS (ESRI, 2011) analysis of the SRTM 90m Digital Elevation Model.

Each station recorded wind speed and wind direction at 5 meters above ground level using horizontal cup anemometers and wind vanes. Wind speeds were recorded at an accuracy of 0.4 ms^{-1}, while wind directions were recorded in 22.5° bins, corresponding to the 16 points of the compass. Data associated with very low wind speeds (below 0.4 ms^{-1}) were excluded from analysis. Data were collected at 1-min intervals from 10th July to 15th December 2014. With a station sampling frequency of 3 s, wind direction observations were recorded as the dominant wind direction sampled over 1 min, while wind speed observations were the average of wind speeds sampled over the minute. **Table 2** details the number of non-zero observations taken for each wind characteristic (speed and direction) over the study period at each site across FCV.

Wind data at these spatial and temporal resolutions, collected with these equipment, are limited to two-dimensional analysis of wind fields at the terrain scale. Although finer resolution three-dimensional data would allow more detailed analysis of fine-scale wind field movements, including the effects of the canopy and turbulence behavior, these are not within the scope of this study. The coarser resolution of this dataset allows for useful insights into terrain-level wind fields, at spatial resolutions akin to those predicted by operational down-scaling models like WindNinja, i.e., 90 m spatial resolutions (which are limited by availability

TABLE 1 | Topographic and vegetation details for each site across Flea Creek Valley.

	Elevation (m)	Aspect (°)	Slope (°)	Vegetation
F1	1,077	280	5	Clear within 5 m of station. Brush up to 2 m, with sparse canopy up to 15 m surrounding, intermediate foliage throughout.
F2	1,019	130	8	Clear within 2–3 m of station. Thick brush up to 5 m, and 10–15 m canopy surrounding.
F3	984	118	16	Acacia up to 5 m surrounding. Higher canopy cleared for powerlines.
F4	968	130	19	Clear within 3 m of station. Dense scrub up to 2 m, canopy up to 15 m with intermediate foliage around 5 m. Clear on SE side, down slope.
F5	922	140	26	Clear within 10m of station, with dense forest surrounding. Very steep slope covered in moss/grasses.
F6	767	159	16	Top of knoll. Thick scrub to 1 m, sparse canopy up to 10 m.
F7	771	254	15	Scrub to 1 m. Sapling growth to 2 m around station. Sparse canopy overhead within 4 m.
F8	831	244	10	Scrub to 1 m. Sapling growth to 2 m around station. Sparse canopy overhead within 4 m. Nearby gully and stream approximately 10 m away.
F9	879	381	12	Brush to 1 m. Canopy clear within 5 m. Medium density canopy to 10–15 m surrounding.
F10	912	275	19	Low density scrub. Intermediate foliage at 5 m surrounding station. Thicker trunks surrounding station 3 m away.
F11	999	308	20	Dense scrub up to 1.5 m surrounding station. Medium density canopy up to 12 m, with intermediate foliage from 5 m.

TABLE 2 | Summary of sample sizes for observed non-zero ($\geq$ 0.4 ms^{-1}) wind characteristics across Flea Creek Valley.

	Wind speed	Wind direction
F1	128,601	128,556
F2	32,812	32,768
F3	20,585	20,585
F4	47,440	47,396
F5	30,295	27,767
F6	61,492	61,456
F7	22,438	22,441
F8	21,740	21,709
F9	16,501	16,546
F10	42,098	42,142
F11	70,718	70,761

of topography data) for real-time fire modeling at, say, 10-min intervals. An analysis, shown in later sections, also highlights consistent wind behaviors captured by this dataset, providing useful meteorological insights.

At 5 m above ground, the anemometers were located within the vegetation canopy, with efforts made to ensure stations were not directly impeded by vegetation, within a few meters (**Table 1**). Modeled wind fields were predicted at 5 m above the canopy and so cannot be directly compared due to the well-known effects of canopies on wind fields (e.g., Finnigan, 2000; Finnigan and Belcher, 2006; Belcher et al., 2012). In application to bushfire modeling, predicted wind speeds from above the canopy are transformed to within-canopy winds using wind reduction factors (Andrews, 2012; Quill et al., 2016; Moon et al., 2019). However, predicted wind directions undergo no such transformation. Therefore, in the context of bushfire prediction, wind directions modeled at 5 m above the canopy are equivalent to wind directions predicted within the canopy and, on this basis, are compared to those observed for this study.

Observed within-canopy wind directions across Flea Creek Valley show consistent behaviors across the study period, suggesting that winds beneath the canopy are structured in relation to the prevailing winds above the canopy, rather than dominated by canopy effects. Such wind field structures are important to the driving of fires beneath and within canopies and quantifying such behaviors (where they are not well modeled) is an important step in understanding uncertainty propagation in surface fire prediction.

2.2. Wind Observations

Figure 2 summarizes the winds observed over the collection period at each site across FCV. Wind data collected from the ridge top stations on both the western and eastern sides of the valley (F1, F2, and F11) indicate the most frequently observed westerly to north-westerly prevailing wind direction. Less frequent easterly prevailing winds were also observed at F1. On the western slopes of the valley (F3 and F4), the dominant easterly wind direction indicates the prevalence of wind reversals when these slopes were leeward to the westerly prevailing winds. At F5, on this western slope, south-westerly winds are experienced most frequently. The site is located on a steep south-facing slope and winds are likely impacted by mechanical or thermal flows driven by this sheer topography.

On the valley floor (F6 and F7), northerly and southerly modes (northeast and southwest at F6) suggest that channeling along the valley axis may have dominated wind movement through this region. On the eastern slope at F8, the wind speeds are very low, leading to considerable variability in wind direction. Finally, on the eastern slope (F9 and F10), south-westerly observations indicate a southerly bias in the winds, most often observed when this slope was windward to the WNW prevailing winds. Local topographical features such as small-scale gullies running up the side of Flea Creek Valley (see contours in **Figure 1C**) may also cause a deviation from the prevailing wind direction.

To better understand the drivers behind observed wind behaviors at each site, **Figure 3** shows the average hourly wind speed and the average hourly wind direction at times which exemplify diurnal patterns, i.e., 03000 h, 0900 h, 1500 h, and 2100 h. Unfortunately, taking the mean of bimodal distributions such as those observed at F1, F2, and F7 can cause issues with such analysis. For instance, the northerly wind direction shown at F1 at 0900 h and 2100 h is not strongly indicated in **Figure 2**. These are in fact a result of significant intra-hourly west to north-westerlies despite more prominent easterlies

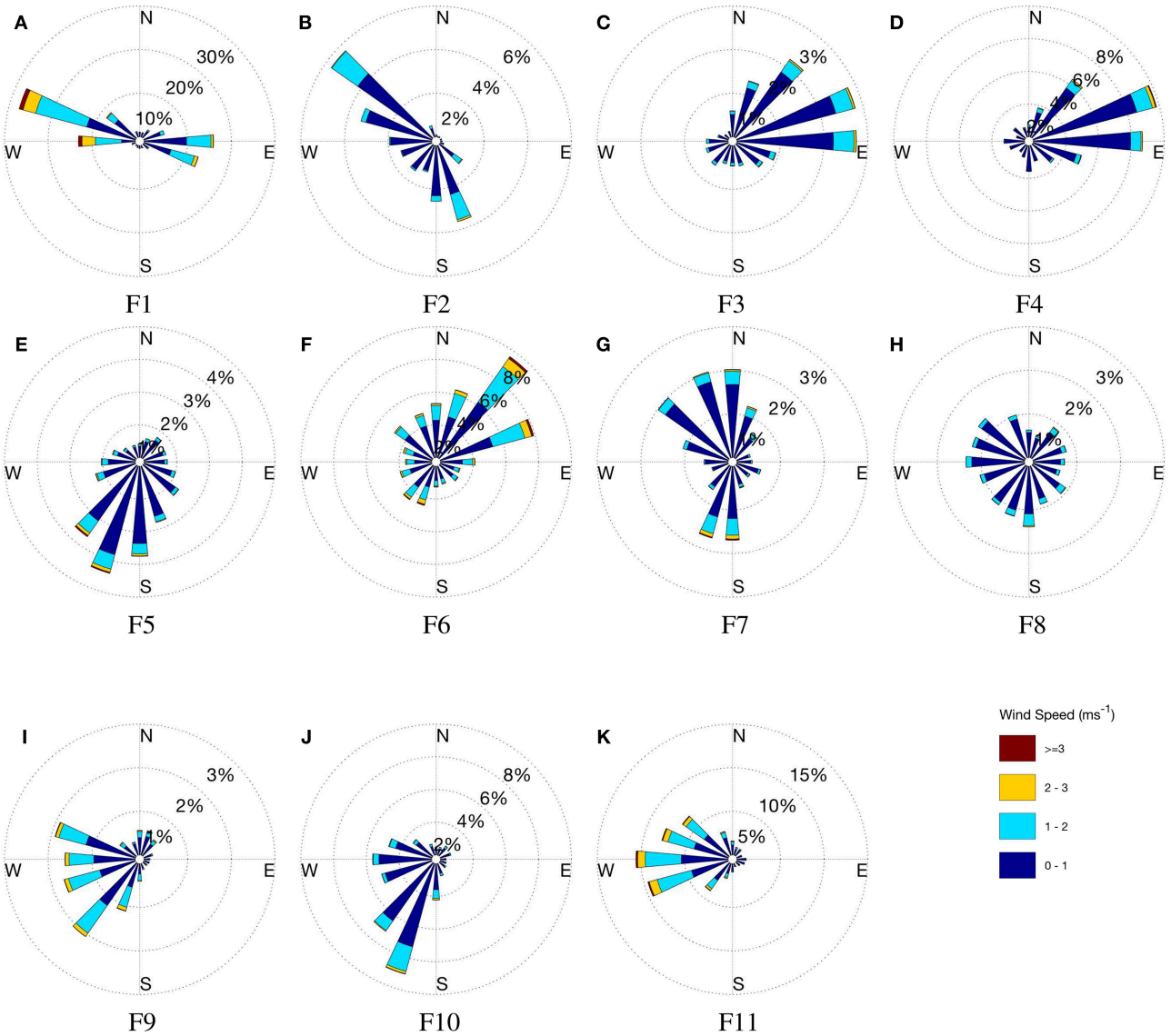

FIGURE 2 | Observed wind roses for each site **(A–K)** F1 to F11, across Flea Creek Valley.

over-night. Similarly, the south-western ridge top station at F2 shows SW winds in **Figure 3**, which result from averaging the NW and SE modes indicated in **Figure 2**. These intra-hour variations suggest no strong diurnal patterns, with mechanical forcing a more likely explanation for the bimodal wind directions.

Despite the northerly bias, average hourly wind directions at the north-western ridge top station (F1) rotated from NE over-night (0300 h) through to NW in the afternoon (1500 h). The easterly shift in wind direction at F1 was echoed by a similar regional wind direction change observed at Canberra Airport, and was coupled with an increase in wind speed across the valley. The higher afternoon wind speeds were predominantly felt along the valley floor and on the west-facing (or windward) slope. The leeward slope winds remained relatively low during the afternoon period.

Despite the change in wind direction observed at F1, the remaining stations showed stable wind directions throughout **Figure 3**, corresponding to the unimodal distributions shown in **Figure 2**. Each other station experienced consistent wind directions throughout the night and day, suggesting that diurnal effects had little impact on wind flow beneath the canopy across the valley. Most prominently on the valley floor at F6, northerly average flows agreed with the dominant northerly and north-easterly modes shown in **Figure 2**. The average northerlies were experienced throughout the day and night, with no southerly hourly average wind direction shown across the 24 hour period. The strong southerly mode shown by F7 in **Figure 2** appears

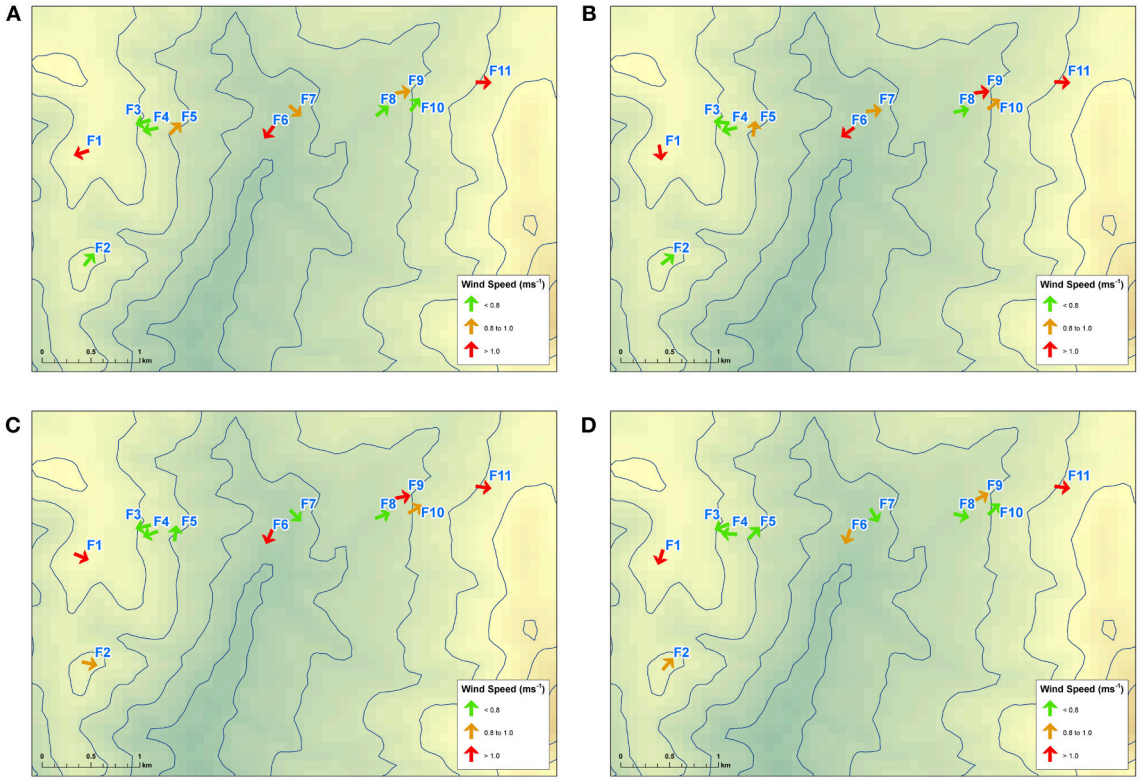

FIGURE 3 | Observed average hourly wind directions at each site across Flea Creek Valley, at **(A)** 0300 h, **(B)** 0900 h, **(C)** 1500 h, and **(D)** 2100 h.

to have been averaged out by consistent northerly winds. As suggested above, this lack of a clear diurnal pattern in the hourly averages suggests that channeling through the valley was mechanically, rather than thermally, driven.

On the western slope of the valley, F3 and F4 experienced consistent low speed easterly winds, directed up the slope of the valley wall. The easterlies experienced at 1500 h are in contrast with the westerlies observed at F1, indicating the existence of a recirculation region within the canopy. These average hourly wind directions concur with the wind roses in **Figure 2** as well as the analysis conducted by Sharples et al. (2010) which showed the prevalence of lee-slope eddies across Flea Creek Valley.

Finally, on the eastern slopes (F8, F9, F10, and F11) consistent average westerly winds were observed throughout the day and night (**Figure 3**), in agreement with **Figure 2**. When easterlies were experienced at F1 on the western ridge top at 0300 h, westerlies were still recorded on the eastern slope. This identifies a second recirculation region on the leeward west-facing slope under easterly prevailing winds, i.e., the inverse to those shown at F3 and F4 on the east-facing slope under westerly winds at 1500 h.

2.3. Wind Direction Distributions

For input into ensemble-based fire prediction frameworks, it is useful to recast wind observations in a probabilistic context. To this end, the wind direction observations from Flea Creek Valley are represented as frequency distributions of all wind directions observed at each of the stations across the valley transect over the study period. These distributions provide a representation of the likelihood of each wind direction being experienced. Such probabilistic representation can be used to inform the construction of ensemble members for fire modeling and help to better understand uncertainty through the prediction process. Since wind speed and direction cannot be considered independently, the impact of wind speed on wind direction distributions is assessed using three minimum speed thresholds observed at the ridge top station F1; 0 ms^{-1} (capturing all observed winds), 2 ms^{-1} and 4 ms^{-1}.

The western ridge top site, F1, was used as an indicator of the prevailing wind conditions across the valley. In application to real-time fire modeling, the use of a local wind reference point is common place where observations are taken on the ground. Utilizing a local reference point in this research therefore helps to understand how such local observations relate to winds in the local region. To verify the choice of F1 as the reference station, comparison of data given by the BoM weather stations at Mount Ginini and Canberra Airport showed observed surface wind directions coincided with prevailing ones (**Figure 4**). Joint wind direction distributions between the BoM wind direction data and that from F1, indicate that dominant prevailing westerlies occurring at both Mount Ginini and Canberra Airport were experienced concurrently at F1, and similarly for the less dominant easterly prevailing winds.

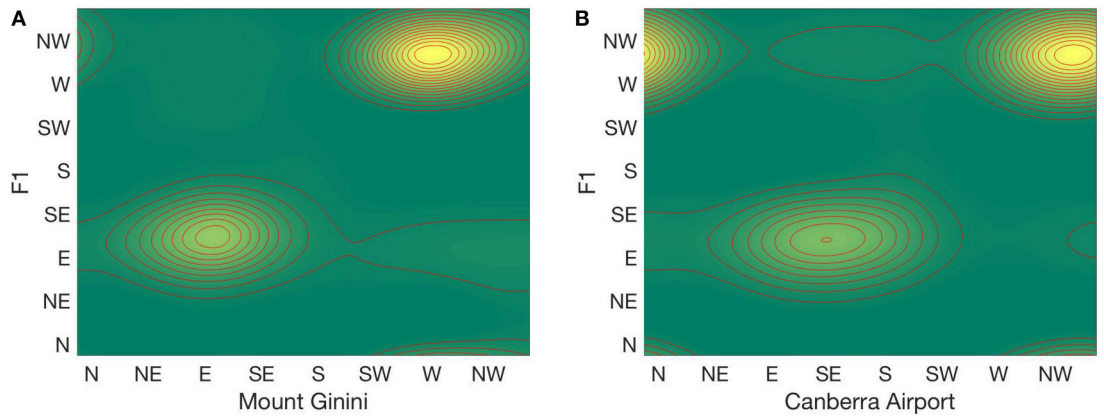

FIGURE 4 | Joint wind direction distributions between F1 and **(A)** Mount Ginini and **(B)** Canberra Airport during the study period. Yellow coloring indicates higher frequency of wind direction pairs observed. Dotted line indicates equal wind direction at the two sites.

3. METHODS

3.1. Conditional Wind Direction

The diagnostic wind model WindNinja was used to predict wind speed and wind direction across Flea Creek Valley using the SRTM 90 m digital elevation model, with the individual run calibrated to give a west-northwesterly wind direction at F1. Two solver options were used within the model; a mass conserving solver (packaged within WindNinja 2.5.2, referred to herein as the "native solver"), and a beta version of a mass and momentum conserving solver (later modified and released within WindNinja 3.0.0, referred to herein as the "momentum solver"). The model was run over a 10.3 km × 10.5 km domain with a vegetation choice of "Trees" and 1 ms^{-1} domain-average wind speeds at 5 m above the vegetation layer. The selection of "Trees" allows a surface roughness length of 1 m with zero-plane displacement of 12 m (assuming a 15.4 m canopy height). The vegetation layer is also assumed to be uniform across the entire domain. Modeled wind directions were predicted to align with observations of WNW (298°) winds at F1 on the western ridge top. For each location, the modeled wind direction from a single model run was compared to the observed wind direction distributions, conditional on a WNW wind being observed at F1. Using a domain averaged wind speed of 1 ms^{-1}, modeled wind speeds at F1 were approximately 2 ms^{-1} using both solvers.

As discussed previously, the wind field prediction was defined at 5 m above the vegetation layer, whereas wind observations were taken at 5 m above the ground within the approximately 15-m-high vegetation layer. To account for this in fire modeling applications, it is common to adjust wind speeds using wind reduction factors (e.g., Andrews, 2012; Quill et al., 2016; Moon et al., 2019), however wind directions are not transformed beneath the canopy. Therefore, the wind directions predicted at 5 m above the canopy using WindNinja are taken to indicate the predicted within-canopy wind directions used for operational fire modeling.

To compare the deterministically predicted wind direction to the observed conditional wind direction distribution, a percentage agreement value was calculated for the predicted wind direction segment. This was defined as the number of observations in the predicted segment as a proportion of the total observations for the time period.

3.2. Unconditional Wind Direction Distributions

For ensemble-based modeling of fire spread, input variables are varied around known distributions. For this purpose, it is therefore desirable to predict the probability distributions of wind speeds and directions. This study utilized a novel application of the deterministic WindNinja model to predict the distribution of wind direction at each location across Flea Creek Valley. Modeled unconditional wind direction distributions were constructed by running WindNinja with the momentum solver in an ensemble-type framework using the following procedure.

1. **Generate look-up table:** WindNinja was used to generate a wind direction look-up table for each site across the valley, using F1 as the reference station. Since the model is deterministic and the observations are discrete, it was only necessary to run WindNinja 16 times, each time calibrated to a different wind direction segment at F1. The look-up table therefore provided the modeled wind directions at each site, given the modeled wind direction at the reference station F1.
2. **Model through time:** Using the observed data at F1 as the representative domain average wind direction, the look-up table was cross-referenced to model wind direction at each site throughout the observation period. The look-up table, generated by the deterministic model, replaced the need to model the entire wind field at each time point.
3. **Construct frequency distributions:** The modeled time series were then used to construct modeled frequency distributions of wind direction at each site. The modeled wind direction distributions were compared to the unconditional distributions of all observed wind directions at each station site across the valley and throughout the study period.

To compare the modeled and observed unconditional wind direction distributions, both empirical and parametric measures are used. Firstly, the proportions of time that the predictions give a wind direction within the same wind direction sector, within one sector ($\pm 22.5^{\circ}$) and within two sectors ($\pm 45^{\circ}$) are calculated and analyzed. Secondly, the following 2-component mixture of von Mises distributions (often considered the circular equivalent to the Gaussian distribution) is fitted to the observed and predicted wind direction data (θ, in radians) for each site (Carta et al., 2008a);

$$f(\theta; p, \mu_1, \kappa_1, \mu_2, \kappa_2) = p \times g(\theta; \mu_1, \kappa_1) + (1 - p) \times g(\theta; \mu_2, \kappa_2), \quad (1)$$

with

$$g(\theta; \mu, \kappa) = \frac{1}{2\pi I_0(\kappa)} \exp(\kappa \cos(\theta - \mu)). \quad (2)$$

The function $I_0(\cdot)$ represents the modified Bessel function of the first kind and zeroth order, defined as

$$I_0(\kappa) = \frac{1}{2\pi} \int_0^{2\pi} \exp(\kappa \cos\theta) d\theta. \quad (3)$$

The structures of the observed and predicted wind direction distributions are compared using the estimated parameters; p, the mixing proportions, μ_i, the mean direction of each component and κ_i, the concentration parameter of each component. Maximum likelihood estimation is used to fit the parameters of Equation (1) in MATLAB (2016).

4. RESULTS

4.1. Deterministic Modeling of Conditional Wind Direction

Output from the single runs of both deterministic models (native solver and momentum solver) were analyzed in ArcGIS (ESRI, 2011) to generate the 5 meter predicted wind fields shown in **Figures 5**, **6**. **Table 3** shows the wind speed and wind direction outputs for each of the station sites. Using WindNinja with native solver (**Figure 5**), the predicted wind field was relatively smooth across the valley, maintaining a dominant WNW direction across both the leeward and windward slopes, as highlighted in the predictions given in **Table 3**. Wind speeds were highest across the western and eastern ridge tops, with very low speeds predicted on the valley floor.

Using the momentum solver (**Figure 6**), the domain-average wind direction was shifted significantly northward to achieve a WNW output at F1. This resulted in considerable northerly channeling through the valley. In addition, the predicted wind field using the momentum solver showed more spatial variation across the valley. This variation was most prominent on the leeward slope where, for instance, small lateral circulations were shown around gully features near F2 and F5. Wind speeds were again highest along the ridge tops, with the addition of some variations around small topographical features. In particular, wind speeds were shown to be much faster across the eastern windward slope around F10 and F12, as well as around F2 on the western ridge, than speeds modeled using the native solver.

Figure 7 shows the observed conditional wind direction distributions for a prevailing wind speed threshold of 0 ms^{-1} and wind direction of WNW measured at F1. Predictions from

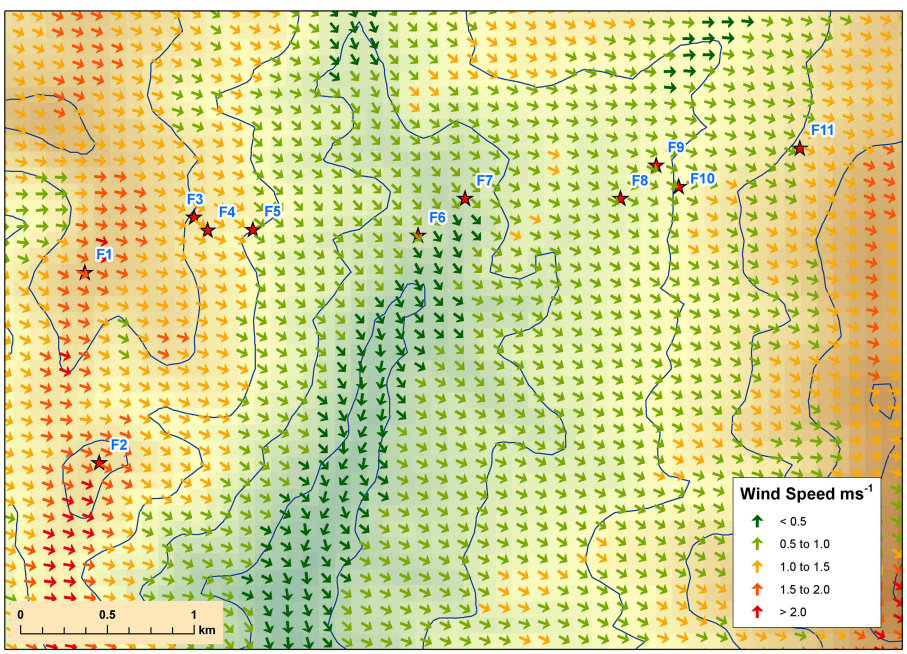

FIGURE 5 | WindNinja with native solver prediction over Flea Creek Valley, using domain-average wind speeds of 1 ms^{-1} and domain-average wind direction of 252°.

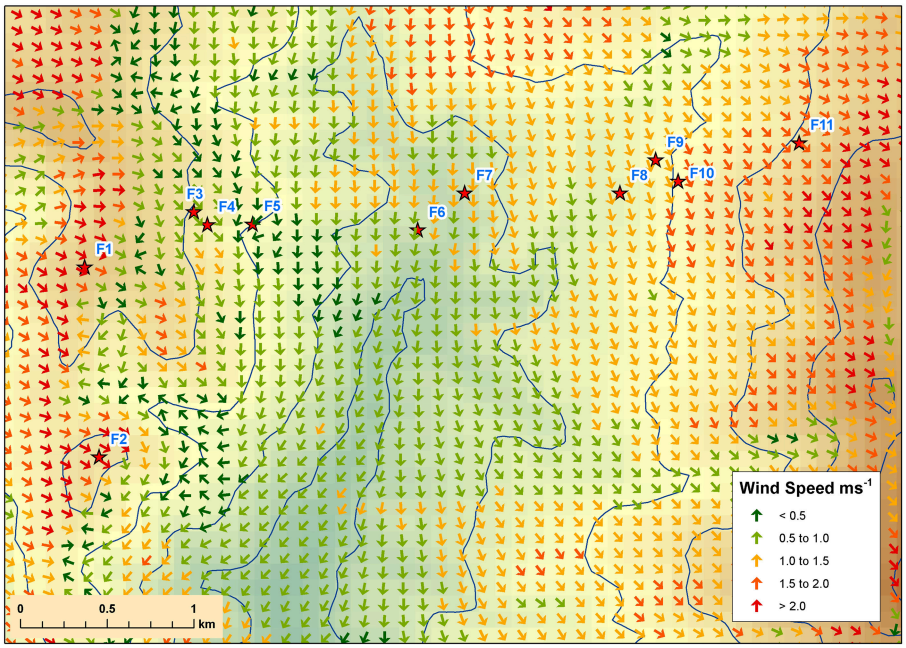

FIGURE 6 | WindNinja with momentum solver prediction over Flea Creek Valley, using domain-average wind speeds of 1 ms^{-1} and domain-average wind direction of 305°.

Table 3 are shown in green for WindNinja with the native solver, and red for WindNinja with the momentum solver. **Table 4** gives the proportion of the observed distributions that agree with each model prediction for increasing wind speed thresholds observed at F1. In general, the percentage agreements are low due to the deterministic nature of the individual predictions, with the individual model outputs not capable of capturing the variability of the observed wind direction distributions.

The highest agreements for the deterministic predictions with either solver (**Table 4**), were found on the ridge tops (F2 and F11) and valley floor (F6 and F7) where the models predict the dominant wind direction modes of the broader scale wind field. On the western ridge top (F2), there is no difference between the predictions from either model, whereas on the eastern ridge top (F11) and valley floor (F6 and F7), the momentum solver prediction shows a bias toward northerly winds. This bias has little impact on the percentage agreements observed on the valley floor, but the agreement values between observation and prediction at F11 are much lower for the momentum solver than for the native solver at all wind speed thresholds, i.e., 2.5% at T = 0 ms^{-1} as opposed to 15.6% for the native solver.

The highest individual deterministic agreement values were found at F2; with a wind speed threshold of 2 ms^{-1}, the percentage agreement reaches above 20% for both solvers. This agreement reduces at F2 as the wind speed threshold increases. Similar decreases in percentage agreement between model predictions and observations as wind speeds increase are shown across nearly all of the sites for both model versions.

On the western wall of the valley, leeward to the WNW prevailing winds, neither model predicts the easterly winds observed when applied as a single deterministic run. As seen in **Figures 5**, **6**, the model with either solver predicts predominantly westerly flows across the entire valley when the prevailing winds are WNW. The observations at F3 and F4 clearly show dominant easterly modes at these stations (**Figure 7**), suggesting the existence of recirculation within the vegetation on the leeward slope. The discrepancies between predictions and observations result in extremely low agreement percentages of 3.2% or less for the native solver, and 3.7% or less for the momentum solver. This percentage agreements dropped to below 1% and 1.5% for the

TABLE 3 | Wind direction (°, compass point) and wind speed (ms^{-1}) predictions using WindNinja with native solver and momentum solver for each site across Flea Creek Valley.

	Native solver			Momentum solver		
	Direction		Speed	Direction		Speed
F1	298	WNW	1.99	298	WNW	2.28
F2	299	WNW	1.94	303	WNW	2.08
F3	298	WNW	1.25	316	NW	0.86
F4	298	WNW	1.25	317	NW	0.96
F5	312	NW	0.93	48	NE	0.07
F6	322	NW	0.60	9	N	0.97
F7	331	NNW	0.55	359	N	1.13
F8	309	WNW	0.54	344	NNW	1.16
F9	300	WNW	0.58	341	NW	1.28
F10	300	WNW	0.60	335	NNW	1.48
F11	297	WNW	1.03	313	NW	1.91

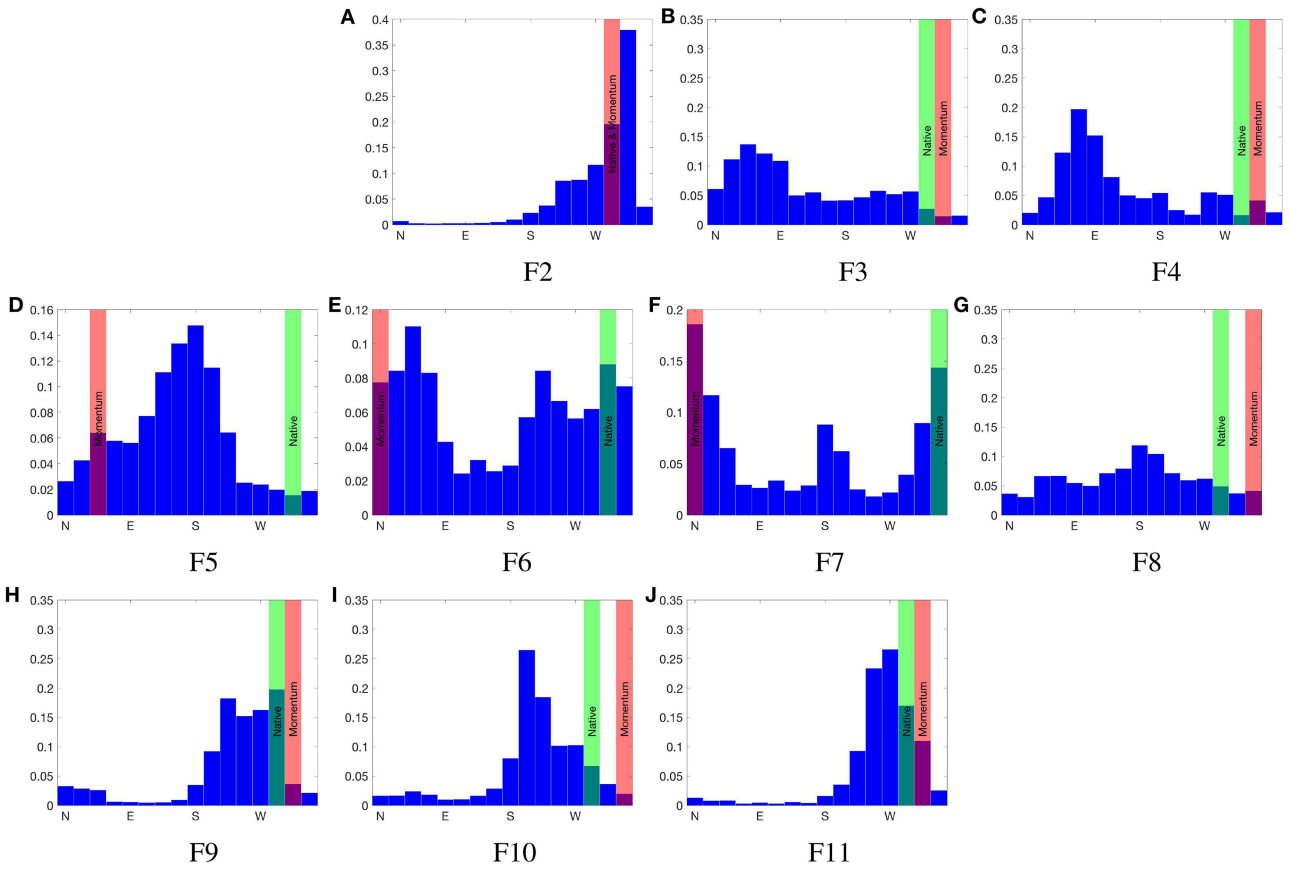

FIGURE 7 | Observed wind direction distribution at sites **(A–K)** F1 to F11, across Flea Creek Valley, conditional on a WNW wind observed at F1. Predicted wind directions using WindNinja with native solver are indicated in green, and with momentum solver are indicated in red.

native and momentum solvers, respectively, as prevailing wind speeds increased.

Finally, on the eastern slope (F8, F9, and F10) single agreement percentages shown in **Table 4** were larger than those shown for the western slope. The momentum solver predicts a considerable northerly bias to the flow through the valley, and this appears to have the greatest impact on the eastern slope. Therefore, the native solver performs better than the momentum solver at all three sites for all wind speed thresholds. In particular, at F9 the native solver predicts a WNW direction which captures the edge of the mode shown in **Figure 7**, while the momentum solver misses the mode by predicting a NW direction, resulting in agreement values of less than 3% as opposed to values up to 20% given by the native solver. This dramatic difference may in part be due to the discretization of wind direction, i.e., the binning of observations, which results in a significant difference in observations between two adjacent bins.

4.2. Modeling Unconditional Wind Direction Distributions

Figure 8 shows the observed unconditional wind direction distributions for each site across Flea Creek Valley (with a wind speed threshold of 0 ms^{-1}), as well as the predicted wind direction distributions produced using the probabilistic application of WindNinja with momentum solver. **Table 5** shows the proportion of time that WindNinja, with the momentum solver, predicted the same wind direction as observed, or within one or two compass sectors (i.e., $\pm 22.5^{\circ}$ or $\pm 45^{\circ}$). On the western and eastern ridge tops (F1 and F11, respectively), the predictions captured the dominant modal structures observed at the stations. In particular, at F1 the model captured the dominant WNW prevailing wind directions and the secondary easterly prevailing wind direction. At F11, although a bimodal distribution was predicted, the modes were concentrated, covering only a single wind direction bin.

For each site, the model generally predicts at least one mode coincident with the observed dominant wind direction shown in **Figure 8**. At F3 and F4, in contrast to the deterministic predictions, the predicted distributions pick up the wind reversal modes, i.e., the dominant easterly modes, with a relatively high prediction overlap of 60% within $\pm 45^{\circ}$ (**Table 5**). Similarly, at F9 and F10, the dominant westerly modes are better predicted than by the deterministic model. Through the valley floor (F6 and F7), the model indicates strong bimodal structures to the wind direction distributions which are somewhat evident in the observations but obscured by considerable variation.

TABLE 4 | Proportion of agreement between predicted wind direction (as compass point) and observed wind direction distribution at each site across Flea Creek Valley, conditional on observing a wind direction of WNW at F1.

	Native solver				Momentum solver			
	Pred.	**0 ms^{-1}**	**2 ms^{-1}**	**4 ms^{-1}**	**Pred.**	**0 ms^{-1}**	**2 ms^{-1}**	**4 ms^{-1}**
F1	WNW	–	–	–	WNW	–	–	–
F2	WNW	0.19	0.21	0.16	WNW	0.19	0.21	0.16
F3	WNW	0.03	0.02	0.02	NW	0.02	0.01	0.01
F4	WNW	0.02	0.01	0.01	NW	0.04	0.02	0.01
F5	NW	0.02	0.01	0.00	NE	0.07	0.05	0.01
F6	NW	0.09	0.06	0.05	N	0.09	0.07	0.08
F7	NNW	0.13	0.12	0.09	N	0.18	0.16	0.09
F8	WNW	0.05	0.04	0.01	NNW	0.04	0.04	0.00
F9	WNW	0.20	0.18	0.15	NW	0.03	0.01	0.02
F10	WNW	0.06	0.08	0.06	NNW	0.03	0.03	0.04
F11	WNW	0.16	0.17	0.18	NW	0.03	0.03	0.10

Three observed minimum wind speed thresholds, T, are used; 0 ms^{-1}, 2 ms^{-1}, and 4 ms^{-1}.

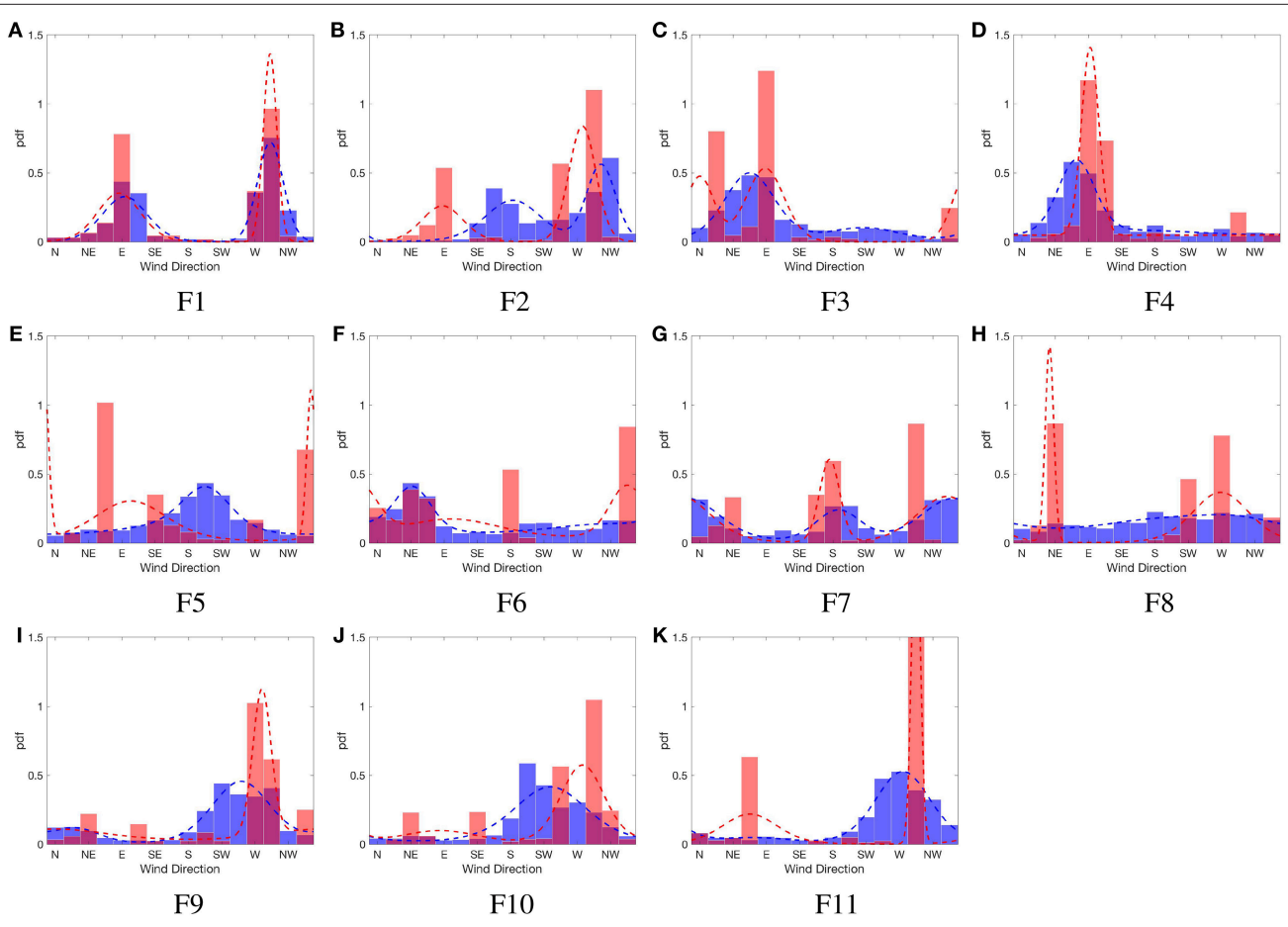

FIGURE 8 | Observed (blue) and predicted (red, using momentum solver) unconditional wind direction distributions at sites **(A–K)** F1 to F11, across Flea Creek Valley. Dotted lines indicate fitted 2-component mixture von Mises distributions with parameters given in **Table 6**.

Table 5 clearly shows the model to be accurate at the western ridge top (F1), with consistent wind direction predictions within one sector of the observations. At the remaining ridge top stations (F2 and F11), as well as on the western slope (F3 and F4) and on the eastern slope (F9), the model predicted wind directions within the same compass quadrant as those observed

(i.e., within ±45°) over 50% of the time. As seen in the predicted distributions in **Figure 8**, these sites show the greatest similarity between the observed and predicted wind direction distributions.

The proportions of overlap between observed and predicted wind directions shown in **Table 5** are lowest at locations across the valley where greater variation was observed (F5, F6, F7, F8, and F10). **Table 5** shows an overlap within ±45° of 47% for F6, where a strong bimodal distribution was predicted, while a secondary wind direction mode was not strongly observed. The lowest overlap proportions are shown at F5, with only 17% overlap within two compass sectors. From the distribution shown in **Figure 8**, it is clear that the model did not capture the structure of the observed wind direction distribution.

Table 6 shows the maximum likelihood estimates for parameters of the 2-component mixture von Mises model used to fit the observed and predicted wind direction distributions. In general, the predicted distributions show modes with considerably higher concentration parameters, showing the models inability to capture the observed variability in wind direction. However, many location parameters were well predicted, with mismatched location estimates potentially due to small-scale topography or high variability which were unable to be resolved by the deterministic model, i.e., F2, F5, and F8.

For stations with clearly observed and predicted bimodal distributions, the 2-component mixture von Mises parameter estimates give similar location parameters, i.e., F1, F7, F9, F10, and F11. However, for other distributions (both observed and predicted) the 2-component mixture may not be the most appropriate fit. For example, F3 and F4 appear to show unimodal distributions, and so the estimated bimodal parameters either show an extremely unbalanced mix (i.e., predicted mixture at F4 gives $\kappa_1 = 24.07$ and $\kappa_2 = 0.00$), or modes at close locations (i.e., predicted mixture at F3 gives $\mu_1 = 1.55$ and $\mu_2 = 6.28$). For stations with very high observed variability such as F8, the predicted and observed parameter estimates were very poorly aligned; firstly, the location parameter for the observed distribution had limited meaning with such low concentration parameters, and secondly the predicted distribution had far greater concentrations than observed.

TABLE 5 | Proportional overlap between predictions and observations at 1-min time steps.

	Same sector	Within one sector	Within two sectors
F1	0.74	1.00	1.00
F2	0.12	0.39	0.55
F3	0.18	0.42	0.60
F4	0.15	0.42	0.60
F5	0.03	0.10	0.17
F6	0.13	0.34	0.47
F7	0.07	0.20	0.32
F8	0.05	0.16	0.29
F9	0.15	0.40	0.30
F10	0.07	0.23	0.41
F11	0.13	0.41	0.63

"Overlap" is taken to be a prediction of wind direction in the same compass sector, within one sector (i.e., ±22.5°) or within two sectors (i.e., ±45°).

5. DISCUSSION

5.1. Deterministic Modeling

In general, the best agreement between the individual deterministic predictions and the conditional wind direction distributions occurred on the ridges and valley floor. These areas can be thought to represent broader scale terrain features, while the valley sides represent areas where more complex physical features dominate wind flows, such as the recirculation regions on leeward slopes caused by flow separation over ridges. As discussed in the introduction, the modeling framework behind the WindNinja software simplifies some of the physical

TABLE 6 | Estimated parameters for a 2-component mixture von Mises model fit to the observed and predicted wind direction distributions across Flea Creek Valley.

	Observed					Predicted				
	p	μ_1	κ_1	μ_2	κ_2	p	μ_1	κ_1	μ_2	κ_2
F1	0.45	1.64	3.66	5.07	10.96	0.46	1.50	4.00	5.07	40.11
F2	0.52	3.19	2.42	5.28	8.65	0.32	1.53	4.32	4.83	9.98
F3	0.76	1.18	2.97	3.87	1.40	0.61	1.55	5.10	6.28	9.34
F4	0.58	1.28	5.41	2.75	0.22	0.70	1.61	24.07	0.01	0.00
F5	0.57	2.82	0.34	3.55	3.25	0.73	1.78	1.40	6.03	100.00
F6	0.33	0.83	5.67	5.55	0.30	0.63	1.74	0.66	5.88	6.00
F7	0.31	3.26	3.61	5.99	1.73	0.36	3.06	18.00	5.83	2.06
F8	0.72	3.23	0.34	5.09	1.02	0.36	0.65	99.81	4.69	2.36
F9	0.16	0.49	3.26	4.38	2.17	0.43	6.28	0.56	4.87	21.68
F10	0.00	3.50	1.30	4.08	1.40	0.25	1.47	1.25	4.83	3.91
F11	0.11	1.32	1.34	4.79	2.49	0.37	1.18	2.48	5.10	99.45

p denotes the mixing proportion, μ_i denotes the locations parameters (in radians) and κ_i denotes the concentration parameter for the respective modes.

equations governing such flows to enable operational use, and thus is known to be limited in such areas (Forthofer et al., 2014b). The results of the deterministic application in this study further confirm this, but add probabilistic information to these limitations, finding that percentage agreements at individual sites can be extremely low.

With the addition of the momentum solver, WindNinja was able to better capture some topographic impacts on wind flow across the valley, including recirculation within gullies and on leeward slopes, and larger-scale channeling along the valley floor. With a comparison of only a select few individual sites, the ability of the momentum solver to capture some of these more complex flows is not shown with the analysis presented here. For example, on the leeward slope, recirculation is not predicted within the pixel overlapping the two observation sites, yet it is observed elsewhere on this slope in **Figure 2**. The discrete nature of the observed wind direction (22.5° sectors) may also contribute to some of the low percentage agreement values seen throughout this analysis. Through estimation of distributions in the ensemble-style analysis, some of these discrepancies may be smoothed.

Other broad-scale flows shown by the deterministic momentum solver prediction, such as the strong northerly bias on the eastern slopes, was not observed in the data. This northerly-skewed prediction by the momentum solver was due to the adaptation of input parameters to optimize the model run but led to lower performance on the windward slope—reducing percentage agreements from 20% with the native solver down to only 3%. In the context of fire, this significant difference between predicted and observed wind direction may cause considerable difference between predicted and observed fire spread.

Across the valley, it is shown that as observed wind speed thresholds increase, the percentage agreement between the individual predictions and observed conditional wind direction distributions decreases. This decrease is to be expected since analysis [not shown here, but also highlighted by Sharples et al. (2010)] indicates that the variance of dominant modes decreases as wind speed thresholds increase, resulting in a lower percentage agreement if the model does not accurately predict the key mode. Due to the relatively low wind speeds experienced throughout the study period the highest wind speed thresholds also have smaller sample sizes to construct the distributions for comparison, thus somewhat reducing the reliability of subsequent conclusions. Further model runs with higher domain-averaged wind speed, larger simulation domains and higher model resolution might also indicate different predicted behaviors across the region. However, it was found that increased wind speeds under the native solver had little impact on predicted wind direction.

The lack of a diurnal pattern at F3 and F4, as shown in **Figure 3**, and the persistence of lee-slope easterly modes under higher wind speed conditions suggests that they are due to recirculation eddies driven by flow separation over the leeward slope rather than upslope thermal winds. Analysis of the timing of similar easterly modes experienced in the same location across the valley by Sharples et al. (2010) also showed limited diurnal patterns, suggesting that this recirculation region is in fact an area of persistent lee-slope eddies within the vegetation layer. Another possibility is that the easterly modes could be due to pressure-driven recirculation under the canopy but given the agreement between these results and those of Sharples et al. (2010), which were obtained in the absence of an intact canopy, flow separation is likely the main driver. While WindNinja with either solver is not intended to predict within canopy flows, with no mechanism for wind direction adjustment, these eddies are consequently often not captured within fire modeling frameworks.

5.2. Modeling Wind Direction Distributions

The ensemble-style application of WindNinja, using wind libraries, allows for a prediction of the full distribution of wind direction at each point across the valley. This probabilistic representation of wind predictions is better suited to emerging ensemble-style fire modeling frameworks, where uncertainty can be quantified and analyzed. In general, the ensemble-style application of WindNinja with momentum solver predicted coincidental modes for wind direction distributions across the valley. However, the modeled data shows considerably lower variation than the observed.

The limited predicted variation is to be expected due to the deterministic nature of the model, with simplified physical equations. Equally, the model predicts above canopy winds while observations were taken beneath the canopy, thus influenced by additional turbulence. Despite this, the within canopy winds showed distinct structures which evidence the existence of consistent wind behaviors such as beneath canopy recirculation zones. Due to the lack in predicted variability, the model was least effective at the most variable sites, where wind speeds were low. In areas where wind directions were highly variable, overlap percentages (to within an entire compass quadrant) could be as low as 17%, and estimated location and concentration parameters were poorly aligned. However, it should be noted, that at some sites, the estimation of a 2-component mixture distribution may be inappropriate, leading to misalignment between observation and prediction estimates. A more flexible modeling approach may be required, where the number of mixture components is also a parameter to be estimated.

The high variation in the wind directions observed at the valley floor sites, reduces the efficacy of the prediction, but the variation itself may also be induced by local features affecting the wind field which are not adequately resolved by the model. For instance, F6 is located on top of a knoll at the bottom of the valley which may induce localized flows or eddies which cannot be represented at the resolution used to predict the wind field. This is again evident at F8 on the eastern slope; observed wind directions are almost uniform around the compass, whereas the model predicts an approximately bimodal distribution representative of mechanical valley winds.

Indeed, there are clearly other factors that influence the variability of wind directions (and wind speeds), aside from the prevailing wind direction. It is this heterogeneity in variation across the landscape (particularly in relation

to deterministic predictions) that requires further study to understand how to best account for these factors in deterministic models (yet maintain computational efficiency). Probabilistic approaches may help to fill such gaps with efficient statistical wind models that can inherently capture heterogeneity in relationships between influencing factors across spatial domains.

6. CONCLUSION

In the pursuit of accurate fire spread prediction, the accuracy of model inputs must be considered. In emerging bushfire research, the accuracy of outputs is being framed in terms of uncertainty, with an increasing focus on ensemble methods and probabilistic representations. Traditional deterministic models must now be complemented with probabilistic information informed by empirical data. This study shows a stark comparison between the application of a diagnostic wind model using the traditional approach and a novel ensemble-style application. The demonstrated ability of this novel method in capturing observed wind field variability highlights a significant advance in modeling input variables (not limited to wind fields) and forms an understanding of the uncertainty in ensemble-based bushfire prediction.

The application of WindNinja with both native and momentum solvers is limited by its deterministic nature, leading to small agreement percentages between single predictions and observed wind direction distributions. As previously noted in the literature (Forthofer et al., 2014a,b; Butler et al., 2015; Wagenbrenner et al., 2016), the models perform poorly on the leeward slopes, with observations representative of recirculation regions not captured at the study sites. However, some areas of recirculation were predicted by the momentum solver in other areas of the leeward slope. It has been shown in the literature that lee-slope eddies can create necessary conditions for dangerous and extreme fire behavior (Sharples et al., 2012; Simpson et al., 2013), and the inability of a single model run to identify such wind behaviors can lead to the misrepresentation of fire spread and behavior across the landscape. Individual model runs can be extremely sensitive to the set of input variables, including domain-averaged wind direction as well as the size and resolution of the domain. Fire managers are encouraged to better understand this sensitivity by running multiple wind input scenarios, however, very limited formal sensitivity analysis exists within the literature. Quantifying the effects of probabilistic prediction of input variables, including wind speed and direction, is an ongoing focus of further research in wildland fire prediction.

The novel ensemble-style application of WindNinja with the momentum solver resulted in the modeling of wind direction distributions which were able to capture some of the key structures of wind flow observed across the valley. Bimodal distributions were predicted at a number of sites where the deterministic application of the model was only able to predict a single outcome. In particular, predicted distributions were able to capture observed leeward slope recirculation which would lead to a strengthened ability of fire models to identify regions prone to extreme and erratic fire behavior. Although distributional predictions were able to model key wind direction modes at each site, the predictions lacked considerable variability compared to observed distributions.

There is always room for improvement to better capture underlying physical processes, but dynamic downscaling models can still be limited by resolution. Mechanisms existing at finer scales will continue to contribute uncertainty to model outputs. From this study, it is clear that an ensemble-style application of WindNinja shows differing levels of accuracy across the landscape, where different physical processes may dominate wind flow. To address some of these gaps, physical processes can be modeled using probabilistic approaches. While statistical approaches have their own limitations, such as relying upon previous system behaviors (including outliers), they are able to capture some of the variability of wind and fire spread across the landscape, which is not resolved by current physical models and can be better suited to emerging ensemble-based fire prediction frameworks. Probabilistic models not only provide more informative inputs for bushfire prediction but can also be used to identify areas where different driving forces may have varying impacts on fire behavior, such as significant terrain effects or fire-atmosphere coupling. In additional further research, sensitivity analysis of fire modeling frameworks is required to understand the quantitative effects of capturing (or not capturing) the true variability of wind fields over complex terrain. Using such analysis alongside ensemble-based or probabilistic modeling approaches will allow for formal and quantitative assessments of uncertainty in operational fire spread and behavior predictions.

DATA AVAILABILITY

The dataset analyzed for this study can be found in the University of Adelaide Figshare repository: Flea Creek Valley Data, Jul to Dec 2014 (Quill and Sharples, 2018), accessed via https://doi.org/10.25909/5c13258d1407a.

AUTHOR CONTRIBUTIONS

RQ, JS, and LS conceived and designed the initial study, with further development provided by NW and JF. RQ coordinated the study. RQ and JS undertook data collection. RQ and NW conducted the analysis and modeling, with JS, LS, and JF providing critical comments. RQ drafted the manuscript. JS, NW, LS, and JF provided revisions of the manuscript. All authors read and approved the final manuscript.

FUNDING

RQ acknowledges the financial support of UNSW Canberra and the Bushfire and Natural Hazards Cooperative Research Centre (BNHCRC; Ref: RG142924) in conducting this research.

REFERENCES

Albini, F. A. (1976). *Estimating Wildfire Behavior and Effects. General Technical Report Int-30*. Report, USDA Forest Service, Intermountain Forest and Range Experiment Station, Ogden, UT.

Alegría, A., Bevilacqua, M., and Porcu, E. (2016). Likelihood-based inference for multivariate space-time wrapped-Gaussian fields. *J. Stat. Comput. Simulat.* 86, 2583–2597. doi: 10.1080/00949655.2016.1162309

Alexander, M. E., and Cruz, M. G. (2013). Limitations on the accuracy of model predictions of wildland fire behaviour: a state-of-the-knowledge overview. *For. Chronic.* 89, 372–383. doi: 10.5558/tfc2013-067

Andrews, P. L. (2012). *Modeling Wind Adjustment Factor and Midflame Wind Speed for Rothermel's Surface Fire Spread Model*. United States Department of Agriculture/Forest Service, Rocky Mountain Research Station. doi: 10.2737/RMRS-GTR-266

Belcher, S. E., Harman, I. N., and Finnigan, J. J. (2012). The wind in the willows: flows in forest canopies in complex terrain. *Annu. Rev. Fluid Mech.* 44, 479–504. doi: 10.1146/annurev-fluid-120710-101036

Butler, B. W., Wagenbrenner, N. S., Forthofer, J. M., Lamb, B. K., Shannon, K. S., Finn, D., et al. (2015). High-resolution observations of the near-surface wind fields over an isolated mountain and in a steep river canyon. *Atmospher. Chem. Phys.* 15, 3785–3801. doi: 10.5194/acp-15-3785-2015

Carta, J. A., Bueno, C., and Ramírez, P. (2008a). Statistical modelling of directional wind speeds using mixtures of von Mises distributions: case study. *Energy Convers. Manage.* 49, 897–907. doi: 10.1016/j.enconman.2007.10.017

Carta, J. A., Ramírez, P., and Bueno, C. (2008b). A joint probability density function of wind speed and direction for wind energy analysis. *Energy Convers. Manage.* 49, 1309–1320. doi: 10.1016/j.enconman.2008.01.010

Cruz, M. G. (2010). Monte carlo-based ensemble method for prediction of grassland fire spread. *Int. J. Wildl. Fire* 19, 521–530. doi: 10.1071/WF08195

Cruz, M. G., and Alexander, M. E. (2013). Uncertainty associated with model predictions of surface and crown fire rates of spread. *Environ. Modell. Softw.* 47, 16–28. doi: 10.1016/j.envsoft.2013.04.004

Erdem, E., and Shi, J. (2011). Comparison of bivariate distribution construction approaches for analysing wind speed and direction data. *Wind Energy* 14, 27–41. doi: 10.1002/we.400

ESRI (2011). *ArcGIS Desktop: Release 10*. Redlands, CA: Environmental Systems Research Institute.

Finney, M. A., Grenfell, I. C., McHugh, C. W., Seli, R. C., Trethewey, D., Stratton, R. D., et al. (2011). A method for ensemble wildland fire simulation. *Environ. Model. Assess.* 16, 153–167. doi: 10.1007/s10666-010-9241-3

Finnigan, J. (2000). Turbulence in plant canopies. *Annu. Rev. Fluid Mech.* 32, 519–571. doi: 10.1146/annurev.fluid.32.1.519

Finnigan, J. J., and Belcher, S. E. (2006). Flow over a hill covered with a plant canopy. *Q. J. R. Meteorol. Soc.* 130, 1–29. doi: 10.1256/qj.02.177

Forthofer, J. M. (2007). *Modelling Wind in Complex Terrain for Use in Fire Spread Prediction*. Thesis, Department of Forest, Rangeland and Watershed Stewardship, Colorado State University.

Forthofer, J. M., Butler, B. W., McHugh, C. W., Finney, M. A., Bradshaw, L. S., Stratton, R. D., et al. (2014a). A comparison of three approaches for simulating fine-scale surface winds in support of wildland fire management. Part II. an exploratory study of the effect of simulated winds on fire growth simulations. *Int. J. Wildl. Fire* 23, 982–994. doi: 10.1071/WF12090

Forthofer, J. M., Butler, B. W., and Wagenbrenner, N. S. (2014b). A comparison of three approaches for simulating fine-scale surface winds in support of wildland fire management. Part I. Model formulation and comparison against measurements. *Int. J. Wildl. Fire* 23, 969–981. doi: 10.1071/WF12089

French, I., Cechet, B., Yang, T., and Sanabria, A. (2013). "FireDST: fire impact and risk evaluation decision support tool-model description," in *MODSIM2013, 20th International Congress on Modelling and Simulation,* eds J. Piantadosi, R. S. Anderssen, and J. Boland (Adelaide, SA: Modelling and Simulation Society of Australia and New Zealand Inc.).

French, I. A., Duff, T. J., Cechet, R. P., Tolhurst, K. G., Kepert, J. D., and Meyer, M. (2014). "FireDST: a simulation system for short-term ensemble modelling of bushfire spread and exposure," in *Advances in Forest Fire Research,* ed D. X. Viegas (Coimbra: Imprensa da Universidade de Coimbra), 1147–1158.

Kourtz, P. (1972). Probability makes fire danger index more reliable. *Fire Control Notes* 33, 11–12.

Lagona, F., and Picone, M. (2016). Model-based segmentation of spatial cylindrical data. *J. Stat. Comput. Simulat.* 86, 2598–2610. doi: 10.1080/00949655.2015.1122791

Lopes, A. M. G. (2003). WindStation: a software for the simulation of atmospheric flows over complex topography. *Environ. Model. Softw.* 18, 81–96. doi: 10.1016/S1364-8152(02)00024-5

MATLAB (2016). *R2016b*. Natick, MA: The MathWorks, Inc.

McRae, R. H. D. (2004). "Breath of the dragon–observations of the January 2003 ACT bushfires," in *Proceedings of Bushfire 2004* (Adelaide, SA).

McRae, R. H. D., and Sharples, J. J. (2013). "A process model for forecasting conditions conducive to blow-up fire events," in *MODSIM2013, 20th International Congress on Modelling and Simulations,* eds J. Piantadosi, R. S. Anderssen, and J. Boland (Adelaide, SA: Modelling and Simulation Society of Australia and New Zealand), 2506–2512.

Moon, K., Duff, T. J., and Tolhurst, K. G. (2019). Sub-canopy forest winds: understanding wind profiles for fire behaviour simulation. *Fire Saf. J.* doi: 10.1016/j.firesaf.2016.02.005. [Epubh ahead of print].

Noble, I. R., Gill, A. M., and Bary, G. A. V. (1980). McArthur's fire-danger meters expressed as equations. *Aust. J. Ecol.* 5, 201–203. doi: 10.1111/j.1442-9993.1980.tb01243.x

Penman, T. D., Collins, L., Price, O. F., Bradstock, R. A., Metcalf, S., and Chong, D. M. O. (2013). Examining the relative effects of fire weather, suppression and fuel treatment on fire behaviour - a simulation study. *J. Environ. Manage.* 131, 325–333. doi: 10.1016/j.jenvman.2013.10.007

Quill, R. (2017). *Statistical Characterisation of Wind Fields Over Complex Terrain With Applications in Bushfire Modelling*. Thesis, School of Physical, Environmental and Mathematical Sciences, UNSW Canberra.

Quill, R., Moon, K., Sharples, J. J., Sidhu, L. A., Duff, T. J., and Tolhurst, K. G. (2016). "Wind speed reduction induced by post-fire vegetation regrowth," in *Research Forum at the Bushfire and Natural Hazards CRC & AFAC Conference,* ed M. Rumsewicz (Brisbane, QLD: Bushfire and Natural Hazards CRC), 15–29.

Quill, R., and Sharples, J. J. (2018). *Flea Creek Valley Data, Jul to Dec 2014*. Figshare. doi: 10.25909/5c13258d1407a

Sharples, J. J., McRae, R. H. D., and Weber, R. O. (2010). Wind characteristics over complex terrain with implications for bushfire risk management. *Environ. Model. Softw.* 25, 1099–1120. doi: 10.1016/j.envsoft.2010.03.016

Sharples, J. J., McRae, R. H. D., and Wilkes, S. R. (2012). Wind–terrain effects on the propagation of wildfires in rugged terrain: fire channelling. *Int. J. Wildl. Fire* 21, 282–296. doi: 10.1071/WF10055

Simpson, C. C., Sharples, J. J., Evans, J. P., and McCabe, M. F. (2013). Large eddy simulation of atypical wildland fire spread on leeward slopes. *Int. J. Wildl. Fire* 22, 599–614. doi: 10.1071/WF12072

Tolhurst, K. G., Shields, B. and Chong, D. (2008). Phoenix: development and applications of a bushfire risk management tool. *Austral. J. Emerg. Manage.* 23, 47–54.

Twomey, B., and Sturgess, A. (2016). "Simulation analysis-based risk evaluation (SABRE) fire: operational stochastic fire spread decision support capability in the Queensland Fire and Emergency Service," in *Proceedings of AFAC 2016* (Brisbane, QLD).

Wagenbrenner, N. S., Forthofer, J. M., Lamb, B. K., Shannon, K. S., and Butler, B. W. (2016). Downscaling surface wind predictions from numerical weather prediction models in complex terrain with WindNinja. *Atmos. Chem. Phys. Discuss.* 2016, 1–32. doi: 10.5194/acp-2015-761

Conflict of Interest Statement: The authors declare that the research was conducted in the absence of any commercial or financial relationships that could be construed as a potential conflict of interest.

frontiers in Mechanical Engineering

ORIGINAL RESEARCH
published: 28 March 2019
doi: 10.3389/fmech.2019.00008

A Data-Driven Fire Spread Simulator: Validation in Vall-llobrega's Fire

Oriol Rios, Mario Miguel Valero, Elsa Pastor and Eulàlia Planas*

Department of Chemical Engineering, Centre for Technological Risk Studies, Universitat Politècnica de Catalunya, Barcelona, Spain

While full-physics fire models continue to be unsuitable for wildfire emergency situations, the so-called operational fire spread simulators are incapable of providing accurate estimations of the macroscopic fire behavior while quickly reacting to a change of governing spread mechanisms. A promising approach to overcome these limitations are data-driven simulators, which assimilate observed data with the aim of improving their forecast with affordable computation times. Although preliminary results obtained by several data-driven simulators are promising, this scheme needs intensive validation. Detailed studies of the particular aspects related to data assimilation are essential to gain insight about the applicability of this approach to operational wildfire simulation. This paper presents the validation of the simulator presented in Rios et al. (2014b, 2016, 2018) with a large scenario of real complexity with intricate terrain. The study case corresponds to a wildfire of significant repercussions occurred in Catalonia in March 2014. We employed as reference data the event reconstruction performed by the Catalan Fire Service and validated with operational observations. Detailed information about fuel and meteorology was collected by the fire brigades and allowed reconstructing the fire development with Farsite, a widely employed simulator. Subsequently, our simulator was tested without a detailed description of the fuel and wind parameters, i.e., imitating its intended deployment conditions. It proved capable of automatically estimating them and correctly simulating the fire spread. Additionally, the effect of the assimilation window on the forecast accuracy was analyzed. These results showed that the simulator is able to correctly handle complex terrain and wind situations to successfully deliver a short-term fire-front forecast in those real and complex scenarios.

Keywords: wildfire, front spread, Rothermel, forecast, Wind-Ninja

OPEN ACCESS

Edited by:
Michael John Gollner, University of Maryland, College Park, United States

Reviewed by:
Arnaud C. Trouve, University of Maryland, College Park, United States
Wei Tang, National Institute of Standards and Technology (NIST), United States

****Correspondence:***
Elsa Pastor
elsa.pastor@upc.edu

Specialty section:
This article was submitted to Thermal and Mass Transport, a section of the journal Frontiers in Mechanical Engineering

Received: *22 January 2019*
Accepted: *04 March 2019*
Published: *28 March 2019*

Citation:
Rios O, Valero MM, Pastor E and Planas E (2019) A Data-Driven Fire Spread Simulator: Validation in Vall-llobrega's Fire. Front. Mech. Eng. 5:8. doi: 10.3389/fmech.2019.00008

1. INTRODUCTION

Wildfires are a global phenomenon that have a dramatic impact in terms of human lives, property, and environmental losses. Moreover, they exhibit an increasing trend in both burned area and fire severity. In order to face them, better tools to tackle and envisage fire propagation are required. Fire spread is determined by a number of physico-chemical phenomena intimately interconnected. The complex mathematical description of these underlying phenomena has prevented, so far, scientists from successfully modeling forest fire spread with acceptable computation resources and meaningful lead times. Simulators based on Computational Fluid Dynamics require hardware and computing times far beyond the current available capacity. Consequently, operational fire spread simulation is, at present, performed using semi-empirical models (e.g., Rothermel's, 1972) that

are highly sensitive to input parameter's uncertainty and thus, cannot be applied universally. The expectable heterogeneities in fuel, terrain, and wind properties, added to the intrinsic difficulty to measure such parameters in a wildfire scenario, usually lead to an important decrease in the accuracy of these models.

To address this issue, Mandel et al. (2009) pioneered the application of data assimilation concepts into the wildfire modeling problem by using Kalman filters to assimilate fire locations and predict flame temperature using an atmosphere-coupled wildfire model. While the results were promising they also raised concerns on spurious fire corrections and the needed computing time. Following those ideas, Rochoux et al. (2014a,b, 2015) implemented a data-driven system based on a level-set description of Rothermel (1972) model and studied the difference between parameters and state assimilations. The system was further used in an interesting application to reproduce the front location of a three-hectare field-scale tests (Zhang et al., 2018) and a simulation recreating of a medium-scale (800 x 400 m) wildfire test (Zhang et al., 2017). The later case used a spatially-distributed parameter estimation to tackle the issue of spatial heterogeneity of the resolved parameters. Despite the strategy showed improved capacity to reproduce observations, the extrapolation to forecast application is not clear as assimilated parameters remain valid on their pre-stated observables region.

In parallel to those developments, we explored a data-driven system based on marker-tracking implementation of Rothermel model (Rios et al., 2014b, 2016). This tool integrates data assimilation techniques in order to calibrate a semi-empirical fire behavior model on-line. By matching modeled and observed fire evolution, fuel and wind properties are estimated and periodically updated. In addition to the observed fire spread, our simulator accounts for terrain and spatially distributed wind. For the terrain interaction, Digital Elevation Model maps (DEM) are used to compute the Rate of Spread corrected by slope projection according to Rothermel's model (Rothermel, 1972). For the wind input, we considered high-resolution simulated wind fields that interact with the fire spread according to the correction of Rothermel's model proposed by André and Gonçalves (2013). Additionally, wind fields that account for topography are generated with WindNinja (Forthofer et al., 2009; Wagenbrenner et al., 2016). This software projects overall values of wind speed and direction onto the DEM in order to output a detailed wind field at low height (1.5 m in our case).

A significant drawback of the computation of high-resolution topographic wind fields is its high computational cost. For instance, a 800 x 800 cell domain needs about 20 min to be resolved in a single core machine. Recent works conducted by Sanjuan et al. (2016a,b,c) made use of advanced parallelization computing techniques to reduce this time to the order of several minutes using multicore machines. However, those are still unaffordable times in a data-driven approach where hundreds of iterations are typically required. As the wind speed and direction are part of the key parameters to be resolved by the assimilation process, every time that a new parameter set is estimated, the wind field needs to be updated. In order to work around this limitation, our modeling system integrates the interpolation approach described in Rios et al. (2018). This strategy makes use of a set of pre-run wind field maps within the fire domain and all new values of wind magnitude and direction are automatically interpolated. This approach allows delivering updated maps with low computational time (in the order of 1E-3 seconds).

After the correct validation of the concept with flat experiments (Rios et al., 2016), this data-driven modeling system needs validation against a case as close as possible to real wildfire conditions. In order to be applied in a real fire scenario, our simulator should ideally be coupled with a real-time fire monitoring system. Previous studies have proposed intelligent computer vision algorithms to process aerial infrared imagery automatically with this purpose (Valero M. et al., 2017; Valero M. M. M. et al., 2017; Valero et al., 2018). However, there is at present no airborne system that can be deployed operationally to track the fire perimeter in real time with a high temporal resolution. Currently, quantitative information about the fire spread is usually limited to scattered observations of the approximate fire front positions at temporal resolutions in the order of hours. We overcame this difficulty using the simulated reconstruction of a recent wildfire, which had been previously validated, as synthetically observed fire evolution. The usage of reconstruction data implies that the validation is not performed on the overall system but on the assimilation step and capacity to reproduce a set of fire perimeter with a given initialization data. Whereas, the validation of the whole system is needed (with real data usage), this particular validation of the assimilation step can also be useful to detect weaknesses and strengths while enabling the further upgrade of the embedded fire spread model while keeping the overall system unchanged.

This paper presents the validation of the simulator presented in Rios et al. (2014b, 2016, 2018) in a large-scale wildfire scenario of real complexity with intricate terrain. We employed, as reference data, the event reconstruction performed by the Catalan Fire Service and validated with operational observations. Point observations of the fire evolution were collected by the fire brigades and allowed, together with detailed information about fuel and meteorology, the reconstruction of the fire development. Subsequently, our simulator was tested based on this synthetic observations and using the data potentially available in a real operation, i.e., rough and general fuel information and domain averaged wind measurements. The rest of the paper is structured as follows: firstly, section 2 provides background information about the real fire incidence as well as its simulation; section 3 explains the data driven system employed in the present study and the results are presented and discussed in sections 4.

2. VALL-LLOBREGA WILDFIRE

Detailed information about fuel and meteorology was collected by the fire brigades and allowed reconstructing the fire development with Farsite, a widely employed simulator. This reconstruction was validated using observed data about the burned perimeter evolution by L. Castell (personal communication, 2016).

The fire started near the village of Vall-llobrega, on the northern shore of Catalunya (see origin sign in **Figure 1**) at

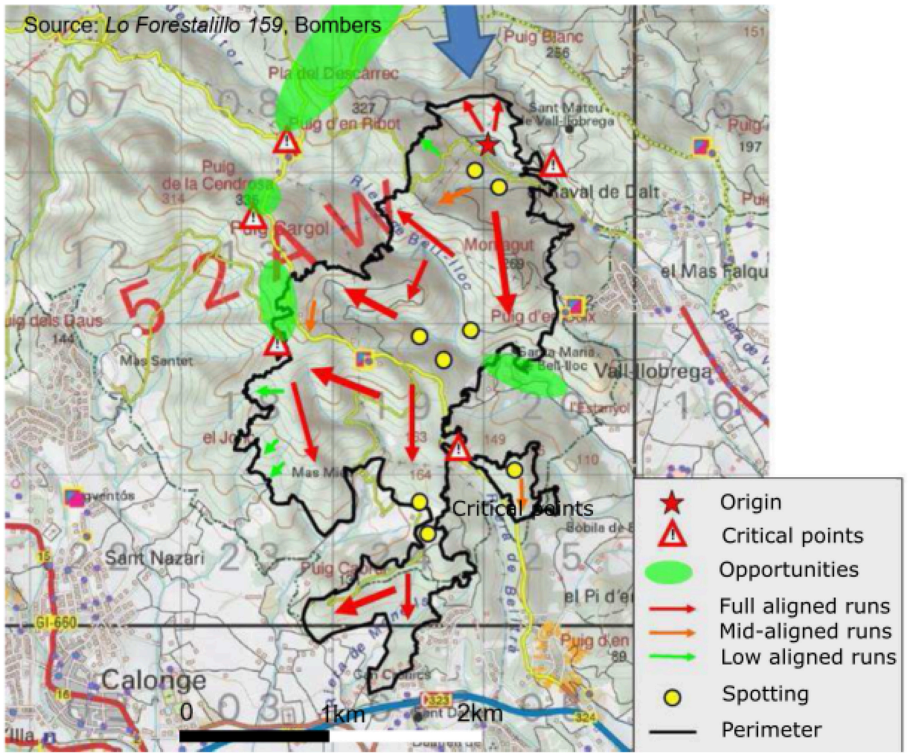

FIGURE 1 | Vall-llobrega fire development and final perimeter. Source: GRAF (2014), adapted.

13:04 h of 16th march 2014 and it ended burning 359 ha. The extinguishing operation involved more that 50 fire engines, 7 aerial means, and more than 150 fire fighters. The fire took place off-season but showed similar behavior to summer fires (**Figure 2**) in terms of propagation speeds and fire intensity. The main and secondary runs together with observable spotting propagation were reported by the emergency responders and displayed in **Figure 1**. Reasons were twofold: the severe drought regime present at the time [see drought index values (Turner, 1972) displayed in **Figure 3**] and the presence of large dead fuel on the ground due to an uncommon snowfall in a precedent year (2010), which provided additional available fuel.

The weather conditions were dry and windy. When the fire was initiated, the relative humidity was of 20% and the wind was blowing from north at a speed over 36 km $h^{-1}$with reported wind gusts of 80 km h^{-1}. Data logged by the automatic weather station located at 10 km from the fire are reported in **Figure 4**.

3. METHODOLOGY: DATA ASSIMILATION

3.1. SmartQFire Tool

SmartQFire is a data-driven wildfire spread modeling system explained in detail in Rios et al. (2014a, 2016, 2018). The system is based on the Rothermel (1972) model to estimate the Rate of Spread of a fire front given the fuel, terrain, and wind characteristics. The fire front is generated by coupling the rate of spread with the Huygens wave principles for elliptical expansion by means of the partial differential equations established by Richards (1995). The equations are integrated in a discretized form implemented in a Lagrangian markers tracking approach. The enveloping front produced by those equations is filtered with algorithms to prevent loop entanglements, sharp edges, and homogeneously distributed markers along the entire fire front perimeter.

The version used in this paper includes a built-in fuel structure to adapt the standard fuel model classification developed by Scott and Burgan (2005a) to a simplified implementation that reduces the number of fuel parameters to 5: Fine Fuel Load (W), Surface-area-to-volume ratio (SAV), Moisture content (M_f), Moisture of extinction (M_x), and Fuel Bed Depth (D). The reduction methodology was proposed and evaluated in Rios (2018). This reducing strategy allows for a simplified description of the standard fuel model (Scott and Burgan, 2005a) which uses those five parameters for each of the five fuel particle classes, namely, 1, 10, 100 h, live herbaceous, live woody. The equivalent parameter set is build up by means of numerical optimization within all families of fuel models that contain the same fuel particle classes.

Additionally, the data driven system at hand includes topographic wind simulations that are being run at each iteration step. The wind maps are generated by means of the interpolation framework presented in Rios et al. (2018), which uses the diagnoses software WindNinja (Forthofer et al., 2009; Wagenbrenner et al., 2016) to generate base maps. This strategy

FIGURE 2 | Aerial images of the Vall-llobrega wildfire. Source: La Vanguardia.

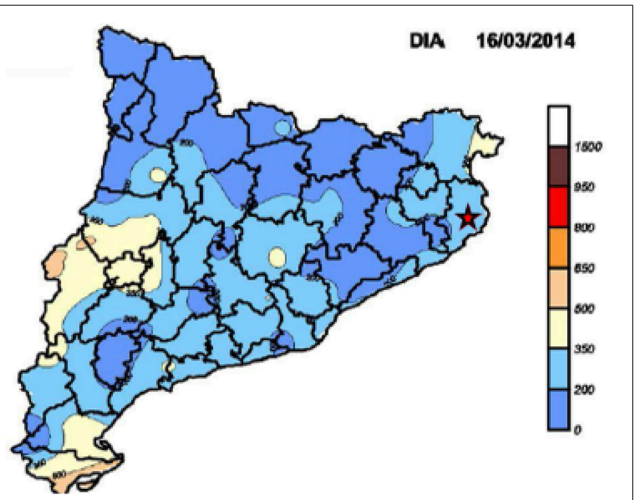

FIGURE 3 | Drought index values on 16/03/14 over Catalunya. The star symbol marks Vall-llobrega location. Source: GRAF (2014).

proved to be computationally efficient and accurate enough for operational wildfire simulations.

3.2. Optimization Strategy

The cost function used to perform the optimization process is based on the Shape Dissimilarity Index (SDIa) stated by Cui and Perera (2010). The original index was corrected by subtracting the area of the front used to initialize the assimilation to avoid the bias given by this already contained area. The SDIa index can then be expressed as:

$$\mathrm{SDIa} = \frac{M_i \oplus O_i}{O_i - I_a} \tag{1}$$

Where M_i and O_i are, respectively, the modeled and observed fronts' burned areas in a given time and I_a is the initial front area used to perform the first perimeter expansion.

The optimization step is performed by means of the active set method as this algorithm was found to overperform other existing line-search based methods in terms of computing efficiency and capacity to find the closest solution to the global minimum. Active-set methods can be applied to both convex and non-convex problems and have been the most widely used methods since 1970s (Nocedal and Wright, 1999). They are based on a trust-region strategy. This technique establishes a sub-domain near the current objective function evaluation point (trust region) where the cost function is approximated using a quadratic model. Then, the constrained problem is solved using a sequence of parametrized unconstrained optimizations, which in the limit converge to the constrained problem. The method can be mathematically formulated with the Kuhn-Tucker equations (Kuhn and Tucker, 1951). Lagrange multipliers are necessary to balance the deviations in magnitude of the objective function and constraint gradients. Particular care on the implementation of this algorithm must be taken regarding *Maratos effect*. This effect states that bounds and equalities might be violated to find the fastest way to the minimum. In our present problem, this is important in two of the parameter bounds. Lower wind speed (i.e., 0 ms^{-1}) and the inequality $M_f \leq M_x$. If any of those constraints is violated, negative and complex values of Rate of Spread are output producing an error in the spread algorithm. To solve this issue (and prevent the optimization from halting) the spread model must be tweaked to handle those scenarios and produce a `NaN` output that can be further interpreted by the optimization method.

3.3. Reference Data for Model Validation

The fire described in section 2 was recreated using Farsite (Finney, 1998) by members of the Catalan Fire Department closely involved with the emergency response operations developed during the fire. The Farsite input files, together with the adjustment factors, were manually tuned to closely reassemble the 2 h 50 min initial development of the fire. Those are depicted in **Figure 5**.

Taking those 35 isochrones as ground-truth, three cases are run varying the number of isochrones used for assimilation and forecast validation. Those allocations are gathered below. The corresponding time is given in parentheses.

- **Case A**: 5 assimilated fronts (20 min), 29 forecast (145 min)
- **Case B**: 10 assimilated fronts (45 min), 24 forecast (120 min)
- **Case C**: 22 assimilated fronts (105 min), 12 forecast (60 min)

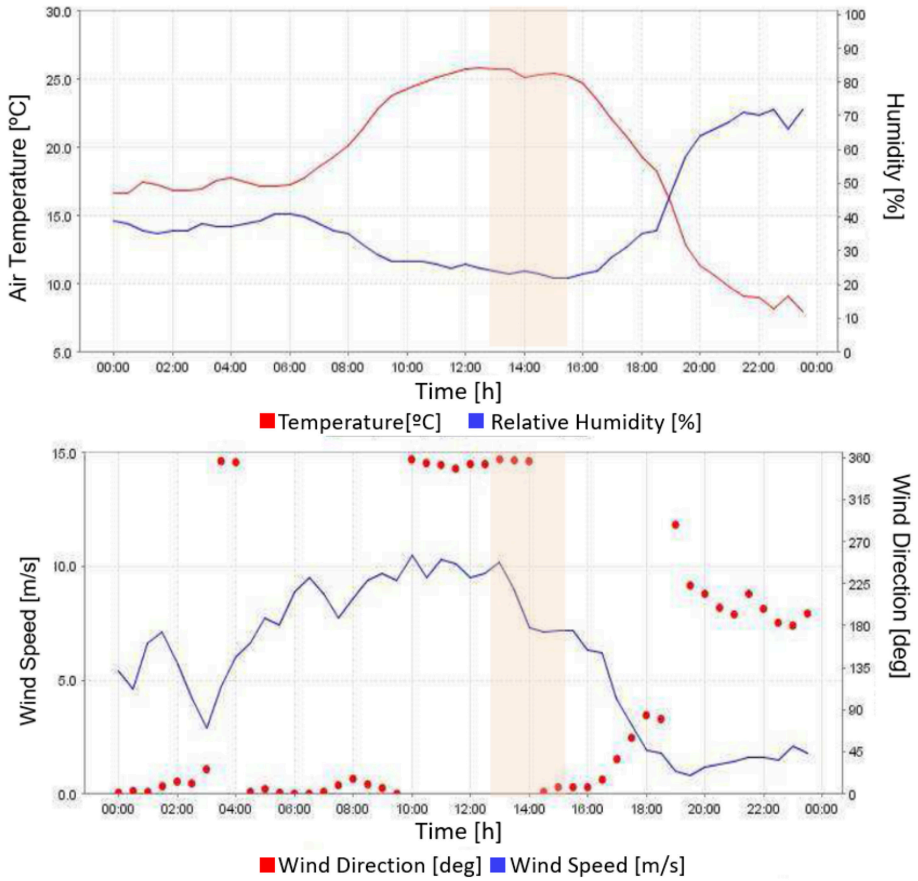

FIGURE 4 | Wind, temperature and relative humidity data logged at the automatic station of La Bisbal d'Empordà (10 km from the fire) on the 16/03/2014. Shaded area corresponds to the period of interest. Source: Servei Meteorològic de Catalunya.

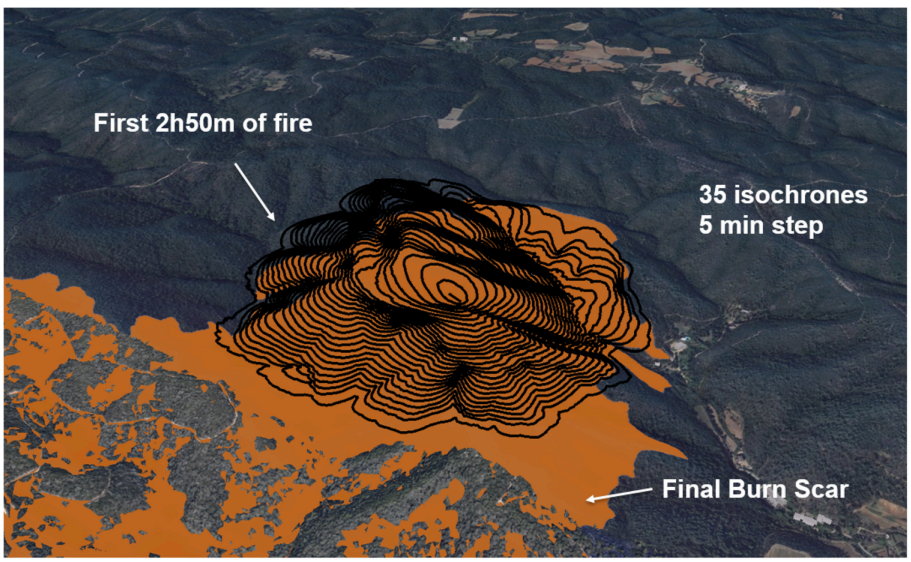

FIGURE 5 | Farsite validated reconstruction of Vall-llobrega fires for the initial 170 min. Black lines are 35 isochrones at 5 min frequency. Orange solid contour is the satellite-based final scar (source: ICGC, 2018).

To initialize SmartQFIRE software, the 7 parameters to be optimized were estimated with the values gathered in **Table 1**. This could be a blind estimation done in real situations as it only requires a rough idea on the scenario conditions. As example, for the case at hand, the fuel characteristics had been paired to the fuel model TU5 *Very High Load, Dry Climate Timber-Shrub* (Scott and Burgan, 2005b) as fire responders already knew that packed and dead under-story was present. Similarly, a representative wind speed and direction was taken from a nearby station at the time of fire initiation (see **Figure 4**) .

4. RESULTS AND DISCUSSION

4.1. Assimilation Results

The results of the assimilated fronts for the three cases explored are plotted in **Figure 6**. Dashed-green lines in this figure correspond to the estimated propagation with the values in **Table 1**. Black lines correspond to the observed fronts whereas red dashed lines are the calibrated fire spread. In the three cases, it is clear that the front generated with the initialization values highly differs from observations. On the contrary, the assimilation process converges into a situation that closely resembles the observations, especially in the cases where 5 and 10 fronts are assimilated. In particular, the topographic effect in both flanks is well-resolved. The 10 front case, however, shows some divergence on the tail as converged fronts spread slightly further than observations. This effect is more remarkable in the third case, (**Figure 6C**) where this overspread is larger. In this case, however, flanks and fronts are still correctly resolved. The difficulty to properly simulate the tail part of the fire may lie on the fact that backwards spread (fire spreading against wind and topography) is not well-characterized yet. A dedicated sub-model should be implemented once theoretically available, to improve this weakness.

4.2. Parameters Convergence

To assess the convergence of the assimilation process we analyzed, on one side, the convergence of the simulated fronts

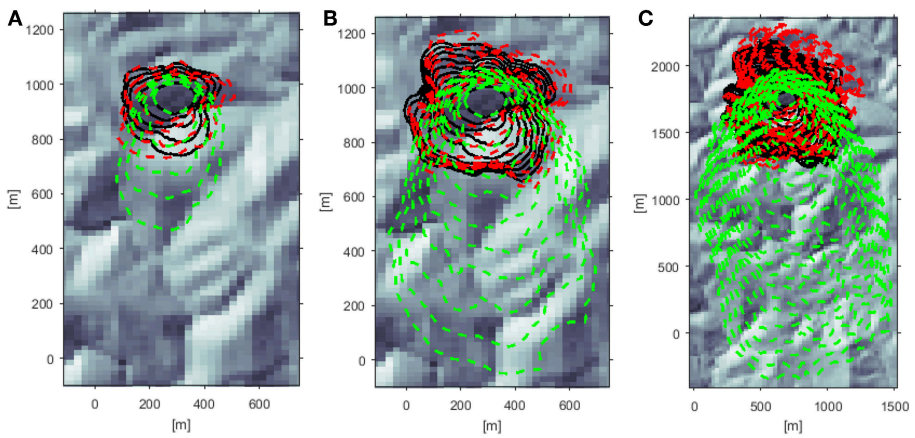

FIGURE 6 | Three different assimilations runs. North direction is toward the top of the image. Black solid lines are observations, dashed green lines are initial run, and dashed red lines are the optimized fronts at the end of the assimilation period. Background image is the hillshade representation of the domain. **(A)** 5 fronts. **(B)** 10 fronts. **(C)** 22 fronts.

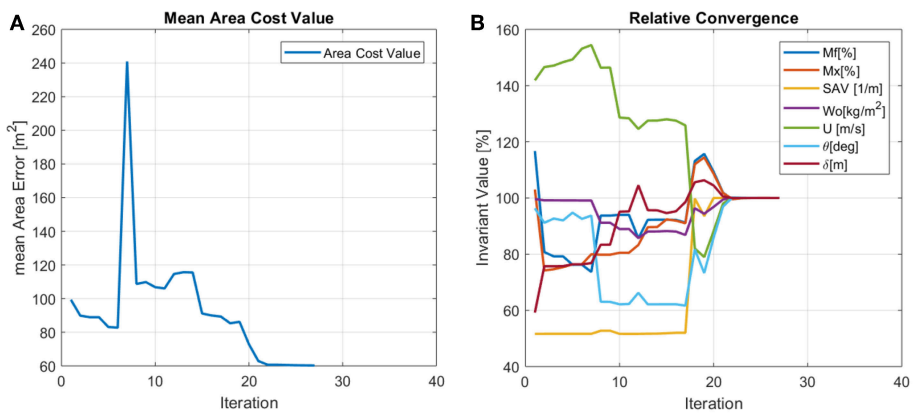

FIGURE 7 | Convergence of the assimilation process for Case A (20 min of assimilation). **(A)** Mean area error between observed and assimilated fronts. **(B)** Relative convergence for each of the 7 optimized parameters.

and, on the other, the convergence of the seven assimilated parameters. **Figure 7** shows those two convergences for the first case presented here (20 min of assimilation). As the optimization engine made use of the active-set strategy, each of the iterations indicated in the Figure make use of multiple evaluations of the forward model in order to define the following step direction. The mean area cost value depicted in the left panel of **Figure 7** is the absolute areal difference between each of the observed and simulated fire perimeters averaged by the number of simulated fronts. It is remarkable that in the 9th iteration this value diverges rising to 240 m^2. The explanation for this behavior might lie on the fact that despite the optimization is constrained, the active-set converging process could exceed the boundaries of the optimization domain before the parameters are forced to fall back into the valid range. Those processes have been sometimes identified to produce this local divergence of the optimization process.

The relative parameters value convergence (**Figure 7B**) is expressed as a percentage of the final converged value. Thus, all parameters converge to 100%. We can identify here that the convergence is not smooth and steady as there are large jumps (*SAV* and *u* at iteration 17 for example). This supports the finding identified in Rios et al. (2017): the optimization problem at hand is not a smooth problem and, thus, simple linear search algorithms do not provide an acceptable solution.

Converged values for each parameter and case are gathered in **Table 2**. Analyzing them one-by-one we find that all three cases generated here mostly converge toward the same set of parameters, except for the wind speed in case C, which is considerably lower than the other cases. The fine fuel load (w) is reduced for all cases with respect to the initial value as well as the moisture content. This could provide a larger fire spread, which would be inexplicable regarding the fronts produced with the initial guess (see green dashed lines in **Figure 6**), but the dramatic wind reduction prevents this. Indeed, for all cases the domain representative wind speed is lowered below 10 ms^{-1}. The wind direction pivots around the 360° value, i.e, wind blowing from north. It is worth to recall here that the direction (θ) is internally expressed in radians and values are always projected into [π - 3π] bounds for numerical reasons (see **Table 3**). Another remarkable output is the converged value of the surface-area-to-volume ratio (*SAV*). In all cases, it increases largely, and even in case A, it gets close to the upper bound (stated at 7,270 m^{-1}). These values indicate that from our simulator standpoint, mostly the thinner fuel is the principal contributor to fire spread. To validate this results, post-fire data would be needed to assess the principal fuels involved in the fire. Despite the lack of this information, the observations of high intense fire behavior and its high propagation speed support this outcome.

4.3. Fire Spread Forecast

Once the seven parameters are calibrated by means of the assimilation process, the forecast is launched and compared to the ground-truth fronts that remain available in each case. These results are depicted in **Figure 8**. For all cases, the last assimilated perimeter is the one used to initiate the forecast model run.

TABLE 1 | Values of the parameters estimated to initialize the assimilation run.

	W [kg m^{-2}]	*SAV* [m^{-1}]	δ [cm]	M_x [%]	M_f [%]	*U* [km h^{-1}]	θ [deg]
Ini. Guess	1.73	4,015	110	25	20	36.6	360

TABLE 2 | Final absolute values for all seven parameters after the assimilation process.

	W [kg m^{-2}]	*SAV* [m^{-1}]	δ [cm]	M_x [%]	M_f [%]	*U* [km h^{-1}]	θ [deg]
Ini. Guess	1.73	4,015	110	25	20	36.6	360
Case A	1.72	7,234	183	24.0	16.9	34.9	371.1
Case B	1.51	6,915	167	25.3	17.4	32.3	351.6
Case C	1.32	6,859	172	23.6	16.3	27.7	358.2

The initial estimated values are also depicted in the first row.

TABLE 3 | Summary of the proposed fuel model variables, ranges, and constant values.

Parameter		Range (value)	Units
CHARACTERISTIC VARIABLES			
Fuel Load	W	0.067–2.925	[kg m^{-2}]
Surface-area-to-volume ratio	SAV	3753–7270	[m^{-1}]
Moisture content	M_f	5–40	[%]
Moisture of extinction	M_x	12–40	[%]
ORIGINAL VARIABLES			
Fuel Bed Depth	δ	0.06–1.83	[m]
Mid-flame Wind Speed	U	0.06–1.83	[m s^{-1}]
Mid-flame Wind Dir	θ	π-3π	[rad]
CONSTANT PARAMETERS			
Low heat content (all fuel particles)	h	18609	[kJ kg^{-1}]
Ovendry particle density	ρ_p	512.59	[kg m^{-3}]
Effective mineral content	s_e	5.55	[%]
Total mineral content	s_t	1.0	[%]
TERRAIN INPUT PARAMETERS			
Slope	slp	–	[rad]
Aspect	α	–	[rad]

As it could be expected, case A (with the shortest assimilation window) performs poorer than the other two cases. This case correctly forecasts the back of the fire and the right flank after 145 min (2 h 25 min) (**Figure 8A**), however it over-predicts the position of the front part of the perimeter by approximately 200 m. Case B also manages to forecast the back of the fire and it matches correctly the front and the flanks. The last three isochrones show a burst on the rear part of the right flank. This might be due to bad terrain handling, as it seems that this part of the front accelerates suddenly. Contrary to the previous cases, case C, which is the one that has more fronts assimilated, under-predicts the back of the fire and slightly over-predicts the

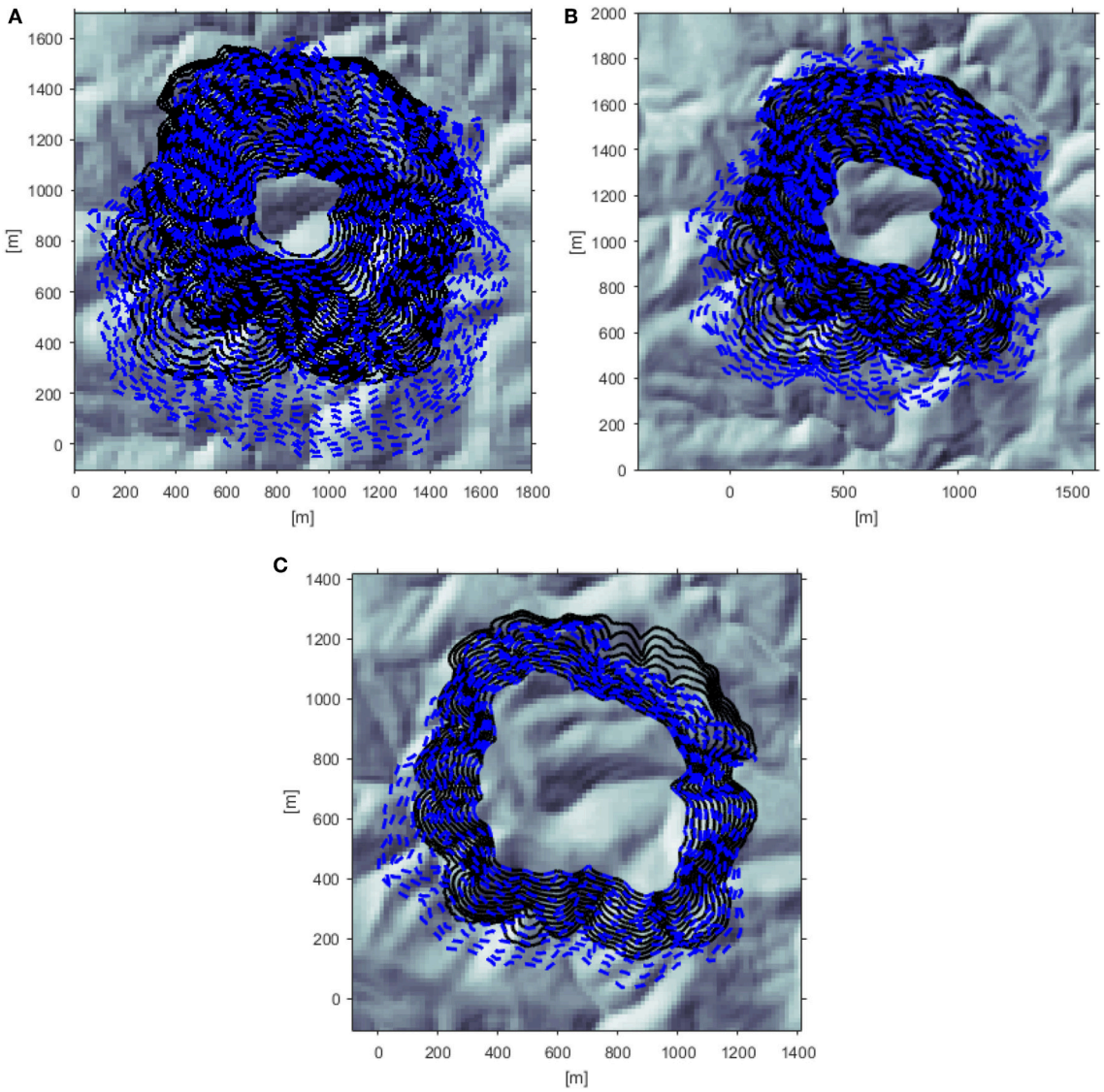

FIGURE 8 | Forecast run (blue dashed lines) vs. observations (black solid lines) for the three cases. **(A)** 5 assimilated fronts, 29 forecast fronts. **(B)** 10 assimilated fronts, 24 forecast fronts. **(C)** 22 assimilated fronts, 12 forecast fronts.

front. Nevertheless, the right flank is better resolved than in the previous cases.

To help in the analysis of the forecast performance of each case, the SDIa index for each forecast perimeter is plotted in **Figure 9**. Each marker in the Figure corresponds to a single SDIa value for a given time. One can observe, for example, that the best 110 min-forecast is provided in case C. However, this is probably due to the fact that case C was initialized at minute 90 so it is actually a forecast at 20 min horizon. Indeed, as time passes by case C performs worse than case B. Case A delivers an acceptable forecast during the first 30 min. Beyond this time, performance decreases with time until reaching rather unacceptable values for the last 50 min. As the whole systems is build up on finding representative parameters that are assumed constant over time, there is a trade-off between the assimilating time and this averaging effect. Ideally, once enough validations are performed, the optimal assimilation windows for a given case could be defined and it should be shifted over time (without increasing the number of assimilated fronts) as the emergency evolves. As this window might depend on the overall fire behavior, different window length could be set based on some index, as head front Rate of Spread. The study of this optimal assimilation window linked to scenario (observed fire behavior, domain characteristics, parameters values, etc.) should be further investigated with more validation cases as it is one of the key aspects to render this tool operational.

Finally, the computation time needed to perform all assimilation and forecast runs for each case are reported

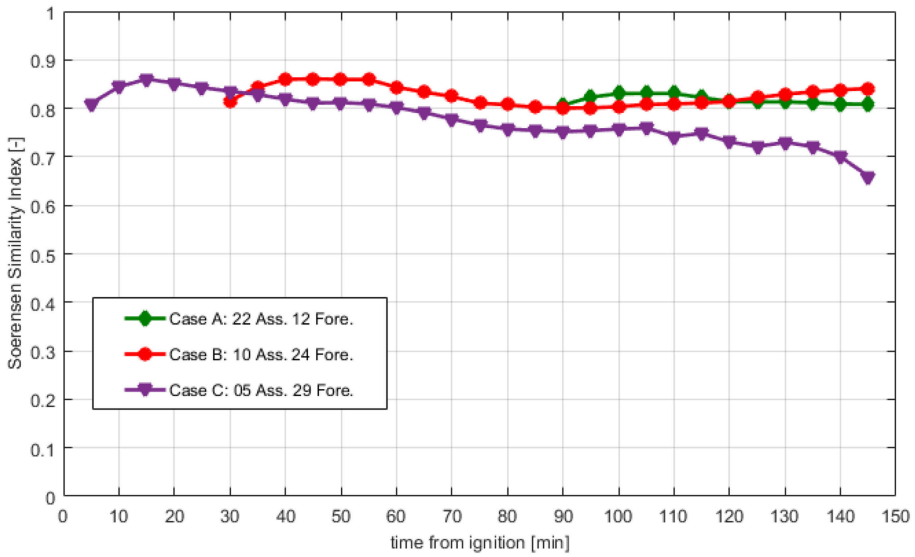

FIGURE 9 | Similarity index (SDIa) performance for all forecast fronts and the three different strategies explored. Ass, assimilated fronts; Fore, forecasted fronts.

TABLE 4 | Running times and lead times for all cases.

Case	Elapsed wall-clock time [s]	Forecast horizon [s]([min])	Lead time [s]([min])
Case A	115	8700 (145)	8585 (143)
Case B	251	7200 (120)	6949 (115.8)
Case C	380	3600 (60)	3220 (53.6)

The simulations are conducted with an Intel(r) Core(MT) i7-6700CPU 3.4Ghz (8 physical cores).

in **Table 4**. In all cases, the lead time (time between the results delivery and the forecast time) exceeds 50 min. This aspect, together with an accuracy estimation to set the reliable forecasting horizon, are key aspects if SmartQFIRE is to be employed in operational situations.

5. CONCLUSIONS

The data driven system SmartQFIRE was tested with the reconstruction of a real wildfire in order to explore its potential performance in a real emergency scenario. The a-posteriori simulation of a real fire had been generated with Farsite and validated by operational responders with *in-situ* point observations. This simulation was used in the present study as synthetic observed fire evolution. Synthetic fire spread was used instead of real observations in order to decouple the data-assimilation problem from the fire-spread-simulation scheme. Whereas comparison of this simulator against real data will be essential, the measurement of its performance in a real scenario would complicate the identification of the forecast error sources. Operational fire spread simulators are based on semi-empirical models which are built upon strong simplifications and do not fully describe fire dynamics. Consequently, the inaccuracies of a data-driven simulator when compared against observed data could be a result of deficient data-assimilation performance just as well as inherent physical limitations of the forward models.

By decoupling both problems, this study aimed to assess our data assimilation system independently from the fire spread model employed. We achieved this by using, as synthetic ground-truth data, simulation results obtained with Farsite. Farsite implements Rothermel's fire spread model, which is also incorporated in SmartQFIRE. Therefore, results obtained in this study can be understood as a direct assessment of the accuracy of our data assimilation system.

The evaluation was performed with the initial 2 h and 50 min of isochrones with a frequency of 5 min. Three different assimilation cases were studied. They could be representative of different times where the assimilating system could be deployed. The algorithm showed great potential to handle complex wind and terrain entangled scenarios. The coupling with WindNinja enhanced successfully delivered realistic fronts that could closely match observation without jeopardizing the operational application due to computing time. Indeed, for all cases studied, the lead time exceeded the 50 min. It was found that, in general terms, more assimilated fronts provides better results although the analysis also showed that it exists a trade-off on the averaging calibration parameters and correct forecast. More research is needed to determine the ways to establish the correct assimilation window that optimizes the forecasting results.

Finally, one of the identified limitations of this approach is the lack of spatial variation of the fuel parameters that are being resolved by means of the assimilation. In most real situations and long lasting wildfires, the canopy cover affected will be heterogeneous and thus, the present system

will not be capable of correctly resolving a single set of fuel parameters for the entire domain. A possible solution lies on the ability to pre-classify the entire domain into different sub-domains with certain homogeneity. If this division is possible (for example, employing available canopy cover information coming from lidar sensors) then, it is possible to resolve the parameters independently for each of the sub-domains. An initial exploration of this concept was performed by Zhang et al. (2017) although in their case the aim was to capture wind heterogeneity (already considered in the system at hand) and the division was not based on canopy cover but structured in a grid shape. Thus, this upgrade is a necessary future work to be conducted prior to the deployment of the system into real scenarios.

DATA AVAILABILITY

All datasets generated for this study are included in the manuscript.

AUTHOR CONTRIBUTIONS

All authors listed have made a substantial, direct and intellectual contribution to the work, and approved it for publication.

FUNDING

The authors thank the Spanish Ministry of Economy and Competitiveness (project CTQ2017-89990-R) founded with FEDER funds, the Spanish Ministry of Education, Culture and Sport (Formación de Profesorado Universitario Program) and the Autonomous Government of Catalonia (project no. 2017-SGR-413).

ACKNOWLEDGMENTS

The authors would like to thank the GRAF division of the Catalan Fire Service (*Bombers de la Generalitat de Catalunya*) for sharing the data to conduct this validation.

REFERENCES

André, J., and Gonçalves, J. (2013). Angular variation of fire rate of spread. *Int. J. Wildland Fire* 1991, 970–979. doi: 10.1071/WF12028

Cui, W., and Perera, A. H. (2010). Quantifying spatio-temporal errors in forest fire spread modelling explicitly. *J. Environ. Informatics* 16, 19–26. doi: 10.3808/jei.201000174

Finney, M. (1998). *FARSITE: Fire Area Simulator: Model Development and Evaluation*. Technical report, USDA Forest Service, Ogden, UT.

Forthofer, J., Shannon, K., and Butler, B. (2009). "Simulating diurnally driven slope winds with WindNinja," in *Proceedings of 8th Symposium on Fire and Forest Meteorological Society* (Kalispell, MT), 13.

GRAF (2014). *Incendis, Estratègies i Ecologia del foc Forestal. Nº 159. 2014: Incendis tot l'any, Llamps i pluja a l'Estiu i Cremes a la Tardor*. Technical Report 159, Bombers de Catalunya. Unitat tècnica GRAF.

ICGC (2018). *Perímetres del Cercador D'incendis Forestals*. Technical report.

Kuhn, H. W., and Tucker, A. (1951). "Nonlinear Programming," in *Proceedings of the Second Symposium on Mathematical Statistics and Probability* (Berkeley, CA), 481–492.

Mandel, J., Beezley, J. D., Coen, J. L., and Kim, M. (2009). Data assimilation for wildland fires. *Control Syst. IEEE* 29, 47–65. doi: 10.1109/MCS.2009.932224

Nocedal, J. and Wright, S. J. (1999). *Numerical Optimization*. Springer Series in Operations Research and Financial Engineering. New York, NY: Springer-Verlag.

Richards, G. D. (1995). A general mathematical framework for modeling two-dimensional wildland fire spread. *Int. J. Wildland Fire* 5, 63–72.

Rios, O. (2018). *Inverse Modelling in Wildfire Spread Forecasting: Towards a Data-driven System*. Ph.D thesis, Polytechnic University of Catalunya.

Rios, O., Jahn, W., Pastor, E., Valero, M. M., and Planas, E. (2018). Interpolation framework to speed up near-surface wind simulations for data-driven wildfire applications. *Int. J. Wildland Fire* 27, 257–270. doi: 10.1071/WF17027

Rios, O., Jahn, W., and Rein, G. (2014b). Forecasting wind-driven wildfires using an inverse modelling approach. *Nat. Hazards Earth Syst. Sci.* 14, 1491–1503. doi: 10.5194/nhess-14-1491-2014

Rios, O., Pastor, E., Tarragó, D., Rein, G., Planas, E., and Viegas, D. X. (2014a). "Short term forecasting of large scale wind-driven wildfires using thermal imaging and inverse modelling techniques," in *Advances in Forest Fire Research* (Coimbra: Imprensa da Universidade de Coimbra), 949–960.

Rios, O., Pastor, E., Valero, M., and Planas, E. (2016). Short-term fire front spread prediction using inverse modelling and airborne infrared images. *Int. J. Wildland Fire* 20, 1015–1032. doi: 10.1071/WF16031

Rios, O., Valero, M., Pastor, E., and Planas, E. (2017). "Optimization strategy exploration in a wildfire propagation data driven system," in *International Conference on Computational Science, ICCS 2017* (Zurich).

Rochoux, M., Emery, C., Ricci, S., Cuenot, B., and Trouvé, A. (2015). Towards predictive data-driven simulations of wildfire spread– Part II: ensemble Kalman Filter for the state estimation of a front-tracking simulator of wildfire spread. *Nat. Hazards Earth Syst. Sci.* 15, 1721–1739. doi: 10.5194/nhess-15-1721-2015

Rochoux, M., Emerya, C., and Riccia, S. (2014a). "A comparative study of parameter estimation and state estimation approaches in data-driven wildfire spread modeling," in *VII International Conference on Forest Fire Research*, ed D. Viegas (Coimbra: Rochoux), 1–12.

Rochoux, M., Ricci, S., Lucor, D., Cuenot, B., and Trouvé, A. (2014b). Towards predictive data-driven simulations of wildfire spread – Part I: Reduced-cost Ensemble Kalman Filter based on a Polynomial Chaos surrogate model for parameter estimation. *Nat. Hazards Earth Syst. Sci.* 14, 2951–2973. doi: 10.5194/nhess-14-2951-2014

Rothermel, R. (1972). *A Mathematical Model for Predicting Fire Spread in Wildland Fuels*. Research Paper INT-115. Technical report, USDA Forest Service. Intermountain Forest and Range Experiment Station, Odgen, UT.

Sanjuan, G., Margalef, T., and Cortés, A. (2016a). Applying domain decomposition to wind field calculation. *Parallel Comput.* 57, 484–490. doi: 10.1109/HPCSim.2015.7237080

Sanjuan, G., Margalef, T., and Cortés, A. (2016b). Hybrid application to accelerate wind field calculation. *J. Comput. Sci.* 17, 576–590. doi: 10.1016/j.jocs.2016.07.011

Sanjuan, G., Tena, C., Margalef, T., and Cortés, A. (2016c). Applying vectorization of diagonal sparse matrix to accelerate wind field calculation. *J. Supercomput.* 73, 240–258. doi: 10.1007/s11227-016-1696-9

Scott, J. H., and Burgan, R. E. (2005a). "Standard fire behavior fuel models: a comprehensive set for use with Rothermel's surface fire spread model," in *The Bark Beetles, Fuels, and Fire Bibliography* (Fort Collins, CO: USDA), 72.

Scott, J. H., and Burgan, R. E. (2005b). *Standard Fire Behavior Fuel Models: A Comprehensive Set for Use with Rothermel's Surface Fire Spread Model*. Technical report.

Turner, J. (1972). *The Drought Code Component of the Canadian Forest Fire Behavior System*. Technical Report 1316, Canadian Forestry Service, Ottawa, ON.

Valero, M., Rios, O., Pastor, E., and Planas, E. (2017). An integral system for automated tactical monitoring and data-driven spread forecasting of wildfires. *Fire Safety J.* 91, 835–844. doi: 10.1016/j.firesaf.2017.03.085

Valero, M., Rios, O., Planas, E., and Pastor, E. (2018). Automated location of active fire perimeters in aerial infrared imaging using unsupervised edge detectors. *Int. J. Wildland Fire* 27, 241–256. doi: 10.1071/WF17093

Valero, M. M., Verstockt, S., Rios, O., Pastor, E., Vandecasteele, F., and Barcelonatech, D. C. (2017). "Flame filtering and perimeter localization of wildfires using aerial thermal imagery," in *SPIE 10214, Thermosense: Thermal Infrared Applications XXXIX* (Anaheim, CA).

Wagenbrenner, N. S., Forthofer, J. M., Lamb, B. K., Shannon, K. S., and Butler, B. W. (2016). Downscaling surface wind predictions from numerical weather prediction models in complex terrain with WindNinja. *Atmos. Chem. Phys.* 16, 5229?-5241. doi: 10.5194/acp-16-5229-2016

Zhang, C., Collin, A., Moireau, P., Trouvé, A., and Rochoux, M. C. (2018). "Front shape similarity measure for data-driven simulations of wildland fire spread based on state estimation: application to the RxCADRE field-scale experiment," in *Proceedings of the Combustion Institute*, 1–9. doi: 10.1016/j.proci.2018.07.112

Zhang, C., Rochoux, M., Tang, W., Gollner, M., Filippi, J. B., and Trouvé, A. (2017). Evaluation of a data-driven wildland fire spread forecast model with spatially-distributed parameter estimation in simulations of the FireFlux I field-scale experiment. *Fire Safety J.* 91, 758–767. doi: 10.1016/j.firesaf.2017.03.057

Conflict of Interest Statement: The authors declare that the research was conducted in the absence of any commercial or financial relationships that could be construed as a potential conflict of interest.

frontiers in Mechanical Engineering

ORIGINAL RESEARCH
published: 02 April 2019
doi: 10.3389/fmech.2019.00011

The Role of Fuel Bed Geometry and Wind on the Burning Rate of Porous Fuels

*Sara McAllister**

RMRS Missoula Fire Sciences Lab, USDA Forest Service, Missoula, MT, United States

The vast majority of wildland fires occur in windy conditions. However, most operational wildland fire models do not account for changes in burning rate or duration due to wind as no simple model exists. To gain some understanding of how wind and fuel bed properties interact to influence the burning rate and duration of wildland fuels, a relatively simple fuel bed, wood cribs, was first considered. The burning rate of 23 crib designs was measured in a wind tunnel under a range of windspeeds from 0 to 0.7 m/s. Fuel element thickness varied from 0.32 to 1.27 cm and fuel bed width from 12.7 to 60.96 cm. A range of crib porosities was tested as well covering the loosely-packed to densely-packed regime. A clear threshold behavior of the burning rate was seen depending on fuel bed geometry. For fuel beds with element length to thickness ratio (l/b) <30, the burning rate increased with wind. However, for fuel beds with element length to thickness ratio larger than 30, the burning rate actually decreased with wind. This change in burning rate was linked to a visual change in burning behavior. When the burning rate increased, the wind and flames were observed to penetrate the internal portions of the fuel bed and the crib would burn uniformly. When the burning rate decreased, the wind and flames did not penetrate the entire fuel bed and the burning front would most often propagate from the upwind edge to the downwind edge. It appeared that for these fuel bed geometries the wind was forced around the fuel, preventing any horizontal or, more importantly, vertical flow through the bed. These results are likely most applicable to isolated, small clumps of elevated fuel where the wind has the opportunity to divert around the fuel bed. Future work will include experiments that force the airflow through the fuel bed.

Keywords: wildland fire, burning rate, forced ventilation, wind, cribs

OPEN ACCESS

Edited by:
Xinyan Huang,
Hong Kong Polytechnic University,
Hong Kong

Reviewed by:
Wei Tang,
National Institute of Standards and Technology, United States
Jorge Rafael Nogueira Raposo,
University of Coimbra, Portugal

***Correspondence:**
Sara McAllister
sara.mcallister@usda.gov

Specialty section:
This article was submitted to Thermal and Mass Transport, a section of the journal Frontiers in Mechanical Engineering

Received: *07 December 2018*
Accepted: *07 March 2019*
Published: *02 April 2019*

Citation:
McAllister S (2019) The Role of Fuel Bed Geometry and Wind on the Burning Rate of Porous Fuels. Front. Mech. Eng. 5:11. doi: 10.3389/fmech.2019.00011

INTRODUCTION

Burning and heat release rate are important fire behavior metrics for both structure and wildland fires. Some general insights into burning rate behavior of porous fuel beds can be found from the literature on crib fires from the fire protection engineering field. The burning rate behavior of porous fuel beds has long been understood to be separated into two regimes (Gross, 1962; Block, 1971). In the loosely-packed regime, the burning rate is more closely approximated by the free burning rate of the individual sticks and is governed by heat and mass transfer processes near the surfaces. In this regime, the burning rate is more of a function of the stick dimensions, and is independent of the "porosity" of the fuel bed. In the densely-packed regime, the burning rate is limited by availability of oxidizer within the fuel bed. In this regime, the burning rate increases with the inter-stick spacing or the "porosity" of the fuel bed. There have been several proposed

definitions for the porosity (φ) of the fuel bed, but perhaps the most widely used is that of Heskestad (1973):

$$\varphi = s^{\frac{1}{2}} b^{\frac{1}{2}} \left(\frac{A_v}{A_s} \right)$$

where s is the spacing between sticks (cm), b is the stick thickness (cm), A_v is the area of the vertical shafts in the crib (cm^2), and A_s is the exposed stick surface area (cm^2), with the result that the porosity has units of cm. The transition between burning regimes occurs at a porosity of approximately 0.05 cm, with densely-packed and loosely packed cribs having porosities below and above this threshold, respectively. The fuel bed porosity and the identification of these two regimes not only gives an impression about the appearance of the fuel bed, but also describes the mechanisms that govern the burning behavior.

Unfortunately, the variation of the burning rate with forced ventilation is not well-understood, despite its obvious relevance and importance to wildland fires. In the only study dedicated to answering this question, Harmathy (1978) showed an increase in burning rate of cribs built with charring materials, but an insensitivity in non-charring materials, indicating that char oxidation is an important mechanism. Unfortunately, this was a relatively early paper, and consideration of the crib porosity [such as from Gross (1962), Block (1971), or Heskestad (1973)] was not carefully included so the full range of expected behavior was not elucidated. Other clues exist in the fire protection engineering literature as well. For example, for baskets of unordered wood cubes, Grumer and Strasser (1965) saw an increase in the burning rate of more than six times when air was blasted into the fuel bed. There have also been several studies of the effects of forced ventilation on burning rate for fuel beds in tunnel fires [for example, see (Carvel et al., 2001; Lönnermark and Ingason, 2008; Ingason and Li, 2010; Ingason and Lönnermark, 2010)] and compartment fires [for example, see (Alvares et al., 1984; Beyler, 1991; Chow and Chan, 1993; Peatross and Beyler, 1997)]. However, the interaction of the fire with the tunnel or enclosure adds significant complexity to the problem.

The understanding of the variables effecting the burning rate, and the related flame residence time, in the wildland fire literature is also poor. There are studies that suggest that no effect is seen and others that suggest an increase with wind. For example, Steward and Tennankore (1981) measured the burning rate of a single wooden dowel within a fuel bed consisting of vertical rods arranged in a uniform matrix. While the burning rate of the dowel was proportional to the diameter to the 3/2 power, no effect of wind speed was seen. On the contrary, Beaufait (1965) saw an increase in the residence time with wind speed for heading fires in beds of ponderosa pine needles. Beaufait (1965), however, noted that there was no effect of wind on the residence time for backing fires. Nelson (2003) argues in his model development that there is only a weak dependence of residence time with wind speed through the convective heat transfer coefficient. Many of these studies were performed for spreading fires which complicates the measurement and even the definition of these parameters (Nelson, 2003).

Our own previous work on the matter (McAllister and Finney, 2016a) was also inconclusive. Published as part of the proceedings of the Operation Tomodashi—-Fire Research workshop, the work was merely a preliminary investigation that raised more questions than it answered. In that work, seven crib designs were tested in a wind tunnel under a wind ranging from 0 to 0.7 m/s. It was seen that the burning rate of cribs with thicker (1.27 cm) sticks increased with wind speed, whereas the burning rate of cribs with thinner (0.64 cm) sticks decreased. Possible mechanisms were discussed, but it was clear that more experimentation was needed to fully understand the results. Our current work presents the results of significantly more testing and a clearer picture of the controlling mechanisms.

EXPERIMENT DESCRIPTION

Twenty three crib designs were tested to examine the combined effect of forced ventilation and fuel bed properties. The full list of crib designs is shown in **Table 1**. The cribs were built out of square ponderosa pine sticks that were free of knots and other obvious defects. Three stick thicknesses were used (0.32, 0.64, and 1.27 cm). The length of the sticks, the number of sticks per layer, and the number of layers were varied to provide a wide variety of geometries and porosities (φ). Though no particular experiment design scheme was followed, the fuel bed parameters were varied in an exploratory manner, probing for any unexpected or non-linear behaviors.

The moisture content of the cribs was controlled by conditioning them in a conditioning chamber set to 35°C and 3% relative humidity for at least 3 days before testing. The equilibrium moisture content was ∼1%. Simultaneous ignition of the crib was achieved by quickly dunking the entire crib in 99% isopropyl alcohol and allowing it to drain. The total mass of alcohol used was 10% or less of the crib weight.

The weighing platform consisted of a 91.4 cm square, thin aluminum sheet that was supported by three 6-kg capacity load cells as in **Figure 1**. The load cells were calibrated to 0.1 g. Heat transfer to these load cells was minimized by covering the aluminum sheet with multiple layers of ceramic paper insulation, and by using 1.3 cm diameter ball bearings as contact points between the aluminum sheet and the load cells themselves. Because previous work indicated that the burning rate could be very sensitive to the spacing between the bottom of the crib and the weighing platform (McAllister and Finney, 2016b), two 7.62-cm-tall steel spacers were used to eliminate this effect. This weighing apparatus was placed inside of a 3 m by 3 m wind tunnel which was large enough for the flames to not interact with the walls. A gentle ramp was built ahead of the platform to compensate for the height of the load cells and platform so as to smooth out and guide the airflow. Wind speeds of 0, 0.24, 0.37, and 0.7 m/s were tested with the primary set of 15 crib designs, designated in **Table 1**. The remaining eight crib designs were only tested with 0 and 0.7 m/s, as these cribs were designed to help clarify the threshold behavior observed. The reported wind speeds are the free-stream value, measured at a height of 2.2 m above the wind tunnel floor. Boundary layer thickness at 0.7 m/s

TABLE 1 | Crib designs tested.

Crib design #	Stick thickness (b) [cm]	Stick length (l) [cm]	l/b [ ]	Number of sticks per layer (n) [ ]	Number of layers (N) [ ]	Stick spacing (s) [cm]	Surface area (A_S) [cm^2]	Heskstad porosity (φ) [cm]
1	1.27	12.7	10	2	25	10.16	3077.4	0.1205
2	1.27	12.7	10	7	10	0.64	3319.3	0.0039
3	1.27	20.3	16	6	14	2.54	7432.2	0.0390
4	1.27	25.4	20	4	21	6.77	10077.4	0.1202
5	1.27	40.6	32	13	3	2.01	7087.1	0.1313
6	1.27	43.2	34	14	3	1.95	8083.9	0.1257
7	1.27	45.7	36	13	4	2.43	10609.7	0.1414
8	0.64	12.7	20	6	24	1.78	4093.5	0.0205
9	0.64	15.2	24	10	35	0.99	11088.7	0.0057
10	0.64	19.1	30	8	14	2.00	4838.7	0.0454
11	0.64	19.1	30	5	15	3.97	3407.3	0.1174
12	0.64	19.7	31	8	16	2.09	5729.0	0.0429
13	0.64	20.3	32	3	45	9.21	6757.2	0.1213
14	0.64	20.3	32	8	16	2.18	5935.5	0.0460
15	0.64	21.0	33	9	14	1.91	5958.9	0.0429
16	0.64	21.6	34	9	15	1.98	6597.6	0.0429
17	0.64	25.4	40	10	10	2.12	5806.4	0.0725
18	0.64	25.4	40	14	15	1.27	11504.8	0.0213
19	0.64	61.0	96	20	9	2.54	25435.4	0.1163
20	0.32	10.2	80	2	80	9.53	2033.1	0.0776
21	0.32	25.4	80	14	30	1.61	12487.1	0.0252
22	0.32	25.4	80	27	20	0.65	14735.7	0.0087
23	0.32	30.5	96	6	40	5.72	9055.6	0.1215

Cribs in bold were tested at all four wind speeds.

has been measured to be ∼0.3 m at the location of the test section with freestream turbulence intensities of <2% (Rothermel, 1967). Because the height of the platform and load cells is about 0.2 m, the fuel beds sit just at the top of the boundary layer and are largely exposed to the freestream velocity.

The mass data from the load cells was recorded at 10 Hz. A sample of the raw mass and mass loss rate data are shown in **Figure 2**. The rate data was calculated here as the derivative of the mass data with time using a spline fit with ten degrees of freedom. In this particular example, ignition occurs at approximately 10 s, giving rise to considerable noise in the data. Because of this noise in the data, the spine fit to obtain the mass loss rate is unreliable for the short period around ignition. Even so, three phases of burning are seen in this data. The first phase, characterized by a short and steep drop in the mass, is the alcohol burning off which occurs relatively quickly. The second phase is the steady burning portion. The reported data is taken as the slope of the best fit line through this second phase of burning. The final phase is when the crib collapses and flaming ceases. All test combinations are repeated at least three times (for a total of 228 tests) and the results averaged.

RESULTS AND DISCUSSION

Before discussing the results in detail, some mention of the scaling of these experiments should be made. Several non-dimensional parameters can be used to provide some context. One such parameter is the non-dimensional heat release rate, or Q* defined as (for example see Quintiere, 2017 or Zukoski, 1995):

$$Q^* = \frac{\dot{Q}}{\rho_\infty c_p T_\infty g^{\frac{1}{2}} D^{\frac{5}{2}}} = \frac{\dot{m}\Delta h_c}{\rho_\infty c_p T_\infty g^{\frac{1}{2}} D^{\frac{5}{2}}}$$

where $\dot{Q}$ is the heat release rate (kW), ρ_∞ is the density of the ambient air (kg/m^3), c_p is the specific heat of the ambient air (kJ/kg-K), T_∞ is the ambient air temperature (K), g is the acceleration due to gravity (m/s^2), D is the characteristic length (m), $\dot{m}$ is the burning rate (g/s), and Δh_c is the heat of combustion (kJ/g). For our purposes, we assumed that the heat of combustion was 14.1 kJ/g (Heskestad, 2006) and the properties of air were evaluated at 300 K. Using the average burning rate values from **Table 2**, Q* values ranged from 0.60 (crib design #5 at 0.7 m/s) to 12.72 (crib design #20 at 0 m/s). Q* for outdoor fires typically ranges from 0.5 up to 100 (Quintiere, 2017). Most fires will have $Q^* < 10$ and, because Q* is related to the ratio of the flame height to the fire diameter, larger area fires have $Q^* < 2$ (Zukoski, 1995). Given this range, the fires in these experiments are representative of the flame and plume regime expected for wildland fires.

Another scaling consideration to keep in mind is the relation of the wind speed to the amount of heat that is released. This can be done a number of ways. In some flame tilt literature (see for example Thomas, 1965 and Beyler, 2008), the ratio of the wind velocity (u_w) to the buoyant velocity (u_b) can be useful. This

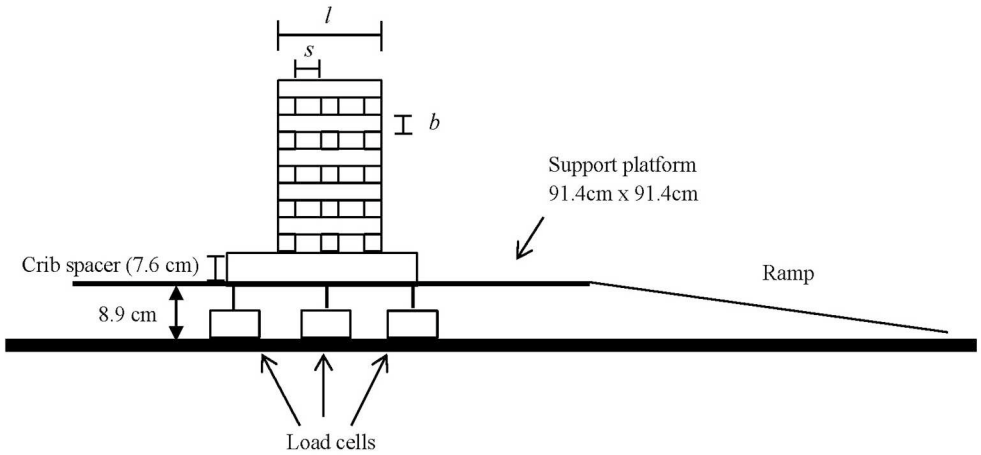

FIGURE 1 | Sketch of apparatus for a crib with 3 sticks per layer ($n = 3$) and 10 layers ($N = 10$).

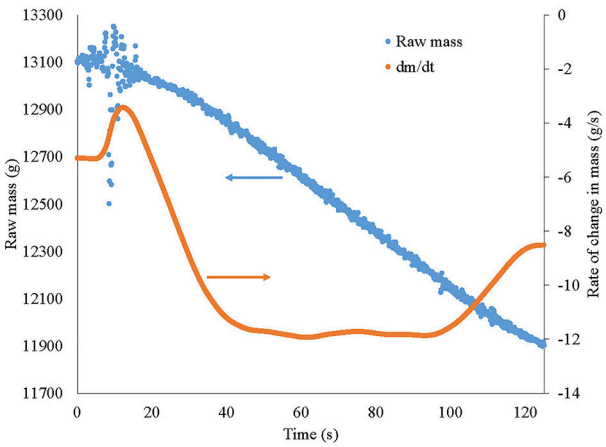

FIGURE 2 | Raw mass and rate of change data for crib design #4 in 0.24 m/s wind. Ignition occurs at about 10 s, alcohol burnoff and stick ignition is complete by around 40 s, and steady burning occurs between about 40 and 100 s.

non-dimensional velocity is defined as,

$$u^* = \frac{u_w}{u_b} = \frac{u_w}{\left(\frac{g\dot{m}''D}{\rho_\infty}\right)}$$

where $\dot{m}''$ is the burning rate per unit area. If $u^* < 1$, the buoyant velocity dominates and the flames remain upright. If greater than one, the inertia of the wind becomes important and the flames tilt. Using the burning rates from **Table 2**, u^* for the experiments here ranged from 0.33 (crib design #4 at 0.24 m/s) up to 1.75 (crib design #22 at 0.7 m/s), covering a wide range of behaviors. In the engineering literature, the Froude number is regularly used to quantify this balance between inertia and buoyancy forces. Using the flame length given by Quintiere (2006), the Froude number is defined here as (for example Pagni and Peterson, 1973):

$$Fr = \frac{u^2}{gL} = \frac{u^2}{g\left(\frac{\dot{Q}}{\rho_\infty c_p T_\infty \sqrt{g}}\right)^{\frac{2}{5}}} = \frac{u^2}{g\left(\frac{\dot{m}\Delta h_c}{\rho_\infty c_p T_\infty \sqrt{g}}\right)^{\frac{2}{5}}}$$

Using data from **Table 2**, the Froude number ranged from 0.013 (crib design #4 at 0.24 m/s) to 0.2191 (crib design #22 at 0.7 m/s) using the wind speeds at the fuel level. In wildfire situations, wind speeds are often reported at a particular height above the ground (10 m or 20 ft), so the reported wind conditions are not necessarily the conditions experienced by the flames. In calculating wind speeds in operational fire spread models, often a logarithmic wind profile is assumed and the wind speed is reduced to the mid-flame height (Albini and Baughman, 1979). For comparison purposes, the range of Froude numbers tested here would correspond to 1.5 m tall shrubs with 3 to 8.5 m flames in 0.7 to 4.5 m/s mid-flame winds (see for example Scott and Burgan, 2005, shrub fuel model SH9).

As discussed in earlier work, distinct changes in the burning pattern were observed. In still air, loosely-packed cribs burned very uniformly with equal consumption rates throughout the entire fuel bed (see **Figure 3**). Densely-packed cribs in still air burned symmetrically from the outside edges inward, with the center core as the last portion to be consumed (see **Figure 4**). In wind, however, the burnout patterns were asymmetric. With only a couple of exceptions, most of the cribs burned faster on the windward side as the wind speed was increased. One of the most exaggerated cases is shown in **Figure 5**, where the burning resembled a propagating flame front from the front, windward side of the crib down wind. Additionally, some of the densely-packed cribs, when exposed to wind, seemed to burn out a bit faster on the bottoms, such that the crib appeared to decrease in height over the course of the test.

Table 2 shows the average burning rate for all tests conducted. Also included in **Table 2** is the standard deviation as a percent of the mean value to give an indication of the repeatability. The

TABLE 2 | Burning rate results averaged over three replicates.

Crib design #	l/b [ ]	Stick spacing (s) [cm]	Heskstad porosity (φ) [cm]	Average burning rate (R) [g/s] at 0 m/s (% std)	Average burning rate (R) [g/s] at 0.24 m/s (% std)	Average burning rate (R) [g/s] at 0.37 m/s (% std)	Average burning rate (R) [g/s] at 0.7 m/s (% std)
1	10	10.16	0.1205	2.98 (6.0)	3.07 (3.3)	3.27 (2.2)	3.38 (1.0)
2	10	0.64	0.0039	0.71 (2.0)	0.87 (1.7)	0.99 (7.1)	1.14 (5.5)
3	16	2.54	0.0390	6.16 (4.6)	6.60 (3.2)	6.25 (2.0)	6.56 (3.1)
4	20	6.77	0.1202	10.69 (1.8)	11.57 (1.0)	12.41 (0.7)	13.21 (5.7)
5	32	2.01	0.1313	7.64 (0.7)	–	–	5.10 (7.1)
6	34	1.95	0.1257	8.53 (2.9)	8.11 (13.0)	6.85 (5.8)	6.55 (1.8)
7	36	2.43	0.1414	12.83 (8.1)	8.26 (5.0)	8.05 (3.6)	7.68 (7.8)
8	20	1.78	0.0205	2.95 (1.9)	3.02 (9.5)	3.18 (2.2)	3.30 (7.1)
9	24	0.99	0.0057	2.63 (16.0)	3.79 (8.8)	4.47 (5.1)	4.29 (3.3)
10	30	2.00	0.0454	5.55 (2.9)	–	–	3.16 (2.7)
11	30	3.97	0.1174	4.90 (7.3)	–	–	4.05 (1.5)
12	31	2.09	0.0429	6.24 (1.4)	–	–	3.88 (4.1)
13	32	9.21	0.1213	10.32 (4.5)	9.90 (16.2)	10.73 (11.9)	12.42 (6.1)
14	32	2.18	0.0460	6.64 (1.3)	–	–	3.99 (3.2)
15	33	1.91	0.0429	6.68 (3.5)	–	–	3.57 (4.4)
16	34	1.98	0.0429	6.62 (4.6)	4.12 (8.3)	4.02 (2.0)	4.39 (6.0)
17	40	2.12	0.0725	7.00 (8.3)	4.43 (8.8)	3.46 (2.8)	4.23 (4.1)
18	40	1.27	0.0213	7.38 (13.4)	3.75 (1.7)	3.90 (9.2)	4.09 (3.9)
19	96	2.54	0.1163	34.54 (21.1)	–	–	17.44 (3.4)
20	80	9.53	0.0776	3.35 (11.9)	–	–	2.84 (10.4)
21	80	1.61	0.0252	8.94 (5.7)	4.75 (5.1)	4.40 (4.5)	4.40 (4.5)
22	80	0.65	0.0087	4.49 (4.3)	2.80 (9.0)	2.77 (6.2)	1.99 (6.7)
23	96	5.72	0.1215	16.95 (4.9)	13.70 (3.7)	13.77 (4.9)	10.98 (2.8)

The values in the parentheses indicate one standard deviation as a percent of the mean. Cribs in bold were tested at all four wind speeds.

FIGURE 3 | Loosely-packed crib (crib design #11) burning in a quiescent environment showing the entire fuel bed burning uniformly throughout.

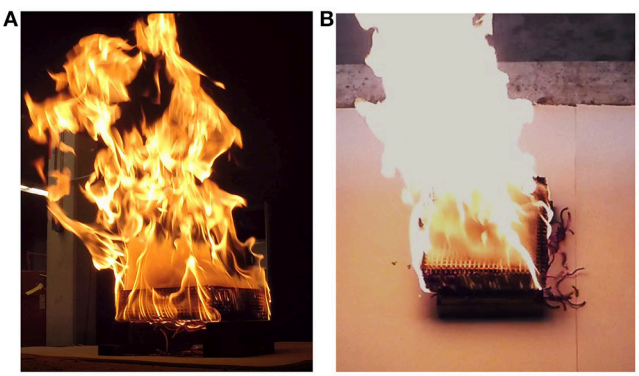

FIGURE 4 | Densely-packed crib (crib design #22) from the side **(A)** and from above **(B)** burning in a quiescent environment. The crib burns primarily from the outside inward, with lots of unburnt, white gases being emitted from the top of the fuel bed.

average standard deviation over all tests was 5.4% of the mean value, with a maximum value of 21.1%, demonstrating good consistency between tests.

Figures 6–8 plot the normalized burning rate results as a function of wind speed for the 1.27, 0.64, and 0.32 cm thick sticks, respectively. All data are scaled by the exposed surface area (A_s) and the inverse square root of the stick thickness ($b^{-0.5}$) as in Block (1971) and Heskestad (1973). Each point represents the average of three tests, and though it may not be visible in

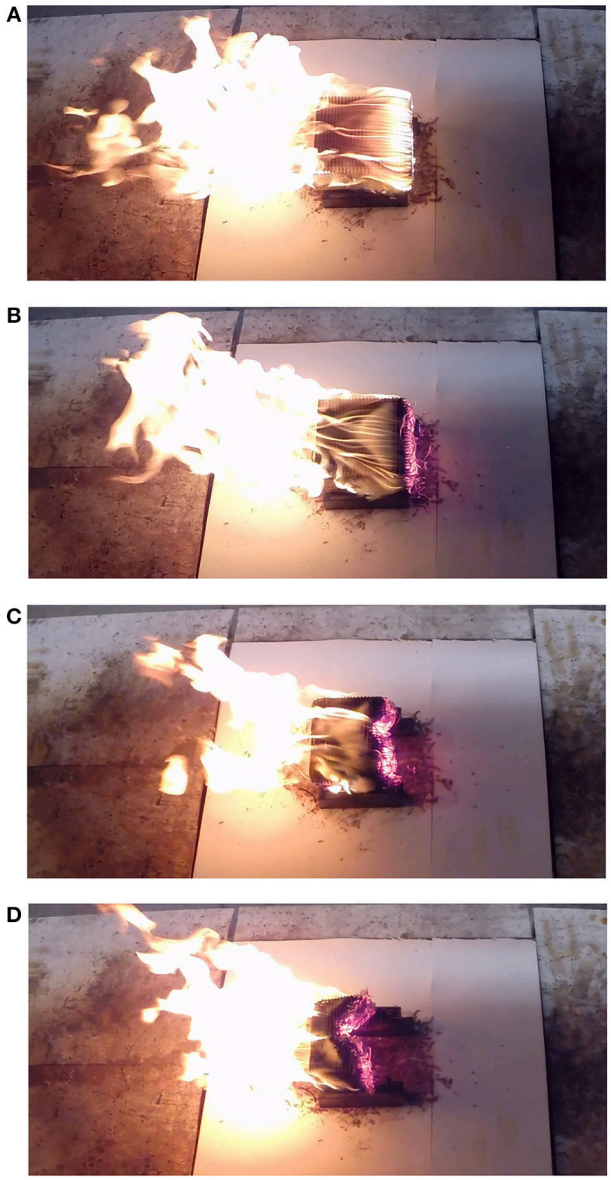

FIGURE 5 | Crib design #22 in 0.7 m/s wind at various times after ignition: **(A)** approximately 30 s, **(B)** approximately 70 s, **(C)** approximately 195 s, **(D)** approximately 360 s.

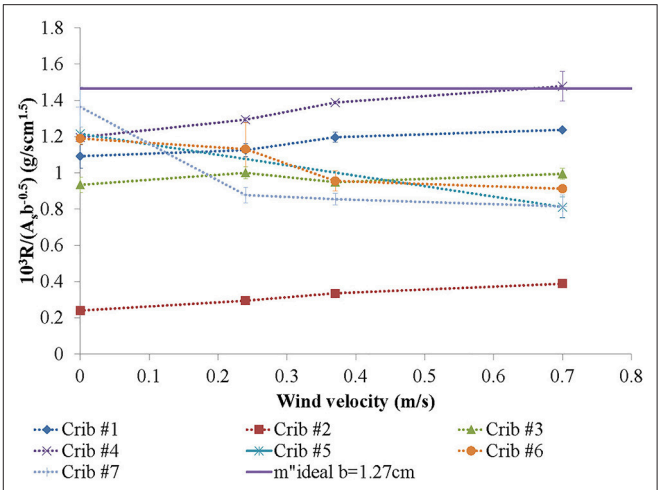

FIGURE 6 | Scaled burning rate as a function of wind speed for cribs with 1.27 cm thick sticks. Ideal burning rate is from Tewarson and Pion (1976). See **Table 1** for details on fuel bed parameters.

all cases, the error bars show one standard deviation for each condition. Also shown in the figures is the ideal burning rate for each stick thickness according to Tewarson and Pion (1976). The ideal burning rate is defined as the burning rate where the additional heat flux (such as from nearby burning surfaces) is just balanced by the heat losses. Some difference in the ideal rate may be expected due to differing wood species. The values from Tewarson and Pion (1976) are for Douglas-fir while ponderosa pine was tested here.

As shown in **Figure 6** through **Figure 8**, the burning rate either increases or decreases with wind speed. Contrary to what was observed in previous work (McAllister and Finney, 2016a), this trend is not dependent upon stick thickness, but seems to depend on other factors that will be discussed further below. The maximum increase in burning rate was 69.9% percent from crib design #9, one of the most densely-packed cribs tested ($\varphi = 0.0057$ cm). In general, the largest increases in burning rate were seen for the densely-packed cribs. These cribs are generally considered to be ventilation limited, so logically, forcing air through these densely-packed cribs will lean out the gaseous air and fuel mixture internally, allowing for greater reaction rates and thus heat release rates. Interestingly, even some loosely-packed cribs (#s 1, 4, and 13) also showed modest increases in the burning rates of 13 to 23%. As pointed out by Harmathy (1978), char oxidation can be an important contributor to the overall burning rate. With forced ventilation, the char oxidation rate is increased, resulting in increased burning rate even in fuel beds that aren't ventilation limited.

In the case of crib designs #4 and 13, the addition of wind allowed the burning rate of the fuel bed to approach or exceed the estimated ideal of Tewarson and Pion (1976) (see **Figures 6**, **7**). In general, for loosely-packed and transition-regime cribs, such as crib designs #4–7 (**Figure 6**), 10–17, 19 (**Figure 7**), 20, and 23 (**Figure 8**), the burning rate in no wind was already within about 20% of this ideal (or exceeded it). However, the burning rate of many of these crib designs dropped considerably as wind was added, indicating a shift in the balance between heat generated and heat lost. In general, this balance is what governs whether the burning rate will increase or decrease, but how this balance is achieved in all cases here is not obvious.

Though all cribs burned with some level of asymmetry in the wind, the cases with decreased burning rate had increasingly asymmetric burning patterns. In some cases, the downwind half of the crib chars but is nearly completely unconsumed before the upwind half burns out and collapses (see **Figure 5**). Visually, it appears as if the crib geometry is preventing the airflow through the crib. As the flow resistance through the crib increases, the

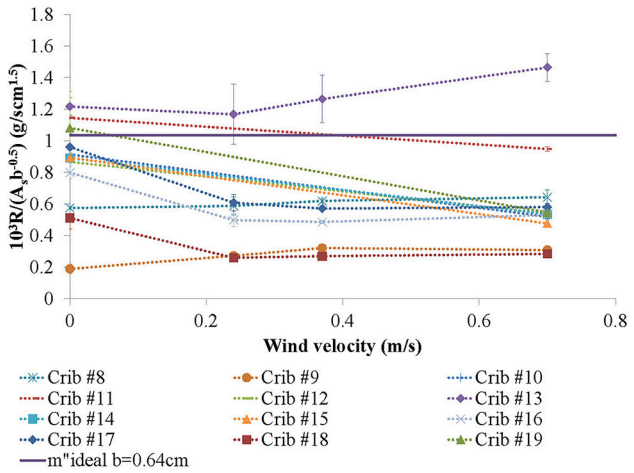

FIGURE 7 | Scaled burning rate for cribs with 0.64 cm thick sticks. Ideal burning rate is from Tewarson and Pion (1976). See **Table 1** for details on fuel bed parameters.

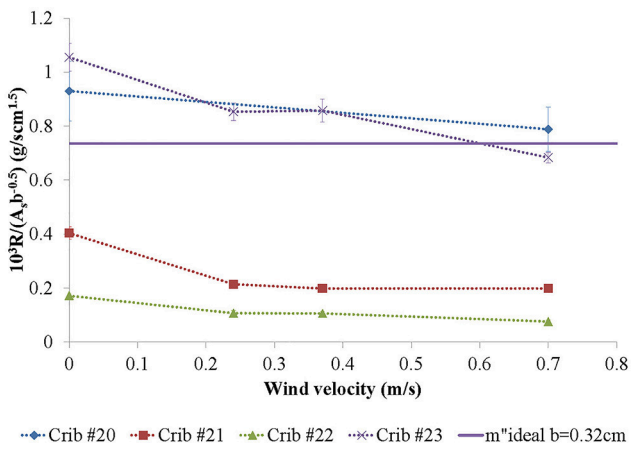

FIGURE 8 | Scaled burning rate for cribs with 0.32 cm thick sticks. Ideal burning rate is from Tewarson and Pion (1976). See **Table 1** for details on fuel bed parameters.

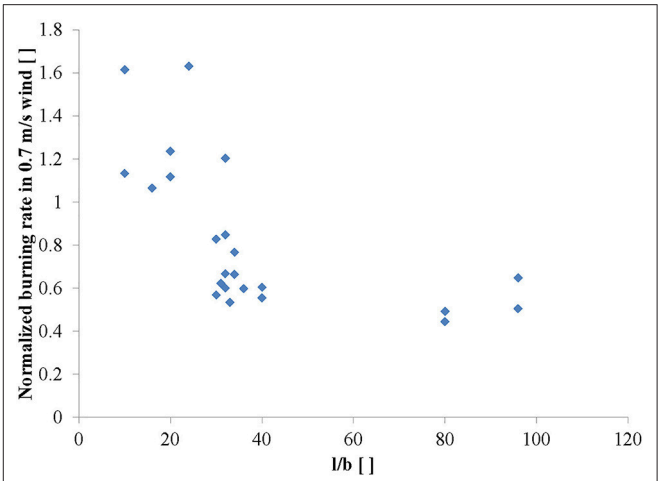

FIGURE 9 | Burning rate under 0.7 m/s normalized by quiescent case as a function of the aspect ratio of the crib (l/b).

path of least resistance for the flow is around, not through, starving portions of the internal area of the fuel bed of air. This, however, does not seem to be related to the porosity of the fuel bed, at least as defined by Heskestad (1973) or as bulk density (volume of fuel per fuel bed volume), as even loosely-packed cribs exhibit this behavior as well (for example, crib designs #5, 6, 7, 11, 19, 20, and 23). Interestingly, this transition from flow *through* to flow *around* occurred for cribs with large aspect ratios (long sticks relative to the stick thickness, or l/b). **Figure 9** shows the burning rates at the highest wind speed tested (0.7 m/s) normalized by the quiescent case as a function of the aspect ratio (l/b). Despite one exception (crib design #13), there is a rather sharp threshold at an l/b ratio between about 25 and 30. Some exploratory statistical analysis was conducted to find an alternate explanation, but no other fuel bed property was found that explained this behavior in any meaningful way.

Though a surprisingly simple criteria, this ratio has physical meaning. In a quiescent environment, cribs with small aspect ratios are able to entrain air into the fuel bed from the sides efficiently enough so that the burning rate does not change significantly when flow from the bottom is completely blocked, for example by placing the crib directly on the ground (McAllister and Finney, 2016b). Because the sticks are relatively short, the horizontal distance to the center of the crib is relatively small. As cribs are built by stacking the sticks, the gap the air must pass through is a function of the stick thickness, so the thicker the stick, the less flow resistance encountered. In contrast, cribs with large aspect ratios rely heavily on airflow from underneath the crib. In these cases, the burning rate can decrease dramatically if the flow from underneath is blocked or restricted at all (McAllister and Finney, 2016b). When the sticks are long and thin, the air must travel further horizontally to the center and encounters a larger flow resistance. Additionally, though the fuel elements here are in arrays, Hoerner (1965) shows that the drag coefficient for a rectangular plate in cross flow doubles as the aspect ratio increases from 10 to ∞ as the flow transitions from three dimensional flow to two dimensional flow. Note that the drag coefficient for aspect ratios less than this is nearly constant at the minimum value. It is unsurprising then, that the air flow in from the sides of the cribs is much reduced as the aspect ratio increases.

However, the large aspect ratio cribs never relied on flow from the sides, so this horizontal flow diversion around the fuel bed shouldn't have a large effect on the burning rate. Thus, a second factor limiting the airflow in the crib may be at play here as well. In the wind, the flames are blown over so that they hug both the top and bottom of the crib as demonstrated in **Figure 10A**. The flames act to block air from diffusing into the fuel bed, but also are a great visible flow tracer indicating that there is very little flow entering the bottom of the crib. This perhaps could be because the flow going underneath is forced through a relatively

FIGURE 10 | Crib design #22 in 0.7 m/s **(A)** and 0.24 m/s **(B)** wind from behind demonstrating flames hugging the top and bottom sides of the fuel bed, blocking airflow from below.

small gap, generating an increased horizontal momentum that is difficult to redirect vertically. Additionally, by tipping the plume over, the driving force pulling air up through the bottom of the crib is significantly reduced. Because the plume is tilted in even the lowest wind speed tested here (see **Figure 10B**), this absence of flow from underneath could not only explain the decreasing burning rate but also why it is nearly constant with wind speed for several of these diminished cases (crib design #s 7, 16, 17, 18, 21, and 23).

SUMMARY

The burning rate and residence time of porous fuel beds are important fire behavior metrics relevant to both structure and wildland fires. Unfortunately, the effect of wind is largely unknown. This work set out to understand how the fuel bed properties interact with the wind to dictate the burning rate. Twenty three crib designs were tested in a range of wind speeds and it was seen that the effect of wind was dependent on the fuel bed structure. For cribs with a small aspect ratio, defined as the ratio of the stick length to the thickness (l/b), the burning rate increased with wind speed. This increase was more pronounced for densely-packed fuel beds that are, by definition, ventilation limited. Loosely-packed fuel beds also had a modest increase in the burning rate due to increased char oxidation. For cribs with a large aspect ratio (l/b $>$ 30), the burning rate decreased with wind. This decrease was likely due to flow patterns that limited flow through the sides, but primarily up through the bottom of the crib.

These results are likely most applicable to isolated, small clumps of elevated fuel (trees and shrubs) where the wind has the opportunity to divert around the fuel bed and would ordinarily flow vertically up into the fuel. Future work will include experiments that will force the airflow to actually pass through the fuel bed. To understand the effect of wind in surface fires, these experiments will include tests that block the flow from below.

DATA AVAILABILITY

The datasets generated for this study are available on request to the corresponding author.

AUTHOR CONTRIBUTIONS

The author confirms being the sole contributor of this work and has approved it for publication.

FUNDING

The work was funded by the National Fire Decision Support Center.

ACKNOWLEDGMENTS

The authors would like to thank Sophia Vernholm for her tireless and careful construction of the fuel beds; Cyle Wold for setting up the data acquisition system; Mark Finney, Jason Forthofer, and Torben Grumstrup for many discussions; and Isaac Grenfell for help with data analysis.

REFERENCES

Albini, F. A., and Baughman, R. G. (1979). *U.S. Forest Service Research Note INT-221.* Intermountain Forest and Range Experiment Station. Ogden, Utah.

Alvares, N. J., Foote, K. L., and Pagni, P. J. (1984). Forced ventilation enclosure fires. *Combust. Sci. Technol.* 39, 55–81. doi: 10.1080/00102208408923783

Beaufait, W. R. (1965). *Characteristics of Backfires and Headfires in a Pine Needle Fuel Bed.* U.S. Forest Service Research Note INT-39, Intermountain Forest and Range Experiment Station. Ogden, Utah.

Beyler, C. L. (1991). "Analysis of compartment fires with overhead forced ventilation," in *Fire Safety Science–Proceedings of the Third International Symposium*, 291–300. doi: 10.3801/IAFSS.FSS.3-291

Beyler, C. L. (2008). "Fire hazard calculations for large, open hydrocarbon fires," in *SFPE Handbook of Fire Protection Engineering*, 4th Edn, eds P. J. DiNenno, D. Drysdale, C. L. Beyler, W. D. Walton, R. L. P. Custer, J. R. Hall Jr., and J. M. Watts (Quincy, MA: National Fire Protection Association), 2591–3493.

Block, J. A. (1971). A theoretical and experimental study of non-propagating free-burning fires. *Symp. Combust.* 13, 971–978. doi: 10.1016/S0082-0784(71)80097-8

Carvel, R. O., Beard, A. N., Jowitt, P. W., and Drysdale, D. D. (2001). Variation in the heat release rate with forced longitudinal ventilation for vehicle fires in tunnels. *Fire Saf. J.* 36, 569–596. doi: 10.1016/S0379-7112(01)00010-8

Chow, W. K., and Chan, W. L. (1993). Experimental studies on forced-ventilated fires. *Fire Sci. Technol.* 13, 71–87. doi: 10.3210/fst.13.1_71

Gross, D. (1962). Experiments on the burning of cross piles of wood. *J. Res. Nat. Bureau Stand. C Eng. Instrument.* 66c, 99–105. doi: 10.6028/jres.066C.010

Grumer, J., and Strasser, A. (1965). Uncontrolled fires–specific burning rates and induced air velocities. *Fire Technol.* 1, 256–268. doi: 10.1007/BF02588468

Harmathy, T. Z. (1978). Experimental study on the effect of ventilation on the burning of piles of solid fuels. *Combust. Flame* 31, 259–264. doi: 10.1016/0010-2180(78)90138-4

Heskestad, G. (1973). Modeling of enclosure fires. *Symp. Combust.* 14, 1021–1030. doi: 10.1016/S0082-0784(73)80092-X

Heskestad, G. (2006). Heat of combustion in spreading wood crib fires with application to ceiling jets. *Fire Saf. J.* 41, 343–348. doi: 10.1016/j.firesaf.2006.01.008

Hoerner, S. F. (1965). *Fluid-Dynamic Drag, 2nd Edn.* Midland Park, NJ, 3-15, 3-16.

Ingason, H., and Li, Y. Z. (2010). Model scale tunnel fire tests with longitudinal ventilation. *Fire Saf. J.* 45, 371–384. doi: 10.1016/j.firesaf.2010.07.004

Ingason, H., and Lönnermark, A. (2010). "Effects of longitudinal ventilation on fire growth and maximum heat release rate," in *Fourth International Symposium on Tunnel Safety and Security* (Frankfurt), 17–19.

Lönnermark, A., and Ingason, H. (2008). "The effect of air velocity on heat release rate and fire development during fires in tunnels," in *Fire Safety Science –Proceedings of the Ninth International Symposium*, 701–712. doi: 10.3801/IAFSS.FSS.9-701

McAllister, S., and Finney, M. (2016a). The effect of wind on burning rate of wood cribs. *Fire Technol.* 52, 1035–1050. doi: 10.1007/s10694-015-0536-4

McAllister, S., and Finney, M. (2016b). Burning rates of wood cribs with implications for wildland fire. *Fire Technol.* 52, 1755–1777. doi: 10.1007/s10694-015-0543-5

Nelson, R. M. (2003). Reaction times and burning rates for wind tunnel headfires. *Int. J. Wildl. Fire* 12, 195–211. doi: 10.1071/WF02041

Pagni, P. J., and Peterson, T. G. (1973). Flame spread through porous fuels. *Symp. Combust.* 14, 1099–1107. doi: 10.1016/S0082-0784(73)80099-2

Peatross, M. J., and Beyler, C. L. (1997). "Ventilation effects on compartment fire characterization," in *Fire Safety Science–Proceedings of the Fifth International Symposium*, 403–414. doi: 10.3801/IAFSS.FSS.5-403

Quintiere, J. G. (2006). *Fundamentals of Fire Phenomen*a. West Sussex: John Wiley and Sons. doi: 10.1002/0470091150

Quintiere, J. G. (2017). *Principles of Fire Behavior, 2nd ed*. New York, NY: CRC Press.

Rothermel, R. C. (1967). *Airflow Characteristics–Wind Tunnels and Combustion Facilities Northern Forest Fire Laboratory*. Laboratory Report, Northern Forest Fire Laboratory, Intermountain Forest & Range Experiment Station, Forest Service, U.S. Department of Agriculture, Missoula, Montana.

Scott, J. H., and Burgan, R. E. (2005). *Standard Fire Behavior Fuel Models: A Comprehensive Set for Use With Rothermel's Surface Fire Spread Model.* General Technical Report RMRS-GTR-153. U.S. Department of Agriculture, Forest Service, Rocky Mountain Research Station, Fort Collins, CO.

Steward, F. R., and Tennankore, K. N. (1981). The measurement of the burning rate of an individual dowel in a uniform fuel matrix. *Symp. Combust.* 18, 641–646. doi: 10.1016/S0082-0784(81)80069-0

Tewarson, A., and Pion, R. F. (1976). Flammability of plastics- I. Burning intensity. *Combust. Flame* 26, 85–103. doi: 10.1016/0010-2180(76)90059-6

Thomas, P. H. (1965). *Fire Spread in Wooden Cribs: Part III the Effect of Wind*. Fire Research Note No. 600, Fire Research Station, Ministry of Technology and Fire Offices' Committee Joint Fire Research Organization.

Zukoski, E. E. (1995). "Properties of fire plumes," in *Combustion Fundamentals of Fire*, ed G. Cox (London: Academic Press), 101–219.

Conflict of Interest Statement: The author declares that the research was conducted in the absence of any commercial or financial relationships that could be construed as a potential conflict of interest.

frontiers in Mechanical Engineering

ORIGINAL RESEARCH
published: 21 May 2019
doi: 10.3389/fmech.2019.00027

Design Bushfire Selection for Bushfire Protection in Adaptation to Global Warming

*Grahame B. Douglas and Yaping He**

School of Computing, Engineering and Mathematics, Western Sydney University, Penrith, NSW, Australia

In this article, a risk based approach to design for bushfire protection in view of adaptation to global warming is discussed. The concept of design bushfire is explained in an analogy to design flood or design earthquake in terms of event of prescribed return period. In lieu of using the Global Climate Model, the current study is based on the analysis of historical fire weather data from multiple locations in a state wide region. The generalized extreme value (GEV) analysis method is employed to establish the recurrence models for predicting the fire weather index of given return period and the associated fire intensity. To examine the impacts of the climate change, a moving GEV method is utilized to the weather data records over the period of 44 years. The result demonstrated a heterogeneity in the impact of climate change in terms of a given recurrence fire danger index and the potential bushfire severity over the region studied. The implication of this outcome is that the traditional prescriptive approach to design for bushfire protection may not be suited for adaptation to climate change.

Keywords: adaptation, design bushfire, extreme value, heterogeneous, recurrence, severity, weather

OPEN ACCESS

Edited by:
Michael John Gollner, University of Maryland, United States

Reviewed by:
Wei Tang, National Institute of Standards and Technology (NIST), United States
Alexis Cantizano, Comillas Pontifical University, Spain

****Correspondence:***
Yaping He
y.he@westernsydney.edu.au

Specialty section:
This article was submitted to Thermal and Mass Transport, a section of the journal Frontiers in Mechanical Engineering

Received: *01 February 2019*
Accepted: *23 April 2019*
Published: *21 May 2019*

Citation:
Douglas GB and He Y (2019) Design Bushfire Selection for Bushfire Protection in Adaptation to Global Warming. Front. Mech. Eng. 5:27. doi: 10.3389/fmech.2019.00027

INTRODUCTION

Bushfires (wildfires or forest fires) can be a more complicated phenomenon than other kinds of natural disasters. For example, unlike tsunami, earthquake or storms where only the natural force is at work, the contributing factors to bushfires include vegetation, weather, topography, and even human activities. Notwithstanding, bushfires possess some similar features when compared with some other natural hazards (such as floods, drought, and heatwaves) in that they are predominantly influenced by weather and climate conditions (Douglas et al., 2015; Steffen et al., 2017). Recent bushfire events in many parts of the world have given strong indications that the global warming is having an impact on the geographical location, frequency, and severity of such disasters (Norway Today, 2018; The Guardian, 2018).

The potential impacts of climate change on natural events such as heat waves, storms, floods and, particularly, bushfires have been the subject of many theoretical and empirical investigations (Kiern et al., 2006; Semenov and Stratonovitch, 2010; Fox-Hughes et al., 2014; Barbero et al., 2015; Ayar et al., 2016; Abatzoglou et al., 2017). These investigations have included the applications of global climatic models (GCM) and other models to predict future scenarios for developing climate change adaptation strategies (Hennessey et al., 2005).

At the international level, the Intergovernmental Panel on Climate Change (IPCC) met and agreed to its 5th Assessment Report which confirms and extends previous concern for global warming and increased losses from natural hazards, including bushfires (IPCC, 2014). In 2018, the IPCC issued its Special Report on Global Warming, warning that major changes in extreme events

were likely with temperatures up to and exceeding average increased temperatures of 1.5°C. These reports have given rise to concerns that climate change will have a significant impact on bushfire behavior (Steffen et al., 2018).

When considering the implications of climate change on bushfires, the trends in annual or seasonal frequency of fire and fire severity need to be accompanied by information on recurrence of fire weather. As such, climate change can be translated into changes in fire frequency and severity (Hennessey et al., 2005). These changes are correlated with fire danger indices that incorporate drought as a pre-conditioning factor, and temperature, relative humidity, and wind speeds as ambient conditions (Noble et al., 1980).

Traditional building design practice for bushfire protection has been relying on the so called prescriptive approach (e.g., AS3959, 2018). Even though performance based building regulations have been introduced in many countries in the world since the last quarter of the last century, very little consideration has been given to adaptation strategies to climate change so far as design for bushfire protection is concerned. Recognizing the challenges faced by performance based codes, the idea of risk-informed performance-based building codes was proposed by a number of scholars in recent years (Meacham and Van Straalen, 2018). The hierarchy of the risk-informed performance-based building code is a multi-tiered system which includes the performance criteria based on risk concept and the verification methods. Such a hierarchy gives rise to the need to: (a) establish acceptable risk criteria; and (b) develop appropriate risk assessment or verification methods.

Current risk based approaches consider climatic conditions as being invariant from the past, both spatially and temporally (AS3959, 2018). While climate models can be used to indicatively show that changes in fire weather are likely to occur, there has not been much discussion on verification methods that are ready for use by practitioners and engineers to incorporate the effect of climate change in their design practice for bushfire protection.

In this article, a risk based approach to design for bushfire protection is discussed. The concept of design bushfire is introduced as an analogy to design flood or design earthquake in terms of event of prescribed return period (or annual exceedance probability). The focus is then given to the selection of design bushfires incorporating the effect of climate change. The ultimate aim of the study is to assist in the development of appropriate verification methods for bushfire protection design in adaptation to the global warming.

In lieu of using the GCM, the current study is based on the analysis of historical fire weather data. A number of methods are employed to demonstrate the effect of climate change on fire weather which is characterized with a fire danger index and the associated fire intensity. One of these methods, namely the generalized extreme value (GEV) analysis is employed to establish the recurrence models for predicting the fire weather of given return period. To examine the impacts of the climate change, a moving GEV method is introduced, where the GEV is applied to a series of consecutive timeframes with fixed duration to reveal the changes in the control parameters of the recurrence models. The methods of analysis have been applied to the weather data records of a number of weather districts in the state of New South Wales in Australia for the period of 1972–2015.

Section Bushfire Weather and Global Warming of this paper presents a literature review of fundamental concepts of fire danger index, its correlation with bushfire severity, and design bushfire. The relevant building regulation and design standard for bushfire protection in Australia, as well as the previous studies on the effect of climate change on bushfires are also reviewed. Section Determination of the Impact of Climate Change describes the data and the method used in the current study. The results are presented in section Results. Section Discussion presents the application of the results and the regression analyses to the selection of 50-year recurrence value of fire danger index for determining the design bushfire conditions. The spatial uncertainty in the results is also discussed in this section, followed by conclusion in Section Conclusion. An error analysis and tabulated results are delivered in **Appendices A, B**, respectively.

BUSHFIRE WEATHER AND GLOBAL WARMING

Fire Danger Indices and Fire Severity

In many countries, bushfire behavior has been linked to various fire danger rating (FDR) systems, such as those in the USA, Canada, Portugal, and Australia (Sullivan, 2009). Extensive work has been undertaken to relate bushfire risk in Australia (Verdon et al., 2004), Canada (Cruz et al., 2003; Abbott et al., 2007; Beverly and Wotton, 2007), USA (Hardy and Hardy, 2007), and Europe (Fernandes, 2001; Good et al., 2008) to various fire danger index systems, and the correlations between such indices and fire intensity appear useful in determining fire severity.

In Australia, the Forest Fire Danger Index (FFDI) (Luke and Mcarthur, 1978) is commonly used as a measure of fire weather conditions. This index is a dimensionless parameter and is a function of multiple weather variables as shown in the following (Noble et al., 1980):

$$F = 2\exp[-0.45 + 0.987\ln(D) - 0.0345H + 0.0338T + 0.0234U_{10}] \quad (1)$$

where F stands for FFDI, D is drought factor, H is relative humidity, T is temperature (°C), and U_{10} is the mean wind speed (km/h) at the reference height of 10 m.

It has been well-established that house loss rate in terms of average loss per bushfire event is related to FFDI (Gibbons et al., 2012). The data presented in **Table 1** was extracted from Blanchi et al. (2010). This table illustrates that house losses are relatively rare at Fire Danger Rating below HIGH but increases significantly at VERY HIGH to CATASTROPHIC ranges. These results confirm that bushfire severity can be correlated to FFDI.

The bushfire severity factors such as forward rate of spread, fire intensity, and flame height can be correlated to FFDI by the following empirical equations (Byram, 1959; Noble et al., 1980; AS3959, 2018):

$$R = 0.0012FW_s\exp(0.069\theta) \quad (2)$$

TABLE 1 | House losses of some major bushfire events in Australia (1957–2009) (Blanchi et al., 2010).

Fire danger rating	FFDI range	No. of events	% of total events	No. of houses lost	% of total loss	Average loss per event
CATASTROPHIC	100+	8	14.8	5,319	64.4	665
EXTREME	75-99	9	16.7	1,181	14.3	131
SEVERE	50-74	27	50.0	1,163	14.1	43
VERY HIGH	25-49	9	16.7	589	7.1	65
HIGH	12-24	1	1.9	4	0.1	4
LOW-MODERATE	≤12	0	0.0	0	0.0	-
Total		**54**	**100.0%**	**8,256**	**100.0%**	**153**

$$I = HW_tR/36 \quad (3)$$

$$Z = (13R + 0.24W_t)/2 \quad (4)$$

where R is the rate of forward spread (kph), W_s is surface related fuel density (t/Ha) (i.e., surface, near-surface and elevated fuel, AS3959, 2018), W_t is total fuel density (including W_s, bark and canopy fuel), θ is slope in degrees ($-15^\circ \leq \theta \leq 20^\circ$), I is bushfire line intensity (MW/m), H the heat yield of fuel (MJ/kg), and Z is flame height (m). For a given design site, the topography information is known. Provided that the fuel density is also known, then the bushfire condition is predominantly determined by FFDI.

It is noted that historically the FFDI value was originally presumed to have an upper limit of 100 which corresponded to the deemed worst possible conditions for bushfire that occurred in the state of Victoria, Australia in 1939 (Sullivan, 2004). However, these conditions and the FFDI 100 limit were exceeded significantly on many occasions (Douglas et al., 2015). In practice, whole integers rather than fractional numbering are used (NSW Rural Fire Service, 2009). Fire agencies across Australia introduced a categorized FDR system to assist the public's perception of bushfire events. This rating system and the corresponding range of FFDI values are illustrated in the first two columns of **Table 1**.

Design Bushfire in Engineering Approach to Bushfire Protection

Determining the severity of a potential bushfire for land-use planning and construction practice purposes is crucial in the planning assessment processes (Douglas and Ellis, 2000). Property protection measures are related to the concept of "design bushfire" (Ramsay et al., 2006). A design bushfire is a reference bushfire condition against which bushfire protection strategies or engineering solutions are to be developed. The "design bushfire" can be considered as the dimensions and characteristics of a bushfire flame, its initiation, spread, and development, which arises from assumed weather conditions, topography, and fuel (vegetation) in a given regional setting. The design bushfire can therefore be used to determine consequences including radiant heat flux, sustained flame contact, and wind speeds arising from the assumed bushfire event (Douglas and He, 2017).

Obtaining the correct inputs for developing the design bushfire is therefore critical in considering the protection of life and property assets, including resident, and fire fighter safety, protection of homes, and other infrastructure and the need to balance environmental objectives.

Deterministic and empirical approaches to bushfire behavior modeling combined with fire engineering principles have been applied to determine defendable space for fire fighters and building protection in North America (Butler and Cohen, 1998; Gettle and Rice, 2002), in Portugal (Zárate et al., 2008), and in Australia (Douglas and Tan, 2005). These defendable space arrangements are contingent on an appropriate design bushfire.

Attempts have been made in the past to quantify suitable design bushfires based on a frequency distribution profile of fire weather. Andrews et al. (2003) considered the utilization of logistic regression and percentile analysis in describing severe weather. Blanchi et al. (2010) compared bushfire statistics in Australia from 1957 to 2009 with local meteorological conditions to determine conditions under which house loss was likely.

A major difficulty is in defining bushfire scenarios for design and assessment purposes. Inappropriate selections of design bushfire can result in either additional costs to the environment and construction, or the failure of the building systems to withstand the likely fire event. So the question arises, on what basis can the design bushfire be determined.

Risk Based Approach in Verification Method

Natural and man-made disasters often exhibit themselves as random events which cannot be predicted with high certainty (Coles, 2001). Regulations or codes for structural designs against flood and cyclonic wind disasters often use events with known likelihood or frequency as benchmarks. For example, annual exceedance probabilities are provided for structural provisions within the National Construction Code of Australia (NCC, 2019). This has led to the development of performance criteria for various construction arrangements, in the hope of supporting innovation, reducing costs, and improving productivity.

The implementation of performance based building codes, however, have not been without criticism and reservations. The qualitative or descriptive nature of the performance requirements are sometimes criticized for being subject to interpretations and being lack of quantifiable or verifiable performance requirements

and criteria (Almgren and Hansson, 2010). To address these concerns, verification methods have been introduced which aim to establish more quantitative approaches to design and construction practice. A recent development by the Australian Building Codes Board is the introduction of a verification method for bushfire protection design into the National Construction Code of Australia (NCC, 2019) in support of the performance requirements for construction in bushfire prone areas. This is seen as a significant advancement toward a risk informed performance based building code and the supporting verification methods (Douglas and He, 2017).

The performance requirement for bushfire protection can be found in Vols. 1 and 2 of the National Construction Code of Australia (NCC, 2019) and is not repeated herein. So as to meet this requirement, the new verification method (NCC, 2019), provides the acceptance criteria in terms of the probability of fire initiation of a building that is exposed to the bushfire conditions with prescribed recurrence. More specifically, the verification method GV5.1 states that fire ignition probability of a building should be <10% when it is exposed to design bushfire conditions with prescribed recurrence based on building importance. For a residential (Class 1) building, the annual exceedance probability is specified in Table G5.1 of the code as 1:50, with higher recurrence levels for other residential and vulnerable types of buildings (NCC, 2019).

The proposed ignition probability limit is essentially a benchmark for acceptable conditional failure probability. The prescription of the recurrence period of bushfire event in effect sets up a reference bushfire condition against which fire protection strategies or solutions are to be developed. This reference bushfire condition is referred as the design bushfire as discussed in the previous subsection.

Generalized Extreme Value Method for Selection of Design Bushfires

As can be seen in subsection Fire Danger Indices and Fire Severity, the fire severity parameters that are used in bushfire protection design are associated with fire weather. The selection of design bushfire conditions is reduced to the selection of appropriate fire weather, fuel, and topography. In accordance with GV5.1, it is eventually reduced to the determination of design bushfire conditions within the prescribed recurrence, or return period.

In statistical terms, the use of a return period (or annual probability of exceedance or APE) is an appropriate mechanism for determining design parameters for rare but extreme conditions (Coles, 2001). As such, the *extreme* value analysis can be used when considering planning for *extreme* weather events (Holmes and Moriarty, 1999). *Extreme* value analysis (EVA) allows, through regression analysis, the prediction of certain conditions for planning, and construction practice purposes. *Extreme* value analyses are used in determining flood outcomes, temperatures (Dury, 1972), storms (Holmes and Moriarty, 1999), and other natural phenomena.

Katz et al. (2005) noted the potential advantages of extreme value theory when modeling ecological disturbances. Such approaches can be combined with moving average methods to detect shifts among alternate states through non-linear methods (Ives and Dakos, 2012). Where data is of a longer duration (20 years or more), the GEV method was found to usually suffice (Coles, 2001).

Some work has been done recently in relation to fire weather or fire behavior in Australia at the extreme by Douglas et al. (2014). In their study, the prevailing extreme values were determined by comparing different statistical approaches at the 1:50 year recurrence with existing policy values based on previously limited data. However, this work assumed static climatic conditions.

Impact of Climate Change on Bushfires

It has already been ascertained by previous investigations (Hasson et al., 2008) that fire weather conditions, and hence fire behavior will alter in the future as the effects of climate change will become more pronounced over time. However, the possible extent of such changes has not been quantified. Increases in average temperature due to climate change may occur (Hasson et al., 2008) but do not directly indicate increased bushfire severity. Based on the McArthur bushfire behavior model (Noble et al., 1980), it is difficult to ascertain whether or not the recurrence of the EXTREME forest fire danger would differ significantly from the current range without a careful analysis of each variable used to determine FFDI (Hennessey et al., 2005; Lucas et al., 2007; Clarke et al., 2011).

Previous studies (Hennessey et al., 2005; Lucas et al., 2007) described changes in annual average cumulative FFDI (denoted ΣFFDI) under different climate change scenarios using. Hennessey et al. (2005) generated future fire weather data from GCM simulations of FFDI. They then studied the number of events per year which have FFDI $\leq$ 25 or FFDI $\leq$ 50 over the period of data and found that there were indeed shifts in both seasonal and annual threshold events, although the numbers vary across the NSW landscape. Lucas et al. (2007) combined the historical weather data and the predicted changes using GCM to study daily-average and monthly-average FFDI, annual average cumulative FFDI (or ΣFFDI), average number of days of FFDI $\leq$ 25, and average number of days of FFDI $\leq$ 50 for the period 1973–2007 and predicted increases in these parameters to 2020.

Changes using FFDI as an indicator in modeled scenarios provided some insight into possible shifts in fire weather. However, GCM is not generally accessible and operable by bushfire protection practitioners. It is expensive and time consuming to run and the results may contain large uncertainty. More importantly, straightforward application of GCM do not address climate change impacts in terms of recurrence events.

Summary

Climate change is almost certain to give rise to increased frequency of prolonged periods of adverse bushfire conditions and potentially increased severity of bushfires. The understanding of these changes alone is not sufficient for developing the bushfire scenarios for adaptation strategies in land use planning or construction. The question is how to

TABLE 2 | NSW weather stations selected in the current study.

Weather district no.	Weather district name	Weather station
2	North Coast	Coffs Harbor
3	Greater Hunter	Williamtown
4	Greater Sydney	Sydney
5	Illawarra /South Coast	Nowra
8	ACT	Canberra
13	North Western	Moree
15	Lower Central West	Dubbo
17	Eastern Riverina	Wagga Wagga

determine design bushfires, knowing that climate change is making impact on individual fire weather events?

Albeit having been used in the literature to predict future climate conditions, GCM does have limitations in engineering practice to develop design bushfire conditions for the risk based approaches. The historical climate data, in conjunction with a statistical approach to extreme weather events can be used to develop design bushfire scenarios. This approach is more robust than either cumulative FFDI or changes in number of threshold days which by its nature does not consider the distribution of weather data.

DETERMINATION OF THE IMPACT OF CLIMATE CHANGE

Data Source and Distributions

The dataset used in the current study was primarily obtained from Australia's National Historical Fire Weather Dataset program (Lucas, 2009) which covers 77 stations nationwide for the period beginning 1972 to the end of 2015. This dataset contains the evaluated daily FFDI and all the associated weather parameters.

Eight weather stations were identified in the state of New South Wales (NSW) of Australia to illustrate the geographical spread of the impacts of climate change on fire weather. The weather stations and associated weather districts are listed in **Table 2** and the geographic distribution of the eight weather stations is depicted in **Figure 1**.

As seen in Equation (1), FFDI is calculated using temperature, relative humidity, wind speed, and daily drought factor. The National Historical Fire Weather Database comprises calculated FFDI based on:

- Daily drought factor (1–10);
- 3:00 p.m. wind speed (km/h, 10 min average at 10 m height);
- 3:00 p.m. relative humidity (%RH); and
- Maximum daily temperature (°C).

Lucas (2009) has quantified some of the errors associated with this dataset, notably that wind speed may have errors associated with changes in instrumentation, changes in station location or changes in recording procedures. The 3:00 p.m. dataset is used due to the long term accumulation of weather station data, although improved technology will allow for a more accurate and continuous daily dataset in the future. Historically, data was collected between 1 and 8 times per day, with 9:00 a.m. and 3:00 p.m. being the most common. As such, the 3:00 p.m. data for relative humidity and wind speed will not necessarily identify the true daily maximum FFDI, which would be ideal for GEV analysis. The deviations in the input parameters from the worst case scenario may raise a concern in relation to the level of uncertainty associated with the calculated FFDI data. A detailed analysis is presented in **Appendix A** to estimate the level of uncertainty associated with the use of these four weather parameters in calculating FFDI. The result shows that the uncertainty in the recorded FFDI values is in the order of 20%. This is a quite significant error and aligns with the issues considered by Lucas (2009). However, it should be noted that, although drastic, this error consistently leads to under-estimate of FFDI and does not consider the correlations between the contributing variables. It can therefore be concluded that the data is suitable for climatic studies (Lucas, 2009).

Method of Analysis

As reviewed in Subsection Generalized Extreme Value Method for Selection of Design Bushfires, the extreme value analysis has now been adopted for risk based approaches in bushfire design. The collected daily FFDI over the data period of 44 years were subjected to GEV analysis to establish the relationship between FFDI and their return period. The method is based on the work of Makkonen (2006). A detailed description of the application of GEV method to historical weather data can be found in Douglas et al. (2014). From a sufficient length of data, a log-linear model of the form

$$F_r = a\ln r + b \tag{5}$$

is established, where r is the return period or recurrence, F_r is the forest fire danger index corresponding to the give recurrence r, parameters a and b are constants obtained from the log-linear regression of GEV result.

In order to reveal the changes in fire weather as the consequence of climate change, an attempt is made in the current study to apply the GEV analysis to the FFDI index subject to a moving 20-year data window over the data period of 1972–2015.

The moving window technique is a simple and widely used technique for local averaging or smoothing in data processing to identify some main features imbedded in otherwise noisy background. It is often referred to as the Savitzky–Golay filter (Chen et al., 2004). The advanced use of such technique can be found in Schulze et al. (2012) for spectral analysis. In the current study, this technique is extended to the GEV analysis whereby the recurrence value of FFDI is modeled on the basis of a relatively small (short) time window of data over a long period of data record. The window is then successively traversed through the entire data record period to reveal the changes in a given recurrence value.

For a finite length of the total data record, there is a trade-off between the window width and the accuracy of the GEV model. Generally speaking, the wider the window width, the better the GEV result. However, the wider window might smooth out the

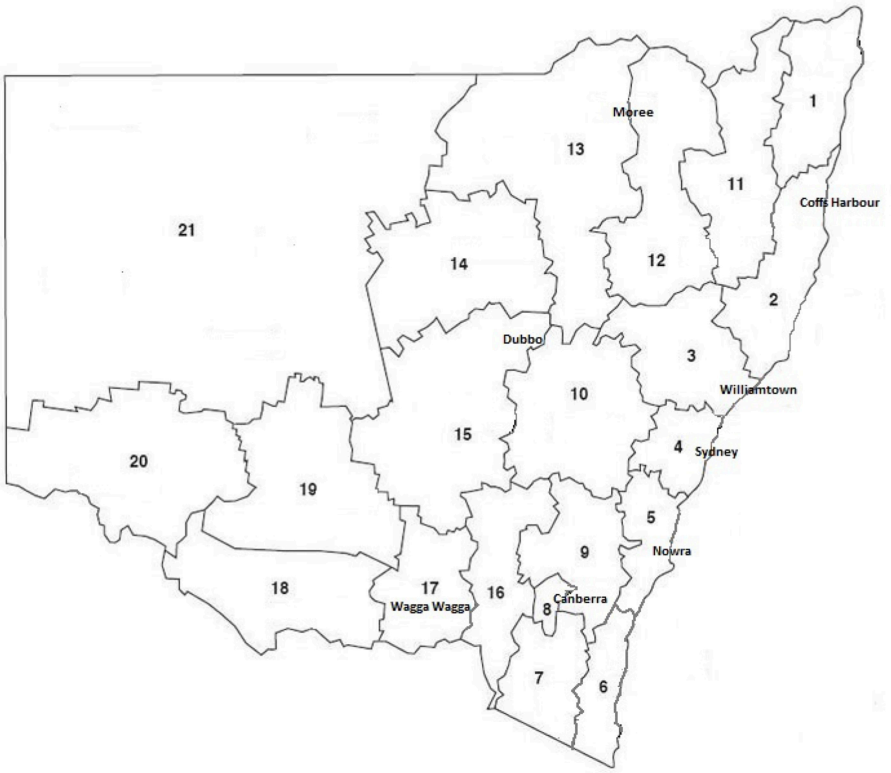

FIGURE 1 | New South Wales Fire Weather Districts and the locations of the eight weather stations involved in the current study. Adapted from NSW Rural Fire Service (2006).

imbedded variations in the change of recurrence value. The 20-year window is considered the minimal number of years required for reasonable accuracy for prediction of recurrence values (see Gumbel, 1958). This width is adopted in the current study.

The window is traversed consecutively year by year for 24 times to cover the entire data span of 44 years. A number of 24 predictive equations in the form of Equation (5) are obtained. These equations are then used to estimate the 50-year recurrence values of FFDI, or F_{50}, of which the variation may indicate the impact of climate change.

The outcome of the moving window GEV analysis is then fitted with three types of regression functions, namely power, linear and logarithm as given in Equations (6–8) to discern the trend of variation:

$$F_{50} = cx^d \tag{6}$$

$$F_{50} = cx+d \tag{7}$$

$$F_{50} = c\ln(x)+d \tag{8}$$

where c and d are regression constants, x is the period sequence number. For a given calendar year y, x is evaluated according to the following equation:

$$x = y - 1992 + 1 \qquad (y \geq 1992) \tag{9}$$

RESULTS

An analysis was undertaken for the weather data of each of the eight weather stations using the method described in section Method of Analysis. As an example, the daily forest fire danger index extracted from the data sources for Coffs Harbor (D2) for the period of 44 year are plotted in **Figure 2**. Three data windows among the 24 in total for the moving window GEV analysis are also indicated in this figure. The results of the recurrence forest fire danger index values for a sequence of moving window GEV analysis are presented in **Figure 3** showing windows 1, 5, and 13 in the series. The figure also contains the corresponding regression lines as in the form given in Equation (5) from which the F_{50} value is estimated.

Twenty-four F_{50} values are derived from the moving window GEV analysis for each weather district. The results are presented in **Figure 4** and tabulated in **Table B1** of Appendix B. Also included in **Figure 4** are the three regression lines, namely power, linear, and logarithm, of which the regression parameters are listed in **Table B2**.

As can be seen, the moving GEV assessment of Coffs Harbor (D2) fire weather data indicates that the 50-year recurrence FFDI values have increased from ∼70 in the first period to nearly 120 in the last. The significant jump occurred in the 10th period, or the period including the year 1983 when the historical Ash Wednesday fire event

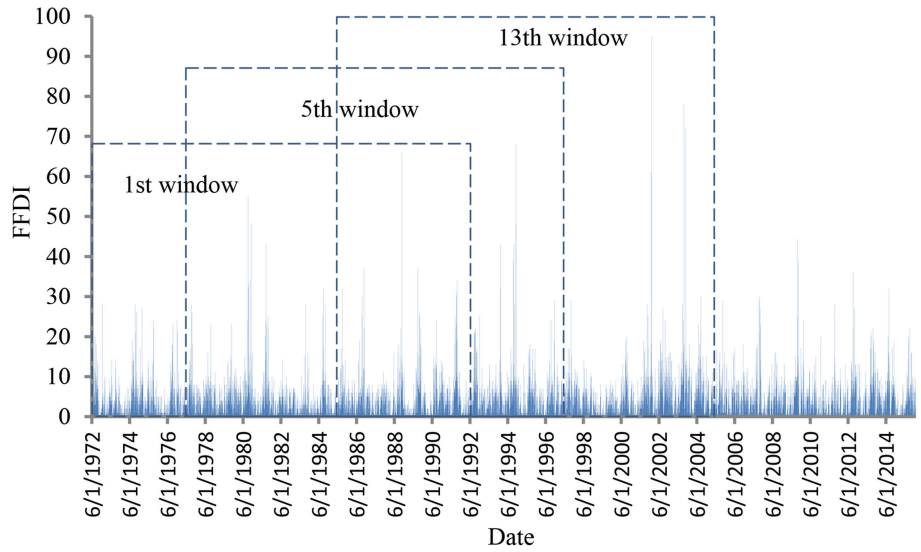

FIGURE 2 | Raw data of FFDI for Coffs Harbor (D2) over the period of 1972–2015 and the 1st, 5th, and 13th moving window for GEV analysis.

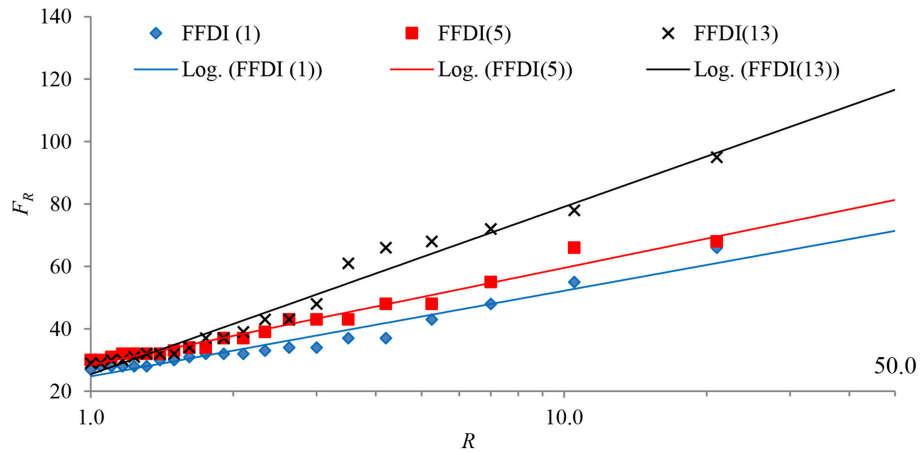

FIGURE 3 | Plots of recurrence FFDI and the log-linear model [Equation (5)] of the 1st, 5th, and 13th moving window for Coffs Harbor (D2).

took place (Blanchi et al., 2010). The increases in F_{50} for D13 and D17 also exhibit stepwise increments at different periods, respectively. The reason for this kind of behavior is not known.

It can also be discerned that the trend in F_{50} is increasing over the period for the majority of the sites. An exception to this can be found with the Williamtown (D3) weather station, where the trend is clearly declining. The F_{50} value of Nowra district (D5) is quite peculiar, showing a trace of bath-tab curve. These results indicate that the impact of climate change on fire weather conditions over a portion of the landscape in New South Wales is heterogeneous.

Figure 4 and **Table B2** also reveals that, except for districts 4 and 5, the three regression functions generally produce reasonable approximations of variations in F_{50}. On average, the power and logarithm regression functions produce more conservative and, perhaps, more reasonable, estimates of future variations than the linear regression.

DISCUSSION

Determination of Design Bushfire Conditions

To demonstrate the application of the GEV analysis and modeling results the selection of recurrence values of FFDI for determining future design bushfire conditions, a comparison between each of the three regression methods [see Equations (6–8)] is made in **Table 3** for the year 2015 and 2025. The parameters in **Table B2** were substituted into Equations (6–8) for each of the eight districts investigated.

Equation (7) should be used with caution, as linear regression may not be the most appropriate choice for some cases. For

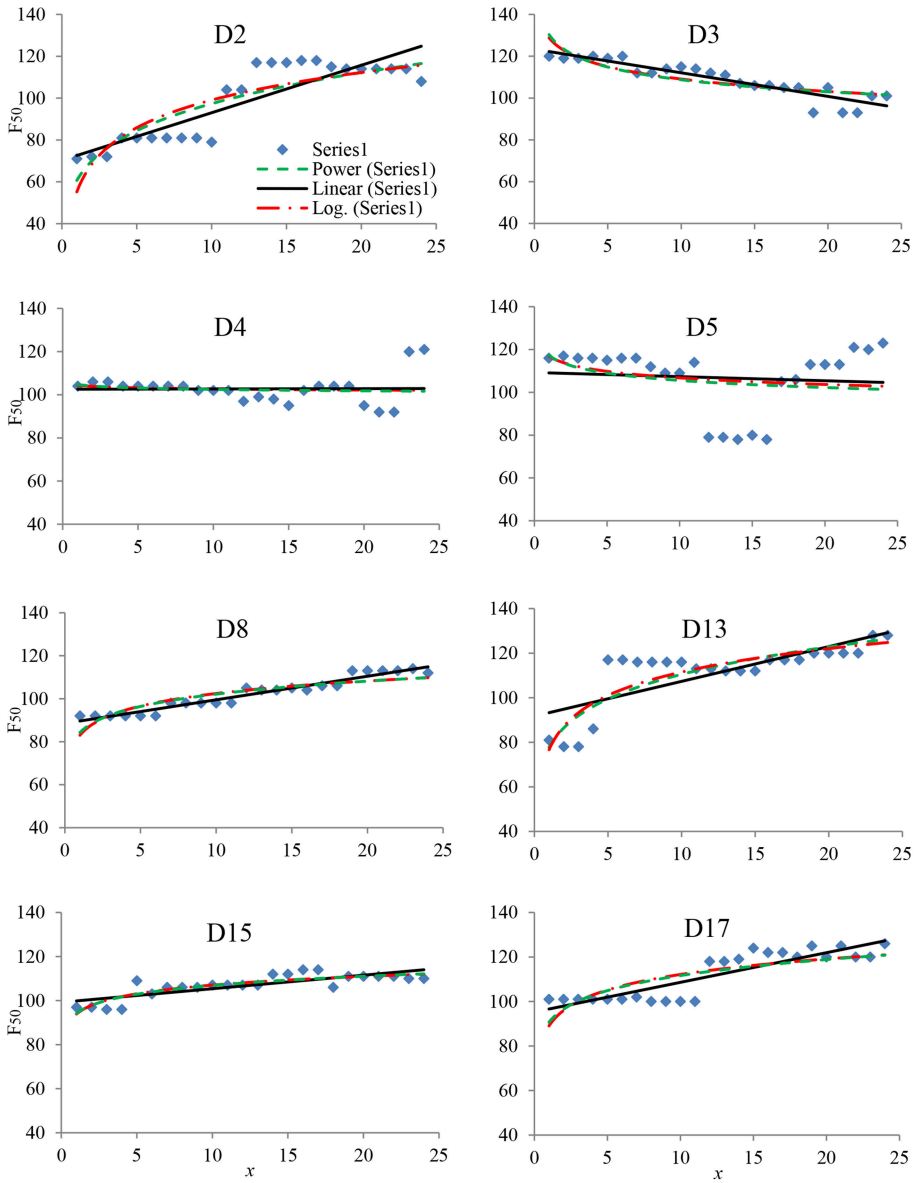

FIGURE 4 | Moving window GEV and regression results for weather stations in the eight districts.

example, the F_{50} for Coffs Harbor (D2) exhibits stepwise increments over the 24 window periods and remains almost constant for quite a long period since the last change as shown in **Figure 4**. The use of the linear regression could result in significant over prediction of the future variation in F_{50}. Equations (6, 8) however exhibit a lower level of deviation for all stations, either trending positively or negatively.

In the districts where correlation coefficient is small, the variation in the 50-year recurrence FFDI value is very irregular. The linear form was not a good choice of regression. In such a case, the overall F_{50} value may be considered for the same purpose. For example, no regular variation trend was discernible in the Sydney district (D4). Then the overall F_{50} of 116 as given in **Appendix B** can be used to determine the design bushfire condition. As for D5 (see **Figure 4**), the latest trend of variation could be taken into account in order to err on the conservative side for the selection of design bushfires.

Uncertainty

The accuracy of the result by the moving window GEV method depends on the total length of the available data and the width of the moving window. Generally, the longer of the total data period and the wider of the moving window are, the better the result. Since the total available data length was 44 years and the minimum 20-year window was used to estimate the F_{50} values, large uncertainties in the results may expected. Such uncertainties will be based on inference of the likelihood function and therefore consistent at the moving window selected (Coles, 2001).

TABLE 3 | Comparison between three regression methods for predicted F_{50} at eight weather stations.

Regression	Year	D2	D3	D4	D5	D8	D13	D15	D17
Log	2015	116	89	102	103	110	125	112	121
	2025	122	89	102	101	113	130	114	124
Linear	2015	125	96	103	105	115	129	114	127
	2025	147	85	103	103	126	145	120	141
Power	2015	117	80	102	101	110	126	112	121
	2025	125	78	101	100	113	133	114	125

It should be noted that spatial resolution of the data and the results need to be considered in the design application of the regression models. The limited numbers of weather stations within the landscape can only produce representative data and results for the entire weather districts. Variations within a district are expected as much as variations between districts, which have been revealed in the current study. The spatial distribution of weather stations can therefore also build in some level of uncertainty when considering the role of the design bushfire for a specific development proposal. It is recommendable that for a proposed development, the weather data, and the derived regression models from the nearest weather station be used to determine the recurrence FFDI values for design bushfire selection purpose.

A further issue associated with climate change is the potential impact on fuel accumulation and or curing. It should be noted that bushfire severity is determined not only by fire weather, but also by fuel load which may also be influenced by climate change (DECCW, 2010; Cary et al., 2012). The GEV study of the effect of climate change on fuel load and further on bushfire severity is not within the scope of the current paper.

CONCLUSION

This study has examined the impact of climate change on the forest fire danger index, which incorporates a range of weather parameters. The design bushfire concept in terms of fire weather conditions and the related fire severity was explained. A novel approach of moving window GEV analysis was applied to historical record of weather data to reveal the variation in the fire danger index with prescribed return period.

It has been found through the application of the GEV analysis to the data from limited number of weather stations selected across the NSW landscape, the impact of the climate change on the design bushfire with nominated return period is heterogeneous and geographically dependent. The trends predicted by the GEV results differ dramatically, from coastal locations to the inland, as well as latitudes from north to south of the State. The severity of the design bushfire would be aggravated in some weather districts by climate change but may be alleviated in other districts or neutral in others.

The moving window GEV analysis method not only revealed the heterogeneity in the impact of climate change on bushfire conditions, it also assisted in the selection of design bushfire conditions within the risk based framework to cater for protections against future bushfire attacks.

Based on the outcome of this research it is recommended that bushfire protection strategies for climate change adaptation should be flexible and take into account the local and regional conditions in order to generate economic benefit as well as provide safety for communities. Because of the limited length of available data and the minimum window width used in the current study, the results of moving window GEV may contain significant uncertainty. Future studies should, if possible, extend the data length and examine the sensitivity to window width.

The current study did not include the impact of climate change on fuel load on which bushfire severity is also dependent. It will be worth investigating this issue for the long term adaptation to climate change.

AUTHOR CONTRIBUTIONS

GD initiated the study on the topic. He contributed to the work by conducting literature review, collecting data, developing the methodology, and the implementation of it. He started the preliminary draft of the manuscript. YH contributed to the work by providing an outline. He oversaw the progress of the study, refined, and verified the methodology and its implementation. He contributed to the analysis of the results. He drafted 40% of the manuscript.

ACKNOWLEDGMENTS

The authors wish to acknowledge the constructive comments of the reviewers, which have led to significant improvements in the content of the paper. This work was funded in part by the Australian Research Council grant ARC-DP160103248.

SUPPLEMENTARY MATERIAL

The Supplementary Material for this article can be found online at: https://www.frontiersin.org/articles/10.3389/fmech.2019.00027/full#supplementary-material

REFERENCES

Abatzoglou, J. T., Kolden, C. A., Williams, A. P., Lutz, J. A., and Smith, A. M. S. (2017). Climatic influences on interannual variability in regional burn severity across western US forests. Int. J. Wildland Fire 26, 269–275. doi: 10.1071/WF16165

Abbott, K. N., Leblon, B., Staples, G. C., McLean, D. A., and Alexander, M. E. (2007). Fire danger monitoring using RADASAT1 over Northern Boreal Forests. *Int. J. Remote Sens.* 28, 1317–1378. doi: 10.1080/01431160600904956

Almgren, E., and Hansson, P. (2010). *Finding the Performance in Performance Based Codes-Lesson Learned From the Pre-Study for the Renewal of the Swedish*

Fire Safety Code due to 2010. 8th Performance-Based Codes and Safety Design Methods. Lund University, Sweden: Society of Fire Protection Engineers.

Andrews, P. L., Loftsgaarden, D. O., and Bradshaw, L. S. (2003). Evaluation of fire danger rating indexes using logistic regression and percentile analysis. *Int. J. Wildland Fire* 12, 213–226. doi: 10.1071/WF02059

AS3959 (2018). *Construction of Buildings in Bushfire-Prone Areas. Standards Australia; SAI Global*. Available online at: https://infostore.saiglobal.com/en-au/Standards/AS-3959-2018-122340_SAIG_AS_AS_2685241/

Ayar, P. V., Vrac, M., Bastin, S., Carreau, J., Déqué, M., and Gallardo, C. (2016). Intercomparison of statistical and dynamical downscaling models under the EURO- and MED-CORDEX initiative framework: present climate evaluations. Clim. Dyn. 46, 1301–1329. doi: 10.1007/s00382-015-2647-5

Barbero, R., Abatzoglou, J. T., Larkin, N. K., Kolden, C. A., and Stocks, B. (2015). Climate change presents increased potential for very large fires in the contiguous United States. Int. J. Wildland Fire 24, 892–899. doi: 10.1071/WF15083

Beverly, J. L., and Wotton, B. M. (2007). Modelling the probability of sustained flaming: predictive value of fire weather index components compared with observations of site weather and fuel moisture conditions. *Int. J. Wildland Fire* 16, 161–173. doi: 10.1071/WF06072

Blanchi, R., Lucas, C., Leonard, J., and Finkele, K. (2010). Meteorological conditions and wildfire-related house loss in Australia. *Int. J. Wildland Fire* 19, 914–926. doi: 10.1071/WF08175

Butler, B. W., and Cohen, J. D. (1998). Firefighter safety zones: A theoretical model based on radiative heating. *Int. J. Wildland Fire* 8, 73–77. doi: 10.1071/WF9980073

Byram, G. M. (1959). "Combustion of forest fuels," in *Forest Fire: Control and Use*, ed K. P. Davies (New York, NY: McGraw-Hill), 61–89.

Cary, G. J., Bradstock, R. A., Gill, A. M., and Williams, R. J., (2012), "Global change and fire regimes in Australia," in *Flammable Australia – Fire Regimes, Biodiversity and Ecosystems in a Changing World,* eds R. A. Bradstock, A. M. Gill, and R. J. Williams (Melbourne, VIC: CSIRO Publishing), 149–169.

Chen, J., Jonsson, P., Tamura, M., Gu, Z., Matsushita B., and Eklundh, L. (2004). A simple method for reconstructing a high-quality NDVI time series data set based on the Savitzky-Golay filter. Rem. Sens. Environ. 91, 332–344. doi: 10.1016/j.rse.2004.03.014

Clarke, H. D., Smith, P. L., and Pitman, A. J. (2011). Rural signatures of future regional fire weather over south-eastern Australia from global climate models. *Int. J. Wildland Fire* 20, 550–562. doi: 10.1071/WF10070

Coles, S. (2001). An Introduction to Statistical Modelling of Extreme Values. London: Springer-Verlag.

Cruz, M. G., Alexander, M. E., and Wakimoto, R. H. (2003). Assessing canopy fuel stratum characteristics in crown fire prone fuel types of western North America. *Int. J. Wildland Fire* 12, 39–50. doi: 10.1071/WF02024

DECCW (2010). *NSW Climate Impact Profile: The Impacts of Climate Change on the Biophysical Environment of NSW*. Sydney, NSW: Department of Environment, Climate Change and Water. Available online at: https://climatechange.environment.nsw.gov.au/Impacts-of-climate-change/2010-NSW-climate-impact-reporting

Douglas, G., and Ellis, P. (2000). *Integrating Land Use Planning and Construction Standards for Protection for Bushfires in New South Wales – A Model*. Christchurch: Bushfire 2000.

Douglas, G., and He, Y. (2017). *Moving Forward on a Verification Method for Bushfire Protection Under the National Construction Code*, *Quantify Fire Safety - Fire Australia 2017*. Australia Fire Protection Association. Available online at: http://www.fpaa.com.au/media/229666/d2-fse-p5-douglas.ppt.pdf

Douglas, G., He, Y., Yang, X., and Morris, E. (2015). "Construction practice and planning in bushfire prone environments," in *Research Proceedings of the Natural Hazards and Bushfire Cooperative Research Centre & AFAC Conference* (Adelaide, SA). Available online at: https://www.bnhcrc.com.au/events/2015-annual-conf

Douglas, G., He, Y. Yang, X., and Morris, E. C. (2014). "Use of extreme value analysis in determining annual probability of exceedance for bushfire protection design," in *Proceedings of the 11th International Symposium on Fire Safety Science*, ed P. Van Hees (Christchurch: International Association of Fire Safety Science; University of Canterbury), 1379–1392.

Douglas, G., and Tan, Z. (2005). *Integrating Site Assessment and Performance Planning Outcomes for Bushfire Prone Areas at Planning for Natural Hazards - How We Can Mitigate the Impacts?* University of Wollongong.

Dury, D. H. (1972). High temperature extremes in Australia. *Ann. Assoc. Am. Geogr*. 62, 388–400. doi: 10.1111/j.1467-8306.1972.tb00871.x

Fernandes, P. A. M. (2001). Fire Spread prediction in shrub fuels in Portugal. *Forest Ecol. Manage.* 144, 67–74. doi: 10.1016/S0378-1127(00)00363-7

Fox-Hughes, P., Harris, R., Lee, G., Grose, M., and Bindoff, N. (2014). Future fire danger climatology for Tasmania, Australia, using a dynamically downscaled regional climate model. Int. J. Wildland Fire. 23, 309–321. doi: 10.1071/WF13126

Gettle, G., and Rice, C. L. (2002). "Criteria for determining the safe separation between structures and wildlands," in *Forest Fire Research & Wildland Fire Safety*, ed D. X. Viegas (Rotterdam; Holland: Millpress), 18–23.

Gibbons, P., van Bommel, L., Gill, M., Cary, G. J., Driscoll, D. A., Bradstock, R. A. et al. (2012). Land management practices associated with house loss in wildfires. *PLoS ONE* 7:e29212.

Good, P., Moriondo M., Giannakopoulos, C., and Bindi, M. (2008). The meteorological conditions associated with extreme fire risk in Italy and Greece: relevance to climate model studies. *Int. J. Wildland Fire*. 17, 155–165. doi: 10.1071/WF07001

Gumbel, E. J. (1958). *Statistics of Extremes*. New York, NY: Dover Publications, 2004 reprint.

Hardy, C. C., and Hardy, C. E. (2007). Fire danger rating in the United States of America: an evolution since 1916. *Int. J. Wildland Fire* 16, 217–231. doi: 10.1071/WF06076

Hasson, A. E. A., Mills, G. A., Timbal B., and Walsh, K. (2008). *Assessing the Impact of Climate Change on Extreme Fire Weather in Southeast Australia*. CAWCR Techical Report 007, The Centre for Australian Weather and Climate Research.

Hennessey, K., Lucas C., Nicholls N., Bathols J., Suppiah R., and Ricketts, J. (2005). *Climate Change Impacts on Fire-Weather in South-East Australia*. Melbourne, VIC: CSIRO.

Holmes, J. D., and Moriarty, W. W. (1999). Application of the generalized Pareto distribution to extreme value analysis in wind engineering. J. Wind Eng. Ind. Aerodyn. 83, 1–10. doi: 10.1016/S0167-6105(99)00056-2

IPCC (2014). "Climate change 2014: synthesis report," in *Contribution of Working Groups I, II and III to the Fifth Assessment Report of the Intergovernmental Panel on Climate Change*, eds R. K. Pachauri and L. A. Meye (Geneva: IPCC), 151.

Ives, A. R., and Dakos, V. (2012). Detecting dynamical changes in nonlinear time series using locally linear state-space models. *Ecosphere* 3, 1–15. doi: 10.1890/ES11-00347.1

Katz, R. W., Brush, G. S., and Parlange, M. B. (2005). Statistics of extremes: modelling ecological disturbances. Ecology 86, 1124–1134. doi: 10.1890/04-0606

Kiern, A., Stewart, F., and Danielle, V. (2006). Climate variability in the land of fire and flooding rain. *Austr. J. Emerg. Manag.* 21, 52–56. Available online at: https://search.informit.com.au/documentSummary;dn=158193333195283;res=IELHSS

Lucas, C. (2009). On developing a historical fire weather dataset for Australia. Austr. Meteorol. Oceanogr. J. 60, 1–14. doi: 10.22499/2.6001.001

Lucas, C., Hennessey K., Mills G., and Bathols J. (2007). *Bushfire Weather in Southeast Australia: Recent Trends and Projected Climate Change Impacts*. Melbourne, VIC: CSIRO and Bushfire CRC.

Luke, R. H., and Mcarthur, A. G. (1978). Bushfires in Australia. Canberra, ACT: Australian Government Publishing Service.

Makkonen, L. (2006). Plotting positions in extreme value analysis. *J. Appl. Meteor. Climatol.* 45, 334–340. doi: 10.1175/JAM2349.1

Meacham, B. J., and Van Straalen, I. J. (2018). A socio-technical system framework for risk-informed performance-based building regulation. *Build. Res. Inf.* 46, 444–462. doi: 10.1080/09613218.2017.1299525

NCC (2019). *National Construction Code of Australia*, Vol. 1 and 2, Building Code of Australia. Canberra, ACT: Australian Building Code Board. Available online at: https://ncc.abcb.gov.au/ncc-online/NCC

Noble, I. R., Bary, G. A. V., and Gill, A. M. (1980). McArthur's fire-danger meters expressed as equations. Austr. J. Ecol. 5, 201–203. doi: 10.1111/j.1442-9993.1980.tb01243.x

Norway Today (2018). *Nearly 300 Forest Fires So Far This Year*. Available online at: http://norwaytoday.info/news/nearly-300-forest-fires-far-year/ (accessed 29 April, 2019).

NSW Rural Fire Service (2006). *Planning for Bush Fire Protection*. Sydney, NSW.

NSW Rural Fire Service (2009). *Fire Danger Ratings* [Brochure]. Available online at: https://www.rfs.nsw.gov.au/__data/assets/pdf_file/0005/9428/Fire-Danger-Ratings-Factsheet.pdf (accessed 29 April, 2019).

Ramsay, G.C., Wynn-Jones M., Wood C., Douglas G., and Robeson P. (2006). "The Australian bushfire safety engineering guidelines," in *Proceedings of Fire Safety Engineering Conference* (Gold Coast, QLD: Society of Fire Safety).

Schulze, H. G., Foist, R. B. Okuda, K., Ivanov, A., and Turner, R. F. B. (2012). A small-window moving average-based fully automated baseline estimation method for Raman spectra. Appl. Spect. 66, 757–764. doi: 10.1366/11-06550

Semenov, M. A., and Stratonovitch, P. (2010). Use of multi-model ensembles from global climate models for assessment of climate change impacts. Clim. Res. 41, 1–14. doi: 10.3354/cr00836

Steffen, W., Hughes, L., Alexander, D., and Rice, M. (2017). Cranking Up the Intensity: Climate Change and Extreme Weather Events. Climate Council. Available online at: https://www.climatecouncil.org.au/resources/cranking-intensity-report/

Steffen, W., Rice, M., Hughes, L., and Dean, A. (2018). The Good, the Bad and the Ugley: Limiting Temperature Rise to 1.5°C. Climate Council. Available online at: https://www.climatecouncil.org.au/resources/limiting-temperature-rise/

Sullivan, A. L. (2004). *Nature of Severe Fire Events*. Client Report for Fire Management Unit, Department of Urban Services ACT Government (CSIRO: Canberra, ACT).

Sullivan, A. L. (2009). Wildland surface fire spread modelling, 1990-2007. Part 2: Empirical and quasi-empirical models. *Int. J. Wildland Fire* 18, 369–386.

The Guardian (2018). *Sweden Calls for Help as Arctic Circle Hit by Wildfires*. Available online at: https://www.theguardian.com/world/2018/jul/18/sweden-calls-for-help-as-arctic-circle-hit-by-wildfires (accessed December 5, 2018).

Verdon, D. C., Kiem, A. S., and Franks, S. W. (2004). Multi-decadal variability of forest fire risk-eastern Australia. *Int. J. Wildland Fire* 13, 165–171. doi: 10.1071/WF03034

Zárate, L. J., Arnaldos, J., and Casal, J. (2008). Establishing safety distances for wildland fires. Fire Safety J. 43, 565–575. doi: 10.1016/j.firesaf.2008.01.001

Conflict of Interest Statement: The authors declare that the research was conducted in the absence of any commercial or financial relationships that could be construed as a potential conflict of interest.

NOMENCLATURE

a, b	constants in the log-linear GEV regression model
c, d	constants in regression models for moving window GEV analysis
D	is drought factor
H	relative humidity (%)
I	bushfire line intensity (MW/m)
R	rate of forward spread (kph)
r	recurrence year
r^2	correlation coefficient
T	temperature (°C)
U_{10}	mean wind speed at the reference height of 10 m (m/s)
W_S	surface fuel density (t/Ha)
W_t	total fuel density (t/Ha)
x	moving window sequence number
y	calendar year
Z	flame height (m)
Greek	
ΔH	heat yield of fuel (MJ/kg) (heat of combustion)
Θ	slope in (°)

frontiers in Mechanical Engineering

ORIGINAL RESEARCH
published: 14 June 2019
doi: 10.3389/fmech.2019.00032

Firebrand Generation From Thermally-Degraded Cylindrical Wooden Dowels

Sara E. Caton-Kerr[1], *Ali Tohidi*[2*] *and Michael J. Gollner*[3]

[1] Jensen Hughes, Baltimore, MD, United States, [2] One Concern Inc., Palo Alto, CA, United States, [3] Department of Fire Protection Engineering, University of Maryland, College Park, MD, United States

During wildland fires, firebrands form once they break off of burning vegetation or structures. Many are then lofted into the fire plume where they are transported long distances ahead of the fire front, igniting new "spot" fires as they land. To date, very few studies have been conducted on the breakage mechanism of thermally-degraded vegetative elements. Knowledge of these mechanisms is needed to feed mathematical models of firebrand transport from traditional wildfires as well as those that spread into communities. First, a framework to understand the behavior of thermally-degraded wooden elements under simultaneous external loading is presented. A set of experiments were designed such that cylindrical wooden dowels of different species are exposed to different heating conditions similar to wildland fires, in order to model the breakage mechanisms of these elements in the absence of wind. The thermally-degraded elements are subjected to the three-point bending test to obtain the mechanical response of the materials after combustion. Assuming Hookean Orthotropic behavior for combusted dowels, dimensional analysis of the results reveals that the ultimate strength of the dowels is affected by the recoverable elastic strain during loading, which is found to occur under two distinct regimes. These results are not only important for better understanding of the breakage mechanisms but also are advantageous for developing a failure theory of thermally degrading wooden elements under simultaneous wind loading conditions.

Keywords: firebrand, wildfire, thermal-degradation, wildland-urban interface, dimensional analysis

OPEN ACCESS

Edited by:
Guillermo Rein,
Imperial College London,
United Kingdom

Reviewed by:
Jie Ji,
University of Science and Technology of China, China
Pedro Reszka,
Adolfo Ibáñez University, Chile

***Correspondence:**
Ali Tohidi
tohidiarchives@gmail.com

Specialty section:
This article was submitted to Thermal and Mass Transport, a section of the journal Frontiers in Mechanical Engineering

Received: *27 November 2018*
Accepted: *22 May 2019*
Published: *14 June 2019*

Citation:
Caton-Kerr SE, Tohidi A and Gollner MJ (2019) Firebrand Generation From Thermally-Degraded Cylindrical Wooden Dowels. Front. Mech. Eng. 5:32. doi: 10.3389/fmech.2019.00032

INTRODUCTION

Over the past few decades, wildland fires have been increasing in size, frequency, and severity (Caton et al., 2016; Balch et al., 2017). These fires result in many large-scale disasters, in particular at the Wildland-Urban Interface (WUI), where human development and unoccupied land intermingle. This trend is projected to increase due to fire management policies, an increase in land development adjacent to wildlands, and climate change (Howard, 2014; Tohidi, 2016; Tohidi and Kaye, 2017a). In order to improve land development and wildfire management policies, map the risks from wildfires, and improve the resilience of WUI communities, it is imperative to understand and model the mechanisms by which fires ignite communities and pose serious threats to people, properties, infrastructure, and ecosystems.

Three pathways for wildland fire spread and ignition in WUI communities have been identified. These include direct flame impingement on fuel sources, radiation, and firebrand showers. Firebrands are combusting pieces of vegetation or structural elements that break off of burning

elements during wildfires or other large conflagrations. During many of these fires, a large number of firebrands are formed creating a "shower" of brands lofted into the fire plume. These lofted firebrands travel downwind and upon landing eventually ignite spot fires far ahead of the main fire front (Koo et al., 2010; Tohidi and Kaye, 2017a,b) (**Figure 1**). Investigations of several past WUI fires have revealed that firebrand showers are often responsible for more than half of the reported ignitions (Manzello et al., 2008; Caton et al., 2016).

Among the three phases important for firebrand showers: generation, transport and ignition, firebrand transport has received the most attention both experimentally and numerically (Albini, 1979; Sardoy et al., 2007; Tohidi and Kaye, 2017b,c). Numerous studies have collected data on the general characteristics of firebrands, i.e., the mass, surface area, and shape, that are formed from trees (Manzello et al., 2006a, 2008, 2009, 2007a; Mell et al., 2009), structural elements (Suzuki et al., 2012a,b), and during small prescribed fires (El Houssami et al., 2016). Studies on the ignition of fuel beds and some structural components have also been reported (Manzello et al., 2006b; Hadden et al., 2010), however very few works on the actual formation processes of firebrands from thermally-degraded vegetative elements can be found in the literature (Barr and Ezekoye, 2013; Tohidi et al., 2015); (Chen et al., 2017).

Barr and Ezekoye (2013) proposed a thermo-mechanical breakage model for firebrands formed from a fractal tree. Later, Tohidi et al. (2015) presented a mechanical break-off model for firebrand formation from cylindrical twigs and tree branches with relatively high aspect ratios, i.e., length over diameter ($\eta = L/D$). Chen et al. (2017) also recently investigated, both experimentally and numerically, the burning rate and burning lifetime of wooden particles of different ellipsoid shapes and, similar to Tohidi et al. (2015) concluded that the aspect ratio of the elements is an important factor in material failure. Although findings from these studies lay the foundation of break-off analysis, the effects of thermal-degradation of the material under external loading is not directly addressed.

Therefore, the present study focuses on the behavior of thermally-degraded cellular solids (wooden elements) under subsequent external loading. With the lack of current knowledge in the area, this work is meant to propose a framework and a model to understand the behavior of thermally-degraded wooden elements with a cylindrical shape under external loading such as wind-induced drag. Beyond its importance in wildland and WUI fires, wood is the most widely used structural material (Gibson and Ashby, 1999), however there are few studies on the behavior of thermally-degraded wooden elements under external loading. After a review of the processes applied to this problem, a series of experiments are presented which capture the effects of thermal-degradation on failure mechanisms of wooden dowels that are exposed to flames and subsequently subjected to external loading. Utilizing the collected data during experiments, a dimensional analysis is conducted on the parameter space. The results of the scaling analysis suggest that there are two distinct failure regimes dominating the breakage and ultimately the formation of firebrands from thermally-degraded wooden elements.

FORMATION MECHANISMS (EVOLUTION) OF FIREBRANDS

The mechanisms that lead to firebrand formation from wooden elements may be related to the physical properties of the materials both prior and after thermal-degradation. Previous studies have proposed mechanical break-off models which relates the physical properties to the failure mechanism of the samples. For instance, Barr and Ezekoye (2013) report a linear correlation between the flexural stress (corresponding to the critical fracture load) and the density of pyrolyzed firebrands (wooden cylinders) in three-point-bending tests. This is similar to Easterling et al. (1982) results from balsa wood samples, where the collapse stress (σ_L^c) was found to be linearly proportional to the relative density of the wood,

$$\sigma_L^c \propto \left(\frac{\rho}{\rho_s}\right). \tag{1}$$

Here, σ_L^c is the stress recorded at the point of collapse in the longitudinal direction (parallel to the grain), ρ is the density of the wood species, and ρ_s is the density of the wood cell-wall material. Following this, Tohidi et al. (2015) assumed that failure occurs once the distortion energy of the wood from bending moment-induced shear exceeds the yield energy of the wood. This is assuming the maximum allowable stress of the wood sample remains constant during the generation process. While this is a simplified mechanical model, decoupled from combustion effects, it incorporates the effects of mass in addition to drag forces due to vertical and horizontal velocities in the fire plume to calculate the bending moments of tree branches. A non-dimensional parameter was also introduced that quantifies the relative importance of firebrand weight and vertical drag on the bending moment that connects individual branches to the main element. Using this parameter, it was shown that drag-driven (wind-driven) firebrand formation is the dominant formation mechanism and that firebrands with large aspect ratios ($\eta > 3$) are more likely to form and be lofted through the fire plume. These results are consistent with experimental observations from burning trees by Manzello et al. (2007b). In addition, results presented by Chen et al. (2017) support previous models as it concludes that the larger aspect ratio firebrands decompose faster, which makes them more susceptible to failure due to external loading.

The micro-structure of wood plays a critical role in its physical degradation and failure (Gibson and Ashby, 1999). At fine scales, wood is a cellular composite with different geometric configurations that depend on the type and species of the wood. Generally, wood species can be categorized as hardwoods (dense) and softwoods (light) (Easterling et al., 1982). Hardwoods are deciduous angiosperms with pores and vessels in their micro-structure, whereas softwoods are gymnosperms (conifers) that do not have pores and vessels (Dinwoodie, 2000). In angiosperms (hardwood), more than 90% of the wood is aligned in the longitudinal direction, whereas in gymnosperms (softwoods), this cell distribution varies between 80 and 90%. The rest of the material is distributed through rays in radial and tangential

FIGURE 1 | Schematic of a firebrand shower scenario in the wildland-urban interface (WUI); excerpted from Tohidi and Kaye (2017c) with permission.

directions, which implies a high degree of anisotropy in wood structure (Dinwoodie, 2000). **Figure 2** illustrates a typical wood structure from a full tree down to the micro-scale structures within. While the behavior of composite or tapered wood samples are also of interest in firebrand formation, their physical and chemical properties might be different and are not included in this work. This also holds true for samples with a shell-type geometry, such as tree bark, although the introduced framework may be applicable to their study in the future.

A framework for understanding firebrand formation is first presented here, as such a description does not yet exist in the literature. The process is viewed in three phases which occur across different scales. First, a thermo-mechanical instability (buckling) develops at the micro-scale, leading to crack formation. Second, a series of physiochemical degradation processes that involve pyrolysis and oxidation occurs through which the material losses its structural integrity, and finally thermo-mechanical break-off due to external loading, most likely via wind or body forces such as gravity occurs at the macro-scale. In a real scenario, these three phases occur sequentially or, more likely, simultaneously depending on the intensity of heat exposure and mechanical loading scenarios.

At the micro-scale, natural wood is a fiber-reinforced composite made up of crystalline cellulose fibers embedded in a matrix of (amorphous) hemicellulose and lignin (Easterling et al., 1982; Gibson and Ashby, 1999) (see **Figure 2**). Previous studies, i.e., Gibson and Ashby (1999), Easterling et al. (1982) and Ashby (1983) have shown that the material's density, dimensions, and shape of the cell walls at the microscale determine the anisotropy and mechanical properties of the wood in macroscale (RTL coordinates), that is the modulus of elasticity, bending, buckling, plastic collapse, and fracture mechanisms (Easterling et al., 1982; Ashby, 1983; Gibson and Ashby, 1999). If the samples of wood are extracted at sufficient distance from the pith where the curvature of the growth rings are relatively small (i.e., a large radius), it is reasonable to assume that wood in the tangential (T) and radial (R) directions is orthotropic, i.e., $E_L \propto \rho/\rho_s$, $E_{RT} \propto (\rho/\rho_s)^3$, $\nu_{TL} = \nu_{RL} \approx \mathcal{O}(0.01)$, and $\nu_{TR} = \nu_{RT} \approx \mathcal{O}(0.5)$ (Easterling et al., 1982; Gibson et al., 1982) where E is the module of elasticity, ν is Poisson's ratio, and subscripts show the directions in RTL coordinates system. This is consistent with the fact that, as a tree grows, pores and vessels in the outer layers (latewood) get smaller relative to the ones in the center (earlywood) (Dinwoodie, 2000). The longitudinal direction (L) would be different as the microfibrils of cellulose in the cells are mostly aligned in the L-direction and prismatic cells are stiffer under tension and compression in the L-direction in relation to bending in the R and T directions. Other factors such as age and moisture content play an influential yet secondary role on the mechanical properties of the wood.

It should be noted that the orthotropic assumption could be violated in this study due to the small diameter of samples used. However, samples are oven-dried and deliberately chosen such that the grains are aligned with the longitudinal direction (length of the samples). Therefore, as demonstrated in the experimental results, the differences between physical properties in the longitudinal direction compared to the ones in the radial/tangential direction are significant, which suggests that the orthotropic assumption is still valid and appropriate. For a detailed description of the mechanical properties, deformation, and behavior of wood, refer to either Gibson and Ashby (1999) or Dinwoodie (2000). Having reviewed the micro-structure of wooden elements, a three-phase thermal-degradation mechanism can now be described.

Phase I: Thermo-Mechanical Instability (Buckling)

Burning cellulosic materials, such as wood, forms a layer of char that significantly reduces heat conduction to virgin wood at the inner layers and subsequently reduces the burning rate of the uncharred material. However, the charred layer may shrink and crack, which notably affects the pyrolysis and oxidation of the sample material (Bryden and Hagge, 2003; Li et al., 2014). It was initially thought that pyrolysis and oxidation were the primary mechanisms of crack formation for heat-exposed wood samples. However, recent work by Baroudi et al. (2017) showed that, due to a global thermo-mechanical instability in the heat-exposed layer at temperatures below the pyrolysis temperature $\left(T_p \approx 573\,^{\circ}K\right)$, macro-crack patterns are established before physiochemical processes dominate.

External heating of wood samples, either through radiation or direct flame exposure (convection), not only boils entrapped water within the virgin wood, but also leads to the transformation of some of the chemical components of the material to gases (pyrolysis). Accumulation of the water vapor and gases builds

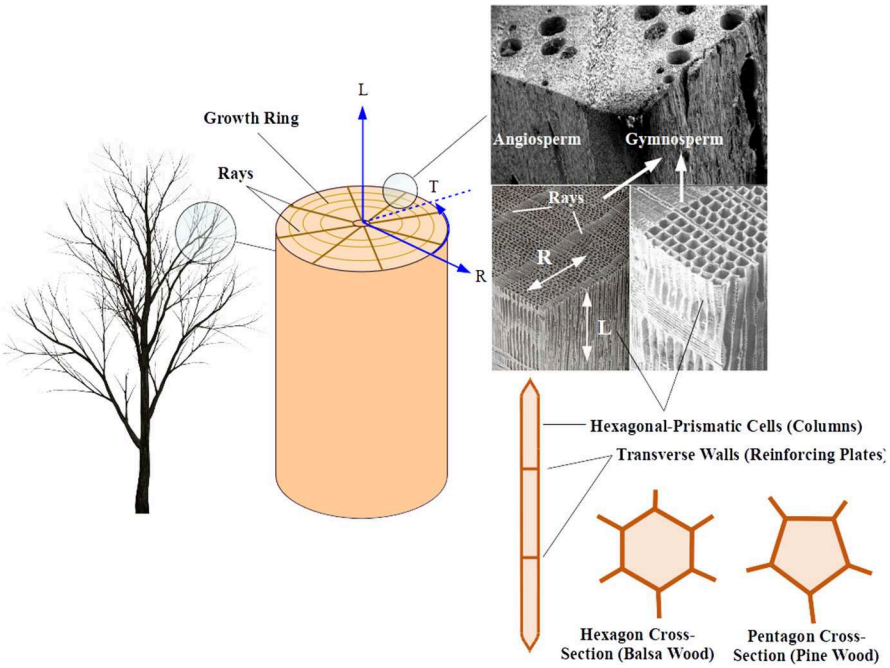

FIGURE 2 | Schematic of wood structure at different scales; shown are the customary coordinates aligned with rays, growth rings and fibers (grain), i.e., Radial, Tangential, and Longitudinal (RTL), along with a Scanning Electron Microscopy (SEM) image of typical angiosperm and gymnosperm wood species, here, Pinus and Balsa wood. The SEM images show the general micro-structure of the hardwood (top) and softwood (bottom) which are, respectively, excerpted from **Wikipedia** and raw materials of Koch (1972a,b).

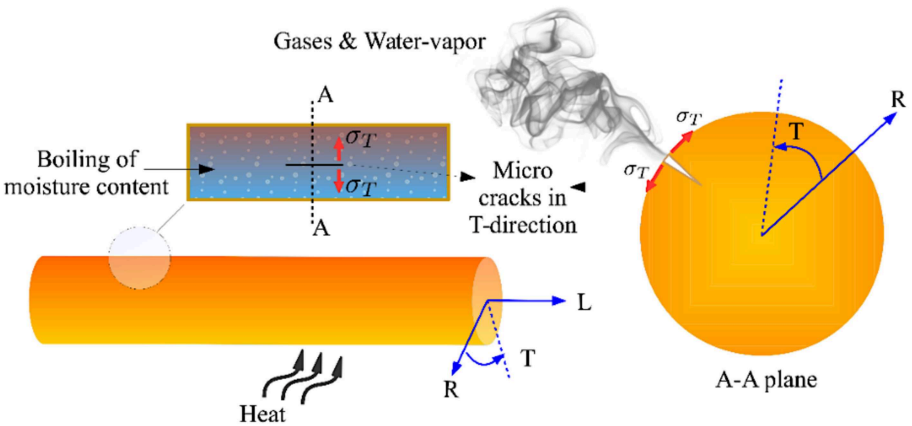

FIGURE 3 | Schematic of the evolution of micro-crack patterns through the heat-exposed wooden material.

up a hydrostatic pressure inside the material and increases the internal pressure, shown illustratively in **Figure 3**.

As the internal hydrostatic pressure increases, preliminary micro-cracks evolve in the tangential direction, eventually leading to the rupture and exit of gases, shown in **Figure 3**. This is expected as the tangential moduli (E_T) of the wood varies with the cube of the relative density as opposed to the linear relation of E_L with relative density; wood is a much stronger and stiffer material in the longitudinal direction than the transverse (tangential/radial) direction (Easterling et al., 1982; Ennos and Van Casteren, 2010). This is partly due to the fact that more than 80% of the microfibrils in the cell walls lie along the longitudinal direction, which makes the cell walls stiffest in that direction (Mark, 1907; Dinwoodie, 2000), and partly due to the prismatic shape of the cell walls that are stiff axially and less stiff transversely (Gibson and Ashby, 1999). Depending on the age of the wood, its moisture content, and species type, this process is likely to continue even at the macro-scale and leads to a crack in the longitudinal direction. In addition, after release of water vapor and gasses the material shrinks due to lower external ambient

pressure which increases the opening of micro-cracks. As shown in **Figure 4**-right, the evolution of micro and macro cracks on the surface of the heat-exposed layer not only generates a temporary path for the discharge of gases and water vapor, but also induces a negative pore pressure which may pull the flame sheet closer to the wood surface (Li et al., 2015). After the release of water vapor and gases from the sample and generation of a negative pressure field, the material starts to shrink at the micro-scale, exacerbating the effects of micro-cracks.

In addition to the previously-described effects, the negative-pressure increases the heat feedback from the flame to the fuel surface and amplifies thermomechanical effects. With persistent heat exposure, wood enters a rubber-like state and softens as the temperature exceeds the sample's glass transition temperature; here denoted by T_g. For dry wood with 10% moisture content, $T_g$is about 373 K, which is well-below the pyrolysis temperature of the wood (Salmén, 1984, 2004; Bažant, 1985; Antoniow et al., 2012; Baroudi et al., 2017). Because wood is an elasto-viscoplastic natural composite consisting of cellulose and hemicellulose-lignin matrices, e.g., polyermic materials, the elasticity modulus in all directions decreases around close to the glass transition temperature, while the thermal expansion coefficient of the wood increases dramatically (Li et al., 2016; Baroudi et al., 2017). This behavior induces substantial thermal stresses on the surface of the heat-exposed layer (hot-layer) before the formation of any char layer (Baroudi et al., 2017; Tohidi et al., 2017). Baroudi et al. (2017) showed that the thermal stresses, indicated as σ_T in **Figure 4**-left, are due to resistance against thermal expansion from the cold elastic sublayer (virgin wood). Assuming a thin-plate approximation for cases when $T_g < T < T_p$ and utilizing the Kirchhoff-Love theory of plates (Ventsel and Krauthammer, 2001; Li et al., 2016; Baroudi et al., 2017), it can be shown that by increasing thermal stresses, buckling occurs during transition from a membrane bi-axial state (flat plate) to a post-critical membrane and bending state (wrinkle-shaped plate), see **Figure 4**-left. At nodes of the buckled plate in a post-critical state, principal tension stresses exist which may lead to the development of macro-crack patterns perpendicular to the grains (Baroudi et al., 2017) as well as elongating and deepening existing cracks. Importantly, macro-crack patterns appear to emerge before char formation (Baroudi et al., 2017). **Figure 5** shows evidence of the development of global macro-crack patterns on birch dowels exposed to a propane flame at different times in this study; the experimental methods shall be discussed in section Experimental Methodology. Concepts of this framework may apply to shell-type wooden elements, e.g., tree bark, however this is beyond the scope of this study.

Phase II: Physiochemical Processes (Pyrolysis and Oxidation)

During pyrolysis, elevated temperatures initiate reactions within the organic material that changes its chemical composition and primarily forms char (Turns, 2000). Several studies (Ragland et al., 1991; Spearpoint and Quintiere, 2001; Haas et al., 2009; Liu et al., 2013; Sedighi Gilani et al., 2013; Li et al., 2016), however, have shown that the micro-structure of charred wood has a cellular form and wood charring due to pyrolysis does not change the micro-structure of the wood. Despite the fact that a consensus on this behavior does not exist, Hagge et al. (2004) argues that this is primarily due to reconstruction of chemical bonds and carbon atom connections. Thermal decomposition under pyrolysis transforms the material to char which produces a considerable amount of gas and leaves behind a porous media (Shen et al., 2009; Li et al., 2016). This porous media shrinks considerably under ambient pressure. Non-uniform shrinkage may lead to the generation of internal stress and, subsequently, unbalanced penetration of developed cracks in previous phases through the affected (char) layer; see **Figure 5**. As pyrolysis transforms a wooden element into a porous medium, its surface density and subsequently its stiffness will significantly decrease. Hence, the combined effects of the stress concentration at the tip of the already developed cracks (see **Figure 4**-right) and loss of structural stiffness (integrity), help the cracks gain sufficient depth through the charred layer. Once these macro-cracks or fissures are established, their number and path generally does not change (Li et al., 2016). It is also shown that the length of the crack is directly proportional to the square root of the heating time (Li et al., 2016). This is consistent with the findings of Nguyen et al. (2017) on crack morphology, where it is shown that short cracks develop after long fissures are established. Eventually, short and long cracks converge and, so long as a heat source exists, pyrolysis continues until full degradation of the wooden element's cross section.

With the presence of ambient oxygen, oxidation of the surface material also occurs, during which the surface of the solid material reduces without a significant change in density and remaining strength (Barr and Ezekoye, 2013). This process is associated with the formation of oxides from oxygen molecules (formation of ash over the charred layer). Continuation of pyrolysis and oxidation leads to the full thermal degradation of the material. As a result, established macro-cracks penetrate throughout the entire depth of the material thickness and cause brittle failure/break-off from the main wooden branches that are not yet fully degraded (Tohidi et al., 2017).

Phase III: Presence of External Loading or Constraints

While thermal degradation of the wooden elements alone can cause failure, during a typical fire scenario external loading of the elements will also contribute to failure. External loading is often applied due to a buoyancy-driven updraft flow in the fire plume, wind or entrainment-driven horizontal flow, and the weight of the wooden branches. These are considered in a simple mechanical break-off model by Tohidi et al. (2015). In a real fire scenario, the flame exposure and consequently heat conduction are not uniform throughout heated samples. The resulting temperature gradient leads to non-uniform thermal expansion and compression, as shown in **Figure 6**.

The thermal effects due to this temperature gradient will be manifested as either internal stresses, if the element is restrained, or displacement, if the element is unrestrained (Usmani et al., 2001). Most tree branches and twigs can be considered cantilever

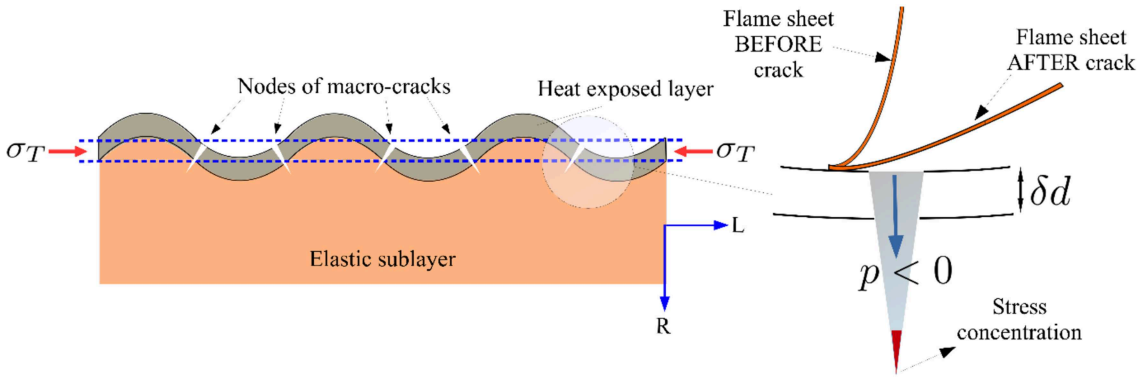

FIGURE 4 | Development of global macro-crack patterns.

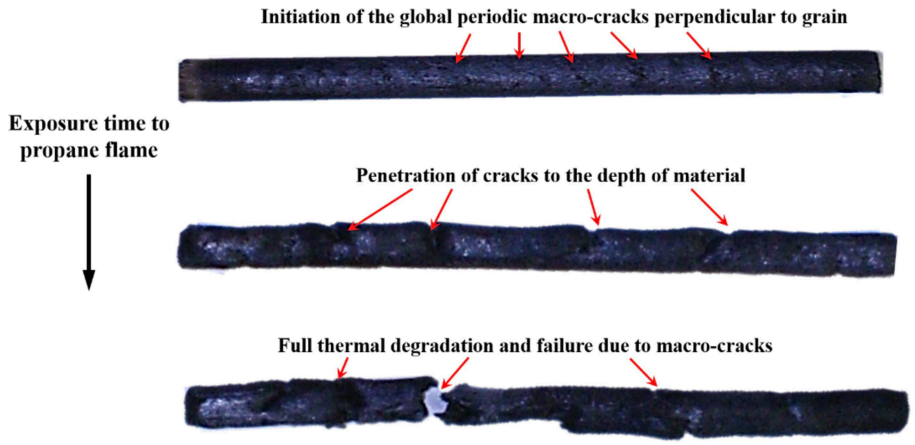

FIGURE 5 | Shown are the of the global periodic macro-crack patterns due to thermo-mechanical instabilities. From top to bottom the flame exposure times are 10, 15, and 20 s for the 6.35 mm diameter birch dowels.

FIGURE 6 | Observations of the combined effect of thermal rolling and thermal degradation in firebrand formation from a burning Leyland Cypress tree performed under wind at the IBHS wind tunnel.

beams where there is at least one boundary constraint at the joints. These restraints play a major role in determining the response of wooden elements to fire (heat) exposure. In fact, for branches at the top of what could be considered a fractal chain, the induced thermal strains lead to continuous rolling of the branch as it is simultaneously being thermally-degraded. We call this phenomenon thermal rolling. Upon close investigation of burn scenarios with various fuels, this behavior can be directly observed. **Figure 6** shows some evidence of thermal degradation and subsequent rolling along a single branch during combustion of a Leyland Cypress tree at the Insurance Institute for Business & Home Safety's (IBHS) wind tunnel.

In real fire scenarios, thermal rolling occurs when branches experience non-uniform heating as the fire (flame) approaches and heats them more from one side than the other, often upwind. This temperature gradient most likely causes thermal expansion

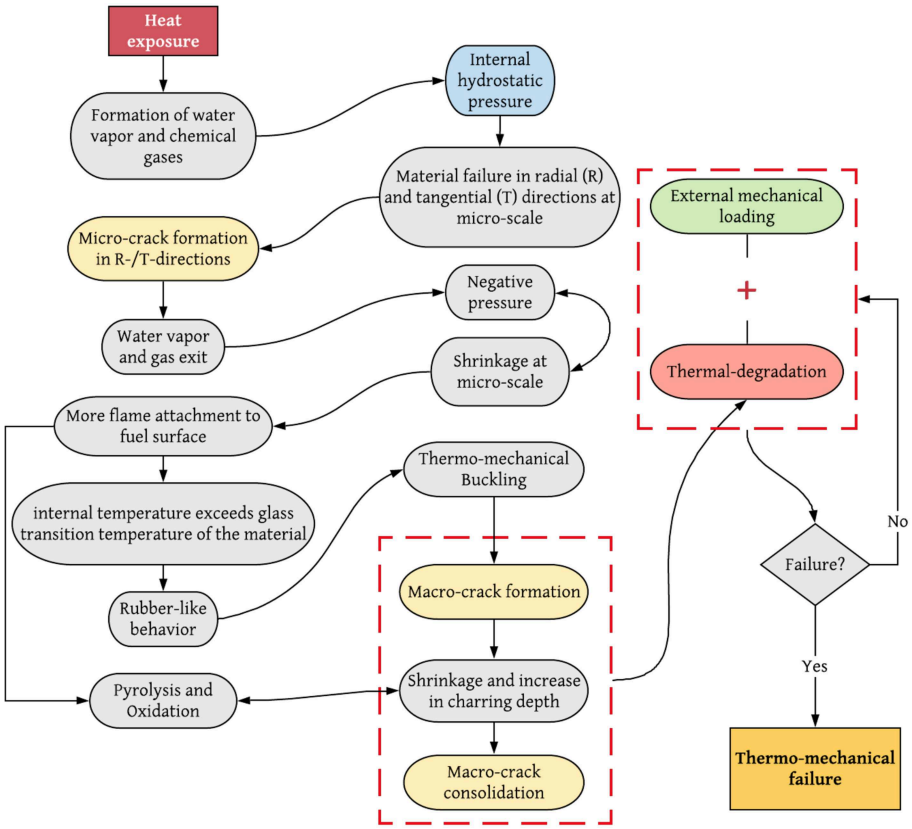

FIGURE 7 | Thermo-mechanical failure cycle for a cylindrical wooden element under continuous heat exposure. Here, arrows with two heads show concurrent processes.

of the lee side and, since one end of the branch is constrained, the cooler material above the neutral axis experiences compression. Therefore, assuming a constant and linear temperature gradient, Hookean-Orthotropic behavior, and a circular cross section, the equivalent uniform moment that develops at the cross-section due to thermal rolling may be characterized as

$$M_{r,R} = \left(\frac{3\pi}{128}\right) \beta E_L \frac{\partial T}{\partial z} D^5, \tag{2}$$

where β is the thermal expansion coefficient, T is temperature, and z is the distance from the neutral axis of the circular cross section. The bending moment in Equation (2) is time-dependent and applies to cylindrical dowels in which the temperature gradient can be resolved. However, this still applies to cylindrical dowels with a relatively small diameter as tree branches show fractal behavior (Barr and Ezekoye, 2013) and only the time scale for the presence of the gradient would be shorter. Due to the time-dependent nature and difficulties of capturing temperature gradients across the cross section of samples within our current experimental setup, the thermal-rolling induced bending moments are not measured in this study. Nevertheless, based on our experimental observations, the time-varying bending moment causes small deflections in elements where thermal degradation is not dominant yet. As time passes, E_L will decrease, but β will increase, and micro and macro cracks will develop throughout the wooden elements. This may further increase the temperature gradient and subsequently the thermal rolling moment, see Equation (2). Hence, the softened element starts to bend, as shown in **Figure 6** where thermal rolling is acting simultaneously during the softening of the branch that eventually leads to the brittle failure and detachment or lofting of the firebrand through the wind field. To summarize these processes, the thermo-mechanical failure cycle for a cylindrical wooden element under persistent heat exposure and external mechanical loading is shown in **Figure 7**.

In a real scenario, thermal-degradation of the material occurs concurrently with a variety of dynamic loading combinations. These are primarily due to thermal rolling, traction forces, and body forces which depending on the extent of degradation and magnitude of loading, one of the failure modes in tree branches could occur. The failure modes are (1) diffuse fracture (greenstick), (2) fibrous (clean) fracture, (3) transverse buckling, and (4) brittle rupture. For a detailed explanation of the failure modes in tree branches refer to Ennos and Van Casteren (2010); Casteren et al. (2012).

The process of firebrand generation includes heat transfer in cellular solids, pyrolysis, elastic and elastoplastic deformation,

and eventually crack formation and failure. Previous studies (Wichman and Atreya, 1987; Baroudi et al., 2017; Nguyen et al., 2017) are available where the governing equations are presented and numerical simulations of wood charring and crack propagation are conducted. However, very few works discuss the dominant parameters, processes, and failure modes in thermally-degraded wooden elements that lead to firebrand generation. Given this and the detailed explanatory framework of the processes, an experimental methodology along with a series of experiments are devised to investigate the dominant modes of firebrand generation from thermally degraded wooden dowels.

EXPERIMENTAL METHODOLOGY

Previous studies (Manzello et al., 2006b) have shown that many firebrands generated from burning vegetation (e.g., conifers) are in cylindrical form. Thus, cylindrical wooden dowels of three different wood species, i.e., birch, oak, and poplar, were chosen for testing. This provides a range of material properties as well as allowing for testing of smaller wooden dowels. The average initial densities measured before testing were 610, 700, and 540 kg/m^3 for the birch, oak, and poplar, respectively. Since Barr and Ezekoye (2013) found a relationship between strength and density, a range of initial densities was studied to better understand the role of density in firebrand generation. The density of Douglas fir and pine species, which are more typical species in WUI fires, overlap with the lower range of densities tested in this study. Due to an inability to source hardwoods such as pines in the desired diameter ranges, we chose to use birch, oak, and poplar as surrogates which could be readily supplied for experiments.

The diameter of dowels tested range from about 3 mm to 13 mm (1/8 in to 1/2 in). Previous works (Albini, 1979; Suzuki et al., 2012a,b) have found that the average firebrand diameter ranges from 3 to 5 mm, which motivated the dowel sizes used in these experiments. All of the dowels were cut to 10.16 cm (4 in) in length for the three-point bending tests. Moisture contents were measured with a moisture content analyzer which dried the fuel over a load cell. The moisture content ranged from 5 to 8% on a dry basis for all three species. Drying the dowels to lower moisture contents was tested but did not have an effect on the results of the bending tests.

Dowels were weighed and then exposed to a propane flame created by a large Bunsen-type burner to induce flaming combustion. While the temperatures produced by this burner were likely higher than those produced in a real wildland fire, they were much more representative of the temperatures and heating rates expected compared to the other heating methods tried in preliminary tests, such as a hot plate and oven (Caton, 2016). The effect of the flaming time on degradation was determined by increasing the exposure time in 5 s intervals from 10 to 20 s. It should be noted that the exposure times are corroborated with the charring depth that is estimated from image processing of the cross section of the extinguished samples. In order to ensure that all pyrolysis and combustion reactions stopped, and that the heating times were as accurate as possible, the dowels were placed in a 22.9 × 33 × 6.35 cm aluminum box after each exposure time. The box was lined with Kaowool ceramic insulation fiber, such that the dowels would not fracture when placed inside. Then, nitrogen gas (N_2) was injected through an inlet hole in the top of the enclosure box. N_2 acted as an inert to extinguish any combustion processes, flaming or smoldering, that were still occurring. After ensuring the combustion reactions cease, the samples were weighed again in order to calculate the mass loss rate.

Finally, three-point bending tests were performed using a PASCO Materials Testing System with the bending accessory on all of the heated dowels. There was also a set of three-point bending tests conducted with virgin dowels of all the species to produce data on initial mechanical properties. The length span between the supports, L_0, was 8.65 cm, with supports located 0.76 cm from the edge of the 10.16 cm long dowel. The Materials Testing System's software measured the force applied to the specimen through the plunger by a 7,100 N load cell in the base of the machine, and the position of the tip of the plunger was measured when the software was recording data by an optical encoder. The loading history of the bending force as well as the associated strain, measured based on the location of the plunger's tip, were collected for each sample until it failed.

RESULTS

The maximum force that each dowel could withstand prior to breakage was measured based on the three-point-bending tests. Ten dowels were tested for each scenario and the mean of the maximum force for each condition was calculated. In the birch tests, the maximum force decreased with increasing time for each diameter. The results of the oak tests demonstrate that increasing the exposure time from 15 to 20 s did not significantly change the maximum force measured for any of the sizes. The poplar dowels lost a significant amount of strength after burning for 10 s but increasing the exposure time beyond 10 s only created small decreases in the ultimate force. **Figure 8** shows the observed breakage modes for birch dowels of the same diameter but with different flame exposure times. This trend has been consistently observed for other species as well.

On the left-hand side of **Figure 8**, samples with shorter flame exposure times (10 s) are shown. Fibrous failure can be observed which implies that the stiffness of the thermally degraded material is the dominating mode of failure. In addition, the presence of the common 45-degrees angle cracks, which show propagation along the longitudinal direction, supports this. By increasing the exposure time (20 s), a change in the crack propagation mode and form of the failure can be observed, shown in **Figure 8**-right. This type of failure, namely a sudden 90-degree crack, suggests failure of the material in a brittle form. Due to prolonged exposure to the propane flame, the material's cross-section is thermally degraded such that the stiffness of the cross-section is no longer sufficient to withstand the load. Therefore, it suddenly ruptures. These modes of mechanical behavior are effects of the combustion process, which increases the proportion of char within the sample.

FIGURE 8 | Birch dowels with a diameter of 6.35 mm (1/4 in) heated in the flame for 10 s (left) and 20 s (right) which, respectively, show fibrous and brittle fracture modes. This result provides evidence that the breakage mechanisms are dependent on the heating exposure time.

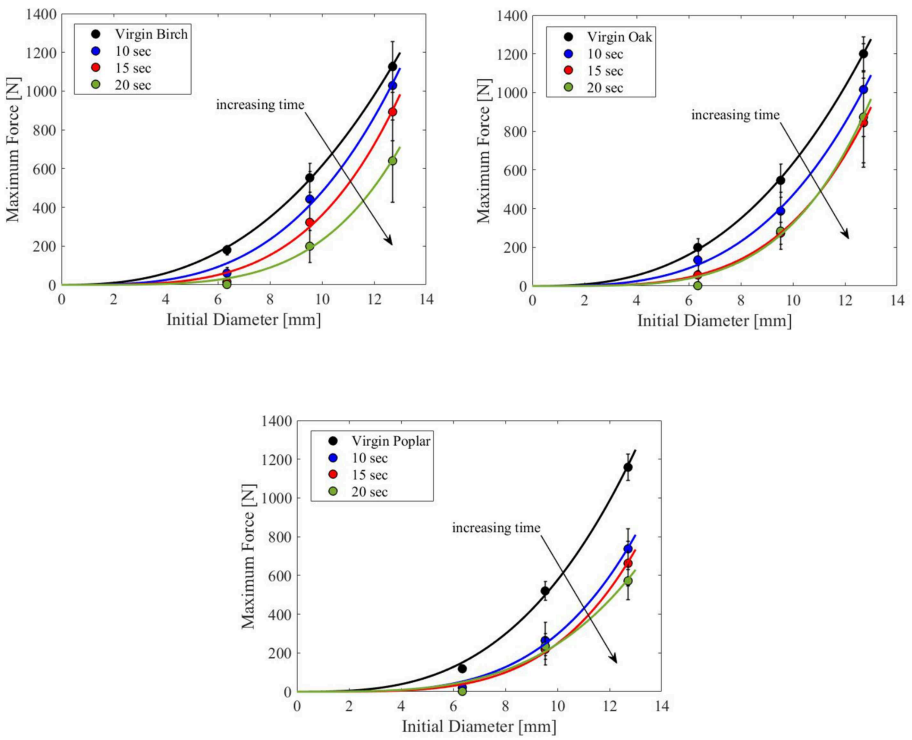

FIGURE 9 | Variation of the maximum force as a function of initial diameter for the birch (top left), oak (top right), and poplar (bottom) in the flaming tests.

The maximum forces that each dowel could withstand prior to breakage were studied as a function of the initial diameter of the dowels for all the tests. Ten dowels were tested for each scenario and the mean of the maximum force for each testing condition was calculated to find the average value associated with the test parameters. The results for the flaming tests are shown in **Figure 9** for all three species to demonstrate the differences between the species tested. In the birch tests, the maximum forces decreased with increasing time for each diameter. The results of the oak tests demonstrate that increasing the exposure time from 15 to 20 s did not significantly change the maximum force measured for any of the sizes. The poplar dowels lost a significant amount of strength after burning for 10 s but increasing the exposure time beyond 10 s only resulted in small decreases in the ultimate force. To capture the underlying physics, influential parameters of the experiment are summarized using dimensional analysis in the next section.

DIMENSIONAL ANALYSIS

The three-point bending tests provide valuable knowledge about the effects of the combustion processes on breakage mechanisms of cylindrical wooden dowels; however, due to the specificity of the results to the species and size of the dowels, it is beneficial to use non-dimensional analysis to extend and generalize the observations. This approach extracts relationships between a variety of physical quantities based on the identified independent variables and their base physical units (e.g., mass, length, time, etc.), and represents the dependent variables as a function of them. One of the common methods of using this technique is the Buckingham-Π theorem; for details of this method refer to Kundu et al. (2002). As one of the dependent variables, the critical breakage force should be scaled in the parameter space of the experiments. This can be shown by summarizing the parameter

space as

$$\psi\left(F_{\max},\ P_{\infty}, \rho_s,\ \rho_{\infty},\ L_0,\ \nu_{RT}, E_L,\ \alpha \mid \dot{m},\ \rho_0,\ D_0\right) = 0 \quad (3)$$

where $F_{\max}$ is the maximum (critical) force before breakage, ρ_0 the initial species' density, L_0 is the length span between the supports of the three-point bending test, D_0 denotes the initial dowel diameter, ν_{RT} is Poisson's ratio in the radial plane R and in transverse direction T in the RTL coordinate system, α is species' thermal diffusivity, $\dot{m}$ is the mass loss rate, E_L is the modulus of elasticity in the longitudinal direction, ρ_s is the density of wood cell wall material, and P_{∞} and ρ_{∞} are the ambient pressure and density, respectively. In Equation 3, respectively from left to right, the dependent variables are separated from the independent variables with a vertical line. Also, the mass loss rate represents the time dependent effects of the flame exposure time. Here, it is assumed that wooden dowels follow Hookean-Orthotropic behavior, i.e., having material properties that differ along three mutually-orthogonal 2-fold axes of rotational symmetry. By utilizing the Buckingham-Π theorem, two governing non-dimensional parameters can be obtained,

$$\Pi_1 = \left(\frac{\alpha \dot{m} \rho_{\infty}}{P_{\infty} D_0^3 \rho_0}\right), \Pi_2 = \left(\frac{F_{max}\, L_0 \nu_{RT}}{E_L D_0^3}\right)\left(\frac{\rho_0}{\rho_s}\right) \quad (4)$$

Π_1 can be interpreted as the ratio of the average burning rate of the material to its scaled mechanical stiffness and Π_2 is a non-dimensional representation of the recoverable plastic strain in the transverse direction of the dowels. **Figure 10** illustrates the variation of these non-dimensional groups under the parameter space of the experiments. As the ratio of the burning rate to the scaled stiffness increases (combustion intensifies), the recoverable transverse strain remains relatively constant until it exceeds the maximum plasticity potential of the wooden dowels, where the failure occurs. Once the magnitude of the recoverable strain tends toward zero, the failure strain tends toward infinity, which effectively causes rupture of the dowels.

Based on the results shown in **Figure 10**, two distinct regimes describe the effects of combustion on the breakage mechanism of dowels. The first regime can be shown by an approximately horizontal exponential fit, i.e., $\Pi_2 = e^{-13.51}\Pi_1^{-0.21}$, which demonstrates that the recoverable plastic strain is weakly affected by the burning rate parameter Π_1. This shows that, for cylindrical samples with either short flame exposure times or large (residual) diameters, the stiffness of the material cross section is the dominant parameter in describing the failure mechanism of the sample during bending tests.

The second regime, fitted by the vertical steep line in **Figure 10**, i.e., $\Pi_2 = e^{-131.51}\Pi_1^{-4.38}$, shows that material strain is strongly affected by changes in the burning rate. Throughout the second regime, the critical breakage force drops significantly, which indicates that samples were more susceptible to failure by a slight increase in the burning rate parameter. This is indicative of the fact that, for samples with either longer exposure times or smaller (residual) diameters, the dominant factor that accounts for the failure is thermal degradation, as the stiffness of the cross section is not sufficient to overcome the thermal degradation effects. Further, it is evident that the diameter, size, and plasticity of the samples are the controlling factors for the observed transition between the failure regimes. The flaming time (shown by the changing colors of the symbols) which to some extent represents variations in the plasticity of the thermally degraded samples, shows that the exposure time is another controlling parameter as well since the dowels with longer exposure time were more susceptible to fracture. Moreover, the presented analysis is invariant with respect to the species type.

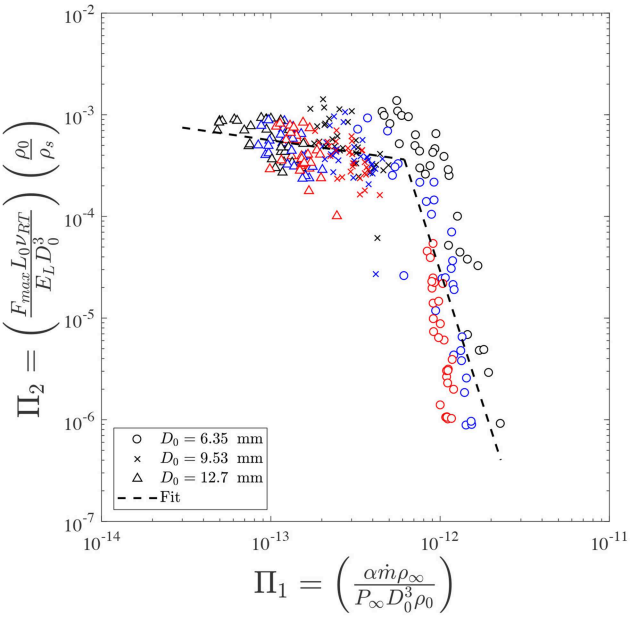

FIGURE 10 | Non-dimensional analysis of the effects of combustion on the breakage mechanisms of wooden dowels of different species. Two distinct failure regimes are shown that control the failure mechanism regardless of the species type and initial physical properties. The exponential fits for the first and second failure modes are $\Pi_2 = e^{-13.51}\Pi_1^{-0.21}$ (approximately horizontal fit) and $\Pi_2 = e^{-131.51}\Pi_1^{-4.38}$ (steep line). (Colored version) Black, blue, and red symbols correspond to 10, 15, and 20 s heat exposure, respectively.

CONCLUSIONS

With the eventual goal of modeling the generation of firebrands from diverse vegetative species, a phenomenological framework was presented to understand thermal-degradation and failure of cylindrical wooden elements under simultaneous external loading. Depending on the state of thermal degradation and extent of external loading, four failure modes are possible: (1) diffuse fracture (greenstick), (2) fibrous (clean) fracture, (3) transverse buckling, and (4) brittle rupture. To further investigate the dominant modes, an experimental methodology for testing the effects of combustion on the strength of small cylindrical wooden dowels in the laboratory utilizing a propane flame, nitrogen extinction, and three-point bending tests is presented.

Scaling analysis of the experimental results suggests that the fracture mode, i.e., fibrous or brittle, primarily depends on the ratio of burning rate to initial stiffness, regardless of species type and initial physical properties. These two regimes summarize the thermal degradation of the wooden dowels in terms of the recoverable transverse strain. Despite these preliminary results, more detailed experiments and analysis are needed in order to extend the observed results, including development of an improved plasticity model and testing of more species, diameters and lengths so that results can eventually be incorporated into a time-dependent firebrand release model for different species.

AUTHOR CONTRIBUTIONS

SC-K did the experiments, some initial analysis, and visualization of the experimental results. AT provided the description of firebrand generation from thermally-degraded material and did the dimensional analysis of the experimental results. MG advised the work and edited the manuscript.

FUNDING

This work was partially performed with support from financial assistance awards 70NANB15H176 and 70NANB16H284 from the U.S. Department of Commerce, National Institute of Standards & Technology, Fire Research Grants Program. SC-K was employed by NIST as a Pathways Intern during the course of this research. Additional support is also acknowledged from the USDA Forest Service through cooperative agreement 15-CA-11272167-058 funded through the Joint Fire Science Program award 15-1-04-4 for tests conducted at IBHS.

ACKNOWLEDGMENTS

We would like to thank Nelson Bryner of NIST for multiple suggestions which have contributed to this work, Stephen Quarles and the rest of the staff at IBHS for running the experiments demonstrated in **Figure 6** and Raquel Hakes for her assistance in laboratory experiments.

REFERENCES

Albini, F. A. (1979). *Spot Fire Distance From Burning Trees—A Predictive Model*. Ogden: Intermountain Forest and Range Experiment Station, Forest Service; US Department of Agriculture.

Antoniow, J. S., Maigret, J.-E., Jensen, C., Trannoy, N., Chirtoc, M., and Beaugrand, J. (2012). Glass-transition temperature profile measured in a wood cell wall using scanning thermal expansion microscope (SThEM). *Int. J. Thermophy* 33, 2167–2172. doi: 10.1007/s10765-012-1313-y

Ashby, M. F. (1983). The mechanical properties of cellular solids. *Metall. Trans. A* 14, 1755–1769. doi: 10.1007/BF02645546

Balch, J. K., Bradley, B. A., Abatzoglou, J. T., Nagy, R. C., Fusco, E. J., and Mahood, A. L. (2017). Human-started wildfires expand the fire niche across the United States. *Proc. Natl. Acad. Sci. U.S.A.* 11, 2946–2951. doi: 10.1073/pnas.1617394114

Baroudi, D., Ferrantelli, A., Li, K. Y., and Hostikka, S. A. (2017). thermomechanical explanation for the topology of crack patterns observed on the surface of charred wood and particle fibreboard. *Combust. Flame* 182, 206–215. doi: 10.1016/j.combustflame.2017.04.017

Barr, B. W. W., and Ezekoye, O. A. (2013). Thermo-mechanical modeling of firebrand breakage on a fractal tree. *Proc. Combust. Inst.* 2, 2649–2656. doi: 10.1016/j.proci.2012.07.066

Bažant, Z. P. (1985). Constitutive equation of wood at variable humidity and temperature. *Wood Sci. Technol.* 2, 159–177. doi: 10.1007/BF00353077

Bryden, K. M., and Hagge, M. J. (2003). Modeling the combined impact of moisture and char shrinkage on the pyrolysis of a biomass particle. *Fuel* 82, 1633–1644. doi: 10.1016/S0016-2361(03)00108-X

Casteren, A. V., Sellers, W. I., Thorpe, S. K. S., Coward, S., Crompton, R. H., Ennos, A. R. (2012). Why don't branches snap? The mechanics of bending failure in three temperate angiosperm trees. *Trees* 26, 789–797. doi: 10.1007/s00468-011-0650-y

Caton, S. (2016). *Laboratory Studies on the Generation of Firebrands From Cylindrical Wooden Dowels*.

Caton, S. E., Hakes, R. S. P., Gorham, D. J., Zhou, A., and Gollner, M. J. (2016). Review of pathways for building fire spread in the wildland urban interface part I: exposure conditions. *Fire Technol.* 53, 1–45. doi: 10.1007/s10694-016-0589-z

Chen, Y., Aanjaneya, K., and Atreya, A. (2017). A study to investigate pyrolysis of wood particles of various shapes and sizes. *Fire Saf. J.* 91, 820–827. doi: 10.1016/j.firesaf.2017.03.079

Dinwoodie, J. M. (2000). *Timber; Its Nature and Behaviour, 2nd Edn*. London: Taylor & Francis.

Easterling, K. E., Harrysson, R., Gibson, L. J., and Ashby, M. F. (1982). On the Mechanics of Balsa and Other Woods. *Proc. R. Soc. A Math. Phys. Eng. Sci.* 1784, 31–41. doi: 10.1098/rspa.1982.0118

El Houssami, M., Mueller, E., Filkov, A., Thomas, J. C., Skowronski, N., Gallagher, M. R., et al. (2016). Experimental procedures characterising firebrand generation in wildland fires. *Fire Technol.* 3, 731–751. doi: 10.1007/s10694-015-0492-z

Ennos, A. R., and Van Casteren, A. (2010). Transverse stresses and modes of failure in tree branches and other beams. *Proc Biol Sci.* 277, 1253–1258. doi: 10.1098/rspb.2009.2093

Gibson, L. J., and Ashby, M. F. (1999). *Cellular Solids: Structure and Properties, 2nd Edn*. Cambridge: Cambridge University Press.

Gibson, L. J., Ashby, M. F., Schajer, G. S., and Robertson, C. I. (1982). The mechanics of two-dimensional cellular materials. *Proc. R. Soc. London A Math. Phys. Eng. Sci.* 382:1782. doi: 10.1098/rspa.1982.0087

Haas, T. J., Nimlos, M. R., and Donohoe, B. S. (2009). Real-time and post-reaction microscopic structural analysis of biomass undergoing pyrolysis. *Energy Fuels* 23, 3810–3817. doi: 10.1021/ef900201b

Hadden, R. M., Scott, S., Lautenberger, C., and Fernandez-Pello, A. C. (2010). Ignition of combustible fuel beds by hot particles: an experimental and theoretical study. *Fire Technol.* 2, 341–355. doi: 10.1007/s10694-010-0181-x

Hagge, M. J., Bryden, K. M., and Dietenberger. M. A. (2004). "Effects of backing board materials on wood combustion performance," in *Wood & Fire Safety: Proceedings, 5th International Scientific Conference*. Svolen, Slovakia: Faculty of Wood Sciences and Technology; Technical University of Zvolen, 51–58. Available online at: https://www.fs.usda.gov/treesearch/pubs/7019

Howard, P. (2014). *Flammable Planet: Wildfires and the Social Cost of Carbon*. New York, NY: Institute for Policy Integrity; New York University School of Law.

Koch, P. (1972a). "Utilization of the Southern pines, Vol. 1," in *Agricultural Handbook SFES-AH-420* (Asheville, NC: USDA-Forest Service, Southern Forest Experiment Station), 1–734.

Koch, P. (1972b). "Utilization of the Southern pines, Vol. 2," in *Agricultural Handbook SFES-AH-420* (Asheville, NC: USDA-Forest Service, Southern Forest Experiment Station), 735–1663.

Koo, E., Pagni, P. J., Weise, D. R., and Woycheese, J. P. (2010). Firebrands and spotting ignition in large-scale fires. *Int. J. Wildl. Fire* 19:818. doi: 10.1071/WF07119

Kundu, P. K., Cohen, I. M., Hu, H. H., and Publishers, E. S. (2002). *Fluid Mechanics*. San Diego, CA: Academic Press.

Li, K., Hostikka, S., Dai, P., Li, Y., Zhang, H., and Ji, J. (2016). Charring shrinkage and cracking of fir during pyrolysis in an inert atmosphere and at different ambient pressures. *Proc. Combust. Inst.* 36, 3185–3194. doi: 10.1016/j.proci.2016.07.001

Li, K., Pau, D. S. W., Wang, J., and Ji, J. (2015). Modelling pyrolysis of charring materials: determining flame heat flux using bench-scale experiments of medium density fibreboard (MDF). *Chem. Eng. Sci.* 123, 39–48. doi: 10.1016/j.ces.2014.10.043

Li, K. Y., Cheng, X., and Zhang, H. A. (2014). simplified model on vertical density profile and shrinkage ratio of virgin and charred medium density fibreboard. *Fire Mater* 6, 659–672. doi: 10.1002/fam.2207

Liu, Q., Shen, D., Xiao, R., and Fang, M. (2013). Thermal behavior of wood slab under a truncated-cone electrical heater: experimental observation. *Combust. Sci. Technol.* 5, 848–862. doi: 10.1080/00102202.2012.760548

Manzello, S. L., Cleary, T. G., Shields, J. R., Maranghides, A., Mell, W., and Yang, J. C. (2008). Experimental investigation of firebrands: generation and ignition of fuel beds. *Fire Saf. J.* 3, 226–233. doi: 10.1016/j.firesaf.2006.06.010

Manzello, S. L., Cleary, T. G., Shields, J. R., and Yang, J. C. (2006b). On the ignition of fuel beds by firebrands. *Fire Mater.* 1, 77–87. doi: 10.1002/fam.901

Manzello, S. L., Maranghides, A., Shields, J. R., Mell, W. E., Hayashi, Y., and Nii, D. (2007a). Measurement of firebrand production and heat release rate (HRR) from burning Korean pine trees. *Fire Saf. Sci.* 7:108. Available online at: https://www.iafss.org/publications/aofst/7/108

Manzello, S. L., Maranghides, A., and Mell, W. E. (2007b). Firebrand generation from burning vegetation. *Int. J. Wildl. Fire* 16:4. doi: 10.1071/WF06079

Manzello, S. L., Maranghides, A., Mell, W. E., Cleary, T. G., and Yang, J. C. (2006a). Firebrand production from burning vegetation. *For. Ecol. Manag.* 234:S119. doi: 10.1016/j.foreco.2006.08.160

Manzello, S. L., Maranghides, A., Shields, J. R., Mell, W. E., Hayashi, Y., and Nii, D. (2009). Mass and size distribution of firebrands generated from burning Korean pine (Pinus koraiensis) trees. *Fire Mater.* 33:1. doi: 10.1002/fam.977

Mark, R. E. (1907). *Cell Wall Mechanics of Tracheids*. New Haven, CT: Yale University Press.

Mell, W., Maranghides, A., McDermott, R., and Manzello, S. L. (2009). Numerical simulation and experiments of burning douglas fir trees. *Combust. Flame* 156, 2023–2041. doi: 10.1016/j.combustflame.2009.06.015

Nguyen, Y., Pence, T. J., and Wichman, I. S. (2017). "Crack formation during material thermal degradation in combustion," in *10th U.S. National Combustion Meeting* (College Park, MD).

Ragland, K. W., Aerts, D. J., and Baker, A. J. (1991). Properties of wood for combustion analysis. *Bioresour. Technol.* 2, 161–168. doi: 10.1016/0960-8524(91)90205-X

Salmén, L. (1984). Viscoelastic properties of in situ lignin under water-saturated conditions. *J. Mater. Sci.* 9, 3090–3096. doi: 10.1007/BF01026988

Salmén, L. (2004). Micromechanical understanding of the cell-wall structure. *Comptes Rendus Biol.* 9–10, 873–880. doi: 10.1016/j.crvi.2004.03.010

Sardoy, N., Consalvi, J.-L., Porterie, B., and Fernandez-Pello, A. (2007). Modeling transport and combustion of firebrands from burning trees. *Combust. Flame* 150, 151–169. doi: 10.1016/j.combustflame.2007.04.008

Sedighi Gilani, M., Fife, J. L., Boone, M. N., and Ghazi Wakili, K. (2013). Dynamics of microcrack propagation in hardwood during heat treatment investigated by synchrotron-based X-ray tomographic microscopy. *Wood Sci. Technol.* 5, 889–896. doi: 10.1007/s00226-013-0545-8

Shen, D. K., Gu, S., Luo, K. H., and Bridgwater, A. K. (2009). Analysis of wood structural changes under thermal radiation. energy fuels. *Am. Chem. Soc.* 23, 1081–1088. doi: 10.1021/ef800873k

Spearpoint, M. J., and Quintiere, J. G. (2001). Predicting the piloted ignition of wood in the cone calorimeter using an integral model—effect of species, grain orientation and heat flux. *Fire Saf. J.* 4, 391–415. doi: 10.1016/S0379-7112(00)00055-2

Suzuki, S., Manzello, S. L., and Hayashi, Y. (2012a). The size and mass distribution of firebrands collected from ignited building components exposed to wind. *Proc. Combust. Inst.* 3, 2479–2485. doi: 10.1016/j.proci.2012.06.061

Suzuki, S., Manzello, S. L., Lage, M., and Laing, G. (2012b). Firebrand generation data obtained from a full-scale structure burn. *Int. J. Wildl. Fire.* 21, 961–968. doi: 10.1071/WF11133

Tohidi, A. (2016). *Experimental and Numerical Modeling of Wildfire Spread via Fire Spotting*. Boston, MA: Northeastern University.

Tohidi, A., Caton, S., Gollner, M., and Bryner, N. (2017). "Thermo-mechanical breakage mechanism of firebrands," in *10th US National Combustion Meeting* (College Park, MD: University of Maryland College Park).

Tohidi, A., Kaye, N., and Bridges, W. (2015). Statistical description of firebrand size and shape distribution from coniferous trees for use in Metropolis Monte Carlo simulations of firebrand flight distance. *Fire Saf. J.* 77, 21–35. doi: 10.1016/j.firesaf.2015.07.008

Tohidi, A., and Kaye, N. B. (2017a). Aerodynamic characterization of rod-like debris with application to firebrand transport. *J. Wind Eng. Ind. Aerodyn.* 168, 297–311. doi: 10.1016/j.jweia.2017.06.019

Tohidi, A., and Kaye, N. B. (2017b). Comprehensive wind tunnel experiments of lofting and downwind transport of non-combusting rod-like model firebrands during firebrand shower scenarios. *Fire Saf. J.* 90, 95–111. doi: 10.1016/j.firesaf.2017.04.032

Tohidi, A., and Kaye, N. B. (2017c). Stochastic modeling of firebrand shower scenarios. *Fire Saf. J.* 91, 91–102. doi: 10.1016/j.firesaf.2017.04.039

Turns, S. R. (2000). *An Introduction to Combustion*. Boston, MA: MacGraw Hill.

Usmani, A. S., Rotter, J. M., Lamont, S., Sanad, A. M., and Gillie, M. (2001). Fundamental principles of structural behaviour under thermal effects. *Fire Saf. J.* 8, 721–744. doi: 10.1016/S0379-7112(01)00037-6

Ventsel, E., and Krauthammer, T. (2001). *Thin Plates and Shells: Theory: Analysis, and Applications*. New York, NY: CRC press.

Wichman, I. S., and Atreya, A. A. (1987). Simplified model for the pyrolysis of charring materials. *Combust. Flame* 68, 231–247. doi: 10.1016/0010-2180(87)90002-2

Conflict of Interest Statement: SC-K was employed by the company Jensen Hughes and AT was employed by the company One Concern Inc.

The remaining author declares that the research was conducted in the absence of any commercial or financial relationships that could be construed as a potential conflict of interest.

frontiers in Mechanical Engineering

ORIGINAL RESEARCH
published: 20 June 2019
doi: 10.3389/fmech.2019.00034

An Experimental Study of Intermittent Heating Frequencies From Wind-Driven Flames

Wei Tang[1], Mark Finney[2], Sara McAllister[2] and Michael Gollner[1]**

[1] Department of Fire Protection Engineering, University of Maryland, College Park, MD, United States, [2] United States Forest Service (USDA), Missoula Fire Sciences Laboratory, Missoula, MT, United States

An experimental study was conducted to understand the intermittent heating behavior downstream of a gaseous line burner under forced flow conditions. While previous studies have addressed time-averaged properties, here measurements of the flame location and intermittent heat flux profile help to give a time-dependent picture of downstream heating from the flame, useful for understanding wind-driven flame spread. Two frequencies are extracted from experiments, the maximum flame forward pulsation frequency in the direction of the wind, which helps describe the motion of the flame, and the local flame-fuel contact frequency in the flame region, which is useful in calculating the actual heat flux that can be received by the unburnt fuel via direct flame contact. The forward pulsation frequency is obtained through video analysis using a variable interval time average (VITA) method. Scaling analysis indicates that the flame forward pulsation frequency varies as a power-law function of the Froude number and fire heat-release rate, $f_F \tilde{} \left(Fr/Q^{*1/2}\right)^{0.4}$. For the local flame-fuel contact frequency, it is found that the non-dimensional flame-fuel contact frequency f_C^+ remains approximately constant before the local Ri_x reaches 1, e.g., attached flames. When $Ri_x > 1$, f_C^+ decreases with local as Ri_x flames lift up. A piece-wise function was proposed to predict the local flame-fuel contact frequency including the two Ri_x scenarios. Information from this study helps to shed light on the intermittent behavior of flames under wind, which may be a critical factor in explaining the mechanisms of forward flame spread in wildland and other similar wind-driven fires.

Keywords: wind-driven, wildfire, flame spread, pulsation frequency, flame contact

OPEN ACCESS

Edited by:
Guillermo Rein, Imperial College London, United Kingdom

Reviewed by:
Longhua Hu, University of Science and Technology of China, China
Khanh Duc Cung, Southwest Research Institute, United States

****Correspondence:***
Wei Tang
wtang125@gmail.com
Michael Gollner
mgollner@umd.edu

Specialty section:
This article was submitted to Thermal and Mass Transport, a section of the journal Frontiers in Mechanical Engineering

Received: *28 February 2019*
Accepted: *28 May 2019*
Published: *20 June 2019*

Citation:
Tang W, Finney M, McAllister S and Gollner M (2019) An Experimental Study of Intermittent Heating Frequencies From Wind-Driven Flames. Front. Mech. Eng. 5:34. doi: 10.3389/fmech.2019.00034

INTRODUCTION

Wind-driven fires have been studied extensively over the past few decades, however, there are still significant gaps in understanding, especially applied to wind-driven fires resembling a line fire configuration. Most of the current literature on wind-driven fire spread has focused on the steady-state burning characteristics of these fires, preferring this time-averaged view of flame tilt angles, burning rates and downstream heat fluxes to the more complicated, stochastic movements that flames in reality make (Putnam, 1965; Albini, 1982; Weckman and Sobiesiak, 1988). The fluctuation of the flame front has recently been determined to follow some scaling laws and play a role in flame spread, in particular for wildland fires (Finney et al., 2015). The movement of flames therefore may have implications in a variety of wind-driven scenarios, wherever flames reside long enough to heat unburnt fuels and thus contribute to forward fire spread.

Flame "pulsations," or brief cyclical motions, have been studied for various fire configurations. Under stagnant conditions, an intermittent "puffing" phenomenon has been extensively studied using pool fires where the puffing frequency of the flame has been found to be well correlated with the diameter of the fire source (Grant and Jones, 1975; Hamins et al., 1992; Hu et al., 2015). These experiments on buoyant plumes suggest that puffing is primarily the result of a buoyant flow instability, which involves the strong coupled interaction of a toroidal vortex formed a short distance above a fuel or burner surface (Cetegen and Ahmed, 1993). Scaling of this phenomena has also been represented as a Strouhal–Froude relationship $St \sim Fr^{-0.5}$ (Cetegen and Ahmed, 1993). In wind-driven fires, the pulsation of the flame is not expected to scale with burner size in the same way as fires under stagnant conditions as wind plays a significant role in the fire behavior, too. These fires have already been shown to be strongly influenced by a competition between upward buoyant forces from the flame and forward momentum from the wind (Tang et al., 2017a), suggesting a combination of these forces will also play a role in generating intermittent motions within the flame.

A detailed look at the time-dependent nature of wind-blown flames reveals that there are a variety of structures and regions which vary in both time-dependent and averaged characteristics. **Figure 1** shows an image of a wind-blown flame from a stationary burner that, at first, appears attached along the downstream surface, but eventually lifts into a tilted flame. Three regions are thus defined to describe the flame behavior. First, an attachment region exists where the flame is visibly attached to the surface, occurring for some distance downstream of the burner since the wind overpowers buoyancy from the flame. As the flame moves forward, buoyancy increases in proportion to the momentum from the wind and the flame enters a transitional, "intermittent" region, where the flame fluctuates as a result of the competition with momentum from the wind and flame-generated buoyancy. After this region, the flame is finally lifted due to the dominant role of buoyancy, growing with distance as distributed heat release reactions continues to occur within the flame.

In the process of the flame moving forward, a two-directional fluctuating behavior is anticipated, indicated on **Figure 1**. One is *flame forward pulsation*, where the flame intermittently flickers forward onto the downstream surface ahead of the flame front. In a spreading fire scenario, this may potentially reach more unburnt fuels and heat them, albeit for short times. This likely occurs due to a competition between momentum-driven wind and a counter-clockwise recirculation zone at the flame front, a buoyant instability similar to puffing pool fires, or a combination of the two. The other is *flame-fuel contact*, which appears most rapid in the region between the attached flame length and the lifted region. The up-and-down motion of the flame here is most likely due to a local buoyant instability and may be subject to change along the downstream distance. Independently measuring these two components will help to determine the influence intermittent heating has in each of the mentioned regions. Flame *forward pulsation* and *flame-fuel contact* will each play a significant role in the ignition of unburnt fuels within the flame's reach in wind-driven fires.

In our previous work (Tang et al., 2017a), the local total heat flux distribution on the downstream surface of wind-driven line fires was investigated and a local Richardson number [$Ri_x = Gr_x/Re_x^2$, describing flame buoyancy over wind momentum (Subbarao and Cantwell, 1992; Johnson and Kostiuk, 2000)] was employed to scale measured non-dimensional heat fluxes. Inertial forces would be expected to dominate the flame behavior when $Ri_x < 0.1$, and buoyant forces when $Ri_x > 10$. However, the details and implications of the heat transfer modes in the mixed region ($0.1 < Ri_x < 10$), where the transition from an inertial-dominant to buoyancy-dominant regime, has not been well studied. Because most fires with cross-flow reside in this region, e.g., flames that begin attached near the surface and tend to "lift off" into a more plume-like scenario downstream, study of the fire behavior in this region is important to improve understanding of heating during flame spread.

In this study, a stationary, non-spreading gas-burner fire configuration was chosen as it allows for a thorough statistical analysis of the flame structure. Long-duration experiments allow for a large sample size and more control over variations in experimental parameters, such as decoupling the heat-release rate of the fire from flow conditions. High speed video is useful on these fires to reveal and track buoyant instabilities in the fire flow which resemble those appearing in spatially-uniform fuel beds. The same flame movements observed in previous spreading fire experiments were observed with the stationary burner (Finney et al., 2015), but with the ability to collect a larger data set of intermittency. Both forward and vertical movements of the flame were studied. The flame forward pulsation frequency was extracted from videos using the VITA method, similar to previous work (Tang et al., 2017b), while the local flame-fuel contact frequency on the downstream surface was obtained through Fast Fourier Transform (FFT) of heat flux sensor data. Scaling laws were then developed for these two frequencies and equations derived to correlate the frequency with related controlling parameters.

EXPERIMENTAL SETUP

Experiments were performed on a specially-designed 30 cm cross-section laminar blower built for uniform forced-flow combustion experiments. The blower pressurizes a 0.75 cubic-meter plenum with a centrifugal fan. The flow then travels through a converging section into a 30 × 30 cm rectangular duct, where multiple mesh screens and honeycomb flow straighteners were installed in the converging section to help generate a uniform wind profile. Finally, the flow travels another 1.35 m in the duct resulting in a fully-developed laminar boundary layer before it is exhausted at the outlet. The outlet velocity from the tunnel can be as high as 6 m/s, with a turbulence intensity, u'/u controlled below 3%. The wind velocity ranged from about 0.8 to 2.5 m/s in experiments, confirmed to be

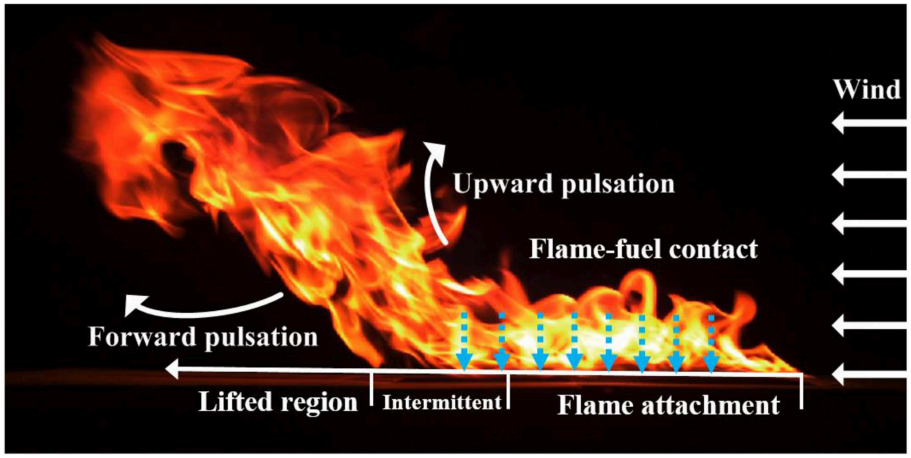

FIGURE 1 | The movement of a stationary, wind-driven flame is depicted here with forward and upward pulsations and flame-fuel contact depicted throughout the attached, intermittent and lifted regions of the flame.

uniform at multiple locations across the space with a hot-wire anemometer.

The experimental platform was placed immediately following the outlet of the exhaust tunnel. A sand-filled gas burner was used with a 10 cm deep sand-filled plenum and a 25 cm (length) ×5 cm (width) surface. The top surface of the burner was mounted flush with a sheet of ceramic insulation board in the center of the blower outlet. The ceramic board had dimensions of 90 (length) × 45 (width) × 2 (height) cm^3, over which the flame fluctuates, providing a quasi-adiabatic boundary condition. Propane from a gas cylinder was passed through a programmable flow meter to provide a steady flow rate of fuel during experiments. Three different fire heat-release rates, 6.3, 7.9, 9.5 kW, which correspond to 4, 5, and 6 liters per minute of propane gas were used during the experiments. High-speed videography using a Nikon DX was recorded at 250 frames per second at a 1,000 × 720 pixel resolution to capture digital images of the flame in all configurations from the side view. The wind tunnel and test section setup are shown in **Figures 2A,B**.

For the frequency of the flame intermittently attaching to the downstream surface, a Gardon-type high frequency Vatell heat flux gauge (model HFM 1000-0) sampled at 1 kHz was used to capture the heat flux signal, and a FFT is applied to the heat flux data to extract the dominant frequency. These gauges were placed at six downstream locations 5.5 cm apart, starting 5.5 cm away from the trailing edge of the burner. Experimental conditions were chosen following our previous work on the total heat flux distribution and flame attachment, representing a wide range of wind momentum (Re number) and flame buoyancy (non-dimensional heat release rate) (Tang et al., 2017a). For the flame-forward pulsation frequency, a dominant frequency is not as apparent in the video analysis, as it is thought to be more affected by transport of stochastic turbulent structures. A technique used to analyze such turbulent flows, the variable-interval time-average (VITA) method, essentially a level-crossing technique, is applied through a MATLAB script which was previously found to show good results for turbulent flows (Tang et al., 2017b).

RESULTS AND DISCUSSIONS

Flame Forward Pulsation Frequency

The flame forward pulsation was measured for stationary burners under wind. The flame location was determined using side-view high speed videos. Each image in the video was cropped to the same region-of-interest, a region defined from the downstream edge of the burner surface to the end of the image in the downstream direction, with a certain height above the surface. This region, in theory, could represent a flame zone depth in a spreading fire (see the dashed rectangle in **Figure 3A**). Flame images were then converted to greyscale images in MATLAB by averaging all three color channels and a threshold applied to result in a black-and-white image of flame and no-flame regions. As shown in **Figure 3A**, the flame position and flame shape are constantly changing when there is a perpendicular wind. The flame location is determined in the region of interest by tracking the furthest downstream tip of the flame detected from thresholding. This location fluctuates in time and would "burst" or quickly enter into what would be the unburnt fuel region, resulting in the intermittent heating of unburnt fuels by flame contact.

Resultant flame locations as a function of time were analyzed using the VITA method (Blackwelder and Kaplan, 1976; Audouin et al., 1995) for a 1 cm window in the video at different distances downstream of the burner. Other window sizes up to 4 cm wide required more processing but produced similar results. Level-crossing was only considered for the forward direction, thus only when the flame appeared after absence in the previous frame, was it considered a crossing to avoid double-counting. The resulting flame forward pulsation frequency was then determined at each downstream location by dividing the number of crossings by the total number of frames,

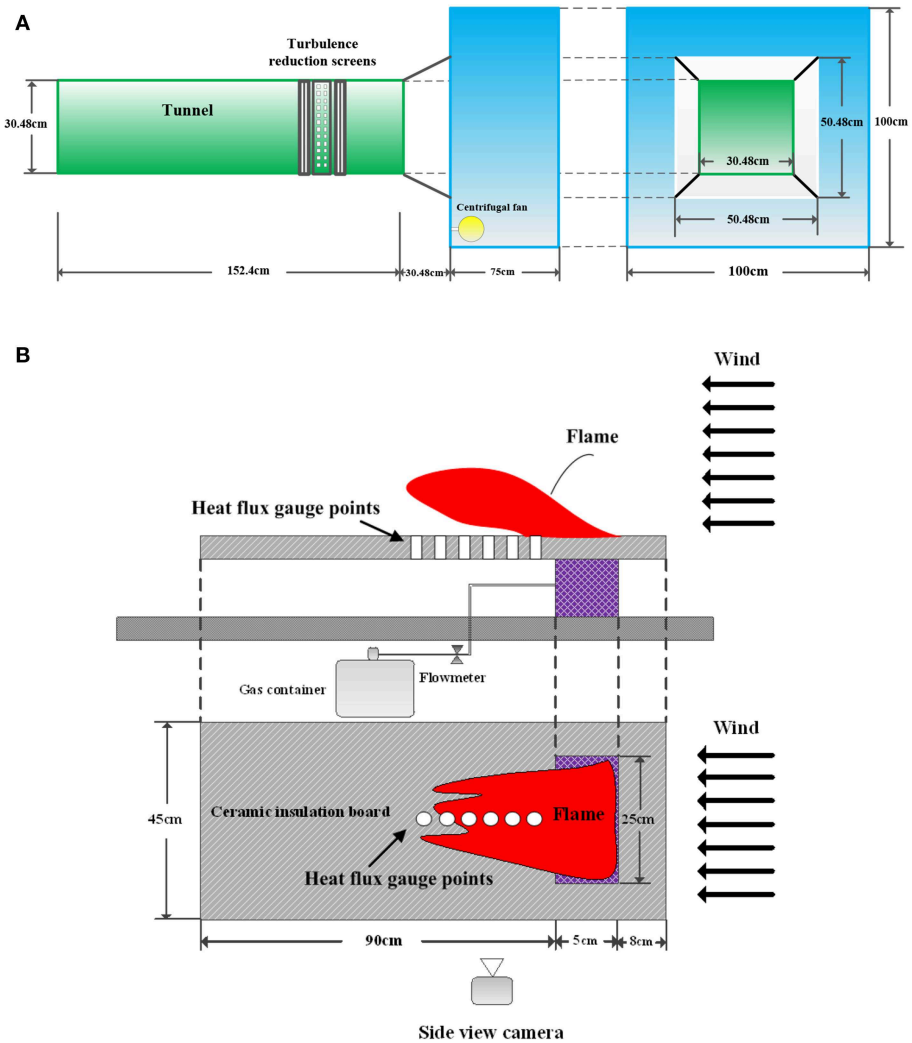

FIGURE 2 | Experimental setup. **(A)** Wind tunnel apparatus. **(B)** Test section setup.

multiplied by the frame rate of the video. The mean values of the frequency data obtained from all the thresholds was used for later analysis. To connect results to flame spread in solid fuels, a fuel bed height will need to be defined for the scenario at hand. **Figure 3B** shows resultant frequencies following application of the VITA technique. As the flame intermittently moves forward and backwards, it enters and leaves the downstream window position producing a parabolic distribution of frequencies. A maximum frequency therefore occurs at some downstream location between the continuous flame region and the maximum forward extension of the flame. The frequency at this location is used in the analysis as a maximum representative frequency of the flame along the surface.

Applying the VITA method to all fire sizes and wind velocities, maximum frequencies are extracted, shown in **Figure 4**. It shows that the flame pulsation frequency increases relatively linearly with the wind velocity, while it decreases with fire size in all the experiments tested. The frequencies observed range from <10 Hz to about 15 Hz.

Flame-Fuel Contact Frequency

The flame-fuel contact frequency can help determine how much heat flux is received by unburnt fuels ahead of the flame front through direct flame contact, which has recently been found to be a primary mechanism of ignition of fuels in a wind-driven wildland fire (Finney et al., 2015). For each of the experimental conditions, raw heat flux signals were taken at different locations on the downstream board. The flame-fuel contact frequency was extracted from measured heat flux signals by applying a FFT which results in a frequency spectrum.

The same method was applied to three cases with different wind velocities but the same fire size (9.5 kW) at 11 cm downstream, shown in **Figure 5**. FFT data smoothed by a Savitzky–Golay filter revealed the peak intensity used to choose the peak frequency at that location. In **Figure 5**, it can be seen

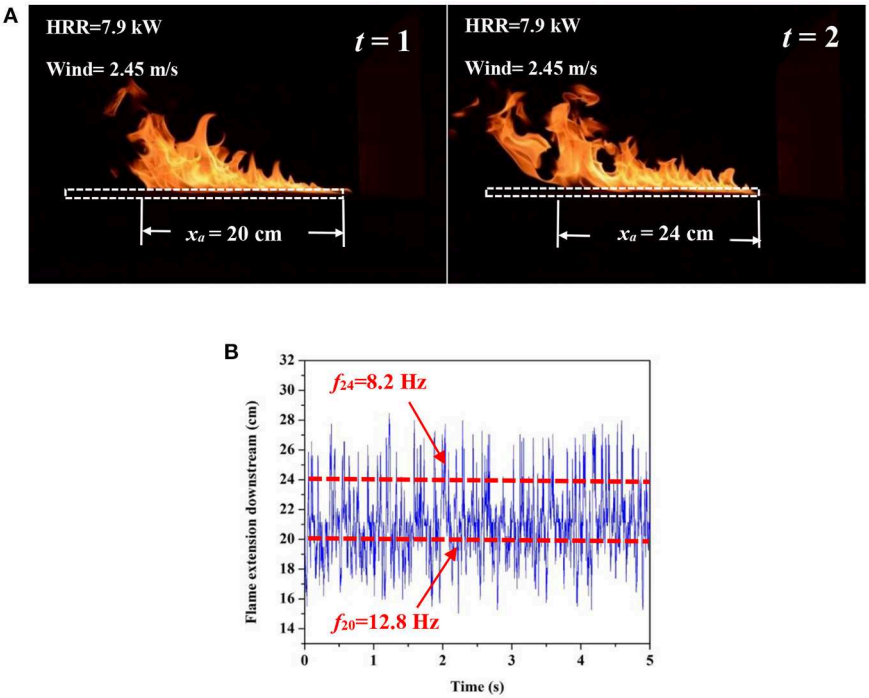

FIGURE 3 | Flame location between two time steps in a forced flow experiment and resultant flame locations with time. **(A)** Flame image in two consecutive time steps. **(B)** Flame extension distance downstream.

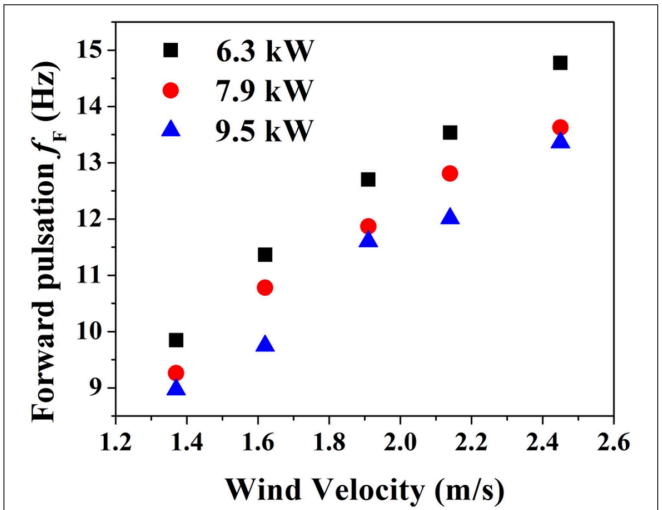

FIGURE 4 | Forward pulsation frequencies with different wind velocities and fire sizes.

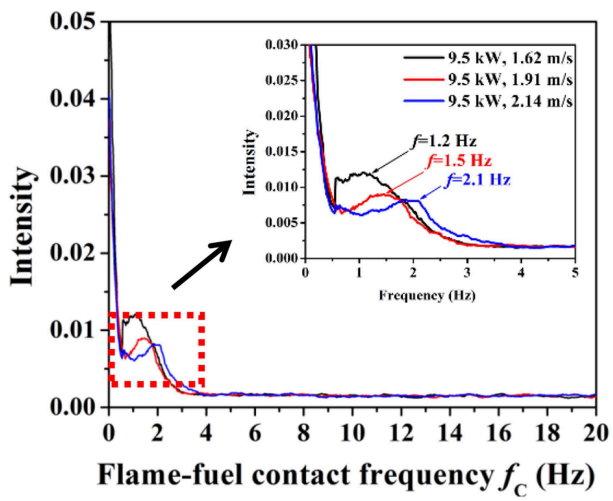

FIGURE 5 | Comparison of frequencies obtained from a FFT for different wind velocities.

that the flame-fuel contact frequency slightly increases with increasing wind velocity, however the intensity of this peak decreases indicating a reduced dominance of this peak frequency and more turbulent structures.

The local flame-fuel contact frequency was further plotted for different wind velocity and fire sizes. **Figure 6** shows one example where the fire size is 7.9 kW, for a given wind velocity, the local frequency tends to decrease with downstream distance from the burner. It is worth noting that, under high wind speeds, the flame starts to behave differently as the leading edge of the flame becomes highly strained i.e., the flame length approaches a constant value instead of extending further with high wind

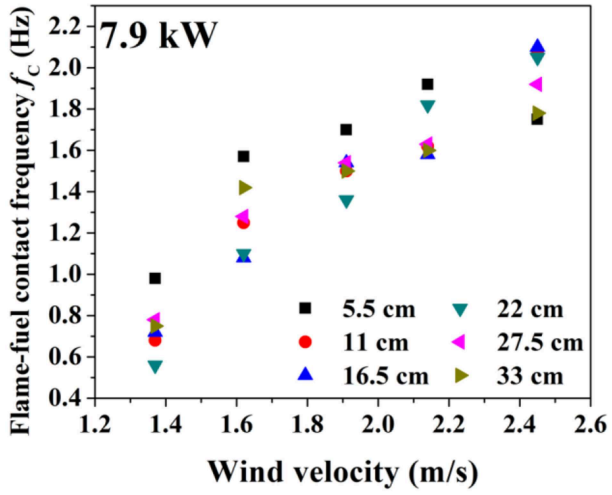

FIGURE 6 | Local flame fuel contact frequency for a 7.9 kW fire under different wind velocities.

speed, the leading edge also starts to briefly extinguish and blue flames appear, which might explain some of the decrease shown in **Figure 6** for the high wind at 5.5 cm data point.

Discussion

Unlike previous studies on flame frequencies (Hamins et al., 1992; Cetegen and Ahmed, 1993), which focused on puffing under stagnant conditions, this paper investigated the flame pulsation frequency under a cross-wind flow. The puffing frequency without wind has been found to be a function of burner size. Under wind conditions, however, two movements have been clearly identified. One is the global forward pulsation, where the flame is driven by the wind, and possibly buoyancy as well, and intermittently moves back and forth in the stream-wise direction. The other is an upward pulsation, which is found to be a more local phenomenon, where the flame is touching and directly transferring heat to the local unburnt fuel within the attachment and intermittent regions shown in **Figure 1**. This section will discuss these two pulsation frequencies and their correlations with relevant parameters.

Global Flame Forward Pulsation Frequency

The global flame forward pulsation frequency is thought to be the result of a competition between forward momentum from the ambient wind and buoyancy from the flame itself. A scaling analysis can be performed, assuming relevant parameters, which reveals two primary groups that the forward pulsation frequency is dependent on, the Froude number (wind momentum over inertial force) and Q* (buoyancy). A phenomenological explanation can be arrived at by first assuming the flame forward-pulsation frequency can be related to both the ambient wind velocity, u and the flame length, l_f, which characterizes buoyancy from the fire, as

$$f_F \tilde{} \frac{u}{l_f}. \tag{1}$$

In a wind-driven fire, the flame length has previously been found to be a function of the wind velocity and mass burning rate in the form (Thomas, 1963; Moorhouse, 1982),

$$\frac{l_f}{D} = a\left(\frac{\dot{m}''}{\rho_a\sqrt{gD}}\right)^b \cdot (u^*)^c, \tag{2}$$

where D is the characteristic diameter or length of the burner, $\dot{m}''$ the mass burning rate of the fire, and a, b, and c are constants, previously found to be 62, 0.25, −0.044, respectively for gas fires (Thomas, 1963). A non-dimensional velocity can be defined as a ratio of the ambient wind velocity and a characteristic buoyant velocity of the fire (Hu, 2017),

$$u^* = \frac{u}{\left(g\dot{m}''D/\rho_a\right)^{1/3}}, \tag{3}$$

where g is the acceleration due to gravity and ρ_a the density of ambient air. Assuming the fuel burns completely, $\dot{m}''$can be related to the heat-release rate of the fire, $\dot{Q}$ as

$$\dot{Q} = \Delta H_c \dot{m}'', \tag{4}$$

which provides a more functional and universal parameter from which to define the fire. The heat-release rate can be non-dimensionalized as Q^* (Quintiere, 1989) for a fire plume and expressed in terms of $\dot{m}''$ as

$$Q^* = \frac{\dot{Q}}{\rho_a T_a C_p \sqrt{gD^5}} \tilde{} \dot{m}'', \tag{5}$$

Combining Equations (1–5), we arrive at Equation (6), which relates the flame forward-pulsation frequency with the Froude number and the non-dimensional heat-release rate,

$$f_F \sim \frac{u^{1.044}}{Q^{*0.265}} \approx \frac{\mathrm{Fr}^{1/2}}{Q^{*1/4}} = \sqrt{\frac{\mathrm{Fr}}{Q^{*1/2}}}, \tag{6}$$

where Fr is defined as $\mathrm{Fr} = u^2/gL$, u is the wind velocity, and L is the flame length. The flame forward pulsation frequency is then plotted against this parameter derived in **Figure 7**, and a power-law relationship is found relating them. An empirical fit can then be found from the data,

$$f_F = 15.7\left(\frac{\mathrm{Fr}^{1/2}}{Q^{*1/4}}\right)^{0.8} = 15.7\left(\frac{\mathrm{Fr}}{Q^{*1/2}}\right)^{0.4}. \tag{7}$$

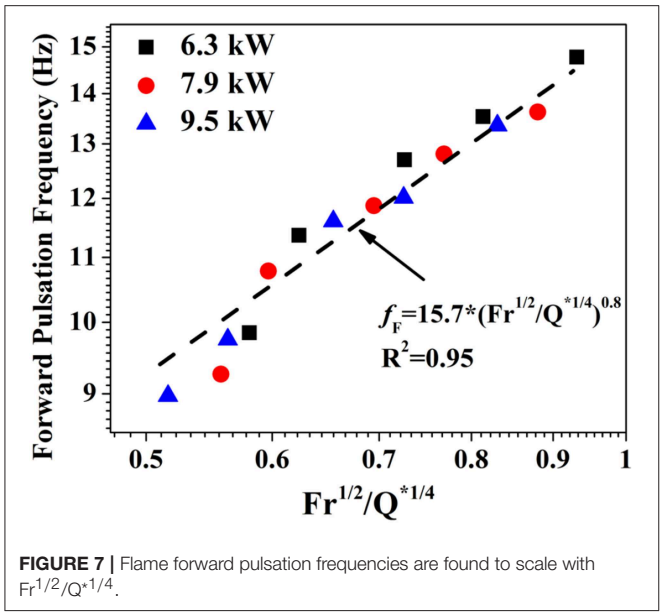

FIGURE 7 | Flame forward pulsation frequencies are found to scale with $Fr^{1/2}/Q^{*1/4}$.

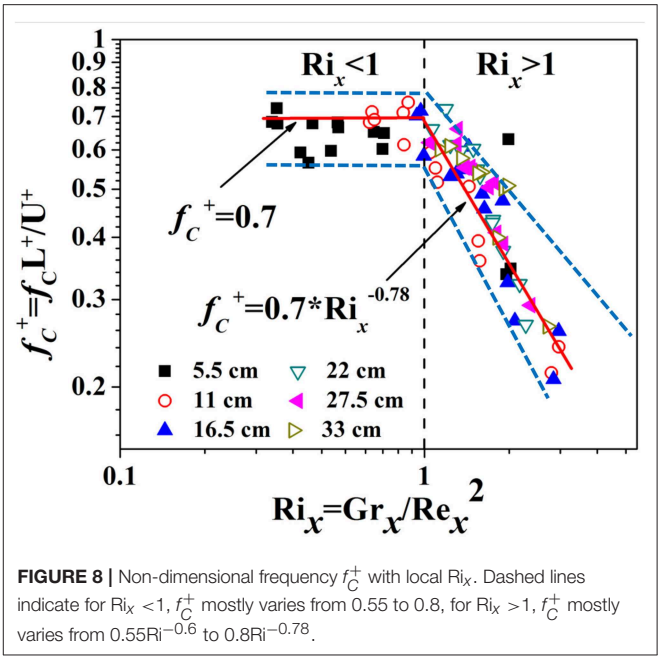

FIGURE 8 | Non-dimensional frequency f_C^+ with local Ri_x. Dashed lines indicate for Ri_x <1, f_C^+ mostly varies from 0.55 to 0.8, for Ri_x >1, f_C^+ mostly varies from $0.55Ri^{-0.6}$ to $0.8Ri^{-0.78}$.

with an R^2 of 0.95. While f_F could be presented in non-dimensional form, such as through a Strouhal number, the choice of a relevant length scale known *a priori* is difficult to define and, if properly applied, will result in a straight line similar to puffing pool fires (Hamins et al., 1992). Therefore, only f_F is shown in **Figure 7**.

Local Flame-Fuel Contact Frequency

For the local flame-fuel contact frequency, the local Grashof ($Gr_x = g\beta(T_h - T_\infty)L^3/\nu^2$) and Reynolds ($Re_x = UL/\nu$) numbers arise as critical parameters describing the flow and heat transfer in our setup, where T_h and $T_\infty$are the hot gas and ambient temperatures, respectively, L is the characteristic length, g the acceleration due to gravity, β the thermal expansion coefficient, and ν the kinematic viscosity of the ambient air. The relative role of buoyant and inertial forces in the flow have been found to be well-described by comparing the relative influence of these two parameters, often determined to be Gr_x/Re_x^a, with a varying constant a (Imura et al., 1978; Miller et al., 2017).

A non-dimensional flame-fuel contact frequency f_C^+ is proposed based on a characteristic gas fuel flow rate and downstream distance,

$$f_C{}^+ = \frac{f_C L^+}{u^+}, \tag{8}$$

$$u^+ = \left(g\dot{m}'' D/\rho_a\right)^{1/3}. \tag{9}$$

where $f_C$is the raw frequency data we obtained from heat flux gauge sensor, L^+ is the downstream distance from the measuring point to the leading edge of the burner chosen as characteristic length scale, u^+ is the characteristic fuel velocity based on mass flow rate, $\dot{m}''$ is the mass flow rate, D the burner hydraulic diameter, and ρ_a the air density.

Note that this non-dimensional flame-fuel contact frequency is not a typical form of the Strouhal number, such as those previously defined in pool fire studies. St-Fr correlations have been found to correlate the pool fire puffing frequency under stagnant conditions, where only natural convection is controlling the flame behavior, and the length scale chosen for the study was the pool diameter. This appears to be more of a global instability of the system driven by buoyancy. In our study, we introduce forced convection (wind), and the length scale is chosen as the distance from the measuring point to the leading edge of the burner, where the thermal boundary layer starts to develop. The length scale chosen in this paper follows our previous work on the effect of forced and natural convection on the heat flux distribution in wind-driven line fires (Tang et al., 2017a).

In **Figure 8** the local Ri_x is plotted against the non-dimensional frequency. When Ri_x is smaller than 1, f_C^+ varies around 0.7 with ranges from 0.55 to 0.8, however after Ri_x reaches 1, f_C^+ starts to decrease with Ri_x. A piece-wise function was obtained based on a correlation with experimental data to describe the local frequency trend with Ri_x. Equation (10) indicates that in a wind-driven fire, the flame-fuel contact frequency before the local Ri_x reaches 1 will remain unchanged, fluctuating around $f_C^+ = 0.7$. After Ri_x reaches 1, which means natural convection and forced convection approximately balance each other, f_C^+ will decrease with Ri_x in a power law trend as $f_C^+ = 0.7Ri_x^{-0.78}$. Correlations are provided here is to aid in understanding the trend of local flame-fuel contact frequency as it changes in different Ri_x regimes. Within the two Ri_x regimes representing lifted and attached flames, data are still scattered to some degree. Further investigations are needed to look into each of these regimes and isolate the parameters related to this scatter, which may include the fuel heat-release rate, geometry of the burner, etc., to obtain a full understanding of this relationship.

$$f_C{}^{+} = \begin{cases} 0.7 & Ri_x < 1 \\ 0.7\mathrm{Ri}_x^{-0.78} & Ri_x > 1 \end{cases} \quad (10)$$

This investigation revealed multiple patterns of movement within a wind-driven flame resulting from different forces controlling the competition between buoyancy and forward momentum along the length of the flame. Neither puffing pool fires nor jets in cross flow correctly describe this phenomenon.

The forward motion is more "messy" than the up and down contact of the flame. This likely occurs due to a competition between momentum-driven wind and a counter-clockwise recirculation zone at the flame front, a buoyant instability similar to puffing pool fires, or a combination of the two. It is also thought to be more affected by transport of stochastic turbulent structures. The up and down motion of the flame, described by $f_C^+$and $\mathrm{Ri_x}$ is seen in two regions, similar to previous studies investigating the heat flux downstream of the burner. The changes here were attributed to attachment and liftoff of the flame, which appears to be occurring here as well. It is near the end of this attachment region where the highest frequencies are observed, indicating this is also an inflection point where an unstable transition between attachment and liftoff occurs.

The way in which the flame moves within both the forward region ahead of and close within the attachment region may have important implications for fire spread modeling. Current flame spread models assume either a constant heat flux for some distance ahead of the burning region, which heats unignited fuels, or a profile of decaying heat flux constant with time. Both approaches neglect the time-dependence of heating that becomes increasingly important when fine fuels primarily carry the fire, such as in wildland fires.

CONCLUSIONS

Experiments were conducted on a variety wind-driven line fires where the intermittent behavior of the flame was studied. Both the flame forward-pulsation frequency and flame-fuel contact frequency were independently measured. Trends in these quantities were reviewed and non-dimensional scaling proposed for each. It was found that the flame forward pulsation frequencyf_F, can be well correlated and predicted by a non-dimensional parameter, $^{\mathrm{Fr}}/_{Q^{*1/2}}$ in a power law trend. The mechanism for this forward pulsation has been found to be related to the competition of wind momentum and flame buoyancy. For the flame-fuel contact frequency, which describes the local heating process of the flame to unburnt fuels along the flame attachment and intermittent regions, a piece-wise function was found with local Ri_x, indicating that when $\mathrm{Ri}_x < 1$, the non-dimensional flame contact frequency f_C^+ remains approximately constant, and when $\mathrm{Ri}_x > 1$, it decreases with Ri_x. The description of global flame forward pulsation frequency and local flame-fuel contact frequency will help to explain wildland fuel ignition and flame spread in the future.

DATA AVAILABILITY

All datasets generated for this study are included in the manuscript and/or the supplementary files.

AUTHOR CONTRIBUTIONS

WT and MG designed the tests and conducted the tests. WT, MF, MG, and SM wrote the paper.

ACKNOWLEDGMENTS

The authors would like to acknowledge financial support for this work from the USDA Forest Service Missoula Fire Sciences Laboratory and National Fire Decision Support Center under collaborative agreement 13-CS-11221637-124 and CBET 1554026. The authors also would like to thank Dr. Arnaud Trouve, Dr. Colin Miller, Mr. Daniel Gorham for their fruitful discussions and insightful comments.

REFERENCES

Albini, F. A. (1982). Response of free-burning fires to nonsteady wind. *Combust. Science Tech*. 29, 225–241. doi: 10.1080/00102208208923599

Audouin, L., Kolb, G., Torero, J. L., and Most, J. M. (1995). Average centreline temperatures of a buoyant pool fire obtained by image processing of video recordings. *Fire Safety J*. 24, 167–187. doi: 10.1016/0379-7112(95)00021-K

Blackwelder, R. F., and Kaplan, R. E. (1976). On the wall structure of the turbulent boundary layer. *J. Fluid Mech*. 76, 89–112. doi: 10.1017/S0022112076003145

Cetegen, B. M., and Ahmed, T. (1993). Experiments on the periodic instability of buoyant plumes and pool fires. *Combust. Flame* 93, 157–184. doi: 10.1016/0010-2180(93)90090-P

Finney, M., Cohen, J., Forthofer, J., McAllister, S., Gollner, M., Gorham, D., et al. (2015). Role of buoyant flame dynamics in wildfire spread. *Proc. Natl. Acad. Sci. U.S.A*. 112, 9833–9838. doi: 10.1073/pnas.1504498112

Grant, A. J., and Jones, J. M. (1975). Low-frequency diffusion flame oscillations. *Combust. Flame* 25, 153–160. doi: 10.1016/0010-2180(75)90081-4

Hamins, A., Yang, J. C., and Kashiwagi, T. (1992). An experimental investigation of the pulsation frequency of flames. *Proc. Combust. Inst*. 24, 1695–1702. doi: 10.1016/S0082-0784(06)80198-0

Hu, L. (2017). A review of physics and correlations of pool fire behaviour in wind and future challenges. *Fire Safety J*. 91, 41–55. doi: 10.1016/j.firesaf.2017.05.008

Hu, L., Hu, J., and de Ris, J. (2015). Flame necking-in and instability characterization in small and medium pool fires with different lip heights. *Combust. Flame* 162, 1095–1103. doi: 10.1016/j.combustflame.2014.10.001

Imura, H., Gilpin, R. R., and Cheng, K. C. (1978). An experimental investigation of heat transfer and buoyancy induced transition from laminar forced convection to turbulent free convection over a horizontal isothermally heated plate. *J. Heat Transf*. 100, 429–434. doi: 10.1115/1.3450826

Johnson, M. R., and Kostiuk, L. W. (2000). Efficiencies of low-momentum jet diffusion flames in crosswinds. *Combust. Flame* 123, 189–200. doi: 10.1016/S0010-2180(00)00151-6

Miller, C., Tang, W., Finney, M., McAllister, S., Forthofer, J., and Gollner, M. (2017). An investigation of coherent structures in laminar boundary layer flames. *Combust. Flame* 181, 123–135. doi: 10.1016/j.combustflame.2017.03.007

Moorhouse, J. (1982). Scaling criteria for pool fires derived from large-scale experiments. *Intl. Chem. Sym*. 71, 165–179.

Putnam, A. A. (1965). A model study of wind-blown free-burning fires. *Proc. Comb. Inst.* 10, 1039–1046. doi: 10.1016/S0082-0784(65)80245-4

Quintiere, J. (1989). Scaling applications in fire research. *Fire Safety J.* 15, 3–29. doi: 10.1016/0379-7112(89)90045-3

Subbarao, E. R., and Cantwell, B. J. (1992). Investigation of a co-flowing buoyant jet: experiments on the effect of Reynolds number and Richardson number. *J. Fluid Mech.* 245, 69–90. doi: 10.1017/S0022112092000351

Tang, W., Gorham, D., Finney, M., McAllister, S., Cohen, J., Forthofer, J., et al. (2017b). An experimental study on the intermittent extension of flames in wind-driven fires. *Fire Safety J.* 91, 742–748. doi: 10.1016/j.firesaf.2017.03.030

Tang, W., Miller, C., and Gollner, M. (2017a). Local flame attachment and heat fluxes in wind-driven line fires. *Proc. Combust. Inst.* 36, 3253–3261 doi: 10.1016/j.proci.2016.06.064

Thomas, P. H. (1963). The size of flames from natural fires. *Proc. Combust. Inst.* 9, 844–859. doi: 10.1016/S0082-0784(63)80091-0

Weckman, E. J., and Sobiesiak, A. (1988). The oscillatory behaviour of medium-scale pool fires. *Proc. Combust. Inst.* 22, 1299–1310. doi: 10.1016/S0082-0784(89)80141-9

Conflict of Interest Statement: The authors declare that the research was conducted in the absence of any commercial or financial relationships that could be construed as a potential conflict of interest.

frontiers in Mechanical Engineering

ORIGINAL RESEARCH
published: 28 June 2019
doi: 10.3389/fmech.2019.00035

Physics-Based Simulation of Heat Load on Structures for Improving Construction Standards for Bushfire Prone Areas

Nazmul Khan[1,2], *Duncan Sutherland*[1,2,3], *Rahul Wadhwani*[1,2] *and Khalid Moinuddin*[1,2]*

[1] *Institute for Sustainable and Livable Cities, Victoria University, Melbourne, VIC, Australia,* [2] *Bushfire and Natural Hazards Cooperative Research Centre, Melbourne, VIC, Australia,* [3] *School of Science, University of New South Wales, Canberra, ACT, Australia*

OPEN ACCESS

Edited by:
Michael John Gollner, University of Maryland, College Park, United States

Reviewed by:
Shiyou Yang, Ford Motor Company, United States
Xinyan Huang, Hong Kong Polytechnic University, Hong Kong
Eric Link, National Institute of Standards and Technology (NIST), United States

***Correspondence:**
Khalid Moinuddin
khalid.moinuddin@vu.edu.au

Specialty section:
This article was submitted to Thermal and Mass Transport, a section of the journal Frontiers in Mechanical Engineering

Received: *29 January 2019*
Accepted: *31 May 2019*
Published: *28 June 2019*

Citation:
Khan N, Sutherland D, Wadhwani R and Moinuddin K (2019) Physics-Based Simulation of Heat Load on Structures for Improving Construction Standards for Bushfire Prone Areas. Front. Mech. Eng. 5:35. doi: 10.3389/fmech.2019.00035

Australian building standard AS 3959 provides mandatory requirements for the construction of buildings in bushfire prone areas in order to improve the resilience of the building to radiant heat, flame contact, burning embers, and a combination of these three bushfire attack forms. The construction requirements are standardized based on the bushfire attack level (BAL). BAL is based on empirical models which account for radiation heat load on structure. The prediction of the heat load on structure is a challenging task due to many influencing factors: weather conditions, moisture content, vegetation types, and fuel loads. Moreover, the fire characteristics change dramatically with wind velocity leading to buoyancy or wind dominated fires that have different dominant heat transfer processes driving the propagation of the fire. The AS 3959 standard is developed with respect to a quasi-steady state model for bushfire propagation assuming a long straight line fire. The fundamental assumptions of the standard are not always valid in a bushfire propagation. In this study, physics based large-eddy simulations were conducted to estimate the heat load on a model structure. The simulation results are compared to the AS 3959 model; there is agreement between the model and the simulation, however, due to computational restrictions the simulations were conducted in a much narrower domain. Further simulations were conducted where wind velocity, fuel load, and relative humidity are varied independently and the simulated radiant heat flux upon the structure was found to be significantly greater than predicted by the AS 3959 model. The effect of the mode of fire propagation, either buoyancy-driven or wind dominated fires, is also investigated. For buoyancy dominated fires the radiation heat load on the structure is enhanced compared to the wind dominated fires. Finally, the potential of using physics based simulation to evaluate individual designs is discussed.

Keywords: wildland fire, wildfire, forest fire, emissions, fire spread, physics-based simulation, building standards

1. INTRODUCTION

Bushfire or wildfire is an integral part of the Australia environment and costs millions of dollars every year in terms of losses to the economy. The infamous *Black Saturday* bushfire of 2009 alone had an estimated economic cost of AUD 4.4 billion and destroyed ∼3,500 structures (McLeod et al., 2010; Ronchi et al., 2017). Previously, the 2003 Canberra fire (Blanchi and Leonard, 2005) destroyed roughly 390 houses and cost an estimated AUD 0.35 billion in losses. Over the past decade, the frequency of bushfire around the world has increased (Jolly et al., 2015). Ronchi et al. reported some of the economic costs of wildfire in North America to be between 0.4 and 7 billion USD in the last decade. The size of fires is also increasing. Recently, large and devastating bushfires, termed mega bushfire or mega wildfire, have emerged. Wildfires are classified as mega wildfires if the fire occurs at large spatial scale coupled with strong wind reaching up to 100 km/h, firestorm events and massive ember generation can cause massive evacuation, devastation, and loss of life. These fires are dynamic and difficult to manage (Mell et al., 2010). Dynamic bushfire behavior is also present in smaller bushfires. Empirically-based operational fire models struggle to account for extreme and dynamic bushfire behavior and existing operational fire model show significant difference in predicting the bushfire propagation (Cruz and Alexander, 2013). Some of the recent "mega wildfires" are the 2016 Fort McMurray fire, Canada; the 2017 Californian wildfires, USA; the 2017 Portugal wildfires, Portugal (Ronchi et al., 2017). The effect of these bushfires is not limited to economical damages, the fires also cause massive evacuation of communities and present challenges to emergency personnel. The Black Saturday fire, Australia, caused 7500 people to evacuate (McLeod et al., 2010). Many people, who did not evacuate early, died during their attempted late evacuation. The high number (173) of fatalities in 2009 Black Saturday fire is one such identified bushfire case where late evacuation resulted in the loss of life (McLeod et al., 2010; Whittaker et al., 2013). Expansion of suburban areas into previously undeveloped forest and grassland also increases the impact of fires on the population. As the populations of major cities grows, so does the area of residential areas bordering fire prone bushland. City planners and building authorities must therefore plan new developments to be resilient to the risks of bushfires.

1.1. Building in Bushfire Prone Areas

A recent study in the US (Radeloff et al., 2018) showed that there is a significant increase in the wildland-urban-interface (WUI), WUI houses, and people living in WUI from 1990-2010. One definition of the WUI (Radeloff et al., 2005) is as an area in which:

- There are at least 6.17 housing units/km^2 with vegetation area of more than 50% of terrestrial area, or
- There are more than 6.17 housing unit/km^2 with vegetation area less than 50% of terrestrial area and is less than 2.4 km away from vegetation which has an area of greater than 5 km^2 and have vegetation area of greater than 75%.

These definitions depend somewhat on the jurisdiction. In Australia, bushfire prone areas (BPA) are classified by Australian Standard 3959 (AS 3959, 2009). The BPA is classified into three classes:

- Bushfire hazard level 2 (BHL2): Areas of forest, woodlands, scrub, shrublands, mallee, and rainforest where there is potential for bushfire behavior such as a crown fire, extreme levels of radiant heat, and extreme ember attack. BHL2 does not include grasslands. An area of BHL2 that is larger than 4 hectares will be mapped as BPA including a buffer of 300 m.
- Bushfire hazard level 1 (BHL1): Areas of forest, woodlands, scrub, shrublands, mallee, rainforest, and unmanaged grasslands where there is potential for bushfire behavior such as crown fire, grassfire, and ember attack. An area of BHL1 that is between 2 and 4 hectares that is not unmanaged grassland will be mapped as BPA including a buffer of 150 m. An area of unmanaged grassland larger than 2 hectares will be mapped as BPA including a buffer of 60 m.
- Bushfire hazard level low (BHL low): Areas where extent of bushfire attack is very low e.g., managed grassland park, airports, or botanical gardens.

Australian standard 3959 (AS 3959, 2009) was developed to specify the necessary design for the structures located at BPA. The intention of AS 3959 was improving the resilience of buildings against the bushfire attack (radiant heat, direct flame contact, burning ember, or a combination of these three factors) to mitigate the risk of bushfire through better adaptability of structures situated in the WUI. While the topic of this paper is limited to AS 3959, the US standard developed by National Fire Protection Association (NFPA). NFPA 1144 (NFPA 1144, 2013) uses a similar model to prescribe design requirements for structures in the WUI areas of the US. There are several drawbacks of AS 3959 that have previously been reported (Roberts et al., 2017; Sharples, 2017). A particular limitation of AS 3959 is the lack of quantified ember loading during a fire event. Embers are the leading cause of house loss; in the Canberra 2003 fires, 229 houses were destroyed in the suburb of Duffy and 106 of the houses were ignited by embers alone (Blanchi and Leonard, 2005). AS 3959 only provides a small amount of guidance about ember attack increasing with fire danger. AS 3959 is based upon an empirical model for radiation heat load upon the structure. The model and its limitations will now be discussed.

1.2. Empirical Models and FDI

Fire danger index (FDI) is a measure of the degree of fire danger quantified based on wind speed, relative humidity, some measure of fuel load, and fuel moisture content. Fuel moisture content is typically modeled based upon the dryness of fuel, rainfall, vegetation type, and past fire history. For this discussion, we will assume only flat terrain, however, there are multiplicative corrections for slopes that can be applied. FDI is a scaled version of the quasi-steady rate of fire spread on flat ground expected

Abbreviations: FDI, Fire Danger Index; GFDI, Grass Fire Danger Index; RoS, Rate-of-spread (of a fire); BAL, Bushfire attack level.

under the weather and fuel conditions. The McArthur Forest fire danger index FDI has a reference value set to 100 for the 1939 *Black Friday* bushfire (McArthur, 1967). There are many instances where this reference value was breached, for example, the *Black Saturday* bushfire of 2009, where FDI value for forest was more than 172 and 241 for grass lands (Tollhurst, 2009). In the state of New South Wales, Australia, FDI of above 100 suggests that structures will not survive and hence evacuation of occupants is required. There are several versions of the fire danger index for different fuel types and for different fire spread models and all FDI are based on the same principles. Given that this work focus on grassland fuels, the relevant fire danger index is the grassland fire danger index (*GFDI*):

$$GFDI = \begin{cases} 3.35w\exp(-0.097m_c + 0.0403u) & m_c \leq 18.8\%, \\ 0.299w\exp(-1.686m_c + 0.0403u)(30 - m_c) & \\ \qquad\qquad 18.8\% < m_c < 30\%. \end{cases} \quad (1)$$

where w is the fuel weight (T/Ha), m_c is fuel moisture content as a percentage, and u is the wind speed at 10 m high in km/h. The moisture content is modeled by the following correlation

$$m_c = \frac{97.7 + 4.06RH}{T + 6} - 0.00854RH + \frac{3000}{C} - 30, \quad (2)$$

where RH is relative humidity (%), T is ambient temperature (°C) is the curing index ($0 - 100\%$), a measure of the amount of dead material in the grassland. The *GFDI* is used to determine the rate of spread of the fire *RoS*, which is used to model the intensity of the fire. The *RoS* is

$$RoS = 0.13GFDI. \quad (3)$$

The fire intensity model for grassland [AS 3959 fuel class G, and also class C (shrubland), D (scrub), and E (Mallee/Mulga)] is given by Byram's model:

$$I = \frac{H\,w\,RoS}{36}, \quad (4)$$

where H is heat of combustion (in the Byram model $H = 18.6$ MJ/kg) and flame length L_f is subsequently calculated using

$$L_f = 0.0775I^{0.46}, \quad (5)$$

and flame height may be determined using:

$$F_h = L_f cos\alpha, \quad (6)$$

where α is the angle between the ground surface and the flame height which is not subsequently modeled. An algorithm in AS 3959 is provided to compute the flame angle which gives the maximum view factor between the flame and the structure to provide an estimate of heat load in the worst-case scenario. On a flat ground the view factor will be maximized at $\alpha = \pi/2$. The lack of a model of α is a limitation of the standard, especially since some limited flame angle correlations, for example Weise and Biging (1996), do exist in the literature. To calculate emitted radiant heat flux, an estimated flame temperature (1090 K) is used instead of fire intensity; note that intensity does determine the flame length.

The emitted radiant heat flux is computed from the flame temperature, flame height, and flame width. Here flame width refers to the length of the fire front taken as arbitrarily as 100 m in the AS 3959 standard. These fire behavior parameters are used to compute the emitted radiant heat flux load available from the fire present in the particular vegetation. The radiant heat emitted by the flame is

$$q_{r,emitted} = L_f \cos\alpha F_w \sigma \epsilon T_f^4, \quad (7)$$

where T_f is the flame temperature (K), σ is the Stefan-Boltzmann constant ($5.67^{-8} W/m^2K^4$), ϵ is called emissivity and represents the non-ideal blackbody characteristics of the material. ϵ is taken as the value for soot (0.9). F_w is the flame width.

AS 3959 assumes a constant value of flame temperature of 1090 K however the instantaneous value of flame temperature can be higher than 1200 K (Worden et al., 1997). It can be seen from Equation (7) that the thermal radiation is proportional to the fourth power of the flame temperature and directly proportional to effective area of the flame. Because the flame temperature is raised to the fourth power and so any errors in flame temperature lead to much larger errors in emitted radiant heat flux. The radiant heat flux received at the structure depends on two more parameters: the view factor $F_{1,2}$, which represents the effective solid angle between the flame in the classified vegetation and structure, and ϕ, the atmospheric transmissivity to account for how much radiative heat is absorbed before reaching the structure. These two parameters are combined with the calculation of heat flux load at the site to estimate effective radiant heat flux at the structure. That is,

$$q_{r,effective} = L_f \cos\alpha F_w F_{1,2} \phi \sigma \epsilon T_f^4. \quad (8)$$

AS 3959 (table 3.1) classifies the bushfire attack level (BAL) into six categories based on the radiant heat flux $q_{r,effective}$ at the structure

- BAL- LOW: considered safe situation for heat flux less 12.5 kW/m^2 and no ember attack. Hence, no special construction requirements.
- BAL- 12.5, 19, 29, 40: special construction is required, the numbers correspond to heat fluxes of 12.5, 19, 29, and 40 kWm^{-2}, respectively. These cases involve ember attack however there is no quantification of ember attack, only that ember attach is suggested to increase with the heat flux.
- BAL- FZ: are considered situations in which direct flame contact in addition to heat flux more than 40 kWm^{-2} and ember showers are expected to the structure.

There are several drawbacks in the AS 3959 approach. Firstly, there is no model for ember attack, and only limited guidance (see above) about when embers can be expected. Other limitations include a fixed value of flame temperature, limitations to the flame length calculation, an ambiguous flame angle, the view factor model, and assumption of a planar flame. Hence, the AS

3959 radiation model in certain situations and generally in mega-bushfire might severely under predict radiation heat flux load. In the 2017 Iberian wildfires, Portugal, social media posts showed that many of the structure were exposed to multiple fire fronts showing a higher heat flux exposure on the structure (Viegas, 2017). The other aspect that radiant heat flux depends upon is view factor. The dynamic nature of a fire front changes the structure of flame hence affecting the view factor. The view factor can also change significantly due to different topography that is, if the fire is progressing down a slope toward the structure would have higher view factor than a fire progressing up the slope toward the structure. AS 3959 does include the topography in the computation of the view factor. Because we are only considering flat ground for this study, we omit discussion of the slope corrections to view factor. Another potential limitation of the AS 3959 approach is the lack of consideration of any flame geometry. The lack of a flame angle model may also be a critical flaw; it has been established for some time that there are two modes of fire propagation in wild, industrial, and building fires (Apte et al., 1991; Morvan and Frangieh, 2018). Grassfires have been characterized as wind dominated and buoyancy dominated fires (Dold and Zinoviev, 2009; Moinuddin et al., 2018; Morvan and Frangieh, 2018). In the wind dominated mode the shearing fluid flow (that is, the wind) dominates over the buoyant flow (the updraft from the fire plume). The flame is elongated and confined to a boundary layer structure, **Figure 1A**. In the buoyancy dominated mode, the updraft from the fire is sufficient to overcome the shearing forces of the driving wind and the flame becomes more vertical, see **Figure 1B**. In the wind dominated mode, the flame height is low and so the view factor will be small compared to the buoyancy dominated mode, however, because the fire plume is confined to a boundary layer there will be a high convective heat flux downstream of the fire. In the buoyancy dominated mode the plume is vertical and therefore the convective heat flux ahead of the fire will be small compared to the wind dominated mode. However, because the flame is vertical, the radiant heat flux ahead of the fire will be high compared to the wind dominated mode. For a realistic parameter range, wind dominated fires will have high *GFDI* (Equation 1) because of the exponential growth with wind speed. As a fire transitions from a buoyancy dominated fire to a wind dominated fire due to an increase in wind speed the *GFDI* will increase. The fire intensity is expected to increase due to the increase in *GFDI* and *RoS* (Equation 3). The AS 3959 model (Equation 5) predicts monotonic increase in flame height with increasing *RoS* and therefore, assuming flat ground, increased radiation load upon a structure. However, we hypothesize that if the fire becomes wind dominated the flame height will decrease and the corresponding increase in intensity may not be sufficient to ensure that the heat load on the structure increases with increasing wind speed.

The Byram convective number, N_c is used to quantify if a fire is buoyancy dominated or wind dominated (Morvan and Frangieh, 2018). The Bryam number is defined by

$$N_c = \frac{2gI}{C_p \rho T_a (u_{10} - RoS)^3}, \tag{9}$$

where $g = 9.8\ \mathrm{ms}^{-2}$ is the gravitation acceleration constant, $T_a$is the ambient temperature, $T_a = 305$ K in the simulations presented here, the density $\rho = 1.2\ \mathrm{kg/m}^3$ and specific heat of air $C_p = 1.0$ kJ/kg K. u_{10} is the driving wind speed at 10 m high. u_{10} is a chosen because wind speed measured at 10 m is a meteorological standard. The factor of two in the definition of N_c is merely conventional. Fires are conclusively buoyancy dominated if $N_c \geq 10$, wind dominated if $N_c \leq 2$, and ambiguous if $2 < N_c < 10$.

1.3. Present Study

In this work we conduct simulations to compare the radiation heat load upon a structure, as close as computationally possible, from the fire scenario in AS 3959 predicted by the BAL set out in the standard, to the radiation heat load simulated by a physics based model. The idea is to assess the validity of the standard as it stands, rather than looking to extend the standard to include new features such as ember attack. Specifically, we will

1. identify if the BAL classification values are supported by physics-based simulation,
2. assess the sensitivity of the radiation heat load to the wind speed, fuel load, and relative humidity,
3. and examine the differences in heat load on a structure between buoyancy dominated fires and wind dominated fires.

The simulations are as close to the AS 3959 standard as computationally practical. However, due to computational restrictions the fire width is considerably reduced from 100 to 20 m. However, if the radiative heat load predicted by a 20 m wide fire is larger than predicted by AS 3959, it is reasonable to assume that the 100 m wide fire will exceed the standard by a larger amount. For simplicity we consider a grassland fuel at $GFDI = 50$ to match the fuel class *G* in AS 3959. Further simulations are conducted to assess the effect of varying the driving wind speed and fuel load on the heat flux received by a structure and to determine if the different modes (wind dominated or buoyancy dominated) fire propagation effects the radiative heat load upon a structure. This work is intended to provide an introductory framework for the use of physics-based models in construction standards for properties in bushfire prone areas.

2. PHYSICS BASED SIMULATION

2.1. Fire Dynamics Simulator (FDS)

The code used to conduct the simulations is FDS (McGrattan et al., 2013a). FDS uses a large eddy simulation (LES) methodology to solve the equations governing fluid momentum. LES resolves large scale fluid motions but smaller, subgrid scale, turbulent motions are modeled with an eddy viscosity approach. The grass is modeled as fuel particles located in a layer on the ground using the boundary fuel model. The boundary fuel model assumes that the fuel bed is thin and that the combustion largely occurs above the fuel bed. The gas phase to be resolved on a user-specified coarse grid and the fuel pyrolysis and the heat transfer to the fuel bed is resolved on a finer grid (in this case determined by the program). As the solid fuel decays due to heating, the fuel acts as a source of combustible gas. The height

and structure of the grass, which exerts an aerodynamic drag force, is also represented as a momentum sink in the Navier-Stokes equations. Conduction within the solid fuel is modeled, but the contribution of conduction to the overall heat transfer is negligible. The convective heat transfer from the flame to the fuel bed is modeled using an empirical correlation for convective heat transfer to vertical circular cylinders. Radiation heat transfer is approximated by solving the radiation transport equation using a discrete ordinates method. A problem arises with this approach; because the combustion zone is difficult to resolve with LES the gas temperature can be under predicted in the flame. Because radiation depends on the fourth power of flame temperature, care is required so that unacceptable errors in radiative heat flux do not occur. The source of radiation is modeled by a piecewise function for the flaming and non-flaming regions. Outside the flaming zone, where T is well resolved and there is no difficulty. Inside the flaming zone the radiation source is a function of the local heat release per unit volume.

FDS uses a fast chemistry model of combustion and where the mixture fraction of fuel and air is higher than the stoichiometric value, the fuel is considered burnt. See Mell et al. (2007), Mell et al. (2009), and McGrattan et al. (2013b) for a full and careful discussion of the physics-based model and the numerical methods used. FDS has been carefully validated for the simulation of grassfires. Both Mell et al. (2007) and Moinuddin et al. (2018) have compared simulation results to experimental results from Cheney et al. (1998). The simulations were shown to reproduce the measured rate-of-spread.

2.2. Model Setup

AS 3959 assumes a straight line fire of width 100 m, that is, the fire is assumed to behave like a two-dimensional line fire. However, due to computational restrictions a fire width of 20 m is used here. Linn et al. (2012) has demonstrated that this width is adequate for quasi-two-dimensional simulations. Linn et al. (2012) notes that the *RoS* of a straight-line fire is significantly greater than the *RoS* of a naturally curved fire. It is important to note that the fire is still three dimensional, although the fire is similar at every location in the span-wise direction. This approach was adopted for these simulations because the standard assumes a straight line fire. In reality, a perfectly straight line fire is unlikely, fire fronts often propagate in an elliptical shape. As such, the distance from the fire front to the structure, and therefore the radiative heat load, would vary as a function of position along the curved fire line.

The lateral boundaries are free slip to ensure that the fireline remains approximately straight as the fire progresses through the domain. The total domain height is chosen to be at four times the structure height, to avoid spurious fluid acceleration above the canopy (Bou-Zeid et al., 2009). The ground is a no-slip boundary and the top boundary is a free-slip surface as is standard for atmospheric surface layer simulations.

The driving wind is prescribed using a logarithmic mean velocity profile that is

$$u_{inlet} = A \log(\frac{z}{z_0}), \tag{10}$$

The roughness length is taken as $z_0 = 0.03$ m, representative of open grassland (Rüedi, 2006). The amplitude A is chosen so $u(0, 10)$= 5.83, 8.33, and 12.50 ms^{-1}. To introduce turbulent fluctuations, the synthetic eddy method of Jarrin et al. (2006) is used. This method introduces artificial perturbations in with randomized length and velocity scale. N_{eddy} synthetic eddies with length scale L_{eddy} and velocity scale σ_{eddy} are prescribed on the inlet plane $x = 0$.

A structure of size 5x5x2.5 is located at 240x10x2.5. The structure is a solid object with no-slip boundary conditions and thermally inactive material properties. Therefore, no re-radiation from the structure to the fire is included in the simulations and combustion of the structure is not simulated; these assumptions are also implicitly made by AS 3959. The wind-only flow is firstly allowed to spin-up for a time of 300 s, to ensure a statistically stationary wind field throughout the domain. The fire was ignited by a temperature anomaly of 1200 K imposed for 10 s over a line which runs across the domain at $x = 40$ m and this causes the fuel to ignite. A schematic of the domain is sketched in **Figure 2**.

The resolution follows Moinuddin et al. (2018) with a uniform grid spacing in all variables $\delta x = \delta y = \delta z = 0.25$ m. δx is approximately half of the extinction length scale (Morvan et al., 2013). Moinuddin et al. (2018) found that a stretched grid, as used by Morvan et al. (2013) converged more slowly than a uniform grid. The other parameters for the fuel properties are shown in **Table 1**.

The quantities measured in the simulations are the radiative and convective heat fluxes located on the walls of the structure and the boundary temperature. The heat fluxes are measured at a single point on each face of the structure, although only the face of the structure nearest to the approaching fire front is relevant. The boundary temperature allows measurement of the fire front location and correspondingly the RoS of the fire. The

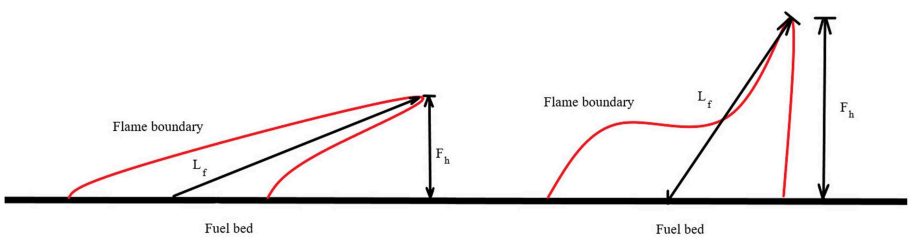

FIGURE 1 | Cartoon showing a sketch of the two different flame geometries expected from the two fire propagation modes. **(left)** A wind dominated flame, **(right)** a buoyancy dominated flame.

pyrolysis model used in these simulations is the linear model of Morvan and Dupuy (2004). Thus, fuel with a temperature above $T = 400$ K is pyrolyzing. The $T = 400$ K contour is then a clear measure of the pyrolysis front and the fire front location is taken as midpoint of the pyrolysis region. Because the fire is a straight line fire in the spanwise direction, the pyrolysis region may be averaged in the $y-$direction to give a single mean fire location x_*. Because the flame may be quite long and elongated, the fire front location based on the center of the pyrolysis region may be significantly further away from the structure than the location of the leading edge of the flame. The effect of different flame measurements on the radiative heat load was tested.

Seven simulations are conducted, notice that some cases in the parametric study are duplicates. The first simulation is control case aimed at replicating the AS 3959 scenario as faithfully as possible. Three further sets of simulations are conducted systematically varying driving wind velocity, vegetation load, and relative humidity to assess how the radiative heat flux upon the structure depends on these quantities. Assuming that the lowest wind velocity fire is buoyancy dominated. As the driving wind speed increases (with all other parameters constant), the fires should be more dominated by wind than buoyancy. If the fire is wind dominated, the radiative heat flux should be low but the convective heat flux should be high relative to a fire where the fire is buoyancy dominated. However, if the fire is buoyancy dominated, the increase in wind speed should tilt the flame, allowing more fuel to be involved in the fire and thus increase the intensity of the fire. Correspondingly the radiative heat flux on the structure will increase. As the vegetation load increases (with all other parameters constant), the intensity of the fire should increase and correspondingly the radiative heat flux should increase. Decreasing the relative humidity with other parameters fixed should lead to a increase in fire intensity and radiative heat flux on the structure. The parameters for all cases are shown in **Table 2**.

3. RESULTS AND ANALYSIS

3.1. Basecase

To check that the simulation is reasonable we examine the frontal position as a function of time and the *RoS* (ie the time derivative of the position) of the fire. The frontal location and *RoS* are shown in **Figure 3**. Because of the noise in the *RoS* results, a five-point moving average smoothing was applied to the data to reveal informative trends. The frontal location in time shows a brief ignition phase over the first 5 s of the simulation before becoming approximately linear, indicative of a quasi-steady fire. The *RoS* shows a slight decreasing trend after the ignition phase. The average rate of spread ($\sim$2.2 ms^{-1}) is commiserate with the observations of Cheney et al. (1998), simulations of Linn et al. (2012) and Moinuddin et al. (2018), and empirical model predictions (Moinuddin et al., 2018) for similar wind speeds and fuel conditions.

The simulated heat load of the basecase, following AS 3959 as closely as possible, is compared to the AS 3959 BAL predictions. The radiative and convective heat fluxes received on all surfaces of the structure as a function of fire front distance from the structure are shown in **Figure 4**. Because the fire location moves over time the distances between the fire and the structure changes in time. Because AS 3959 quantifies BAL in terms of distance and because different fire parameters lead to different *RoS*, these plots are made with respect to fire distance, rather than time. The

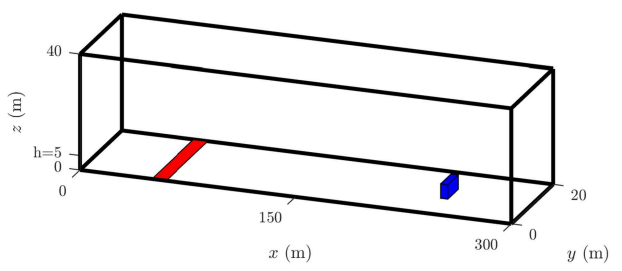

FIGURE 2 | The simulation domain showing the line ignition source (red strip), and the house structure (blue object).

TABLE 1 | Simulation parameter values and characteristics.

Numerical parameters	
Domain size:	$300 \times 20 \times 40$ m
Grid spacing	$\delta x = \delta y = \delta z = 250$ mm (fire simulations)
Filtering	Implicit at the grid spacing scale
Turbulence model	Smagorinsky constant $C_s = 0.1$
Boundary conditions	
Lateral	Free-slip, no normal velocity
Bottom (ground)	No-slip
Top (sky)	Free-slip, no normal velocity
Inlet	Log profile with SEM parameters
Roughness length z_0	0.03 m
L_{eddy}	0.5 m
N_{eddy}	1200
σ_{eddy}	1.0 ms^{-1} if $z < 5$ m
	0.5 ms^{-1} if $5 \geq z < 15$ m
	0 ms^{-1} if $z \geq 15$ m
Outlet	constant pressure
Temperature BCs	zero fluxes
Fuel parameters	**Moinuddin et al. (2018)**
Drag coefficient	0.125
Vegetation height	0.315 m
Moisture content	5 %
Element surface/volume ratio	9,770 m^{-1}
Element density	440 kg m^{-3}
Char fraction	17 %
Emissivity	99 %
Maximum mass loss rate	0.15 kg m^2 s^{-1}
Sampling	
Spin-up time	$\sim$300 s
Simulation time	$\sim$450 s
Measurement time	1 s

TABLE 2 | Parameters for base case and parametric study.

Base case parameters	
Driving velocity	$u_{10} = 12.5$ ms^{-1}
Vegetation load	0.375 kgm^{-2}
Relative humidity	25%
Bryam Number	$N_c = 0.6$, $RoS = 2.3$ ms^{-1}
Driving velocity	**Vegetation load: 0.75 kgm^{-}2, Relative humidity :25 %**
Vel. case 1 driving velocity	$u_{10} = 12.5$ ms^{-1}, $N_c = 1.1$,$RoS = 2.0$ ms^{-1}
Vel. case 2 driving velocity	$u_{10} = 8.33$ ms^{-1}, $N_c = 3.6$,$RoS = 1.8$ ms^{-1}
Vel. case 3 driving velocity	$u_{10} = 5.55$ ms^{-1}, $N_c = 49.5$,$RoS = 1.9$ms^{-1}
Vegetation load	**Driving velocity: 12.5 ms^{-1}, Relative humidity :25 %**
Veg. case 1 Vegetation load	1.5 kg m^{-2}, $N_c = 1.1$,$RoS = 2.3$ ms^{-1}
Veg. case 2 Vegetation load	0.75 kg m^{-2}, $N_c = 1.1$,$RoS = 2.0$ ms^{-1}
Veg. case 3 Vegetation load	0.375 kg m^{-2}, $N_c = 0.6$,$RoS = 2.3$ ms^{-1}
Relative humidity	**Vegetation load: 0.375 kgm^{-2}, Driving velocity: 12.5 ms^{-1}**
RH case 1 Relative humidity	25%, $N_c = 0.6$,$RoS = 2.3$ ms^{-1}
RH case 2 Relative humidity	12.5%, $N_c = 1.1$,$RoS = 2.2$ ms^{-1}
RH case 3 Relative humidity	6.25%, $N_c = 1.1$,$RoS = 2.2$ ms^{-1}

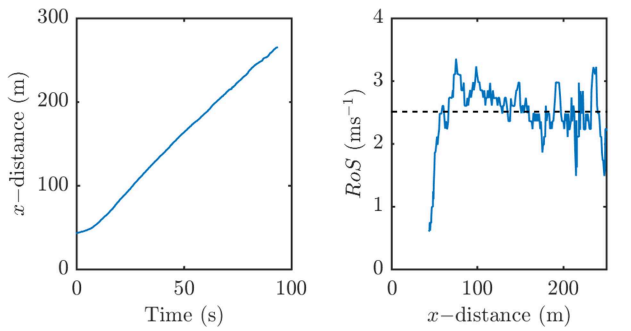

FIGURE 3 | The frontal location **(left)** and *RoS* **(right)** as a function of time. The *RoS* has been smoothed using a five-point moving average. The dashed line shows the mean *RoS* over the simulation.

radiative heat flux on the structure is irregular, although some trends are observable. The heat flux on the front surface increases most quickly as the flame makes contact with the structure. The heat flux on the rear surface increases after the fire has passed the structure. The heat fluxes on the left and right sides both increase at the same distance (∼–10 m) but the peak radiative heat load on the left hand side is much greater than on the right hand side and on the front of the structure. The asymmetry is likely due to a complicated wake behind the structure which leads to intensification of the fire on one side of the structure. While this phenomenon is interesting, a full investigation is beyond the scope of the present study. Furthermore, the peak of radiant heat flux, when the fire is in direct contact with the structure is not important because the structure will likely ignite. The radiant heat flux on the top of the structure is minimal because the top surface is flat and not exposed to the flame. The radiation heat load can be used to estimate the duration of the heat load on the structure. The heat load on all faces is summed and the peak total heat load is measured. The duration of heat exposure is taken as the time period where the heat load exceeds 1% of the peak total heat load. For the basecase the exposure duration is 22 s. Note that all other cases give similarly short exposure periods. The duration of exposure is important when considering ignition by radiation alone, however, in reality most house losses ignitions are piloted by embers (Blanchi and Leonard, 2005).

The convective heat flux on the structure is approximately an order of magnitude less than the corresponding radiative heat flux on the structure and therefore negligible in terms of BAL in this case. However, this does not imply that the convective heat load on the structure is always negligible nor does this imply that the increased windload due to the convective plume can be neglected.

The Byram number is computed from Equation (9) using the quasi-steady rate of spread before the fire impacts on the structure and the mean total heat release rate over the time before the fire impacts on the structure. The Bryam numbers and the *RoS* from the simulations are also listed in **Table 2**. The simulated *RoS* are realistic compared to the grassfire experiments of Cheney et al. (1998). The simulated *RoS* exceeds that of previous simulations by Moinuddin et al. (2018) although we use a straight line fire as opposed to a naturally curved fire which makes significant differences to the *RoS* (Linn et al., 2012). The values of, and the variation in, *RoS* computed here are of similar magnitude to the observations of Linn et al. (2012). The Byram numbers indicate that most of the cases are wind dominated, except the vel. case 2, which is ambiguous and vel. case 3 which is buoyancy dominated. The Bryram numbers are unsurprising; high fuel load and low wind speed should give a buoyancy dominated fire.

The total heat flux, that is the sum of radiant and convective heat flux, and radiation heat flux are also shown in **Figure 5** to see the relative contribution of convective heat load. In this figure, the front face of the structure is located at the origin and the distance to the fire front is measured along the $x-$axis. The fire location is measured by the fire front and leading edge approaches. The simulated heat flux follows the same trends as the BAL model, however, the BAL-12.5 and BAL-19 are apparently excessive. That is, the standard predicts heat flux far greater (between two and more than 10 times) the simulated heat flux. The BAL-29 and BAL-40 regions agree with the simulation results. Recall that the simulated fire is one fifth of the width of the fire modeled by AS 3959. The radiant heat load can be expected to increase with increasing fire width. Therefore, while the simulation results may apparently support the model in the standard, the simulated heat flux from a 100 m wide fire will likely exceed the standard. While this discrepancy could be severe, the standard could be revised fairly easily. The BAL regions are fairly narrow so the regions could be made wider to accommodate larger anticipated heat fluxes. Measuring the distance from the leading edge of the flame shifts the heat flux curve to the right. Consequently the peak heat flux is received well after the fire front has passed the house structure. The flame center measurement, which leads to greatest heat flux when the fire impacts upon the structure is more intuitive. The total heat flux and radiation heat

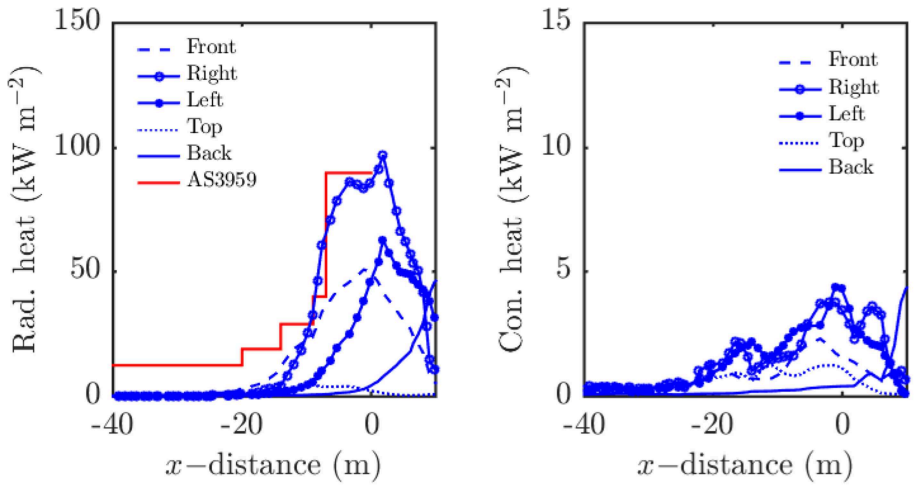

FIGURE 4 | Radiation **(left)** and convective heat load **(right)** on the structure for the base case. The distance is measured to the center of the pyrolysis region.

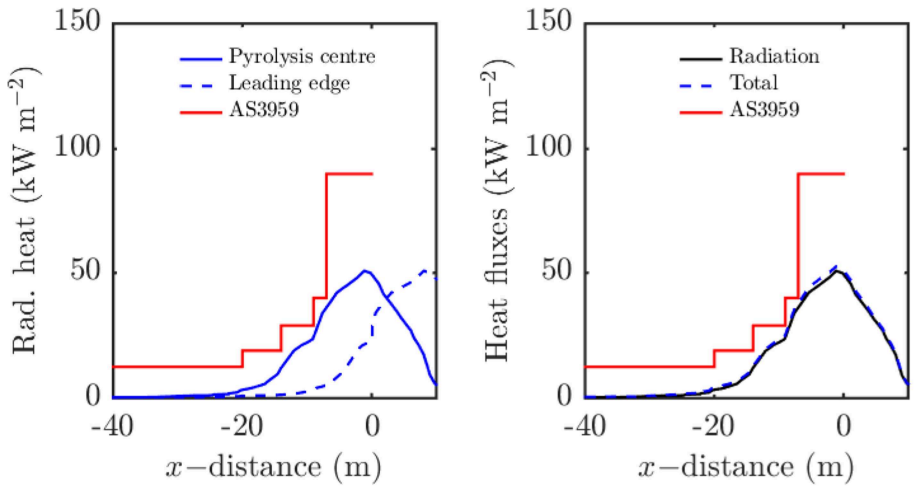

FIGURE 5 | Comparison of heat load with AS 3959 data; the origin is the position of structure. **(Left)** Radiation heat load, **(right)** radiation and total heat load. For **(left)** the fire location is estimated from the center of the pyrolysis region (fire front) and from the leading edge of the fire. For **(right)**, only the center of the pyrolysis region is used.

flux are also shown in **Figure 5** to see the relative contribution of convective heat load and, as expected, the contribution of convection to total heat load is negligible in this case.

3.2. Variation of Driving Velocity

The driving wind velocity is varied with fixed vegetation load (0.75 kgm^{-2} and fixed relative humidity (25%). The wind velocities are decreased from the value of 12.5 to 5.55 ms^{-1}, or 45 to 20 kmh^{-1}.

In this set of simulations the fuel load is high and as such a buoyancy dominated fire may be expected at low wind speeds, whereas the fire will tend to be more wind dominated at high wind speeds. Buoyancy dominated fires tend to have taller and more vertical flames than wind dominated fires, so more radiative heat load on the structure may occur at low wind speeds due to the size of the flame. Increased wind speed wind provides increased fresh oxygen to the fire, this enhances the fuel burning rate, in turn creating a larger fire. If the shear force from the wind is significant relative to the buoyant force from the fire plume, the increased wind speed also inclines the fire plume at a more acute angle, increasing heat transfer to the virgin fuel, subsequently increasing the pyrolysis region and fire intensity. Because the fire intensity increases the flame height and flame temperature both increase leading to greater radiative heat load on the structure. However, if the fire becomes wind dominated (i.e., wind shear dominates buoyancy forces) the flame will effectively attach to the ground (Sharples et al., 2010) leading to a very small flame height and a decrease in radiative heat load on the structure.

Figure 6 shows the heat load with varying wind velocities; 5.55, 8.33, and 12.5 ms^{-1}, respectively. The figure supports the hypothesized effect of buoyancy dominated fire yielding higher radiative heat loads at lower wind velocities. The radiative heat

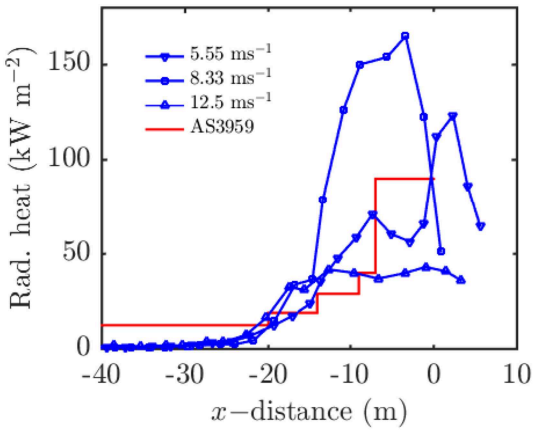

FIGURE 6 | Radiation heat load on the front of the structure as the wind velocity varies. Distance is measured to the pyrolysis center.

load for the 12.5 ms^{-1} case is systematically lower than the other two cases. The radiative heat load at distance 0 m (i.e., where the flame makes contact with the structure) for the 5.55 and the 8.33 ms^{-1} case wind speed case is ∼90 kWm^{-2}. However, for the 12.5 ms^{-1} wind speed case the radiative heat load at distance zero is much lower than the other two cases: ∼45 kWm^{-2}. Unexpectedly, the intermediate wind speed 8.33 ms^{-1} case yields the highest heat load, suggesting that the radiative heat load dependence on the fire dynamics is complicated. For example buoyancy dominated fires with very upright flames may not burn as intensely as a buoyancy dominated fire with a slightly inclined flame. The inclination of the flame will lead to increased preheating and pyrolysis of unburnt fuel and a more intense fire overall, while still yielding a large flame area that enhances radiative heat fluxes on the structure. A more comprehensive investigation of the flame dynamics is required to fully understand this behavior.

The maximum convective heat flux on the structure was measured to be ∼ 7% of the maximum radiative heat flux on the structure, consistent with the findings in **Figure 4**.

The flame profiles are examined when the fire is located at $x \approx -20$ m and $x \approx 0$ m. Here we use the term flame profile to refer to a cross section of the flame determined from the stoichometric mixture fraction contour and are shown in **Figure 7**. Because FDS uses a mixed-is-burnt combustion model these contours in the $xz-$plane represent the simulated flame boundary, with combustion occurring in the region enclosed by the contours. The three fires at $x = -20$ m have different characteristics. For the $u_{10} = 5.55$ and $u_{10} = 8.33$ ms^{-1} cases the average flame height is ∼0.75 m, whereas for the $u_{10} = 12.5$ ms^{-1} case the flame height is less than 0.5 m. This is consistent with the notion that the $u_{10} = 12.5$ ms^{-1} case is wind dominated and the other two cases are buoyancy dominated. When the fire is at $x = 0$, the flame height behavior is no longer systematic, which is likely due to the complexities of the fire engulfing the structure.

The AS 3959 model predicts that the flame height increases monotonically with wind speed. In these cases the $GFDI = 34$, 50, and 92 for $u_{10} = 5.55$, 8.33, and 12. ms^{-1} respectively. AS 3959 considers tussock moorland fires at $GFDI = 50$ and the computed $GFDI$ values are in the very high to severe fire danger rating categories. Basic manipulation of Equations (1)–(5), i.e., substituting all quantities into Equation (5) and assuming only u varies gives the following equation for L_f

$$L_f = 0.0775Be^{0.0185u_{10}}, \tag{11}$$

where B is a constant:

$$B = \begin{cases} \left(\frac{3.35w^2H}{36}\exp(-0.097m_c)\right)^{0.46} & m_c \leq 18.8\%, \\ \left(\frac{0.299w^2H}{36}\exp(-1.686m_c)(30-m_c)\right)^{0.46} & 18.8\% < m_c < 30\%. \end{cases} \tag{12}$$

Recall L_f is the flame length, H is relative humidity, m_c is fuel moisture content, and u_{10} is the driving wind speed.

Because the ground is flat the view factor will be maximized at $\alpha = \pi/2$. Therefore, L_f is the only variable in Equation (8). Hence the AS 3959 model predicts that the (maximum possible) radiation flux at the structure will increase with increasing wind speed; this prediction is not supported by these simulations. The predictions of the standard are also breached, for all wind speed cases, with the exception of the BAL-40 region in the 12.5 ms^{-1} case. The maximum heat flux (from the 8.33 ms^{-1} cases) received in the BAL-19 region is ∼30 kWm^{-2}, 100 kWm^{-2} in the BAL-29 region, and 150 kWm^{-2} in the BAL-40 region not breached in this case. Not correctly predicting the worse-case scenario is a problem for the standard. Structures may be built to withstand the predicted worse-case scenario and receive far greater heat flux from a fire with lower $GFDI$.

3.3. Variation of Vegetation Load

Because the base case (wind speed 12.5 ms^{-1}, 25% relative humidity, and a fuel load of 0.375 kgm^{-2}) is wind dominated, increasing the fuel load should increase the intensity of the fire, and subsequently the radiative heat flux at the structure should increase. The results shown in **Figure 8** support the aforementioned hypothesis. The general trend is that the radiative heat flux at the structure increases with increasing heat load; especially before the fire impacts upon the structure. There is a peak in radiative heat flux in the highest fuel load case, at around $x = -20$ m. The exact cause of the peak is not investigated, but the peak in radiation heat flux corresponds to a peak in total heat release rate suggesting that fire has instantaneously flared up around that point.

3.4. Variation of Relative Humidity

Following the equation for $GFDI$ (1), increasing the relative humidity decreases the $GFDI$ and thus the radiative heat flux at the structure. However, increasing the relative humidity also will modify the fuel moisture content, which will decrease the burning rate of the fuel and the intensity of the fire. Here, in order to systematically investigate the effect of different

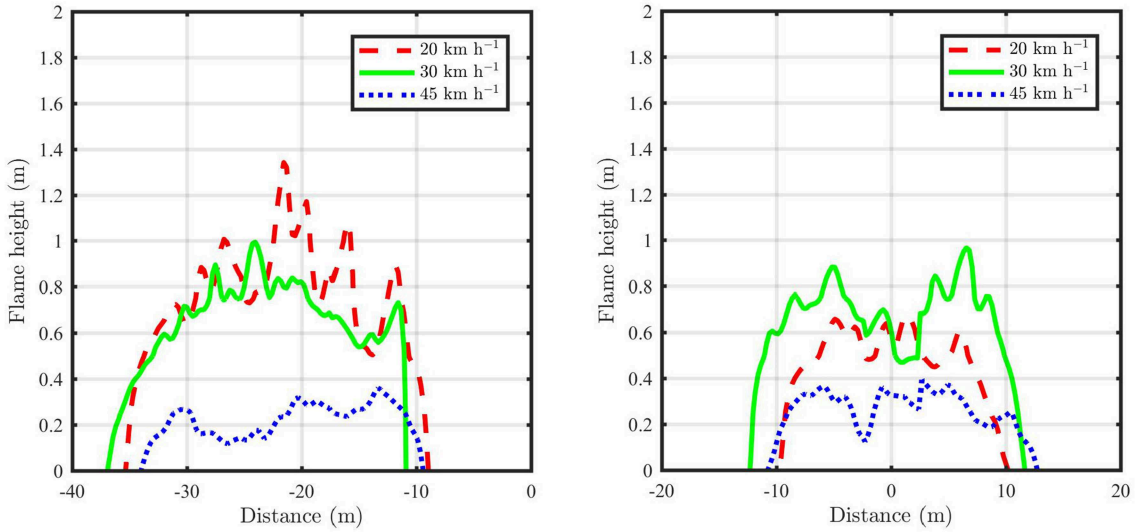

FIGURE 7 | Flame profiles showing characteristics of the flame at different velocities. **(Left)** Flame profiles at 20 m distance, **(right)** flame profiles at the structure location.

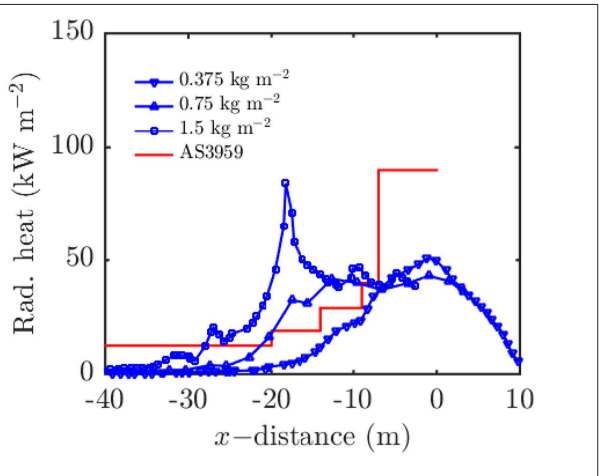

FIGURE 8 | Radiation heat load on the front of the structure with varying vegetation load. Distance is measured to the pyrolysis center.

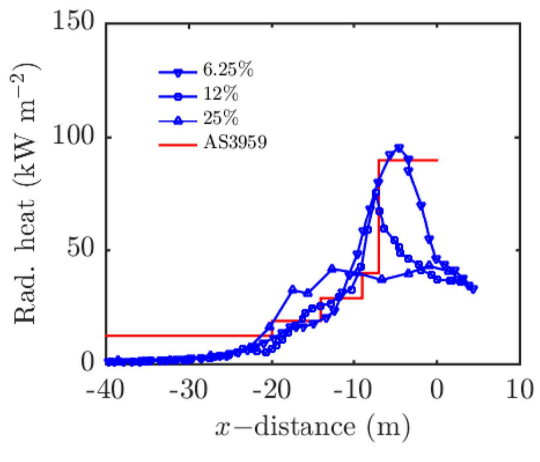

FIGURE 9 | Radiation heat load on the front face of the structure as a function of distance to the flame center with varying relative humidity. Distance is measured to the pyrolysis center.

parameters, we modify the relative humidity without changing the fuel moisture content. Three relative humidities are selected: 6.25, 12, and 25% (basecase) with wind speed and fuel load held constant at 12.5 ms^{-1} and 0.375 kgm^{-2}, respectively. The results in these cases are complicated: the relative humidity (with constant fuel moisture content) does modify the radiative heat flux at the structure however the results are not completely systematic. The general trend is that lower relative humidity yields the peak higher radiative heat load as shown in **Figure 9**. However, the 25% relative humidity case yields the highest radiative heat flux when $-20 < x < -10$ m. At $x = -15$ m the 25% case gives radiative heat flux of $\sim$30 kWm^{-2}, the 12% case gives radiative heat flux of $\sim$22 kWm^{-2}, and the 6.25% case gives radiative heat flux of $\sim$18 kWm^{-2}. At greater distances from the structure, $x < -20$ m, the order of the curves changes again. However, the difference in between the heat fluxes are relatively small for $x < -20$ m and this observation may simply be due to turbulent fluctuations in the fires or some other source of noise in the data. While relative humidity on its own does yield some changes in radiative heat flux at the structure, the changes are not entirely systematic. We therefore conclude that relative humidity largely acts as a proxy for fuel moisture content in the *GFDI* equation and further work is required to assess the effect of fuel moisture content upon the radiative heat flux at the structure.

3.5. The Case to Improve Building Standards With Physics-Based Modeling

Designing building standards is arguably a very difficult task. In the case of building in bushfire prone areas, the basic requirements of the standard are to ensure that a building is resilient to a realistic fire event and the standard is simple and straightforward to apply. Idealized simulations, such as those conducted here, can be considered as a first attempt at providing a framework that can be used to revise existing standards. Controlled physical experiments can also serve as a validation for proposed structural integrity discussed in AS 3959 in a bushfire attack. The controlled experiments have significant cost, risk, and safety, which limits it utilization. Numerical modeling reduces the cost, risk, and safety in exploring the bushfire attack on structure. Previously, numerical simulations have been successfully applied to simulate experimental grassfires (Mell et al., 2007; Moinuddin et al., 2018). Here, we have demonstrated that the same physics-based models can simulate the radiant heat load upon a structure. The computational effort required to simulate fire impact on a structure is currently too great to allow the possibility of simulating a general proposed structure in a given location in detail. However in the future, simulation of fire impact on a proposed design may become part of the design and approval process.

For the data presented here, the idealized models included in AS 3959 were found to under predict the simulations results near the structure. Furthermore, the models in AS 3959 do not account for the differences between buoyancy dominated and wind dominated fires. Given these limitations and the omission of any kind of ember attack model, in the AS 3959 the standard should be re-examined.

Because computational technology and physics-based simulation have advanced considerably since the standard was originally implemented, physics-based simulations of bushfire attack on a structure could be used to strengthen the standard. It is important to examine the limitations of the approach presented here. Firstly, it is unlikely that a house structure would be built in unmaintained grasslands; most houses have a garden with watered or mowed grass forming a buffer region from the fire. Nonetheless the simulations conducted here reflect the situations outlined in AS 3959. The present research only considers surface fuels whereas the standard is mostly concerned with elevated forest or shrub like fuels. In planning this study, it was thought that surface fuels were likely to be better predicted by the idealized model used by the standard. The geometry of the vegetation, the possibility of crown fuel involvement, and wind reduction due to the vegetation are expected to complicate the fire impact upon a structure. Similarly this study did not address the effect of sloping terrain on the fire spread and radiative heat load. Therefore, a further study should be conducted in future to address these limitations.

4. CONCLUSIONS

Physics based simulations are performed following the model outlined in the building standard AS 3959. The basecase simulation was designed to replicate the AS 3959 grassland (tussock moorland) fire as close as computationally feasible. That is, a straight line fire approaching a small cubiod structure was simulated and the radiative heat flux at the front face of the structure was analyzed as a function of the distance from fire front to the structure. The AS 3959 standard is based upon the radiative heat flux received at the structure. The standard sets several BAL levels; the BAL level is the radiative heat flux permitted if the fire is a particular difference away from the structure. Due to computational constraints, the width of the simulated fire is 20 m instead of the 100 m outlined in the standard. As the fire width increases, the radiative heat flux on the structure should also increase. The simulated radiative heat flux was similar in magnitude to the modeled radiative heat flux. However, the simulation was conducted at a much smaller width than the standard considers. Because radiative heat flux will increase with increasing fire width, therefore, the standard is likely insufficient for these fires. A parametric study shows that the relative humidity alone does vary the radiative heat flux on a structure, but not entirely in a systematic manner. Relative humidity will also vary the fuel moisture content, held constant in these simulations, and effect of varying the fuel moisture content needs to be investigated. The fuel load increases the radiative heat flux on a structure. As wind speed increases the fire changes from a buoyancy dominated fire leading to high radiative heat flux upon a structure, to a wind dominated fire with lower heat flux on the structure and this occurs despite the *GFDI* monotonically increasing.

Overall, building standards based on radiative heat flux alone will require revision to account for other forms of bushfire impact such as ember attack. Physics based modeling has the potential to simulate realistic fires and physics based simulations could be used to revise the radiative heat flux levels used in AS 3959. As computational capacity increases, physics based simulations may be used in performance based design of structures in bushfire prone areas.

AUTHOR CONTRIBUTIONS

NK conducted and analyzed the bulk of the simulations presented in this work and contributed to writing the manuscript. DS conducted preliminary simulations, proposed the study presented, and contributed writing the manuscript. RW conducted a literature review, performed an assessment of AS 3959, and contributed to writing the manuscript. KM contributed to writing the manuscript and provided guidance and expertise throughout the project.

FUNDING

This project was funded by the Commonwealth of Australia through the Bushfire and Natural Hazards Cooperative Research Centre. Project: Fire spread prediction across fuel types, 2014–2020.

ACKNOWLEDGMENTS

The authors are grateful to the administrators of Spartan, a high performance computing cluster at the University of Melbourne.

REFERENCES

Apte, V., Bilger, R., Green, A., and Quintiere, J. (1991). Wind-aided turbulent flame spread and burning over large-scale horizontal pmma surfaces. *Combust. Flame* 85, 169–184. doi: 10.1016/0010-2180(91)90185-E

AS 3959 (2009). *Construction of Buildings in Bush Fire Prone Areas (as 3959)*. Technical report, Standards Australia, Sydney, NSW.

Blanchi, R., and Leonard, J. (2005). *Investigation of Bushfire Attack Mechanisms Resulting in House Loss in the Act Bushfire 2003*. Technical report, Bushfire Cooperative Research Centre (CRC) Report.

Bou-Zeid, E., Overney, J., Rogers, B. D., and Parlange, M. B. (2009). The effects of building representation and clustering in large-eddy simulations of flows in urban canopies. *Bound. Layer Meteorol.* 132, 415–436. doi: 10.1007/s10546-009-9410-6

Cheney, N., Gould, J., and Catchpole, W. R. (1998). Prediction of fire spread in grasslands. *Int. J. Wildland Fire* 8, 1–13. doi: 10.1071/WF9980001

Cruz, M. G., and Alexander, M. E. (2013). Uncertainty associated with model predictions of surface and crown fire rates of spread. *Environ. Model. Softw.* 47, 16–28. doi: 10.1016/j.envsoft.2013.04.004

Dold, J., and Zinoviev, A. (2009). Fire eruption through intensity and spread rate interaction mediated by flow attachment. *Combust. Theor. Model.* 13, 763–793. doi: 10.1080/13647830902977570

Jarrin, N., Benhamadouche, S., Laurence, D., and Prosser, R. (2006). A synthetic-eddy-method for generating inflow conditions for large-eddy simulations. *Int. J. Heat Fluid Flow* 27, 585–593. doi: 10.1016/j.ijheatfluidflow.2006.02.006

Jolly, W. M., Cochrane, M. A., Freeborn, P. H., Holden, Z. A., Brown, T. J., Williamson, G. J., et al. (2015). Climate-induced variations in global wildfire danger from 1979 to 2013. *Nat. Commun.* 6:7537. doi: 10.1038/ncomms8537

Linn, R., Canfield, J., Cunningham, P., Edminster, C., Dupuy, J.-L., and Pimont, F. (2012). Using periodic line fires to gain a new perspective on multi-dimensional aspects of forward fire spread. *Agric. For. Meteorol.* 157, 60–76. doi: 10.1016/j.agrformet.2012.01.014

McArthur, A. G. (1967). *Fire Behaviour in Eucalypt Forests*. Leaflet number 107.

McGrattan, K., Hostikka, S., and Floyd, J. (2013a). *Fire Dynamics Simulator, User's Guide*. Gaithersburg, MD: NIST special publication, 1019.

McGrattan, K., Hostikka, S., Floyd, J., Baum, H. R., Rehm, R. G., Mell, W., et al. (2013b). *Fire Dynamics Simulator (Version 6), Technical Reference Guide*. Gaithersburg, MD: NIST special publication, 1018.

McLeod, R. N., Pascoe, S. M., and Teaguea, B. G. (2010). *Final Report, Royal Commission into Victoria's Bushfires*. Technical report, State of Victoria.

Mell, W., Jenkins, M. A., Gould, J., and Cheney, P. (2007). A physics-based approach to modelling grassland fires. *Int. J. Wildland Fire* 16, 1–22. doi: 10.1071/WF06002

Mell, W., Maranghides, A., McDermott, R., and Manzello, S. L. (2009). Numerical simulation and experiments of burning douglas fir trees. *Combust. Flame* 156, 2023–2041. doi: 10.1016/j.combustflame.2009.06.015

Mell, W. E., McDermott, R. J., and Forney, G. P. (2010). "Wildland fire behavior modeling: perspectives, new approaches and applications," in *Proceedings of 3rd Fire Behavior and Fuels Conference* (Birmingham, AL), 25–29.

Moinuddin, K., Sutherland, D., and Mell, W. (2018). Simulation study of grass fire using a physics-based model: striving towards numerical rigour and the effect of grass height on the rate of spread. *Int. J. Wildland Fire* 27, 800–814. doi: 10.1071/WF17126

Morvan, D., and Dupuy, J. (2004). Modeling the propagation of a wildfire through a mediterranean shrub using a multiphase formulation. *Combust. Flame* 138, 199–210. doi: 10.1016/j.combustflame.2004.05.001

Morvan, D., and Frangieh, N. (2018). Wildland fires behaviour: wind effect versus byram's convective number and consequences upon the regime of propagation. *Int. J. Wildland Fire* 27, 636–641. doi: 10.1071/WF18014

Morvan, D., Meradji, S., and Mell, W. (2013). Interaction between head fire and backfire in grasslands. *Fire Saf. J.* 58, 195–203. doi: 10.1016/j.firesaf.2013.01.027

NFPA 1144 (2013). *Nfpa 1144 Standard for Reducing Structure Ignition Hazards from Wildland Fire*. Technical report, National Fire Protection Association and others.

Radeloff, V. C., Hammer, R. B., Stewart, S. I., Fried, J. S., Holcomb, S. S., and McKeefry, J. F. (2005). The wildland–urban interface in the united states. *Ecol. Appl.* 15, 799–805. doi: 10.1890/04-1413

Radeloff, V. C., Helmers, D. P., Kramer, H. A., Mockrin, M. H., Alexandre, P. M., Bar-Massada, A., et al. (2018). Rapid growth of the us wildland-urban interface raises wildfire risk. *Proc. Natl. Acad. Sci. U.S.A.* 115, 3314–3319. doi: 10.1073/pnas.1718850115

Roberts, M., Sharples, J., and Rawlinson, A. (2017). "Incorporating ember attack in bushfire risk assessment: a case study of the Ginninderry region," in *MODSIM2017 Proceedings - MSSANZ, Modelling and Simulation Society of Australia and New Zealand, The 22nd International Congress on Modelling and Simulation* (Hobart, TAS), 1152–1158.

Ronchi, E., Gwynne, S. M., Rein, G., Wadhwani, R., Intini, P., and Bergstedt, A. (2017). *e-Sanctuary: Open Multi-Physics Framework for Modelling Wildfire Urban Evacuation*. Technical report, National Fire Protection Association.

Rüedi, I. (2006). *WMO Guide to Meteorological Instruments and Methods of Observation: WMO-8 Part i: Measurement of Meteorological Variables*. Geneva: World Meteorological Organization.

Sharples, J. J. (2017). *Risk Implications of Dynamic Fire Propagation*. Report for Ginninderra Falls Association (Non-peer reviewed report).

Sharples, J. J., Gill, A. M., and Dold, J. W. (2010). "The trench effect and eruptive wildfires: lessons from the kings cross underground disaster," in *Proceedings of Australian Fire and Emergency Service Authorities Council 2010 Conference* (Darwin, NT), 8–10.

Tollhurst, K. (2009). *Report on the Physical Nature of the Victorian Fires Occurring on the 7th of February 2009*. Technical report, University of Melbourne.

Viegas, D. X. (2017). *O Complexo de Incéndios de Pedr og ao Grande e Concelhos limtrofes, Iniciado a 17 de Junho de 2017*. Technical report, Universidade de Coimbra.

Weise, D., and Biging, G. (1996). Effects of wind velocity and slope on flame properties. *Can. J. For. Res.* 26, 1849–1858. doi: 10.1139/x26-210

Whittaker, J., Haynes, K., Handmer, J., and McLennan, J. (2013). Community safety during the 2009 Australian 'Black Saturday' bushfires: an analysis of household preparedness and response. *Int. J. Wildland Fire* 22, 841–849. doi: 10.1071/WF12010

Worden, H., Beer, R., and Rinsland, C. P. (1997). Airborne infrared spectroscopy of 1994 western wildfires. *J. Geophys. Res. Atmos.* 102, 1287–1299. doi: 10.1029/96JD02982

Conflict of Interest Statement: The authors declare that the research was conducted in the absence of any commercial or financial relationships that could be construed as a potential conflict of interest.

NOMENCLATURE

Symbols

w	fuel weight (T/Ha)
m_c	fuel moisture content (percentage)
u	driving wind speed (ms^{-1})
RH	relative humidity (percentage)
C	the curing index (percentage)
N_c	Byram number
L_f	flame length (m)
F_h	flame height (m)
F_w	flame width (m)
α	flame angle
T_f	flame temperature (K)
T_a	is the ambient temperature (K)
ϵ	emissivity (unitless 0 to 1)
q	heat flux (kW/m^2)
z_0	roughness length (m)
A	Imposed velocity magnitude (inlet condition) (ms^{-1})
L_{eddy}	eddy length scale (inlet condition)
N_{eddy}	number of eddies (inlet condition)
σ_{eddy}	velocity scale of eddies (inlet condition)
δx, δy, δz	grid sizes in x, y, and z

Standard constants

$\sigma = 5.67 \times 10^{-8} W/m^2K^4$	Stefan-Boltzmann constant
$g = 9.8\ ms^{-2}$	gravitation acceleration constant
$\rho = 1.2\ kg/m^3$	density of air
$C_p = 1.0$ kJ/kg K	specific heat of air
$H = 18.6\ MJ\ kg^{-1}$	heat of combustion

Subscripts

inlet	at $x = 0$
eddy	pertaining to the synthetic inlet turbulence
10	measured ten meters from the ground
r	radiant
emitted	emitted from the flame
effective	received at the structure

frontiers in Mechanical Engineering

ORIGINAL RESEARCH
published: 05 July 2019
doi: 10.3389/fmech.2019.00041

Effect of Canyons on a Fire Propagating Laterally Over Slopes

André Rodrigues[1], Carlos Ribeiro[1], Jorge Raposo[1,2], Domingos Xavier Viegas[1,2] and Jorge André[2]*

[1] Association for the Development of Industrial Aerodynamics, Department of Mechanical Engineering, Faculty of Sciences and Technology, Forest Fire Research Center, University of Coimbra, Coimbra, Portugal, [2] Department of Mechanical Engineering, Faculty of Sciences and Technology, University of Coimbra, Coimbra, Portugal

In this paper, the problem related with a fire front propagating laterally on a slope with a nearby canyon is presented. The presence of the canyon can modify the intensity of the fire and create a difficult situation for elements involved in fire suppression. When a fire propagating laterally in a slope enters the canyon, a rapid increase in the fire's rate of spread occurs and a strong convective activity is generated due to the burning inside the canyon. The convective flow generated will then induce a change in the propagation of the fire in the slope. In certain conditions the rate of spread and the intensity of the fire will be strongly increased. This type of extreme fire behavior is referred to as eruptive fire behavior (or blow-up), and usually happens over slopes or in canyon configurations. In this study, we analyzed the results of laboratory-scale experiments that model a fire spreading latterly over a slope and then enter a canyon that is embedded in the slope. Three configuration parameters were used in the experiments. The first is the inclination α of the slope, the second is the orientation γ of the axis of the canyon and the third is the angle β of the ignition line. The fire spread is very complex and dynamic resulting in situations in which very high values of the ROS can be reached for several configurations, creating dangerous situations for firefighters.

Keywords: forest fires, fire safety, extreme fire behavior, eruptive behavior, fire in canyons

OPEN ACCESS

Edited by:
Xinyan Huang,
Hong Kong Polytechnic University,
Hong Kong

Reviewed by:
Houzhi Wang,
University of Adelaide, Australia
Franz Richter,
Imperial College London,
United Kingdom
Jiuling Yang,
National Institute of Standards and Technology (NIST), United States

****Correspondence:***
André Rodrigues
andrerodrigues@adai.pt

Specialty section:
This article was submitted to Thermal and Mass Transport, a section of the journal Frontiers in Mechanical Engineering

Received: *28 February 2019*
Accepted: *18 June 2019*
Published: *05 July 2019*

Citation:
Rodrigues A, Ribeiro C, Raposo J, Viegas DX and André J (2019) Effect of Canyons on a Fire Propagating Laterally Over Slopes. Front. Mech. Eng. 5:41. doi: 10.3389/fmech.2019.00041

INTRODUCTION

Forest fires are a phenomenon that can be characterized by a great level of destruction of material and human assets. In the worst cases, forest fires may cause accidents and fatalities among firefighters and civilians. Many of these accidents and fatalities are associated with canyons. Accidents involving firefighters related to forest fires are often due to insufficient knowledge about fire and its behavior, especially in the case of Extreme Fire Behavior (EFB) (Viegas, 2006, 2012; Werth et al., 2011).

In 2013, in Portugal at Serra do Caramulo, several firefighters were fighting a flank fire on a sloped terrain with a nearby canyon (Viegas et al., 2013). When the fire entered the bottom of the canyon the behavior of the fire was modified dramatically. Several firefighters were hurt by the fire and two of them lost their lives. This particular accident motivated us to study the change of the fire behavior over slopes when the flank fire enters canyons, with the aim to improve the safety of the teams involved in the suppression of wildfires in similar conditions.

TABLE 1 | Classes of fire behavior regime.

Class	R'	I ($kW.m^{-1}$)	L (m)	Description	Color code
1	$0 < R' < 2$	<750	<1.63	Static or quasi-static fire regime	White
2	$2 \leq R' < 5$	<1,875	<2.48	Dynamic fire behavior	Green
3	$5 \leq R' < 10$	<3,750	<3.41	Mild extreme fire behavior	Yellow
4	$10 \leq R' < 15$	<5,625	<4.11	Strong extreme fire behavior	Orange
5	$R' \geq 15$	>5,625	>4.11	Very strong extreme fire behavior	Red

Color code to associate with the scale of intensity values.

STATIC AND DYNAMIC FIRE BEHAVIOR

Most fire behavior models are based on the assumption that the fire propagation properties are quasi static and can be determined from three groups of essential factors: topography, fuel and meteorology, which are called the "fire triangle" (Byram, 1959). Recognizing that in the general case the convective flow induced by the fire modifies its behavior in the course of time, even in the case of permanent boundary conditions, Viegas (2006) proposed, as an alternative to this classic formulation, the concept of "square of fire," adding a fourth factor: time. According to this concept the fire behavior is dynamic in the sense that it changes in the course of time even with permanent boundary conditions.

Designating by R_o the basic rate of spread (ROS) of a fire line spreading on a horizontal surface in the absence of wind we can define the non-dimensional rate of spread R' by:

$$R' = \frac{R}{R_o}$$

Viegas (2006) showed that only if $R' \approx 1$ the behavior of a fire can be considered as static as its properties remain constant.

If the value of R' is large, the acceleration of the fire front can be quite large and lead to what we designate as Extreme Fire Behavior that is normally associated to rapid changes of the ROS and to large values of fire line intensity.

As a reference, a fire spreading in a shrub fuel bed with a load of 1.5 kg, a typical value of R_o is of the order of $50\ m.h^{-1}$ ($\approx 0.014\ m.s^{-1}$). The corresponding value of the fire line intensity is 5,625 kW/m. This intensity was determined according to Byram (1959).

In the present study we consider the ranges of values of R' that are shown in **Table 1** to differentiate various fire behavior regimes. In **Table 1** we included the reference values of fire line intensity and estimated flame length as an indication of the meaning of these limits.

Fires spreading on slopes have been studied by several authors, namely by Dupuy (1995), Dupuy and Maréchal (2011), Dupuy et al. (2011), and Silvani et al. (2012), with it found that fire induced convection becomes dominant for values of slope angle $\alpha > 30°$.

Fire spread in canyons is of particular relevance in fire safety analysis as a large number of fatalities are related to this type of terrain configuration (cf. Viegas, 2005; Schemel et al., 2008; Viegas and Simeoni, 2011; Lahaye et al., 2018). This type of fires was extensively studied by Viegas and Pita (2004) and Dold and Zinoviev (2009). The steady increase of the ROS of the fire front, even in the absence of wind or any other contributing factor was also reported in Pyne et al. (1996) and Dold (2010). The designation of "eruptive" fire behavior was coined in Viegas and Pita (2004), to designate this type of fire behavior. Viegas (2005, 2006) proposed a mathematical model to predict the ROS of the head fire in canyons. According to this model the presence of the flame induces a local enhancement of the flow velocity around the fire front that produces an increase in its ROS in the course of time. The positive feedback between both processes leads to a gradual increase of R' that can reach quite high values.

The merging of two fire fronts that was studied in Viegas et al. (2012), Sharples et al. (2013), and Raposo et al. (2015, 2018), also exhibits a behavior similar to a fire eruption leading to extremely high values of R' and are accompanied by very strong convective effects.

To the knowledge of the present authors, the problem of fires spreading in slopes with embedded or nearby canyons, which is the object of the present paper, is not reported in the literature. As described above, the problem of fire spread on slopes was studied quite extensively both empirically and using analytical and numerical models. The spread of fires in canyons was studied as well but the interaction between fires spreading on a slope with a nearby canyon that is relevant for applications, was not considered before. As pointed out by Silvani et al. (2012) even in the absence of wind, heat transfer is not only achieved by radiation, but also by convection, therefore the presence of fire inside or near the canyon modifies the flame geometry and the spread of the fire. Depending on the slope angle, the orientation of the canyon axis and the inclination of the fire front, as a result of this complex interaction very high values of the ROS can be achieved due to the presence of the canyon.

The main objective of this paper is a detailed and exhaustive analysis of the phenomenon has an interaction on lateral spread of fire on a slope with a canyon. The intent is to understand the variation of fire propagation velocity and direction and the values of the fire intensity, and contribute toward the increase of scientific knowledge in this case of EFB. Different ignition angles will be tested to evaluate their influence on the development in the forest fires. The acquisition of images in the visible and infrared range to determine the velocity and direction of fire propagation, the flame geometry and the energy release rate are purposed in this work. This study also aims to propose behavior models and operation rules to personal safety when people fight against forest fires on slopes with canyons, based on previous studies and in the research that will be carried out.

METHODOLOGY

Definition of the Problem

The geometry of a canyon embedded in a slope is described schematically in **Figure 1**. Let us consider an absolute reference frame $O_oX_oY_oZ_o$ in which the horizontal datum plane is defined

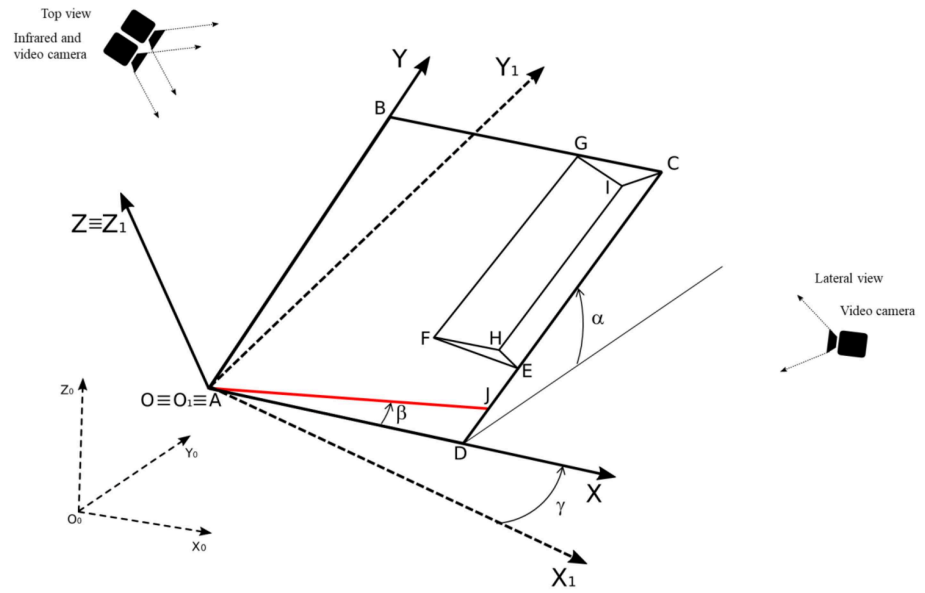

FIGURE 1 | The variation of test table geometry.

by the axis X_o and Y_o. A second reference frame is defined by $O_1X_1Y_1Z_1$ in which the axis OX_1 is parallel to OX_o and the axis OY_1 is rotated by an angle α in relation to OX_o. Henceforth this angle will be designated as slope angle.

Rotating the system of axis O_1 X_1 Y_1 Z_1 by an angle γ around axis OZ we can define a new system OXYZ that is shown in **Figure 1** in which $OZ \equiv OZ_1$.

The surface of the slope is a square ABCD in which A≡O. The canyon is embedded in this slope in the rectangle CEFG as shown in **Figure 1**. The canyon has two lateral faces of equal slope and therefore its section has a constant triangular shape. The base of the canyon is HI, that is designated as its "axis" and is parallel to OY. More details on the canyon geometry are given in the next section.

In this study we consider a linear fire front AJ that is spreading across the surface of the ground. The angle between this line and OX axis is β, as indicated in **Figure 1**. Henceforth, this is designated as Line *i*. In the present study the following values of β were used: 0, 10, and 20°.

FIGURE 2 | Table of laboratory tests.

Experimental Setup

For the experimental study an original test table (**Figure 2**) was built. The test table has a burn area of 3 × 3 m^2 and one embedded canyon of 0.94 × 2.34 m^2. The test table permits an angle change of the slope (α) between 0 and 45° and the orientation of the canyon axis (γ) between 0 and 360°, as demonstrated in **Figure 1**. It also allows for a change in the canyon configuration, but in these tests only the configuration shown in **Figure 3** was used.

The canyon that was used in the tests is a "U shape" canyon with the dimensions shown in **Figure 3**, with an approximately 38° in the lateral slopes and 40° in the entrance of the canyon. The depth of the canyon is 0.35 m and its length is 2.34 m. **Figure 3** exhibits the technical drawing of the canyon configuration.

Methods

In all experiments the fuel bed was composed of a layer of *Pinus pinaster* dead needles with a load of 0.6 $kg.m^{-2}$ (on a dry basis) that covered the entire surface of the slope and the canyon.

The conditions of fuel load and bulk density were controlled during the preparation of the fuel bed; air temperature, relative humidity and fuel moisture (m_f) were monitored. The time between preparation of the fuel bed and burning did not exceed 10 min to avoid changes in moisture content of the fuel in contact with ambient air.

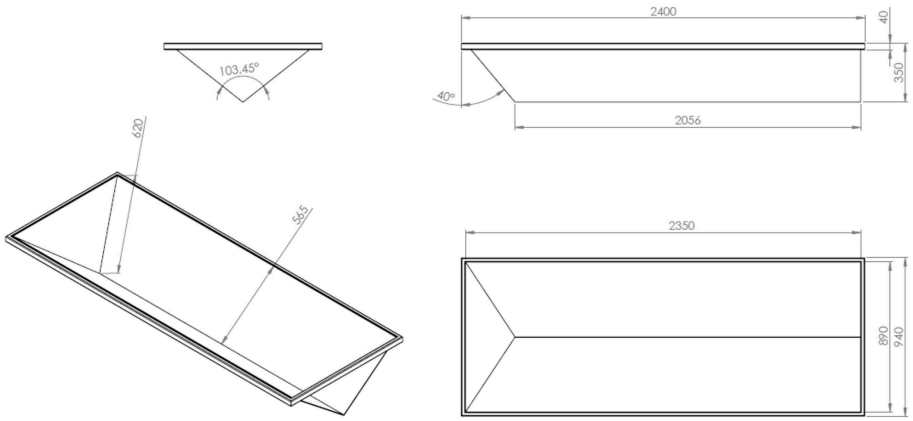

FIGURE 3 | Technical drawing of the canyon configuration.

The fuel moisture content (m_f) is a critical factor that has significant effects on the combustion process. According to Byram (1959) and Pyne et al. (1996), the fuel moisture content determines the possibility of a forest fuel to ignite and what proportion of it is available for the combustion process. In each test the fuel moisture content was measured twice: at the beginning of the preparation of the fuel bed and immediately before each test. The value presented in **Table 2** corresponds to the one measured immediately before the test. A moisture analyser (A&D ML50) was used for the measurement. This machine enables the quantification of water inside the fuel in a drying period of 10 min.

The tests were monitored using a photographic camera (Canon EOS 550D), two video cameras—one in the frontal plane (Sony AVCHD MPEG2 SD) and one in the lateral plane (Sony HD DCR-SR87). An infrared camera (FLIR SC660) was used to record all tests in the range of 300–1,500°C, with a rate of acquisition of 15 Hz. Before each test a reference test to determine the basic ROS (R_o) was performed using a horizontal table of 1 × 1 m^2 with the same fuel cover.

We analyzed the infrared recorded images to obtain the fire contour at pre-defined times. The time between frames was adapted for each test, in order to determine the evolution of the fire front, following the methodology referred in Raposo (2016). In order to have an overall assessment of the fire front evolution during the experiment and also to analyse the spatial distribution of temperature along the fuel bed, infrared images (IR) from each experiment were recorded. Using IR methodology, the position of the fire perimeter at given time frames was assessed and from these images the ROS at various positions of the fire perimeter. The threshold of 350°C was used to avoid the obstruction of the view by the plume of the fire. The adjustment of this threshold can be set even after the recording of the images. Any digital frame of the video of the IR camera is stored on the PC hard disk frame, with the name corresponding to time t, then each frame is imported. In this program, a specifically written application allows the capture of the fire line in the image and for each point, the Cartesian coordinates of the frame are converted into true physical Cartesian coordinates in the plane of the combustion table. This conversion encompasses a simple but non-trivial image calibration technique in which the camera is assimilated to a pin-hole optical system without aberration. Eventually, the fire line is described by an ordered set of points, in the OXY Cartesian system defined above. The program computes the average and instantaneous values of ROS at each point of the fire line and the isochrones of the fire perimeter.

As the IR recording was continuous it was possible to estimate the local value of the ROS at any point of the fuel bed or at any time. This feature was used to determine the value of ROS at predefined distances along the reference lines mentioned below to allow the estimation of average values of ROS at given locations and their standard deviation.

These tests were performed with four different slope angles (α): 0, 10, 20, and 30° and for three values of the orientation of the canyon axis (γ): −20, 0, and 20° (**Figure 4**).

For each angle of slope and rotation of the table, three angles (β) of ignition line were used (0, 10, and 20°).

Data of the tests performed, are presented in **Table 2**. In order to reduce uncertainty three replications (T1, T2, and T3) were performed for each set of parameters for $\alpha = 20°$ and $\alpha = 30°$. Preliminary tests with $\alpha = 0°$ and $\alpha = 10°$ showed that for these low values of slope *R'* was always lower than 2 and therefore only one test was performed for these slope angles.

As an example, in **Figure 5** the isochrones of one of the tests (SC324) are shown together with some reference lines that were used to analyse the spread of the fire. Line *a* (yellow line) is along the center of the table; Line *b* (green line) is at mid distance between line *a* and the left border of the canyon (FG); Line *c* (blue line) is along the waterline of the canyon (HI); Line *d* (orange line) is along the propagation of the head fire that coincides with the maximum slope direction of the plane OXY. Lines *a*, *b* and *c* are all parallel to OY axis.

TABLE 2 | Data of the tests performed (for experiments with slope angles of $\alpha = 20^{\circ}$ and $\alpha = 30^{\circ}$ three tests were performed).

Ref.	Designation			m_f (%)			R_o (cm.s^{-1})			α (°)	γ (°)	β (°)
	T1	T2	T3	T1	T2	T3	T1	T2	T3			
1	SC131	SC210	SC334	15.47	–	–	0.37	–	–	0	+20	0
2	SC108	SC230	SC328	14.16	–	–	0.30	–	–	0	+20	10
3	SC130	SC225	SC309	14.47	–	–	0.31	–	–	0	+20	20
4	SC101	SC228	SC325	15.47	–	–	0.29	–	–	0	0	0
5	SC136	SC201	SC331	16.14	–	–	0.33	–	–	0	0	10
6	SC132	SC211	SC301	16.14	–	–	0.32	–	–	0	0	20
7	SC135	SC235	SC305	15.01	–	–	0.29	–	–	0	−20	0
8	SC113	SC213	SC335	15.61	–	–	0.28	–	–	0	−20	10
9	SC114	SC236	SC330	15.61	–	–	0.34	–	–	0	−20	20
10	SC102	SC222	SC336	14.81	–	–	0.33	–	–	10	+20	0
11	SC103	SC232	SC315	15.47	–	–	0.36	–	–	10	+20	10
12	SC117	SC234	SC307	14.81	–	–	0.37	–	–	10	+20	20
13	SC104	SC206	SC321	14.03	–	–	0.30	–	–	10	0	0
14	SC119	SC221	SC314	14.68	–	–	0.26	–	–	10	0	10
15	SC106	SC205	SC319	12.74	–	–	0.28	–	–	10	0	20
16	SC134	SC215	SC333	13.25	–	–	0.28	–	–	10	−20	0
17	SC109	SC231	SC308	13.77	–	–	0.29	–	–	10	−20	10
18	SC133	SC202	SC332	17.01	–	–	0.27	–	–	10	−20	20
19	SC112	SC223	SC303	16.41	16.28	16.82	0.30	0.36	0.26	20	+20	0
20	SC128	SC217	SC320	16.82	17.51	16.96	0.34	0.42	0.26	20	+20	10
21	SC107	SC226	SC310	16.28	17.51	16.96	0.40	0.35	0.30	20	+20	20
22	SC105	SC227	SC329	15.47	17.10	16.55	0.33	0.31	0.28	20	0	0
23	SC118	SC207	SC317	15.21	17.37	16.82	0.31	0.23	0.26	20	0	10
24	SC111	SC229	SC302	14.03	17.37	16.82	0.30	0.23	0.31	20	0	20
25	SC110	SC219	SC322	17.37	16.82	16.55	0.42	0.28	0.29	20	−20	0
26	SC126	SC208	SC304	16.14	16.96	16.55	0.36	0.29	0.28	20	−20	10
27	SC125	SC204	SC323	16.14	16.96	16.55	0.24	0.28	0.25	20	−20	20
28	SC115	SC220	SC306	16.38	17.51	17.10	0.36	0.37	0.27	30	+20	0
29	SC121	SC209	SC316	17.51	16.55	17.10	0.26	0.34	0.29	30	+20	10
30	SC127	SC218	SC311	16.38	16.55	17.23	0.28	0.36	0.25	30	+20	20
31	SC122	SC214	SC312	16.41	16.41	17.79	0.38	0.38	0.21	30	0	0
32	SC129	SC233	SC313	15.34	15.21	17.79	0.36	0.55	0.23	30	0	10
33	SC123	SC203	SC326	16.28	15.34	18.06	0.31	0.50	0.26	30	0	20
34	SC124	SC212	SC318	16.96	17.10	16.69	0.24	0.45	0.37	30	−20	0
35	SC120	SC224	SC324	17.10	17.10	16.69	0.24	0.44	0.40	30	−20	10
36	SC116	SC216	SC327	17.10	17.23	16.69	0.33	0.40	0.36	30	−20	20

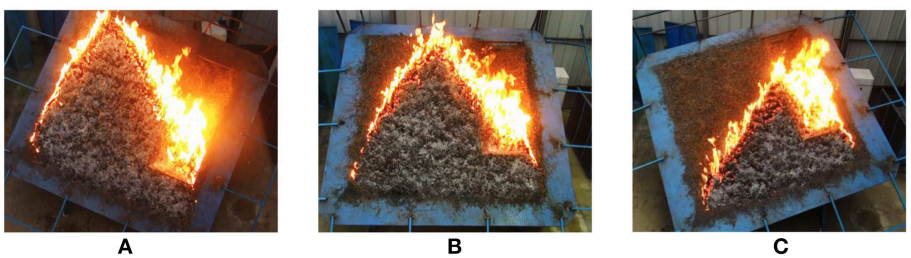

FIGURE 4 | Effect of the inclination of the axis of the canyon (γ): **(A)** −20° (Test SC124); **(B)** 0° (Test SC122); **(C)** +20° (Test SC115).

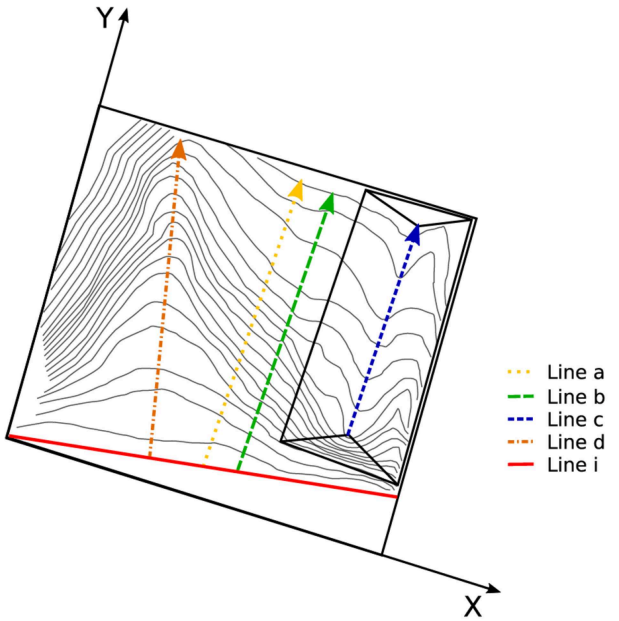

FIGURE 5 | The measurement directions of the fire propagation. The isochrones correspond to test SC324 ($\alpha = 30°$, $\gamma = -20°$, $\beta = 10°$).

RESULTS AND DISCUSSION

Overall Fire Behavior Regimes

In the present analysis we considered a non-dimensional rate of spread (R'), defined by equation (1) to allow the extension of the results to other fuel bed properties. In order to assess the overall danger associated to the problem of a flank fire entering in the canyon for the set of conditions that were analyzed in the present study we analyzed the maximum local value of R' along each line of reference mentioned above. The results are shown graphically in **Table 3**, using the color codes for each Class of fire behavior as defined in **Table 1**.

As can be seen in **Table 3** for $\alpha \leq 10°$ the fire behavior is only in Classes 1 and 2. For $\alpha = 20°$, Class 3 is observed only along lines *b, c,* and *d*, near or inside the canyon, for some sets of values of β and of γ. Class 4 regime was only observed along line *b* for $\gamma = 0°$ and $\beta = 20°$.

For $\alpha = 30°$, Class 3 regime is observed in all cases. Class 4 regime occurs in most situations for lines *b* and *c*. Class 5 regime is also observed along these lines and along line *d* as well for some sets of values of the control parameters.

We can conclude that besides the interior of the canyon its vicinity (near line *b*) is a potentially dangerous area to stay and to operate in the case of a fire spreading in the geometric conditions that were considered. This was actually the case in the accident that was mentioned above that occurred in Portugal.

Linear Ignition With $\beta = 0°$

In the previous analysis we indicated that the maximum value of R' along a reference line was in a certain range of values, without actually stating the location where this maximum value occurs. Although we have this information in our database, it would require much more space to present it. In order to illustrate the variation of R' along the reference lines, as an example, we present part of the results for $\beta = 0°$.

Effect of Slope Angle

To analyse the effect of slope angle α we consider the evolution of R' along line *b* for $\gamma = -20°$ for four values of α, that are shown in **Figure 6**. Each data point in this figure corresponds to the local average value from three replications that were performed for $\alpha = 20°$ and $\alpha = 30°$. The corresponding bars represent the confidence intervals for a 90% level. As can be seen, the values of R' are in generally lower than 3 for $\alpha \leq 20°$. The case of $\alpha = 30°$ is of particular interest as the value of R' increases initially, then it decreases to values lower than one and increases up to 8, corresponding to Class 3 regime.

Effect of Canyon Axis Inclination

In order to analyse the effect of the inclination angle γ of the axis of the canyon we consider the case of slope angle $\alpha = 30°$. The results are shown in **Figure 7** for each line *a*, *b*, *c* and *d*. The scale of R' is the same in the four figures to facilitate a comparison.

In line *a* (**Figure 7A**) the value of R' is always lower than 10 but the effect of angle γ can be observed. The case of $\gamma = 0°$ registers the higher values of R' in the lower part of the slope but the difference between the three cases of inclination angle γ is reduced in its upper part. In **Figure 7B** the results for line *b*, near the canyon are shown. In this case the values of R' are also lower than 10 and an influence of angle γ can be observed. In the first part of the slope the values of R' decrease with distance but are larger for larger values of γ. In the upper part of the slope the values of R' increase due to the proximity of the canyon, but the opposite occurs in the upper part of the slope. The increase of R' for the case of $\gamma = 0°$ is particularly noteworthy as it is directly influenced by the fire eruption in the canyon as line *b* is parallel to the maximum slope direction.

The results for line *c* in the bottom of the canyon are shown in **Figure 7C**. There is a marked influence of the inclination angle γ: for $\gamma = -20°$ the fire behavior is almost always in Class 2. For $\gamma = +20°$ the value of R' is practically constant along line *b* and of the order of 12. For $\gamma = 0°$ the value of R' increases along line *c* reaching Class 5.

The results for line *d* of maximum slope are shown in **Figure 7D**. The values of R' decrease along the slope for the three values of γ. The values of R' are higher for $\gamma = 0°$ and decrease symmetrically with γ.

CONCLUSIONS

In this paper the complex situation of a linear fire line spreading on a slope in the vicinity of an embedded canyon was analyzed in a laboratory simulation. Three geometrical parameters were considered in the study: the slope of the fuel bed α, the inclination angle of the axis γ of the canyon and the orientation of the ignition line β.

The spread of the fire in this terrain configuration can create very high risk situations for firefighters due to the potential

TABLE 3 | Distribution of the class of FB according to the maximum local value of *R'* along the reference lines.

α °		0				10				20				30			
γ °	β °	a	b	c	d	a	b	c	d	a	b	c	d	a	b	c	d
-20	0																
	10																
	20																
0	0																
	10																
	20																
+20	0																
	10																
	20																

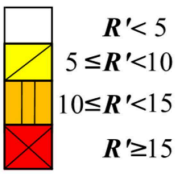

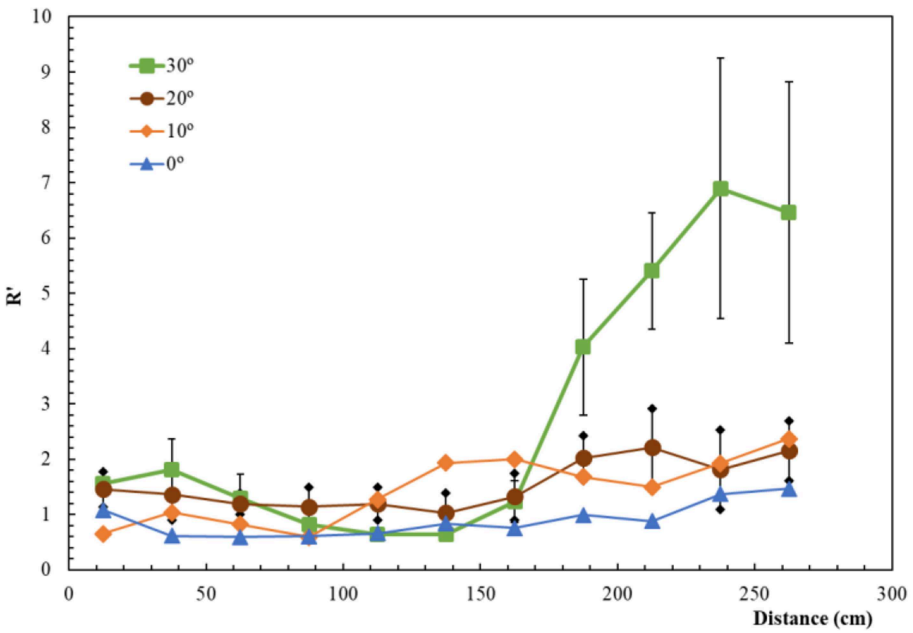

FIGURE 6 | Mean values of R' along line b for tests with $\beta = 0°$ and $\gamma = -20°$ for various of slope angle α. The error bars correspond to a level of confidence of 90%.

increase of the ROS. In order to assess this potential of having areas of very high fire line intensity, we defined five Classes of fire behavior according to the maximum local values of the non-dimensional ROS *R'*.

In the overall analysis it was verified that for slope angles $\alpha \leq 10°$ the fire behavior is always Classes 1 or 2 and therefore not considered very dangerous. For $\alpha = 20°$, we may have fire behavior of Class 3 or even of Class 4 in some configurations. For $\alpha = 30°$, fire behavior is mostly in Class 3 but quite often it reaches Classes 4 and 5, especially for $\gamma = +20°$, making this range of configurations the most dangerous.

More detailed results were presented for the ignition line configuration corresponding to $\beta = 0°$. It was observed that the orientation angle of the canyon axis has a complex influence on fire spread along the reference lines. Analysis of the ROS along line *b* for $\gamma = -20°$ indicate that the value of *R'* remains below 2 in average for $\alpha \leq 20°$ but can reach a value of 7 for $\alpha = 30°$.

The results for $\alpha = 30°$ show that for lines *a*, *b* and *d* the fire behavior is always in Classes 1 to 3 for each orientation of the canyon axis. For line *c*, when $\gamma = -20°$ the fire behavior is in Classes 2 and 3 but when $\gamma = +20°$ the fire behavior is in Classes 3 and 4. In this line, for $\gamma = 0°$ initially the fire behavior starts in Class 3 but along the distance inside the canyon the ROS increases and we have Classes 4 and 5, being dangerous situations for the firefighters.

Analysis of the ROS along the line *a* and *b* for $\gamma = -20°$ show that the value of *R'* is below 2 in average at the base of

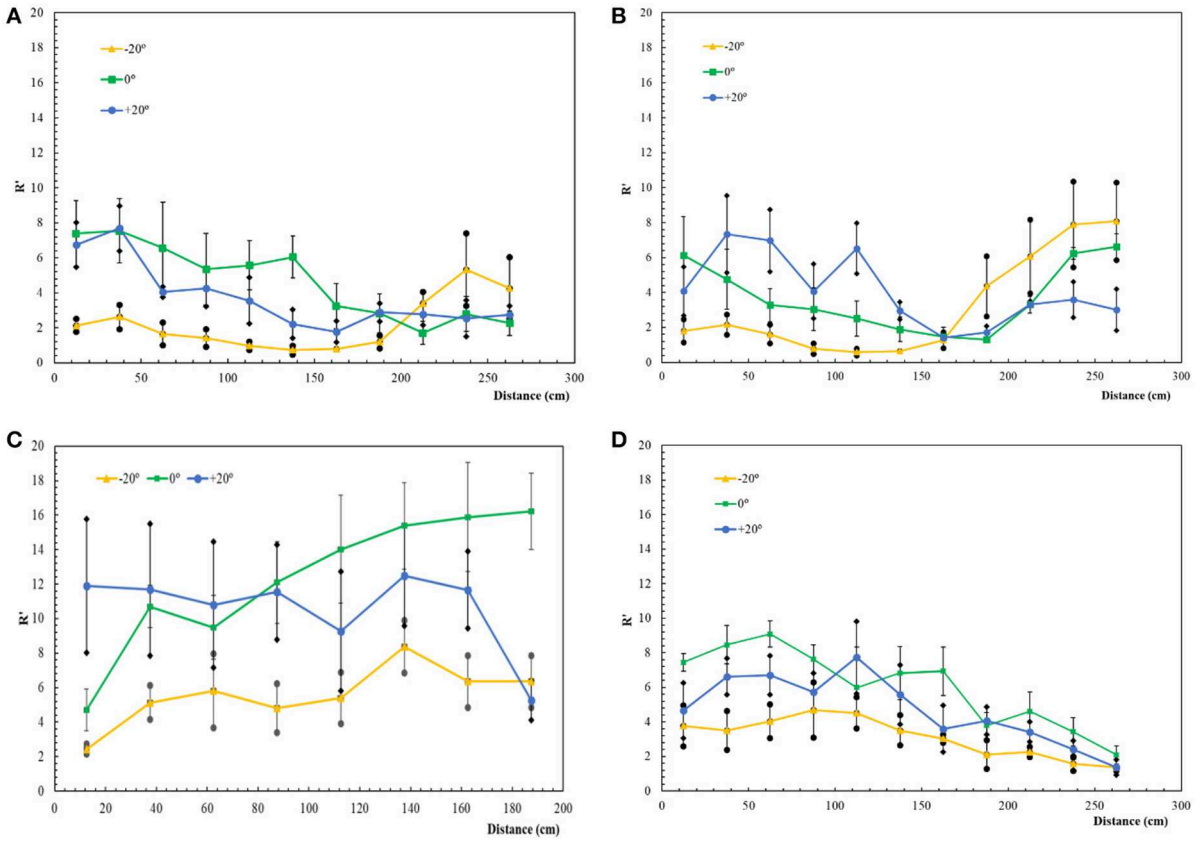

FIGURE 7 | Mean value of R' for tests with $\alpha = 30°$ and $\beta = 0°$–**(A)** Line a; **(B)** Line b; **(C)** Line c; **(D)** Line d. The error bars correspond to a level of confidence of 90%.

the slope but can reach a value >5 when the fire enters the canyon and it influences the adjacent points. For line *c* when $\gamma = 0°$ the canyon axis is aligned with the maximum slope and the eruptive effect occurs. For $\gamma = -20°$ and $\gamma = +20°$ the waterline is not aligned with maximum slope and the convective flow is affected, therefore the values of *R*' are lower but are higher in line *c*. For line *d* the fire has an acceleration initially but then the value of *R*' decreases for all values of γ. It is observed that the presence of the canyon interferes with the direction of propagation when the fire spreads with a higher ROS in the direction of the canyon's waterline affecting the adjacent points.

In the future, we intend to insert pitot tubes to the test table to analyze the convective flow and use thermocouples to measure the transfer of heat by radiation, for the different slope angles and to model this complex problem numerically.

DATA AVAILABILITY

The datasets generated for this study are available on request to the corresponding author.

AUTHOR CONTRIBUTIONS

All authors listed have made a substantial, direct and intellectual contribution to the work, and approved it for publication.

FUNDING

We would like to thank the FCT-Foundation for Science and Technology for the Ph.D. Grants (SFRH/BD/138235/2018 and SFRH/BD/140923/2018) and for the Projects FIREWHIRL (PTDC/EMS-ENE/2530/2014), FIRESTORM (PCIF/GFC/0109/2017), and RENATURE (CENTRO-01-0145-FEDER-000007) that allowed this work to be performed.

ACKNOWLEDGMENTS

We would like to express our gratitude to Gonçalo Rosa and Nuno Luís for their support in laboratory tests. We also would like to express our appreciation to Doctor Aileen Gracias for reviewing our paper.

REFERENCES

Byram, G.M. (1959). "Combustion of forest fuels," in *Forest Fire Control and Use, Vol. 3*, eds K. P. Davis (New York, NY: McGraw-Hill), 61–89.

Dold, J. (2010). "Flow attachment in eruptive fire growth," in *VI International Conference on Forest Fire Research* (Coimbra).

Dold, J. W., and Zinoviev, A. (2009). Fire eruption through intensity and spread rate interaction mediated by flow attachment. *Combust. Theory Model.* 13, 763–793. doi: 10.1080/13647830902977570

Dupuy, J.-L., and Maréchal, J. (2011). Slope effect on laboratory fire spread: contribution of radiation and convection to fuel bed preheating. *Int. J. Wildl. Fire* 20, 289–307. doi: 10.1071/WF09076

Dupuy, J. L. (1995). Slope and fuel load effects on fire behavior: laboratory experiments in pine needles fuel beds. *Int. J. Wildland Fire* 5, 153–164.

Dupuy, J. L., Maréchal, J., Portier, D., and Valette, J. C. (2011). The effects of slope and fuel bed width on laboratory fire behaviour. *Int. J. Wildland Fire* 20, 272–288. doi: 10.1071/WF09075

Lahaye, S., Sharples, J., Matthews, S., Heemstra, S., Price, O., and Badlan, R. (2018). How do weather and terrain contribute to firefighter entrapments in Australia? *Int. J. Wildland Fire* 27, 85–98. doi: 10.1071/WF17114

Pyne, S. J., Andrews, P. L., and Laven, R. D. (1996). *Introduction to Wildland Fire*. New York, NY: John Wiley and Sons.

Raposo, J. R., Cabiddu, S., Viegas, D. X., Salis, M., and Sharples, J. (2015). Experimental analysis of fire spread across a two-dimensional ridge under wind conditions. *Int. J. Wildland Fire* 24:1008. doi: 10.1071/WF14150

Raposo, J. R., Viegas, D. X., Xie, X., Almeida, M., Figueiredo, A. R., Porto, L., et al. (2018). Analysis of the physical processes associated with junction fires at laboratory and field scales. *Int. J. Wildland Fire* 27, 52–68. doi: 10.1071/WF16173

Raposo, J. R. N. R. (2016). *Extreme Fire Behaviour Associated to Merging of Two Linear Fire Fronts*. Coimbra: University of Coimbra.

Schemel, C. F., Simeoni, A., Biteau, H., Rivera, J. D., and Torero, J. L. (2008). A calorimetric study of wildland fuels. *Exp. Ther. Fluid Sci.* 32, 1381–1389. doi: 10.1016/j.expthermflusci.2007.11.011

Sharples, J. J., Towers, I. N., Wheeler, G., Wheeler, V., and Mccoy, J. A. (2013). "Modelling fire line merging using plane curvature flow," in *20th International Congress on Modelling and Simulation* (Coimbra).

Silvani, X., Morandini, F., and Dupuy, J.-L. (2012). Effects of slope on fire spread observed through video images and multiple-point thermal measurements. *Exp. Ther. Fluid Sci.* 41, 99–111. doi: 10.1016/j.expthermflusci.2012.03.021

Viegas, D. X. (2005). A mathematical model for forest fires blowup. *Combust. Sci. Technol.* 177, 27–51. doi: 10.1080/00102200590883624

Viegas, D. X. (2006). Parametric study of an eruptive fire behaviour model. *Int. J. Wildland Fire* 15, 169–177. doi: 10.1071/WF05050

Viegas, D. X. (2012). "Extreme fire behaviour," in *Forest Management: Technology, Practices and Impact*, eds A. C. B. Cruz and R. E. G. Correa (New York, NY: Nova Science Publishers, Inc.), 1–56.

Viegas, D. X., and Pita, L. P. (2004). Fire spread in canyons. *Int. J. Wildland Fire* 13, 253–274. doi: 10.1071/WF03050

Viegas, D. X., Raposo, J. R., Davim, D. A., and Rossa, C. G. (2012). Study of the jump fire produced by the interaction of two oblique fire fronts. Part 1. Analytical model and validation with no-slope laboratory experiments. *Int. J. Wildland Fire* 21, 843–856. doi: 10.1071/WF10155

Viegas, D. X., Ribeiro, L. M., Almeida, M. A., Oliveira, R., Viegas, M. T. P., Reva, V., et al. (2013). *Os Grandes Incêndios Florestais e os Acidentes Mortais Ocorridos em 2013*. Coimbra: University of Coimbra.

Viegas, D. X., and Simeoni, A. (2011). Eruptive behaviour of forest fires. *Fire Technol.* 47, 303–320. doi: 10.1007/s10694-010-0193-6

Werth, P. A., Potter, B. E., Clements, C. B., Finney, M. A., Goodrick, S. L., Alexander, M. E., et al. (2011). *Synthesis of Knowledge of Extreme Fire Behavior. Vol. 1*. Portland, OR: USDA.

Conflict of Interest Statement: The authors declare that the research was conducted in the absence of any commercial or financial relationships that could be construed as a potential conflict of interest.

frontiers in Mechanical Engineering

ORIGINAL RESEARCH
published: 09 July 2019
doi: 10.3389/fmech.2019.00040

Reduced Gas-Phase Kinetic Models for Burning of Douglas Fir

Jeffrey F. Glusman[1], Kyle E. Niemeyer[2], Amanda S. Makowiecki[1], Nicholas T. Wimer[1], Caelan Lapointe[1], Gregory B. Rieker[1], Peter E. Hamlington[1] and John W. Daily[1]*

[1] Department of Mechanical Engineering, University of Colorado, Boulder, CO, United States, [2] School of Mechanical, Industrial, and Manufacturing Engineering, Oregon State University, Corvallis, OR, United States

New skeletal chemical kinetic models have been obtained by reducing a detailed model for the gas-phase combustion of Douglas Fir pyrolysis products. The skeletal models are intended to reduce the cost of high-resolution wildland fire simulations, without substantially affecting accuracy. The reduction begins from a 137 species, 4,533 reaction detailed model for combustion of gas-phase biomass pyrolysis products, and is performed using the directed relation graph with error propagation and sensitivity analysis method, followed by further reaction elimination. The reduction process tracks errors in the ignition delay time and peak temperature for combustion of gas-phase products resulting from the pyrolysis of Douglas Fir. Three skeletal models are produced as a result of this process, corresponding to a larger 71 species, 1,179 reaction model with 1% error in ignition delay time compared to the detailed model, an intermediate 54 species, 637 reaction model with 24% error, and a smaller 54 species, 204 reaction model with 80% error. Using the skeletal models, peak temperature, volumetric heat release rate, premixed laminar flame speed, and diffusion flame extinction temperatures are compared with the detailed model, revealing an average maximum error in these metrics across all conditions considered of less than 1% for the larger skeletal model, 10% for the intermediate model, and 24% for the smaller model. All three skeletal models are thus sufficiently accurate and computationally efficient for implementation in high-resolution wildland fire simulations, where other model errors and parametric uncertainties are likely to be greater than the errors introduced by the reduced kinetic models presented here.

Keywords: combustion, chemical kinetics, Douglas Fir, biomass, computer simulations

OPEN ACCESS

Edited by:
Xinyan Huang,
Hong Kong Polytechnic University,
Hong Kong

Reviewed by:
Liming Cai,
RWTH Aachen Universität, Germany
Shiyou Yang,
Ford Motor Company, United States

****Correspondence:***
Jeffrey F. Glusman
jeff.glusman@colorado.edu

Specialty section:
This article was submitted to Thermal and Mass Transport, a section of the journal Frontiers in Mechanical Engineering

Received: *31 January 2019*
Accepted: *18 June 2019*
Published: *09 July 2019*

Citation:
Glusman JF, Niemeyer KE, Makowiecki AS, Wimer NT, Lapointe C, Rieker GB, Hamlington PE and Daily JW (2019) Reduced Gas-Phase Kinetic Models for Burning of Douglas Fir. Front. Mech. Eng. 5:40. doi: 10.3389/fmech.2019.00040

1. INTRODUCTION

In order to reduce the computational cost of high-fidelity numerical simulations of wildland fire, computationally efficient—yet still physically accurate—reduced chemical kinetic models are required for the prediction of gas-phase combustion. In this paper, we present three such skeletal models for the combustion of gas-phase products resulting from the pyrolysis of Douglas Fir. The computational savings enabled by these models are substantial when compared to detailed models, making the skeletal models suitable for wildland fire simulations spanning large spatial and temporal scale ranges.

The need for such scale-resolving simulations arises from the considerable environmental and economic cost of wildland fires, as well as the difficulty in establishing future mitigation and

avoidance strategies. It is anticipated that climate change will contribute to increased wildland fire activity, particularly in the Western U.S. (Barbero et al., 2015; Westerling, 2016), further increasing the importance of simulations in fire management efforts.

Predicting wildland fires using computational models remains, however, an inexact science. Such models can generally be divided into two categories: semi-empirical operational models used for nearly real-time incident response, and physics-based models used to understand the dynamics of fire spread (Coen et al., 2013). Although there is a growing trend in wildland fire research toward physics-based models (Linn et al., 2002, 2010; Sullivan, 2009; Mell et al., 2010; Morvan, 2011), these models remain limited by the daunting challenge of incorporating the physics of wildland fuel combustion in landscape-scale numerical simulations that are coupled to atmospheric dynamics and weather (Coen et al., 2013).

As a possible solution to this challenge, high-resolution numerical simulations at much smaller scales (e.g., 10 m and below) can, in principle, be used to develop improved subgrid-scale models for landscape-scale wildland fire simulations. As the scale of the simulations decreases, however, there is a greater need to more accurately model all relevant small-scale chemical and fluid processes. To adequately model fire spread, simulations must be able to resolve small-scale turbulent mixing, as well as capture the pyrolysis and subsequent gas-phase combustion of geometrically complex and spatially heterogeneous wildland fuels. The challenge of resolving turbulence can be addressed through advanced computational techniques such as adaptive mesh refinement (Wimer et al., 2019a,b), but the chemical models used for pyrolysis and combustion must be sufficiently detailed without significantly increasing the computational cost.

Although typical biomass pyrolysis models are not excessively large, gas-phase combustion models routinely involve hundreds or even thousands of different species and reactions. For example, Ranzi et al. (2008) have provided a gas-phase biomass combustion model—which is the basis for the present skeletal models—that contains 4,533 reactions and 137 species. Skeletal and other reduced models are typically an order of magnitude smaller. The widely-used multi-step DRM19 kinetic model, for instance, is a 19 species (plus N_2 and Ar), 84 reaction reduced model for methane combustion based on GRI-Mech 1.2 (Kazakov and Frenklach, 1995).

In the following, we outline the development of three new skeletal chemical kinetic models for gas-phase combustion of Douglas Fir pyrolysis products. The three models are targeted at large-scale simulations on high-performance computing resources, but are intended to provide three different levels of accuracy and computational cost. Users may thus choose the model best suited to their needs and available computational resources. All skeletal mechanisms include a similar number of species (i.e., 71 and 54 species), but have vastly different numbers of reactions (i.e., 1,179, 637, and 204 reactions).

The skeletal models are obtained by reducing the detailed chemical kinetic model for gas-phase biomass combustion from Ranzi et al. (2008). The reduction is performed using the directed relation graph with error propagation and sensitivity analysis method in a perfectly stirred reactor. We then show that all three skeletal models introduce relatively small errors, as compared to the detailed model, for various properties of premixed and diffusion flames.

The paper is organized as follows. In the next section, we outline the detailed model and reduction procedure, followed by a presentation of results from the three new skeletal models. Finally, we provide conclusions at the end.

2. METHODOLOGY

The overall reduction procedure tracks errors in ignition delay time and peak temperature in a constant-pressure, fixed volume perfectly stirred reactor (PSR) for the combustion of gases resulting from the pyrolysis of Douglas Fir. In the following, we describe the model and procedure used to obtain the Douglas Fir pyrolysis products, followed by descriptions of the detailed chemical kinetic model and the reduction process.

2.1. Pyrolysis Model

The pyrolysis kinetic model is that of Debiagi et al. (2015), which includes extractives and is a refined version of the model published by Corbetta et al. (2014). The model involves 28 reactions and 47 species (including volatile, non-volatile, and condensed phase species) and provides pathways for the thermal decomposition of the three main polymer components of wood: cellulose, hemicellulose, and lignin, in addition to two extractives. It predicts light fractions directly, while heavy fractions are described by lumped species. The advantage of using this model is that the gaseous lumped product species correspond to those in an associated gas-phase detailed kinetic model (Ranzi et al., 2008), which is the starting point for the model reduction performed here. Of the 47 species in the pyrolysis mechanism, 18 are gaseous or volatile.

The major components of wood are polymers, and the pyrolysis model reflects this by starting with de-polymerization reactions, although in a highly simplified manner. Cellulose is assumed to transform into active cellulose; i.e., a reactive form that leads to the monomeric form and other products like levoglucosan. Hemicellulose is assumed to decompose into intermediate species `HCE1` and `HCE2` that successively decompose with different activation energies, with different propensities to char. Lignin is assumed to be composed of `LIG-C`, `LIG-O`, and `LIG-H` (carbon, oxygen, and hydrogen rich derivatives of the β-O-4 molecule, respectively), that then decompose into intermediate components that lead to other products (Ranzi et al., 2008).

Extractives extend the applicable types of biomass that can be represented with this kinetic model. Previous versions of the pyrolysis mechanism (e.g., Corbetta et al., 2014) were only valid for specific types of biomass, depending on their carbon and hydrogen makeup. Extractives fall into two categories: hydrophilic and hydrophobic. Debiagi et al. (2015) chose to use a tannin (`TANN`) as the hydrophilic extractive and a triglyceride (`TGL`) as the hydrophobic extractive.

TABLE 1 | Weight percentages of the main components of Douglas Fir, including molecular structures.

Molecule	Structure	Weight percentage
Cellulose	$C_6H_{10}O_5$	44.06
Hemicellulose	$C_6H_8O_5$	22.01
LIG-C	$C_{15}H_{14}O_4$	4.73
LIG-H	$C_{20}H_{22}O_{10}$	12.05
LIG-O	$C_{22}H_{28}O_9$	10.89
TANN	$C_{15}H_{12}O_7$	1.26
TGL	$C_{57}H_{100}O_7$	5.01

2.2. Douglas Fir Pyrolysis Products

To carry out reduction of the gas-phase kinetic model, a realistic set of gas-phase pyrolysis products is required as input to the gas-phase calculations. Therefore, we have run simulations using the pyrolysis model described in the previous section over a range of times and temperatures. This requires selecting a target wood species to work with, since the initial concentrations of cellulose, hemicellulose, and lignin vary by species. We have selected Douglas Fir because of its widespread availability and native presence in the Rocky Mountain region. We obtained the initial mole fractions of cellulose, hemicellulose, LIG-C, LIG-H, LIG-O, TANN, and TGL for Douglas Fir from Debiagi et al. (2015), Faravelli et al. (2010), and Schwetz and Lipp (1985); **Table 1** lists these in terms of weight percentages.

The pyrolysis model is solved using an experimentally measured temperature time series (shown in **Figure 1**) as input. In the experiments, Douglas Fir samples were heated with a cone-calorimeter while simultaneously measuring surface temperature (via an infrared camera), gas temperature, and H_2O mole fraction. The latter two quantities were measured using dual-frequency comb laser diagnostics (Schroeder et al., 2017). Since the model describes pyrolysis (i.e., decomposition at high temperature in the absence of air), an approximately stoichiometric amount of air was assumed for comparison with the experimental dataset. The formation of pyrolysis gases is modeled using the surface temperature measured by the infrared camera, prior to any combustion occurring. More extensive details on the experiments are available in Makowiecki et al. (in preparation).

Figure 1 shows the evolution of the top five gaseous pyrolysis products as a function of time; at 80 s, these species account for approximately 74% of the total moles in the gas-phase. This figure indicates that the pyrolysis model accurately captures the production of H_2O vapor measured experimentally.

2.3. Detailed Combustion Model

The detailed gas-phase kinetic model bio1412 from the CRECK modeling group is used as the starting point for the reduced skeletal models. This model is publicly available at the website http://creckmodeling.chem.polimi.it, with verification data given by Ranzi et al. (2008). The model contains 4,533 reactions and 137 species and is built upon earlier work from the CRECK group (Ranzi et al., 2001). Although this model has been shown to give good agreement for the gas-phase combustion of solid fuel pyrolysis gases (Ranzi et al., 2008), it is generally too large for inclusion in already demanding simulations of wildland fire. Consequently, in the following we reduce this model to a size that is appropriate for high-fidelity numerical simulations.

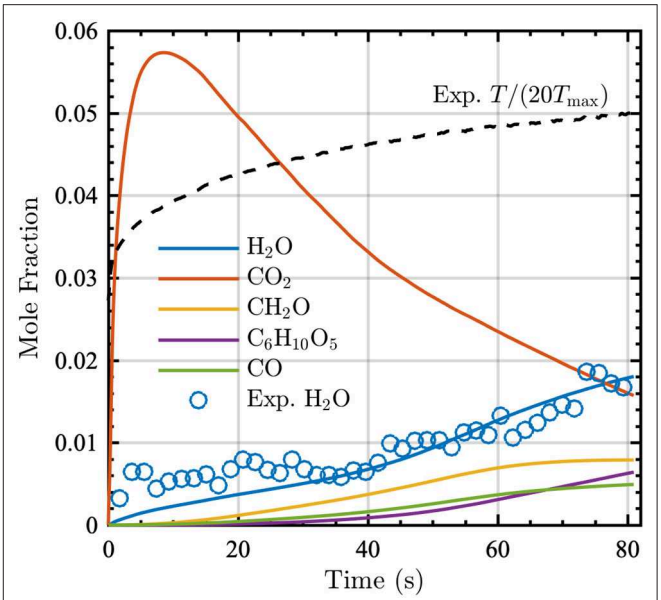

FIGURE 1 | Mole fraction time series of the five most prevalent (by mole fraction at 80 s) gaseous pyrolysis products (indicated by lines) and the corresponding experimentally measured H_2O mole fraction (indicated by open circles). The normalized experimental temperature time series is also shown (black dashed line), where $T_{\max} = 639$ K.

2.4. Reduction Methodology

The CRECK detailed gas-phase combustion model is reduced using the Model Automatic Reduction Software (MARS) package (Niemeyer et al., 2010; Niemeyer and Sung, 2011, 2014, 2015). The reduction employs the directed relation graph with error propagation (DRGEP) and sensitivity analysis (SA) methods, followed by reaction elimination, which Niemeyer and colleagues have shown to be effective for reducing various surrogate fuel models.

Briefly, the process begins by applying DRGEP, which determines the importance of each species to the production or consumption of chosen target species (e.g., fuel, oxidizer, important pollutants). Next, a "greedy" SA removes individual species one-by-one and evaluates the error induced; it removes the species that least affect error and repeats the process on the remaining species until reaching the specified error limit. The error limit is determined by comparing predictions of the full, detailed kinetic model via autoignition and PSR simulations across expected conditions (e.g., pressure, temperature, equivalence ratio, and initial reactants) with those of the skeletal model. Ignition delay time and points along the upper PSR temperature response curve are chosen as metrics for the reduction, consistent with typical target parameters for premixed combustion mechanisms. Then, the contributions of each remaining reaction are examined, with the goal of

eliminating reactions that are unimportant to the overall progression of the kinetic model, while remaining below the specified error tolerance. The final resulting model is considered the skeletal model.

This process is carried out for each targeted condition (e.g., pressure, temperature, equivalence ratio, initial reactants), resulting in a single skeletal model that consists of the union of species remaining over all conditions. This guarantees that the reduced model maintains error below the specified limit for autoignition and PSR results. Further, targeted species cannot be removed, regardless of their impact on the overall kinetics.

3. RESULTS

3.1. Skeletal Combustion Models

Reduction calculations were performed using the fuel set composed of all 18 gas-phase pyrolysis products. The pressure was set to 1 atm, with temperatures ranging from 800 to 2,000 K and equivalence ratios from 0.5 to 1.5. The wide range of conditions included in the reduction reflects the similarly wide-ranges of temperatures and equivalence ratios found in real-world wildland fires.

To create a robust gas-phase combustion model, various sets of products from the pyrolysis model were used in the reduction, corresponding to the products at 20, 50, and 80 s (shown in **Figure 1**). However, the resulting reduced gas-phase models were all roughly the same size, with similar numbers of species and reactions. Therefore, only the reductions on the final pyrolysis products at 80 s will be discussed in the following sections.

Figure 2 shows the reduction process via DRGEPSA for the number of species remaining in the kinetic model as a function of error limit. Applying DRGEP with a maximum error of 30% (in ignition delay time and peak temperature in a PSR) to the detailed kinetic model removed 75 species and any reaction containing them, leaving 62 species. At this point in the reduction, the error in ignition delay time between the detailed model and the reduced model was approximately 21%. Applying sensitivity analysis removed 8 additional species and their associated reactions, resulting in a reduced model with 54 species and 637 reactions, giving approximately 24% error in ignition delay time, as compared to the detailed model. The reaction elimination step removed an additional 433 reactions, yielding a skeletal model with 204 reactions. For the ignition delay time in a PSR, this final skeletal model has 82.9% maximum error when compared to the detailed model. However, this most-reduced skeletal model retains only 54 species and 204 reactions, corresponding to 39.4% of the total number of species and 4.5% of the total number of reactions in the detailed model.

During the DRGEP process, **Figure 2** indicates a significant increase in error at 81 species, corresponding to a jump from 1% to greater than 15% error. Consequently, we created another reduced model with 1% error for gas-phase combustion, hereby noted Skeletal-A. Following the same naming convention, Skeletal-B is the reduced model produced by DRGEPSA with 30% error, and Skeletal-C is the model obtained from Skeletal-B after the reaction elimination step. The numbers of species and reactions in these three models are summarized in **Table 2**, along with the detailed model. After the DRGEPSA process, the Skeletal-A model has only 1.00% error in ignition delay time compared to the detailed model, which increases to 24.1% error for Skeletal-B and 82.9% after the reaction elimination step in Skeletal-C. With the introduction of tabulated and dimensional reduction of chemistry, models on the order of one-thousand reactions and one-hundred species are suitable for computations (Hiremath et al., 2013), and thus all of the skeletal models developed here are sufficiently compact for implementation in high-resolution simulations. The final skeletal models and associated information on thermodynamic and transport properties are provided as text-based files in the **Supplemental Material**.

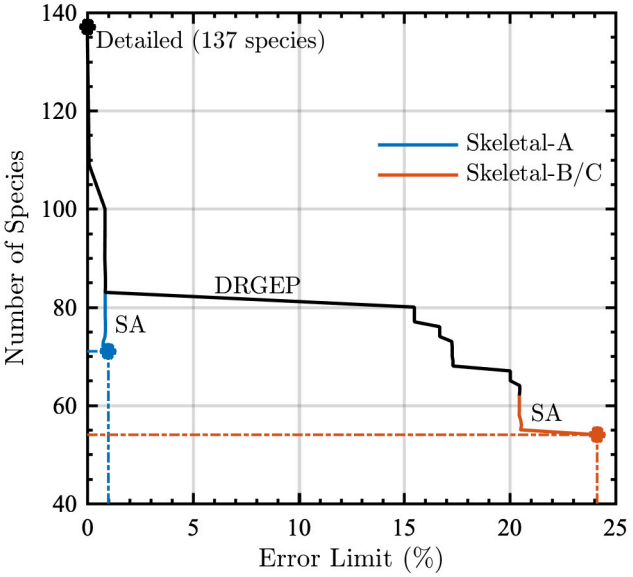

FIGURE 2 | Number of species as a function of error limit during the reduction of the detailed model using the directed relation graph with error propagation (DRGEP) and sensitivity analysis (SA) method. Dash-dot lines indicate the number of species for the given error limit in skeletal models A (blue lines) and B (red lines) prior to the reaction elimination step (which produces Skeletal-C).

TABLE 2 | Detailed and skeletal model details, indicating the final number of species and reactions, as well as the error in the ignition delay time with respect to the detailed model.

Model	# Species	# Reactions	Error %
Detailed	137	4,533	–
Skeletal-A	71	1,179	1.00
Skeletal-B	54	637	24.1
Skeletal-C	54	204	82.9

3.2. Validation of Skeletal Models

To validate the accuracy of the reduced skeletal models, which were obtained based solely on consideration of the ignition delay time and peak temperature in PSR calculations, here we compare PSR ignition delays, peak temperatures, and

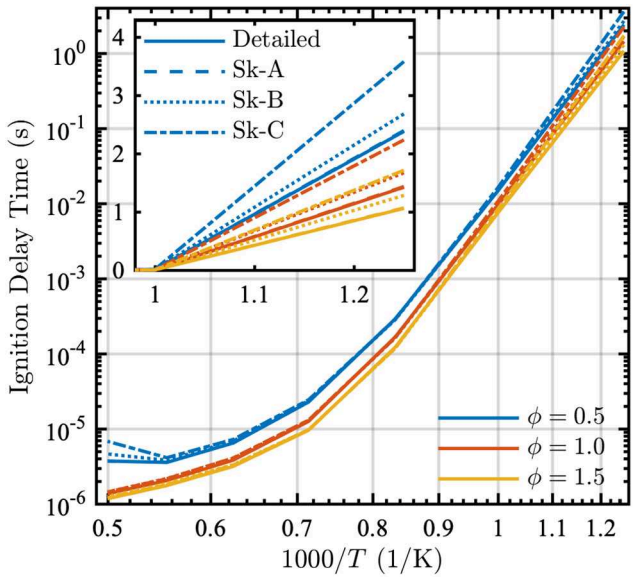

FIGURE 3 | Ignition delay as a function of $1000/T$ in a PSR at equivalence ratios ϕ=[0.5, 1.0, 1.5] and $P = 1$ atm for the detailed (solid lines), Skeletal-A (dashed lines), Skeletal-B (dotted lines), and Skeletal-C (dash-dot lines) models. The inset shows ignition delay time vs. $1000/T$ for lower temperatures.

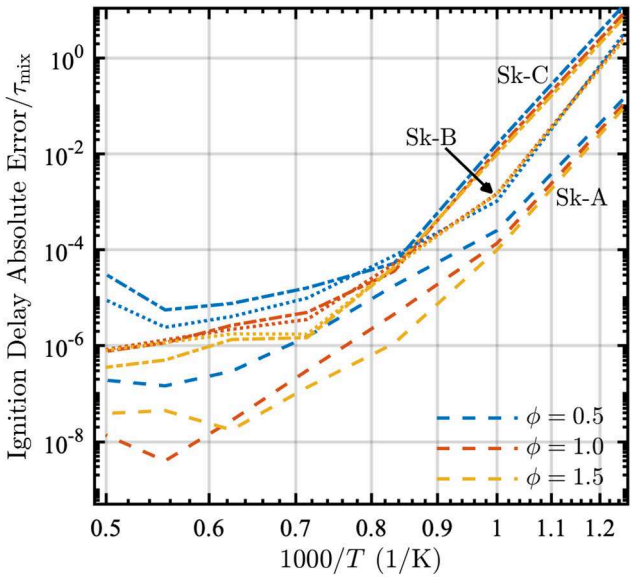

FIGURE 4 | Absolute error relative to the mixing time $\tau_{mix} = 0.1$ s as a function of $1000/T$ in a PSR at equivalence ratios $\phi = [0.5, 1.0, 1.5]$ and $P = 1$ atm for the Skeletal-A (dashed lines), Skeletal-B (dotted lines), and Skeletal-C (dash-dot lines) models.

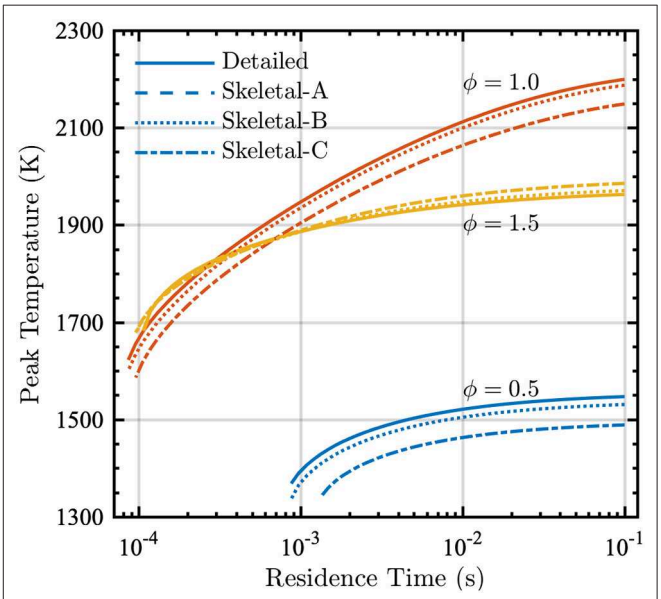

FIGURE 5 | Peak temperature vs. residence time in a PSR at equivalence ratios ϕ=[0.5, 1.0, 1.5] and $P = 1$ atm for detailed (solid lines), Skeletal-A (dashed lines), Skeletal-B (dotted lines), and Skeletal-C (dash-dot lines) models.

volumetric heat-release rates, premixed laminar flame speeds, and diffusion flame extinction points from the detailed and skeletal models.

Figure 3 shows that all three skeletal models match the ignition delay times of the detailed model for equivalence ratios from 0.5 to 1.5 over a wide range of temperatures. Although discrepancies do exist between the models at low temperatures, such temperatures are not of primary interest for wildland fire. In general, as expected, the larger Skeletal-A model is in better agreement with the detailed model, as compared to the Skeletal-B and Skeletal-C models.

To assess the importance of the error in ignition delay, we compare the absolute error in the ignition delay time to an approximate characteristic turbulent mixing time τ_{mix}. This time is estimated as $\tau_{mix} \approx 0.1$ s based on a convective velocity of 1 cm/s and a characteristic length of 1 mm. For most practical conditions, the ignition delay will be dominated by mixing and therefore the error introduced by the reduction is reasonably small, as seen in **Figure 4**. The highest error occurs at low temperatures where the characteristic turbulent mixing time would be much longer than the approximate one used here, due to a lower convective velocity. While the deviations at T = 2,000 K look large, it must be kept in mind that the non-dimensional errors are on the order of 10^{-4} to 10^{-8}, and therefore trivial for this application when compared to the mixing time.

The PSR calculations performed during the reduction process also provide the peak temperature and the volumetric heat-release rate as functions of residence time. These results are shown in **Figures 5** and **6** for the detailed and skeletal models over equivalence ratios from 0.5 to 1.5.

For each of the models and at all equivalence ratios, the peak temperatures in **Figure 5** decrease as the residence time decreases, consistent with the increased incidence of incomplete combustion for small residence times. The detailed and Skeletal-A models are in nearly perfect agreement, with small deviations in the Skeletal-B model for all conditions considered.

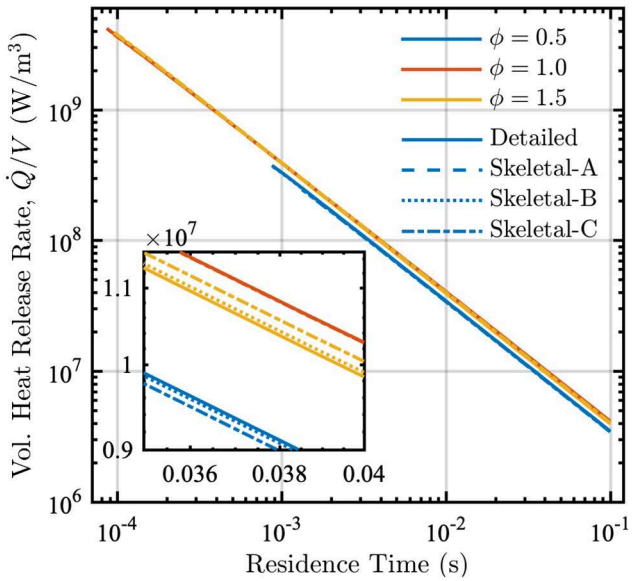

FIGURE 6 | Volumetric heat release rate vs. residence time in a PSR at equivalence ratios $\phi = [0.5, 1.0, 1.5]$ and $P = 1$ atm for detailed (solid lines), Skeletal-A (dashed lines), Skeletal-B (dotted lines), and Skeletal-C (dash-dot lines) models.

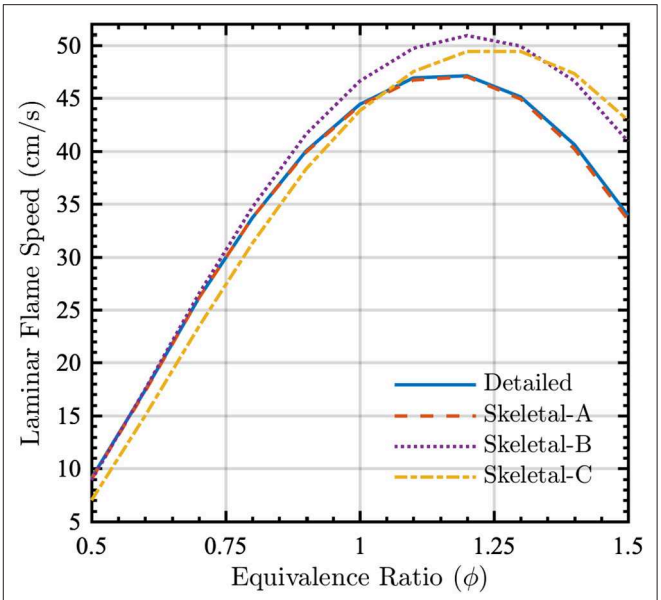

FIGURE 7 | Laminar flame speed for a one-dimensional premixed flame as a function of equivalence ratio ϕ for detailed (solid lines), Skeletal-A (dashed lines), Skeletal-B (dotted lines), and Skeletal-C (dash-dot lines) models. The reactants were at 300 K and $P = 1$ atm.

Peak temperatures from the Skeletal-C model show a slight discrepancy with respect to the detailed and Skeletal-A and -B models, but the correct trends with varying residence time are nevertheless still captured.

The variation of the volumetric heat-release rate with residence time is nearly identical for the detailed and all three skeletal models, as shown in **Figure 6**. In particular, the volumetric heat release rate increases substantially as the residence time decreases. This occurs because more heat must be removed relative to the volume in order to maintain a constant-pressure reactor.

To validate the model reduction in non-homogeneous flame configurations, laminar flame speeds were computed for a one-dimensional premixed flame in Cantera (Goodwin et al., 2018) using both detailed and skeletal chemical kinetic models with mixture-averaged diffusion coefficients. The physical domain length was 50 cm, the reactants were at a temperature of 300 K and pressure of 1 atm, and flame speeds were computed over a range of equivalence ratios. **Figure 7** shows that, once again, there is essentially no discrepancy between the detailed and Skeletal-A models. Although errors are larger for the Skeletal-B and -C models, these errors will generally be tolerable in simulations of real-world fires given the typically larger errors introduced by other physical models in the simulations (e.g., for turbulence, heat transfer, and fuel properties), as well as uncertainties in boundary and initial conditions.

Because wildland fires exhibit characteristics of both premixed and diffusion flames, the skeletal models were also used to compute the extinction temperature as a function of maximum strain rate for an opposed-jet diffusion flame. The simulations

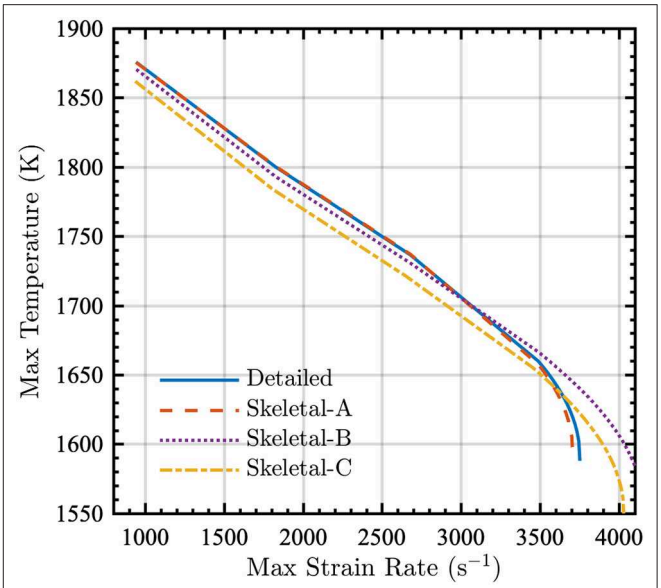

FIGURE 8 | Maximum temperature in an opposed-jet diffusion flame as a function of maximum strain rate for detailed (solid lines), Skeletal-A (dashed lines), Skeletal-B (dotted lines), and Skeletal-C (dash-dot lines) models. The conditions of the opposed-jet configuration were $T_{\text{fuel}} = 500$ K, $T_{\text{air}} = 300$ K, and $P = 1$ atm.

were performed using Cantera in an 18 mm domain with radiation. The fuel and air temperatures were $T_{\text{fuel}} = 500$ K and $T_{\text{air}} = 300$ K, respectively, and the pressure was $P = 1$ atm.

The results shown in **Figure 8** indicate that the reduction process generally has minimal effect on the relation between

TABLE 3 | Root mean square (RMS) and maximum error percentages from the Skeletal-A, Skeletal-B, and Skeletal-C reduced models for various properties of interest over the range of conditions considered in this study.

	Skeletal-A error		Skeletal-B error		Skeletal-C error	
	RMS (%)	Max (%)	RMS (%)	Max (%)	RMS (%)	Max (%)
Ignition delay time (PSR)	0.40	1.00	9.40	24.13	28.82	82.85
Peak temperature (PSR)	0.03	0.33	0.73	1.46	2.54	6.17
Vol. heat release rate (PSR)	0.01	0.13	0.34	0.82	1.24	2.65
Flame speed (LP)	0.64	1.18	9.12	20.65	13.5	26.5
Extinction temperature (OJD)	0.52	1.40	1.00	1.98	0.54	1.16

Errors are computed relative to results from the detailed model. Properties are computed for a perfectly stirred reactor (PSR), a 1D laminar premixed (LP) flame, and an opposed-jet diffusion (OJD) flame.

the maximum temperature and strain rate at the extinction point. As with other metrics for the PSR and the premixed flame, the Skeletal-A model is in nearly perfect agreement with the detailed model, and the Skeletal-B and -C models display relatively small discrepancies when compared to the detailed model.

As a quantitative summary of the errors in the skeletal models with respect to the detailed model, **Table 3** shows the root-mean square (RMS) and maximum errors for various quantities of interest over all conditions (i.e., temperatures and equivalence ratios) considered in the present study. In general, the errors for the Skeletal-A model are extremely low and the maximum errors for the Skeletal-B model are below 25% for all metrics considered. As expected, the Skeletal-C model shows the greatest amount of error, although the RMS errors are maintained below 30%.

Table 3 shows that the maximum errors across all reduced models occur in the ignition delay time. As noted before, these errors are likely to be acceptable in most high-fidelity simulations of wildland fire given the significant increase in computational efficiency resulting from the reduction in number of species and reactions. Moreover, although the errors in ignition delay time are somewhat large in relative terms, they are small in absolute terms when compared to characteristic flow mixing times.

4. CONCLUSIONS

Three new skeletal chemical kinetic models (provided in the **Supplemental Material**) have been developed and validated for the combustion of gas-phase products resulting from the pyrolysis of Douglas Fir. The skeletal models were obtained by using the directed relation graph with error propagation method, "greedy" sensitivity analysis, and unimportant reaction elimination to reduce a detailed gas-phase model with 137 species and 4,533 reactions.

The three skeletal models had different sizes and resultant errors. The larger 71 species, 1,179 reaction skeletal model had a maximum error of 1% for combustion properties of interest over a wide range of conditions, while a more reduced model with 54 species and 637 reactions yielded maximum errors of roughly 21% and 24% in ignition delay time and laminar flame speed, respectively. The smallest 54 species, 204 reaction model had a maximum error of roughly 83% in ignition delay, with an average maximum error of 24%. These errors are reasonable given the complexity and uncertainty involved in modeling solid biomass combustion, although the larger skeletal model, with smaller error, is preferable if sufficient computational resources are available to allow its integration within high-fidelity simulations of wildland fire. It should also be noted that the largest errors were observed for all three skeletal models in the prediction of the ignition delay time, but these errors were small in absolute terms, particularly when compared to characteristic flow mixing times.

Ongoing work is focused on the use of additional performance measures in different flows, such as diffusion flames, as targets for MARS. A multi-dimensional finite volume model in OpenFOAM is currently under development to allow full coupling of pyrolysis and gas chemistry, thus permitting more direct comparisons with experimental data. An additional study will also be performed to quantify the maximum reduction allowable before the induced errors affect major simulation outcomes, as well as to expand to more general biomass flora.

AUTHOR CONTRIBUTIONS

JG, KN, and JD were jointly responsible for the selection of the detailed model, the model reduction, and the validation of the skeletal model. AM and GR provided experimental data. Frequent discussions with NW, CL, and PH guided reduced model development, particularly with respect to computational constraints.

FUNDING

This research was supported by the Strategic Environmental Research and Development Program (SERDP) under grant W912HQ-16-C-0026 as project number RC-2642. Work by KN was supported by SERDP under project number RC-2651. CL is supported by the National Science Foundation Graduate Research Fellowship Program under Grant No. NSF GRFP, DGE 1144083.

SUPPLEMENTARY MATERIAL

The Supplementary Material for this article can be found online at: https://www.frontiersin.org/articles/10.3389/fmech.2019.00040/full#supplementary-material

The final skeletal models and associated information on thermodynamic and transport properties are provided as text-based files in the **Supplemental Material**.

REFERENCES

Barbero, R., Abatzoglou, J., Larkin, N., Kolden, C., and Stocks, B. (2015). Climate change presents increased potential for very large fires in the contiguous united states. *Int. J. Wildl. Fire* 24, 892–899. doi: 10.1071/WF15083

Coen, J. L., Cameron, M., Michalakes, J., Patton, E. G., Riggan, P. J., and Yedinak, K. M. (2013). Wrf-fire: coupled weather–wildland fire modeling with the weather research and forecasting model. *J. Appl. Meteorol. Climatol.* 52, 16–38. doi: 10.1175/JAMC-D-12-023.1

Corbetta, M., Frassoldati, A., Bennadji, H., Smith, K., Serapiglia, M. J., Gauthier, G., et al. (2014). Pyrolysis of centimeter-scale woody biomass particles: kinetic modeling and experimental validation. *Energy Fuels* 28, 3884–3898. doi: 10.1021/ef500525v

Debiagi, P. E. A., Pecchi, C., Gentile, G., Frassoldati, A., Cuoci, A., Faravelli, T., et al. (2015). Extractives extend the applicability of multistep kinetic scheme of biomass pyrolysis. *Energy Fuels* 29, 6544–6555. doi: 10.1021/acs.energyfuels.5b01753

Faravelli, T., Frassoldati, A., Migliavacca, G., and Ranzi, E. (2010). Detailed kinetic modeling of the thermal degradation of lignins. *Biomass Bioenergy* 34, 290–301. doi: 10.1016/j.biombioe.2009.10.018

Goodwin, D. G., Speth, R. L., Moffat, H. K., and Weber, B. W. (2018). *Cantera: An Object-Oriented Software Toolkit for Chemical Kinetics, Thermodynamics, and Transport Processes*. Version 2.4.0. Available online at: https://www.cantera.org

Hiremath, V., Lantz, S. R., Wang, H., and Pope, S. B. (2013). Large-scale parallel simulations of turbulent combustion using combined dimension reduction and tabulation of chemistry. *Proc. Combust. Inst.* 34, 205–215. doi: 10.1016/j.proci.2012.06.004

Kazakov, A., and Frenklach, M. (1995). *Reduced Reaction Sets Based on GRI-Mech 1.2.* Available online at: http://combustion.berkeley.edu/drm/

Linn, R., Reisner, J., Colman, J., and Winterkamp, J. (2002). Studying wildfire behavior using FIRETEC. *Int. J. Wild. Fire* 11, 233–246. doi: 10.1071/WF02007

Linn, R., Winterkamp, J., Weise, D., and Edminster, C. (2010). A numerical study of slope and fuel structure effects on coupled wildlfire behavior. *Int. J. Wild. Fire* 19, 179–201. doi: 10.1071/WF07120

Mell, W. E., McDermott, R. J., and Forney, G. P. (2010). "Wildland fire behavior modeling: perspectives, new approaches and applications," in *Proceedings of 3rd Fire Behavior and Fuels Conference, Spokane* (Washington, DC), 45–62.

Morvan, D. (2011). Physical phenomena and length scales governing the behaviour of wildfires: a case for physical modelling. *Fire Technol.* 47, 437–460. doi: 10.1007/s10694-010-0160-2

Niemeyer, K. E., and Sung, C.-J. (2011). On the importance of graph search algorithms for drgep-based mechanism reduction methods. *Combust. Flame* 158, 1439–1443. doi: 10.1016/j.combustflame.2010.12.010

Niemeyer, K. E., and Sung, C.-J. (2014). Mechanism reduction for multicomponent surrogates: a case study using toluene reference fuels. *Combust. Flame* 161, 2752–2764. doi: 10.1016/j.combustflame.2014.05.001

Niemeyer, K. E., and Sung, C.-J. (2015). Reduced chemistry for a gasoline surrogate valid at engine-relevant conditions. *Energy Fuels* 29, 1172–1185. doi: 10.1021/ef5022126

Niemeyer, K. E., Sung, C.-J., and Raju, M. P. (2010). Skeletal mechanism generation for surrogate fuels using directed relation graph with error propagation and sensitivity analysis. *Combust. Flame* 157, 1760–1770. doi: 10.1016/j.combustflame.2009.12.022

Ranzi, E., Cuoci, A., Faravelli, T., Frassoldati, A., Migliavacca, G., Pierucci, S., et al. (2008). Chemical kinetics of biomass pyrolysis. *Energy Fuels* 22, 4292–4300. doi: 10.1021/ef800551t

Ranzi, E., Dente, M., Goldaniga, A., Bozzano, G., and Faravelli, T. (2001). Lumping procedures in detailed kinetic modeling of gasification, pyrolysis, partial oxidation and combustion of hydrocarbon mixtures. *Prog. Energy Combust. Sci.* 27, 99–139. doi: 10.1016/S0360-1285(00)00013-7

Schroeder, P., Wright, R., Coburn, S., Sodergren, B., Cossel, K., Droste, S., et al. (2017). Dual frequency comb laser absorption spectroscopy in a 16 MW gas turbine exhaust. *Proc. Combust. Inst.* 36, 4565–4573. doi: 10.1016/j.proci.2016.06.032

Schwetz, K., and Lipp, A. (1985). Ullmann's encyclopedia of industrial chemistry. *VCH: Deerfield Beach* 28:315.

Sullivan, A. L. (2009). Wildland surface fire spread modelling, 1990–2007. 1: physical and quasi-physical models. *Int. J. Wildl. Fire* 18, 349–368. doi: 10.1071/WF06143

Westerling, A. L. (2016). Increasing western us forest wildfire activity: sensitivity to changes in the timing of spring. *Philos. Trans. R. Soc. B* 371:20150178. doi: 10.1098/rstb.2015.0178

Wimer, N. T., Day, M. S., Lapointe, C., Makowiecki, A. S., Glusman, J. F., Daily, J. W., et al. (2019a). High-resolution numerical simulations of a large-scale helium plume using adaptive mesh refinement. *arXiv 1901.10554*. doi: 10.1103/APS.DFD.2018.GFM.V0083

Wimer, N. T., Lapointe, C., Christopher, J. D., Nigam, S. P., Hayden, T. R., Upadhye, A., et al. (2019b). Scaling of the puffing strouhal number for buoyant jets. *arXiv[Preprint].arXiv:1901.01580*.

Conflict of Interest Statement: The authors declare that the research was conducted in the absence of any commercial or financial relationships that could be construed as a potential conflict of interest.

frontiers in Mechanical Engineering

ORIGINAL RESEARCH
published: 12 July 2019
doi: 10.3389/fmech.2019.00043

A Framework to Facilitate Firebrand Characterization

Faraz Hedayati[1], *Babak Bahrani*[2], *Aixi Zhou*[2]*, *Stephen L. Quarles*[1] *and Daniel J. Gorham*[1]

[1] *Insurance Institute for Business & Home Safety, Richburg, SC, United States,* [2] *Department of Applied Engineering Technology, North Carolina A&T State University, Greensboro, NC, United States*

Generation of firebrands from various fuels has been well-studied in the past decade. Limited details have been released about the methodology for characterizing firebrands such as the proper sample size and the measurement process. This study focuses on (1) finding the minimum required sample size to represents the characteristics of the population, and (2) proposes a framework to facilitate the tedious measurement process. To achieve these goals, several firebrand generation tests were conducted at a boundary layer wind tunnel with realistic gusty wind traces. Firebrands were generated from burning structural fuels and collected in 46 strategically located water pans. The statistical analysis showed that the minimum required sample size based on the chosen statistical parameters (standard deviation, confidence interval, and margin of error) is 1,400 for each test. To facilitate characterizing such a large sample of firebrands, an automated image processing algorithm to measure the projected area of the firebrands was developed, which can automatically detect the edges of the background sheet, rotate the photo if its tilted before cropping, detect edges of firebrands, remove erroneous particles (e.g., ash) and finally measures the projected area. To facilitate the weighing process, a Gaussian process regression was performed to predict the mass based on projected area, traveling distance and wind speed. The model can predict the firebrand mass within 5% error compared to the measurement. This framework and model can provide a probabilistic range of firebrand characteristics over the continuous range of the collection region.

Keywords: firebrand, machine learning, Gaussian process regression, image processing, ember, wildfire, WUI

OPEN ACCESS

Edited by:
Michael John Gollner, University of Maryland, College Park, United States

Reviewed by:
Nigel Berkeley Kaye, Clemson University, United States
Wei Tang, National Institute of Standards and Technology (NIST), United States

***Correspondence:**
Aixi Zhou
azhou@ncat.edu

Specialty section:
This article was submitted to Thermal and Mass Transport, a section of the journal Frontiers in Mechanical Engineering

Received: *06 April 2019*
Accepted: *27 June 2019*
Published: *12 July 2019*

Citation:
Hedayati F, Bahrani B, Zhou A, Quarles SL and Gorham DJ (2019) A Framework to Facilitate Firebrand Characterization. Front. Mech. Eng. 5:43. doi: 10.3389/fmech.2019.00043

INTRODUCTION

Large-scale wildland and wildland-urban interface (WUI) fires have happened more frequently in recent years. Direct flame contact, radiant heat, and burning firebrands (or embers) have been identified as three principal ways that cause fire spread in the wildland and WUI (Clements, 1977; Maranghides and Mell, 2011; Koo et al., 2012; Caton et al., 2017). However, only burning firebrands can initiate a new spot fire at distances further than 60-m away from the main fire front (Cohen, 2008). Spotting due to firebrands, also referred as the firebrand phenomenon, can overpower fire suppression efforts and become the dominant fire spread mechanism (Koo et al., 2010). The spotting process includes three phases: firebrand generation, transportation, and ignition of the recipient fuel.

The ability of a firebrand to travel far way and start a new fire is a function of its physical properties and the environmental parameters (Tohidi et al., 2015). Primary physical properties of a firebrand include mass, size (aerodynamic) shape, surface temperature, heat flux, and the heat of combustion of the fuel. The shape and

dimensions are critical factors in firebrand transport. In previous studies, firebrand size has been treated as a 2-dimentional parameter that is represented by the projected area of the firebrand (Manzello et al., 2012b; Zhou et al., 2015; Suzuki and Manzello, 2016; Caton et al., 2017; Manzello and Suzuki, 2017). The mass and heat of combustion determine the total available heat energy from the firebrand. Surface temperature and heat flux play an important role in heat transfer from the firebrand to the recipient fuel. Environmental conditions influence all three phases of the firebrand phenomena. Key parameters include relative humidity, environmental temperature, wind speed, terrain conditions, and the condition of the recipient fuel. Among the environmental parameters, wind speed is critical effecting breakage of burning fuel leading to the generation of firebrands, transport mechanism (e.g., travel distance) and the burning behavior.

Several studies have been conducted to obtain a better understanding of the firebrand generation in structural fires. The methodology for characterizing firebrands in this work was expensive (time/labor/money). In the 1960's Vodvarka conducted full scale building fire tests (Vodvarka, 1969, 1970) and used plastic sheets downwind of fire to measure size of the firebrands. The hot firebrands melted through the sheets, and by measuring the size of the remaining hole, the projected area and traveling distance of the firebrands were calculated. A challenge of this method is distinguishing between measurement of individual firebrands and accumulations when multiple land in the same hole. Recent work has employed water-filled pans to collect and quench firebrands (Manzello et al., 2012a,b; Suzuki et al., 2012, 2013, 2014; Manzello and Suzuki, 2013, 2017; Zhou et al., 2015; Suzuki and Manzello, 2016). Quenching firebrands preserves their mass and shape at the point of landing which changes as the firebrand burns. The center of each pan is considered as the landing position for each ember, so the data is discrete. The wet pan method also requires the drying of the collected firebrands which involves handling the fragile firebrands and may break some firebrands during handling and drying if not done properly, and thus contribute to measurement uncertainties and errors.

The process of measuring or characterizing the physical properties of firebrands can be more tedious than conducting the tests because the burning fuel generates many firebrands which need to be individually measured. For a single experiment the number of generated firebrands in the complete sample (or the whole firebrand population) is often extremely large. This makes the complete collection, enumeration, and characterization of the whole firebrand population impractical or impossible. Sampling techniques play a pivotal role in the validity of the measurements. Statistical sampling should be used so that a subset of manageable size can be used to represent the whole firebrand population. Ideally, a firebrand collection process should have unbiased representative firebrands during the sampling process. In practice, only firebrands larger than a certain size can be collected and enumerated by researchers. For example, in some early firebrand studies, expressions such as "unaccountable" or "many" were used for very small firebrands (Vodvarka, 1970). In strict terms, firebrand collection is not a random sample selection process because some firebrand (i.e., the very small ones) of the population will not be selected. This exclusion bias is a source of uncertainty and brings limitations on how much information a firebrand sample can provide about the whole population. The sample of the full-scale building component experiments conducted in the past varied between 50 and 500 firebrands (Manzello et al., 2012b; Suzuki et al., 2012; Suzuki and Manzello, 2016; Manzello and Suzuki, 2017). The vital question is how many firebrands are needed to sufficiently quantify the characteristics of entire population of the firebrands in an experiment. If the answer suggests a sample size far larger than 500, the efficiency of the current measurement methodology to count and measure thousands of firebrands must be explored. Furthermore, it is not practical to cover the entire area of the downwind of fire in water pans to catch all the firebrands; therefore, no information could be obtained at the uncovered locations. There is a need to determine (or at least estimate) different characteristics of the firebrands at those spots.

To address these issues, this study aims to develop and test a new statistics-based framework that incorporates a machine learning predictive model for the sampling and measurement processes in firebrand generation experiments so that the obtained firebrand data can achieve the desired level of statistical reliability with increased efficiency. To achieve this goal, sampling based on statistical analysis was performed to determine a statistically acceptable sample size for each experiment. To test the proposed framework, firebrand generation experiments were performed, firebrands were collected, and their physical properties were measured. The process of measuring the mass and projected area is a tedious task, so an advanced automated image processing algorithm was developed to minimize the human effort in measuring the projected area. By incorporating a machine learning predictive model into the framework, instead of physically weighing the firebrands, their mass can be estimated based on the desired level of accuracy.

The structure of this paper is as the followings. The framework and firebrand generation experiments are explained in Section Statistics-Based Framework and Firebrand Generation Experiments. This includes information about specimens and test facility, firebrand collection design, test procedures, and sampling design. Section Firebrand Characterization addresses the measurement and characterization of the collected firebrands, including their traveling distance, mass, and projected area. In this section, an advanced automated image processing algorithm is presented and then the uncertainty analysis of the measurements is discussed. In Section Firebrand Characterization Results, the framework for employing machine learning is presented to minimize the tedious weighing process.

STATISTICS-BASED FRAMEWORK AND FIREBRAND GENERATION EXPERIMENTS

Proposed Framework

The overview of the framework is depicted in **Figure 1**. Projected area and mass are the most tedious parameters to measure. To ease the former one, an image processing algorithm is developed.

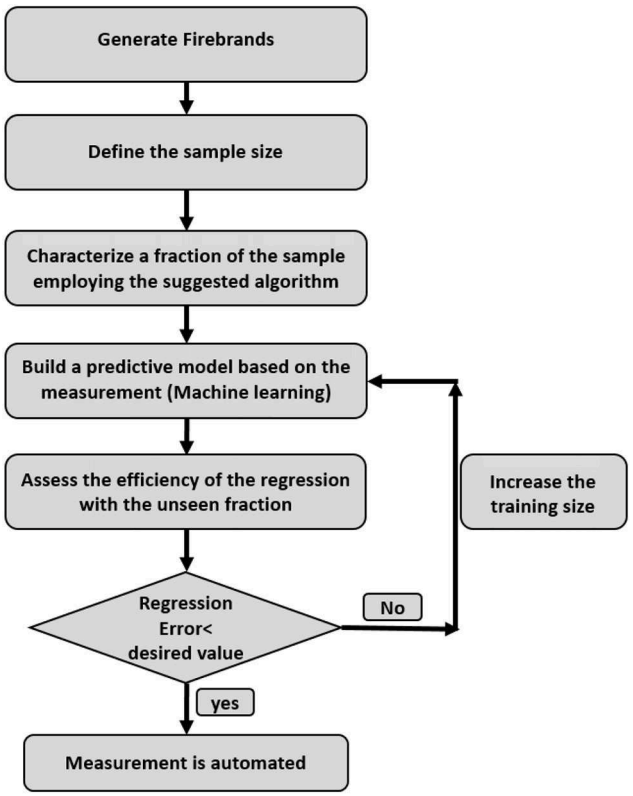

FIGURE 1 | The overview of the framework.

To facilitate the weighing process, Gaussian process regression is employed.

Specimens and Test Facility

Several parameters were considered in the experimental design including burning fuel material, geometry, layout of the pans and wind speed. In a set of experiments, several full-scale structural assemblies with different materials were tested under different environmental conditions as part of a multi-year, multi-institutional project. For the purpose of this paper, only firebrands generated from 90° corner assemblies at three different wind speeds were used. The corner assemblies were built from typical residential building construction materials in wildfire prone areas of the United States. Corner assemblies were made with solid or composite wood horizontal lap attached to a ½-in. nominal oriented strand board (OSB) or CDX plywood. A picture of a burning corner assembly is shown in **Figure 2A**. Each wall in the corner assembly is 32-in. (81-cm) long, using 2-in.× 4-in. (5- × 10-cm) southern yellow pine (SYP) framing, 16-in. (41-cm) on center. A nominal ½-in. (1.3-cm) gypsum board is attached to the non-fire exposed walls. Wall sheathing on the fire-exposed side is nominal ½-in. (1.3-cm) OSB. Siding on the fire exposed side is solid cedar wood. All the samples were conditioned in a kiln to reach the nominal moisture content of 5% prior to firebrand production experiments. Fuel packages were ignited with custom-build natural gas burners. These tests were performed in the test chamber at the Insurance Institute for Business & Home Safety (IBHS) Research Center in Richburg, South Carolina, USA. The facility has a 148-ft. × 148-ft (45- × 45-m) open-jet wind tunnel with a clear height of 59-ft. (18-m). The wind flow is produced using arrays of 105 approximately 6-ft. (1.8-m) diameter fans with active and passive control elements to simulate atmospheric boundary layer flow up to 130-mph (58-m/s) wind speeds 33-ft. (10-m) above the ground (Standohar-Alfano et al., 2017). The three designated fluctuating wind speed levels used in the experiments are: low (average 12-mph or 5-m/s), medium (average 25-mph or 11-m/s), and high (average 40-mph or 18-m/s).

Firebrand Collection

A rectangular area of approximately 2- × 15-m downwind of fire specimen was available in the test chamber for water pans. **Figures 2B,C** depict the layout of the water pans in this collection area. Wake flows immediately downwind of the object are strong which may cause a large number of firebrands to land a short distance from the burning object so six rows of pans were placed immediately downwind of the fuel package. Assuming a symmetrical distribution of firebrands about the central line water pans were located on alternate sides for rows 6 through 17 to maximize distance covered. In total, 46 aluminum water pans, each with a capture area of 0.65- × 0.45-m, were strategically located to optimize collection of firebrands. Window screens (mesh) were submerged in each water pan to facilitate the collection of firebrands.

Test Procedure

The ignition source was an arrow shaped stainless steel burner placed at the base of the insider corner assembly. Test start time was at burner ignition with fans on. Burner was removed after 10 min and total test time was 30 min. Three corner assembly fuel packages were tested at each wind speed. Firebrands at each wind speed were collected after all three tests. The firebrands were oven-dried to reach zero moisture content level and then were sealed in plastic bags and clearly marked for each test. The number of firebrands in one bag was intentionally limited to ensure that only one layer of firebrands was stored in one bag. The bags were separated from each other with layers of paper towels and were gently placed in boxes to avoid firebrand breakage during transportation to the University of North Carolina at Charlotte. Although extreme care was taken during transportation and handling, some of them might have been broken. We recognize this is a source of uncertainty in this study.

Sampling

In order to estimate the characteristics of the entire population, either simple or stratified random sampling can be used. Stratified random sampling is suggested when there are different groups in the population (de Vries, 1986). Since each of the experiments is considered as a separate group, stratified sampling was chosen for this research. Assuming normality (Zhou et al., 2015), the sample size can be obtained using the confidence interval relation which requires defining the sample standard deviation, confidence interval and margin of error (Hosmer and

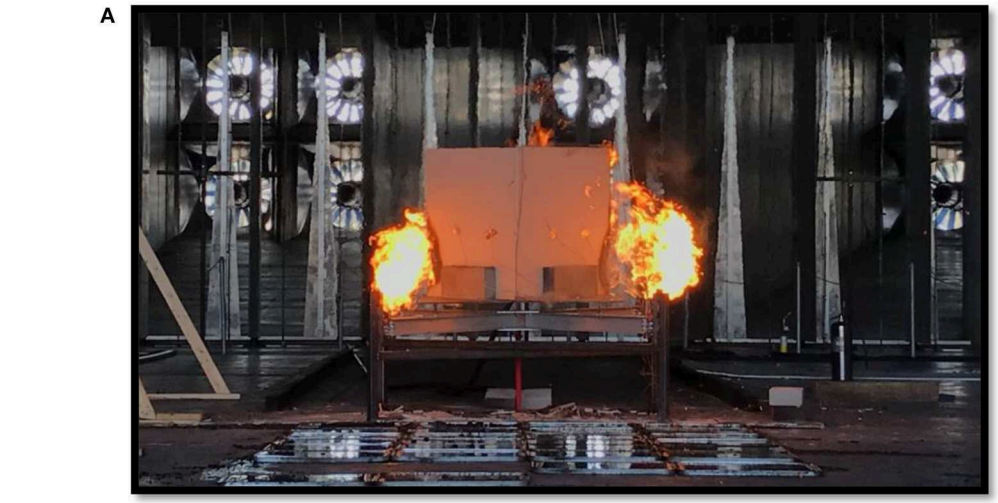

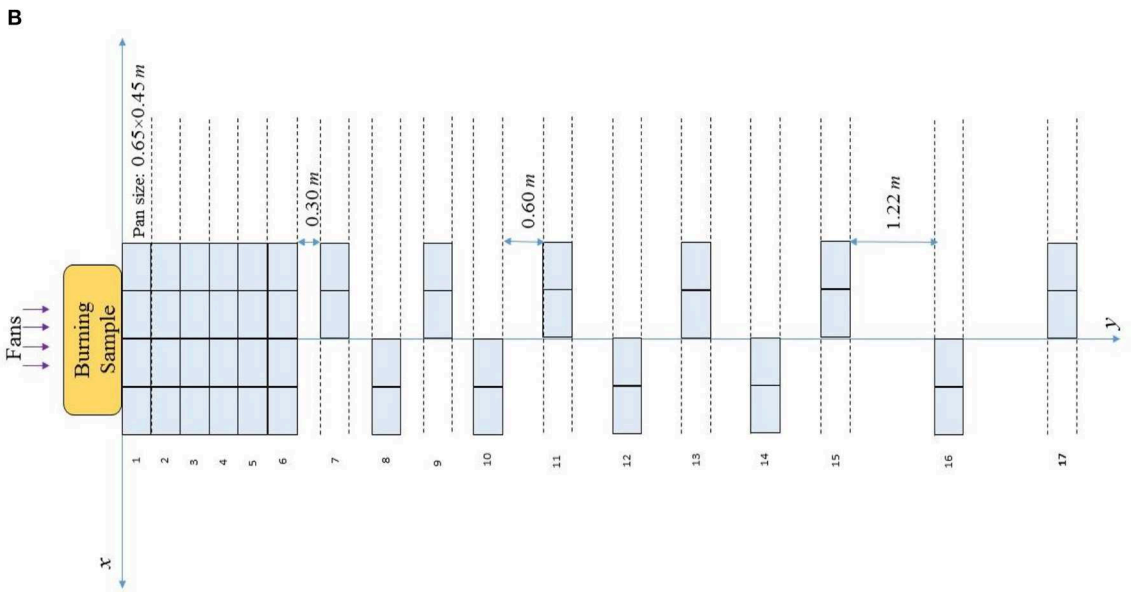

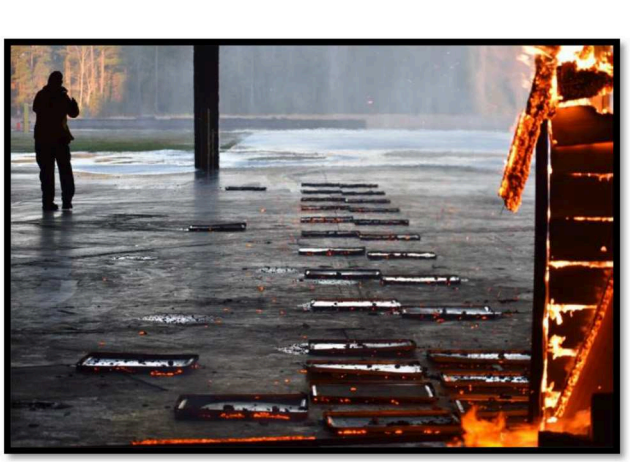

FIGURE 2 | (A) Burning sample (corner assembly) inside the wind tunnel. **(B)** Layout of the water pans. **(C)** Water pans downwind of fire.

Lemeshow, 1992). The larger the standard deviation becomes, the larger the sample size will be. The correlation of sample size with margin of error, however, is reversed. Since no information about the standard deviation of tests was available, the average of standard deviations of firebrands in previous studies (since the 1960s) (Hedayati and Zhou, 2017) was used, which showed the minimum threshold of 0.42 grams. However, to be more conservative, a standard deviation of 0.55 grams was used for this study. The margin of error was set to be 0.03 which is smaller (and thus more reliable) than the typical value of 0.05. Based on these requirements the sample size estimator function of Minitab suggests approximately 1,300. To be conservatives the minimum sample size was specified as 1,400 firebrands for each experiment. The sample included firebrands from all water pans which in some cases exceeded the minimum size. In this study, a total of 4,415 firebrands were collected and analyzed: 1,400 at idle, 1,520 at medium speed, and 1,495 at high wind speed.

FIREBRAND CHARACTERIZATION

Three key parameters of firebrand were investigated: traveling distance, mass, and projected area. The first two are straightforward to measure and are grouped together in Section Traveling Distance and Mass. The technique for measuring projected area is explained separately in Section Projected Area.

Traveling Distance and Mass

Traveling distance represents the horizontal distance from the point the firebrand was generated to where it lands. For these tests the travel distance can be calculated by over the straight length of the straight line from the burning corner assembly to the center of the collection pan which is known by the row and column (as shown in **Figure 2**). The mass of the firebrand changes from when it is generated from the source fuel as it burns, and virgin fuel combusts. When the firebrand lands the water quenches the combustion and stops mass loss. Individual firebrands were weighted using a digital balance (Sartorius H51, resolution of $\pm$ 0.0001 gram).

Projected Area

The size and shape of firebrands can impact the aerodynamics during transport and accumulation geometry. In the literature, there is not much detail about the calculation of the surface area of the firebrands (Manzello et al., 2012a,b; Suzuki and Manzello, 2016; Manzello and Suzuki, 2017). A new process was developed to expedite measuring the projected area of firebrands. Firebrands were placed on a white sheet which provided a contrasting background to black objects. High-resolution pictures were captures of each sheet using a Nikon D5600 and light setup that provided adequate lighting from three directions at 120° interval on the sheet to avoid shadows. To increase the efficiency in measuring the projected area and minimize human labor, a MATLAB code was developed to automate the process, with the steps illustrated in **Figure 3**. Images were processed to remove noise on the white sheet and outside of it (**Figure 3A**). A histogram of the image colors was stretched to adjust the contrasts. The algorithm detected the edges of the sheet and calculated the angle between the edges and the vertical axis (**Figure 3B**) and the image was rotated, thresholded, and cropped to remove noises beyond the sheet borders (**Figures 3C,D**). The thresholding value is a source of uncertainty in the measurement which will be discussed in Section Uncertainty in the Measurement. In **Figure 4.1**, two sources of noise can be observed; the scratches on the sheet that occurred by scattering the firebrands on the sheets, and the white ashes on the firebrands. In **Figure 3E**, both are removed, and the borders are cleaned so the remaining objects (white pixels) were individual firebrands. Each firebrand was labeled (**Figure 3F**), and the projected area of each firebrand with respect to Object 1 (rectangle with known area) were calculated. Using this automated method, counting and calculating the projected area of hundreds of firebrands can be accomplished in a few seconds. Note that in the traditional method, each of these steps were done manually which increases the measurement time significantly.

FIREBRAND CHARACTERIZATION RESULTS

The measured firebrand data are summarized in **Table 1**. In addition to mean, standard deviation, median, and correlation values, the skewness of each parameter is also provided. Correlation value of positive one indicates a direct relationship between the parameters while negative one indicates an inverse relationship. Zero correlation means no relation between the parameters exists. The correlation values in the table show that mass and projected area are strongly correlated, as observed in some experimental (Manzello et al., 2012b; Suzuki and Manzello, 2016; Manzello and Suzuki, 2017) and theoretical studies (Tohidi et al., 2015) The corrections between mass and traveling distance as well as projected area and traveling distance are small. The mean and median of travel distance, projected area, and mass increased as wind speed increased. Wind speed can have competing effects on generation of firebrands, higher wind speed can force departing larger firebrands and at the same time will increase the combustion rate during the flight. Since the flying distance in this experiment was limited by the dimensions of the test chamber, **Table 1** suggests that stronger wind causes larger firebrands to depart which can travel further away. Also, the standard deviation of projected area and mass increased when wind speed increased, which implies that the range of variation in the size and mass of the firebrands was larger at stronger winds (more variability in the sample).

Measuring the density of firebrand can be a challenging task, but worth investigating. Strong correlation between mass (m) and projected area (a) suggests that there is a linear correlation between them. This correlation can be approximated as $m = K\,a$, where K is a constant. Since we know that $m = (\rho h)a$ (where ρ is the density and h is the thickness of a firebrand), recording the thickness of firebrands can provide useful information about the distribution of the density of firebrand.

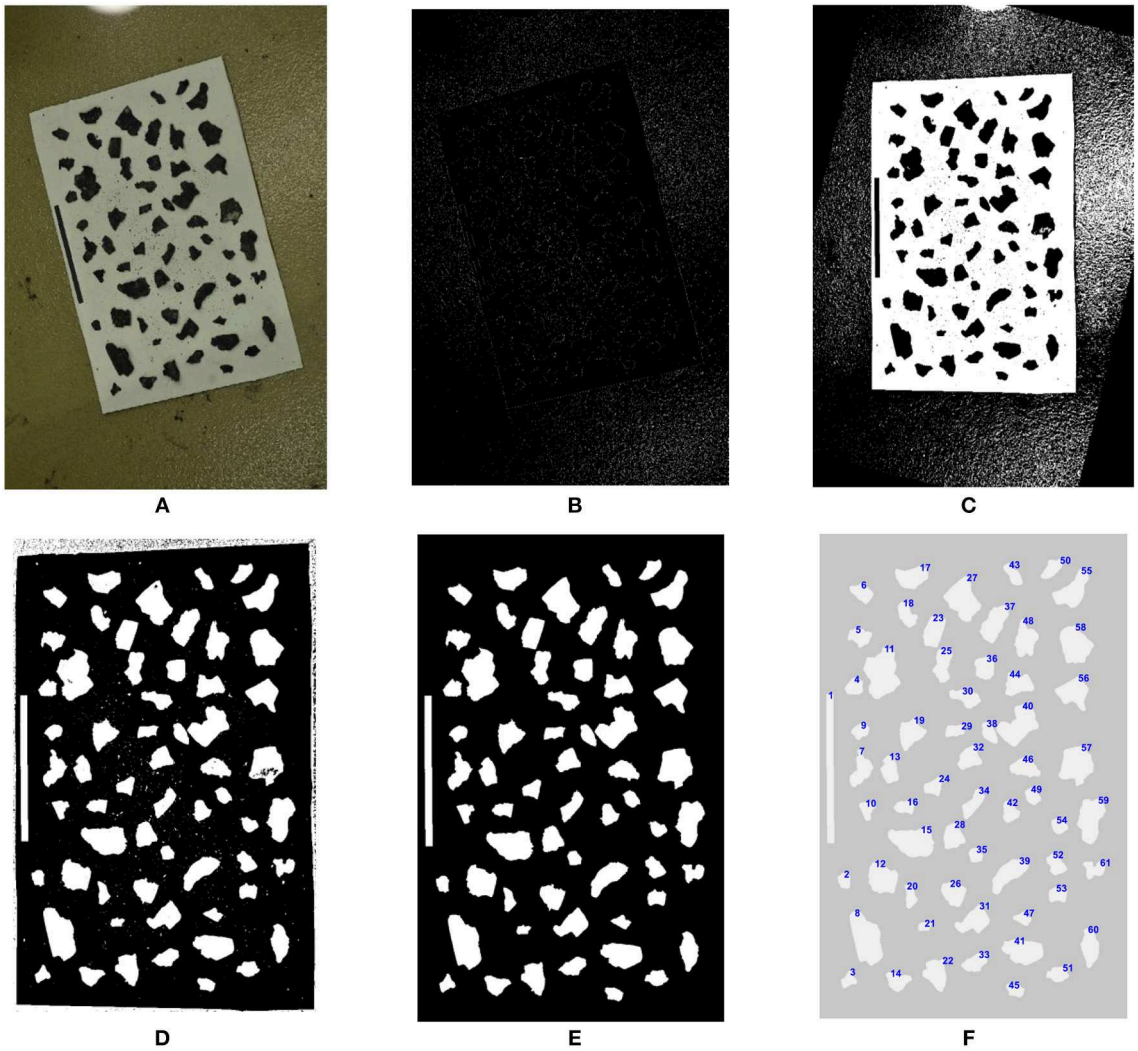

FIGURE 3 | Detailed steps to calculate the projected area. **(A)** Original image. **(B)** Edge detection. **(C)** Rotation. **(D)** Corner detection and cropping. **(E)** Noise removal. **(F)** Labeling firebrands with known projected areas.

Uncertainty in the Measurement

To investigate the uncertainty of the projected area measurement, different geometries have been plotted on a sheet with known pixel numbers and areas. As Photoshop plots with three significant digits (0.01-cm^2 resolution), the calculations also presented three significant digits. Miscounting the pixels typically happens at the borders of an object, which depends on the user-defined binary image threshold. The threshold defines how sensitive the MATLAB code should be when it converts different shades of gray in an RGB image to a binary one. To investigate the effects of thresholding reference objects with various and known pixel configurations were used (**Figure 4**). At a granular level angular and curved edges of these objects are square pixels which effects the uncertainty of the measurement based on the thresholding value. A thresholding value (α) to 0.20 resulted in loosing numerous pixels in counting (**Figure 4B**) while a value of 0.9 led to identifying any dark point on the sheet as an object, which can be seen in **Figure 4C**.

To find the proper range for α in which the minimum error-difference between the best estimated value and the measured value- occurs, the surface area of the objects in **Figure 4A** were calculated at several thresholding levels (from 0.1 to 1 with 0.1 intervals). The minimum relative error happens when $0.6 < \alpha < 0.8$. This threshold range was validated on a sample of 27 firebrands. Using the same code, the differences between the projected areas were calculated at $\alpha = 0.6$ and $\alpha = 0.8$ for each firebrand. It was determined that the maximum difference is 0.11-cm^2 which can be considered as the uncertainty of the projected area for each measurement.

The standard uncertainty of the measurement can be calculated by dividing the standard deviation by the square root of the sample size. The standard uncertainty of measuring mass,

TABLE 1 | Summary of the measured parameters at different mean wind speeds.

Physical quantity	Statistical quantity	Low wind (5.36 m/s)	Medium wind (11.17 m/s)	High wind (17.88 m/s)
Flying distance (m)	Mean	2.71	3.2	5.07
	S. D.	3.72	3.24	3.88
	Skewness	0.47	0.52	0.27
	Median	1.11	1.99	3.20
Projected area (cm^2)	Mean	2.10	3.90	4.87
	S. D.	2.72	6.48	7.87
	Skewness	5.17	6.62	13.47
	Median	1.26	2.08	2.99
Mass (g)	Mean	0.09	0.25	0.38
	S. D.	0.24	1.28	1.44
	Skewness	7.63	25.37	21.99
	Median	0.02	0.06	0.14
Mass and area correlation		0.83	0.72	0.90
Mass and flying distance correlation		−0.20	−0.11	−0.07
Area and flying distance correlation		−0.24	−0.20	−0.10

traveling distance, and projected area were determined to be 0.0169-grams, 0.22-m, and 0. 0.09-cm^2, respectively. Among the three parameters traveling distance measurements has additional sources of uncertainty because a two-dimensional collection area was reported as a single point (the center of the pan). For this case, the theoretical uncertainty is rounded up to the measurement resolution which is half of the width of the water pans (0.22m).

As mentioned earlier, skewness is an important parameter to study asymmetry of Probability Density Functions (PDFs). Equation (1) shows that the uncertainty in skewness depends on the uncertainties of the mean and individual firebrands.

$$b = \frac{\frac{1}{n}\sum_{i=1}^{n}(x_i - \bar{x})^3}{\left[\frac{1}{n-1}\sum_{i=1}^{n}(x_i - \bar{x})^2\right]^{3/2}} \tag{1}$$

The uncertainty can be calculated with Equation (2), where and are already calculated as 0.05 and 0.11, respectively.

$$u_c = \sqrt{\left(\frac{\partial b}{\partial \bar{x}}u(\bar{x})\right)^2 + \left(\frac{\partial b}{\partial x_i}u(x_i)\right)^2} \tag{2}$$

The numerical values for the derivatives are shown in Equation (3) (work shown in **Appendix**).

$$\begin{aligned} \sum_{i=1}^{n} \frac{\partial b}{\partial \bar{x}}\Big|_{\bar{x}=3.62, n=4414} &= 0.48 \\ \sum_{i=1}^{n} \frac{\partial b}{\partial x_i}\Big|_{\bar{x}=3.62, n=4414} &= 2.64 \end{aligned} \tag{3}$$

The numerical value for the combined uncertainty for skewness reduces to 0.29-cm^2. Employing a similar approach, the uncertainty in measuring the skewness for mass and traveling distance are 0.047-gr, and 0.33-m, respectively.

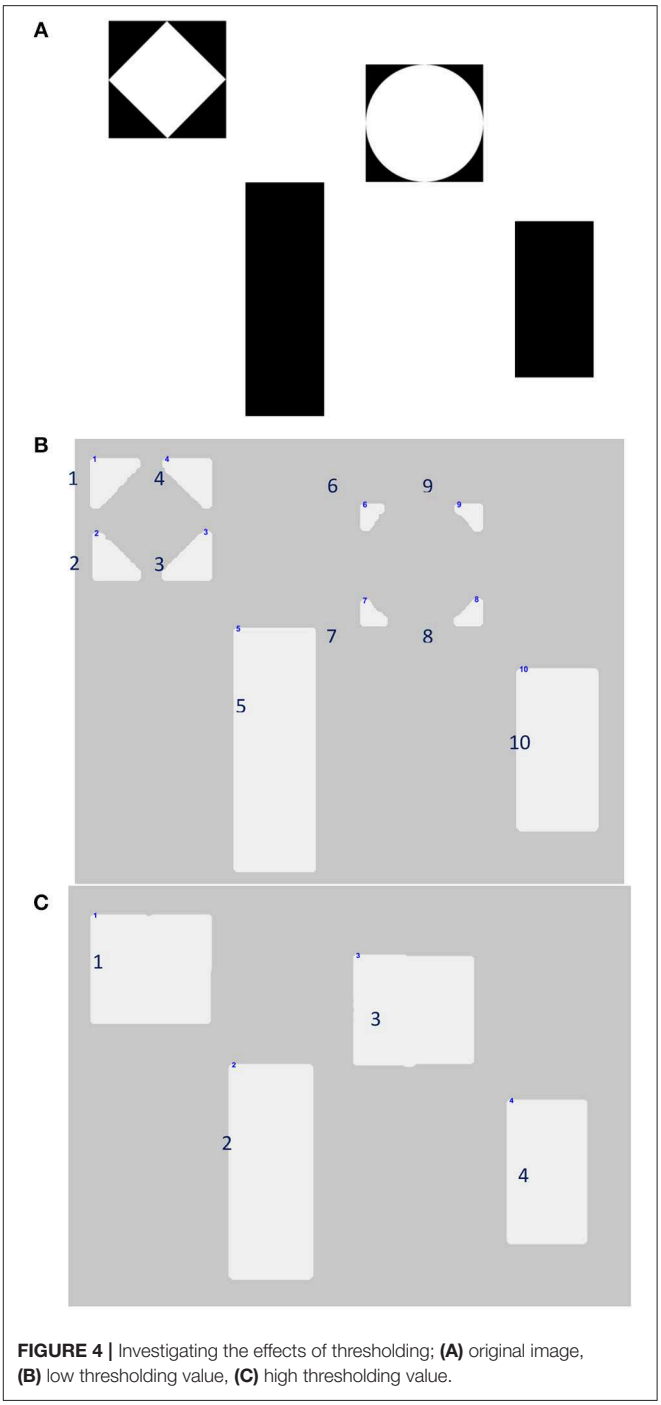

FIGURE 4 | Investigating the effects of thresholding; **(A)** original image, **(B)** low thresholding value, **(C)** high thresholding value.

Mass Prediction Model

Employing the proposed algorithm in Section Projected Area, measuring the projected area becomes a straightforward task. Measuring the mass, however, remains a tedious task because each of the 4,415 firebrands must be weighed individually using the high-precision balance. Machine learning, a type of artificial

intelligence that enables the computer to predict or classify a set of data (Carbonell et al., 1983), can be employed to expedite the weighing process. There are several different algorithms available to predict (regress) a variable with machine learning techniques. For this project Gaussian process regression is employed which is useful when the relationship between the predictors and the predicted value is unclear (Williams and Rasmussen, 1996; Bernardo et al., 1998). This type of regression also works well for continuous regressed values, such as mass. This method provided the best estimated value for the prediction as well as a probabilistic range defined the certainty about the predicted values. The mathematical formulation of the Gaussian process regression is beyond the scope of this paper; however, the method is explained briefly in the following for the purpose of this study.

Gaussian Process Regression

The idea of Gaussian process regression (Rasmussen, 2003; Rasmussen and Williams, 2006) is the extension of probability distribution of numbers to the probability distribution of functions. In this study four attributes describe each firebrand, where the obtained data set can be analyzed in two different ways. The conventional way is to see all the points in a four dimensional space. The alternative look is to consider them as the values of a function sampled at four points. In the first perspective, points can be chosen from a probability distribution which are typically determined by a mean vector and a covariance matrix. In the second analyzation, we can have a probability distribution of functions determined by mean and covariance functions. This covariance function depends on the Kernel function which describes the influence of each point on its neighbors.

To predict the value of an input that the model has not yet seen before (validation subset), Gaussian regression built a multidimensional normal distribution with the seen data (training subset). In other words, in order to regress the $n+1^{st}$ value, an n dimensional normal distribution is built. Having conditioned (sliced) the multivariate PDF, the dimensions of the PDF reduces and ultimately the most probable value, as well as a probabilistic range for the prediction, can be estimated (Bernardo et al., 1998). The probabilistic range depends on the covariance function between the inputs that the user provides for the algorithm.

Before discussing the results of the predictive model, it is necessary to address the effects of the training and validating subsets on the model. The training subset is used to build a model to predict the response value and the validation set is utilized to assess the accuracy of the build model based on the training data set. Typically, 70% of the data is implemented to train the model and 30% is held out for the validation set (Rasmussen, 2003). However, the accuracy of the model heavily depends on how the data is split and trained. Although one may have chosen the subset elements randomly, it would be more accurate if the division process was repeated for multiple times in a random way to minimize the dependency of the model on the subsets. This process is known as cross validation (Refaeilzadeh et al., 2009). In this method, the data would randomly be divided into k sets. *K-1* of the sets would be used to train and 1 will be saved for validation. This process continues until all the subsets have been employed for validation at least once (Refaeilzadeh et al., 2009). The larger the k is, the more computational efforts we will have but the model will be more robust.

Results and Discussion of the Predictive Model

To evaluate the influence of different inputs on predicting the mass of each firebrand, a decision tree model was built for the different attributes in the data and uses them to split the data into subsets (Safavian and Landgrebe, 1991). The obtained split subsets are called *pure* if all the elements in that subset are homogenous and called *impure* otherwise. Once all the predictors are split, the algorithm starts to split each subset in order to find the purest subset. Clustering the data into an absolutely *pure* subset rarely happens.

The importance of the predictors to estimate the response value is measured by the magnitude of a fraction; the numerator is the purity of each branch and the denominator is the number of binary decisions to reach the final step in each subset. The larger the ratio is, the more significant that parameter is to predict the response variable. Projected area, distance, and wind speed are the three important predictors and mass is the response variable. Having employed 3/2 Matérn kernel function and taken the cross-validation factor equal to five ($k = 5$), a Gaussian regression was built over the training set with the size of 950.

Figure 5 depicts the results of the prediction of the mass for the medium wind speed experiment. Red dots depict the measured mass with the balance, and the blue circles illustrate the predicted value with the predictive model. The dotted line shows the maximum probabilistic range that the mass of a firebrand could be based on the given surface area, traveling distance, and the wind speed. This can be helpful to simulate the worst-case scenario and monitor how large/heavy a firebrand may be at any desired distance or wind speed. Errors between measured and calculated firebrand mass values can be seen in **Figure 6**.

To visualize the relative error between the predicted and measured values, the validation subset is plotted for each firebrand as illustrated in **Figure 8**. The model was able to predict the mass within 0.5%. Although the individual values for mass have been predicted sufficiently accurate, the individual values do not play an important role when one intends to create a PDF based on the data. Regardless of the underlying PDF, all the PDFs require the mean, standard deviation and correlations between the predictors which will be addressed subsequently.

The relative error of mean, standard deviation, and correlations vs. the training size are plotted in **Figures 7–10** with a sample size of 1,400. In each figure, 5 and 10% error lines are plotted with red dotted lines. What stands out in these figures is that when setting the training size to 700, the model can predict the mean, standard deviation and correlations of the mass with $<$10% error. In other words, employing this model, the results that one may obtain by counting 700 firebrands is $<$10% deviated from counting 1,400 firebrands. Hence, employing this technique can significantly reduce the labor (e.g., 50%) involved in the measurement process.

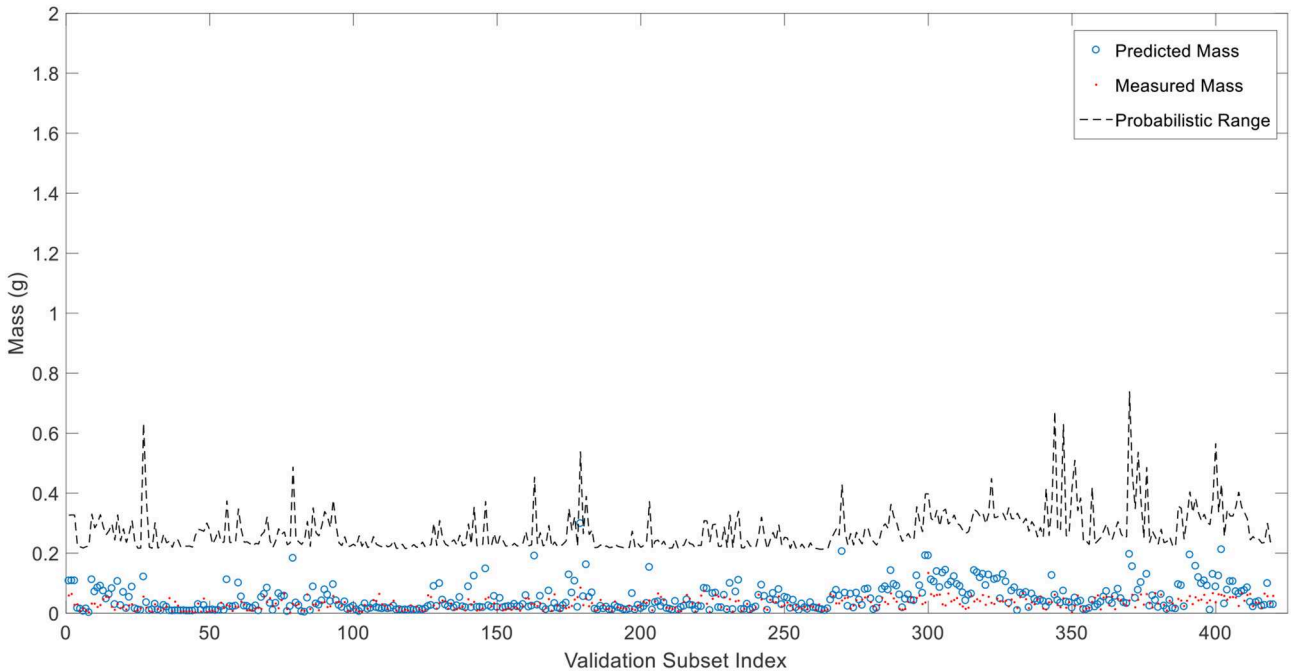

FIGURE 5 | Schematic of predicted and measured firebrand mass values.

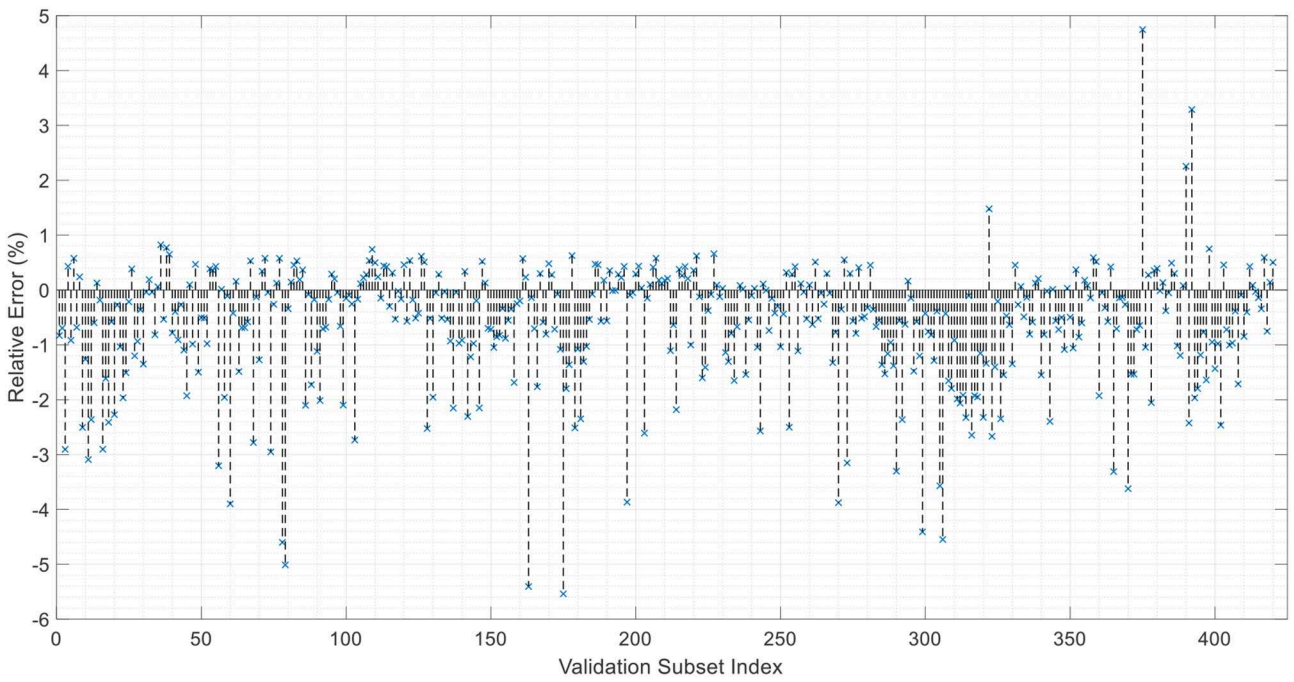

FIGURE 6 | The error between measured and predicted firebrand mass values for unseen firebrands (validation subset index).

Figures 9, **10** show that the relative error starts increasing when the training size is larger than approximately 900 samples, a result of overtraining the model. In any regression problem, if the complexity of the model increases, it is very likely that the model is not capable of predicting the validation set very well. If the model touches every point in the training set exactly, it involves the fluctuations and noises in the training set and will be trained without any uncertainty for the prediction. However, the model

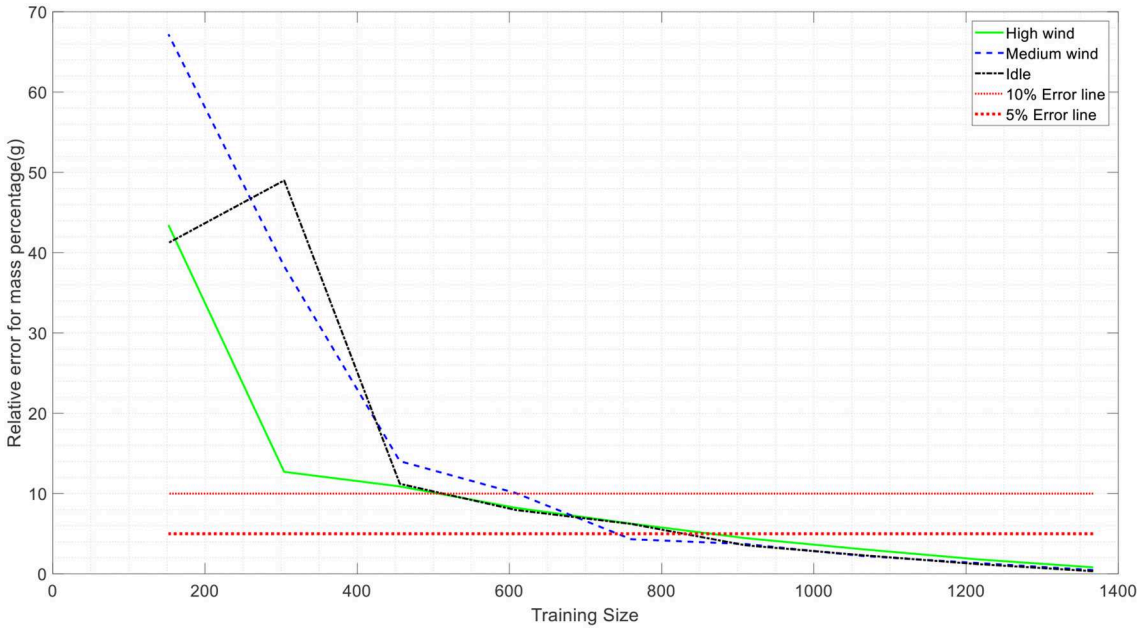

FIGURE 7 | Variation prediction of mean values for firebrand mass with sample size.

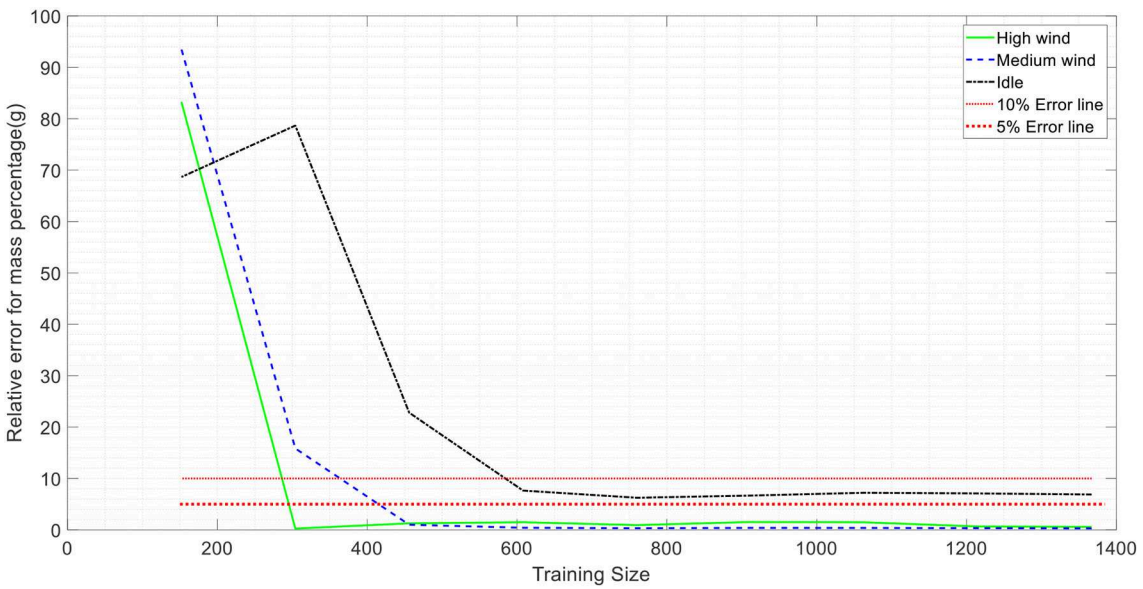

FIGURE 8 | Variation predication of standard deviation values for firebrand mass with sample size.

will lose the ability of predicting the response value for a new unseen point. In **Figures 7**, **8**, since the concept of the mean and standard deviation is to subtract each point from the mean value, the noise in the data set is reduced. For correlations in **Figures 9**, **10**, when the training size gets larger than 900, the model losses its accuracy to predict the mass and then the relative error in calculating the correlations increases. From experimental data the center of pans is the landing position of the firebrand; thus, the data is inevitably discrete. Considering this fact, the calculated correlation between the mass and traveling distance may have less degree of accuracy comparing to other presented parameters.

CONCLUSION

In this study, experiments were conducted to generate firebrands from burning corner assemblies (building materials) in a

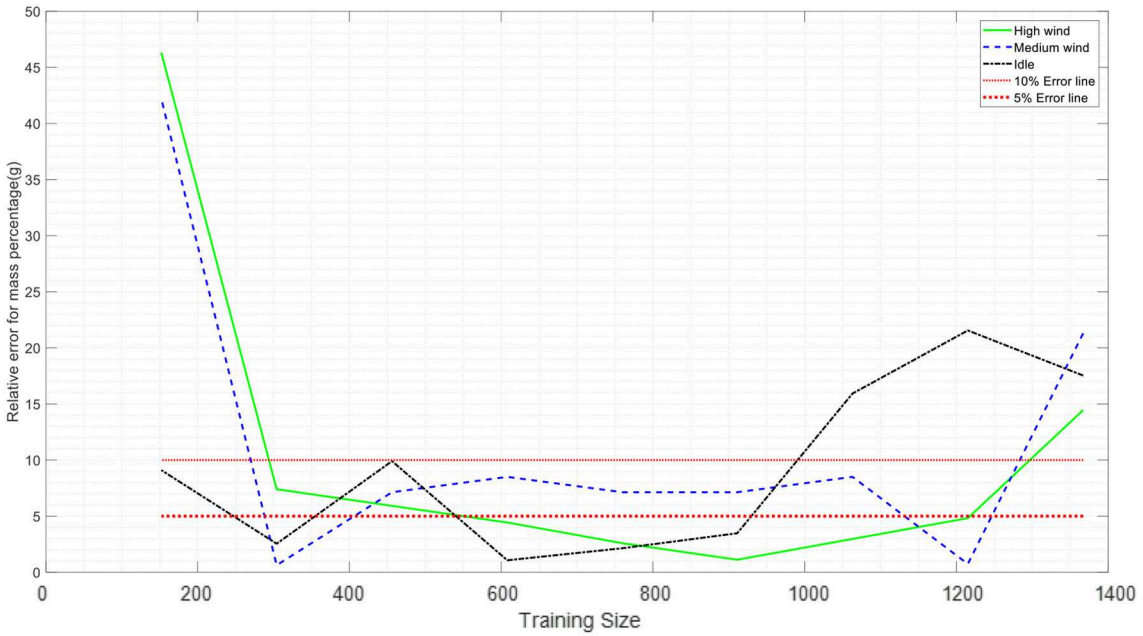

FIGURE 9 | Variation predication of firebrands' mass and projected area correlation with sample size.

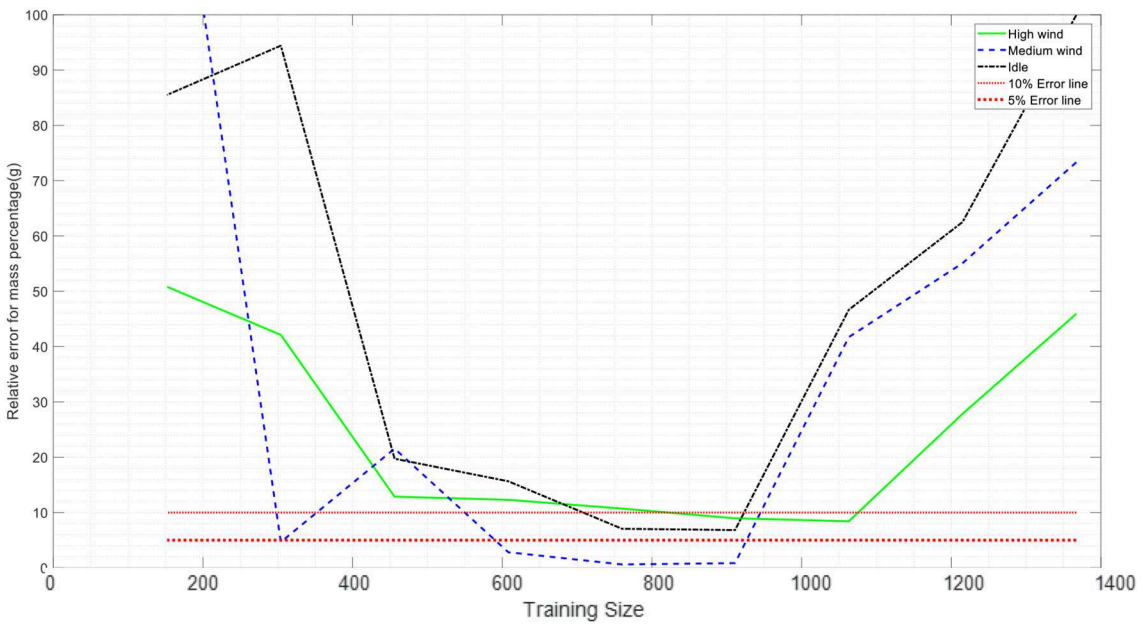

FIGURE 10 | Variation predication of firebrands' mass and flying distance correlation with sample size.

boundary layer wind tunnel. A sample size of 1,400 firebrands for each of the three experimental configurations was necessary to determine the characteristics of the population. A process for efficiently measuring traveling distance and projects area was employed for a large sample size. An image processing algorithm was developed to measuring project area of each firebrand in batches. The projected area accompanied with traveling distance and wind speed was used to train a predictive model for estimating the mass of individual firebrands. The comparison between the predicted mass and measured mass shows a maximum error of 5%, confirming the accuracy of the model. This framework provides a methodology

for efficiently measuring travel distance and project area along with a model that provides a probabilistic range for the estimation of firebrand mass/projected area/flying distance. Using this method for future testing will reduce the resource demands for measuring large sample sizes and reliably characterizing firebrands.

DATA AVAILABILITY

The datasets generated for this study are available on request to the corresponding author.

AUTHOR CONTRIBUTIONS

FH, BB, and DG performed research under the guidance of AZ and SQ. FH, BB, and AZ worked on data analysis, image analysis, and machine learning algorithms. FH, BB, AZ, DG, and SQ worked on the firebrand generation experiments and manuscript preparation.

FUNDING

Research funding is provided by the Joint Fire Science Program (JFSP) with project ID # 15-1-04-4. Open access publication fees are provided by the Insurance Institute for Business and Home Safety (IBHS).

ACKNOWLEDGMENTS

The authors would like to thank the Joint Fire Science Program (JFSP) for sponsoring this project (Project ID # 15-1-04-4). The authors would also like to thank Dr. Christine Alfano for providing the facility to conduct experiments and supplying the samples for this study. The authors appreciate the assistance from Dr. Vahid Hemmati, Gregorio Mesa, Jacob Kadel, Noah Bull, and Ja'Juan Battle from the University of North Carolina at Charlotte. Any opinions, findings, and conclusions or recommendations expressed in this material are those of the authors and do not necessarily reflect the views of the JFSP, the US Department of Agriculture and Department of the Interior.

REFERENCES

Bernardo, J., Berger, J., Dawid, A., and Smith, A. (1998). Regression and classification using gaussian process priors. *Bayesian Statist.* 6:475.

Carbonell, J. G., Michalski, R. S., and Mitchell, T. M. (1983). *An Overview of Machine Learning. Machine Learning* (Palo Alto, CA: Springer), 3–23.

Caton, S. E., Hakes, R. S. P., Gorham, D. J., Zhou, A., and Gollner, M. J. (2017). Review of pathways for building fire spread in the wildland urban interface part i: exposure conditions. *Fire Technol.* 53, 429–473. doi: 10.1007/s10694-016-0589-z

Clements, H. (1977). *Lift-off of Forest Firebrands [Pinus]*. USDA Forest Service Research Paper SE (USA) no. 159

Cohen, J. (2008). The wildland-urban interface fire problem. *Forest History Today*. 11, 20–26. Available online at: https://www.fs.usda.gov/treesearch/pubs/33787

de Vries, P. G. (1986). "Stratified random sampling," in *Sampling Theory for Forest Inventory*, ed D. Mandallaz (New York, NY: Springer), 31–55.

Hedayati, F., and Zhou, A. (2017). "Statistical analysis on firebrand generation from structural fuels," in *Proceedings of the 15th International Conference on Fire and Materials* (San Francisco, CA), 656–667.

Hosmer, D. W., and Lemeshow, S. (1992). Confidence interval estimation of interaction. *Epidemiology* 3, 452–456. doi: 10.1097/00001648-199209000-00012

Koo E, Pagni PJ, Weise DR, Woycheese JP. (2010) Firebrands and spotting ignition in large-scale fires. *Int. J. Wildland Fire* 19, 818–843. doi: 10.1071/WF07119

Koo, E., Linn, R. R., Pagni, P. J., and Edminster, C. B. (2012). Modelling firebrand transport in wildfires using higrad/firetec. *Int. J. Wildland Fire* 21, 396–417. doi: 10.1071/WF09146

Manzello, S. L., and Suzuki, S. (2013). Experimentally simulating wind driven firebrand showers in wildland-urban interface (WUI) fires: overview of the NIST firebrand generator (NIST Dragon) technology. *Procedia Eng.* 62 (Suppl. C):91–102. doi: 10.1016/j.proeng.2013.08.047

Manzello, S. L., and Suzuki, S. (2017). Generating wind-driven firebrand showers characteristic of burning structures. *Proc. Combust. Instit.* 36, 3247–3252. doi: 10.1016/j.proci.2016.07.009

Manzello, S. L., Suzuki, S., and Hayashi, Y. (2012a). Enabling the study of structure vulnerabilities to ignition from wind driven firebrand showers: a summary of experimental results. *Fire Safety J.* 54:181–196. doi: 10.1016/j.firesaf.2012.06.012

Manzello, S. L., Suzuki, S., Yamada, T., Foote, E. I., Lage, M., Laing, G., et al. (2012b). *Exposing Wood Decking Assemblies to Continuous Wind-Driven Firebrand Showers*. Gaithersburg, MD: US Department of Commerce, National Institute of Standards and Technology.

Maranghides, A., and Mell, W. (2011). A case study of a community affected by the witch and guejito wildland fires. *Fire Technol.* 47, 379–420. doi: 10.1007/s10694-010-0164-y

Rasmussen, C. E. (2003). "Gaussian processes in machine learning," in *Summer School on Machine Learning*, eds C. E. Rasmussen and C. K. I. Williams (Berlin, Heidelberg: Springer), 63–71.

Rasmussen, C. E., and Williams, C. K. (2006). *Gaussian Processes for Machine Learning*, Vol. 1. Cambridge: MIT press.

Refaeilzadeh, P., Tang, L., and Liu, H. (2009). "Cross-validation," in *Encyclopedia of Database Systems* (New York, NY: Springer), 532–538.

Safavian, S. R., and Landgrebe, D. (1991). A survey of decision tree classifier methodology. *IEEE Trans. Syst Man Cyber.* 21, 660–674. doi: 10.1109/21.97458

Standohar-Alfano, C., Estes, H., Johnson, T., Morrison, M., and Brown-Giammanco, T. (2017). Reducing losses from wind-related natural perils: research at the IBHS Research Center. *Front. Built Environ.* 3:9. doi: 10.3389/fbuil.2017.00009

Suzuki, S., Brown, A., Manzello, S. L., Suzuki, J., and Hayashi, Y. (2014). Firebrands generated from a full-scale structure burning under well-controlled laboratory conditions. *Fire Safety Journal* 63:43–51. doi: 10.1016/j.firesaf.2013.11.008

Suzuki, S., and Manzello, S. L. (2016). Firebrand production from building components fitted with siding treatments. *Fire Safety J.* 80, 64–70. doi: 10.1016/j.firesaf.2016.01.004

Suzuki, S., Manzello, S. L., and Hayashi, Y. (2013). The size and mass distribution of firebrands collected from ignited building components exposed to wind. *Proc. Combust. Insti.* 34, 2479–2485. doi: 10.1016/j.proci.2012.06.061

Suzuki, S., Manzello, S. L., Lage, M., and Laing, G. (2012). Firebrand generation data obtained from a full-scale structure burn. *Int. J. Wildland Fire* 21, 961–968. doi: 10.1071/WF11133

Tohidi, A., kaye, N., and Bridges W,. (2015) Statistical description of firebrand size and shape distribution from coniferous trees for use in metropolis monte carlo simulations of firebrand flight distance. *Fire Safety J.* 77, 21–35. doi: 10.1016/j.firesaf.2015.07.008

Vodvarka, F. (1969). *Firebrand Field Studies*. Chicago, IL: IIT Research Inst Chicago Ill Engineering Mechanics Division.

Vodvarka, F. (1970). *Urban Burns - Full-Scale Field Studies*. Chicago, IL: IIT Research Inst Chicago Ill Engineering Mechanics Division.

Williams, C. K., and Rasmussen, C. E. (1996). "Gaussian processes for regression," in *Advances in Neural Information Processing Systems*, eds M. C. Mozer, M. I. Jordan, and T. Petsche (NIPS), 514–520. Available online at: https://papers.nips.cc/book/advances-in-neural-information-processing-systems-9-1996

Zhou, K., Suzuki, S., and Manzello, S. L. (2015). Experimental study of firebrand transport. *Fire Technol.* 51, 785–799. doi: 10.1007/s10694-014-0411-8

Conflict of Interest Statement: The authors declare that the research was conducted in the absence of any commercial or financial relationships that could be construed as a potential conflict of interest.

APPENDIX

The details about the partial derivation of skewness is presented below.

$$\frac{\partial b}{\partial \bar{x}} = \frac{-3n\bar{x}^2 + \sum_{i=1}^{n}\left(6x_i\bar{x} - 3x_i^2\right)}{n\left[\frac{n\bar{x}^2 + \sum_{i=1}^{n}\left(-2x_i\bar{x} + x_i^2\right)}{n-1}\right]^{\frac{3}{2}}} - \frac{\frac{3}{2}\left(-n\bar{x}^3 + \sum_{i=1}^{n}\left(3\bar{x}^2x_i - 3\bar{x}x_i^2 + x_i^3\right)\right)\left[\frac{2n\bar{x} + \left(\sum_{i=1}^{n} -2x_i\right)}{n-1}\right]}{n\left[\frac{n\bar{x}^2 + \sum_{i=1}^{n}\left(-2x_i\bar{x} + x_i^2\right)}{n-1}\right]^{\frac{5}{2}}}$$

$$\frac{\partial b}{\partial x_i} = \frac{3n\bar{x}^2 + \sum_{i=1}^{n}\left(-6x_i\bar{x} + 3x_i^2\right)}{n\left[\frac{n\bar{x}^2 + \sum_{i=1}^{n}\left(-2x_i\bar{x} + x_i^2\right)}{n-1}\right]^{\frac{3}{2}}} - \frac{\frac{3}{2}\left(-n\bar{x}^3 + \sum_{i=1}^{n}\left(3\bar{x}^2x_i - 3\bar{x}x_i^2 + x_i^3\right)\right)\left[\frac{-2n\bar{x} + \left(\sum_{i=1}^{n} 2x_i\right)}{n-1}\right]}{n\left[\frac{n\bar{x}^2 + \sum_{i=1}^{n}\left(-2x_i\bar{x} + x_i^2\right)}{n-1}\right]^{\frac{5}{2}}}$$

frontiers in Mechanical Engineering

ORIGINAL RESEARCH
published: 21 August 2019
doi: 10.3389/fmech.2019.00050

On the Use of Semi-empirical Flame Models for Spreading Chaparral Crown Fire

Jeanette Cobian-Iñiguez[1]*, *AmirHessam Aminfar*[1], *David R. Weise*[2] and *Marko Princevac*[1]

[1] Laboratory for Environmental Flow Modeling, Department of Mechanical Engineering, University of California, Riverside, Riverside, CA, United States, [2] Pacific Southwest Research Station, USDA Forest Service, Riverside, CA, United States

Flame geometry plays a key role in shaping fire behavior as it can influence flame spread, radiative heat transfer and fire intensity. For wildland fire, thorough characterizations of flame geometry can help advance the derivation of comprehensive models of wildfire behavior. Within the fire community, a classical flame modeling approach has been to develop semi-empirical models. Many of these models have been derived for surface fuels or for pool fire configurations. However, few have sought to model flame behavior in chaparral crown fires. Thus, the objective of this study is to assess the applicability of semi-empirical models on observed chaparral crown fire behavior. Semi-empirical models of flame tilt, flame height, and flame length from the literature are considered. Comparison with experimental observation of flame height in the crown fuel layer, showed good agreement between the 2/5th power law that relates flame height to heat release rate. Two new power-law correlations relating flame tilt angle to Froude number are proposed. The coefficients for new models are obtained from regression analysis.

Keywords: wildfire, crown fire, flame geometry, semi-empirical model, computer vision

OPEN ACCESS

Edited by:
Jason John Sharples,
University of New South Wales
Canberra, Australia

Reviewed by:
Chuangang Fan,
Hefei University of Technology, China
Xinyan Huang,
Hong Kong Polytechnic University, Hong Kong
Duncan Sutherland,
University of New South Wales
Canberra, Australia
Thomas Duff,
The University of Melbourne, Australia

***Correspondence:**
Jeanette Cobian-Iñiguez
jcobi002@ucr.edu

Specialty section:
This article was submitted to Thermal and Mass Transport, a section of the journal Frontiers in Mechanical Engineering

Received: *01 March 2019*
Accepted: *30 July 2019*
Published: *21 August 2019*

Citation:
Cobian-Iñiguez J, Aminfar A, Weise DR and Princevac M (2019) On the Use of Semi-empirical Flame Models for Spreading Chaparral Crown Fire. Front. Mech. Eng. 5:50. doi: 10.3389/fmech.2019.00050

INTRODUCTION

The occurrence of large fires has increased significantly in many regions around the world. One region particularly impacted by wildfires is southern California, where the terrain, highly flammable fuels, dry ambient conditions and fast foehn type winds (known locally as Santa Ana winds) generate conditions highly favorable to wildfire (Rothermel and Philpot, 1973). Thus, fuel and weather conditions exist such that in the event of an ignition event, the potential for wildfire is high. In the southern California case, growing wildfire potential, and fast population growth have occurred in parallel. This coupled growth has prompted changes to the so-called wildland urban interface, that is, the region separating the wildland from urban settlements. The growth of the wildland urban interface coupled with increased fire risk, places people and their property closer to fire. Because of the growing threat, the ability to accurately predict fire behavior has become paramount. This is contingent on thorough understanding of physical mechanisms driving fire spread and intensity. Because wildfire behavior is shaped by its environment, it is important to define the key conditions shaping fire behavior in a regional landscape and climate. In mediterranean climates, chaparral fires typically burn as crown fires (Barro and Conard, 1991), a category of fire consisting of two fuel layers, an above ground surface fuel layer and an elevated fuel layer known as a crown layer. In chaparral crown fires, fires typically start in the easily ignitable surface fuels and spread in the crown fuel layer (Tachajapong et al., 2014). Before a fire can spread in the crown, the fire must move vertically from the surface fuels to ignite crown fuels, a process defined as transition (Weise et al., 2018a).

Little is known of the exact mechanisms which produce effective transition and spread in chaparral crown fires. Transition and spread in crown fire, involves a dynamic energy exchange between the surface and crown fuel layers. Spread in the crown fuel layer may require energy to be supplied from the surface fuel layer, as in passive or dependent crown fires; or may rely on the crown fuel layer alone to maintain successful spread, as in independent fires (Van Wagner, 1977). In the case of crown fire spread where energy is partially or solely supplied by the crown fuel layer, identifying the mechanism through which energy is exchanged from the crown flame to unburned fuel is necessary to better understand mechanisms for successful crown fire spread. Hence, assessing flame properties in the crown fuel layer, particularly flame geometry, may be a key step in generating a rigorous characterization of chaparral crown fire behavior.

Flame geometry has been shown to influence flame spread through radiative heat transfer (Albini, 1985). Thus, numerous groups have focused on assessing flame geometry properties as they relate to fire spread. It is pertinent then to present a brief review of studies examining flame geometry characteristics for wildland fuels; this now follows. Byram (1959) conducted foundational work to characterize combustion and fire behavior in forest fuels. The Byram intensity which defines heat release rate per unit time per unit length, is perhaps the most widely accepted expression for fire intensity. Byram proposed early correlations relating flame length to fire intensity. Since the first formulation, numerous groups have derived semi-empirical expression of flame length as a function of fire intensity for various fuels. Thomas proposed correlations relating flame height to fuel supply rate and burner dimensions in conditions without wind (Thomas et al., 1961) and with wind (Thomas, 1963). In work by Nelson (1980) theoretical formulations for flame length, height, tip velocity and tilt angle as a function of Byram intensity were examined for light southern pine fuels. In addition to theoretical modeling, the work presents results from semi-empirical power-law modeling of flame length and tip velocity as a function of Byram intensity. Steward (1970) derived mathematical expressions relating mass flow rate to flame height. Zukoski et al. (1980) examined entrainment characteristics in methane diffusion flames and proposed power-law correlations of flame height as a function of heat release rate and burner diameter. Similarly, Heskestad (1983, 1984) related flame height to heat release rate and burner diameter. Other recent studies of flame conditions and flame spread include those by Gang et al. (2017) and Zhou et al. (2018). Fernandes et al. (2009) derived empirical correlations of flame length and flame height for head and back wildfires. They expressed flame length and height of head fires as a function of Byram intensity and fuel loading. For back fires, both flame length and height were expressed as a function of Byram intensity. Alexander and Cruz (2012) surveyed expressions of flame length presented as function of fire intensity. Alexander and Cruz (2012) identify the significance of flame length to crown fuel layer ignition behavior and highlight power-law expressions relating Byram intensity to flame length for various fuels. Fernandes et al. (2000) derived a powerlaw expression relating Byram intensity for flame length in shrublands. Other recent studies of flame spread include those by Gang et al. (2017) and Zhou et al. (2018).

Works focusing on flame geometry for shrub and chaparral fuels include computational evaluation of flame properties such as the one by Padhi et al. (2016) in which flame geometry in a stationary shrub fire was considered. Moreover, a numerical analysis of flame tilt angle and height, in a spreading shrub fire was presented by Morvan (2007). Recent work by Weise et al. (2018b) compared predictions from flame models to results from experimental circular and line fire configurations of chaparral fire. Model predictions of flame height and flame tilt angle, were compared against experimental values in work by Nelson et al. (2012). Laboratory scale work by Weise and Biging (1996) evaluated the effect of wind and slope on flame properties. Importantly, the previous experimental studies did not include a dual layer, crown fire configuration.

Results from the works reviewed above include semi-empirical correlations which show promise in predicting fire spread behavior. However, few of these semi-empirical models have been produced through the study of chaparral fire modeled as crown fire, as done when modeling chaparral fire with distinct fuel layers for surface and crown fuels. Thus, the aim here is to examine crown flame geometry and to survey the applicability of semi-empirical models of flame geometry to chaparral fires modeled as dual-layer crown fires. To the knowledge of the authors, no prior work has attempted to use established models of semi-empirical fire spread for chaparral fuels modeled with distinct layers for the surface and crown fuel beds. We consider that modeling chaparral fires with a dual layer configuration will more precisely replicate spread behavior as it can capture the dynamic energy exchange between the surface and crown fires. To this purpose, this paper compares models of flame geometry to observations of flame data obtained from wind tunnel experiments in which the surface and crown fuel beds were modeled as separate fuel beds. Data from experiments with wind-blown spread are examined. The next section describes the experimental procedure and modeling approach.

METHODOLOGY

Experimental

Experiments were conducted in a specialized wind tunnel located at the USDA Forest Service Pacific Southwest Research Station fire laboratory in Riverside, California. The wind tunnel study area was composed of two distinct fuel beds representing the dead fuel surface layer and the live fuel crown layer. The surface fuel layer was constructed on the wind tunnel floor and a platform mounted on the top of the tunnel frame contained the crown fuel bed (see **Figure 1**). Aspen (*Populus tremuloides* Michx.) excelsior (shredded wood) served as the surface fuel; crown fuels consisted of chamise (*Adenostoma fasciculatum* Hook & Arn.) branches and foliage harvested locally. Custom instrumentation was developed to measure mass loss from the crown fuel layer; full details of this system can be found in Cobian-Iñiguez et al. (2017). Surface fuel mass loss was measured using an electronic scale placed under a portion of the excelsior fuel bed. Fires

were started by igniting the surface fuel bed (excelsior) using a butane torch and ethyl alcohol as lighter fluid. Wind was activated simultaneously with surface fuel bed ignition. Once ignited, the excelsior fuel bed developed a flame and the fire spread. The surface fire spread under the crown fuel thus preheating it to the point of ignition, at this point the fire transitioned to the crown fuel layer. Thereafter, a flame developed in the crown fuel layer and the fire in the crown fuel layer was allowed to spread until extinction.

Before explaining the properties that were measured using the image processing techniques here, it is necessary to note some basics of flame geometry. In microgravity, experiments have shown and demonstrated that a laminar diffusive flame has a spherical shape. When gravity is applied, a good approximation is to assume that gravity forces will stretch the spherical shape of the flame like a candle and the resulting shape will be an ellipsoidal. Following the same logic, when analyzing the shape of a turbulent diffusive flame, an ellipsoidal (in the case of 2D projection, an ellipse) can be used as a reference for flame characteristics such as flame length and flame tilt.

Flame geometry was obtained from video recordings obtained using a Sony Handicam[1] at 30 frames per s. We used two different algorithms for video data processing: one for flame height, H, see **Figure 1**, and another one for flame tilt angle, θ_f, and flame length, L_f, see **Figure 2F**. The flame height algorithm was generated in MATLAB. The script was designed to convert raw red-green-blue (*RGB*) images to black and white images through thresholding in order to isolate the flame and generate a flame perimeter image. Flame height was obtained from the flame perimeter image. Video data was resampled from 30 to 1 Hz. Once the datum were re-sampled, flame height was obtained at 1 s intervals. The resulting data were used to obtain one absolute maximum flame height value for each experiment. The complete flame height dataset included both the surface and crown flame. Therefore, for the purposes of the analysis shown here, the surface flame height was cropped out. Computationally, this was done by identifying the vertical location of the crown fuel bed in a sample image of the experimental setup. The pixel value at this location was extracted and selected as a threshold. A script was developed to filter out values falling under the threshold thus isolating the crown fuel bed.

An algorithm based on computer vision was developed to obtain flame tilt angle and flame length from an experiment video. The use of this methodology is motivated by advancements in computer vision over the past decade through which image processing for fire imaging has improved. Edge detection has been used to identify flame edge contours (e.g. Gupta and Gaidhane, 2014). The fundamental parameters that can be obtained from visual images are flame height, flame tilt, and flame length. The algorithm and process used here to obtain such parameters follow. At first, images were preprocessed to obtain edges of the flame. To do so, first, a homography and prospective transformation was applied to the raw image. The transformation corrected the perspective of the images. Later, the *RGB* channeled image was converted to hue-saturation-value images (*HSV)* format and the value channel (V) was extracted from the image. Subsequently, a threshold value was selected to convert the images to a binary image. Once the image was converted to binary, the flame edge, or perimeter was obtained using an edge detection algorithm, *Sobel* edge detection.

After obtaining the flame edge, the binary or edge images (**Figures 2D,E**) were labeled and segmented into discrete flames (**Figure 2F**) (in case of both surface and crown fuel flames) distinct from each other and the background. This step essentially established what were known in image processing as *regions*. The regions, the crown flame and surface flame, region 1, and region 2, were now the computational objects of interest. Once the regions were established, the image features, flame length and orientation, were computed. This was done by calculating the moments of the region as described by Burger and Burge (2008). Calculations of the second moment returned orientation and major axis of the region. The coordinates and dimensions of the major axis and orientation were used to produce an ellipsoid using the *OpenCV* (Bradski, 2000) library in Python. This produced an ellipsoid which enveloped the flame and had a major axis equal to the flame length and an orientation equal to the flame tilt angle. The last processing step leading up to the generation of the ellipsoid was visualized in **Figure 2G**. For the purposes of the study here, only region 1, the crown flame was analyzed.

Modeling Techniques

Data obtained experimentally was compared to predictions from existing semi-empirical models to be described in this section. The goal was to assess whether currently available models accurately describe the chaparral crown fire system modeled. Flame geometry properties were defined according to naming and measuring conventions described by **Figures 1**, **2**. Predicted flame height was calculated from heat release rate (Q). Theoretical heat release rate was obtained from mass loss rate according to Equation (1)

$$\dot{Q} = h\left(\frac{dm}{dt}\right), \tag{1}$$

where h represented the low heat of combustion (for chamise h = 14.71 KJ/g). Following Zukoski et al. (1980), we modeled flame height using a semi-empirical power-law correlation of the forms in Equations 2 and 3,

$$H_{max} = 0.2\dot{Q}_{max}^{\frac{2}{5}}, \tag{2}$$

where H_{max} and $\dot{Q}_{max}$ represented maximum flame height and maximum heat release rate, respectively. The second approach was to use the power-law correlation proposed by Sun et al. (2006)

$$H_{max} = 0.17\dot{Q}_{max}^{0.43}. \tag{3}$$

We obtained maximum heat release rate using the two methods proposed by Sun et al. (2006) which, for consistency, we name following their convention such that in Method 1, maximum heat

[1]The use of trade or firm names in this publication is for reader information and does not imply endorsement by the U.S. Department of Agriculture of any product or service.

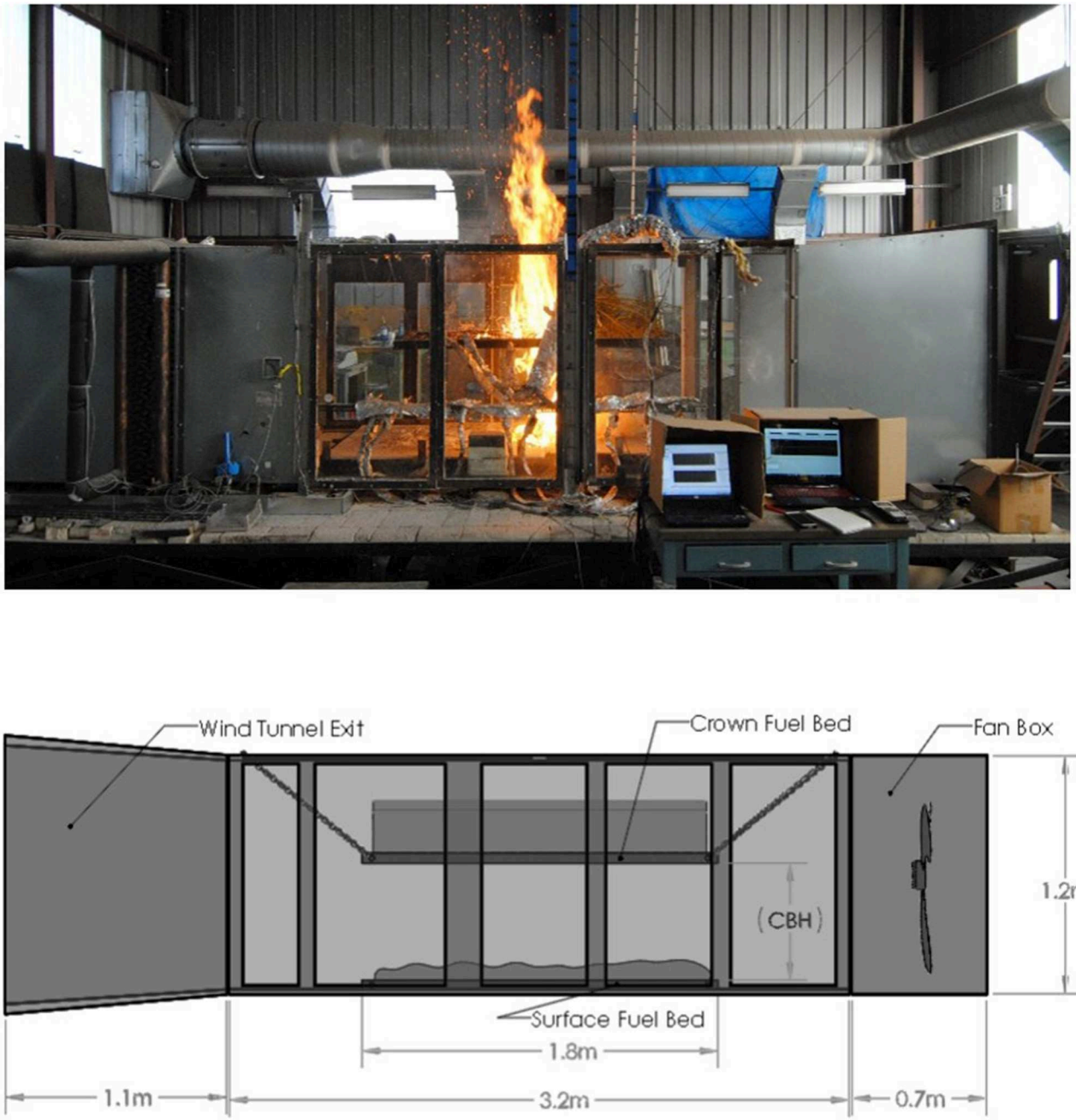

FIGURE 1 | Photograph with wind tunnel configuration with crown base height (*CBH*), flame height (*H*) and experimental configuration labels (top). Schematic of wind tunnel with major dimensions labeled (bottom).

release rate was defined as the heat loss rate occurring at the time of maximum mass loss rate ($\dot{Q}_{max,\ Method\ 1} \sim \dot{m}(t_{\dot{m}_{max}})$). In Method 2, maximum heat release rate was defined as the heat loss rate occurring at the time of maximum flame height $\dot{Q}_{max,\ Method\ 2} \sim \dot{m}(t_{flame\ height,\ max})$. In addition to flame height, we estimated flame tilt from power law and log-log correlations.

Next, we obtained predicted flame tilt values. Predicted flame tilt as a function of Froude number, a dimensionless measure of the relative importance of buoyant and inertial forces Williams (Williams, 1985), was compared to experimental data. The general form for Froude number is given by

$$Fr = \frac{U^2}{gD}, \tag{4}$$

where U is the gas velocity, g is the gravitational constant and D is the characteristic length (Drysdale, 2011). To correlate Froude

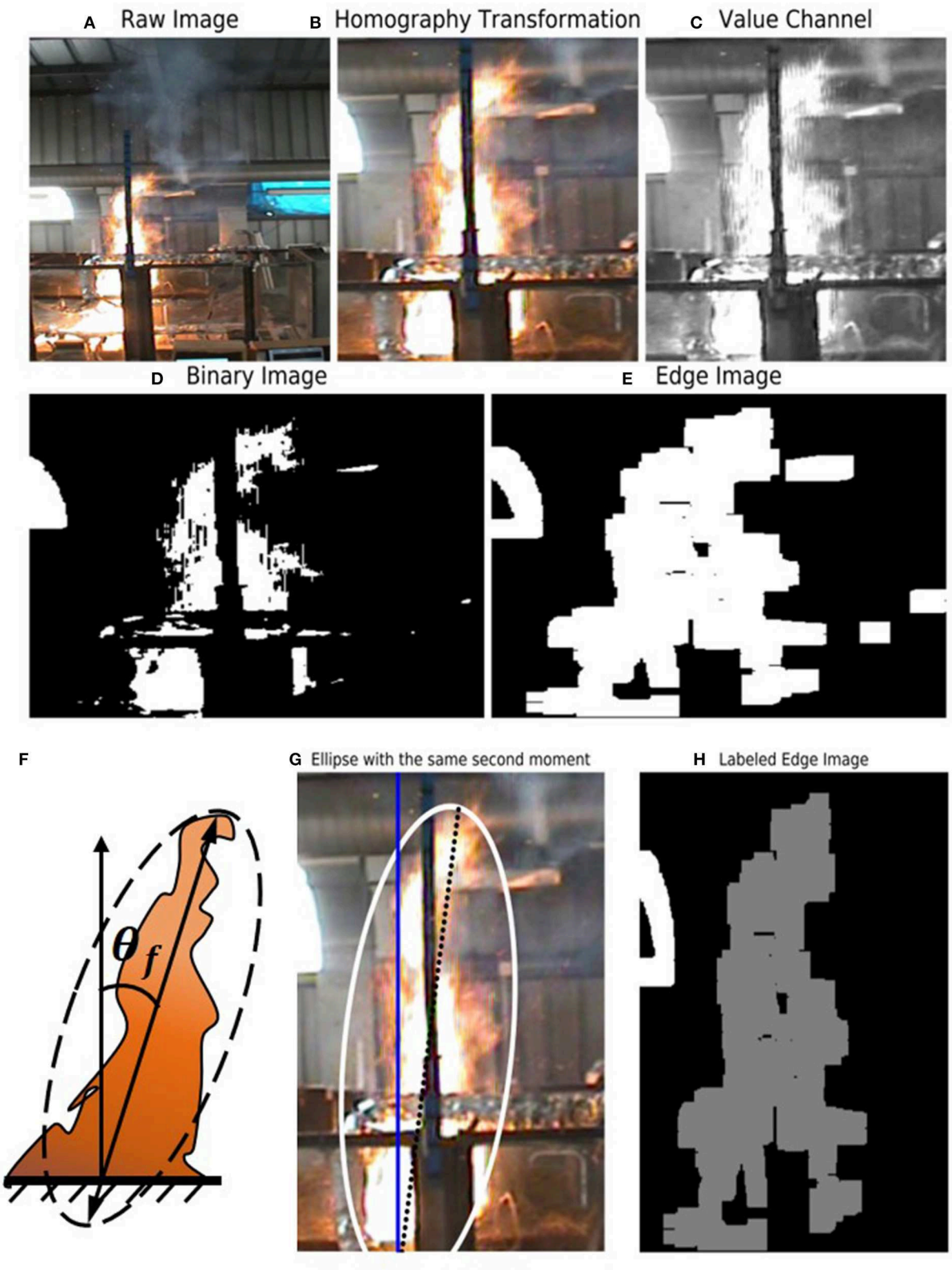

FIGURE 2 | Flame tilt computer vision algorithm image processing steps and schematic (clockwise from the leftmost top corner): **(A)** raw image **(B)** homographic transformation **(C)** value channel extraction **(D)** binary image **(E)** edge image **(H)** labeled edge image **(G)** ellipsoid generated from the processed image overlapped in RGB raw image **(F)** schematic with flame length and flame tilt angle labeled.

number to flame tilt angle, some have used flame height, H, as a characteristic length (Albini, 1981) while others have used flame length, L_f, (Putnam, 1965). In the approach here the latter was used, hence the resulting Froude number expression used was of the final form given by Equation (5)

$$Fr = \frac{U^2}{gL_f}. \tag{5}$$

The empirical correlation between flame tilt angle, θ_f, and Froude number, Fr, was of the form given by Equation (6) (Albini, 1981; Nelson and Adkins, 1986; Weise and Biging, 1996)

$$\tan\left(\theta_f\right) = \alpha Fr^{\beta}. \tag{6}$$

In Equation 5, θ_f is the flame tilt angle as measured from the vertical as presented in **Figure 2B**. The coefficient α and power dependence β can be estimated following the regression analysis in Weise and Biging (1996) (**Figure 2F**).

Coefficients to fit Equation (6) to the data from chaparral crown fire experiments were obtained through regression analysis.

Error Analysis

Agreement between the observed and predicted values of flame height and flame tilt was quantified using the measures identified in Cruz and Alexander (2013) and Weise et al. (2018b). These error analysis schemes have been previously used in analyzing results from wildland fire behavior studies (Cruz and Alexander, 2013). Perhaps the most elemental form of difference is simply the difference between observed and predicted values or

$$d = \left(P_i - O_i\right), \tag{7}$$

where we have adopted notation from Willmott (1982) to represent observed values by O and predicted values by P. If N is the number of samples, then the mean bias of the error (*MBE*), the mean absolute error (*MAE*) and the root mean square error (*RMSE*) can be given as

$$MBE = N^{-1}\sum_{i=1}^{N}\left(P_i - O_i\right), \tag{8}$$

$$MAE = N^{-1}\sum_{i=1}^{N}\left|P_i - O_i\right|, \tag{9}$$

$$RMSE = \left[N^{-1}\sum_{i=1}^{N}\left(P_i - O_i\right)^2\right]^{0.5}. \tag{10}$$

Willmott (1982) qualified *RMSE* and *MAE* as the best measures of model performance and claimed that *MBE* is not a sufficient measure of error as it is simply an expression of the difference between mean values. Here we included *RMSE* and *MAE* as the primary measures of difference. *MBE* was used as a supplemental measure as it provided a sense of over prediction or under prediction of experimental results. Moreover, we calculated the normalized root mean square error (*NRMSE*) by normalizing *RMSE* with the mean of the observed values

$$NRMSE = \left(\frac{RMSE}{O}\right)\cdot 100. \tag{11}$$

TABLE 1 | Table of experiment classes.

Class	Crown Base Height (CBH)	Wind
1	$CBH_1 = 60$ cm	No wind
2	$CBH_2 = 70$ cm	No wind
3	$CBH_1 = 60$ cm	1 m/s
4	$CBH_2 = 70$ cm	1 m/s

In this way we aimed to provide RMSE as a percentage error. The mean absolute percent error (*MAPE*), Equation 12, was also measured and it provides an additional form of percentage error

$$MAPE = N^{-1}\left[\sum_{i=1}^{N}\left(\frac{P_i - O_i}{O_i}\right)\right]\cdot 100. \tag{12}$$

According to Cruz and Alexander (2013), percentage error as measured by *MAPE* is optimized as it nears zero and an acceptable range for good values is 10%.

Experiment Classification

Four experiment classes were used to quantify the effect of wind and the separation distance between the surface and crown fuel layer, which following Van Wagner (1977) is called crown base height (*CBH*) in this work. **Table 1** summarizes the conditions for each experimental class.

The effect of wind and crown base height on flame height was examined for all experimental classes. A total of 18 experiments were considered for flame height analysis. Flame tilt was primarily observed in wind driven flame spread, experiment classes 1 and 2. For this stage of the study, we focused only on the effect of wind on flame tilt, therefore we focused only on one experimental class for the flame tilt analysis, class 4. Two experiments conducted on the same day were examined. This enabled greater uniformity in fuel conditions as fuels burned for both experiments were collected on the same day under the same ambient conditions. *Experiment A* (experiment burn time = 171 s, RH = 52%, FMC = 54%) was the first experiment analyzed, *Experiment B* (experiment burn time = 385 s, RH = 28%, FMC = 54%) was the second.

RESULTS

Flame Height

Data from experiments with and without wind with two crown base height values (CBH_1= 60 cm and CBH_2= 70 cm) were considered for the analysis. Power law relationships as described by Equations (2) and (3) were used to estimate maximum flame heights from maximum heat release rates for each experiment. For flame height analysis, experiments from all classes were considered.

Comparison of the data with Equations (2) and (3) did not show significant differences between models which is not surprising (**Figure 3**). When comparing observed values to theoretical values using Method 1 to estimate maximum heat release rate (**Figure 3A**), it was observed that just under 70%

TABLE 2 | Error statistics for maximum flame height power-law correlations using method 1, $\dot{Q}_{max}$ obtained from $\dot{m}_{max}$ and method 2, $\dot{Q}_{max}$ obtained from $\dot{m}\,(t_{H_{max}})$ (n = 18).

Model tanθ	Ō	RMSE	NRMSE	MAE	MBE	MAPE (%)
(method 1)	2.007	0.3218	16.0380	0.1303	0.1303	8.61
(method 2)	2.007	0.4098	20.4209	0.1627	−0.1627	6.83

of experiments were over-estimated by the model. Theoretical values estimated using method 2, over 75% of experiments considered were under-estimated (**Figure 3B**). Comparison of observed and predicted values showed that for Method 1, only 10% of experiments fell outside 70% of accuracy (**Figure 4A**). In the case of power law predictions using method 2, 17% of experiments fell outside the bounds of 70% of accuracy (**Figure 4B**).

Model statistics resulting from the power-law predictions of maximum flame height using method 1 and method 2 are shown in **Table 2**. For Method 1, the power law correlation had an *MAE* of 0.1303 (*MAPE* = 8.61%) with a *MBE* of 0.1303. For Method 1 *MAE* is 0.1303, for Method 2 it is 0.1627 (*MAPE* = 6.83%). Method 2 had a lower *MAE* using these numbers. A negative *MBE* was calculated for Method 2, −0.1627. *RMSE* was lower for Method 2, RMSE = 0.2098 (20.4209 %) than for Method 1, RMSE = 0.3218 (NRMSE = 16.0380%).

Predicted Flame Tilt

Experimental flame tilt angle was obtained from videos by using the computer vision algorithm described in the Methods section. The analysis here represents flame tilts in wind-blown flames. Only configurations with CBH_2 are included. We explored derivation of new semi-empirical correlations applicable for flame tilt angles in chaparral crown fire. Two experiments of wind-blown flames with CBH_2 were analyzed. Power law regression coefficients were obtained from linear regression performed on a log-log plot computed using the Python *scipy stats* linear regression library. In the first experiment analyzed, hereby called experiment A, the power-law relationship obtained was,

$$\tan\theta_f = 11Fr^{4.6},\ R^2 = 0.85 \tag{13}$$

Observations compared against the power-law given by Equation (13) are presented in **Figure 5A**. A log-log plot of the data with the corresponding correlation is presented in **Figure 5C**. A linear regression was performed on the log-log plot in order to obtain the required coefficients.

The curve shown in **Figure 5A** shows reasonable agreement between the power-law fit given by Equation (13) and observed data (R^2 = 0.85). Moreover, observed-vs.-predicted analysis showed that only 10% of flame tilt samples considered fell outside of the 70% accuracy bounds when using this modeling method, see **Figure 5B**. A sound degree of agreement was consequentially also observed for the log-log analysis (**Figures 5C,D**).

TABLE 3 | Error statistics of flame tilt angle tanθ as a function of Equation 13 for Experiment A and Equation 14 for Experiment B.

Model tanθ	Ō	RMSE	NRMSE	MAE	MBE	MAPE (%)
Experiment A	0.56	0.14	25.23	0.023	−0.023	2.12
Experiment B	0.59	0.22	36.72	0.054	−0.054	2.29

In the second experiment analyzed, hereby called experiment B, the power-law relationship obtained was,

$$\tan\theta_f = 10Fr^4,\ R^2 = 0.84 \tag{14}$$

Observations compared against the power-law given by (14) are presented in **Figure 6A**. A log-log plot of the data with the corresponding correlation is presented in **Figure 6C**. Similarly, to Experiment A, a linear regression on the log-log plot was used to obtain the required coefficients for modeling.

The power-law correlation represented in **Figure 6**, shows a reasonable correlation between observed values for Experiment B and Equation (14) (R^2 = 0.84). Evaluation of observed-vs-predicted values showed that only 30% of flame tilt samples considered fell outside the model 70% accuracy bounds. Reasonable agreement was also observed in the log-log analysis.

Model statistics resulting from the power-law fit on Experiment A and Experiment B are shown in **Table 3**. For Experiment A, *MAE* of 0.023 (*MAPE* = 2.12 %) and an *MBE* of −0.023 were calculated, hence the model exhibits underprediction of the observed values. For Experiment B, *MAE* of 0.054 (*MAPE* = 2.29%) and an *MBE* of −0.054 were calculated, hence similarly to the model in Experiment B, underpredicting observed values. In addition, *RMSE* was optimized for the model in Experiment A, where *RMSE* was 0.14 (*NRMSE* = 25.23%) as compared to the *RMSE* for Experiment B which was 0.22 (NRMSE = 36.72).

DISCUSSION

Flame height results are discussed in terms of model choice and method of heat release rate calculation. In terms of model choice, we evaluated the use of the two-fifths power law given in Equation 2, and the power law derived for dead Fall fuels proposed by Sun et al. (2006) given in Equation 3. Both power laws express flame height in terms of heat release rate. Our results indicate good agreement between flame height values observed experimentally and predicted flame height. Little variation between the two empirical models (Equations 2 and 3) was observed as exemplified by the almost coinciding curves in **Figure 3**. This suggests the validity of the Fall fuels model, Equation 3, proposed by Sun et al. (2006) for experiments conducted in fire season for chaparral fires modeled as chaparral crown fires.

In terms of heat release calculation method, results showed some variation with respect to flame height obtained from power-law correlations of heat release rate using the time at maximum mass loss rate, Method 1 ($\dot{Q}_{max,\,Method\,1} \sim \dot{m}(t_{\dot{m}_{max}})$), and

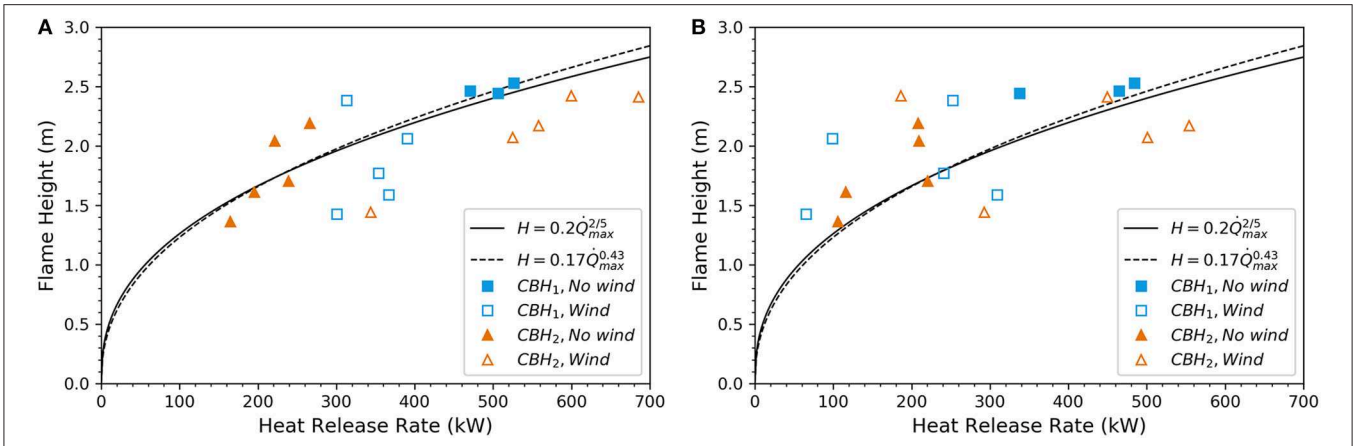

FIGURE 3 | Maximum flame height per experiment as a function of heat release rate plotted against two-fifths power law and Sun et al. power law for chaparral fuels burned in fall season. Maximum heat flux estimated using: **(A)** Method 1, $\dot{Q}_{max}$ obtained from $\dot{m}_{max}$ [$\dot{Q}_{max,\ Method\ 1} \sim \dot{m}(t_{\dot{m}_{max}})$]. **(B)** Method 2, $\dot{Q}_{max}$ obtained from $\dot{m}\ (t_{H_{max}})$ $\dot{Q}_{max,\ Method\ 2} \sim \dot{m}(t_{flame\ height,\ max})$ ($n = 18$).

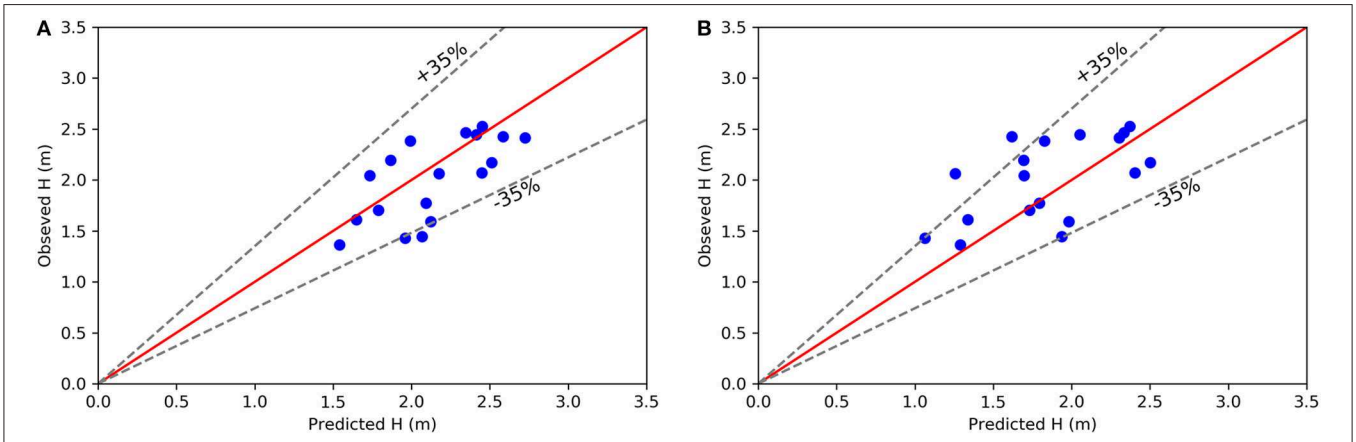

FIGURE 4 | Comparison between predicted and observed flame height values using **(A)** two-fifths power law and $\dot{Q}_{max}$ obtained from $\dot{m}_{max}$ [method 1 of Sun et al. (2006)] **(B)** two-fifths power law and $\dot{Q}_{max}$ obtained from $\dot{m}\ (t_{H_{max}})$ [method 2 of Sun et al. (2006)] ($n = 18$).

the time at maximum flame height as a reference, Method 2 ($\dot{Q}_{max,\ Method\ 2} \sim \dot{m}(t_{flame\ height,\ max})$. When using Method 1, only 10% of experiments fell outside the 70% error bounds, whereas this number increased to 17% when using Method 2. Error analysis also reflected slightly larger error measures for Method 2. *RMSE* was larger for Method 2 than for Method 1. *MBE* exhibited a negative value only for Method 2, thus potentially hinting at the underprediction of the observed values.

Next, we discuss flame tilt results in terms of two representative experiments analyzed. Overall, we found that for the experiments considered, power-law correlations derived had reasonable accuracy, as exhibited by the calculated R^2 coefficient of over 0.80 for both experiments. Moreover, over two thirds of samples fell inside the 70% accuracy bounds. Comparison of predicted flame tilt values to values observed experimentally resulted in negative MBE values for Experiment A and Experiment B which could indicate that models obtained for both experiments underrepresented the data. Moving on to *MAPE*, this measure of error varied by under 1.0 % between the two models. Perhaps the largest variation between statistical error measures of predicted flame tilt was found when assessing *RMSE* which for Experiment A had a normalized value of 25.23% while for Experiment B this number increased to 36.72%. The difference in *RMSE* may indicate that model derived using the dataset from Experiment A yielded a closer fit to observed values.

From the analysis presented here, it can be argued that like in other fire spread applications, power-law semi-empirical models may be used to represent fire spreading in the crown fuel layer of chaparral crown fires. The relatively low variation in error between the two models derived here indicate that with further optimization and by considering an expanded dataset, a unified power-law correlation of flame tilt as a function of Froude number could be derived for flames in chaparral crown fires. In assessing results on flame tilt, it was also observed that when estimating flame tilt angle as a function of Froude

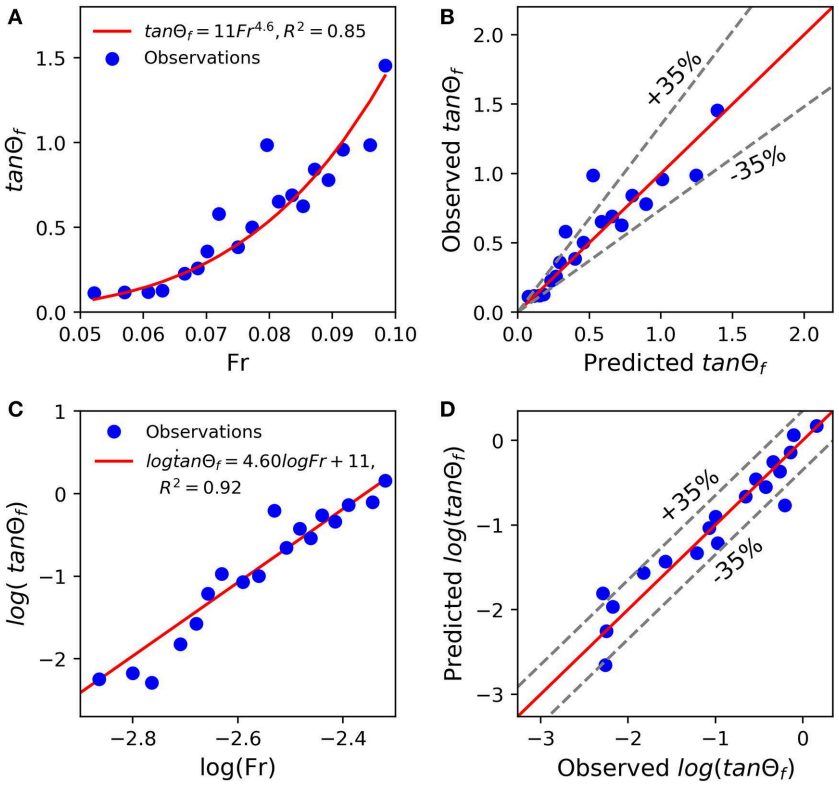

FIGURE 5 | Experiment A, **(A)** Power-law fit **(B)** Predicted vs. Observed values based on power law fit **(C)** log-log fit **(D)** Predicted vs. observed values based on log-log fit.

number in the form given by Equation (6), wind speed did not change and hence, the only varying parameter was flame length or flame height.

Moreover, our results exhibited what could be considered small Froude numbers Fr << 1. The small values points to the dominance of buoyancy forces in governing flame structure. Establishing this feature of fire behavior for the fire system modeled here is significant as it provides information on the modes of heat transfer governing fire spread behavior. This is important as in recent years a great deal of attention has been invested to studying the role of convective and radiative heat transfer in wildland fire behavior. Recent studies examining this aspect of wildfire behavior include those by Finney et al. (2015), Morvan and Frangieh (2018), and Maynard et al. (2016). Results from our work may thus follow others in indicating the role of buoyancy forces driving flame structure and consequently fire behavior. Particular to the work here is a diagnosis on chaparral crown fire fuel beds which illustrates the influence of buoyancy forces on the specific case of crown fire spread and flame behavior in the chaparral. To further understand the role of buoyancy forces in this chaparral crown fire system, future work would benefit from flow visualization such as Schlieren which has been recently used for visualization of convective flow in wildland fire systems (Aminfar et al., 2019).

SUMMARY AND CONCLUSIONS

The work here aimed to serve as proof of concept on the applicability of certain established models of flame properties to spreading chaparral crown fires. Predictions of flame geometry, particularly flame height and flame tilt angle, were compared to observed values obtained from wind tunnel experiments. Maximum flame height was predicted as a function of maximum heat release rate using power law correlations. Additionally, following Sun et al. (2006), we used two methods to calculate maximum heat release rate. Method 1 where maximum heat release is defined at the time of maximum mass loss rate $[\dot{Q}_{max,\ Method\ 1} \sim \dot{m}(t_{\dot{m}_{max}})]$ and Method 2 where maximum heat release rate is defined at the time of maximum flame heat $\dot{Q}_{max,\ Method\ 2} \sim \dot{m}(t_{flame\ height,\ max})$. A good degree of agreement was found between the two-fifths power law correlation of maximum flame height as a function of maximum heat release rate. Similar agreement was found when considering the power-law derived for Fall fuels proposed by Sun et al. (2006).

Error and statistical analysis reflected the positive agreement between predicted and observed values and highlighted some nuances in the predictive potential of the models. Particularly, it was found that Method 1 and Method 2 for maximum heat release estimation showed similar results, but that Method 2 resulted in some degree of underprediction of observed values.

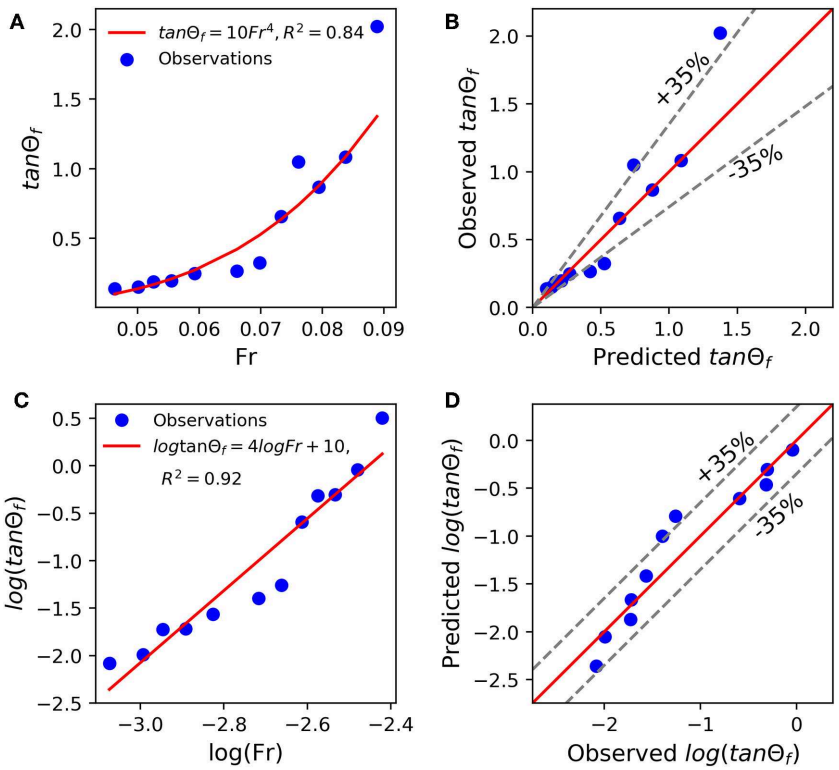

FIGURE 6 | Experiment B **(A)** Power-law fit **(B)** Predicted vs. Observed values based on power law fit **(C)** log-log fit **(D)** Predicted vs. observed values based on log-log fit.

However, most other measures of error showed reasonable agreement with observed data. For this reason, it may be concluded that for the conditions tested here, it was shown that the two-fifths power law may in fact be used to predict flame height from maximum heat release rate in chaparral crown fire spread. Fundamental work in studies including that of Thomas (1963) have successfully applied two-fifths power law correlation to spreading natural fires (without wind). More recent studies have successfully applied of these correlations in chamise chaparral burns in pool fire configurations. Despite the fact that the study here was not conducted for pool fire configurations but instead investigated spread fire, the wind conditions tested (1 m/s) are potentially fit for ensuring that for the conditions tested and the fuels considered, the two fifths power law correlation relating flame height to heat release rate does not fail. In future work it would be worth examining whether increasing wind speed would effect any changes in the applicability of this type of correlation. Additionally, here we considered wind-driven and non-wind driven flames as well as two experimental CBH configurations in our assessment of flame height prediction, future work should examine differences in model agreement between the different experimental conditions.

We derived two sample power-law correlations from selected experiments. Error analysis of flame tilt angle predictions obtained from these new power-law correlations showed good agreement between observed and predicted values. The findings in our study lead to the conclusion that in fact, new semi-empirical power-law correlations may be used to express flame height in spreading crown fires as a function of heat release rate. Finally, the results presented here were obtained from selected experiments and as such are representative of the particular conditions tested. We recognize that the models tested and derived here may be limited to the operational conditions assessed and described in the methodologies section of this work. Nonetheless, they represent important steps toward the derivation of new flame property models for chaparral crown fire applications.

DATA AVAILABILITY

The datasets generated for this study are available on request to the corresponding author.

AUTHOR'S NOTE

This manuscript was prepared, in part, by a U.S. Government employee on official time, is not subject to copyright and subject to copyright is in the public domain.

AUTHOR CONTRIBUTIONS

JC-I designed and conducted the experimental study and analyzed data. AA developed codes and computer vision

algorithms. DW and MP provided guidance in experimental design and data analysis.

FUNDING

This work was supported in part by agreement 13JV11272167–062 between USDA Forest Service PSW Research Station and the University of California–Riverside. This research was partially supported by funding from the DOD/DOE/EPA Strategic Environmental Research and Development Program project RC-2640 administered through agreement 16JV11272167026 between the USDA Forest Service PSW Research Station and the University of California, Riverside.

ACKNOWLEDGMENTS

The authors here would like to thank Gloria Burke and Joey Chong for their assistance during experiments. We would also like to acknowledge and thank Albertina Zuniga, Alejandro Gonzalez, Matthew Choi, Ivan Herrera, and Jake Eagan for their help in experiments and in developing the diagrams presented here.

REFERENCES

Albini, F. A. (1981). A model for the wind-blown flame from a line fire. *Combust. Flame* 43, 155–174. doi: 10.1016/0010-2180(81)90014-6

Albini, F. A. (1985). A model for fire spread in wildland fuels by-radiation. *Combust. Sci. Technol.* 42, 229–258. doi: 10.1080/00102208508960381

Alexander, M. E., and Cruz, M. G. (2012). Interdependencies between flame length and fireline intensity in predicting crown fire initiation and crown scorch height. *Int. J. Wildl. Fire* 21, 95–113. doi: 10.1071/WF11001

Aminfar, A., Cobian-iñiguez, J., Ghasemian, M., Espitia, R., Weise, D. R., and Princevac, M. (2019). Using background-oriented schlieren to visualize convection in a propagating wildland fire using background-oriented schlieren to visualize convection in a propagating wildland fire. *Combust. Sci. Technol.* 0, 1–21. doi: 10.1080/00102202.2019.1635122

Barro, S. C., and Conard, S. G. (1991). Fire effects on California chaparral systems: an overview. *Environ. Int.* 17, 135–149. doi: 10.1016/0160-4120(91)90096-9

Bradski, G. (2000). *The OpenCV Library*. Dr. Dobb's J. Softw. Tools.

Burger, W., and Burge, M. J. (2008). *Principles of Digital Image Processing-Core Algorithms*. Berlin: Springer.

Byram, G. M. (1959). "Combustion of forest fuels," in *Forest Fire: Control and Use*, ed K. P. Davis (New York, NY: McGraw-Hill), 61–89.

Cobian-Iñiguez, J., Aminfar, A., Chong, J., Burke, G., Zuniga, A., Weise, D., et al. (2017). Wind tunnel experiments to study chaparral crown fires. *J. Vis. Exp.* 129, 1–14. doi: 10.3791/56591

Cruz, M. G., and Alexander, M. E. (2013). Uncertainty associated with model predictions of surface and crown fire rates of spread. *Environ. Model. Softw.* 47, 16–28. doi: 10.1016/j.envsoft.2013.04.004

Drysdale, D. (2011). *An introduction to Fire Dynamics*. Second Edition. New York, NY: John Wiley & Sons.

Fernandes, P. M., Botelho, H. S., Rego, F. C., and Loureiro, C. (2009). Empirical modelling of surface fire behaviour in maritime pine stands. *Int. J. Wildl. Fire.* 18, 698–710. doi: 10.1071/WF08023

Fernandes, P. M., Catchpole, W. R., and Rego, F. C. (2000). Shrubland fire behaviour modelling with microplot data. *Can. J. For. Res.* 30, 889–899. doi: 10.1139/x00-012

Finney, M. A., Cohen, J. D., Forthofer, J. M., McAllister, S. S., Gollner, M. J., Gorham, D. J., et al. (2015). Role of buoyant flame dynamics in wildfire spread. *Proc. Natl. Acad. Sci. U.S.A.* 112, 9833–9838. doi: 10.1073/pnas.1504498112

Gang, C., Ji, J., Zhen, Y., and Ingason, H. (2017). Experimental study of sidewall effect on flame characteristics of heptane pool fires with different aspect ratios and orientations in a channel. *Proc. Combust. Inst.* 36, 3121–3129. doi: 10.1016/j.proci.2016.06.196

Gupta, P., and Gaidhane, V. (2014). "A new approach for flame image edges detection," in *International Conference on Recent Advances and Innovations in Engineering (ICRAIE-2014)* (Jaipur: IEEE), 1–6. doi: 10.1109/ICRAIE.2014.6909178

Heskestad, G. (1983). Luminous heights of turbulent diffusion flames. *Fire Saf. J.* 5, 103–108. doi: 10.1016/0379-7112(83)90002-4

Heskestad, G. (1984). Engineering relations for fire plumes. *Fire Saf. J.* 7, 25–32. doi: 10.1016/0379-7112(84)90005-5

Maynard, T., Princevac, M., and Weise, D. R. (2016). A study of the flow field surrounding interacting line fires. *J. Combust.* 2016:12. doi: 10.1155/2016/6927482

Morvan, D. (2007). A numerical study of flame geometry and potential for crown fire initiation for a wildfire propagating through shrub fuel. *Int. J. Wildl. Fire* 16, 511–518. doi: 10.1071/WF06010

Morvan, D., and Frangieh, N. (2018). Wildland fire behaviour: wind kW meffect versus Byram's convective number and consequences on the regime of propagation. *Int. J. Wildl. Fire* 27, 636–641. doi: 10.1071/WF18014

Nelson, R. M. (1980). *Flame Characteristics for Fires in Southern Fuels. Research Paper SE-RP-205*. Asheville, NC: USDA-Forest Service, Southeast Forest Experiment Station, 14. doi: 10.2737/SE-RP-205

Nelson, R. M., and Adkins, C. W. (1986). Flame characteristics of wind-driven surface fires. *Can. J. For. Res.* 16, 1293–1300. doi: 10.1139/x86-229

Nelson, R. M., Butler, B. W., and Weise, D. R. (2012). Entrainment regimes and flame characteristics of wildland fires. *Int. J. Wildl. Fire* 21, 127–140. doi: 10.1071/WF10034

Padhi, S., Shotorban, B., and Mahalingam, S. (2016). Computational investigation of flame characteristics of a non-propagating shrub fire. *Fire Saf. J.* 81, 64–73. doi: 10.1016/j.firesaf.2016.01.016

Putnam, A. A. (1965). A model study of wind-blown free-burning fires. *Symp. Combust.* 10, 1039–1046. doi: 10.1016/S0082-0784(65)80245-4

Rothermel, R. C., and Philpot, C. W. (1973). Predicting changes in chaparral flammability. *J. For.* 71, 640–643.

Steward, F. R. (1970). Prediction of the height of turbulent diffusion buoyant flames. *Combust. Sci. Technol.* 2, 203–212. doi: 10.1080/00102207008952248

Sun, L., Zhou, X., Mahalingam, S., and Weise, D. R. (2006). Comparison of burning characteristics of live and dead chaparral fuels. *Combust. Flame* 144, 349–359. doi: 10.1016/j.combustflame.2005.08.008

Tachajapong, W., Lozano, J., Mahalingam, S., and Weise, D. R. (2014). Experimental modelling of crown fire initiation in open and closed shrubland systems. *Int. J. Wildl. Fire*. 23, 451–462. doi: 10.1071/WF12118

Thomas, P. H. (1963). The size of flames from natural fires. *Symp. Combust.* 9, 844–859. doi: 10.1016/S0082-0784(63)80091-0

Thomas, P. H., Webster, C. T., and Raftery, M. M. (1961). Some experiments on buoyant diffusion flames. *Combust. Flame* 5, 359–367. doi: 10.1016/0010-2180(61)90117-1

Van Wagner, C. E. (1977). Conditions for the start and spread of crown fire. *Can. J. For. Res.* 7, 23–34. doi: 10.1139/x77-004

Weise, D. R., and Biging, G. S. (1996). Effects of wind velocity and slope on flame properties. *Can. J. For. Res.* 26, 1849–1858. doi: 10.1139/x26-210

Weise, D. R., Cobian-Iñiguez, J., and Princevac, M. (2018a). "Surface to Crown Transition," in *Encyclopedia of Wildfires and Wildland-Urban Interface (WUI) Fires*, ed. S. L. Manzello (Cham: Springer), p. 1–5.

Weise, D. R., Fletcher, T. H., Cole, W., Mahalingam, S., Zhou, X., Sun, L., et al. (2018b). Fire behavior in chaparral–evaluating flame models with laboratory data. *Combust. Flame* 191, 500–512. doi: 10.1016/j.combustflame.2018.02.012

Williams, F. A. (1985). *Combustion Theory*, 2nd Edn. Reading, MA: CRC Press.

Willmott, C. J. (1982). Some comments on the evaluation of model performance. *J. Online* 63, 1309–1313. doi: 10.1175/1520-0477(1982)063<1309:SCOTEO>2.0.CO;2

Zhou, Y., Bu, R., Gong, J., Yan, W., and Fan, C. (2018). Experimental investigation on downward fl ame spread over rigid polyurethane and extruded polystyrene foams. *Exp. Therm. Fluid Sci.* 92, 346–352. doi: 10.1016/j.expthermflusci.2017.12.009

Zukoski, E. E., Kubota, T., and Cetegen, B. (1980). Entrainment in fire *Plumes*. *Fire Safe. J.* 3, 107–121. doi: 10.1016/0379-7112(81)90037-0

Conflict of Interest Statement: The authors declare that the research was conducted in the absence of any commercial or financial relationships that could be construed as a potential conflict of interest.

NOMENCLATURE

CBH	Crown-base-height
d	Difference between observed and predicted values
D	Characteristic length
Fr	Froude number
g	Gravitational constant
h	Low heat of combustion
H	Flame height
HSV	Hue saturation value
L_f	Flame length
m	Fuel mass
$\dot{m}$	Mass loss rate
MAE	Mean average error
$MAPE$	Mean average percentage value
MBE	Mean bias error
N	Number of samples
$NRMSE$	Normalized root mean square
O	Observed values
P	Predicted values
$\dot{Q}$	Heat release rate
$\dot{Q}_{max}, Method1$	Maximum heat release rate for Method 1
$\dot{Q}_{max}, Method2$	Maximum heat release rate for Method 2
RGB	Red-green-blue
$RMSE$	Root mean square
$t_{\dot{m}_{max}}$	Time at maximum mass loss rate
$t_{flame\ height\ max}$	Time at maximum flame height
U	Wind speed
V	Value channel
Greek symbols	
α	Power law coefficient
β	Power law coefficient
θ_f	Flame tilt angle
Subscripts	
i	Individual values
f	Flame
max	Maximum

frontiers in Mechanical Engineering

ORIGINAL RESEARCH
published: 13 September 2019
doi: 10.3389/fmech.2019.00054

Piloted Ignition of Cylindrical Wildland Fuels Under Irradiation

Shaorun Lin[1,2], *Xinyan Huang*[1,2*], *James Urban*[3], *Sara McAllister*[4] and *Carlos Fernandez-Pello*[3]

[1] Research Centre for Fire Engineering, The Hong Kong Polytechnic University, Kowloon, Hong Kong, [2] The Hong Kong Polytechnic University Shenzhen Research Institute, Shenzhen, China, [3] Department of Mechanical Engineering, University of California, Berkeley, Berkeley, CA, United States, [4] United States Forest Service, United States Department of Agriculture (USDA), Rocky Mountain Research Station, Missoula Fire Sciences Lab, Missoula, MT, United States

Recent mega wildfires have become one of the most dangerous and devastating hazards, with a wide range of negative impacts on the economy, society, and environment. As cylindrical shrubs and twigs are typical fuel loads in wildfires, it is important to understand how the diameter and arrangement of cylindrical fuels affect their ignition behaviors. In this work, the piloted ignition of cylindrical wood rods with different diameters (3.2 ∼15.9 mm) are conducted under the irradiation up to 50 kW/m^2. Three fuel groups are tested: (I) single vertical rod, (II) single horizontal rod, and (III) horizontal rod bed attached to the ground. For a single vertical rod, the measured ignition time decreases as the diameter is decreased from 15.9 to 6.4 mm, showing a thermally-thin behavior. However, the ignition of the 3.2-mm rod is more difficult than the 9.5-mm rod, because of the enhanced convective cooling by the larger curvature. Nevertheless, when the rod fuels are placed horizontally on the ground, the curvature-enhanced convective cooling becomes limited. For a single rod, when both the fuel diameter and the irradiation are small, only smoldering ignition occurs, and eventually the sample collapses. For the rod bed, flaming ignition always occurs, and it is easier to ignite because of a smaller convective cooling. For both horizontal configurations, the fuel ignition temperature increases almost linearly with the diameter from 270°C (3.2 mm) to 330°C (15.9 mm) but is insensitive to the irradiation level. This research quantifies the effect of fuel diameter and arrangement on the piloted ignition and reveals that the traditional classification of thermally thin and thick fuel for flat materials may not be suitable for cylindrical wildland fuels.

Keywords: wood rod, rod bed, diameter effect, ignition time, ignition temperature

OPEN ACCESS

Edited by:
Guillermo Rein, Imperial College London, United Kingdom

Reviewed by:
Khanh Duc Cung, Southwest Research Institute, United States
Kathryn Marie Butler, National Institute of Standards and Technology (NIST), United States

***Correspondence:**
Xinyan Huang
seuhxy@gmail.com

Specialty section:
This article was submitted to Thermal and Mass Transport, a section of the journal Frontiers in Mechanical Engineering

Received: *03 March 2019*
Accepted: *19 August 2019*
Published: *13 September 2019*

Citation:
Lin S, Huang X, Urban J, McAllister S and Fernandez-Pello C (2019) Piloted Ignition of Cylindrical Wildland Fuels Under Irradiation. Front. Mech. Eng. 5:54. doi: 10.3389/fmech.2019.00054

INTRODUCTION

Over the past few decades, the size, frequency, and severity of wildfires show a steep increase due to the demographic and climatic changes all over the world, despite the significant development of the fire prevention and suppression technologies (Liu et al., 2010; McClure and Jaffe, 2018; Toledo et al., 2018). Wildfires refer to the unmanageable and unpredictable fires which are free to spread and expand, thus causing severe damage and loss to the economy, society and environment (Jolly et al., 2015; Leuenberger et al., 2018; Montiel Molina et al., 2019). For example, serious wildfires in 2017 swept across British Columbia, Canada; California, USA; Southern Europe, especially in

Portugal and Italy, causing more than 100 fatalities in July (Ronchi et al., 2017). Dead vegetation particles can constitute a bulk of surface fuel loads, so they are closely related to the fire risks and hazards in wildlands (Moghtaderi et al., 1997). Therefore, it is of vital importance to fully understand the fire risks and dynamics of the woody particles for the improvement and innovation of wildfire protection measures (Shen et al., 2013).

The ignition of wildland fuels has been widely studied to associate with the initiation and growth of the devastating wildfires (Moghtaderi et al., 1997; Boonmee and Quintiere, 2005). Fundamentally, the fire spread is a continuous ignition process that is heated and piloted by the flame (Williams, 1977). Both extrinsic (e.g., heating source, oxygen concentration and wind velocity) and intrinsic (e.g., density, composition, moisture, and age) factors can affect the ignitability and flammability of vegetations. Therefore, for different vegetation types, there are different ignition criteria and forms, e.g., piloted or auto-ignition, and flaming or smoldering ignition (Tuyen et al., 1995). For high-density wood particle, the ignition difficulty or the ignition delay time under the external irradiation generally increases from the piloted flaming ignition to flaming autoignition, and then, to smoldering (or glowing and surface) ignition (Boonmee and Quintiere, 2002), but for low-density fuel, the smoldering ignition becomes easier (Lin et al., 2019).

Most literature works studied the ignition of flat materials and depending on the level of irradiation (or radiant heat flux), thermally thick and thin materials can be identified (Drysdale, 1986). In general, based on the thermally-thin theory of flat fuel, only when the sample thickness is <1 mm, the ignition delay time will start to increase with sample thickness (Quintiere, 2006). Comparatively, much fewer studies have addressed the ignition of fuel with shapes other than flat, e.g., the cylindrical, spherical, or amorphous shapes. The cylindrical fuels are dominant in the wildland surface fires, e.g., shrubs, twigs and pine needles, as shown in **Figure 1**. Fons (1950) first studied the auto-ignition mechanism of wood cylinders inside a hot furnace and revealed the ignition time increased with the sample diameter. Several analytical and empirical expressions of the ignition delay time as a function of diameter and critical irradiation have been derived for cylindrical fuels (Delichatsios, 2000; Hernández et al., 2019). McAllister and Finney (2017) investigated the auto-ignition of small wood cylinders with a diameter of 6.4∼19.1 mm under the combined convective and radiative heating, and showed that the auto-ignition delay time increased with the wood diameter. Recent researches revealed the dominant ignition mechanism of fine wildland fuel particles (diameter $\leq$ 1 mm, e.g., pine needle) is convective heating by the hot fire plume or the direct flame contact, rather than the radiant heat in Rothermel's model (Finney et al., 2013, 2015). Fundamentally, this is because for fine fuel like pine needles, convective cooling increases significantly with a smaller diameter or a larger curvature that overcomes the radiant heating effect (Incropera, 2007). However, how the diameter of small and medium cylindrical wildland fuels (>1 mm) affects the piloted ignition behavior; and what is the critical diameter for convective cooling to be dominant is still not clear. Moreover, no study in the literature has investigated the different piloted ignition behaviors between the single fuel particle and a fuel bed of multiple particles, thus bringing a huge research gap.

In this work, the piloted ignition of cylindrical wood rods with diameters of 3.2 ∼15.9 mm are tested under the irradiation up to 50 kW/m^2. Three groups of ignition experiments, (I) single vertical rod, (II) single horizontal rod, and (III) horizontal rod bed attached to the ground, are performed to study the diameter effect. The ignition phenomena, delay time, and ignition temperature will be analyzed.

EXPERIMENT

Wood Rod Sample

Cylindrical wood rods (∼8 cm in length) with four different diameters, 15.9, 9.5, 6.4, and 3.2 mm (or 5/8, 3/8, 1/4, and 1/8 in), were used in the experiment, as shown in **Figure 2A**. Note that they are relatively thicker than the conventional fine particles

FIGURE 1 | Typical wildland surface fire with cylindrical fuels (Credit: Benjamin Knapp/University of Missouri).

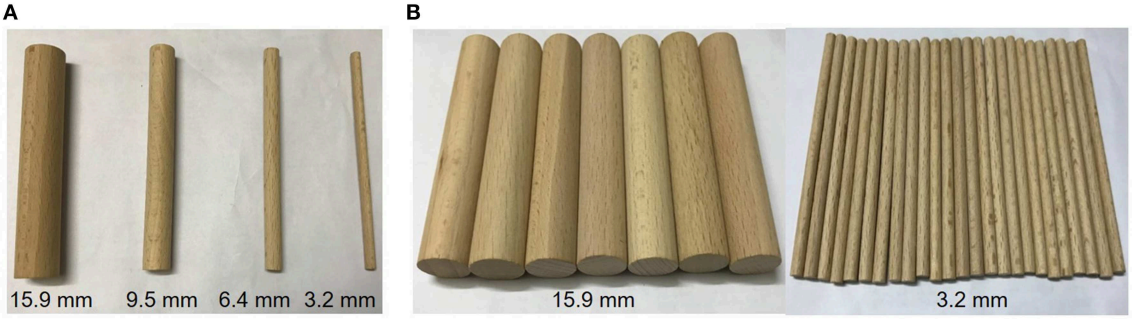

FIGURE 2 | (A) Cylindrical wood samples with different diameters, and **(B)** examples of the array of the rod bed.

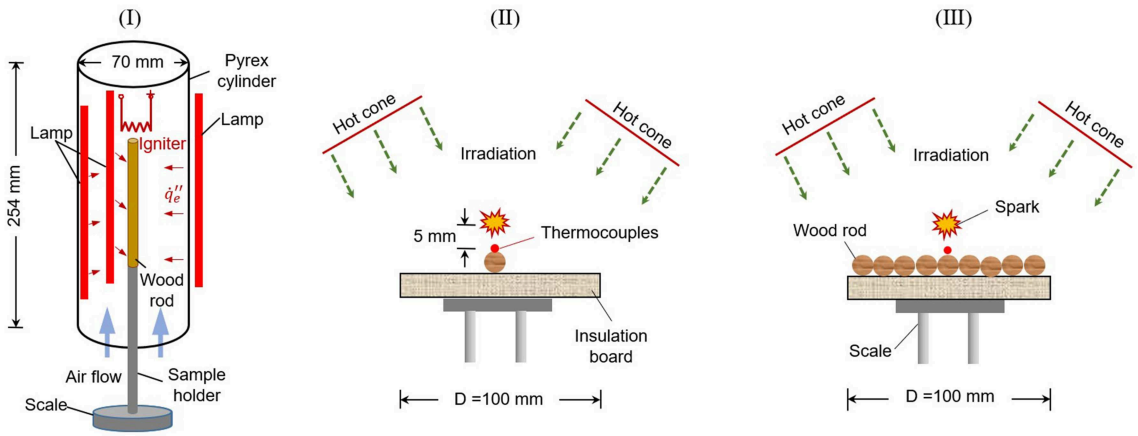

FIGURE 3 | Schematic diagrams for three groups of ignition tests, **(I)** the single vertical rod, **(II)** the single horizontal rod, and **(III)** the horizontal rod bed.

(< 1 mm) (Finney et al., 2013, 2015). Before the experiment, wood rods were first dried at 70°C in the oven for 48 h, and the dry bulk density of rod was measured as ~650 kg/m^3. For the rod bed tests, the wood rods were arranged one against the other without space, as shown in **Figure 2B**, which was to mimic a packed fuel on the wildland surface. As the diameter of the wood rod decreased, the number of wood rods per unit area increased. In particular, as the diameter increased from 3.2 to 15.9 mm, the number of wood rods in the fuel bed decreased from 25 to 7, as seen in **Figure 2B**.

Vertical Rod Test

For the single vertical rod test (Group I), the test section was enclosed by a 25.4 cm long Pyrex glass tube with an outer diameter of 75 mm and an inner diameter of 70 mm, as shown in **Figure 3I**. The vertically oriented cylindrical rod sample was centered in the test section. Three quartz near-infrared halogen tungsten filament lamps (Ushio QIH120-500T/S, 12.7 cm long) were installed with 120° interval to provide more uniform irradiation around the cylindrical wood rod. The average irradiation from 3 lamps to the axial rod surface ($\dot{q}''_e$), up to 35 kW/m^2, was measured by a Schmidt-Boelter radiometer (MEDTHERM Co.) and calibrated with the power supply to be approximately uniform (Hernández et al., 2019). It is expected that most of the irradiation will be absorbed on the fuel surface, i.e., negligible in-depth radiation. To ensure a good air supply to the test section, a small airflow of 25 cm/s was supplied from the bottom of the glass tube throughout the heating process. This experimental setup is the same as the past work on the ignition of electrical wire (Miyamoto et al., 2016).

The ignition process involved turning on the halogen lamps without preheating, because halogen lamp has a quick response to the change of supply power. To fix the sample position, the sample was hung by a hook from the top or supported by a base and a side sample holder. The ignition was achieved by using a hot electrical coil or a ceramic heater, placed 5 mm above the rod. To prevent the direct heating from the igniter, the top of the rod was covered by the aluminum foil. Flaming ignition was considered to have failed if the flame did not occur after heating for 30 min. Then, the irradiation was adjusted to find the critical (or minimum) irradiation for flaming ignition ($\dot{q}''_{crt,f}$). All experiments were repeated at least twice to reduce the random error.

Horizontal Rod Test

Another two piloted ignition tests of the single horizontal rod (Group II) and horizontal rod bed (Group III) were conducted with the cone calorimeter (FTT iCone Plus) (Babrauskas, 2016),

mainly composed of a conical heater, a spark igniter, and a sample holder, as illustrated in **Figures 3II,III**. The conical heater could provide constant irradiation ($\dot{q}''_e$) to the sample area of 10 ×10 cm. During the experiments, the horizontal wood rods were attached to the insulation board without bonding material, mainly to mimic the dead wildland fuel on the surface, different from the floating samples like pine needles and tree twigs (Finney et al., 2013; McAllister and Finney, 2017). Moreover, compared to the vertical rod receiving more uniform surface irradiation, only half of horizontal rod surface receives irradiation. Before the test, the temperature of the conical heater was set at a certain value to generate the correspondingly uniform irradiances over the entire exposed face of the specimens, which was measured and calibrated by a radiometer. The test section (fuel and cone heater) was not enclosed to ensure a good air supply.

A spark was used as the igniter, and the position of spark igniter was adjusted for different rod diameters to ensure that it was located at 5 mm above the top surface of each rod. A 10 × 10 cm insulation board was placed below the horizontal rods. The radiant heating would start when the shield of the conical heater was removed. The surface temperature was monitored by a K-type thermocouple with 0.5-mm bead that was in good contact

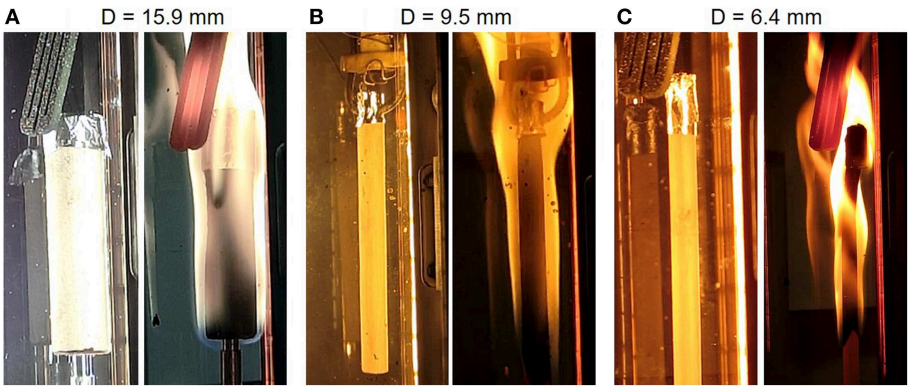

FIGURE 4 | Piloted flaming ignition process of test Group (I) single vertical rod under the irradiation of 20 kW/m^2, **(A)** $D = 15.9$ mm, **(B)** $D = 9.5$ mm, and **(C)** $D = 6.4$ mm.

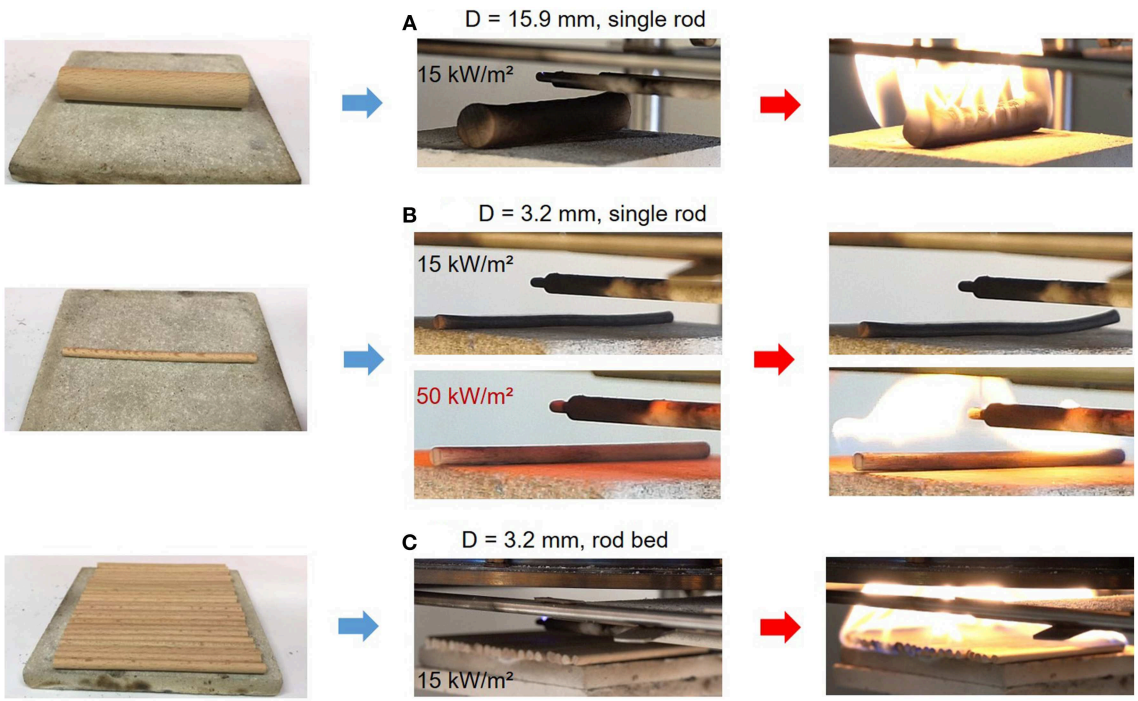

FIGURE 5 | Piloted flaming ignition process of horizontally placed wood rods, **(A)** $D = 15.9$ mm, single rod, 15 kW/m^2, **(B)** $D = 3.2$ mm, single rod, 15 kW/m^2 and 50 kW/m^2, **(C)** $D = 3.2$ mm, rod bed, 15 kW/m^2, where the snapshots in the middle are 5 s before the ignition if it occurs.

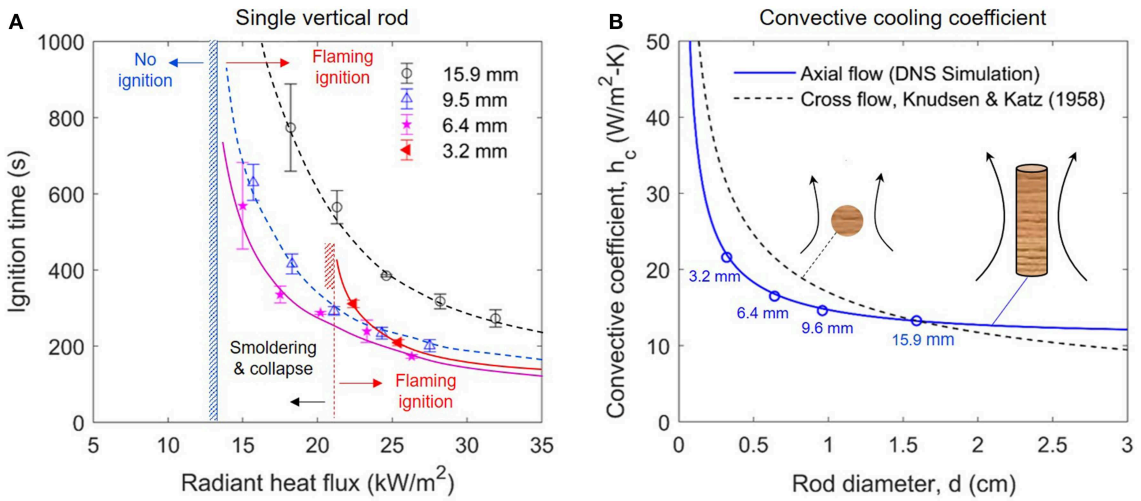

FIGURE 6 | The ignition delay time of **(A)** single vertical rod, and **(B)** convective cooling coefficient of rod sample, where convective cooling coefficient for axial flow is calculated via DNS simulation in FDS, and the convective cooling coefficient for cross-flow is calculated via empirical correlation from Knudsen and Katz (1958).

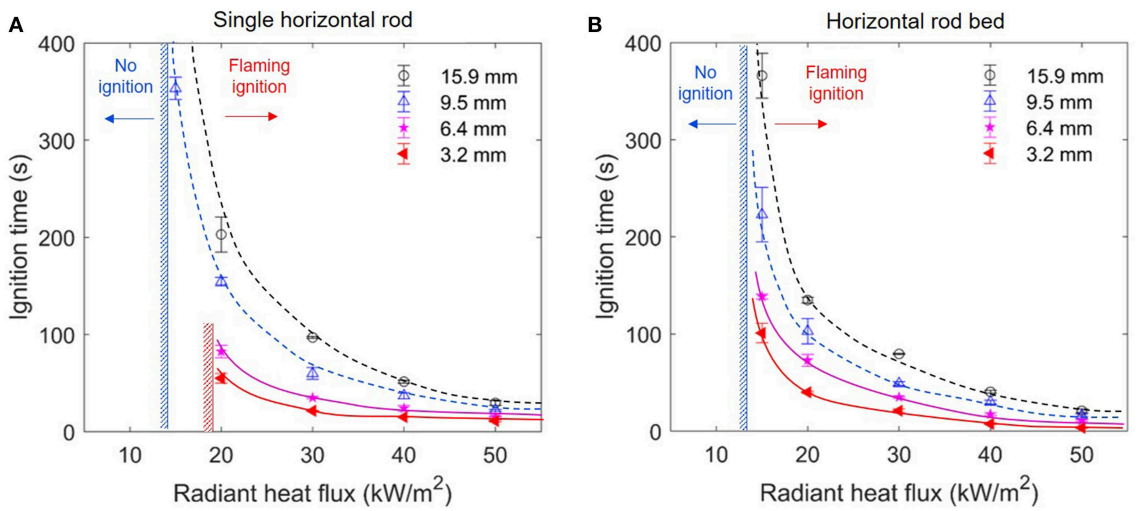

FIGURE 7 | The ignition delay time of **(A)** the single horizontal rod (Group II), and **(B)** the horizontal rod bed (Group III).

with the rod top surface. The heating process, the moment of flaming ignition, and the following burning process were captured by a video camera. Once the flaming ignition occurred, the spark igniter was removed, while the heating was continued until the flaming burning process ended. For each test condition, at least two repeating experiments were conducted to characterize the ignition behaviors and uncertainty.

RESULTS AND DISCUSSIONS

Ignition Phenomena and Critical Irradiation

Figure 4 shows the typical ignition phenomena of the single vertical rod test (Group I), where the original videos can be found in **Supplementary Videos 1–3**. **Figure 5** shows the examples of the piloted ignition process of the single horizontal wood rod (Group II) as well as the wood rod bed (Group III, **Supplementary Videos 4–7**). Before the ignition, smoke was always observed, likely the pyrolysis gases. **Figure 5** also shows a common charring process at the low irradiation of 15 kW/m^2 for all tested rods, where the wood surface turned to black and was bent. This is because a minimum mass flux of pyrolysis gas is required for the spark igniter to pilot a flame (Rich et al., 2007). However, before reaching the minimum mass flux of flaming ignition, a slow pyrolysis or charring process has already taken place under such a long period of slow heating. In contrast, as the heating flux increased to 50 kW/m^2, there is negligible charring and bending process before the ignition, as shown in **Figure 5B**.

If the irradiation decreases to a certain value, no flaming ignition could occur after heating for 30 min. Such value is defined as the critical irradiation ($\dot{q}''_{crt}$), and can be explained by a

TABLE 1 | Measured flaming ignition delay time for the single vertical fuel (Group I), where the radiation level calibrates the change in the gap between lamp and rod due to the change in diameter.

Diameter	15.9 mm (5/8″)		9.6 mm (3/8″)		6.4 mm (1/4″)		3.2 mm (1/8″)	
Heater voltage (V)	$\dot{q}_e''$ (kW/m^2)	$t_{ig,v}$ (s)	$\dot{q}_e''$ (kW/m^2)	$t_{ig,v}$ (s)	$\dot{q}_e''$ (kW/m^2)	$t_{ig,v}$ (s)	$\dot{q}_e''$ (kW/m^2)	$t_{ig,v}$ (s)
100	18.2	774 ± 114	15.7	630 ± 47	15	568 ± 114	14.5	*
110	21.3	565 ± 43	18.3	416 ± 26	17.5	335 ± 22	16.9	*
120	24.6	385 ± 3	21.2	292 ± 11	20.2	288 ± 4	19.5	*
130	28.2	318 ± 19	24.3	234 ± 15	23.3	239 ± 30	22.4	311 ± 10
140	31.9	273 ± 23	27.5	201 ± 16	26.3	173 ± 5	25.4	209 ± 8

*Smoldering ignition where the sample burns to ash and collapses before flaming could occur.

thermal equilibrium with the environmental heat loss ($\dot{q}''_{loss}$) right below the ignition temperature (T_{ig}) (Drysdale, 2011) as:

$$\dot{q}''_{crt} = \dot{q}''_{loss} = (h_c + h_r)\left(T_{ig} - T_a\right) \tag{1}$$

where T_a is the ambient temperature, h_c and h_r are the convective and radiative cooling coefficient, respectively. **Figures 6, 7** summarizes the measured critical irradiation for all three test groups. For (I) the single vertical rod in **Figure 6A**, for the rod diameters between 6.4 and 15.9 mm, the required minimum irradiation are essentially the same, as $\dot{q}''_{crt} = 13$ kW/m^2. However, for the thinnest rod (3.2 mm), no flaming ignition would occur below the irradiation of 20 kW/m^2, because the sample was charred, smoldered into ash, and eventually collapsed. A similar phenomenon also occurred to (II) the single horizontal rod in **Figure 7A**, where the critical irradiation increases from 13 kW/m^2 (9.6 and 15.9 mm) to 17 kW/m^2 (3.2 and 6.4 mm). Therefore, as compared in **Figures 5A,B**, at the low irradiation of 15 kW/m^2, flaming ignition occurs to 15.9-mm rod, while not to the 3.2-mm rod.

In contrast, for (III) the packed rod bed in **Figure 7B**, the critical irradiation is the same 13 kW/m^2 for all rod diameters, probably because the rod bed is essentially similar to a flat wood plate. In other words, it is possible that in real wildland fires, discrete fuel particles of small diameter (∼5 mm) may be ignited and burnt in the form of smoldering fire under a small or medium external radiation from the nearby fires, and they may never ignite with a flame. However, such phenomena may not occur to very small fuel diameters (<1 mm) which do not even smolder because of the strong convective cooling (Finney et al., 2013, 2015), or to a packed fuel bed on wildland surface.

Ignition Delay Time

Figure 6A compares the ignition delay time as a function of rod diameter for (I) the single vertical rod, and all the raw data are listed in the **Table 1**. Not surprisingly, the ignition delay time decreases as the irradiation increases, just like other common fuels (Drysdale, 2011).

Clearly, the ignition delay time increases as the diameter increases from 6.4 to 15.9 mm, but the values become more similar at higher heat fluxes. Therefore, it shows a similar trend of the thermally-thin flat material, although the diameter of rods is much larger than the traditional limit of thin flat material (<1 mm). This is mainly because regardless the diameter of the cylindrical fuel, it has a perfect adiabatic boundary condition in the axis, and two boundary conditions are similar to the classic thermally-thin sample (Quintiere, 2006), as:

$$\dot{q}''_e - \dot{q}''_{loss} = -k\left(\frac{\partial T}{\partial r}\right)_{r=\mathrm{R}} \quad \text{(surface)} \tag{2a}$$

$$0 = \left(\frac{\partial T}{\partial r}\right)_{r=0} \quad \text{(axis)} \tag{2b}$$

Nevertheless, because of different coordinates, the ignition delay time of cylindrical fuels is not proportional to the diameter, different from that of thin flat fuels (proportional to the thickness).

Note that for rod diameter larger than 6 mm, the effect of the radius (or the curvature) on convective cooling coefficient is still relatively small, as illustrated in **Figure 6B**. Thus, the heating of cylindrical rod with different diameters is mainly controlled by the conduction. As a result, the cylindrical rod of a smaller diameter is easier to heat up, and more detailed heat-transfer analysis can be found in Delichatsios (2000) and Hernández et al. (2019). Thus, the traditional classification of thermally thin and thick fuel for flat fuel cannot be applied to cylindrical fuels in the wildlands.

Nevertheless, as the vertical rod diameter decreases to 3.2 mm in **Figure 6A**, its ignition delay time becomes larger than that of 6.4 and 9.5 mm, reversing the trend for diameter larger than 6.4 mm. This is because the convective cooling coefficient (h_c) increases significantly as the diameter is decreased (Knudsen and Katz, 1958), especially below 5 mm, as shown in **Figure 6B**, thus, it may be expressed as:

$$h_c \propto \frac{1}{D^{\alpha}} \tag{3}$$

where the index α quantifies the diameter (or curvature) effect. Therefore, when the rod diameter is smaller than a critical value of about 5 mm, the convective cooling starts to control the piloted ignition under radiation, and the ignition becomes more difficult than larger rod diameters.

However, care is needed to generalize such a conclusion for the size effect. **Figure 7** shows that for the single horizontal rod

TABLE 2 | Flaming ignition delay time for the single horizontal fuel (Group II) and the horizontal fuel bed (Group III).

Diameter	15.9 mm (5/8″)		9.6 mm (3/8″)		6.4 mm (1/4″)		3.2 mm (1/8″)	
$\dot{q}_e''$ (kW/m^2)	Single $t_{ig,1}$ (s)	Bed $t_{ig,bed}$ (s)	Single $t_{ig,1}$ (s)	Bed $t_{ig,bed}$ (s)	Single $t_{ig,1}$ (s)	Bed $t_{ig,bed}$ (s)	Single $t_{ig,1}$ (s)	Bed $t_{ig,bed}$ (s)
15	1380 ± 20	332 ± 57	354 ± 12	223 ± 28	*	139 ± 3	*	101 ± 14
20	203 ± 18	135 ± 3	154 ± 5	103 ± 13	83 ± 7	73 ± 6	55 ± 5	40 ± 2
30	97 ± 12	80 ± 2	60 ± 6	49 ± 2	35 ± 2	35 ± 2	21 ± 2	21 ± 2
40	53 ± 2	41 ± 2	37 ± 3	30 ± 2	24 ± 3	18 ± 2	15 ± 2	8 ± 1
50	32 ± 3	21 ± 2	22 ± 2	17 ± 1	15 ± 2	11 ± 1	11 ± 2	4 ±1

*Smoldering ignition where the sample burns to ash and collapses before flaming could occur.

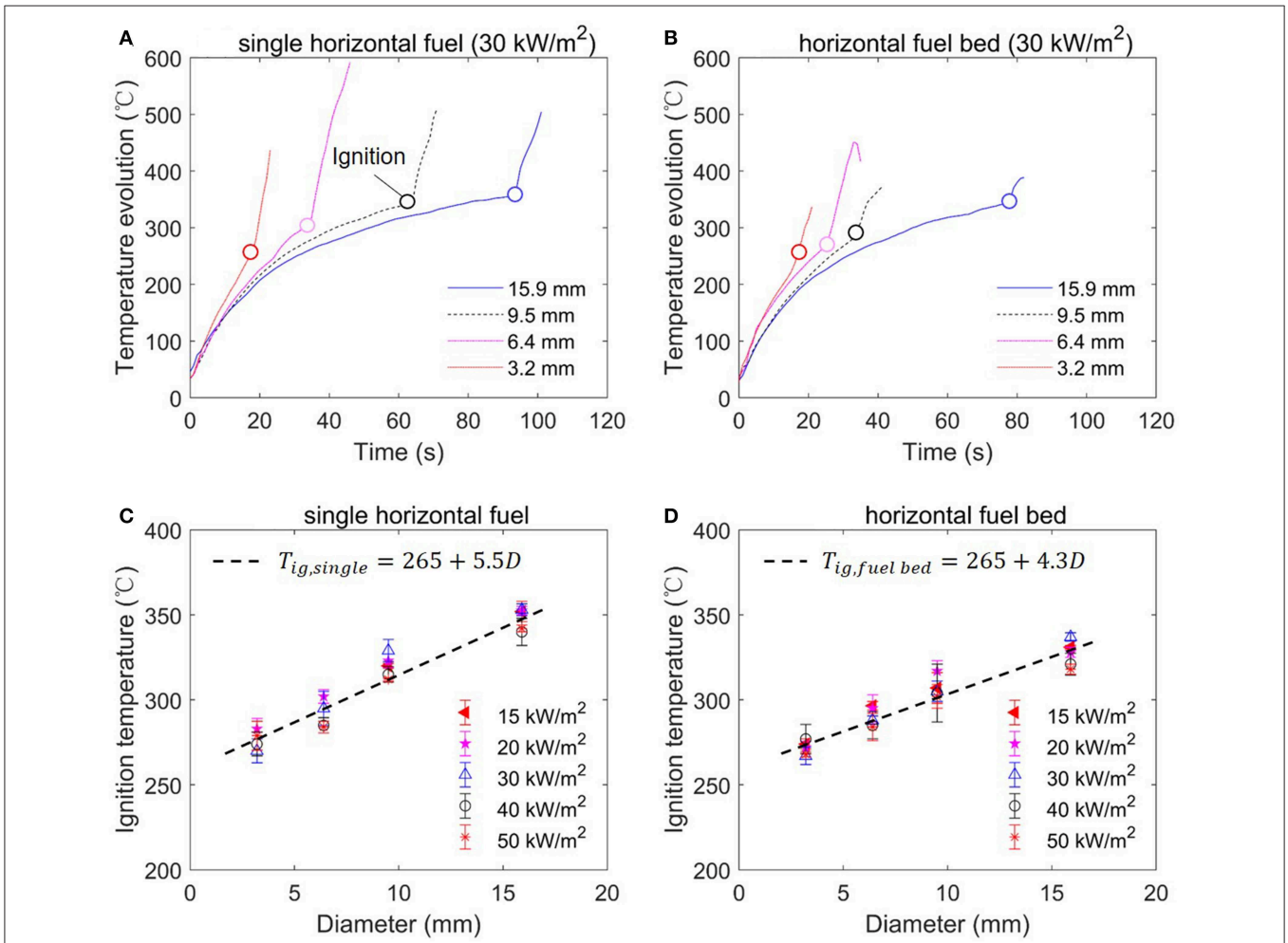

FIGURE 8 | The temperature evolution of rod top surface **(A)** single horizontal rod, and **(B)** horizontal rod bed; and ignition temperature (T_{ig}) as a function of rod diameter, **(C)** single horizontal rod, and **(D)** horizontal rod bed.

or the horizontal rod bed on the ground (Groups II and III), the ignition delay time continuously decreases, as the rod diameter is decreased even to 3.2 mm. All the raw data are listed in **Table 2**. This is mainly because when the wood rod is attached to the ground, the convection flow field is significantly affected by the ground surface, rather than controlled by the curvature of the fuel, that is, a smaller α. Moreover, for the rod bed (Group III), the nearby rods not only limit the convective cooling area, but also reduce the curvature-enhanced convective cooling (i.e., closer to the flat sample). Thus, the convective cooling of each rod is further reduced, resulting in a shorter ignition delay time. For example, under 30 kW/m^2, the ignition time is 60 s for a single

9.5-mm rod but reducing to 49 s for the rod bed. In other words, the curvature-enhanced convective cooling for three test groups ranks as $\alpha_I > \alpha_{II} > \alpha_{III}$.

Ignition Temperature

For the ignition criterion, it is a common practice to assume an ignition temperature (T_{ig}), that is, flaming ignition will occur when the fuel surface temperature reaches a critical value (Quintiere, 2006), and such critical temperature is also most useful to predict the rate of fire spread (Atreya, 1998; Tian and Zhou, 2015). If the irradiation is below the critical value ($\dot{q}''_{crt}$), an equilibrium between radiant heating and environmental cooling will be reached at a surface temperature below T_{ig}. **Figure 8** shows the evolution of surface temperature for (A) the single horizontal rod, and (B) the rod bed with different diameters under the same 30 kW/m^2. Once heated by irradiation, the surface temperature rapidly increases, while the rate of increase becomes smaller because of the increase in the environmental cooling. Afterwards, on the moment of flaming ignition, the surface temperature experiences a sudden jump. Clearly, under the same irradiation, the heating rate of the smaller particle is much faster, especially in **Figure 8A**. Nevertheless, the effect of diameter becomes smaller in the rod bed in **Figure 8B**, the overall top surface of the rod bed configuration becomes more smooth and closer to a flat sample compared to a single rod.

Figure 8 also summarizes the ignition temperature of (C) the single horizontal rod, and (D) the horizontal rod bed as a function of rod diameter and irradiation. It can be found that for both fuel arrangements, the ignition temperature increases with the rod diameter, but it is insensitive to the irradiation level. For example, for the single rod, the ignition temperature increases from about 280 to 350°C, as the rod diameter increases from 3.2 to 15.9 mm. Then, the empirical correlation can be obtained by fitting all the data points for the single horizontal rod as:

$$T_{ig,1} = 265 + 5.5D \quad [^\circ C] \tag{4}$$

and for the horizontal rod bed as:

$$T_{ig,bed} = 265 + 4.3D \quad [^\circ C] \tag{5}$$

Note that these results disagree with the widely assumed constant ignition temperature for a given fuel that is slightly above its pyrolysis point.

One possible reason is that for a rod of the smaller diameter, both the received external radiation and the in-depth conduction are more uniform, leading to a smaller internal temperature gradient. Then, a thicker layer below the surface also has the temperature high enough to pyrolyze, so that sufficient fuel mass flux could be produced. Comparatively, for a rod of larger diameter, the in-depth temperature is much lower than the surface temperature. Only the thin surface layer is pyrolyzing, so that a higher surface (ignition) temperature is needed to reach the minimum fuel mass flux.

Moreover, the trend of ignition temperature also explains the constant critical irradiation of $\dot{q}''_{crt} = 13$ kW/m^2 found in **Figures 6**, **7**. Considering the convective cooling coefficient (h_c) in Equation (3) decreases as the diameter is increased, with the compensation of the increasing ignition temperature (T_{ig}), $\dot{q}''_{crt}$ in Equation (1) will tend to remain as a constant. Comparatively, for the rod bed, a weaker diameter dependence of T_{ig} in Equation (5) also compensates the weak diameter dependence of h_c in Equation (3) where α_{III} is the smallest in all three test groups.

CONCLUSIONS

In this work, we found that for a single vertical rod, the piloted ignition time decreases as the diameter is decreased from 15.9 to 6.4 mm, showing a thermally-thin behavior. However, for the thinnest rod with a diameter of 3.2 mm, the ignition is more difficult, and its ignition time could be longer than that of the 9.5-mm rod. This is because the convective cooling is enhanced when the curvature of fuel is larger, i.e., the curvature effect. Thus, the traditional thermally-thin assumption may fail when the rod diameter is less than about 5 mm. Nevertheless, the arrangement of fuel also influences the piloted ignition behaviors. When the rod fuels are placed horizontally on the ground, such curvature enhanced convective cooling becomes limited.

For the single horizontal rod, when the diameter and irradiation are both small, only smoldering ignition occurs, and eventually the sample collapses. For the single rod with larger diameter and the rod bed, the critical irradiation of ignition is almost constant (13 kW/m^2). For the rod bed, flaming ignition always occurs; the ignition behavior is closer to the flat sample; and its ignition is easier than single rod due to a smaller convective cooling. Moreover, for both horizontal configurations, the measured ignition temperature increases almost linearly from 270 to 330°C as the fuel diameter increases from 3.2 to 15.9 mm, but it is insensitive to the external irradiation up to 50 kW/m^2. This research quantifies the effect of fuel diameter and arrangement on the piloted ignition and reveals that the traditional classification of thermally thin and thick fuel for flat materials may not be suitable for cylindrical wildland fuels.

DATA AVAILABILITY

The raw data supporting the conclusions of this manuscript will be made available by the authors, without undue reservation, to any qualified researcher.

AUTHOR CONTRIBUTIONS

SL conducted experiment Groups (II) and (III) and wrote the first draft of the manuscript. XH conducted experiment Group (I), revised the manuscript, and contributed to the data analysis. JU, SM, and CF-P contributed to the discussion and data analysis.

FUNDING

This study received financial support from the National Natural Science Foundation of China (NSFC No. 51876183), HK PolyU (1-BE04), and US Forest Service.

ACKNOWLEDGMENTS

The authors are grateful to the HK PolyU and UC Berkeley for providing excellent experimental conditions. Meanwhile, the authors would like to thank the NSFC, HK PolyU, and US Forest Service for the experimental funding.

SUPPLEMENTARY MATERIAL

The Supplementary Material for this article can be found online at: https://www.frontiersin.org/articles/10.3389/fmech.2019.00054/full#supplementary-material

Supplementary Video 1 | Vertical test: single wood rod of 15.9-mm diameter, heat flux of 19.1 kW/m2, ignition at 642 s.

Supplementary Video 2 | Vertical test: single wood rod of 9.6-mm diameter, heat flux of 18.3 kW/m2, ignition at 314 s.

Supplementary Video 3 | Vertical test: single wood rod of 6.4-mm diameter, heat flux of 17.5 kW/m2, ignition at 316 s.

Supplementary Video 4 | Horizontal test: single wood rod of 15.9-mm diameter, heat flux of 15 kW/m2, ignition at 1114 s.

Supplementary Video 5 | Horizontal test: single wood rod of 3.2-mm diameter, heat flux of 15 kW/m2, no (flaming) ignition.

Supplementary Video 6 | Horizontal test: single wood rod of 3.2-mm diameter, heat flux of 50 kW/m2, ignition at 10 s.

Supplementary Video 7 | Horizontal test: fuel bed with 3.2-mm rod, heat flux of 15 kW/m2, ignition at 89 s.

REFERENCES

Atreya, A. (1998). Ignition of fires. *Phil. Trans. R. Soc. Lond. A* 356, 2787–2813. doi: 10.1098/rsta.1998.0298

Babrauskas, V. (2016). "The cone calorimeter," in *SFPE Handbook of Fire Protection Engineering*, ed M. Hurley (London: Springer), 952–980. doi: 10.1007/978-1-4939-2565-0_28

Boonmee, N., and Quintiere, J. G. (2002). Glowing and flaming autoignition of wood. *Proc. Combust. Inst.* 29, 289–296. doi: 10.1016/S1540-7489(02)80039-6

Boonmee, N., and Quintiere, J. G. (2005). Glowing ignition of wood: the onset of surface combustion. *Proc. Combust. Inst.* 30, 2303–2310. doi: 10.1016/j.proci.2004.07.022

Delichatsios, M. A. (2000). Ignition times for thermally thick and intermediate conditions in flat and cylindrical geometries. *Fire Saf. Sci.* 6, 233–244. doi: 10.3801/IAFSS.FSS.6-233

Drysdale, D. (1986). An introduction to fire dynamics. *Fire Safe. J.* 10, 161–162. doi: 10.1016/0379-7112(86)90046-9

Drysdale, D. (2011). *An Introduction to Fire Dynamics*, *3rd Edn*. Chichester: John Wiley & Sons, Ltd. doi: 10.1002/9781119975465

Finney, M., Cohen, J. D., McAllister, S. S., and Jolly, W. M. (2013). On the need for a theory of wildland fire spread. *Int. J. Wildl. Fire* 22, 25–36. doi: 10.1071/WF11117

Finney, M. A., Cohen, J. D., Forthofer, J. M., McAllister, S. S., Gollner, M. J., Gorham, D. J., et al. (2015). Role of buoyant flame dynamics in wildfire spread. *Proc. Natl. Acad. Sci.* 112, 9833–9838. doi: 10.1073/pnas.1504498112

Fons, W. L. (1950). Heating and ignition of small wood cylinders. *Ind. Eng. Chem.* 42, 2130–2133. doi: 10.1021/ie50490a035

Hernández, N., Fuentes, A., Reszka, P., and Fernández-pello, A. C. (2019). Piloted ignition delay times on optically thin PMMA cylinders. *Proc. Combust. Inst.* 37, 3993–4000. doi: 10.1016/j.proci.2018.06.053

Incropera, F. P. (2007). *Fundamentals of Heat and Mass Transfer, 7th Edn*. Jefferson City, MO: John Wiley&Sons, Inc.

Jolly, W. M., Cochrane, M. A., Freeborn, P. H., Holden, Z. A., Brown, T. J., Williamson, G. J., et al. (2015). Climate-induced variations in global wildfire danger from 1979 to 2013. *Nat. Commun.* 6:7537. doi: 10.1038/ncomms8537

Knudsen, J. G., and Katz, D. L. V. (1958). *Fluid Dynamics and Heat Transfer*. New York: McGraw-Hill.

Leuenberger, M., Parente, J., Tonini, M., Pereira, M. G., and Kanevski, M. (2018). Wildfire susceptibility mapping: deterministic vs. stochastic approaches. *Environ. Model. Softw.* 101, 194–203. doi: 10.1016/j.envsoft.2017.12.019

Lin, S., Sun, P., and Huang, X. (2019). Can peat soil support a flaming wildfire? *Int. J. Wildl. Fire*. doi: 10.1071/WF19018

Liu, Y., Stanturf, J., and Goodrick, S. (2010). Trends in global wildfire potential in a changing climate. *For. Ecol. Manage.* 259, 685–697. doi: 10.1016/j.foreco.2009.09.002

McAllister, S., and Finney, M. (2017). Autoignition of wood under combined convective and radiative heating. *Proc. Combust. Inst.* 36, 3073–3080. doi: 10.1016/j.proci.2016.06.110

McClure, C. D., and Jaffe, D. A. (2018). Investigation of high ozone events due to wildfire smoke in an urban area. *Atmos. Environ.* 194, 146–157. doi: 10.1016/j.atmosenv.2018.09.021

Miyamoto, K., Huang, X., Hashimoto, N., Fujita, O., and Fernandez-Pello, C. (2016). Limiting Oxygen Concentration (LOC) of burning polyethylene insulated wires under external radiation Limiting Oxygen Concentration (LOC) of burning polyethylene insulated wires under external radiation. *Fire Saf. J.* 86, 32–40. doi: 10.1016/j.firesaf.2016.09.004

Moghtaderi, B., Novozhilov, V., Fletcher, D. F., and Kent, J. H. (1997). A new correlation for bench-scale piloted ignition data of wood. *Fire Saf. J.* 29, 41–59. doi: 10.1016/S0379-7112(97)00004-0

Montiel Molina, C., Karlsson Martín, O., and Galiana Martín, L. (2019). Regional fire scenarios in Spain: linking landscape dynamics and fire regime for wildfire risk management. *J. Environ. Manage.* 233, 427–439. doi: 10.1016/j.jenvman.2018.12.066

Quintiere, J. G. (2006). *Fundamental of Fire Phenomena*. New York, NY: John Wiley. doi: 10.1002/0470091150

Rich, D., Lautenberger, C., Torero, J. L., Quintiere, J. G., and Fernandez-Pello, C. (2007). Mass flux of combustible solids at piloted ignition. *Proc. Combust. Inst.* 31, 2653–2660. doi: 10.1016/j.proci.2006.08.055

Ronchi, E., Gwynne, S. M. V., Rein, G., Wadhwani, R., Intini, P., and Bergstedt, A. (2017). *e-Sanctuary : Open Multi-Physics Framework for Modelling Wildfire Urban Evacuation.* Project Report. National Fire Protection Association.

Shen, D., Xiao, R., Fang, M., and Chow, W. (2013). Thermal-balanced integral model for pyrolysis and ignition of wood. *Korean J. Chem. Eng.* 30, 228–234. doi: 10.1007/s11814-012-0098-9

Tian, T., and Zhou, A. (2015). An ignition criterion for combustible solids integrating surface temperature and heating rate. *Fire Mater.* 39, 139–152. doi: 10.1002/fam/2237

Toledo, T., Marom, I., Grimberg, E., and Bekhor, S. (2018). Analysis of evacuation behavior in a wildfire event. *Int. J. Disaster Risk Reduct.* 31, 1366–1373. doi: 10.1016/j.ijdrr.2018.03.033

Tuyen, B., Loof, R., and Bhattacharya, S. C. (1995). Self-sustained flaming combustion and ignition of single wood pieces in quiescent air. *Combust. Sci. Technol.* 110–111, 53–65. doi: 10.1080/00102209508951916

Williams, F. A. (1977). Mechanisms of fire spread. *Symp. Combust.* 16, 1281–1294. doi: 10.1016/S0082-0784(77)80415-3

Conflict of Interest Statement: The authors declare that the research was conducted in the absence of any commercial or financial relationships that could be construed as a potential conflict of interest.

frontiers in Mechanical Engineering

ORIGINAL RESEARCH
published: 13 September 2019
doi: 10.3389/fmech.2019.00053

Air Permeability of the Litter Layer in Broadleaf Forests

Houzhi Wang[1,2]*, *Philip J. van Eyk*[3], *Paul R. Medwell*[1], *Cristian H. Birzer*[1], *Zhao F. Tian*[1], *Malcolm Possell*[2,4] *and Xinyan Huang*[5]

[1] School of Mechanical Engineering, The University of Adelaide, Adelaide, SA, Australia, [2] Bushfire and Natural Hazards CRC, Melbourne, VIC, Australia, [3] School of Chemical Engineering and Advanced Materials, The University of Adelaide, Adelaide, SA, Australia, [4] School of Life and Environmental Sciences, The University of Sydney, Sydney, NSW, Australia, [5] Research Centre for Fire Engineering, The Hong Kong Polytechnic University, Kowloon, Hong Kong

Fuel on the ground, such as leaves, twigs and decomposing matter, accumulate over time and account for a large percentage of the total fuel load in forests. In fire events, material on the ground is often referred to as a fuel bed. The air permeability of a fuel bed is a critical factor that influences fire behavior because it controls the amount of air or oxygen available for combustion within the fuel bed. The aim of this study is to provide a better understanding of the air permeability of the fuel beds in forests. The air permeability for different fuel beds were determined using experimental and theoretical methods. The pressure drop across the fuel bed samples were experimentally measured using a verified permeability testing rig. The air permeability was then calculated using Darcy's Law or the Forchheimer equation from the pressure drop measurements, depending on the Reynolds number. The particles in the fuel beds were characterized in terms of particle size and shape. Based on the particle characterization, the air permeability of the fuel beds was also calculated using the Kozeny-Carman equation. The results show that the experimental method is preferred when determining the air permeability for natural forest fuel beds due to the variability in the size and shape of the particles. The effect of Reynolds number on effective permeability was aslo investigated, and it was found that the transition from Darcian to non-Darcian flow occur at different Reynolds numbers for different fuel particles. For example, the transition occurs at 5 and 15 for gum bark and decomposing matter, respectively. The significance of this study is that it increases the ability to predict the air permeability of fuel beds in forests, which is essential for modeling wildland fire behaviors involving in porous fuel beds. All the samples were dried at 105°C to remove moisture in the samples.

Keywords: wildfires, bushfires, natural forest fuel bed, porous medium, air permeability

OPEN ACCESS

Edited by:
Satish Kumar,
Georgia Institute of Technology, United States

Reviewed by:
Wei Tang,
National Institute of Standards and Technology (NIST), United States
Daniel Thompson,
Natural Resources Canada, Canada

***Correspondence:**
Houzhi Wang
houzhi.wang@adelaide.edu.au

Specialty section:
This article was submitted to Thermal and Mass Transport, a section of the journal Frontiers in Mechanical Engineering

Received: *25 April 2019*
Accepted: *16 August 2019*
Published: *13 September 2019*

Citation:
Wang H, van Eyk PJ, Medwell PR, Birzer CH, Tian ZF, Possell M and Huang X (2019) Air Permeability of the Litter Layer in Broadleaf Forests. Front. Mech. Eng. 5:53. doi: 10.3389/fmech.2019.00053

INTRODUCTION

Wildfires are a recurring issue throughout summer and the drier months in many parts of the world. In addition to potential loss of life, wildfires cause tremendous economic loss. For example, the cost of the 2009 Victorian Black Saturday disaster in Australia is conservatively estimated at A$4.4 billion (Teague et al., 2010). Climate change is increasing the risk and impact of wildfires (Steffen and Hughes, 2013), hence greater economic impact can be expected without improved methods of wildfire mitigation. It is critical to develop a better understanding of wildfires, and

models can be a good way to provide insights into wildfires. Rothermel's model investigates the influences of the physical fuel bed properties, such as packing ratio, fuel load, bulk density, surface area-to-volume ratio, on fire spread, and intensity (Rothermel, 1972). These physical fuel properties also affect permeability. As permeability affects combustion, fire behavior in fuel beds can be better modeled by improving the physical understanding of permeability in fuel beds.

Fuel beds account for a large percentage of fuel in forests (Biswell, 1989) and are especially important for wildfires, as it accounts for a large part of the fuel (Knapp et al., 2005). Modeling of their combustion needs to consider two different combustion regimes: smoldering and flaming (Wang et al., 2017). The combustion regime of a fuel bed can be controlled by oxygen availability (Hadden et al., 2011; Santoni et al., 2014; Huang and Rein, 2016; Wang et al., 2016, 2017), which is affected by the fuel bed's air permeability. The air permeability of a fuel bed, which can be considered a porous medium, characterizes the ease with which air can pass through it. Determining the air permeability of a fuel bed is challenging because of the diversity of the material in fuel beds. In the literature, fuel beds are often characterized based on particle size in order to simplify the analysis (Anderson, 1982; El-Sayed and Khass, 2013). Previous studies of the air permeability of biomass have been only performed on regular-shaped particles, such as pine needles and soy straw; which reveals a strong dependence of particle shape on the air permeability (Erić et al., 2011; Santoni et al., 2014; Fehrmann et al., 2017; Figueroa et al., 2019). However, to the best of the authors' knowledge, no research has been done on broadleaved forest, and therefore no such data are available in literature. Fuel moisture is a critical property that influences fire behavior and ignition probabilities (Nyman et al., 2018). Previous studies have shown that solar exposure is the driving force behind forest floor drying (Nyman et al., 2015, 2018). While, the pore sizes, and hence the permeability of fuel bed, could affect water infiltration and the propensity of the material to ignite and burn. Therefore, a better understanding of the permeability of fuel bed could help explain the heterogeneity of fuel moisture as well as propensity to burn.

The permeability of a porous medium can be determined using either Darcy's Law, or the Forchheimer equation, depending on the flow regime (Bear, 2013). The fundamental principle in determining the air permeability is based on the pressure gradient, for a particular flow velocity (Sobieski and Trykozko, 2014). The air permeability in fuel beds can also be calculated using the Kozeny-Carman equation, based on the physical properties of the porous medium. The Kozeny-Carman equation has been widely applied to flow through soils, sands, and synthetic materials (Mavis and Wilsey, 1937; Kyan et al., 1970; Chapuis and Aubertin, 2003). However, the validity of the Kozeny-Carman equation has not been demonstrated for particles in other natural forest fuel beds like twigs and leaves. Natural forest fuel beds are highly variable in shape and size, which means that rather than relying on simple correlations, experimental methods are needed to determine characteristics of fuel beds. The results may subsequently be used as an input data for models.

A considerable number of studies have focused on water and oil permeability of porous media, such as rocks and soil, which is relevant to the field of geology (Chapuis et al., 1989; Kamath et al., 1995; Chapuis and Aubertin, 2003). The testing rigs presented in the literature use water as the working fluid to determine the permeability of porous media. However, these testing rigs can only be used to determine the permeability of a porous medium which is not water-sensitive. For instance, these water permeability testing rigs are not suitable for many materials, such as biomass, coal and clay, in which the absorption of water will lead to changes in particle volume and the fuel bed structure. Therefore, the determination of permeability by gaseous fluids, such as air, is needed for these materials. However, there are only a few studies that determine the permeability of a porous medium by air, the air permeability of different materials, such as snow, soil, woven fabrics, and pine litters were determined (Corey, 1957; Shimizu, 1970; Ogulata, 2006; Santoni et al., 2014). The focus of the current study is on natural forest fuel beds, and as these materials are water-sensitive this study determines their permeability by air.

The overall aim of this study is to provide a better understanding of the air permeability of fuel beds and the interaction between flaming and smoldering in wildland fires, since the air permeability has significant effects on the fire behaviors of fuel beds. First of all, it is important to find a robust method of determining the air permeability of fuel beds. It is also necessary to examine whether the fuel bed material can be characterized in a way that is suitable for providing input data into models. The experiments described in this study were designed to investigate the air permeability of natural forest litter layer, and the effects of particle size and particle type on the air permeability. Due to the lack of data in the literature, the air permeability of natural forest fuel beds will be reported.

METHODOLOGY

Experimental Apparatus

The experimental testing rig was designed to determine the air permeability of a fuel bed by measuring the pressure drop across the fuel bed. The experimental testing rig consisted of three parts: a permeability testing rig, an air supply system and a manometer (Model 9565, TSI Inc., Shoreview, United States). The air permeability testing rig shown in **Figure 1** has top and bottom sections. There is a dual air inlet and a bed of ceramic beads in the bottom section to obtain uniform flow through the fuel bed. Fuel bed samples were loaded in the top section of the air permeability testing rig.

The input air flow in this study was supplied by an air compressor, and the moisture in the input air flow was removed by a dehumidifier before introducing into the air permeability testing rig. By removing the moisture in the air, the accuracy of the input flowrate and the pressure drop measurements can be improved, and the uncertainties caused by the moisture in the ambient air can be minimized.

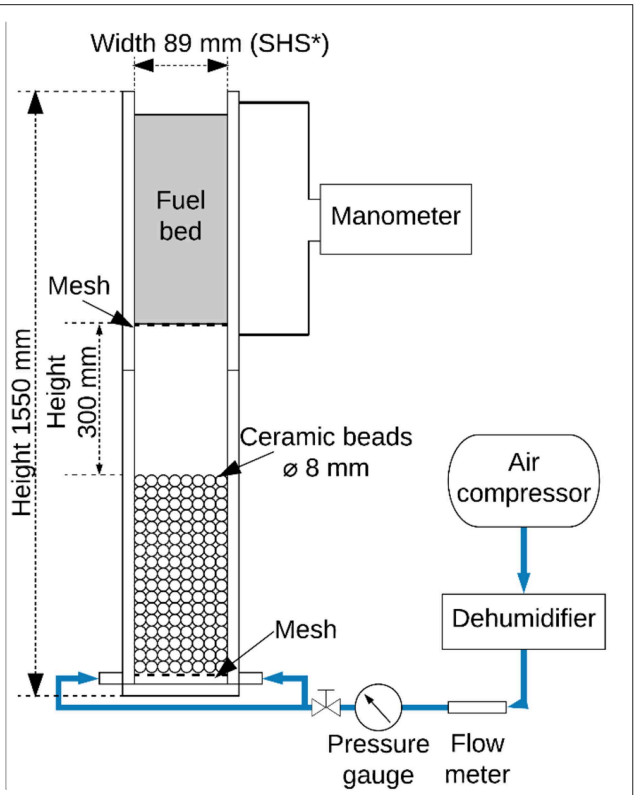

FIGURE 1 | Schematic diagram of the experimental testing apparatus for the air permeability experiments (SHS, Square hollow section; Fuel bed depth varies from 50 to 350 mm).

Experimental Setup and Procedure

The input air flow rate was varied from 20 to 160 L·min^{-1} (42–337 mm·s^{-1}), with a 20 L·min^{-1} increment. Below the lower limit (20 L·min^{-1}), the error in the pressure drop measurement significantly increases due to the range of the manometer. Above the upper limit (160 L·min^{-1}), the bed might start to fluidise. The input air flow rates (superficial velocities) in this paper were chosen to maximize the signal-to-noise ratio of the measurements; however, based on the subsequent curve-fits, these results are applicable at other flow velocities that would be encountered in a wildfire. The pressure before and after the fuel bed (**Figure 1**) was measured using the manometer through holes in the rig.

Prior to each experiment, fuel material was weighed and loaded into the rig. The fuel material was carefully loaded to create an unconsolidated fuel bed; this is to ensure the consistency throughout the fuel bed. The pressure drop (ΔP) across the fuel bed was based on a 60-s averaging period, with a 1 Hz sampling frequency.

Fuel Bed Samples Collection and Preparation

Three categories of fuel bed samples are used in this study: glass beads, milled biomass particles, and natural forest fuel particles. For the milled biomass particles, pulverized and dried pine chips, gum bark and gum leaves were used to represent the three common fuel types on forest floors, namely, leaves, bark, and twig. The pine chips samples are from *Pinus radiata*, and the bark and twig samples are from *Eucalyptus camaldulensis*. To reduce variability between samples, the pine chips, gum bark, and gum leaves were milled and sieved into three size ranges (1–2 mm; 2–3 mm; 3–4 mm).

All the forest fuel bed samples used in this study were collected from a forest in East Gippsland, Victoria (for more details about the collecting site, refer to Possell et al., 2015). This forest is located in one of the wildfire-prone areas of Victoria, Australia. Within the collecting site, three permanent circular plots with a radius of 5 m were established, at least 500 m apart, within similar vegetation types. The fuel samples were collected from these three plots, respectively. When collecting the fuel bed samples, especially the decomposing matter layer, attention was paid to ensure that inorganic matter, such as soils and sands, were not collected. After collecting the natural forest fuel bed, the samples were separated into three types: twig, leaf and decomposing matter. Then, the twig samples were sieved into three size ranges (>10 mm, 5–10 mm, <5 mm); and the decomposing matter samples were sieved into four size ranges (4–5 mm, 3–4 mm, 2–3 mm; 1–2 mm). To reduce uncertainty variability, and ensure experimental repeatability, the samples were dried sufficiently in an oven at 105°C for 24 h prior to experiments. Throughout the paper, the repeatability of measurements represented by ±1 standard deviation error bars.

Fuel Characterization

Fuel material was sieved and the fuel bed samples within each range were characterized based on physical size and projected area. The physical size of particles was measured using a micrometer and repeated for 20 samples of each fuel type. For milled biomass particles, the particle shape was assumed to be cuboid according to their apparent shapes. Hence, the length, width and thickness of particles were measured to calculate the specific area. For twigs, the samples were assumed to be cylindrical; so, the diameter and the length of twigs were measured. In the natural forest fuel particles, the projected areas of 20 randomly selected leaves were measured in order to determine the specific area, rather than assuming a regular shape. The leaf litter was not sieved due to its shape. The specific area of the decomposing matter was calculated based on the sieve aperture rather than measurements of the individual particles. The details of these measurements are listed in **Table 1**. The particle size grouping is based on the size of the sieve used to sort the material, apart from the glass beads which were monodisperse from the manufacturer.

The porosities of the different fuel beds were measured. For glass beads, the porosity was measured using the fluid saturation method, in which water was used to fill the void volume of the glass beads bed. Then, the porosity was calculated through the ratio of the void volume and the total volume of the glass beads bed ($\varepsilon = \frac{V_{void}}{V_{total}}$, where V_{void} is the void volume and V_{total} is the total volume of the glass beads bed). For the milled biomass and

TABLE 1 | Particles physical properties.

Group I: Spherical glass beads						
Type	**Particle size (mm)**	**Diameter, d (mm)**			**Specific area, S_V ($\times 10^3$ m^{-1})**	**Porosity, ε(–)**
Glass beads	6.1	6.07 ± 0.09			1.01 ± 0.02	0.393
	5.1	5.11 ± 0.03			0.85 ± 0.01	0.389
	3.8	3.83 ± 0.07			0.64 ± 0.01	0.386
	2.2	2.16 ± 0.01			0.36 ± 0.01	0.362
Group II: Milled and sieved fuels						
Type	**Particle size (mm)**	**Length, l (mm)**	**Width, w (mm)**	**Thickness, t (mm)**	**Specific area, S_V ($\times 10^3$ m^{-1})**	**Porosity, ε(–)**
Pine chips	1–2	4.26 ± 1.58	1.47 ± 0.50	0.58 ± 0.18	5.74 ± 0.91	0.457
	2–3	6.37 ± 1.78	2.50 ± 0.73	1.16 ± 0.43	3.24 ± 1.01	0.462
	3–4	9.68 ± 2.96	3.37 ± 1.04	1.63 ± 0.48	2.26 ± 0.53	0.502
Gum bark	1–2	4.13 ± 1.28	1.20 ± 0.43	0.95 ± 0.35	4.91 ± 1.34	0.608
	2–3	8.05 ± 2.44	2.25 ± 0.51	1.50 ± 0.35	2.63 ± 0.43	0.674
	3–4	8.90 ± 3.53	4.10 ± 0.70	1.83 ± 0.43	1.94 ± 0.42	0.709
Gum leaf	1–2	2.73 ± 1.36	1.38 ± 0.54	0.3	9.32 ± 1.52	0.450
	2–3	5.55 ± 2.40	2.35 ± 0.76	0.3	7.83 ± 0.42	0.508
	3–4	10.3 ± 4.40	3.53 ± 1.45	0.3	7.42 ± 0.33	0.561
Group III: Natural forest fuels						
Twig	>10 mm	250	11.5	N/A	0.36 ± 0.09	0.800
	5–10 mm	228.7 ± 57.2	6.49 ± 1.14	N/A	0.64 ± 0.10	0.828
	<5 mm	199.5 ± 48.5	2.45 ± 0.92	N/A	1.64 ± 0.24	0.942
Leaf	N/A	N/A	N/A	0.3	3.55 ± 1.02	0.955
Decomposing matter	4–5 mm	19.36 ± 6.36	7.33 ± 2.12	1.07 ± 0.80	2.25	0.550
	3–4 mm	11.95 ± 4.26	4.07 ± 1.35	0.8 ± 0.61	3.16	0.502
	2–3 mm	7.17 ± 3.24	3.10 ± 2.09	0.79 ± 0.64	3.46	0.462
	1–2 mm	4.22 ± 2.52	1.62 ± 0.74	0.40 ± 0.35	6.70	0.450

the natural forests fuel bed, the porosity was calculated based on the weight of the fuel bed and the particle density ($\varepsilon = 1 - \frac{W_{fuel\ bed}}{\rho_p \cdot V_{total}}$, where W_{fuelbed} is the weight of the fuel bed and ρ_p is the particle density), as these fuel beds are all hygroscopic. The porosity measurements are included in **Table 1**.

Figure 2 presents the mass distribution of the (a) twigs and (b) decomposing matter in the forest fuel bed. The results in **Figure 2A** imply that the thin twigs, with <5 mm particle size, contribute ∼50% of the total mass in the twig litter. Similarly, the majority of the decomposing matter is smaller than 5 mm. Even though much of the forest fuel bed visually appears large, the size distribution presented in **Figure 2** shows that the majority of the particles in the twigs and decomposing matter is smaller than 5 mm. From the point view of the air permeability, these small particles have significant effects on the air permeability of fuel bed.

Based on the results of **Figure 2**, the focus of this study is on the air permeability of small particles (<5 mm) within the fuel bed that is an unconsolidated porous medium. To better understand the air permeability of the fuel bed, three common biomass samples, pine chips, gum bark, and gum leaf were milled and sieved. By milling and sieving the particles the results can be better controlled for repeatability, but the generality of the results still applies to the actual particles in the litter layer.

Calculation of the Fuel Bed Permeability

The air permeability of a porous medium particularly an unconsolidated fuel bed can be determined from pressure gradient measurements or from the fuel bed/particle properties. In this study, both methods are used to determine the air permeability of different porous media. A schematic diagram outlining how the air permeability was determined in this study is summarized in **Figure 3**.

The pressure gradient method is an empirical approach that does not need any information about the particle properties such as particle size. For the pressure gradient method, the air permeability was directly determined from the measured pressure gradient using Darcy's Law for Darcian flow regime, while the Forchheimer equation was used to determine the air permeability and the Forchheimer coefficient within the non-Darcian flow regime. It should be noted that Darcy's Law is only applicable in the Darcian flow regime, namely when the

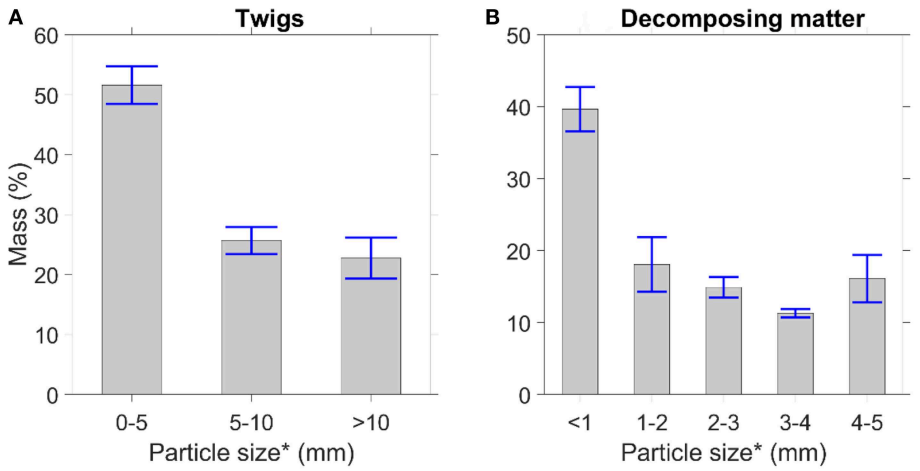

FIGURE 2 | Mass distribution as function of particle size for natural forest fuel bed. Particle size is based on sieve aperture. **(A)** Twigs. **(B)** Decomposing matter. *Sieve opening sizes.

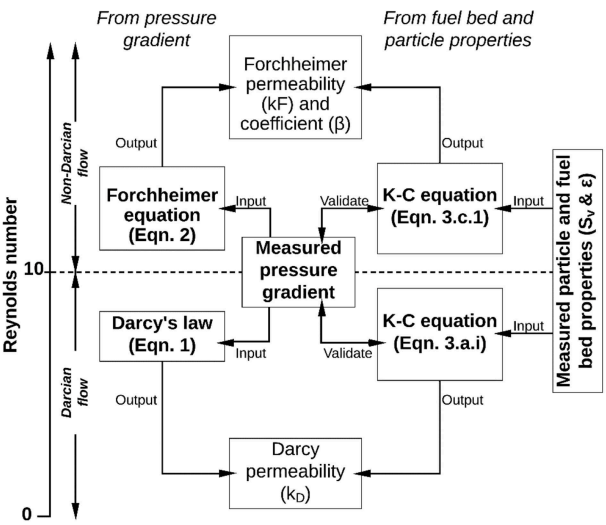

FIGURE 3 | Schematic diagram for determining the air permeability of a fuel bed.

Reynolds number, $Re_d < 10$ (Hassanizadeh and Gray, 1987; Chapman, 2012; Sukop et al., 2013). Here, $Re_d = \rho \cdot U_0 \cdot d/\mu$, where U_0 is superficial velocity and d is the average particle diameter (Sobieski and Trykozko, 2014). For non-Darcian flow ($Re_d > 10$), the Forchheimer equation may be used.

For the fuel bed/particle properties method, the specific area of particle (S_v) and the porosity (ε) of fuel bed were measured to calculate the pressure gradient and the air permeability using the Kozeny-Carman equation. The calculated pressure gradient was compared with the measured pressure gradient to validate the Kozeny-Carman equation. Similar research has been conducted on the air permeability of pine needle fuel beds and the air permeability of fuel bed was calculated using Darcy's Law and the Kozeny-Carman equation (Santoni et al., 2014). However, both Darcy's Law and the Kozeny-Carman equation (Equation 3.a) can only be applied when $Re_d < 10$ (Hassanizadeh and Gray, 1987). This is because, as the air flow velocity increases, the experimental results do not agree with Darcy's law due to inertial effects (Forchheimer, 1901).

Darcy's Law

Permeability (isotropic permeability in this study) can be determined by using Darcy's Law (Equation 1) from the pressure gradient and the superficial velocity. Darcy's Law is only valid for Darcian flow, i.e., $Re_D < 10$, i.e., lower-velocity flow.

$$\nabla P_D = \frac{\Delta P}{L} = \frac{\mu}{k_D} U_0 \tag{1}$$

Equation (1) shows that the pressure drop of Darcian flows in the porous medium is proportional to the fluid dynamic viscosity and velocity. The pressure drop of Darcian flows in porous medium is mainly attributed to the skin friction of porous medium wall surface in porous voids (particle surfaces of the fuel bed in this study).

Forchheimer Equation

The air permeability of a porous medium in a non-Darcian flow ($Re_d > 10$) can be determined based on the Forchheimer equation (Equation 2). The difference between the Forchheimer equation (Equation 2) and Darcy's Law (Equation 1) is that the Forchheimer equation includes an additional new term to incorporate the importance of kinetic energy loss due to inertial effects in non-Darcian flows. When the flow velocity increases, the pressure drop due to inertial effects (for example the change of flow cross section area in porous pores) increases and needs to be considered when Re_d is larger than 10. As a result, the relationship between the superficial velocity and the pressure gradient is a quadratic function in non-Darcian flows. The air permeability determined through the Forchheimer equation

in this paper is referred to as the Forchheimer permeability (k_F), to distinguish it from the permeability from Darcy's Law (k_D). To characterize a porous medium in non-Darcian flow, the Forchheimer permeability and the Forchheimer coefficient are required.

$$\nabla P_F = \frac{\Delta P}{L} = \frac{\mu}{k_F} U_0 + \beta \cdot \rho \cdot {U_0}^2 \tag{2}$$

The air permeability can be determined by either Darcy's Law or the Forchheimer equation, depending on the flow regime. These methods require the experimental data of the pressure gradient and the superficial velocity, which means that a similar experiment (as stated in section Experimental Apparatus) has to be conducted before using Darcy's Law or the Forchheimer equation.

Kozeny-Carman Equation

For flows through unconsolidated beds of fuel particles, the pressure gradient can be calculated from the particle and fuel bed properties using the Kozeny-Carman (K-C) equation (Equations 3.a, b; Holdich, 2002). Equation (3.a) is for Darcian flows, while Equation (3.b) is for non-Darcian flows. In the non-Darcian flow condition, a modified Reynolds number, Re_1 (Equation 5) is required to calculate the friction factor term, $\frac{R}{\rho \bullet U^2}$ (Equation 4). Within the Darcian flow regime, the air permeability can be calculated by rearranging the Kozeny-Carman equation, i.e., Equation (3.a.i). In the non-Darcian flow condition, the air permeability and the Forchheimer coefficient can be calculated by Equations (3.c.i, ii).

$$\nabla P_{KC,D} = \frac{\Delta P}{L} = \mu \left(\frac{K (1-\varepsilon)^2 {S_V}^2}{\varepsilon^3} \right) U_0 \tag{3.a}$$

From Equation (3.a), the air permeability can be calculated using the following equation based on Equation (1):

$$K_{KC,D} = \frac{\varepsilon^3}{K (1-\varepsilon)^2 {S_V}^2} \tag{3.a.i}$$

For non-Darcian flows, the friction factor can be represented using the Carman correlation (Equation 4) and the friction can be represented as a function of the modified Reynolds number (Carman, 1956; Holdich, 2002).

$$\frac{R}{\rho U^2} = \frac{5}{Re_1} + \frac{0.4}{{Re_1}^{0.1}} \tag{4}$$

The modified Reynolds number (Reynolds number varies from 4.9 to 263 in this study) is calculated using Equation (5).

$$Re_1 = \frac{\rho U_0}{(1-\varepsilon) S_V \mu} \tag{5}$$

Thus, for non-Darcian flows, the following equation can be used to calculate the pressure drop in the fuel bed.

$$\nabla P_{KC,F} = \frac{\Delta P}{L} = \left(\frac{R}{\rho U^2} \right) \frac{S_V (1-\varepsilon) \rho {U_0}^2}{\varepsilon^3} \tag{3.b}$$

By substituting the Carman correlation (Equation 4) into the friction factor, $\frac{R}{\rho \bullet U^2}$ in Equation (3.b), Equation (3.c) shows Equation (3.b) in Forchheimer form:

$$\nabla P_{KC,F} = \frac{\Delta P}{L} = \frac{5(1-\varepsilon)^2 {S_V}^2}{\varepsilon^3} \mu U_0 + \left[\frac{0.4\,(1-\varepsilon)^{1.1}\, {S_V}^{1.1} \mu^{0.1}}{\rho^{0.1} \varepsilon^3 U_0} \right] \rho {U_0}^2 \tag{3.c}$$

From Equation (3.c), the air permeability and the Forchheimer coefficient can be calculated using the following equations based on Equation (2):

$$k_{KC,F} = \frac{\varepsilon^3}{5(1-\varepsilon)^2 {S_V}^2} \tag{3.c.i}$$

$$\beta_{KC} = \frac{0.4(1-\varepsilon)^{1.1} {S_V}^{1.1} \mu^{0.1}}{\rho^{0.1} \varepsilon^3 U_0} \tag{3.c.ii}$$

To overcome the discrepancy between experimental results and Darcy's law, Forchheimer (1901) suggested adding a kinetic energy term to Darcy's Law. In this study, for the cases with Re_d >10, the air permeability was calculated using the Forchheimer equation. To calculate the air permeability of fuel bed using the Forchheimer equation, the pressure drop across fuel bed is required. The pressure drop can either be measured experimentally or calculated using the function of pressure gradient and superficial air velocity. Similarly, the Kozeny-Carman equation can be modified to account for non-Darcian flow (Equation 3.b).

Computational Fluid Dynamic Modeling

A CFD model of the testing apparatus for the air permeability has been developed and then been employed to simulate the flows in the testing apparatus with different fuel particles. For further details, please refer to **Supplementary Material Part A**.

RESULTS

Spherical Glass Beads

Due to the diversity and complexity of natural forest particles, benchmarking experiments using well-controlled particles are first presented. These not only verify the reliability of the experimental testing apparatus, but can also be used as a reference for the natural forest samples. Hence, a set of experiments were conducted using the experimental testing apparatus for regular-shaped spherical glass beads.

Figure 4A shows that, for spherical glass bead particles, the pressure gradient calculated using the Kozeny-Carman equation shows good agreement with the measured pressure drop. The results in **Figure 4A** demonstrate that the experimental testing apparatus is reliable and gives an approximate value for the pressure gradient that may be expected for forest fuels of a similar size.

The air permeability and the Forchheimer coefficient of glass beads were calculated using the Forchheimer equation, because at all of the measured flowrates in this study, the flow is non-Darcian (Re_d > 10). The comparison in **Figure 4B** between

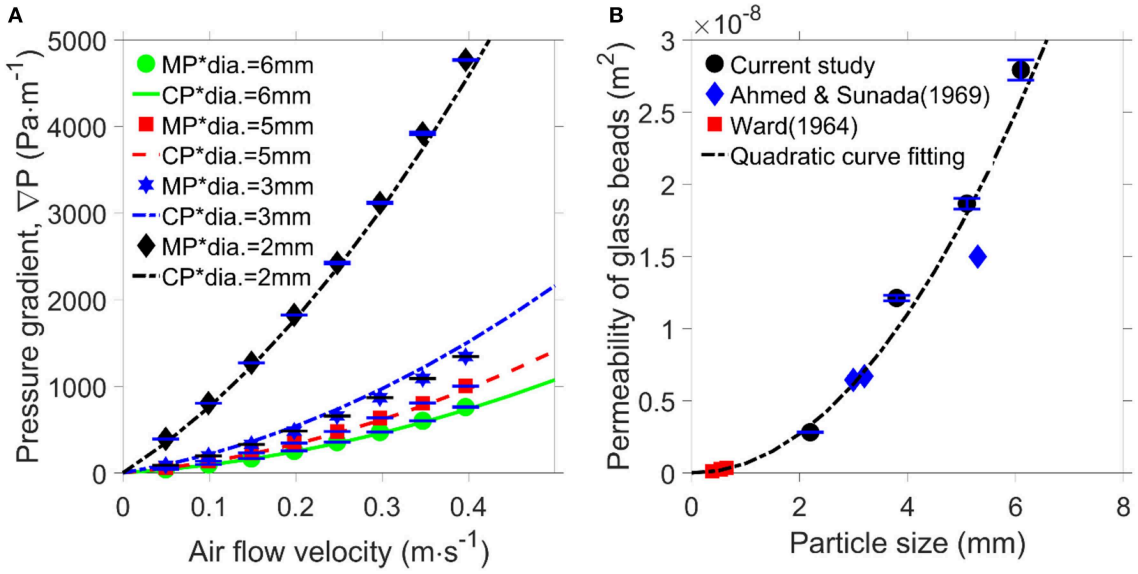

FIGURE 4 | Spherical glass bead particle results. **(A)** Pressure gradient as a function of air flow velocity for various sized particles. MP* is the measured pressure gradient and CP* is the calculated pressure gradient calculated using the Kozeny-Carman equation. **(B)** Air permeability measurement compared with previous studies (Ward, 1964; Ahmed and Sunada, 1969).

the air permeability from the current results and previous studies (Ward, 1964; Ahmed and Sunada, 1969) gives further confidence in the experimental apparatus. Worth noting is that the permeability in the current study is with air as a working fluid, whereas the previous studies used water. Permeability is a fundamental property of a porous bed and ought to be independent of the fluid (Green and Ampt, 1911), which is demonstrated in **Figure 4B**. The equation of the quadratic fitting is $k = 7.02E^{-4} \cdot d^2 - 5.34E^{-11} \cdot d$, and confidence level is. 0.9616. According to Equations (3.a.i) and (3.c.i), the permeability is in inverse proportion to the square of specific surface area (Sv). For glass beads, the specific surface area is also inversely proportional to the diameter of glass beads. Therefore, the permeability of glass beads fit with particle size in a quadratic function. Note that the pore sizes of the fuel beds in the study are much larger than the mean free path of air particles so the Klinkenberg effect can be safely neglected for air flows (Tanikawa and Shimamoto, 2006).

The air permeability can be calculated using the Kozeny-Carman equation (Equations 3.a.i or 3.c.i) if the specific area is known. In the case of a sphere of diameter D, the specific area, $S_V = \frac{6}{D}$. In both Equations (3.a.i) and (3.c.i), the permeability is inversely proportional to the square of the specific area. On this basis, **Figure 4B** includes a quadratic curve fitting which shows a good agreement with the experimental results. Hence, this confirms that a quadratic relationship between the air permeability and particle size may be used for subsequent analysis.

The Forchheimer permeability and the Forchheimer coefficient of glass beads are listed in **Table C.1**. The results of the Forchheimer coefficient show that an increase in the particle size of glass beads decreases the Forchheimer coefficient. According to the Forchheimer equation, the increase in the Forchheimer coefficient implies that the kinetic energy loss of air is higher in small particles than that in large particles.

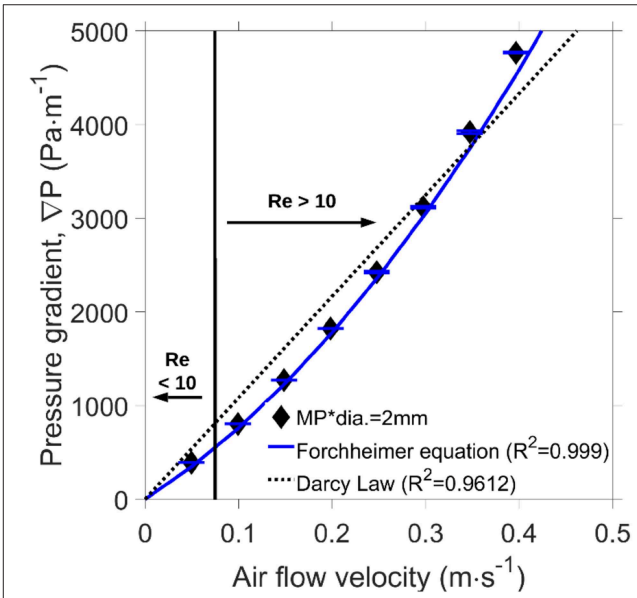

FIGURE 5 | A comparison between the Darcy law and Forchheimer equation on 2 mm spherical particles.

Table C.1 also includes measured air permeability of soy straw (Erić et al., 2011) and pine needles (Santoni et al., 2014), which are other fuel beds reported in the literature. Although the size of soy straw was not reported in the paper (Erić et al., 2011), the size of soy straw particles is typically smaller than 6 mm.

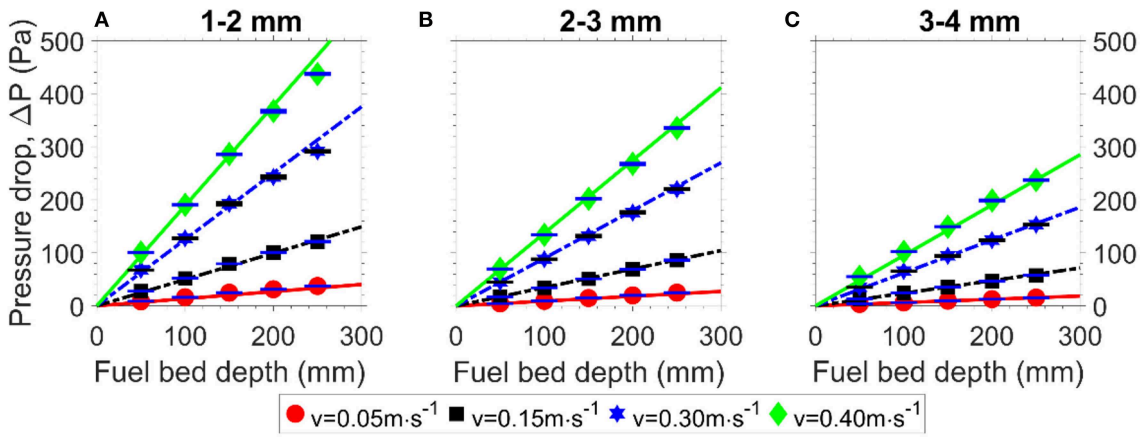

FIGURE 6 | Measured pressure drop as a function of the fuel bed depth for **(A)** 1–2 mm, **(B)** 2–3 mm, **(C)** 3–4 mm milled pine chip particles across a range of air flow velocities.

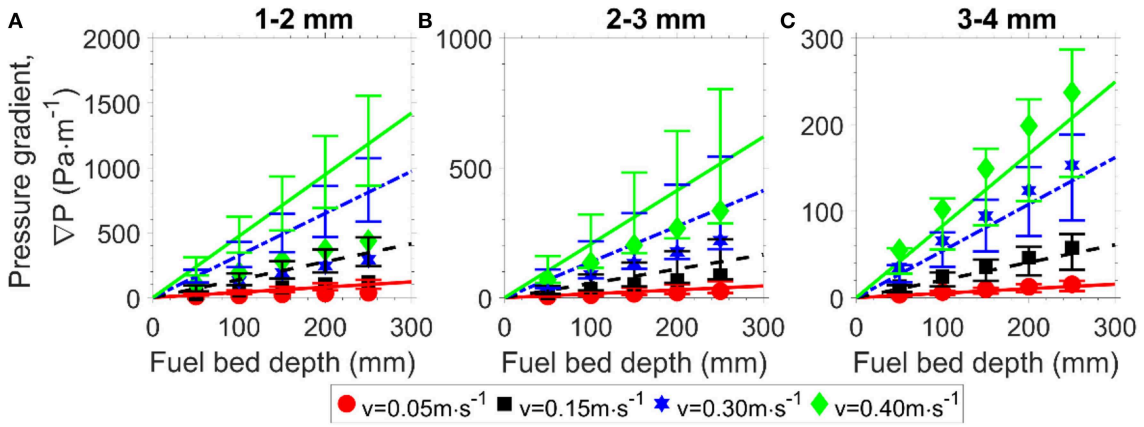

FIGURE 7 | Pressure gradient measured directly (markers) and calculated from the direct measured specific area (lines) as a function of fuel bed depth for pine chips over a range of air flow velocities. Error bars denote the calculated pressure drop based on the measure specific area through the Kozeny-Carman equation. Particle size ranges: **(A)** 1–2 mm, **(B)** 2–3 mm, **(C)** 3–4 mm.

Despite the particle size of the fuels being in the same range as the glass beads, the permeability was much higher. Hence, the results imply that particle shape has an effect on the air permeability and, therefore, needs to be determined for the irregular-shaped particles encountered within the fuel bed.

A comparison between the Darcy law and Forchheimer equation on 2 mm spherical particles is shown in **Figure 5**. The Forchheimer fitting ($R^2 = 0.999$) in **Figure 5**, shows a better agreement with the experimental data than the Darcy fitting ($R^2 = 0.9612$). This is because the Darcy law is only valid under Darcian flow ($Re < 10$); while most of the flows in this study are not in the Darcian flow regime. Hence, the Forchheimer equation should be used to determine the permeability of fuel beds.

Milled Fuel Particles

After verifying the reliability of the experimental testing apparatus using regular-shaped particles (section Results), a set of similar experiments were conducted for milled and sieved pine chips. Compared with glass beads, the milled biomass particles are more irregular in shape, and the behavior of a porous medium made from them is expected to be more complex than that of the glass beads. In the case of spherical particles, it is accepted that the pressure gradient is independent of the bed depth. In the case of the irregular biomass fuel particles, this independence has not yet been confirmed in the literature. Hence, **Figure 6** assesses the linearity of the pressure drop measurements, as a function of bed depth, for a range of different particle size milled pine chips.

Overlaid on the experimental data points in **Figure 6** are lines of best fit. It is apparent that the pressure drop across fuel bed is indeed linear with the fuel bed depth, which means that the pressure gradient of fuel bed is constant with a specific superficial velocity. In other words, the pressure gradient of fuel bed is dependent of fuel type, particle size, and superficial air velocity. Hence, the pressure drop only needs to be measured at a single fuel bed depth, and can be inferred for other depths. For the remainder of the tests,

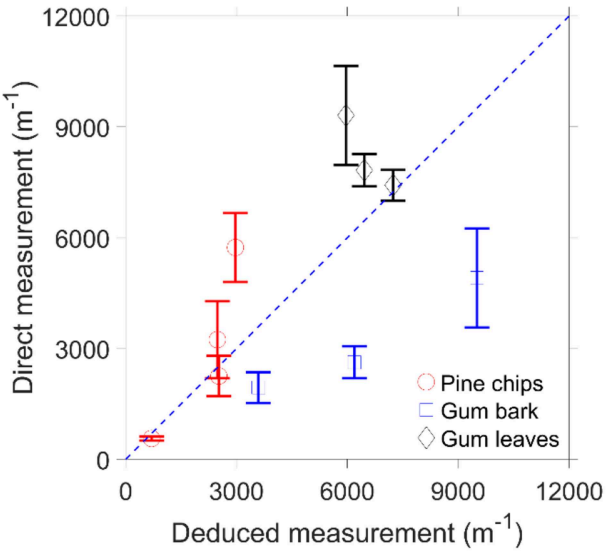

FIGURE 8 | Comparison of the direct measurement and the measurement through pressure gradient of the specific area under the different particle size.

only the deepest fuel bed was used, so as to maximize the pressure drop and thus minimize the uncertainty in the pressure gradient.

In **Figure 7**, the experimentally measured pressure drop is plotted (as per **Figure 7**) and overlaid with the calculated pressure drop using the Kozeny-Carman equation based on the direct measured specific area of the particles and porosity (**Table 1**). The error-bars on the lines are determined from the resultant variability in the specific area, i.e., one standard deviation of the mean. Even accounting for the large error-bars, the calculated pressure drop based on the Kozeny-Carman equation is consistently higher than the measured values. The discrepancy between the calculated and measured pressure drop implies that the direct measured specific area is not the actual specific area of particle. This is because the direct measured specific area assumes a regular shape, which is unlikely to be the case for the biomass fuel. The specific area and the pore structure of the actual fuel bed are different from that of the bed of regular spheres, leading to different energy losses and, therefore, different pressure drops as shown in **Figure 7**.

Based on the results of **Figure 7**, it is deduced that the Kozeny-Carman equation is not able to accurately predict the pressure drop of the actual fuel bed. This could be due to the errors in the assumptions used to determine the specific area. Instead, based on the measured pressure drop, the Kozeny-Carman equation (Equation 3.c) has been used to back-calculate the specific area. The results of this deduced specific area are compared to the direct measurements in **Figure 7** for the various particle types and sizes.

Figure 8 shows the comparison between the direct measurement of the specific area and the deduced specific area, based on the Kozeny-Carman equation and pressure drop measurement, for the milled particles. The deduced measured specific area in **Figure 8** is the average of the specific area calculated at the different superficial velocities. Hence, the specific area cannot accurately be determined for small particles, which are also the ones responsible for the majority of the pressure drop (**Figure 4**) and mass distribution (**Figure 2**) in a forest fuel bed. Therefore, to determine the pressure gradient using the Kozeny-Carman equation a correction of the direct measured specific area of the particles is required.

Figure 9 presents the measured pressure gradient (markers) and the calculated pressure gradient (lines) against the superficial velocity. The consistency between the measured and calculated pressure gradients show that the relationship between the pressure gradient and the superficial velocity is quadratic for the milled biomass fuel beds, as the pressure gradient in the Kozeny-Carman equation is a function of the square of the superficial velocity. The results in **Figure 9** also show that for the same particle size and superficial air velocity, milled gum leaf particles have the highest pressure gradient and milled gum bark has the lowest pressure gradient. The difference in pressure gradient implies that fuel type has significant effects on the pressure gradient of a fuel bed, as different fuel type results in different shapes of milled particles.

The results in **Figure 10** show that the air permeability of the fuel bed with small particles (<4 mm) is much less than that of the fuel bed with large particles (∼15 mm). Furthermore, small particles contribute much more mass in natural forest fuel beds (**Figure 2**). Hence, small particles are expected to dominate the permeability. As discussed in section Spherical Glass Beads, the relationship between the air permeability and particle size is quadratic according to the Kozeny-Carman equation. The results shown in **Figure 9** imply that the Kozeny-Carman equation is applicable for the milled biomass particles. So, theoretically, the air permeability of the milled biomass fuel beds can be presented as a function of the square of particle size. The air permeability can be calculated from either pressure gradient or the particle/fuel bed properties. However, the pressure gradient needs to be obtained by conducting the experiments because the measured specific area of particles is not robust enough for the Kozeny-Carman equation. Alternatively, the air permeability of the milled biomass fuel beds can be estimated based on the average particle size, as it is easier to measure the particle size.

The Forchheimer permeability and the Forchheimer coefficient of milled biomass fuel are listed in **Table C.2**. The results in **Table C.2** show that for the same particle size, the air permeability of the pine chips beds is similar to that of the gum bark beds. The similar air permeability between the pine chips and gum bark beds is because the shape of these two fuel particles is also quite similar. The air permeability of the gum leaf beds is much lower (approximately one fifth) than those of the pine chips and gum bark beds for the same particle size. The shape of the milled leaf particle is flaky, which makes it easier for the leaf particles to create a more

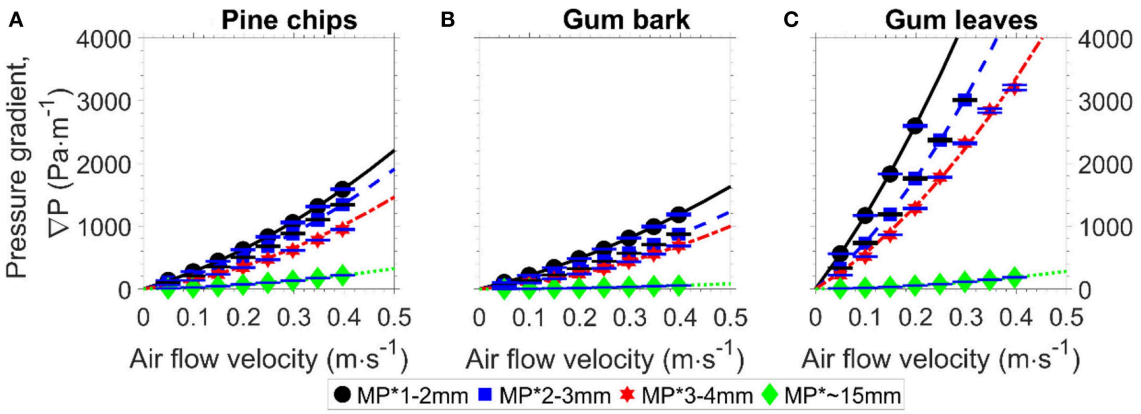

FIGURE 9 | Pressure gradient as a function of air flow velocity for particles: **(A)** pine chips, **(B)** gum bark, **(C)** gum leaves (Marker, measured pressure gradient; Line, calculated pressure gradient based on deduced measured specific area).

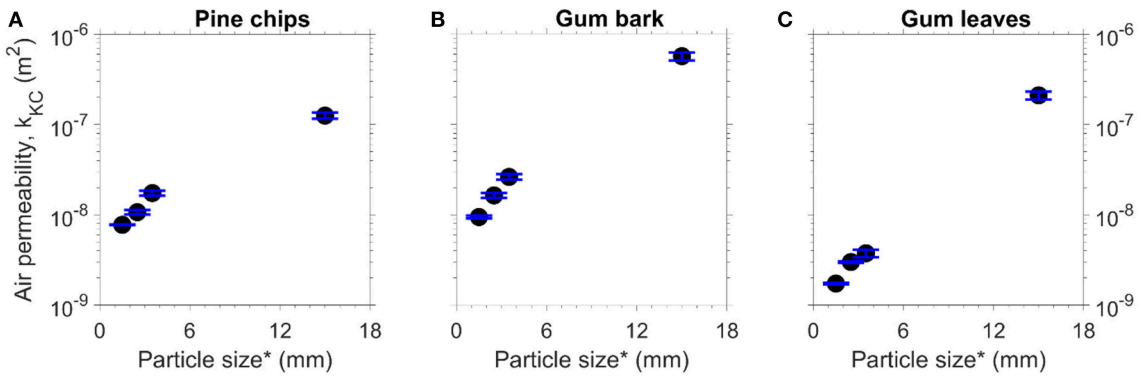

FIGURE 10 | Permeability (k) by K-C Equation as a function of particle size for the milled particles (*average sieve opening size) **(A)** pine chips, **(B)** gum bark, **(C)** gum leaves.

compact fuel bed compared to the milled pine chips and gum bark. Hence, these data imply that the particle shape has a significant effect on the air permeability, and this effect could be much higher than the effect of particle size on the air permeability.

Natural Fuel Particles

The results of the three milled biomass particles are shown in section Conclusions, where the fuel particles were broken down into small sizes using a mill. However, fuel particles in the real world are broken down through the natural decomposition processes so the shape of particles in forests may be quite different from the milled fuel particles. As discussed in section Conclusions, the particle shape has a significant effect on the air permeability. Therefore, it is important to determine the air permeability of the natural forest fuel particles.

The results in **Figure 11** suggest that it is necessary to calculate the specific area for the twig particle no matter the size of the twig particle, as the deduced specific areas do not agree with the measured specific areas. The twig samples were assumed to be cylindrical when calculating their specific area; while the twig samples are so diverse that they cannot be represented by a cylindrical particle. For the decomposing matter particles (**Figure 11**), the deduced specific areas are in good agreement with the measured specific areas.

Figure 12 shows the measured pressure gradients (markers) and the calculated pressure gradients (lines) against the superficial velocity for the natural forest fuel particles. The calculated pressure gradient was calculated using the Kozeny-Carman equation (Equation 3.c) based on the deduced measured specific area. The results in **Figure 12** show that the measured and calculated pressure gradients are in good agreement, and this implies that the fuel bed made of the natural forest fuel material can be represented using the Forchheimer equation and the Kozeny-Carman equation. In comparison to the milled biomass, for the same particle size, the pressure gradient vs. the superficial velocity curves of the decomposing matter beds are similar to those of the pine chips beds.

Based on the quadratic function of the pressure gradient and the superficial air velocity, the pressure gradient for each natural forest fuel bed particle size at a given superficial air velocity

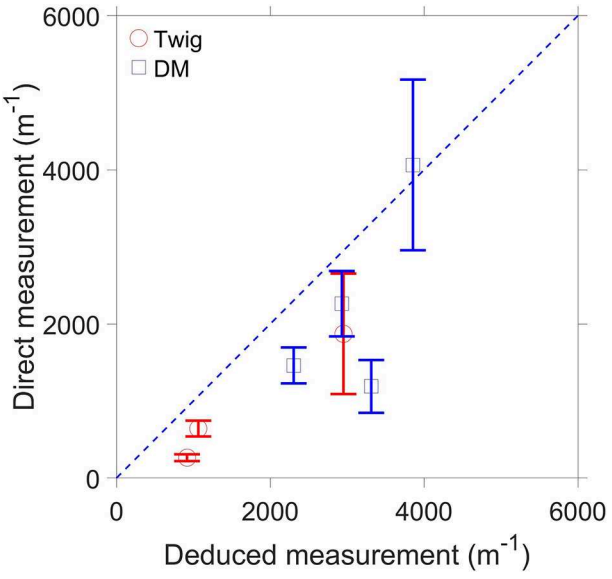

FIGURE 11 | Comparison of the direct measurement and the measurement through pressure gradient of the specific area under the different particle size. DM, decomposing matter.

can be calculated. Similarly, the Forchheimer permeability was calculated based on the Forchheimer equation and the function of the pressure gradient vs. the superficial velocity. However, similar to the milled biomass fuel particles, it is also difficult to measure the specific area of the natural forest fuel particles.

Figure 13A shows that the particle size does not have a significant effect on the air permeability for the twig particles in the range of particle sizes investigated in the current study. **Figure 13B** shows that decomposing matter shows a similar trend to the milled particles, i.e., a decrease in particle size decreases the air permeability. This is because the porosity of the twig fuel bed is much larger than that of the decomposing matter fuel bed. As shown in **Figure 12B**, the Kozeny-Carman equation is validated for the decomposing matter. Hence, the relationship between the air permeability of the decomposing matter beds and particle size is quadratic.

The Forchheimer permeability and Forchheimer coefficient of the natural forest material are listed in **Table C.3**. The results in **Table C.3** show that the Forchheimer permeability of the twig and leaf samples are much higher than that of decomposing matter, which are up to 512 times and 123 times higher for the twig and leaf samples, respectively. In comparison with the results of the milled biomass particles (**Table C.2**), it was found that for the same fuel type, the change in particle size has less effect on the air permeability than the fuel type. In the natural forest material, different fuel types have different particle shapes implying that the particle shape has a significant effect on the air permeability. Therefore, it is expected that fire behavior will be different within the different fuel beds of a natural forest due to differences in air permeability.

DISCUSSION

Darcy's Law and the Forchheimer equation are the two basic equations used to determine the air permeability of a porous medium, depending on flow regime. The Darcy permeability is not always equal to the Forchheimer permeability. Theoretically, the Darcy permeability can only be used to characterize a porous medium in Darcian flow; while the Forchheimer permeability is to characterize a porous medium in non-Darcian flow. In Darcian flows the superficial velocity is very low, leading to a small pressure drop which is difficult to measure accurately. Furthermore, the transition from Darcian to non-Darcian flow in a porous medium is vague. The transition from Darcian to non-Darcian flow can occur over a range of Reynolds number from 1 to 10 (Hassanizadeh and Gray, 1987; Tindall et al., 1999; Chapman, 2012; Bear, 2013).

The effective permeability was calculated using Darcy's law. The effective permeability (markers) and the Darcy's permeability (lines) are presented in **Figure 14**. The results in **Figure 14** show that the effective permeability starts to decrease when Reynolds number is over 10, which is the upper limit of Darcy's law. This is because when Reynolds number is equal to, or below 10, the effective permeability is equal to the Darcy permeability of fuel bed. For the samples with low air permeability (gum leaf and decomposing matter), the upper limit of Darcy's law is slightly higher than 10. This finding is also reported by Sobieski and Trykozko (2014). For these cases, the Darcy permeability is equal to the effective permeability within the Darcian flow regime.

As mentioned previously, it is difficult to measure the pressure drop across the fuel bed in Darcian flow, as the pressure drop is too low to measure. Darcy's law requires the pressure gradient to determine the Darcy permeability. Hence, a different method is needed to determine the Darcy permeability. One method is to calculate the Darcy permeability using the Kozeny-Carman equation. In this way, the Darcy permeability of a porous medium is calculated based on the specific area of particles and the porosity of the porous medium (Equation 3.c). The measured and calculated Darcy permeability for all samples is listed in **Table C.3**. Comparing the Darcy permeability in **Table C.3** with the Forchheimer permeability in **Tables C.1**, **C.2**, and **C.3**, the Darcy permeability of the decomposing matter particles is close (with a maximum difference of 25% at 3–4 mm) to the Forchheimer permeability for the same size, which means that the Darcy permeability can be assumed to be the same as the Forchheimer permeability for the decomposing matter particles.

It has been reported previously that an increase in the moisture content of soy straw fuel bed significant decreased the permeability of that fuel bed (El-Sayed and Khass, 2013). As all the samples was pre-dried in this study, it is expected that the actual permeability of fuel bed in a forest will be lower than the permeability reported in this study due to higher moisture contents.

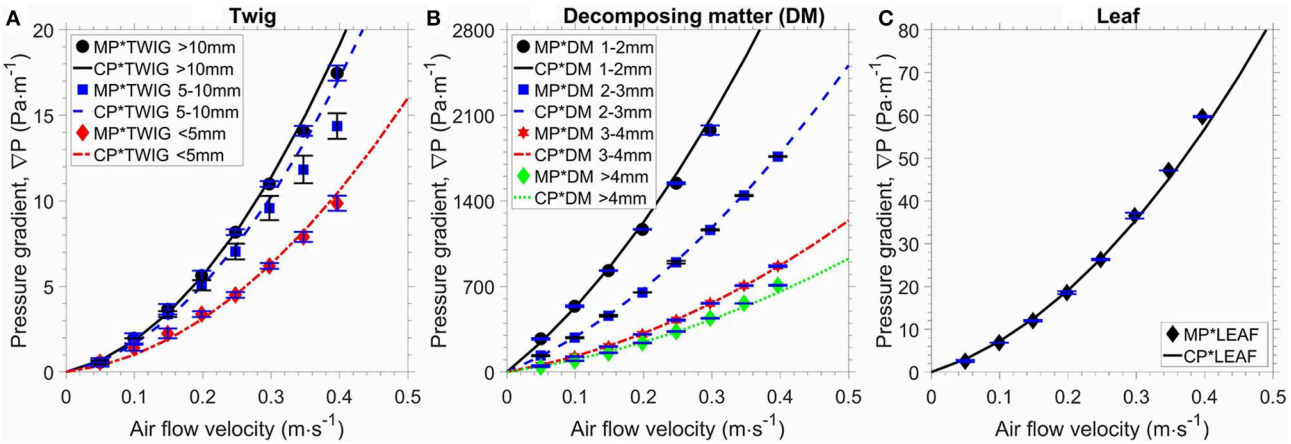

FIGURE 12 | Pressure gradient as a function of air flow velocity for particles: **(A)** twig, **(B)** decomposing matter (DM), **(C)** leaf. (MP*, measured pressure gradient; CP*, calculated pressure gradient based on the deduced measured specific area).

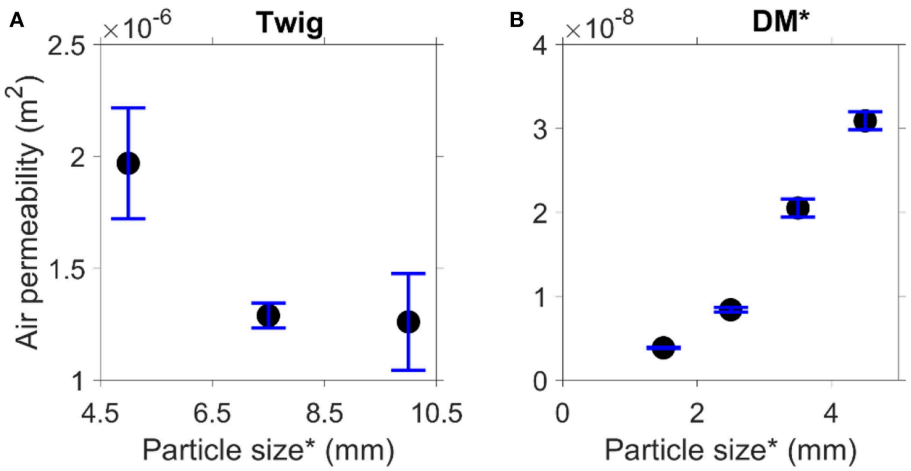

FIGURE 13 | Permeability (k) as a function of particle size (*Average sieve opening size) **(A)** twig, **(B)** decomposing matter (DM).

CONCLUSIONS

This paper investigated the air permeability of fuel beds in forests, from the perspective of its effect on the combustion of fuel beds. An experimental testing apparatus was designed and developed to investigate the effects of particle size and type on the air permeability. Three common biomass fuel types: pine chips, gum bark and gum leaf were milled and sieved into three sizes (1–2 mm; 2–3 mm; 3–4 mm). The air permeability of milled biomass fuel was also determined by experiment and calculation. The results show that the calculated pressure drop (Equation 3.c) is not in good agreement with the measured pressure drop. This is because it is difficult to accurately measure the specific area of particles due to their irregular shape. Hence, the air permeability of the porous medium made of the milled biomass particles can only be determined by experiment.

Natural forest fuel bed samples were separated into three categories: twig, leaf, and decomposing matter; and the twig and decomposing matter were sieved into three (0–5 mm; 5–10 mm; >10 mm) and four sizes (1–2 mm; 2–3 mm; 3–4 mm; >4 mm), respectively. The air permeability of a natural forest fuel bed was determined by experiment and calculation. Similar to the milled biomass fuel particles, the results show that the calculated pressure drop (Equation 3.c) does not match with the measured pressure drop due to the inaccuracy of the specific area estimations. The air permeability in natural forest fuel varies in different fuel types. For example, the air permeability of the twig layer is much larger (~500 times) than that of the decomposing matter layer. Particle size does not have a significant effect for twigs, and the relationship between the air permeability and particle size is quadratic for decomposing matter.

In most of the cases, it is difficult to run the experiments with a Darcian air flow because the pressure drop is too low to reliably measure. By determining the effective permeability, the results show that the upper limit of

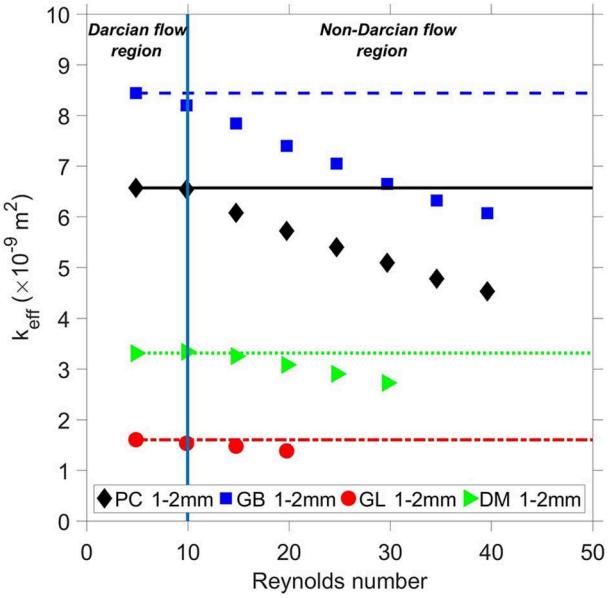

FIGURE 14 | Effective permeability (k_{eff}) as a function of Reynolds number. PC, pine chips; GB, gum bark; GL, gum leaf; DM, decomposing matter.

Darcy's law for the low air permeability fuel bed is slightly higher than 10. The Darcy permeability was calculated using the Kozeny-Carman equation and the results show that the Darcy permeability is similar to the Forchheimer permeability. More research is needed to better understand the relationship between the air permeability and the combustion of the forest fuel beds. The data presented in this paper is intended to be used for validation of subsequent models. The model can then be used to model the air flow in forest fuel beds.

DATA AVAILABILITY

The datasets for this manuscript are not publicly available. Requests to access the datasets should be directed to houzhi.wang@adelaide.edu.au. The datasets for this manuscript are included in **Supplementary Material Part B**.

AUTHOR CONTRIBUTIONS

HW conducted a thorough literature review and identified the research gaps of the paper. After discussion with the other co-authors, a detailed research methodology and experimental plan were decided. According to the plan, HW designed and developed an experiment testing rig. HW tested and calibrated the testing rig. The fuels used in this study were collected by one co-author, MP. HW prepared the fuel samples for the experiments. HW did preliminary experiments using the testing rig. HW discussed the preliminary experiments with the other co-authors, then, HW modified the testing rig based on feedback from the other co-authors. HW set up the experiments. HW conducted all the experiments and collected experimental data independently. HW processed, analyzed, and interpreted all the experimental data. HW performed an analysis of the experimental results, and the analysis was presented in text or figures by HW. HW interpreted data and wrote the manuscript. HW also acted as the corresponding author, responded to the reviewers', the editor's comments and recommendations. PE, PM, CB, ZT, MP, and XH provided feedback, supervised the development of work, helped in data interpretation, and manuscript evaluation.

ACKNOWLEDGMENTS

The support of the University of Adelaide, Australian Government Research Training Program Scholarship, the Bushfire and Natural Hazards CRC, NSFC (No. 51876183), and HK PolyU (1-BE04) are gratefully acknowledged. The authors thank Mr. Marc Simpson for his assistance throughout the experimental campaign. We also thank two reviewers for their insightful comments and suggestions on the previous versions of the manuscript.

SUPPLEMENTARY MATERIAL

The Supplementary Material for this article can be found online at: https://www.frontiersin.org/articles/10.3389/fmech.2019.00053/full#supplementary-material

REFERENCES

Ahmed, N., and Sunada, D. K. (1969). Nonlinear flow in porous media. *J. Hydraul. Div.* 95, 1847–1858.

Anderson, H. E. (1982). "Aids to determining fuel models for estimating fire behavior," in *Research Paper INT-122* (Ogden, UT: US Department of Agriculture, Intermountain Forest and Range Experiment Station), 22.

Bear, J. (2013). *Dynamics of Fluids in Porous Media*. New York, NY: Courier Corporation.

Biswell, H. H. (1989). *Prescribed Burning in California Wildlands Vegetation Management*. Berkeley, CA: University of California Press.

Carman, P. C. (1956). *Flow of Gases Through Porous Media*. Cambridge: Academic Press.

Chapman, R. E. (2012). *Geology and Water: An Introduction to Fluid Mechanics for Geologists*. The Hague: Springer Science & Business Media.

Chapuis, R. P., and Aubertin, M. (2003). *Predicting the Coefficient of Permeability of Soils Using the Kozeny-Carman Equation*. Technical Report no. EPM-RT-2003-03.

Chapuis, R. P., Gill, D. E., and Baass, K. (1989). Laboratory permeability tests on sand: influence of the compaction method on anisotropy. *Can. Geotech. J.* 26, 614–622. doi: 10.1139/t89-074

Corey, A. T. (1957). Measurement of water and air permeability in unsaturated soil 1. *Soil Sci. Soc. Am. J.* 21, 7–10. doi: 10.2136/sssaj1957.03615995002100010003x

El-Sayed, S., and Khass, T. (2013). Smoldering combustion of rice husk dusts on a hot surface. *Combust. Explo. Shock Waves* 49, 159–166. doi: 10.1134/S0010508213020056

Erić, A., Dakić, D., Nemoda, S., Komatina, M., and Repić, B. (2011). Experimental method for determining Forchheimer equation coefficients related to flow of air through the bales of soy straw. *Int. J. Heat*

Mass Transf. 54, 4300–4306. doi: 10.1016/j.ijheatmasstransfer.2011.05.015

Fehrmann, S., Jahn, W., and de Dios Rivera, J. (2017). Permeability comparison of natural and artificial pinus radiata forest litters. *Fire Technol.* 53, 1291–1308. doi: 10.1007/s10694-016-0631-1

Figueroa, S., Rivera, J. d. D., and Jahn, W. (2019). Influence of permeability on the rate of fire spread over natural and artificial pinus radiata forest litter. *Fire Technol.* 55, 1085–1103. doi: 10.1007/s10694-019-00824-w

Forchheimer, P. (1901). Wasserbewegung durch boden. *Zeitz. Ver. Duetch Ing.* 45, 1782–1788.

Green, W. H., and Ampt, G. (1911). Studies on soil phyics. *J. Agric. Sci.* 4, 1–24. doi: 10.1017/S0021859600001441

Hadden, R. M., Scott, S., Lautenberger, C., and Fernandez-Pello, A. C. (2011). Ignition of combustible fuel beds by hot particles: an experimental and theoretical study. *Fire Technol.* 47, 341–355. doi: 10.1007/s10694-010-0181-x

Hassanizadeh, S. M., and Gray, W. G. (1987). High velocity flow in porous media. *Transp. Porous Media* 2, 521–531. doi: 10.1007/BF00192152

Holdich, R. G. (2002). *Fundamentals of Particle Technology*. Nottingham: Midland Information Technology and Publishing.

Huang, X., and Rein, G. (2016). Interactions of Earth's atmospheric oxygen and fuel moisture in smouldering wildfires. *Sci. Total Environ.* 572, 1440–1446. doi: 10.1016/j.scitotenv.2016.02.201

Kamath, J., de Zabala, E., and Boyer, R. (1995). Water/oil relative permeability endpoints of intermediate-wet, low-permeability rocks. *SPE Format. Eval.* 10, 4–10. doi: 10.2118/26092-PA

Knapp, E. E., Keeley, J. E., Ballenger, E. A., and Brennan, T. J. (2005). Fuel reduction and coarse woody debris dynamics with early season and late season prescribed fire in a Sierra Nevada mixed conifer forest. *Forest Ecol. Manage.* 208, 383–397. doi: 10.1016/j.foreco.2005.01.016

Kyan, C. P., Wasan, D., and Kintner, R. (1970). Flow of single-phase fluids through fibrous beds. *Indus. Eng. Chem. Fundam.* 9, 596–603. doi: 10.1021/i160036a012

Mavis, F., and Wilsey, E. (1937). Filter sand permeability studies. *Eng. News Rec.* 118, 299–300.

Nyman, P., Baillie, C. C., Duff, T. J., and Sheridan, G. J. (2018). Eco-hydrological controls on microclimate and surface fuel evaporation in complex terrain. *Agric. Forest Meteorol.* 252, 49–61. doi: 10.1016/j.agrformet.2017.12.255

Nyman, P., Metzen, D., Noske, P. J., Lane, P. N. J., and Sheridan, G. J. (2015). Quantifying the effects of topographic aspect on water content and temperature in fine surface fuel, International Journal of Wildland *Fire*, 24, 1129–1142. doi: 10.1071/WF14195

Ogulata, R. T. (2006). Air permeability of woven fabrics. *J Text. Apparel Technol. Manage.* 5, 1–10. Available online at: https://textiles.ncsu.edu/tatm/wp-content/uploads/sites/4/2017/11/Ogulata_Full_199-06.pdf

Possell, M., Jenkins, M., Bell, T., and Adams, M. (2015). Emissions from prescribed fire in temperate forest in south-east Australia: implications for carbon accounting. *Biogeoscience* 12, 257–268. doi: 10.5194/bg-12-257-2015

Rothermel, R. C. (1972). "A mathematical model for predicting fire spread in wildland fuels," in *Research Paper INT-115* (Ogden, UT: US Department of Agriculture, Intermountain Forest and Range Experiment Station), 40.

Santoni, P., Bartoli, P., Simeoni, A., and Torero, J. (2014). Bulk and particle properties of pine needle fuel beds–influence on combustion. *Int. J. Wildl. Fire* 23, 1076–1086. doi: 10.1071/WF13079

Shimizu, H. (1970). Air permeability of deposited snow. *Contrib. Inst. Low Temperature Sci.* 22, 1–32.

Sobieski, W., and Trykozko, A. (2014). *Darcy's and Forchheimer's Laws in Practice. Part 1. The Experiment*. Technical Sciences/University of Warmia and Mazury, Olsztyn.

Steffen, W., and Hughes, L. (2013). *The Critical Decade 2013, Climate Change Science, Risks and Responses*. Canberra: Climate Commission; Department of Industry; Innovation, Climate Change, Science, Research and Tertiary Education; Commonwealth of Australia.

Sukop, M. C., Huang, H., Alvarez, P. F., Variano, E. A., and Cunningham, K. J. (2013). Evaluation of permeability and non-Darcy flow in vuggy macroporous limestone aquifer samples with lattice Boltzmann methods. *Water Resour. Res.* 49, 216–230. doi: 10.1029/2011WR011788

Tanikawa, W., and Shimamoto, T. (2006). Klinkenberg effect for gas permeability and its comparison to water permeability for porous sedimentary rocks. *Hydrol. Earth Syst. Sci. Discuss.* 3, 1315–1338. doi: 10.5194/hessd-3-1315-2006

Teague, B., McLeod, R., and Pascoe, S. (2010). *Final Report, 2009 Victorian Bushfires Royal Commission*. Parliament of Victoria, Melbourne, VIC.

Tindall, J. A., Kunkel, J. R., and Dean, E. A. (1999). *Unsaturated Zone Hydrology for Scientists and Engineers*. Prentice Hall, Upper Saddle River, NJ.

Wang, H., van Eyk, P. J., Medwell, P. R., Birzer, C. H., Tian, Z. F., and Possell, M. (2016). Identification and quantitative analysis of smoldering and flaming combustion of radiata pine. *Energy Fuels* 30, 7666–7677. doi: 10.1021/acs.energyfuels.6b00314

Wang, H., van Eyk, P. J., Medwell, P. R., Birzer, C. H., Tian, Z. F., and Possell, M. (2017). Effects of oxygen concentration on radiation-aided and self-sustained smoldering combustion of radiata pine. *Energy Fuels* 31, 8619–8630. doi: 10.1021/acs.energyfuels.7b00646

Wang, S., Huang, X., Chen, H., and Liu, N. (2017). Interaction between flaming and smouldering in hot-particle ignition of forest fuels and effects of moisture and wind. *Int. J. Wildl. Fire* 26, 71–81. doi: 10.1071/WF16096

Ward, J. (1964). Turbulent flow in porous media. *J. Hydraul. Div.* 90, 1–12.

Conflict of Interest Statement: The authors declare that the research was conducted in the absence of any commercial or financial relationships that could be construed as a potential conflict of interest.

NOMENCLATURE

d Glass bead diameter [mm]
k Air permeability [m^2]
K Kozeny constant (about 5) (Holdich, 2002)
l Length of the fuel particle [mm]
L Length of the fuel bed [m]
R Drag force in Equation (4) [N]
Re Modified Reynolds number in Equation (5)
S_V Specific surface area [m^{-1}]
t Thickness of the fuel particle [mm]
U_0 Superficial velocity [$m \cdot s^{-1}$]
U Interstitial velocity [$m \cdot s^{-1}$]
w Width of the fuel particle [mm]
ΔP Total pressure drop [Pa]
∇P Pressure gradient [Pa/m]

Greek symbols

β Forchheimer coefficient [m^{-1}]
ε Porosity of fuel bed [-]
μ Dynamic viscosity [Pa·s]
ρ density of air [$kg \cdot m^{-3}$]

Subscripts

D Darcian flows or Darcy's Law
DM decomposing matter
F Forchheimer Law
GB gum bark
GL gum leaf
KC Kozeny-Carman equation
PC pine chips
t twig.

frontiers in Mechanical Engineering

REVIEW
published: 18 September 2019
doi: 10.3389/fmech.2019.00049

Review of the Transition From Smouldering to Flaming Combustion in Wildfires

Muhammad A. Santoso[1], *Eirik G. Christensen*[1], *Jiuling Yang*[2] *and Guillermo Rein*[1]*

[1] Department of Mechanical Engineering, Imperial College London, London, United Kingdom, [2] State Key Laboratory of Fire Science, University of Science and Technology of China, Hefei, China

Wildfires are uncontrolled combustion events occurring in the natural environment (forest, grassland, or peatland). The frequency and size of these fires are expected to increase globally due to changes in climate, land use, and population movements, posing a significant threat to people, property, resources, and the environment. Wildfires can be broadly divided into two types: smouldering (heterogeneous combustion) and flaming (homogeneous combustion). Both are important in wildfires, and despite being fundamentally different, one can lead to the other. The smouldering-to-flaming (StF) transition is a quick initiation of homogeneous gas-phase ignition preceded by smouldering combustion, and is considered a threat because the following sudden increase in spread rate, power, and hazard. StF transition needs sufficient oxygen supply, heat generation, and pyrolysis gases. The unpredictable nature of the StF transition, both temporally and spatially, poses a challenge in wildfire prevention and mitigation. For example, a flaming fire may rekindle through the StF transition of an undetected smouldering fire or glowing embers. The current understanding of the mechanisms leading to the transition is poor and mostly limited to experiments with samples smaller than 1.2 m. Broadly, the literature has identified the two variables that govern this transition, i.e., oxygen supply and heat flux. Wind has competing effects by increasing the oxygen supply, but simultaneously increasing cooling. The permeability of a fuel and its ability to remain consolidated during burning has also been found to influence the transition. Permeability controls oxygen penetration into the fuel, and consolidation allows the formation of internal pores where StF can take place. Considering the high complexity of the StF transition problem, more studies are needed on different types of fuel, especially on wildland fuels because most studied materials are synthetic polymers. This paper synthesises the research, presents the various StF transition characteristics already in the literature, and identifies specific topics in need of further research.

Keywords: fire, forest, flame, wildland urban interface, polymer

OPEN ACCESS

Edited by:
Michael John Gollner, University of Maryland, College Park, United States

Reviewed by:
Sara McAllister, Rocky Mountain Research Station, United States Forest Service, United States
Chris Lautenberger, California Polytechnic State University, United States

***Correspondence:**
Guillermo Rein
g.rein@imperial.ac.uk

Specialty section:
This article was submitted to Thermal and Mass Transport, a section of the journal Frontiers in Mechanical Engineering

Received: *26 February 2019*
Accepted: *24 July 2019*
Published: *18 September 2019*

Citation:
Santoso MA, Christensen EG, Yang J and Rein G (2019) Review of the Transition From Smouldering to Flaming Combustion in Wildfires. Front. Mech. Eng. 5:49. doi: 10.3389/fmech.2019.00049

INTRODUCTION TO SMOULDERING COMBUSTION

Smouldering combustion is the slow, low-temperature, flameless burning of porous fuels, and the most persistent type of combustion phenomena (Rein, 2016). A wide range of materials can undergo smouldering, such as cellulosic insulation, coal, polyurethane (PU) foam, cotton, wood, and peat, making smouldering a serious hazard in both residential and wildland areas. In particular,

TABLE 1 | Smouldering and flaming combustion characteristics (Hadden et al., 2014; Rein, 2016).

Characteristics	Smouldering	Flaming
Peak temperature [°C]	450–700	1,500–1,800
Typical spread rate [mm/min]	1	100
Effective heat of combustion [kJ/kg]	6–12	16–30
Ignition source [kW/m^2]	8	30

the hazard of wildfire increases at the wildland urban interface (WUI), where wildfire fronts meet houses and urban sites. In such an event, two types of fuels are involved, i.e. WUI and wildland fuels. WUI fuels are found in the built environment (e.g., polymers and timber), where the smouldering-to-flaming (StF) transition has been investigated in more studies than wildland fuels (e.g., leaves, twigs, and organic soils), which are rarely discussed in the literature. In any fuel, both smouldering and flaming can occur, and one can lead to the other (Rein, 2016).

The chemical pathways of solid fuel combustion can be broadly simplified to the following equations (Equations 1–3). Notably, smouldering (Equation 2) and flaming (Equation 3) fires of solid fuel. Although flaming is characterisitically different from smouldering; smouldering is the heterogeneous reaction of solid fuel with an oxidiser, whereas flaming is the homogeneous reaction of gaseous fuel with an oxidiser, which releases more heat (**Table 1**); the two fires have their genesis from the same process, namely, pyrolysis (Equation 1).

Pyrolysis:

$$\textit{Fuel}\ (\textit{solid}) + \textit{Heat} \rightarrow \textit{Pyrolyzate}\ (\textit{gas}) + \textit{Char}\ (\textit{solid}) + \textit{Ash}\ (\textit{solid}) \quad (1)$$

Heterogeneous oxidation (smouldering):

$$\textit{Char}\ (\textit{solid}) + O_2\ (\textit{gas}) \rightarrow \textit{Heat} + CO_2 + H_2O + \textit{other gases} + \textit{Ash}\ (\textit{solid}) \quad (2)$$

Gas-phase oxidation (flaming):

$$\textit{Pyrolyzate}\ (\textit{gas}) + O_2\ (\textit{gas}) \rightarrow \textit{Heat} + CO_2 + H_2O + \textit{other gases} \quad (3)$$

The commonality of pyrolysis (Equation 1) prior to both smouldering and flaming combustion allows the transition between them. In one case, a flaming fire can extinguish, and a smouldering fire can proceed in a flaming-to-smouldering transition. This transition may have significant effects on soil consumption during wildfires, as flaming fires quickly spread over the surface of the forest floor and consume shallow layers of ground fuels, while smouldering occurs both above- and belowground, slowly releasing vast amounts of carbon, and is far more detrimental to the ecosystem. For example, during peat fires in Indonesia in 1997, it was found that smouldering combustion consumed organic soils as deep as 51 ± 5 cm and released approximately 2.57 Gt of carbon (Page et al., 2002). At the global scale estimate, the average annual greenhouse gas emissions from smouldering fires are equivalent to 15% of man-made emissions (Rein, 2013). Owing to its low temperature, propensity to travel belowground, and flameless characteristics, smouldering of organic soils is difficult to detect (Page et al., 2002; Rein et al., 2008; Rein, 2016). Additionally, when detected, smouldering is notoriously difficult to extinguish, requiring vastly greater quantities of water (Hadden and Rein, 2011; Rein, 2016; Ramadhan et al., 2017; Ratnasari et al., 2018).

In Southeast Asia, this flaming-to-smouldering transition is common, as it is frequently used in agricultural practices to clean the land and return nutrients for use in plantations—this practice is typically referred to as slash and burn (**Figure 1**). These practices can lead to widespread peat fires during prolonged dry spells, such as El Nino, and are often the cause of dramatic haze episodes, such as those regularly recorded in Indonesia (Page et al., 2002; Huijnen et al., 2016). Additionally, smouldering wildfire produces more toxic compounds per kilogram of fuel compounds than flaming (Rein, 2016; Hu et al., 2019), and due to the low temperature causing weakly buoyant plumes, smoke can be blown into nearby cities, causing severe degradation of air quality and significant adverse health effects (World Health Organization, 2006; Rein, 2016; Hu et al., 2018). In 2015, the haze episode caused an economic loss of 16 billion US$ to Indonesia, not including economic losses to the other affected countries, such as Malaysia, Singapore, and Brunei Darussalam[1].

However, the more dramatic transition is StF, as it represents a sudden increase in spread rate, power, and hazard (**Table 1**). Smouldering ignition requires less energy than flaming ignition, and as such, the StF transition provides a path to flaming *via* heat sources too weak to directly ignite a flame (Hadden et al., 2014). In addition, based on the review of research of fire spread in WUI fires, Caton et al. (2017) identify StF transition as one of the pathways of building fire spread in the WUI fires. There is a rather informal technical term used to express the reignition of fire that previously has been extinguished, i.e., rekindle (NWCG, 2012). StF transition can be one of the mechanisms leading to rekindling in wildfire. This is further discussed in the section *Embers and StF Transition in Wildfires*.

In addition to heat flux from the flame, embers generated by wildfires are a major cause of wildfires spread and ignition in WUI building (Mell et al., 2010). Embers (also called as firebrands or firedrops) are pieces of hot or burning fuel lofted by the plume of the fire (Fernandez-Pello, 2017) (**Figure 2**). Once accumulated, embers can cause WUI structures such as roofing material, decks, and vents to smolder and, in some cases, transition to flaming. The generation of embers, its transport and the vulnerability of ignition of WUI fuels due to flaming and smouldering embers have been widely investigated (Manzello et al., 2008, 2009, 2012, 2017; Manzello, 2014; Manzello and Suzuki, 2014, 2017; Suzuki et al., 2015; Zhou et al., 2015; Hakes et al., 2018). Embers also provide an alternative mode of fire spread during wildfires through spotting, whereby embers land and locally ignite dry fuels, often transitioning from StF and thus

[1]Haze fires cost Indonesia S$ 22 b, twice the tsunami bill: World Bank, *The Straits Times*, Singapore, 16 December 2015.

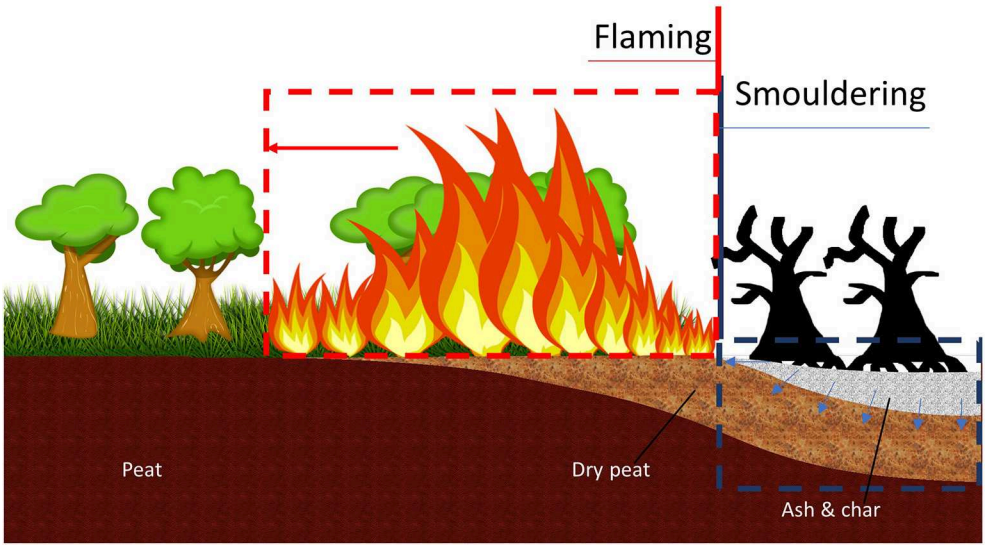

FIGURE 1 | Simultaneous occurrence of smouldering and flaming in peatland forest fires. Flaming wildfire consumes surface fuel vegetation and tree crowns. Smouldering combustion consumes organic soil, dominantly spreading on and below the ground.

advancing the flame (**Figure 2**). This particular behaviour can be highly hazardous to firefighters who may quickly find themselves surrounded by flames. Moreover, the current codes and standards of WUI represent a lack of understanding of how WUI structure can ignite during wildfire, one of which is the WUI structural vulnerability to ember showers (Manzello and Quarles, 2017; Manzello et al., 2018).

Despite the significant risks associated with the transition from StF, limited research is available on the topic, and a fundamental theory of the phenomena has yet to be found. Current research has identified a few key mechanisms but has also found that the transition is inherently difficult to predict. This unpredictable nature of the StF transition both temporally and spatially poses an additional challenge in wildfire prevention and mitigation. This paper aims to synthesise findings in the literature of the StF transition and identify the leading mechanisms and key influencing variables for both wildland and WUI fuels to identify further research required to fully understand the StF transition.

FIGURE 2 | Ember shower during the 2018 Delta Fire in the Shasta-Trinity National Forest, California, USA. Photo courtesy of Noah Berger/Associated Press (noahbergerphoto.com). Photo shows flaming fires of grass due to embers, representing a smouldering-to-flaming transition from embers.

ROLE OF OXYGEN SUPPLY AND HEAT TRANSFER

Airflow has been frequently found to be a factor that influences the StF transition, as it increases the oxygen supply into the reaction zone, increasing the smouldering spread rate. The StF transition is likely to occur with increasing smouldering spread rate as the intensity of combustion and rate of pyrolysis increase, resulting in a greater mass flux of pyrolyzates. Palmer (1957) particularly described that the StF transition was preceded by glowing, which is the visual indication of a high local temperature due to strong smouldering (Rein, 2016). Notably, the wind direction relative to the spread is also markedly important to the spread dynamics of smouldering. Forward smouldering propagates in the same direction as the airflow, whereas opposed smouldering propagates against the flow of air (Rein, 2016). Forward and opposed smouldering propagations represent different heat transfer mechanisms that influence the heating process of the fuel (Ohlemiller, 1985; Rein et al., 2007; Rein, 2009, 2016), thus affecting the occurrence of the StF transition. In opposed smouldering, airflow carries the heat from the smouldering zone away to the ash layer, diminishing the heat supplied for heating the fuel. In forward smouldering, the airflow transfers heat from the smouldering zone to the unreacted fuel, resulting in a

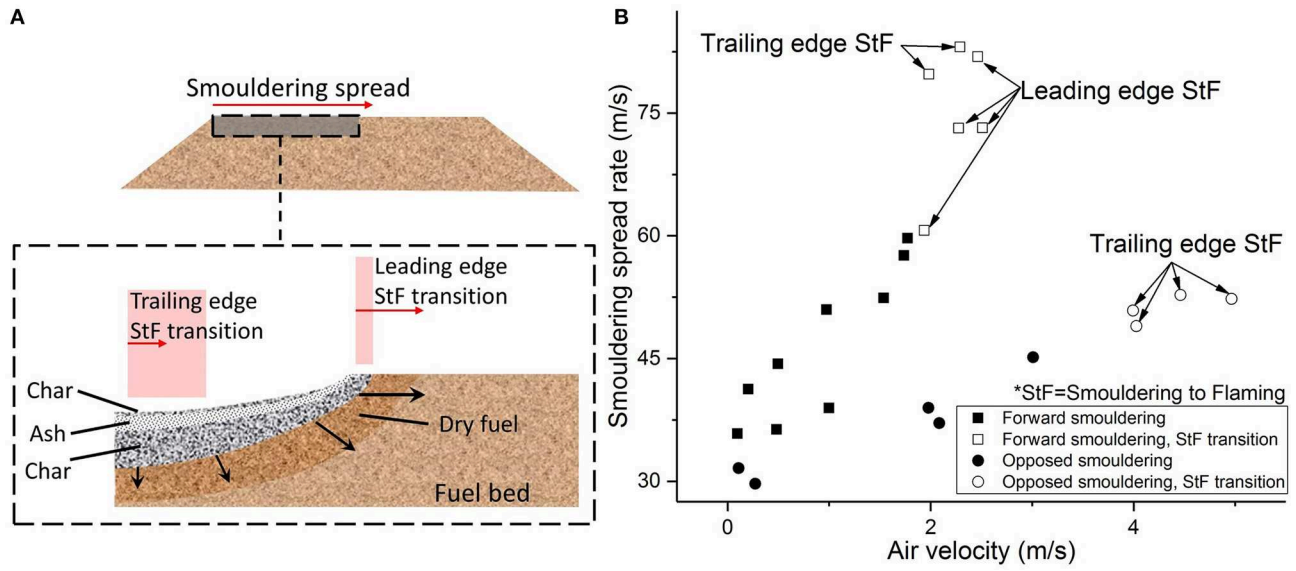

FIGURE 3 | (A) Smouldering front diagram showing leading and trailing edges of the StF transition. No significant smouldering front structures between forward and opposed smouldering in Ohlemiller (1990) other than the relative thickness of each layer, i.e., drying, char, and ash layers. The detailed smouldering front diagram is a modification from X. Huang (CC BY license) in Huang and Rein (2014). The shaded red area represents the rough estimation of the possible location for the StF transition. Red arrow indicates the duration length of the StF transition. **(B)** Smouldering spread rate of cellulosic insulation under forward and opposed smouldering propagation modes. Data from Ohlemiller (1990).

more efficient fuel heating process. The smouldering front is also narrower in opposed smouldering than in forward smouldering, representing the lower amount of heat produced in opposed smouldering (Rein et al., 2007). Due to the stronger influence of airflow on the smouldering spread rate in forward smouldering than in opposed smouldering, forward smouldering has a greater propensity for the StF transition (Palmer, 1957; Chen et al., 1990; Ohlemiller, 1990).

StF transitions can also occur under opposed smouldering (Ohlemiller, 1990, 1991; Aldushin et al., 2009) but with a lower propensity than those under forward smouldering because of the heat transfer direction discussed previously. Basically, the increase in airflow velocity plays two roles in smouldering. Airflow increases both oxygen supply to the smouldering front and convective heat loss. Increased oxygen supply increases the rate of the exothermic reaction needed to sustain smouldering, while increased convective heat losses decrease heat transfer into the unreacted fuel. The latter role is more significant in opposed smouldering propagation than in forward smouldering propagation.

Two types of StF transitions were identified by Ohlemiller (1990): trailing- and leading-edge transitions (**Figure 3A**). **Figure 3A** illustrates smouldering fronts and the location of the leading-edge and trailing-edge StF transitions. The trailing-edge StF transition occurred at the char layer at the trailing edge of the smouldering front. The flame caused by this transition was blue, lasted up to 2 min, and spread up to 10 cm on the residual char. The blue color of the flame was probably due to a lean mix of gaseous fuel with air prior to ignition. In addition to the mixture concentration, the fuel (i.e., hydrocarbon such as CO or pyrolyzate Ohlemiller, 1990) is known to affect the color of the flame, along with the tendency to produce soot. The leading-edge StF transition occurred at the leading edge of the smouldering front, spread downstream onto the unburnt layer of cellulosic insulation, and lasted up to 5 min. **Figure 3B** shows that both leading-edge and trailing-edge StF transitions occurred in forward smouldering, while only the trailing-edge StF transition occurred in opposed smouldering under an airflow of up to 5 m/s. Considering the slower smouldering spread in opposed smouldering, it can be seen that a slower smouldering spread rate results in a lower StF transition propensity.

Building on this fundamental concept of the rate of oxidation being crucial in the transition phenomena, the increase in ambient oxygen concentration has been investigated and found to have a profound effect on the StF transition. StF transitions of smouldering PU foam with no external airflow occurred at oxygen concentrations ranging from 17 to 37 vol%, depending on the ambient pressure, and only for large samples (50 × 120 × 450 mm; Ortiz-Molina et al., 1979). The samples in the form of small cylinders (18 mm in diameter) did not experience a transition. The dimensions of the sample govern the self-sustainability of smouldering since smaller samples lead to higher heat losses (Torero and Fernandez-Pello, 1995). By increasing ambient pressure, the oxygen concentration at which the StF transition occurred (critical oxygen concentration) decreased. This result implies that increased oxygen diffusion penetration into smouldering fuel under increased ambient pressure leads to lower critical oxygen concentration. However, when the ambient oxygen concentration is further increased to 35–54 vol% with assistive heating (4.5–55 kW/m^2), the StF transition can occur in

samples with characteristic lengths as small as 10–12.5 cm (Sato and Sega, 1991; Bilbao et al., 2001; Bar-Ilan et al., 2005; Putzeys et al., 2006, 2007, 2008).

It is important to note that in wildfires, the oxygen concentration will not become higher than the atmospheric oxygen concentration. In fact, the oxygen concentration can be lower. Thus, the effect of airflow velocity and particle diameter in terms of oxygen supply is the most prominent in the StF transition in wildfires. Other important parameters in wildland fuel are moisture content (MC) and inorganic content (IC). MC and IC reduce the propensity to ignition and decrease the lateral fire spread rate of wildland fuel due to their roles as heat sinks (Frandsen, 1987, 1997; Huang et al., 2016; Rein, 2016; Christensen et al., 2019; Santoso et al., 2019). MC absorbs heat for water vaporisation, and IC absorbs heat and does not contribute to further exothermic reactions due to its inert nature, contributing to increased heat losses. Interestingly, it has been recently reported that the in-depth spread rate increases with MC, which is counterintuitive to the widely assumed decrease in spread rate with MC (Huang and Rein, 2017). Thus, the lateral and in-depth spread rates in smouldering fires respond differently to MC. As MC increases, the density of organic matter per unit volume decreases and porosity increases due to volumetric expansion. The spread rates, i.e., lateral and in-depth, are limited and pre-dominantly governed by two different processes of heat loss and oxygen diffusion. However, the mechanism causing these different responses still needs further investigation. Increased propensity of the StF transition with decreased MC has been shown in both WUI and wildland fuels (Chao and Wang, 2001; Manzello et al., 2006a,b; Wang et al., 2017).

The critical velocity of the StF transition occurred as the velocity ranged from 1 to 5 m/s for studies at atmospheric oxygen concentration and without assistive heating, such as radiant heating, deposited embers, and deposited hot particle (**Table 2**). With external heat flux and increased ambient oxygen concentration, the critical velocity decreased because the convective cooling effect was minimised (Bar-Ilan et al., 2005). In turn, the decreasing convective cooling effect decreased the required heat needed to induce the StF transition. In the case of the deposition of embers at atmospheric oxygen concentration, the StF transition was found to occur at velocities as low as 1 m/s (Manzello et al., 2006a,b) or even with no airflow velocity when the assistive heating was from a hot steel particle at a temperature of ∼1,200°C (Wang et al., 2017).

In all investigated consolidated WUI fuels (**Table 2**), the StF transition occurred only if the smouldering sample was assisted with heat insulation, heated boundaries, and increased ambient oxygen concentration (Ortiz-Molina et al., 1979; Tse et al., 1996; Bar-Ilan et al., 2005; Putzeys et al., 2006, 2007, 2008; Chang et al., 2011). However, this finding is not the case when there is a radiation exchange between smouldering char surfaces (Alexopoulos and Drysdale, 1988; Ohlemiller, 1991; Stoliarov et al., 2017). In this case, the critical airflow velocity of the StF transition can be lower than 1 m/s, even without assistive external heating and elevated ambient oxygen concentration. Ohlemiller (1991) found that the StF transition consistently occurred in both forward and opposed smouldering for airflows between 0.2 and 0.25 m/s with a smouldering sample in a U-shaped geometry. The U-shaped geometry increased the radiation heat exchange between the smouldering surfaces of a wood sample. The increased radiation exchange is also the prominent factor in the StF transition mechanism hypothesised from a series of upholstered furniture fire tests (Babrauskas and Krasny, 1985, 1997; Ogle and Schumacher, 1998), as discussed further in the next section.

THE CHIMNEY EFFECT

Many StF transition investigations, especially for upholstered furniture, were conducted during the 1970s and 1980s due to the concern of residential fires in which cigarettes were considered to be the major cause of ignition (Clarke and Ottoson, 1976; Babrauskas and Krasny, 1985). From a series of tests with assorted sofas, chairs, mattresses, and box springs as test materials, the time to StF transition occurred from 20 to 132 min (Clarke and Ottoson, 1976; Bukowski et al., 1977; Harpe et al., 1977; Bukowski, 1979). It was not until the fire tests conducted by Ogle and Schumacher (1998) that the mechanism leading to the StF transition was proposed. The proposed mechanism emphasised the role of oxygen supply and air current in inducing the StF transition. Ogle and Schumacher (1998) performed 11 fire tests on 10 upholstered furniture items, where seven tests were ignited by a smouldering cigarette and four using a flaming liquid fuel. The StF transition was preceded by a "burn-through" of the smouldering cigarette at a crevice location of upholstered furniture (**Figure 4**). This "burn-through" is downward smouldering cigarette propagation through the crevice of cushions forming a narrow vertical channel due to smouldering consumption of the cushion material. The formation of this narrow vertical channel enhances the air entrainment to the smouldering zone from below due to the chimney effect. The greater air entrainment increases both oxygen supply to smouldering reaction and convective heat losses. However, the convective heat losses are compensated for by the radiation exchange between the two smouldering surfaces facing each other, which are also more exothermic due to the enhancement air entrainment. This leads to vigorous smouldering which is favourable for the StF transition.

The radiation exchange between the two smouldering char surfaces in a vertical channel influences the StF transition and induces a StF transition even at low airflow velocities, i.e., 0.1–0.27 m/s (Alexopoulos and Drysdale, 1988; Ohlemiller, 1991). In experiments of chimneys with different shapes, i.e., square, rectangular, and slot shaped, conducted by Alexopoulos and Drysdale (1988) (**Figure 5A**), the time to StF transition was found to be independent of airflow and shortest in the chimney shape with the narrowest vertical channel space, i.e. the slot-shaped chimney (**Figure 5B**). The temperatures inside the vertical channel, i.e., T_1 and T_2 (**Figure 5A**), were higher in the slot-shaped chimney than in the square and rectangular chimneys. This temperature trend and independence of the StF transition time to airflow imply that conservation of heat governs the StF transition mechanism along with oxygen supply. This

TABLE 2 | Studies of the smouldering-to-flaming transition in the literature.

Consolidation/ fuel category	Sample material	Sample shape and orientation (characteristic length [m])	Ignition source (size and duration)	smouldering spread mode	Critical velocity [m/s]	Oxygen concentration [vol%]		External heat flux [kW/m^2]		Location of transition	Time to StF transition [mm:ss]	References
						Experiment range	Critical	Experiment range	Critical			
Unconsolidated/ Wildland fuel	Pine straw mulch, Shredded hardwood mulch, Cut grass, Pine needles	Thin rectangular block/horizontal (0.23)	smouldering embers [four 50 mm (diam.) by 6 mm (thick), 1.5 g]	Forward and opposed (simultaneously)	1	21	21	N/A (ember)	N/A (ember)	Free surface	N/A	Manzello et al., 2006a and Manzello et al., 2006b
	Pine needles	Thin rectangular block/horizontal (0.31)	Spherical metal particle (Diam. 6, 8, 10, 12, 14 mm and temperature 680–1,190°C)	Forward	0–4	21	21	None	From the hot steel particle under high temperatures	Free surface	~01:40–10:20	Wang et al., 2017
	Pine needles	Thin rectangular block/horizontal (0.6)	Flaming wood stick (4 × 4 × 130 mm) on dry pine needle bed (150 × 20 × 40 mm)	Forward	1.1	21	21	None	None	Free surface	N/A	Valdivieso and Rivera, 2014
Unconsolidated/ WUI fuel	Filter paper and cardboard	Cylindrical/vertical (0.1)[#1]	Small flame (N/A)	Opposed	1.52 ± 0.82 (Filter paper) 1.73 ± 0.81 (Cardboard)	18–62	52 ± 2 (Filter paper) 44 ± 4 (Cardboard)	N/A	N/A	N/A	N/A	Sato and Sega, 1991
	Cork dust and deal sawdust[¶]	Rectangular block/horizontal (0.15–0.2)	Small flame (N/A)	Forward	1.8 ± 0.8	21	21	N/A	N/A	Free surface	N/A	Palmer, 1957
	Cellulosic insulation	Flat rectangular with wedge ends/horizontal (0.46)	Electrical heater (375°C and 60 min)	Forward and opposed	2.2 ± 0.22 (forward) 4.4 ± 0.4 (opposed)	21	21	N/A	N/A	Free surface	N/A (50:00[I])	Ohlemiller, 1990
	Wood shavings, shredded papers, beeswings*	Rectangular block/horizontal (0.61)[#2]	Electrical coil (80 V and N/A)	Forward and opposed (simultaneously)	2.23 ± 0.63 (wood shaving) 0 (Shredded paper)	21	21	N/A	N/A	N/A	02:00–76:00	Chen et al., 1990

(Continued)

TABLE 2 | Continued

Consolidation/ fuel category	Sample material	Sample shape and orientation (characteristic length [m])	Ignition source (size and duration)	smouldering spread mode	Critical velocity [m/s]	Oxygen concentration [vol%]		External heat flux [kW/m^2]		Location of transition	Time to StF transition [mm:ss]	References
						Experiment range	Critical	Experiment range	Critical			
Consolidated/ WUI fuel	*Pinus pinaster*	Thin slab/horizontal (0.11)	Spontaneous, Propane-air flame (piloted, no airflow, 10 mm flame length), Electrical spark (piloted, with airflow)	N/A	2.4 ± 1.4	21	21	10–55	35.48 ± 9.61	N/A	00:09–12:17 (spontaneous) 00:10–13:10 (Piloted)	Bilbao et al., 2001
	Fiber-insulated board	Hollow rectangular block/ vertical (0.15)	Bunsen flame	Forward	0.18 ± 0.06	21	21	N/A	N/A	Free surface	10:12–23:36	Alexopoulos and Drysdale, 1988
	Fire-retarded (FR) and Non-fire-retarded (NFR) polyurethane (PU) foam	Rectangular block/horizontal (0.1–0.4)	Electrical heater (40–200 W)	Lateral in natural convection	N/A	21	21	N/A	N/A	Free surface	60:00–138:05	Chao and Wang, 2001
	NFR PU foam	Rectangular block/vertical (0.125)	Electrical heater (23.25 W and until self-sustained smouldering identified)	Forward	0.82 ± 0.5	30–40	37.5 ± 2	7.25–8.75	8 ± 0.6	Within the sample	17:34	Bar-Ilan et al., 2005
	FR PU foam	Rectangular block/vertical (0.125)	Electrical heater (115 W and 250–300 s)	Forward	0.15	30–60	42.5 ± 7.5	4.5 or 5.5	5 ± 0.5	Within the sample	09:12	Putzeys et al., 2006
	NFR PU foam	Rectangular block/vertical (0.125)	Electrical heater (23.25 W and 11.7 min)	Forward	0.5	25 and 40	35 and 40	8 and 8.75	8 and 8.75	Within the sample	17:00 (∼16:00‡)	Putzeys et al., 2007
	PU foam (NFR and FR)	Rectangular block/vertical (0.125)	smouldering: electrical heater (23 W for NFR foam and 115 W for FR foam)	Forward	0.5 (NFR)	15–35	0.2 ± 0.02 (NFR foam)	7.25–8.75 (NFR)	5 ± 0.5 (NFR foam)	Within the sample	∼18:00 (NFR foam at 21 vol% O_2 and 8 kW/m^2)	Putzeys et al., 2008
			Pilot ignition: resistance wire (8.8 A for NFR foam and 10 A for FR foam)		0.15 (FR)		0.28 ± 0.05 (FR foam)	4.5 and 5.5 (FR)	8 ± 0.61 (FR foam)			

(Continued)

TABLE 2 | Continued

Consolidation/ fuel category	Sample material	Sample shape and orientation (characteristic length [m])	Ignition source (size and duration)	smouldering spread mode	Critical velocity [m/s]	Oxygen concentration [vol%]		External heat flux [kW/m^2]		Location of transition	Time to StF transition [mm:ss]	References
						Experiment range	Critical	Experiment range	Critical			
	NFR PU foam	Rectangular block/horizontal (0.23)[#3]	Cigarette ignition	Lateral in natural convection	N/A	21	21	None	None	N/A	~50:00	Chang et al., 2011
	NFR PU foam lined with cotton fabric	Rectangular block/vertical (0.3)	Electrical heater rod (Diam. 0.64 cm, 11 W DC)	Upward natural convection	N/A	21	21	None	None	Free surface	14:00–60:00	Stoliarov et al., 2017
	NFR PU foam	Rectangular block/vertical (0.381)	Electrical heater (70 W and 50 min)	Forward	0.78 ± 0.48	21	21	N/A	N/A	Within the sample	56:54–127:36	Tse et al., 1996
	NFR PU foam	Rectangular block/vertical (0.406)	Electrical heater (70 W and 50 min)	Forward	0.25 and 0.75	21	21	N/A	N/A	Within the sample	96:00–113:00	Tse et al., 1996
	NFR PU foam	Rectangular block/horizontal (0.45)	Heating element (N/A)	Lateral in natural convection	N/A	17–62	27.7 ± 8.1	N/A	N/A	N/A	N/A	Ortiz-Molina et al., 1979
	Red oak and White pine	U-shaped rectangular block/horizontal (0.74)	Electrical heater (N/A and 60 min)	Forward, opposed, and mixed	0.23 ± 0.03	21	21	N/A	N/A	Free surface	N/A	Ohlemiller, 1991
	Upholstered furniture	Upholstered shapes and orientations (N/A)	Cigarette and electrical ignition (N/A)	N/A	N/A	21	21	N/A	N/A	In the crevice between two cushions	18:00–306:00	Babrauskas and Krasny, 1985, 1997; Ogle and Schumacher, 1998
	Cedar, Douglas-fir, Redwood	Slab/horizontal (1.2)	Firebrand showers (17.1 ± 1.7 g/m^{2}s)	Forward and opposed (simultaneously)	6	21	21	N/A [ember(s) shower]	N/A [ember(s) shower]	Free surface	05:56–19:40	Manzello and Suzuki, 2014
	Oriented strand board (OSB); roofing assembly (OSB, tar paper, and shingles); and dried pine needles and leaves	Valley configuration of OSB; and flat configuration of roofing assembly with attached gutter filled by dried pine needles and leaves/angled position (1.22)	Firebrand showers (up to 0.4 g and 6 min)	Forward and opposed (simultaneously)	7	21	21	N/A [ember(s) shower]	N/A [ember(s) shower]	In the crevice[§] and in the gutter[8]	N/A	Manzello et al., 2008

(Continued)

TABLE 2 | Continued

Consolidation/ fuel category	Sample material	Sample shape and orientation (characteristic length [m])	Ignition source (size and duration)	smouldering spread mode	Critical velocity [m/s]	Oxygen concentration [vol%]		External heat flux [kW/m^2]		Location of transition	Time to StF transition [mm:ss]	References
						Experiment range	Critical	Experiment range	Critical			
	Cotton	Cuboid/vertical (0.15)	Electrical heater (12.8 kW/m^2 and 24 min)	Upward natural convection[#4]	N/A	21	21	None	None	Within the sample	117:00, 118:00, 133:00	Hagen et al., 2015
	OSB	Slab/horizontal (0.18)	Fire brand [L 25.4 × Ø 6.35, 9.52, 12.7 mm × piles (1 brand, 20, 50, and 100 g)]	Forward and opposed (simultaneously)	1.84	21	21	N/A [ember(s) deposition]	N/A [ember(s) deposition]	Free surface	∼01:30	Hakes et al., 2018

In some studies, the ignition source also acted as the continuous external heat flux to the sample, i.e., ember accumulation on fuel sample.

[¶]No transition to flaming in samples with particle diameters <0.1 cm.

[l]Computationally predicted by Yang et al. (2018).

[†]Computationally predicted by Dodd et al. (2012).

[*]Transition to flaming only occurred once in thin filmy pieces of bran.

[§]For material construction of valley configuration with only base material (oriented strand board).

[8]For the flat configuration of roofing assembly attached with gutters filled by dried pine needles and leaves.

[#1]Diameter varied from 0.0027 to 0.0054 m.

[#2]Depth varied from 0.1 to 0.2 m.

[#3]Width varied from 0.08 to 0.16 m.

[#4]Sample was in a cube shape and ignited at the bottom.

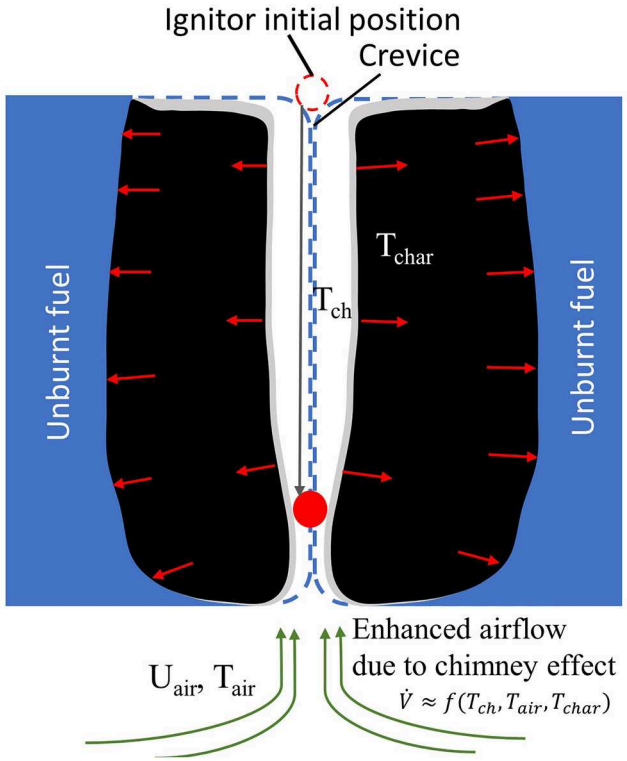

FIGURE 4 | Enhanced oxygen supply in the channel formed by downward smouldering propagation of an ignitor at the crevice location of two adjacent solid fuels. The enhanced airflow increases the oxygen supply to the smouldering fuel, leading to a more exothermic smouldering reaction. This figure is an adaptation from Ogle and Schumacher (1998).

result is in agreement with recent findings by Stoliarov et al. (2017), who performed a series of experiments of smouldering PU foam under natural convection with an adjustable vertical channel gap between the front face of the PU foam and a thermal insulation plate (**Figure 6A**). With a large gap, the oxygen supply was adequate, and smouldering was the dominant reaction (**Figure 6B**). With a smaller gap, smouldering was not the dominant reaction due to insufficient oxygen supply (**Figure 6C**). With the availability of heat from smouldering and a deficient oxygen supply, pyrolysis was more intense in the smaller gap configuration than in the larger channel gap configuration, leading to more pyrolyzates being produced. Moreover, a smaller gap might result in a higher concentration of pyrolyzates inside the channel (**Figure 6B**). The StF transition then occurred when the pyrolyzates were heated by char oxidation up to the point where the pyrolyzate temperature and concentration were above the lower flammability limit. In this case, the StF transition was a piloted ignition of pyrolyzate by char oxidation. This finding was also observed by Alexopoulos and Drysdale (1988), who found that the StF transition time was longer in wider vertical channel gaps. In another study of StF transitions in small *Pinus pinaster* wood samples with dimensions of 11 by 11 by 1.9 cm, Bilbao et al. (2001) found that the radiative heat flux affected the time to StF transition more than convection. A previous ignition study of polyurethane foam found that the critical radiation heat flux to ignite smouldering is lower than that to ignite flaming combustion and decreases with sample size (Hadden et al., 2014). This result represents the important role of radiation heat transfer in smouldering and the following possible StF transition.

The mechanism of the StF transition at a crevice location is particularly important in WUI fires, i.e., where two or more fuels abut each other such as in wood decks and house roofing. The deposition of embers in a crevice of these fuels has been experimentally investigated as a favourable location for ember accumulation that leads to a StF transition (Manzello et al., 2008; Manzello and Suzuki, 2014). Fundamentally, this follows the same mechanism as that shown in **Figure 4**. In addition, wood was found to crack during smouldering. This cracking leads to local crevice formation on the wood surface, leading to a StF transition without heating support from embers (Ohlemiller, 1991).

SECONDARY CHAR OXIDATION

The mechanism of the StF transition due to strong secondary char oxidation (SCO) was first proposed by Torero and Fernandez-Pello (1995), who conducted an experimental study of upward smouldering combustion of polyurethane foam in natural convection (**Figure 7A**). In this experiment, the StF transition was preceded by a second oxidation of char, which was more exothermic than the first. This mechanism is best discussed by referring to **Figure 7B**. Upward smouldering propagation was initiated from t_1 to t_2. At time t_2, the ignitor was turned off. By this time, smouldering had propagated up to the P_5 position. Temperatures at P_1 to P_4 can be observed to decrease, with the temperature at P_1 decreasing the most. The smouldering spread rate decreased, as indicated by a slower temperature increase in downstream positions, i.e., P_6 and P_7. P_5 and P_6 reached a plateau of the pyrolysis temperature (T_p) by the time the experiment approached time t_3. Thus, smouldering fronts propagated to these positions. SCO occurred between times t_3 and t_4. In this time period, the large temperature increase at P_1 indicates a strong char oxidation in the char layer upstream of the smouldering fronts, which is the second char oxidation in that layer. Hence, the name secondary char oxidation is assigned to this process.

Extinguishment of char oxidation at P_1 is not observed prior to SCO since temperatures were still relatively high (~500–600°C). However, its rate of exothermic reaction decreased, as indicated by the temperature decreases, most likely because of the absence of heating from the ignitor. It can be hypothesised that as the smouldering leading edge moved downstream to P_6, the smouldering trailing edge was still around P_1. This process resulted in increases in the smouldering front thickness as smouldering propagated. The term SCO then represents a sudden increase in the exothermic reaction rate at the smouldering trailing edge.

Due to oxygen consumption by secondary char oxidation (SCO), the oxygen concentration was depleted and unable to sustain further oxidation. During this time, t_4 to t_5, endothermic pyrolysis reactions induced by heat provided by previous SCO

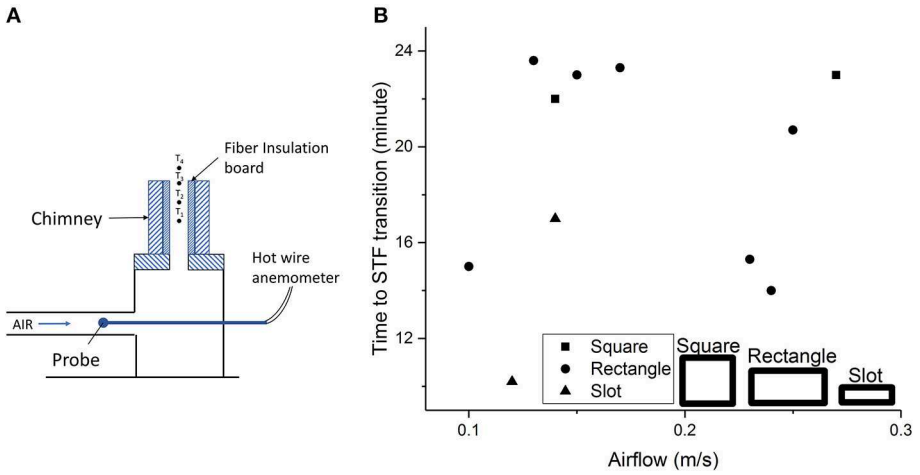

FIGURE 5 | StF transition experiments in a chimney of fiber insulation board (Alexopoulos and Drysdale, 1988). **(A)** Experimental setup of chimney configuration. **(B)** Time to StF transition vs. airflow. Data from Alexopoulos and Drysdale (1988).

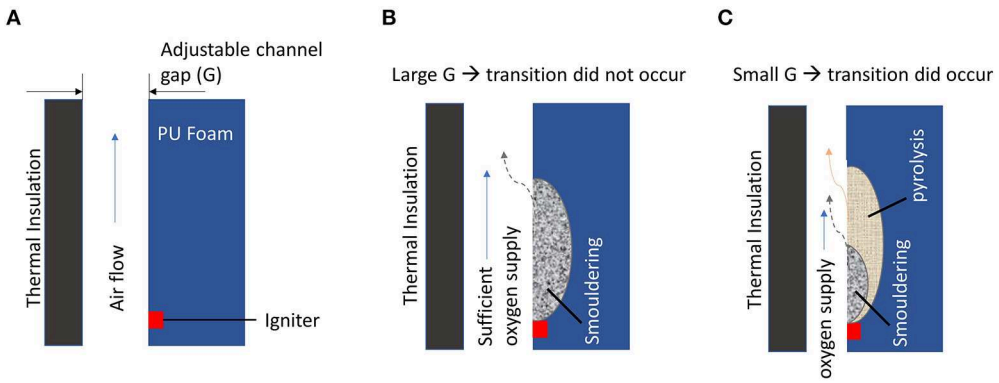

FIGURE 6 | StF transition experiment by Stoliarov et al. (2017). **(A)** Experimental setup. **(B)** Experimental setup in which the StF transition did not occur due to a large channel gap. **(C)** Experimental setup in which the StF transition occurred due to a small channel gap. Solid blue, dotted black, and solid beige arrows indicate oxygen supply, gases and aerosol products from char oxidation, and pyrolyzates, respectively.

took place and produced flammable pyrolyzates, as indicated by the decreasing temperature. Whether char or unreacted PU foam undergoes pyrolysis remains to be determined. Computationally, the pyrolysis of char is one of the key reactions leading to the StF transition (Dodd et al., 2012).

Once the oxygen concentration increased and mixed with the pyrolyzate gases bringin the mixture to within the flammability limits, StF transition occurred (t_5 in **Figure 7B**). This mechanism is consistent with the smouldering of cotton under asymmetric boundary conditions (Hagen et al., 2015). The asymmetric boundary condition was when one face of the cotton sample was closed by a concrete wall. Under this condition, the StF transition occurred due to the slower smouldering spread rate at the closed face than at the open face. One would argue that at the closed face, pyrolysis was more dominant than smouldering due to the insufficient oxygen supply because of the closure by the concrete wall. Pyrolysis provided pyrolyzates that were then ignited by heat provided by smouldering at the open face.

Figure 8A shows a visual observation of the StF transition in a 40-cm-long PU foam slab during upward propagation. In this experiment, one lateral face of the PU foam was exposed to radiant heat flux, the bottom face was in contact with a heater, and the top face as well as the three remaining lateral faces were insulated (Rein, 2009, 2016). Chao and Wang (2001) experimentally investigated the StF transition in PU foam in horizontal propagation under natural convection and found SCO prior to the StF transition. The probability of transition increased with the length of the PU foam.

Recent findings on secondary char oxidation (SCO) were derived from collective works of smouldering PU foam with variable oxidiser supply and radiant heat flux, as shown in **Figure 8B** (Tse et al., 1996; Bar-Ilan et al., 2005; Putzeys et al., 2007, 2008; Dodd et al., 2012). The location of the strong char oxidation upward from the smouldering front, thus located in the char layer upstream of the smouldering leading edge, was confirmed by Tse et al. (1996), who

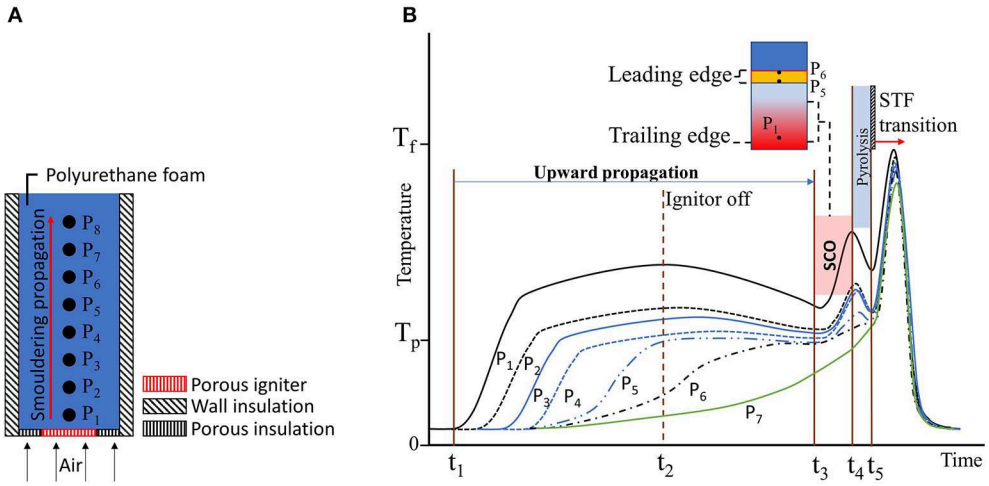

FIGURE 7 | (A) Experimental setup by Torero and Fernandez-Pello (1995). **(B)** Schematic of the temperature distribution in the experiment that led to the StF transition. Figures are redrawn and simplified from the original in Torero and Fernandez-Pello (1995). T_p and T_f are the temperatures at which PU foam undergoes pyrolysis (300°C) and the approximate flaming temperature of PU foam (900–1,000°C).

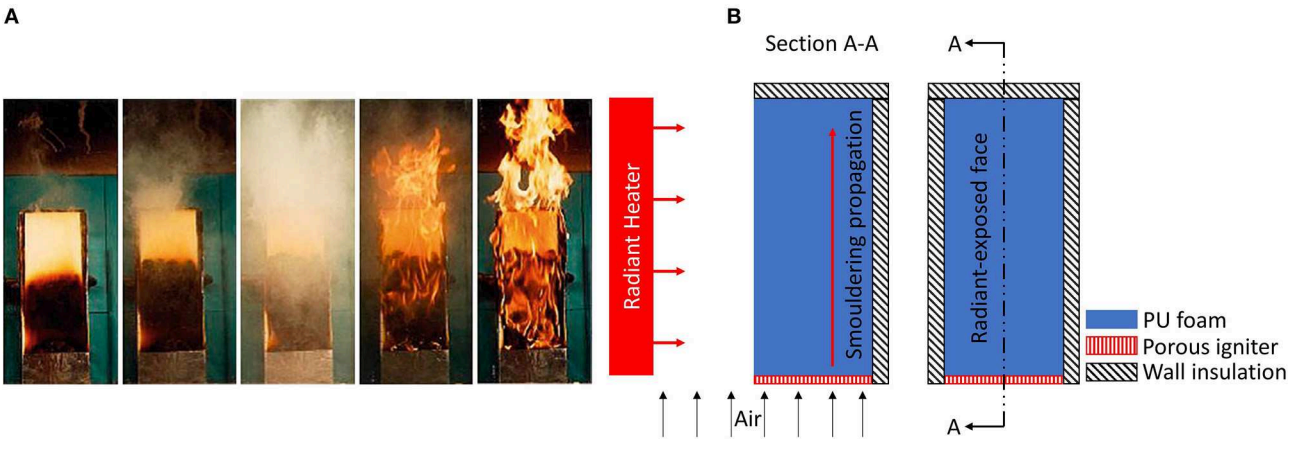

FIGURE 8 | (A) Series of photographs of a combustion experiment illustrating the transition to flaming in a smouldering polyurethane slab 40 cm high under external forced flow (photo by the group of Prof. Carlos Fernandez-Pello, University of California at Berkeley). After 1 h of burning, only half of the sample smouldered (photo 1, far *left*). When the transition took place (photos 2 and 3), the whole sample was engulfed in flames in a few seconds (photos 4 and 5, far *right*). **(B)** Experimental setup of a series of works by Prof. Fernandez-Pello at the University of California at Berkeley, USA (Tse et al., 1996; Bar-Ilan et al., 2005; Putzeys et al., 2007, 2008; Dodd et al., 2012). Figure is redrawn from the original version in Putzeys et al. (2007). Figure on the left shows section A–A cut from the figure on the right.

measured the evolution of permeability inside the PU foam with ultrasonic imaging. The permeability substantially increased as char continued to react. This reaction leads to the formation of voids that provide favourable locations for combustible gas accumulation, thus favouring the StF transition. The SCO, which is more exothermic once reacted, acted as the ignition source for the accumulated gas in the void.

Putzeys et al. (2007) measured the intensity of SCO and concluded that the direction of SCO was downward, while the primary smouldering front was upward. This SCO propagation direction was computationally proven by Dodd et al. (2012), who developed a two-dimensional numerical transport model to predict the StF transition of PU foam in the study by Putzeys et al. (2007). In Dodd et al. (2012) model, there are seven heterogeneous reactions with one global homogeneous gas-phase reaction. Four reactions were important in the model for the StF transition to occur. These reactions are the pyrolysis of thermal char, oxidation of α-char, oxidation of char that produces α-char, and flaming combustion of gaseous fuel. In this scheme, SCO is the oxidation of α-char. The results by Dodd et al. (2012) for temperature and transition time agreed well with the experimental results by Putzeys et al. (2007).

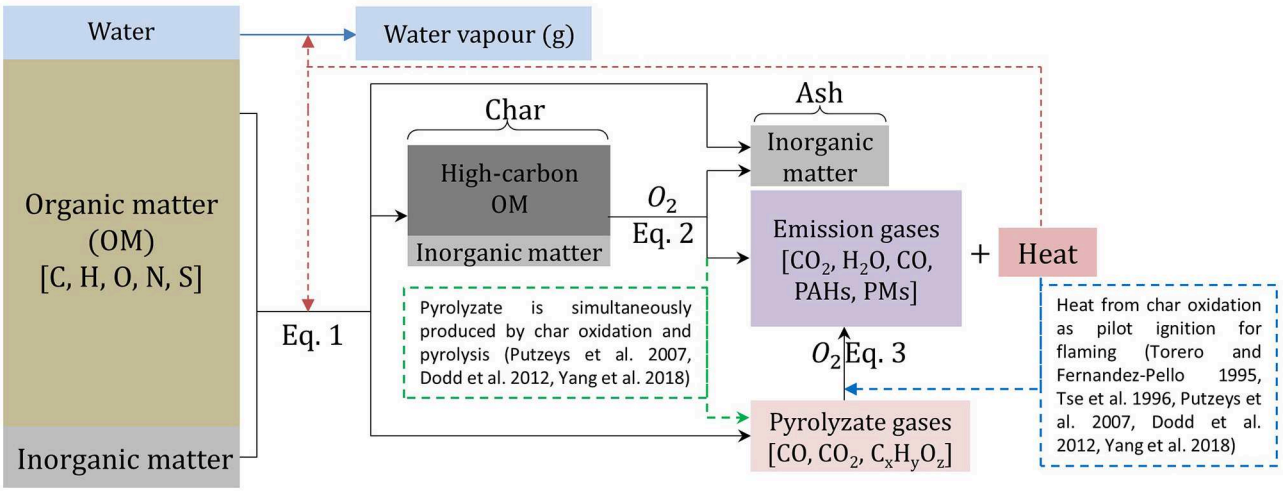

FIGURE 9 | Reaction schematics of organic matter undergoing pyrolysis (Equation 1), smouldering (Equation 2), and flaming (Equation 3). StF transition occurs when oxidation reaction of pyrolyzate (Equation 3) occurs alongside oxidation reaction of char (Equation 2). Solid black lines indicate reaction representing Equations (1–3) in this paper; dotted red line indicates heat feedback from exothermic reaction; blue line indicates evaporation of MC in the fuel; dotted green line indicates pyrolyzate gases production from char oxidation as concluded by Putzeys et al. (2007), Dodd et al. (2012), Yang et al. (2018), and dotted blue line indicates heat feedback from char oxidation that ignite flaming reaction as concluded by Torero and Fernandez-Pello (1995), Tse et al. (1996), Putzeys et al. (2007), Dodd et al. (2012), Yang et al. (2018). Figure after diagram in Lin et al. (2019).

In the kinetic model by Dodd et al. (2012), secondary char oxidation (SCO) is important in providing gaseous fuel and heat required to ignite flaming combustion. This gaseous fuel is produced from SCO and thermal char pyrolysis. Thus, SCO provides gaseous fuel and heat. In addition to sustaining the thermal char pyrolysis which provides the pyrolyzates, heat also acts as the ignitor of the produced gaseous fuel/air mixture once it is above its lower flammability limit. This finding is related to the mechanism proposed by Torero and Fernandez-Pello (1995). To computationally reproduce the experimental work of smouldering cellulosic insulation by Ohlemiller (1990), Yang et al. (2018) found that char oxidation and pyrolysis of cellulose provide gaseous fuel, while the ignitor is the hot char at the surface of the cellulosic insulation (**Figure 9**). There is no SCO in this model. In conclusion, gaseous fuel is simultaneously produced by char oxidation and pyrolysis reaction (**Figure 9**). Whether the prominent pyrolysis reaction takes place on unreacted fuel or char still needs to be determined.

PERMEABILITY AND CONSOLIDATION

Two material properties that particularly seem to control the location of the transition are permeability and consolidation. Permeability is a property of a porous material that represents the ability of fluid to flow through that material (Wang et al., 2019). This paper proposes a material property, namely, consolidation, that represents a material's ability to not collapse during burning and thus remain consolidated. For example, consolidated materials are synthetic polymers and solid wood (embers, timber, and tree trunks), and unconsolidated materials are peat soils and the litter layer made of loose materials such as peat grains, leaves, and needle vegetation. In organic soils, the degree of consolidation depends on the degree of decomposition of parent materials. For example, the presence of partially decomposed hardwood, natural fibers, and tree roots can make organic soils remain consolidated during burning, and once these parent materials are consumed, the organic soils become unconsolidated.

For consolidated materials with high permeability (e.g., PU foam) (**Figure 10A**), the location of the StF transition tends to be initiated within the material (Tse et al., 1996; Bar-Ilan et al., 2005; Putzeys et al., 2007, 2008; Dodd et al., 2012). The high permeability of a material allows oxygen to flow inside the fuel bed. Consolidation of the fuel bed allows the fuel to remain intact as smouldering propagates within the material and forms void spaces. The formation of void spaces is confirmed by the increasing internal permeability of the fuel during smouldering prior to the StF transition (Tse et al., 1996; Putzeys et al., 2007). This void then becomes the favourable space for gaseous fuel to accumulate. The heat produced from the more exothermic char oxidation will ignite the gaseous fuel in the void spaces (**Figure 10A**).

For low permeability and consolidated material (**Figure 10B**). Smouldering propagates at the surface of the material since the oxygen diffusion inside the material is limited. At the surface, the smouldering front also undergoes high convective heat losses. To be self-sustained, smouldering needed to be assisted with decreasing heat loss or external heat flux, i.e., a U-shaped fuel geometry to maximise radiation heat exchange between the smouldering surfaces or deposited embers on fuel bed surface (Ohlemiller, 1991; Manzello et al., 2006b, 2008, 2009, 2012; Manzello and Suzuki, 2014, 2017; Hakes et al., 2018). Under this condition, the transition tends to occur at the surface of the material. Bilbao et al. (2001) conducted an experiment with

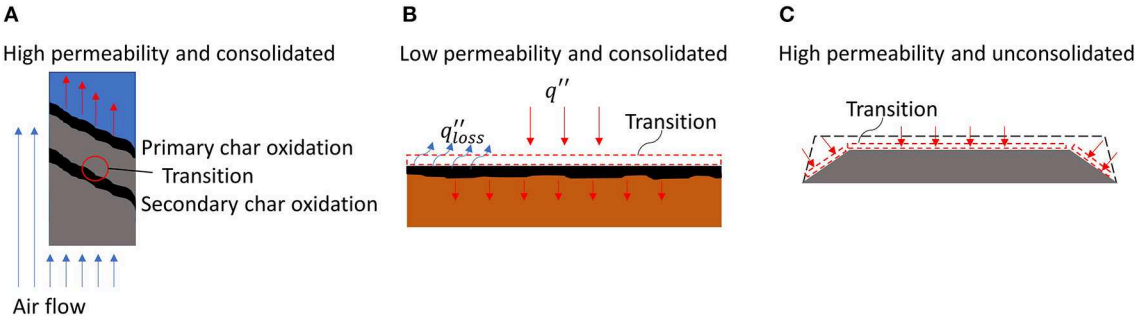

FIGURE 10 | smouldering-to-flaming transition location with respect to permeability and consolidation of the material. **(A)** High permeability and consolidated material, i.e., polyurethane foam, cotton cladding, upholstery material. **(B)** Low permeability and consolidated material, i.e. wood. **(C)** High permeability and unconsolidated material, i.e. dust layer, cellulosic insulation, and organic soil.

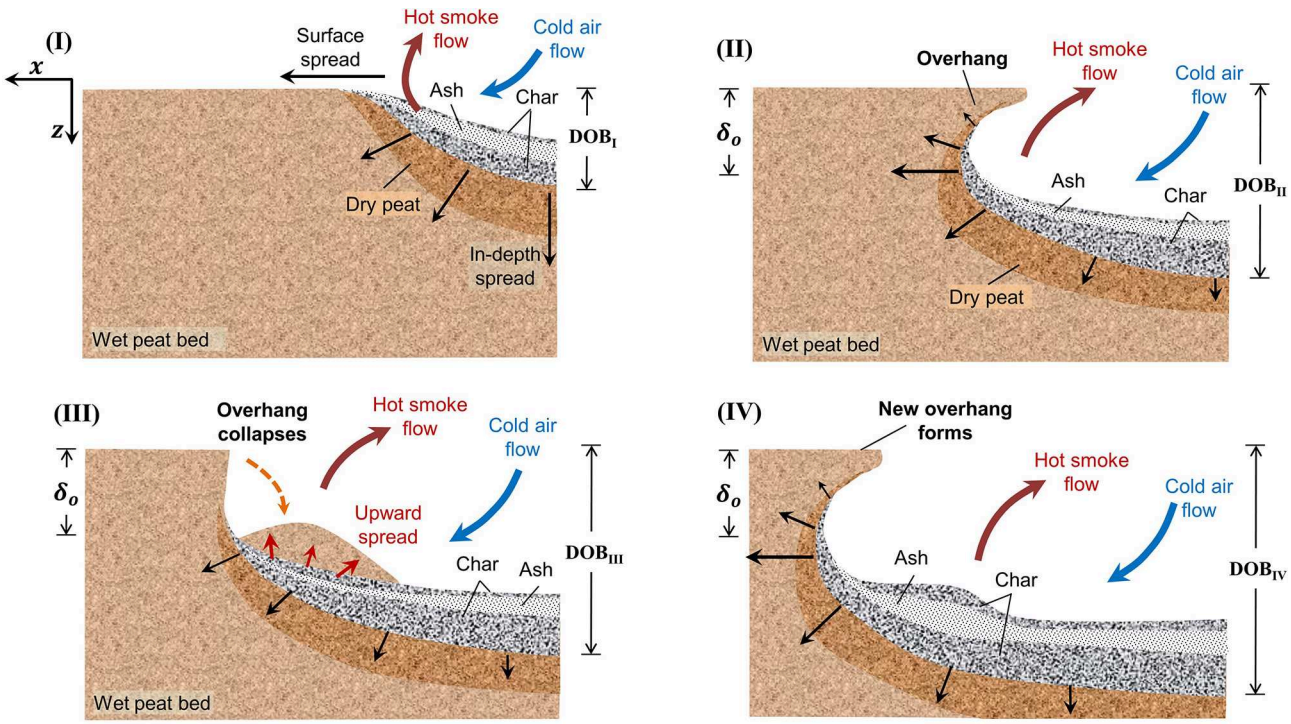

FIGURE 11 | Schematic diagram for the periodic formation and collapse of overhang in smouldering spread over wet peat: **(I)** soon after ignition, **(II)** formation of the overhang, **(III)** collapse and consumption of the overhang, and **(IV)** formation of a new overhang. Illustration from Huang et al. (2016) (X. Huang, CC BY license).

small *P. pinaster* wood, i.e., dimensions of 11 by 11 by 1.9 cm, under radiative heat flux and forced convection. They found that radiative heat flux affected the time to StF transition more than convection did, implying that the low permeability of the material made the smouldering less dependent on airflow and that minimising convective heat losses by assisting smouldering with radiative heat flux governs the StF transition.

In high permeability and unconsolidated materials (**Figure 10C**), the fuel is not able to maintain its structural integrity during burning and thus immediately collapses during fuel consumption. The fuel in this category includes fuel beds made of dusts, cellulosic insulation, vegetation (grasses and pine needles), and organic soils. Most wildland fuels fall in this category, except wood, which is a consolidated fuel with low permeability. In the smouldering of this fuel category, the transition tends to occur at the surface of the fuel bed (Palmer, 1957; Ohlemiller, 1990; Manzello et al., 2006a,b; Valdivieso and Rivera, 2014; Wang et al., 2017; Yang et al., 2018).

For solid fuels that have high permeability and an intermediate degree of consolidation during smouldering, such as peat, an overhang can form and collapse during fire spread (Huang et al., 2016). An overhang is a temporary hanging surface of burning organic soil, where its intermediate layer below has been consumed (**Figure 11**). An overhang is formed because of the

faster horizontal spread rate a few centimeters below the surface due to the reduced convective heat losses compared to the free surface of the organic soil fuel bed (Huang et al., 2016; Rein, 2016). The collapse of the peat overhang is because the char layer is gradually consumed and can no longer support the weight of the above soil. Currently, in the literature, there is no mention of StF transition during overhang formation. However, the possible influence of intermediate consolidation of peat represented by overhang formation and collapse on the StF transition could still be explored since overhang formation and collapse are also recent findings, and their scope of influence on fire dynamics has not yet been identified.

One of the difficulties in mitigating peat fires is its propensity to spread deep below the ground (Page et al., 2002; Rein et al., 2008; Rein, 2016), hence the deep penetration of oxygen diffusion to the smouldering peat. Considering permeability alone, subsurface smouldering propagation can lead to resurfacing of smouldering that can lead to a StF transition. The resurfacing of an underground smouldering front is made possible because of the consolidation of the char layer left behind by oxygen-limited smouldering propagation (Huang and Rein, 2019).

Another parameter found to affect the StF transition, in relation to permeability, is the particle diameter of the fuel bed. For natural fuel beds filled with particles, the permeability is proportional to the square of the particle diameter ($K \sim d_p^2$ $K \sim d_p^2$) (Soulsby, 1997). The particle diameter also affects the heat exchange and mass transfer between the solid matrix and porous pores, thus influencing the chemical reactivity. With increasing particle diameter, the StF transition occurred at a lower critical velocity, which is the velocity at which the StF transition occurs. In smouldering dust beds, the StF transition did not occur when dust particles were <0.1 cm (Palmer, 1957). An increase in particle diameter leads to an increase in the total pore surface area and a decrease in the specific surface area (SSA: total surface area of the fuel bed per unit volume or mass) of the fuel bed. Song et al. (2017) investigated the particle diameter effect on the reaction rate of a heterogeneous coal reaction. Knudsen (intra-particle) diffusion, which is the diffusion of a gas, in this case oxygen, into the interior of particles decreases with increasing particle diameter due to increasing pore surface area or permeability. The decrease in Knudsen diffusion decreases the overall reaction rate of coal oxidation by up to 50%. This finding is contrary to that by Palmer (1957), where increasing particle diameter leads to an increasing tendency for the StF transition. The effects of particle diameter on the Knudsen oxidation rate and StF transition need to be investigated further. Currently, the influence of specific surface area to StF transition cannot be assessed at this point because there are no data available in the literature.

EMBERS AND STF TRANSITION IN WILDFIRES

Embers contribute to the devastating spread of wildfires by being lofted in the fire plume and carried vast distances by strong winds (Pagni, 1993; Butler et al., 1998; Fernandez-Pello, 2017). Embers, commonly called firebrands and different from hot metal fragments, are combustible and rich in carbon. The accumulation of these embers can start local smouldering and, in some cases, exhibit StF transitions that result in fire spread far beyond the original fire front. This behaviour is also known as spotting (**Figure 2**). Field observations of StF are hard to find in the scientific literature, but a few exist. Pagni (1993) qualitatively described the 1991 Oakland Hills wildfire in California, USA, during which embers landed on a downwind region of high fuel load and led to a massive fires conflagration. The report mentions "flaming debris," but we can infer that this term represents a broad range of burning embers, including smouldering embers. This wildfire burned 600 ha, caused 25 fatalities and damaged 2,334 structures (Pagni, 1993). The wind was dry and of high velocity (∼10 m/s), with a strong inversion layer of 600 m, and on a complex hill topography. Field observations of the role of smouldering ember were also recorded in the 1994 South Canyon Fire in Colorado, USA. This fire suddenly shifted from a slow surface fire to a fast crown fire, causing the deaths of 14 firefighters. The surface fire included flaming grass and smouldering litter, with occasional torching of individual trees, which when combined produced flying smouldering embers. This result could imply that the shift from low- to high-intensity fire could have involved the StF transition of smouldering embers. From the survey conducted after the January 1994 wildland fires in Sydney, Australia, 52 of the WUI materials were ignited by embers while the rest, i.e., 18, were ignited by radiation (Babrauskas, 2003). In another investigation, Maranghides and Mell (2009) concluded that 55 of 74 destroyed homes were ignited by embers, 80 min before the arrival of the fire front. This is in agreement with Bell (1985), concluding that radiation alone is rarely the cause of house to be lost.

Manzello et al. (2006a) investigated the ignition of pine straw mulch, shredded hardwood mulch, and cut grass by embers. Fuel MC was either dry or 11% MC and placed inside an aluminum foil pan with dimensions of 23 by 23 by 5.1 cm. The StF transition occurred when four smouldering firebrands 50 mm in diameter were deposited on the samples and exposed to an airflow of 1 m/s. This airflow was lower than the critical velocity of 2 m/s for the StF transition in cellulosic insulation (Ohlemiller, 1990), which may be due to the difference in material or the enhanced radiation feedback between the sample and the firebrands, resulting in more intense smouldering.

To focus the investigation on the ignition of fuel beds, embers can be represented as hot metal particles (Hadden et al., 2011; Wang et al., 2017). This approach eliminates the complexity of the ember reaction process, its variable heat release, and coupled heat transfer interaction between the fuel bed and embers. In addition to these conveniences in investigating fuel bed ignition by hot metal particles, real wildfires are often initiated and accelerated by hot metal particles from clashing power lines and machine processes, such as grinding and welding (Fernandez-Pello, 2017). A smaller particle size leads to a higher temperature required for the flaming ignition of cellulosic fuel beds (Hadden et al., 2011). Particles as small as 19.1 mm with a temperature of 650°C can initiate flaming combustion. Embers with sizes ranging from 25 to 50 mm have been found in studies investigating StF transitions (Manzello et al., 2006a,b, 2008;

Hakes et al., 2018). In pine needle beds, the time to StF transition was ∼2.5–5 min at particle temperatures within the range of smouldering temperatures, ∼630–700°C (Wang et al., 2017). For drier fuel, the StF transition propensity increases, represented by the decreased StF transition time to as short as ∼2 min in fuel with ∼6% MC. In all cases, a larger particle size requires a lower particle temperature to initiate the StF transition in pine needles at higher MC. In comparison, an increasing particle size from 8 to 14 mm at a particle temperature of 925°C placed on a fuel bed at 25% MC can lead from no ignition to the occurrence of a StF transition in pine needle beds. Another interesting finding related to hot metal particle ignition is the effect of the melting process of the metal. It was found that the melting of hot metal particles increases the propensity of smouldering ignition (Urban et al., 2017).

Considering the fire hazard of embers to WUI fuels, Manzello et al. (2008) investigated the showering of firebrands on roofing assemblies. Roofing assemblies were varied into three configurations: (1) valley configuration of only base material, i.e., oriented strand board (OSB); (2) valley configuration of full roofing assembly, i.e., OSB, tar paper, and shingles; and (3) flat configuration of the roofing assembly with gutters filled with dried pine needles and leaves. A StF transition occurred on the (1) valley configuration of only base material and on the (3) flat configuration of the roofing assembly with gutters filled with dried pine needles and leaves. In configuration 1, the StF transition only occurred when the valley configuration was set at a 60° angle. The StF transition occurred due to the accumulation of firebrands in the crevice. The onset of the StF transition was on the back side of the OSB. In this case, the StF transition was due to the chimney effect, as discussed in the section *The Chimney Effect*. The chimney effect was more significant in this case than in the case of upholstered furniture fire due to a smouldering cigarette because the embers continuously accumulated in the crevice. In configuration 3, the StF transition was inside the gutter in the dried pine needles and leaves. The flame did not spread up to the roofing assembly. However, it was able to melt the shingles. It is not discussed whether flaming was preceded by smouldering of the dried pine needles and leaves or went directly to flaming. The time to StF transition was not recorded; however, the experiment was carried out in 6 min, and the StF transition occurred within that time frame. This StF transition time was significantly shorter than the recorded time of the StF transition in the upholstered furniture fire tests due to a smouldering cigarette, i.e., between 20 and 132 min (Clarke and Ottoson, 1976; Bukowski et al., 1977; Harpe et al., 1977; Bukowski, 1979). Extrapolating the scenario of flaming from accumulated vegetation in the gutter, the melted shingles can lead to exposed wood roofing structures. With consistent ember showers lasting longer than 6 min and pre-heated and aged shingles, WUI fires can spread substantially through this mechanism.

The short time to the StF transition in wildland and WUI fuels due to embers certainly shows the scale of wildfire threat, representing sudden fire spread in distant locations. More focused studies closely investigating the mechanism leading to the StF transition of the fuel due to embers are needed. Currently, in the literature, it is not clear whether the StF transition of the fuel is preceded by sustained smouldering of the fuel or only by pyrolysis of the fuel. In the former case, smouldering or flaming embers ignite smouldering of the fuel up to the point where the fuel is self-sustained and spread is uninfluenced by heat from the embers. This self-sustained smouldering later transitions to flaming. In the latter case, the StF transition was piloted ignition of pyrolyzate from the fuel by smouldering embers. Thus, pyrolysis is supported by heat from smouldering embers, and flaming ignition of the fuel occurs in the vicinity of embers where heat is most available. In this case, the StF transition of the embers could also precede flaming ignition of the fuel, where flaming embers act as a heat source for the fuel pyrolysis reaction and pilot ignition of the pyrolyzates from the fuel (Hakes et al., 2018). The comparison of these two cases shows that the embers enhance flaming ignition of the fuel more in the latter case than in the former case, assuming that self-sustained smouldering can take a long time to establish and has equal probability to extinguish as to transition from StF.

Valdivieso and Rivera (2014) investigated the StF transition in self-sustained smouldering of pine needle fuel beds with dimensions of 60 by 15 by 4 cm and, interestingly, they observed that the StF transition is a cyclic transition from smouldering to flaming to smouldering up to the point at which the whole fuel bed is consumed. This cycle occurred with a wind velocity of 1.1 m/s and a fuel MC of 69% (dry mass basis). This cycle was also found in the StF transition of a cellulose fuel bed by Ohlemiller (1990), and was argued to be caused by smouldering fronts that provide heat and pre-heated gaseous fuel. Because the smouldering process is at a lower rate than flaming, the gaseous fuel supply from smouldering fronts soon becomes insufficient to provide self-sustained flaming. In other words, self-sustained flaming could be established if the heat feedback from flaming is sufficient to increase the smouldering rate at a required level of gaseous fuel production. Another way to interpret this cycle is that gaseous fuel is provided by in-depth pyrolysis of fuel. As smouldering progresses, the char layer forms and becomes thick enough to insulate the fuel, decreasing the pyrolyzate diffusion rate to flow outside the fuel bed to mix with oxygen. As smouldering progresses further, the char layer is consumed and becomes thinner. Under this condition, the pyrolyzate diffusion rate increases again and mixes with oxygen. The StF transition occurs once the pyrolyzate/oxygen concentration is above the lower flammability limit. However, whether the StF transition depends on the pyrolysis of unreacted fuel or char or the oxidation of char remains to be determined and could be fuel- and experimental-setup-dependent.

In general, currently there is insufficient statistics and observations of StF transition in field-scale wildfire. These statistics and observations are much-needed data to identify the large gap in the understanding of StF transition and wildfire spread. Largely, rekindle can be initiated by residual smouldering fuel, i.e., wood log, embers, and duff layer, transitioned to flaming, thus starting a new fire front. During the Portugal wildfire in the summer of 2010, rekindle accounted for an additional 2,497 fires (Pacheco et al., 2012). This put a massive burden to firefighters as they need to revisit a reignited fire while under immense pressure to suppress other untreated fires. Pacheco et al. (2012)

discussed the importance of mop-up operation to avoid rekindle. A recent example of rekindle was Canyon Fire 2 in California in October 2017, in which the fire was likely to be started by strong winds pushing smouldering embers from previous fires in late September in the same area (Schwebke, 2017). Rekindle is also an issue when fires survive winter and reignited once weather is warming. This is especially a concern when fires could spread onto organic soils, which is essentially providing a massive amount of fuel supply (Gabbert, 2018). Fires in organic soils have been known to survive under sub-atmospheric oxygen concentration and very wet conditions (Rein, 2016). An example of this is the October 1997 fire in Yeodene peat swamp, Australia. Three weeks after suppression, the fire was thought to be fully extinguished by means of visual observation and infrared signature from aerial operation. However, in March 1998, the fire reignited and burnt 680 ha of the peat swamp area (Gunning, 2019). Due to the unknown cause of the fire, Gunning (2019) also mentioned the possible rekindle of fire in 1881, 1886, 2006, and 2010, emphasising that rekindle possibility can span across years.

CONCLUSIONS

In this paper, 28 studies of StF transition reported in English published from 1957 to 2019 have been reviewed. As shown in **Table 2**, wildland fuels need more attention in terms of their combustion behaviour and StF transition, as only three of the 28 studies observed StF transitions in wildland fuels. By critically reviewing findings in the literature, we identify oxygen supply and heat flux as the primary variables governing the StF transition. Specifically, these two parameters govern the StF transition in fuel subject to external airflow, fuel in a narrow vertical channel configuration, and fuel that undergoes more exothermic SCO. Afterwards, we propose a fuel classification based on the permeability of the fuel and the ability of the fuel to remain consolidated during burning. These two properties of the fuel affect the oxygen supply and heat transfer during fuel combustion, thus affecting the StF transition.

In essence, the StF transition is a spontaneous gas-phase ignition supported by the heat and reaction from smouldering (Tse et al., 1996; Bar-Ilan et al., 2005; Putzeys et al., 2007, 2008; Rein, 2009; Yang et al., 2018). Mechanisms leading to StF transition are governed by complex interactions of heat transfer and chemistry. From studies of widely different experimental setups on samples ranging from 0.1 to 1.2 m (**Table 2**), two variables are found to govern the StF transition, i.e., oxygen supply and heat flux. Airflow has a dual effect on smouldering. Airflow increases the oxygen supply to the fuel, thus increasing the reaction rate of an oxygen-limited spread, which favours the occurrence of the StF transition, but it also increases convective heat losses from the smouldering front, thus decreasing the tendency of the StF transition. The external supply of heat flux minimises heat loss and assists the fuel heating required for self-sustained smouldering progress and pyrolyzate production. Assistive fuel heating can be in the form of external heat flux such as embers in the case of WUI fires or from pertinent features of the fuel configuration such as when heat loss is minimised by the possible presence of radiation exchange between smouldering surfaces, i.e., smouldering at the fuel crevice or smouldering in U-shaped fuels (Alexopoulos and Drysdale, 1988; Ohlemiller, 1991; Ogle and Schumacher, 1998; Manzello et al., 2008, 2009, 2012; Manzello and Suzuki, 2017; Stoliarov et al., 2017; Hakes et al., 2018).

Vertical channel formation in smouldering at a crevice leads to radiation exchange between smouldering char surfaces and the chimney effect, increasing airflow from the buoyant flow (Ogle and Schumacher, 1998; Manzello et al., 2008; Stoliarov et al., 2017). The radiation exchange between smouldering surfaces leads to more effective heating, while buoyant flow increases the oxygen supply to smouldering fronts. The radiation exchange between surfaces minimises the convective cooling effect from the increased buoyant airflow. This mechanism is most relevant to WUI fires (Manzello et al., 2008). The StF transition is favourable at crevice locations in between smouldering fuels, i.e., embers at crevices of wood decks or house roofing, leading to increased buoyant flow through a vertical channel insulated by the char layer, thus minimising heat losses.

Strong char oxidation triggers a StF transition, as it provides heat to accelerate gaseous fuel production from pyrolysis and to ignite gaseous fuel (Torero and Fernandez-Pello, 1995; Tse et al., 1996; Bar-Ilan et al., 2005; Putzeys et al., 2007, 2008; Dodd et al., 2012; Yang et al., 2018). Whether pyrolysis takes place in unreacted fuel or char remains to be determined. SCO represents a sudden increase in the exothermic reaction rate at the smouldering trailing edge and releases more heat than the previous char oxidation at the same location. The role of this strong char oxidation in providing the required gaseous fuel, and regarding its sequentially secondary nature, needs to be further explored in different types of fuel and experimental setups.

Permeability and consolidation of the fuel bed control the location of the StF transition. Both parameters control the propagation of smouldering fronts, ultimately dictating the location of the StF transition (Tse et al., 1996; Putzeys et al., 2007; Dodd et al., 2012). Permeability controls the diffusion of oxygen penetration into the fuel bed, while consolidation controls the availability of space for smouldering to propagate within the fuel bed. Consolidated fuel with high permeability, such as open-celled polyurethane foam, tends to have a transition initiated close to the surface but within the fuel bed. Consolidated fuels with low permeability such as wood and unconsolidated fuels with high permeability such as cellulosic insulation tend to undergo transition at the surface. In a fuel bed such as peat, which is highly permeable and unconsolidated, overhang formation and collapse could alter the StF occurrence due to intermediate production of a char layer that has a tendency to hold its structural integrity but lose it once undergoing further smouldering, leaving only ash.

Deposited embers on a fuel bed increase the propensity of StF due to the embers' role in assisting the fuel heating process. In wildfire propagation, embers contribute to spotting and the quick initiation of new flaming sites (Mell et al., 2010; Caton

et al., 2017; Fernandez-Pello, 2017). The recorded StF transition time from studies of embers deposited on WUI and wildland fuels is <10 min and decreases with drier fuel (Manzello et al., 2008; Wang et al., 2019). With the predicted drier climate in the future, faster and more widespread propagation of WUI fires is to be expected. Considering that population movement contributes to the increase in WUI fire frequency (Mortsch, 2006; Hammer et al., 2007; Tarnocai et al., 2009; Simeoni, 2016) and that current WUI fuels are vulnerable to StF transitions due to embers (Manzello and Suzuki, 2014), more studies should investigate the design of smouldering-resistant material in the WUI area. Fundamentally, this calls for a better understanding of the StF transition mechanism.

This review synthesises the research, identifies regions for further research, and provides information on various StF transition mechanisms in the literature. These mechanisms converge on two fundamental aspects, heat transfer and chemistry. As airflow has a chemical effect (providing oxygen for the exothermic reaction) and a heat transfer effect (convective cooling), vertical channel formation also similarly provides more oxygen (chemistry) from the buoyant effect and a more effective heating process from radiation exchange between smouldering char surfaces (heat transfer). A better understanding of heat transfer and the chemical reactions of the StF transition mechanism can lead to prospective opportunities to better mitigate wildfires and protect the WUI.

AUTHOR CONTRIBUTIONS

MS and GR carried out the literature review. MS, EC, JY, and GR wrote the paper.

FUNDING

The authors would like to thank the European Research Council (ERC) Consolidator Grant HAZE (682587) for research funding and the Doctoral Studies Scholarship funded by the Indonesia Endowment Fund for Education (LPDP).

ACKNOWLEDGMENTS

The authors are grateful for the fruitful discussions with Dr. Haixiang Chen from the University of Science and Technology of China and with Dr. Francesco Restuccia, Dr. Hafiz M. F. Amin, Yuqi Hu, Matthew Bonner, Franz Richter, Dwi M. J. Purnomo, and Benjamin Khoo from Imperial College London.

REFERENCES

Aldushin, A. P., Bayliss, A., and Matkowsky, B. J. (2009). Is there a transition to flaming in reverse smolder waves? *Combust. Flame* 156, 2231–2251. doi: 10.1016/j.combustflame.2009.09.009

Alexopoulos, S., and Drysdale, D. D. (1988). The transition from smouldering to flaming combustion. *Fire Mater.* 13, 37–44. doi: 10.1002/fam.810130106

Babrauskas, V. (2003). *Ignition Handbook: Principles and Applications to Fire Safety Engineering, Fire Investigation, Risk Management and Forensic Science*. Issaquah, WA: Fire Science Pub.

Babrauskas, V. and J. Krasny (1997). Upholstered furniture transition from smoldering to flaming. *J. Forensic Sci.* 42, 1029–1031. doi: 10.1520/JFS14256J

Babrauskas, V., and Krasny, J. F. (1985). *Fire Behavior of Upholstered Furniture*. Washington, DC: National Bureau of Standards; U.S. Department of Commerce.

Bar-Ilan, A., Putzeys, O., Rein, G., and Fernandez-Pello, A. C. (2005). Transition from forward smoldering to flaming in small polyurethane foam samples. *Proc. Combust. Inst.* 30, 2295–2302. doi: 10.1016/j.proci.2004.08.233

Bell, A. (1985). How bushfires set houses alight—lessons from Ash Wednesday. *Ecos* 43, 3–7.

Bilbao, R., Mastral, J. F., Aldea, M. E., Ceamanos, J., Betrán, M., and Lana, J. A. (2001). Experimental and theoretical study of the ignition and smoldering of wood including convective effects. *Combust. Flame* 126, 1363–1372. doi: 10.1016/S0010-2180(01)00251-6

Bukowski, R. W. (1979). *Investigation of the Effects of Heating and Air Conditioning on the Performance of Smoke Detectors in Mobile Homes*. Washington, DC: National Bureau of Standard.

Bukowski, R. W., Christian, W. J., and Waterman, T. E. (1977). *Detector Sensitivity and Siting Requirements for Dwellings*. Boston: National Fire Protection Association.

Butler, B. W., Bartlette, R. A., Bradshaw, L. S., Cohen, J. D., Andrews, P. L., Putnam, T., et al. (1998). *Fire Behavior Associated With the 1994 South Canyon Fire on Storm King Mountain, Colorado*. Ogden, UT: United States Forest Service; Department of Agriculture.

Caton, S. E., Hakes, R. S. P., Gorham, D. J., Zhou, A., and Gollner, M. J. (2017). Review of pathways for building fire spread in the wildland urban interface part I: exposure conditions. *Fire Technol.* 53:429. doi: 10.1007/s10694-016-0589-z

Chang, L., Die, M., Rongkun, P., Bei, P., and Minggao, Y. (2011). "The effect of sample size on smoldering and the transition to flaming combustion," in *2011 Third International Conference on Measuring Technology and Mechatronics Automation*.

Chao, C. Y. H., and Wang, J. H. (2001). Transition from smoldering to flaming combustion of horizontally oriented flexible polyurethane foam with natural convection. *Combust. Flame* 127, 2252–2264. doi: 10.1016/S0010-2180(01)00326-1

Chen, Y., Kauffman, C. W., Sichel, M., Fangrat, J., and Guo, Y. (1990). The transition from smoldering to glowing to flaming combustion. *Chem. Phys. Process. Combust.* 68, 1–4.

Christensen, E., Hu, Y., Restuccia, F., Santoso, M. A., Huang, X., and Rein, G. (2019). "Experimental methods and scales in smouldering wildfires," in *Chapter 17 in Fire Effects in Soil Properties*, eds P. Pereira, J. Mataix-Solera, X. Úbeda, G. Rein, and A. Cerdà (Clayton, VIC: CSIRO), 267–280.

Clarke, F., and Ottoson, J. (1976). Fire death scenarios and fire safety planning. *Fire J.* 70, 20–22.

Dodd, A. B., Lautenberger, C. R, and Fernandez-Pello, C. (2012). Computational modeling of smolder combustion and spontaneous transition to flaming. *Combust. Flame* 159, 448–461. doi: 10.1016/j.combustflame.2011.06.004

Fernandez-Pello, A. C. (2017). Wildland fire spot ignition by sparks and firebrands. *Fire Safety J.* 91, 2–10. doi: 10.1016/j.firesaf.2017.04.040

Frandsen, W. H. (1987). The influence of moisture and mineral soil on the combustion limits of smoldering forest duff. *Canad. J. Forest Res.* 17, 1540–1544

Frandsen, W. H. (1997). Ignition probability of organic soils. *Canad. J. Forest Res.* 27, 1471–1477.

Gabbert, B. (2018). Overwintering fires are a concern in Northern Rockies. *Wildfire Today*. Available online at: https://wildfiretoday.com/2018/05/12/overwintering-fires-are-a-concern-in-northern-rockies/ (cited June 11, 2019).

Gunning, M. (2019). "Managing the complexities and consequences of peat fires around communities," in *Proceedings for the 6th International Fire Behavior and Fuels Conference* (Missoula, MT: International Association of Wildland Fire).

Hadden, R., Alkatib, A., Rein, G., and Torero, J. L. (2014). Radiant ignition of polyurethane foam: the effect of sample size. *Fire Technol.* 50, 673–691. doi: 10.1007/s10694-012-0257-x

Hadden, R., and Rein, G. (2011). "Burning and water suppression of smoldering coal fires in small-scale laboratory experiments," in *Coal and Peat Fires: A Global Perspective*, eds G. B. Stracher, A. Prakash, and E. V. Sokol (Oxford), 317–326. doi: 10.1016/B978-0-444-52858-2.00018-9

Hadden, R. M., Scott, S., Lautenberger, C., and Fernandez-Pello, A.C. (2011). Ignition of combustible fuel beds by hot particles: An experimental and theoretical study. *Fire Technol.* 47, 341–355. doi: 10.1007/s10694-010-0181-x

Hagen, B. C., Frette, V., Kleppe, G., and Arntzen, B. J. (2015). Transition from smoldering to flaming fire in short cotton samples with asymmetrical boundary conditions. *Fire Safety J.* 71, 69–78. doi: 10.1016/j.firesaf.2014.11.004

Hakes, R. S. P., Salehizadeh, H., Weston-Dawkes, M. J., and Gollner, M. J. (2018). Thermal characterization of firebrand piles. *Fire Safety J.* 104, 34–42. doi: 10.1016/j.firesaf.2018.10.002

Hammer, R., Radeloff, V., Fried, J., and Stewart, S. (2007). Wildland–urban interface housing growth during the 1990 in California, Oregon, and Washington. *Int. J. Wildland Fire* 16, 255–265. doi: 10.1071/WF05077

Harpe, S. W., Waterman, T. E., and Christian, W. J. (1977). *Detector Sensitivity and Siting Requirements for Dwellings, Phase 2*. Boston: National Fire Protection Association.

Hu, Y., Christensen, E., Restuccia, F., and Rein, G. (2019). Transient gas and particle emissions from smouldering combustion of peat. *Proc. Combust. Inst.* 37, 4035–4042. doi: 10.1016/j.proci.2018.06.008

Hu, Y., Fernandez-Anez, N., Smith, T. E. L., and Rein, G. (2018). Review of emissions from smouldering peat fires and their contribution to regional haze episodes. *Int. J. Wildland Fire* 27, 293–312. doi: 10.1071/WF17084

Huang, X., and Rein, G. (2014). Smouldering combustion of peat in wildfires: inverse modelling of the drying and the thermal and oxidative decomposition kinetics. *Combust. Flame* 161, 1633–1644. doi: 10.1016/j.combustflame.2013.12.013

Huang, X., and Rein, G. (2017). Downward spread of smouldering peat fire: the role of moisture, density and oxygen supply. *Int. J. Wildland Fire* 26, 907–918. doi: 10.1071/WF16198

Huang, X., and Rein, G. (2019). Upward-and-downward spread of smoldering peat fire. *Proc. Combust. Inst.* 37, 4025–4033. doi: 10.1016/j.proci.2018.05.125

Huang, X., Restuccia, F., Gramola, M., and Rein, G. (2016). Experimental study of the formation and collapse of an overhang in the lateral spread of smouldering peat fires. *Combust. Flame* 168, 393–402. doi: 10.1016/j.combustflame.2016.01.017

Huijnen, V., Wooster, M. J., Kaiser, J. W., Gaveau, D. L., Flemming, J., Parrington, M., et al. (2016). Fire carbon emissions over maritime southeast Asia in 2015 largest since 1997. *Sci. Rep.* 6:26886. doi: 10.1038/srep26886

Lin, S., Sun, P., and Huang X. (2019). Can peat soil support a flaming wildfire? *Int. J. Wildland Fire* 28, 601–613. doi: 10.1071/WF19018

Manzello, S., Cleary, T. G., Shields, J. R., and Yang, J. C. (2006a). Ignition of mulch and grasses by firebrands in wildland-urban interface fires. *Int. J. Wildland Fire* 15, 427–431. doi: 10.1071/WF06031

Manzello, S., Cleary, T. G., Shields, J. R., and Yang, J. C. (2006b). On the ignition of fuel beds by firebrands. *Fire Mater.* 30, 77–87. doi: 10.1002/fam.901

Manzello, S., Shields, J., Hayashi, Y., and Nii, D. (2008). Investigating the vulnerabilities of structures to ignition from a firebrand attack. *Fire Safety Sci.* 9, 143–154. doi: 10.3801/iafss.fss.9-143

Manzello, S. L. (2014). Enabling the investigation of structure vulnerabilities to wind-driven firebrand showers in wildland urban interface (WUI) fires. *Fire Safety Sci.* 11, 83–96. doi: 10.3801/IAFSS.FSS.11-83

Manzello, S. L., Almand, K., Guillaume, E., Vallerent, S., Hameury, S., and Hakkarainen, T. (2018). FORUM position paper, the growing global wildland urban interface (WUI) fire dilemma: Priority needs for research. *Fire Safety J.* 100, 64–66. doi: 10.1016/j.firesaf.2018.07.003

Manzello, S. L., Park, S. –H., and Cleary, T. G. (2009). Investigation on the ability of glowing firebrands deposited within crevices to ignite common building materials. *Fire Safety J.* 44, 894–900. doi: 10.1016/j.firesaf.2009.05.001

Manzello, S. L., and Quarles, S. L. (2017). Special section on structure ignition in wildland–urban interface (WUI) fires. *Fire Technol.* 53, 425–427. doi: 10.1007/s10694-016-0639-6

Manzello, S. L., and Suzuki, S. (2014). Exposing decking assemblies to continuous wind-driven firebrand showers. *Fire Safety Sci.* 11, 1339–1352. doi: 10.3801/IAFSS.FSS.11-1339

Manzello, S. L., and Suzuki, S. (2017). Experimental investigation of wood decking assemblies exposed to firebrand showers. *Fire Safety J.* 92, 122–131. doi: 10.1016/j.firesaf.2017.05.019

Manzello, S. L., Suzuki, S., and Hayashi, Y. (2012). Enabling the study of structure vulnerabilities to ignition from wind driven firebrand showers: a summary of experimental results. *Fire Safety J.* 54, 181–196. doi: 10.1016/j.firesaf.2012.06.012

Manzello, S. L., Suzuki, S., and Nii, D. (2017). Full-scale experimental investigation to quantify building component ignition vulnerability from mulch beds attacked by firebrand showers. *Fire Technol.* 53, 535–551. doi: 10.1007/s10694-015-0537-3

Maranghides, A., and Mell, W. (2009). *A Case Study of a Community Affected by the Witch and Guejito Fires*. Gaithersburg, MD: National Institute of Science and Technology. NIST Technical Note 1635.

Mell, W., Manzello, S., Maranghides, A., Butry, D., and Rehm, R. (2010). The wildland-urban interface fire problem—Current approaches and research needs. *Int. J. Wildland Fire* 19, 238–251. doi: 10.1071/WF07131

Mortsch, L. D. (2006). "Impact of climate change on agriculture, forestry and wetlands," in *Climate Change and Managed Ecosystems*, eds. J. Bhatti, R. Lal, M. Apps, and M. Price (Boca Raton, FL: Taylor & Francis; CRC Press), 45–67.

NWCG (2012). *Glossary of Wildland Fire Terminology*. Available online at: http://www.nwcg.gov/pms/pubs/glossary/ (archived by WebCite® at http://www.webcitation.org/65wjoO4i7) (accessed on March 5, 2012).

Ogle, R. A., and Schumacher, J. L. (1998). Fire patterns on upholstered furniture: Smoldering versus flaming combustion. *Fire Technol.* 34, 247–265. doi: 10.1023/a:1015397907280

Ohlemiller, T. J. (1985). Modeling of smoldering combustion propagation. *Progr. Energy Combust. Sci.* 11, 277–310. doi: 10.1016/0360-1285(85)90004-8

Ohlemiller, T. J. (1990). Forced smolder propagation and the transition to flaming in cellulosic insulation. *Combust. Flame* 81, 354–365. doi: 10.1016/0010-2180(90)90031-L

Ohlemiller, T. J. (1991). Smoldering combustion propagation on solid wood. *Fire Safety Sci.* 3, 565–574. doi: 10.3801/IAFSS.FSS.3-565

Ortiz-Molina, M. G., Toong, T.-Y., Albert Moussa, N., and Tesoro, G. C. (1979). Smoldering combustion of flexible polyurethane foams and its transition to flaming or extinguishment. *Symp. Combust.* 17, 1191–1200. doi: 10.1016/S0082-0784(79)80113-7

Pacheco, A. P., Claro, J., and Oliveira, T. (2012). "Rekindle dynamics: Validating the pressure on wildland fire suppression resources and implications for fire management in Portugal," in *Modelling, Monitoring, and Management of Forest Fires III*, eds. C. A. Brebbia and G. Perona (Southampton: WIT Press), 225–236.

Page, S. E., Siegert, F., Rieley, J. O., Boehm, H. D., Jaya, A., and Limin, S. (2002). The amount of carbon released from peat and forest fires in Indonesia during 1997. *Nature* 420:61. doi: 10.1038/nature01131

Pagni, P. J. (1993). Causes of the 20 October 1991 Oakland Hills conflagration. *Fire Safety J.* 21, 331–339.

Palmer, K. N. (1957). Smouldering combustion in dusts and fibrous materials. *Combust. Flame* 1, 129–154. doi: 10.1016/0010-2180(57)90041-X

Putzeys, O., Bar-Ilan, A., Rein, G., Fernandez-Pello, A. C., and Urban, D. L. (2007). The role of secondary char oxidation in the transition from smoldering to flaming. *Proc. Combust. Inst.* 31, 2669–2676. doi: 10.1016/j.proci.2006.08.006

Putzeys, O. M., Carlos Fernandez-Pello, A., and Urban, D (2006). Ignition of combustion modified polyurethane foam. *J. ASTM Int.* 3, 1–11. doi: 10.1520/JAI13558

Putzeys, O. M., Fernandez-Pello, A. C., Rein, G., and Urban, D. L. (2008). The piloted transition to flaming in smoldering fire retarded and non-fire retarded polyurethane foam. *Fire Mater.* 32, 485–499. doi: 10.1002/fam.981

Ramadhan, M. L., Palamba, P., Ali, I., Fahri, K., Engkos, A., and Nugroho, Y. S. (2017). Experimental study of the effect of water spray on the spread of smoldering in Indonesian peat fires. *Fire Safety J.* 91, 671–679. doi: 10.1016/j.firesaf.2017.04.012

Ratnasari, N. G., Dianti, A., Pither, P., Ramadhan, M. L., Prayogo, G., Sunjarianto, P. A., et al. (2018). Laboratory scale experimental study of foam suppression on smouldering combustion of a tropical peat. *J. Phys.* 1107:052003. doi: 10.1088/1742-6596/1107/5/052003

Rein, G. (2009). Smouldering combustion phenomena in science and technology. *Int. Rev. Chem. Eng.* 1, 3–18. Available online at: https://www.era.lib.ed.ac.uk/handle/1842/2678

Rein, G. (2013). "Smouldering fires and natural fuels," in *Fire Phenomena and the Earth System: An Interdisciplinary Guide to Fire Science*, ed. C. M. Belcher (West Sussex: John Wiley & Sons, Ltd.), 15–33.

Rein, G. (2016). "Smoldering combustion," in *SFPE Handbook of Fire Protection Engineering*, eds M. J. Hurley, D. Gottuk, J. R. Hall, K. Harada, E. Kuligowski, M. Puchovsky, J. Torero, J. M. Watts, and C. Wieczoreks (New York, NY: Springer New York), 581–603.

Rein, G., Carlos Fernandez-Pello, A., and Urban, D. L. (2007). Computational model of forward and opposed smoldering combustion in microgravity. *Proc. Combust. Inst.* 31, 2677–2684. doi: 10.1016/j.proci.2006.08.047

Rein, G., Cleaver, N., Ashton, C., Pironi, P., and Torero, J. (2008). The severity of smouldering peat fires and damage to the forest soil. *Catena* 74, 304–309. doi: 10.1016/j.catena.2008.05.008

Santoso, M. A., Huang, X., Prat-Guitart, N., Christensen, E., Hu, Y., and Rein, G. (2019). "Smouldering fires and soils, Chapter 13," in *Fire effects in soil properties*, ed P. Pereira (Clayton, VIC: CSIRO), 203–216.

Sato, K., and Sega, S. (1991). Mode of burning zone spread in an opposed gas flow. *Combust. Flame* 83, 146–154. doi: 10.1016/0010-2180(91)90209-T

Schwebke, S. (2017). *Canyon Fire 2, Which Torched 9,200-Plus Acres and Destroyed Homes, Ignited by Embers From Previous Fire*. Available from: https://www.ocregister.com/2017/11/06/canyon-fire-2-which-torched-9000-plus-acres-and-destroyed-homes-ignited-by-embers-from-previous-fire/ss (accessed June 11, 2019).

Simeoni, A. (2016). "Wildland fires," in *SFPE Handbook of Fire Protection Engineering*, eds. M. J. Hurley, D. Gottuk, J. R. Hall, K. Harada, E. Kuligowski, M. Puchovsky, J. Torero, J. M. Watts, and C. Wieczorek (New York, NY: Springer New York), 3283–3302.

Song, Z., Huang, X., Luo, M., Gong, J., and Pan, X. (2017). Experimental study on the diffusion-kinetics interaction in heterogeneous reaction of coal. *J. Thermal Anal. Calorim.* 129, 1625–1637. doi: 10.1007/s10973-017-6386-1

Soulsby, R. (1997). *Dynamics of Marine Sands: A Manual for Practical Applications*. London: Thomas Telford.

Stoliarov, S. I., Zeller, O., Morgan, A. B., and Levchik, S. (2017). An experimental setup for observation of smoldering-to-flaming transition on flexible foam/fabric assemblies. *Fire Mater.* 42, 128–133. doi: 10.1002/fam.2464

Suzuki, S., Manzello, S. L., Kagiya, K., Suzuki, J., and Hayashi, Y. (2015). Ignition of mulch beds exposed to continuous wind driven firebrand showers. *Fire Technol.* 51, 905–922. doi: 10.1007/s10694-014-0425-2

Tarnocai, C., Canadell, J. G., Schuur, E. A. G., Kuhry, P., Mazhitova, G., and Zimov, S. (2009). Soil organic carbon pools in the northern circumpolar permafrost region. *Global Biogeochem. Cycles* 23, 1–11. doi: 10.1029/2008GB003327

Torero, J. L., and Fernandez-Pello, A. C. (1995). Natural convection smolder of polyurethane foam, upward propagation. *Fire Safety J.* 24, 35–52. doi: 10.1016/0379-7112(94)00030-J

Tse, S. D., Fernandez-Pello, C. A., and Miyasaka, K. (1996). Controlling mechanisms in the transition from smoldering to flaming of flexible polyurethane foam. *Symp. Combust.* 26, 1505–1513. doi: 10.1016/S0082-0784(96)80372-9

Urban, J. L., Zak, C. D., Song, J., and Fernandez-Pello, C. (2017). Smoldering spot ignition of natural fuels by a hot metal particle. *Proc. Combust. Inst.* 36, 3211–3218. doi: 10.1016/j.proci.2016.09.014

Valdivieso, J. P., and Rivera, J. (2014). Effect of wind on smoldering combustion limits of moist pine needle beds. *Fire Technol.* 50, 1589–1605. doi: 10.1007/s10694-013-0357-2

Wang, F., Jiao, L., Lian, P., and Zeng, J. (2019). Apparent gas permeability, intrinsic permeability and liquid permeability of fractal porous media: carbonate rock study with experiments and mathematical modelling. *J. Pet. Sci. Eng.* 173, 1304–1315. doi: 10.1016/j.petrol.2018.10.095

Wang, S., Huang, X., Chen, H., and Liu, N. (2017). Interaction between flaming and smouldering in hot-particle ignition of forest fuels and effects of moisture and wind. *Int. J. Wildland Fire* 26, 71–81. doi: 10.1071/WF16096

World Health Organization (2006). *Air Quality Guidelines: Global Update 2005: Particulate Matter, Ozone, Nitrogen Dioxide, and Sulfur Dioxide*. Copenhagen: World Health Organization.

Yang, J., Liu, N., Chen, H., and Gao, W. (2018). Smoldering and spontaneous transition to flaming over horizontal cellulosic insulation. *Proc. Combus. Inst.* 37, 4073–4081. doi: 10.1016/j.proci.2018.05.054

Zhou, K., Suzuki, S., and Manzello, S. L. (2015). Experimental study of firebrand transport. *Fire Technol.* 51, 785–799. doi: 10.1007/s10694-014-0411-8

Conflict of Interest Statement: The authors declare that the research was conducted in the absence of any commercial or financial relationships that could be construed as a potential conflict of interest.

frontiers in Mechanical Engineering

ORIGINAL RESEARCH
published: 15 October 2019
doi: 10.3389/fmech.2019.00060

Whole-House Fire Blanket Protection From Wildland-Urban Interface Fires

*Fumiaki Takahashi**

Department of Mechanical and Aerospace Engineering, Case Western Reserve University, Cleveland, OH, United States

Each year, fires in the wildland-urban interface (WUI)—the place where homes and wildlands meet or intermingle—have caused significant damage to communities. To contribute to firefighter and public safety by reducing the risk of structure ignition, fire blankets for wrapping a whole house have been investigated in the laboratory and prescribed wildland fires. The fire blankets aim to prevent structure ignition (1) by blocking firebrands to enter homes through vulnerable spots (gutters, eaves, vents, broken windows, and roofs); (2) by keeping homes from making direct contact with flames of surrounding combustibles (vegetation, mulch, etc.); and (3) by reflecting thermal radiation from a large fire within close range (adjacent burning houses or surface-to-crown forest fires) for a sustained period of time. In the laboratory experiment, two-layer thin fabric assemblies were able to block up to 92% of the convective heat and up to 96% of the radiation (with an aluminized surface). A series of proof-of-concept experiments were conducted by placing instrumented wooden structures, covered with different fire blankets, in various fires in ascending order of size. First, birdhouse-sized boxes were exposed to burning wood pallets in a burn room. Second, wall-and-eave panels were exposed to prescribed fires climbing up slopes with chaparral vegetation in California. Finally, a cedar shed was placed in the passage of the prescribed head fire in the Pine Barrens in New Jersey. The experiments demonstrated both successful performance and technical limitations of thin fire blankets. The key success factors in protecting the WUI structure are (1) the fire blanket's heat-blocking capability, (2) endurance under severe heat-exposure high-wind conditions, and (3) proper installation. Additional studies are needed in the areas of advanced material/layer development, blanket deployment methods, and multi-structure protection strategies.

Keywords: WUI fire, forest fire, passive fire protection, structure wrap, ignition prevention, heat-blocking efficiency, historic cabin

OPEN ACCESS

Edited by:
Michael John Gollner, University of Maryland, College Park, United States

Reviewed by:
Javad Hashempour, University of North Carolina at Charlotte, United States
Wei Tang, National Institute of Standards and Technology (NIST), United States

***Correspondence:**
Fumiaki Takahashi
fxt13@case.edu

Specialty section:
This article was submitted to Thermal and Mass Transport, a section of the journal Frontiers in Mechanical Engineering

Received: *04 June 2019*
Accepted: *20 September 2019*
Published: *15 October 2019*

Citation:
Takahashi F (2019) Whole-House Fire Blanket Protection From Wildland-Urban Interface Fires. Front. Mech. Eng. 5:60. doi: 10.3389/fmech.2019.00060

INTRODUCTION

Background

Housing development in the wildland-urban interface (WUI), i.e., the place where homes and wildlands meet or intermingle, is growing (U.S. Fire Administration, 2002; Radeloff et al., 2005, 2018; Hammer et al., 2007; Stewart et al., 2007; Stein et al., 2013; Kramer et al., 2018). Between 1990 and 2010, the WUI was the fastest-growing land use type in the United States, and 97% of new WUI areas were the result of new housing rather than increases in wildlife vegetation (Radeloff et al., 2018). WUI fires have caused significant damage to communities (Cohen, 1999; Mell et al., 2010; Stein et al., 2013). The magnitude of the fire damage is increasing as well. Major wildfires

California in 2018 caused over $12 billion in property damage (Evarts, 2019). In 2018, the largest (the Mendocino Complex Fire burned 459,123 acres), most destructive (18,804 structures were destroyed in the Camp Fire), and deadliest (86 deaths in the Camp Fire) wildfires in modern California history have occurred at the same time (Cal Fire, 2018; Verzoni, 2019). Like urban conflagrations a century ago, wildfire in urban and suburban settings poses one of the greatest fire challenges of our time (Grant, 2018).

The WUI fire problem can be thought of as a structure ignition problem (Cohen, 1991; Mell et al., 2010) and an effective approach to mitigating the problem is to reduce the potential for structure ignition (Cohen and Stratton, 2008). Thus, if the structure ignition is prevented, WUI fire damage can be reduced and the safety of the public and firefighters will be improved. In a wildland fire, firebrands/embers (i.e., burning branches, leaves, or other materials) are lofted and carried by the wind and start distant spot fires. The cause of the initial structure ignitions in a WUI community is predominately due to exposure to firebrands (embers), generated by a wildfire or burning structures, and/or the heat flux from flames. Post-fire studies (Leonard, 2009; Maranghides and Mell, 2009; Morgan and Leonard, 2010) suggest that the firebrands are a major cause of structural ignition of WUI fires in the U.S. and Australia. A case study (Cohen and Stratton, 2008) revealed that burning homes and surrounding vegetation ignited adjacent homes initiating a "domino effect" of home destruction without wildfire as a major factor. Most of the homes (193 out of 199) destroyed and damaged ignited homes in two ways: (1) from spreading through surface fuels within the residential area that contacted homes and/or from firebrands and/or (2) from thermal exposure directly related to burning residences from structure flames and firebrands. Cohen and Stratton (2008) also concluded, "Firefighters were overwhelmed in their attempt to prevent the residential fire spread due to multiple homes burning simultaneously. However, more homes would have burned without their intervention." Another case study (Maranghides and Mell, 2009) found that firebrands ignited at least 60% of the destroyed structures in the WUI community. The likelihood of a structure's ignition is dependent both on its physical attributes (e.g., roofing material, decks, and vents) and the fire exposure conditions (e.g., magnitude and duration of heat flux from flames and firebrands).

Potential structure ignitions due to uninterrupted fire spread through vegetation to the structure were also reported in the perimeter of the community (Maranghides and Mell, 2009). Thus, the location of the structure in the WUI development community (perimeter or interior) is also an influencing factor (Maranghides and Mell, 2009). Mell et al. (2010) emphasized the research needs to characterize the exposure conditions and the vulnerability of a given structure design or building material when subjected to a given exposure. Butler (2010) pointed out that in the past, it had been stated that, at least for crown fires, radiant energy transport dominated the energy exchange process (Albini, 1986). More recently, laboratory and field studies indicated that convection might be just as critical to the energy transport as radiation (Anderson et al., 2010; Finney et al., 2010; Frankman et al., 2010). In the international crown fire modeling experiments in 1999 (Putnam and Butler, 2004; USDA Forest Service, 2009), one of the fire shelter testing showed that an average heat flux was measured at 80 to 100 kW/m^2, while peak heat flux was over 200 kW/m^2, and maximum (environment) temperature exceeded ≈1,300°C. Ignition of structures by burning vegetation (crown fires) is also possible (Cohen, 1999; Evans et al., 2004). In more recent fire spread experiments (Morandini et al., 2007), the peak heat fluxes measured during the four experiments increased in the range of 39–112 kW/m^2 with flame front size in the field (5 m × 5 m to 30 m × 50 m).

To mitigate risks of ignition of homes, there are resources available to homeowners (Cal Fire, 2006; Ahrens, 2010; Quarles et al., 2010; Stein et al., 2013; ICC, 2018; NFPA, 2018). NFPA 701 (2018)—*Standard for Reducing Structure Ignition Hazards from Wildland Fire* provides a methodology for assessing wildland fire ignition hazards around existing structures, residential developments, and subdivisions. The risk-assessment and risk-reduction guidelines can use the concept of home or structure ignition zone [NFPA 701, 2018] or defensible space (ICC, 2018) to categorize the recommended treatment of structure and vegetative fuels (Mell et al., 2010).

The role of structure-to-structure fire spread in WUI settings has not been given as much attention as vegetative-to-structure fire spread, which is valid for WUI communities with sufficiently low housing density (Mell et al., 2010). Post-fire analysis found that structure-to-structure fire spread played a key role in the overall fire behavior, and heat fluxes from both the flame fronts and firebrands produced by structures were instrumental in maintaining fire spread to surrounding structures and vegetation (Mell et al., 2010). Mell et al. (2010) pointed out a need to assess the effectiveness of the guidelines across a range of WUI fire setting (e.g., housing density, terrain, vegetative fuels, winds, wildland fuel treatments) and exposure conditions (heat flux from flames and firebrands generated by burning vegetation or burning structures). The 2018 Camp Fire in California swept through and destroyed the town of Paradise, possibly by the "domino effect" in structure-to-structure fire. In residential developments and subdivisions with relatively high housing density with limited space surrounding homes, the implementation of the ignition-risk reduction guidelines may not be feasible. Therefore, there is an urgent need to implement technology-based solutions that can diminish ignition vulnerabilities of structures to firebrand showers and heat flux from flames, including structure-to-structure fire spread in high housing density.

While wildfires can rage for days, weeks, or even months, the duration required to protect homes by fire blankets may range widely from minutes to hours, depending on various factors, e.g., housing density, terrain, vegetative fuels, winds, heat flux from flames, and firebrands. In a relatively low housing density, a critical period can be several minutes during a wildfire front passes. Airborne embers or other materials from burning vegetation pose a threat to ignite a house for a much longer time, an order of 30 min before and after the spreading fire front. In a relatively high housing density, e.g., suburban community

or urban setting, neighboring burning houses must threat the ignition of the structure for over an hour, possibly hours, if there is no intervention by firefighters.

Conventional measures in practice to prevent the structure ignition include the application of aqueous fire suppressants and retardants in the forms of foams, gels (USDA Forest Service, 2007), or water sprays, to the structure and/or surroundings prior to the arrival of the wildland fire front. Aerial firefighting using aircraft is also conducted to combat wildfires by dropping water or flame retardant. The advantage of these liquid spray coatings is that they can be applied to the structure parts with complex shapes (including decks, eaves, fences, etc.) and vegetation. The drawback is that they need water (at least 30 psi for ground operations), and spray application is difficult under windy conditions, and foams can be blown away by the wind before the wildfire front arrives. These coatings lose effectiveness with time as a result of water evaporation. Although gels are more effective than foams or water against thermal radiation exposure, their effectiveness decreased significantly even within an hour.

By contrast, more effective and long-lasting means of thermal shielding may be fire blankets, a.k.a. structure wraps. The U.S. Forest Service has occasionally been using the structure wraps to protect historic cabins from wildfires (Kuruvila, 2008; Miller-Carl, 2008; Backus, 2013; Gabbert, 2013; Montanez, 2014; Anon, 2018). Anecdotal evidence and technical know-how on the application of cabin wrapping have been accumulated over the last two decades. A typical description of the structure wrap in the news articles is "the wraps are similar to ones firefighters use for personal safety on the job, though they are thicker and the Forest Service says they are not exactly fireproof (Stephen, 2014)." Despite a common functionality between the fire blanket and the fire shelter as thermal insulation, the design goals (e.g., the interior temperature limit and the content endurance) in protecting a building structure are very different from those for a human body. Unfortunately, scientific research has rarely been conducted.

Literature Review

Fire blankets have been used for both fire suppression and protection. The literature on fire blankets is scarce probably because the basic research has not been fully conducted and the R&D efforts have mainly been made sporadically at manufacturers without dissemination of test results other than the specifications of final products. A few specifications available are: ASTM F 1989 (2005), the British Standards BS EN 1869 (1997), British Standards BS 7944 (1999), and the General Services Administration's procurement specifications (General Services Administration A-A-50230, 1987; General Services Administration A-A-54409, 1991; General Services Administration A-A-54629, 1992). More importantly, there have been no adequate performance-based standards and ongoing third-party certification to those standards specifically designed for fire blankets. As a result, fire blanket industry voluntarily used related compliance standards for flammability tests of blankets or fabrics such as ASTM D 4151 (2001) or NFPA 1144 (2004). In early 2007, the American National Standards Institute adopted ANSI/FM 4950 (2007), a performance-based standard for welding curtains, blankets and pads. Fabrics used for hot work operations such as welding and cutting are also commonly known as fire blankets. The performance of fire blankets for protection of stored ammunition was studied (Tewarson et al., 2001; Hansen and Frame, 2008).

Despite their easiness in handling compared to fire extinguishers, fire blankets have been used for smothering relatively small incipient fires only. They are generally not recommended to be used for a liquid fire or lab equipment as it can cause the fire spread, although some products are claimed to be useable for cooking oil fires. The old fire blankets, made of asbestos, were excellent at putting out fires. However, asbestos blankets were banned because of health hazards, and non-combustible glass fiber was chosen as a substitute material. For general purposes, including personal and burned victim protection, fire-resistant-treated cotton or wool blankets with or without a layer of gelled water are used in the military, fire departments, steel mills, etc. More recent fire blankets are made of fire and heat resistant aramid fabrics, which are more effective than wool blankets, and will not melt, drip, burn, or support combustion in the air. New types of fire blankets have been invented: non-woven polyester impregnated with a hydrous gel (Romaine, 1986), fabric made of mineral material containing basalt or a sodocalcic glass (Calderwood et al., 2006), or chemical compound which melts and reacts endothermically (Goldberg, 2006).

For the protection of building structures, various ideas of fire blanket deployment have been documented as the U.S. patents (Wagner, 1944; Ballinger, 1973; McQuirk, 1989; Gainer, 1992; Floyd, 1997; Hitchcock, 1997; Jones and Smith, 1998; Gleich, 1999; Kilduff and Oswald, 2003; Meyer and Kessler, 2004). Various concepts reported previously include:

1. Blankets, which are rolled around cylinders inside housings attached to various parts of a building, are deployed by rotating the cylinders typically by electric motors.
2. A blanket, which is stored in a container on the roof of a building or transported by a crane or helicopter, is deployed by using thrusting devices (compressed-gas-powered projectiles or rockets), which spread the blanket over the building.
3. A blanket is manually deployed to cover and enclose a building entirely.
4. Blankets are manually deployed to cover windows of a building to prevent the incoming wind, which would fuel the fire.

Although numerous methods for wrapping a home with fire blankets using the thrusting devices (Item 2) have long been proposed, the ideas are not necessarily verified nor validated. Item 1, Item 3, and Item 4 have been put into practice. The USDA Forest Service's effort to protect historic cabins using the commercial structure wraps (Anon, 2019) is among the Item 3 approach.

In contrast to fire blankets, the literature on firefighter protective clothing fabrics and domestic and international standard test methods exist. Various fire-resistive materials and their combinations have been developed for firefighter protective clothing, consisting of shell fabric, vapor barrier, and thermal barrier. These fabrics are resistive in fire fighting environments (Davis et al., 2006; Donnelly et al., 2006;

Madrzykowski, 2007). Furthermore, new materials are also being developed. For example, carbon nanotube fabric, which possesses great thermal conductivity and reflectivity, is currently tested for fire fighter protective clothing at the National Institute of Standards and Technology (Anon, 2006). It may become a candidate for the shell fabric for fire blankets once it becomes economically viable through commercialization in the future. Heat transfer models have been developed for fire fighter's protective clothing (Hirschler, 1997; Mell and Lawson, 1999; Torvi and Dale, 1999a,b; Song et al., 2004; Chitrphiromsri and Kuznetsov, 2005; Chitrphiromsri et al., 2006; Torvi and Threlfall, 2006). The models consist of radiative and conductive heat transfer of several layers of materials. The computed time history compared reasonably with measurement although restricted to lower temperature.

On the other hand, fire shelters are deployed in entrapment situations when firefighters feel they need to use it to prevent possible burn injury or death (National Wildfire Coordinating Group, 2019). In 2002, the U. S. Forest Service selected a new-generation fire shelter possessing improved insulation and a vapor barrier to protect firefighters (USDA Forest Service, 2003, 2008a,b; Petrilli, 2006; Anon, 2009). The old-style fire shelter was deployed 1,100 times and saved 300 lives but caused 20 fatalities, while the new design (Model 2002) statistics are: 166 deployments, 26 saved lives, and 21 fatalities (National Wildfire Coordinating Group, 2019). In 2013, the Yarnell Hill Fire in Arizona overran and killed 19 firefighters. The firefighters had apparently deployed fire shelters against the burnover. More recently, the NASA Langley Research Center and the U.S. Forest Service collaborated and two of the prototype fire shelters are NASA designs. The National Wildfire Coordinating Group (NWCG) board will decide to adopt the new fire shelter designs or continue using the current fire shelter, or a combination of both.

Based on the background and literature survey described above, the following observations can be made:

1. Although the materials for fire blankets for wrapping buildings and fire shelters for firefighter emergency protection are similar, their performance requirements are vastly different.
2. Fire blankets have not undergone proof-of-concept tests as has been done for fire shelters. Fire blankets also lack scientific research compared to firefighter clothing.
3. Although numerous methods for wrapping a home with fire blankets have long been proposed (and often patented), the ideas are not necessarily verified nor validated.
4. U.S. Forest Service used structure wraps (fire blankets) to protect isolated historic cabins during wildfires pass over them. A lot of know-how on proper manual installation must be accumulated but no technical documentation of the data is available in the literature.
5. The effectiveness of fire blankets for longer heat exposures is unknown despite its importance in the case of the structure-to-structure ignition in high housing density areas typical of a WUI community.

Objectives

In previous papers (Hsu et al., 2011; Takahashi et al., 2014), thermal response characteristics of more than 50 relatively thin fire blanket materials have been investigated experimentally and selected cases have been analyzed computationally. Each specimen was exposed to a convective or radiant heat flux. A relatively thin fire blanket operating at high temperatures can efficiently block heat by radiative emission and reflection coupled with thermal insulation. The level of protection afforded depends on the fabric material as well as the incident heat flux level and type (convective or radiative) and exposure time. Among the materials tested, relatively thin (∼1 mm) fiberglass or amorphous silica fabric laminated with aluminum foil performed reasonably well for a wide range of conditions.

The numerical modeling was performed (1) to simulate the heat transfer phenomena in the laboratory experiment (Hsu et al., 2011) and (2) to optimize the performance of fire blanket materials (Brent, 2012). The former is the physics-based modeling using the one-dimensional transient heat-transfer equation, which includes radiation as well as conduction in the interior of layered fire blanket materials. The latter includes three optimization studies on a one-dimensional, quasi-steady-state heat transfer model to optimize the performance of a fire blanket for protecting a structure from an exterior fire. Physical and optimization models would be useful for the development of advanced fabric materials and combined layer ensembles.

There are still various aspects of the subject matter needed to be studied. Topics include the heat-blocking mechanisms and performance of single and multi-layer fabrics in the laboratory and in actual wildland fires. The overall objectives of this study are to gain better understanding of the heat-blocking mechanisms and ignition prevention performance of single and multiple-layer fabric materials through the well-controlled laboratory experiments and larger-scale field fire-exposure tests. This paper reports previously unpublished laboratory experimental results for multi-layer fabric ensembles and the field fire test results using single-layer fabrics in increasing order of scale.

Limitations and Success Criteria

It should be noted that there are limitations of both the laboratory experiments and larger-scale fire-exposure tests. The laboratory experiments yield reproducible data of the thermal protection properties of materials under well-controlled conditions. The large-scale fire-exposure tests are proof-of-concept trials for the feasibility of the fire blanket protection method. When applying findings in the laboratory-scale to large-scale testing or a real fire, there are technical difficulties in scaling up the results. The difficulties stem mainly from differences in the substrate settings and exposure conditions. The laboratory experiments determine the material properties without a specific substrate at a fixed heat flux (84 kW/m^2), whereas the field fire tests examine the damage to the blanket and substrate (wood) (ignition or no-ignition) for particular structures under natural conditions of fluctuating heat flux, wind speed, air temperature, and different fire exposure durations. The incident heat flux by direct flame

contact or a radiant heater in the present laboratory experiments is within a range of values measured in the large-scale crown fire experiments (Putnam and Butler, 2004; USDA Forest Service, 2009) and more recent fire spread experiments (Morandini et al., 2007) as mentioned above. Most importantly, in the outdoor field tests, such exposure conditions are dependent on the weather (winds, humidity, and sunlight), terrain, vegetative fuels, vegetation moisture content, wildland fuel treatments, firebrands, and thus, largely uncontrollable by the experiment operator. Babrauskas (2001) has pointed out that the measured wood ignition heat flux data vary widely and that for short-term exposures, a value of 20 kW/m^2 perhaps best captures the research results. Therefore, the present approach intends to achieve the fire exposure greater than this value up to that of the laboratory experiment. The heat flux from firebrand is assumed to be covered in the range of the present laboratory experiments. This paper reports the measurements and observations of fire blanket performance in the limited cases.

Success of the fire blanket performance will be judged on meeting the stated objectives of ignition prevention; i.e., "pass or fail," under given fire exposure conditions. "Pass" is defined to mean that flaming ignition of the substrate structure material (wood) is prevented successfully and "fail" is defined to mean that substrate is ignited. For the "pass" criterion, two different levels of success—minimum and complete success—are defined. "Minimum success" is defined to mean ignition prevention with significant damage to the blanket and extensively charred substrate. "Complete success" is defined to mean ignition prevention with minimal damage to the blanket and substrate (up to ∼6 mm char depth).

LABORATORY EXPERIMENTS

Experimental Methods

First, material-level experiments have been conducted in the laboratories to determine the thermal insulation characteristics of various fabric materials. The material characteristics measured include (1) the thermal protective performance (TPP) rating against convective heat, (2) the radiation protective performance (RPP) rating, and (3) the transient and steady-state thermal responses to each heat exposure mode. The TPP test uses a direct flame contact based on ASTM D 4108 (1982). The RPP test is similar to ASTM F 1939 (2007), except that the radiant heat source is different. The experimental method is described in more detail in the previous paper (Takahashi et al., 2014).

The thermal protective performance (TPP) rating for protective clothing (ASTM D 4108, 1982) is measured by a test apparatus (Govmark[1] TPP-2) equipped with a 40 mm-diameter copper calorimeter. The Meker burner is modified so that the flow rates of propane and air are controlled with mass flow controllers to maintain a stoichiometric mixture. First, the apparatus is calibrated by placing the calorimeter directly on the lower specimen holder above the Meker burner and set an incident heat flux (83 ± 2 kW/m^2, or 2 cal/cm^2) by adjusting the fuel and air flows.

The TPP rating is the product of the incident heat flux and the exposure time when the heat flux through the specimen causes second-degree burn to human tissues (Stoll and Chianta, 1968) on the back side. The crossover time when the temperature (measured with a J-type thermocouple) of the copper calorimeter disc placed over the fabric reaches the value corresponding to the critical heat-flux condition is used as the exposure time (t_{exp}) to obtain the TPP rating:

$$\text{TPP rating}\,(\text{cal/cm}^2) = (\text{incident heat flux}: 2\,\text{cal/cm}^2\text{s}) \times t_{exp}\,(\text{s})$$

The fabric specimens are cut to 150 mm by 150 mm strips (exposed area: 51 mm by 51 mm square) and placed horizontally between a stainless steel mounting plate and a spacer (6.4 mm thickness), 52 mm above the burner surface.

In addition to the standard TPP test, a heat flux transducer (HFT) holder is newly fabricated (Takahashi et al., 2014) to measure the through-the-fabric heat-flux and the specimen temperature for the convective or radiative heat source. The HFT holder consists of a water-cooled total (convective plus radiative) heat flux transducer (Medtherm; Gardon Type 64-10G-20 or Schmidt-Boelter Type 64-10-20, 100 or 50 kW/m^2), mounted in an insulating ceramic board, a spacer, and a mounting plate. Thermocouples (K type, 0.020" sheath diameters; unexposed and exposed beads, respectively) are positioned touching the front (lower) and back (upper) surfaces of the fabric to measure the front and back surface temperatures (T_{front} and T_{back}), respectively.

The radiant heat exposure apparatus uses an upward radiant cone heater [the same design used in a cone calorimeter standard (ASTM E 1354, 2002)] to provide a uniform long wavelength radiative heat flux (up to 84 kW/m^2). For a calibration purpose, the incident radiative heat flux was measured by a water-cooled dual-sensor heat flux transducer (Medtherm 64-10T-10R[ZnSe]-21735, 100 kW/m^2), prior to the material's heat exposure experiment. The fabric specimens are 25 mm above the cone heater's exit plane. The tests are repeated at least three times for each material under the same exposure condition. By using the radiant cone heater, the radiation protective performance (RPP) rating was determined from the critical radiative incident heat flux when the heat flux through the specimen causes second-degree burn to human tissues (Stoll and Chianta, 1968) on the back side. By integrating the measured heat flux through the fabric specimen over the elapse time, the cumulative heat is calculated. The exposure time (t_{exp}) at the crossover was determined when the integrated value reaches the critical total heat to obtain the RPP rating:

$$\text{RPP rating}\,(\text{cal/cm}^2) = (\text{incident radiant heat flux}: 2\text{cal/cm}^2\text{s}) \times t_{exp}\,(\text{s})$$

In this study, three transient and steady-state thermal response characteristics are newly defined for each of convective and

[1]Certain commercial equipment, instruments, or materials are identified in this article to adequately specify the procedure. Such identification does not imply recommendation or endorsement by the author or CWRU, nor does it imply that the materials, equipment, or materials are necessarily the best available for the intended use.

radiative heat transfer. Thus, the effects of each mode of heat transfer can be determined independently on the thermal protective performance of fire blanket materials. In this manner, it will be possible to analyze the heat-blocking effectiveness of each fire blanket material against different ignition sources (direct flame contact and thermal radiation) and their synergistic effects as the property independent of substrate to be protected. The time for the heat flux through the fabric to reach 13 kW/m^2 and the time for the fabric's backside temperature to reach $T_{back} = 300°C$. These values are selected arbitrarily based on the critical heat flux for ignition of cellulosic (wood) materials (13 to 20 kW/m^2) and the typical solid pyrolysis temperatures (250 to 300°C), respectively (Babrauskas, 2001). In a recent work on the flame penetration and burn testing of fire blanket materials for munitions protection (Hansen and Frame, 2008), 500°C was chosen as representative because a high-temperature oxy-acetylene torch was used.

The time period required to protect a building structure varies from a few-minute exposure from a passing wildfire to hours of exposure from neighboring burning houses. Therefore, the heat flux through the fabric after reaching a steady state is an important property. In this study, the heat-blocking efficiency (HBE) is defined as:

$$\text{HBE} = [1 - (\text{steady} - \text{state transmitted heat flux})/(\text{incident heat flux})] \times 100\ (\%).$$

In addition to the experiments using the direct flame and radiant incident heat sources as described aobove, a preliminary trial has been conducted in consideration of the firebrands as a heat source. In the experiment, pieces of red-hot charcoal are dropped on the fabric specimen. However, the temperature of the charcoal appared to be much lower than those of the burner flame gases or the radiant heater element (∼850°C). Thus, the incident heat flux from the charcoal mainly through thermal conduction and radiation was assumed to be much lower than that from the burner flame or the radiant heater (84 kW/m^2). Therefore, the laboratory experiment related to firebrands was not persued further. Nonetheless, firebrands in a real WUI fire can accumulate particulaly along inside corners of walls around a building structure under high-wind conditions, and the the firebrand temperature and the heat flux may increase capable to ignite the structure. Thus, the topic needs to be studied in the future.

Materials

The results of the laboratory experiments and a complete list of more than 50 fabrics have been reported previously (Takahashi et al., 2014). Fabrics of four different fiber material groups (aramid, fiberglass, amorphous silica, and pre-oxidized carbon) and their composites are used. **Table 1** shows physical properties of selected fire blankets materials reported in this paper. The continuous operating temperature varies widely, depending on the base material group; i.e., aramid composite, 260–320°C; fiberglass, 540°C; amorphous silica, 980°C; and pre-oxidized carbon, 1,427°C. The continuous operating temperature of aluminized materials is much lower (148°C) because it is based on adhesive temperature resistance. The material description, the continuous operating temperature, area density, and thickness are extracted from manufacturers' literature, unless otherwise noted. The manufacturers' code name is for exact identification purpose only. **Table 2** is an excerpt from the previous paper (Takahashi et al., 2014). It lists the measured thermal response characteristics of selected single-layer blanket materials used in this paper, including the times to reach $T_{back} = 300°C$ and $q = 13$ kW/m^2, TPP, and RPP ratings, and the heat blocking efficiencies for both convective and radiative heat sources.

Results and Discussion

Table 3 shows the measured thermal response characteristics of double- and triple-layered blankets, including the times to reach $T_{back} = 300°C$ and $q = 13$ kW/m^2, TPP, and RPP ratings, and the heat-blocking efficiencies for both convective and radiative heat sources. The assembly number (**Table 3**) is based on the type of materials and the fabric alignment configurations as summarized below.

A: Aramid/fiberglass (Group No. 4 in **Tables 1**, **2**)
B: Aramid/carbon/fiberglass (Group Nos. 2 and 4)
C: Fiberglass (Group Nos. 6 and 15)
D: Fiberglass (Group No. 12)
E: Fiberglass (Group No. 13)
F: Fiberglass (Group No. 14)
G: Fiberglass and amorphous silica (Group No. 13)
1: Fabric/fabric (exposed)
2: Fabric/fabric/Al (exposed)
3: Fabric/Al/fabric (exposed)
4: Al/fabric/fabric (exposed)
5: Fabric/Al/fabric/Al (exposed)
6: Al/fabric/fabric/Al (exposed)
7: Fabric/Al/fabric/Al/fabric/Al (exposed)
8: Al/fabric/fabric/Al/fabric/Al (exposed)

Many layered blankets did not reach the conditions of $T_{back} = 300°C$ and $q = 13$ kW/m^2, and the TPP and RPP exceeded 60 cal/cm^2, which corresponds to the maximum exposure time (30 s) tested for second-degree burn of human tissues. The aluminized blankets (2 to 2.8 mm thickness) of aramid/fiberglass (A6) and aramid/carbon/fiberglass (B1-B6) composite materials exhibited good insulation against convective heat and the HBE values reached around 90%, although the values against radiation decreased to <90%. Even for thinner (<1.4 mm) double-layered blankets of aluminized fiberglass (particularly C6 and F6), the heat blocking efficiency against convection reached as close as 90%.

Figure 1 shows effects of the layer alignment on the heat-blocking efficiency of double-layered aluminized materials using the Meker burner (**Figure 1A**) and the radiant cone heater (**Figure 1B**). In the Meker burner (**Figure 1A**), the HBE decreased by adding a single aluminized layer on the exposed side (Alignment No. 1 to 2) but increased by placing Al in-between (No. 1 to 3) or on the backside (No. 1 to 4). The HBE decreased by adding another Al layer on the exposed side (No. 3 to 5). The best performer of double layer blankets was the alignment with Al on the exposed and interior sides (No. 6). The triple layered blankets (C7 and C8 in **Table 3**) did not improve much

TABLE 1 | Fabrics evaluated.

Group no.	Code name	Fabric description	Continuous operating temperature (°C)	Area density (kg/m^2)	Thickness (mm)
Aramid/Carbon/Fiberglass Fabrics					
2	FLPN1500	Aramid-partially carbonized acrylic blend (non-woven)/aramid outer layer (woven)/fiberglass core (woven)	260	0.509	2.54
4	AFL1700	Aramid blend outer layer/fiberglass inner core	148[a]	0.644	1.32
	AFLPN1500	Aramid- carbonized acrylic blend (non-woven)/aramid outer layer (woven)/fiberglass core (woven)	260	0.570	1.78
Fiberglass Fabrics					
6	GL2025	100% fiberglass	540	0.610	0.91
12	1299-074	Fiberglass		0.180	0.15
	1025	Fiberglass		0.375	0.30
13	FS-NEW-I	Fiberglass (new-style fire shelter, inner shell)		0.100 [b]	0.08[b]
14	SW-STD	Fiberglass (structure wrap, standard duty)		0.207[b]	0.15[b]
	SW-HD	Fiberglass (structure wrap, heavy duty)		0.441[b]	0.40[b]
15	AGL2025	100% fiberglass	148[a]	0.666	0.79
Amorphous Silica Fabrics					
18	FS-NEW-O	Amorphous silica (new-style fire shelter, outer shell)		0.367[b]	0.33[b]
19	AAS1800	96% amorphous silica	148[a]	0.746	0.89
Carbon/Aramid Fabrics					
21	CK-3	Carbon (oxidized polyacrylonitrile)/aramid strengthening fiber, woven	1427	0.261	0.53[b]

[a] *Adhesive temperature resistance.*
[b] *Measured.*

in the HBE in the Meker burner. In the radiant cone heater (**Figure 1B**), the HBE depends primarily on the exposed surface reflectivity. Therefore, the HBE jumped up from 84.5% to > 90% by adding an aluminum layer on the exposed side (C1 to C2–C6), and again alignment No. 6 performed the best. However, for aramid/carbon/fiberglass composite materials (B1, B5, and B6), the HBE was not improved much by adding an aluminized (polyester) layer (B1 to B5 and B6) probably because of the surface optical property change.

Summary

In this work, the transient and steady-state thermal response characteristics have been determined for more than 20 multiple-layered fire blanket materials using a convective (Meker burner) or radiant (cone heater) heat source, independently. The findings are summarized as follows.

In addition to conventional thermal protective performance (TPP) ratings for protective clothing, the following two transient thermal response times and a steady-state heat-blocking efficiency (HBE) are introduced both convective and radiant heat sources in this study:

1. Fabric exposure time for the back side temperature to reach 300°C.
2. Fabric exposure time for the through-the-fabric transmitted heat flux to reach 13 kW/m^2.
3. HBE = [1—(transmitted heat flux)/(incident heat flux)] × 100 (%).

The data base provides basic information required by the industry in a product development of structure protective fire blankets. The HBE data are particularly important.

Multiple-layered materials combinations demonstrated high thermal protective characteristics: for the double-layered, HBEs up to 92% for convection and 96% for radiation. Triple-layered blankets of thin fabrics do not improve significantly compared to double-layered blankets.

For convective incident heat flux, the heat loss by radiative emission from the high-temperature surfaces and the efficient thermal insulation by the blanket material are the primary heat transfer mechanisms for relatively high HBE's. For radiative incident heat flux, highly reflective aluminized materials result in exceptionally high HBE's.

As multiple-layered fire blankets become heavier and costlier, they may be more suitable for partial structure coverage (e.g., windows) or other high-temperature intense-exposure applications, e.g., protection of firefighters (fire curtains for bulldozers and fire engines), vehicles, and equipment.

FIELD FIRE EXPERIMENTS

Preliminary Experiments in Burn Rooms

In cooperation with Cuyahoga Community College's Fire Academy (Parma, Ohio), small-scale preliminary experiments have been conducted by placing two dollhouse-size wooden structures, covered with different fire blanket materials, in a

TABLE 2 | Measured thermal characteristics of single-layer fire blankets.

Group no.	Code name	Time to $T_b = 300^\circ$C C: Conv. R: Rad. (s)	Time to $q = 13$ kW/m^2 C: Conv. R: Rad. (s)	TPP or RPP rating[a,b] C: Conv. R: Rad. (cal/cm^2)	HBE[c] C: Conv. R: Rad. (%)
Aramid/Carbon/Fiberglass Fabrics					
2	FLPN1500	C: 12.4 R: 13.3	C: 16.6 R: 16.0	C: 33.0 R: 41.7	C: 82.0 R: 78.5
4	AFL1700	C: 7.0 R: Not reached	C: 10.5 R: Not reached	C: 21.3 R: >60	C: 74.1 R: 97.4
	AFLPN1500	C: 9.7 R: 222.6	C: 11.3 R: 365.1	C: 21.2 R: >60	C: 78.1 R: 97.8, 69.6[d]
Fiberglass Fabrics					
6	GL2025	C: 6.1 R: 8.2	C: 6.9 R: 8.6	C: 18.2 R: 26.9	C: 67.1 R: 75.1
12	1299-074	C: 4.1 R: 440.9	C: 2.6 R: Not reached	C: 8.9 R: >60	C: 65.0 R: 95.3
	1025	C: 7.5 R: 631.4	C: 6.8 R: Not reached	C: 15.4 R: >60	C: 66.0 R: 93.0
13	FS-NEW-I	C: 2.4 R: 103.7	C: 2.8 R: Not reached	C: 7.0 R: >60	C: 54.6 R: 90.3
14	SW-STD	C: 5.2 R: Not reached	C: 3.8 R: Not reached	C: 10.2 R: 25.9	C: 56.0 R: 94.5
	SW-HD	C: 6.6 R: 134.9	C: 6.4 R: Not reached	C: 16.5 R: 27.3	C: 67.7 R: 92.1
15	AGL2025	C: 6.6 R: Not reached	C: 8.5 R: Not reached	C: 24.0 R: 58.8	C: 61.1 R: 93.6
Amorphous Silica Fabrics					
18	FS-NEW-O	C: 8.6 R: 110.8	C: 8.5 R: Not reached	C: 9.9 R: >60	C: 61.1 R: 89.6
19	AAS1800	C: 12.6 R: Not reached	C: 2.5 R: Not reached	C: 6.3 R: >60	C: 70.4 R: 97.2
Carbon/Aramid Fabrics					
21	CK-3	C: 6.1 R: N/A	C: 4.8 R: N/A	C: 13.1 R: N/A	C: 66.9 R: N/A

[a] *Thermal Protective Performance (TPP). Measured with the Meker burner (incident heat flux: 83 ± 2 kW/m^2) and a calorimeter with a 6.4 mm-thick air gap.*
[b] *Radiative Protective Performance (RPP). Measured with the cone heater (incident radiative heat flux: ≈83.5 kW/m^2) and a water-cooled heat flux transducer with a 6.4 mm-thick air gap.*
[c] *Heat Blocking Efficiency (HBE) = 1—[(transmitted heat flux)/(incident heat flux)]. Convective: Meker burner, radiative: cone heater.*
[d] *HBE-r decreased to ∼70% at 500 s.*

burn room inside donated residential buildings during firefighter training sessions.

Figure 2A shows a house (L-shaped flat) used for firefighter training. The experiment was conducted by exposing two dollhouse-size wooden structures (0.31 m W × 0.31 m D × 0.41 m H, 19 mm (3/4")-thick cedar walls and roof) to a wooden pallet/straw fire in a room inside the house. Each structure was wrapped with different fire blankets: metallic polyester coated amorphous silica (AAS1800) and pre-oxidized carbon fiber (CK-3) (see **Table 1**). The blankets were secured with staples using a manual staple gun. Each structure was equipped with three thermocouples (K type, 0.5 mm [0.020"] diameter stainless steel sheath, ungrounded) for measuring the temperatures of the blanket fabric outer (exposed) surface, wood outer surface (between the blanket and wood), and the wood inner surface. **Figure 2B** shows the covered wooden structures placed on sintered blocks surrounded by wooden pallets inside the house before fire. **Figure 2C** shows the wooden structure after fire exposure. Although the fire blankets were significantly damaged (scorched) and the wood charred, ignition of the structures is successfully prevented. Thus, the based on the success criteria definition, both fire blankets passed with a minimum success.

Figure 3 shows the temporal variations in the measured temperatures. Red and black curves are for metallic amorphous silica and pre-oxidized carbon, respectively. For the pre-oxidized carbon blanket, the fabric outer surface increased rapidly to ≈700°C in 120 s after exposure and increased more gradually to the maximum of ≈850°C at 400 s just before fire suppression by water began. Although the continuous operating temperature of pre-oxidized carbon was very high (1,427°C, see **Table 1**), the fabric was severely damaged and became brittle. The wood outer surface (between the blanket and wood) temperature was 100°C to 250°C lower than the fabric outer surface temperature. Therefore, the pyrolysis and charring of wood, which started

TABLE 3 | Measured thermal characteristics of multiple-layer fire blankets.

Assembly no.	Layered fabrics	Alignment	Thickness[a] (mm)	Time to $T_b = 300^\circ C$ C: Conv. R: Rad. (s)	Time to $q = 13$ kW/m^2 C: Conv. R: Rad. (s)	TPP rating[b] C: Conv. R: Rad. (cal/cm^2)	HBE[d] C: Conv. R: Rad. (%)
Aramid/Fiberglass/Carbon Fabrics							
A6	AFL1700 AFL1700	Al Fabric Fabric Al (exposed)	2.0	C: 39.7 R: N/A	C: Not reached R: N/A	C: >60 R: N/A	C: 89.5 R: N/A
B1	FLPN1500 FLPN1500	Fabric Fabric (exposed)	3.1	C: 49.0 R: 26.2	C: Not reached R: 58.0	C: >60 R: 55.9	C: 87.0 R: 82.1
B2	FLPN1500 AFLPN1500	Fabric Fabric Al (exposed)	2.6	C: 35.9 R: N/A	C: Not reached R: N/A	C: >57.4 R: N/A	C: 86.3 R: N/A
B3	AFLPN1500 FLPN1500	Fabric Al Fabric (exposed)	2.6	C: 67.8 R: N/A	C: Not reached R: N/A	C: >60 R: N/A	C: 89.0 R: N/A
B4	AFLPN1500 FLPN1500	Al Fabric Fabric (exposed)	2.8	C: 49.1 R: N/A	C: Not reached R: N/A	C: >60 R: N/A	C: 90.0 R: N/A
B5	AFLPN1500 AFLPN1500	Fabric Al Fabric Al (exposed)	2.4	C: 63.2 R: 215.6	C: Not reached R: 269.3	C: >60 R: > 60	C: 87.5 R: 80.1
B6	AFLPN1500 AFLPN1500	Al Fabric Fabric Al (exposed)	2.5	C: 35.0 R: 201.9	C: Not reached R: 361.5	C: >60 R: > 60	C: 91.6 R: 85.2
Fiberglass Silica Fabrics							
C1	GL2025 GL2025	Fabric Fabric (exposed)	1.4	C: 21.4 R: 65.7	C: 27.0 R: 138.1	C: 47.0 R: > 60	C: 77.9 R: 84.5
C2	GL2025 AGL2025	Fabric Fabric Al (exposed)	1.3	C: 20.3 R: 608.2	C: 27.4 R: Not reached	C: 48.7 R: > 60	C: 75.1 R: 92.5
C3	AGL2025 GL2025	Fabric Al Fabric (exposed)	1.3	C: 32.3 R: 94.9	C: 64.3 R: Not reached	C: 57.5 R: > 60	C: 77.8 R: 90.3
C4	AGL2025 GL2025	Al Fabric Fabric (exposed)	1.3	C: 18.5 R: 23.0	C: 250.0 R: Not reached	C: >60 R: > 60	C: 79.8 R: 91.4
C5	AGL2025 AGL2025	Fabric Al Fabric Al (exposed)	1.3	C: 30.8 R: Not reached	C: 36.2 R: Not reached	C: >60 R: > 60	C: 77.5 R: 93.7
C6	AGL2025 AGL2025	Al Fabric Fabric Al (exposed)	1.4	C: 16.5 R: 157.2	C: 63.5 R: Not reached	C: >60 R: > 60	C: 87.9 R: 96.2
C7	AGL2025 AGL2025 AGL2025	Fabric Al Fabric Al Fabric Al (exposed)	2.3	C: 76.8 R: 469.3	C: 124.9 R: Not reached	C: >60 R: > 60	C: 84.5 R: 90.5
C8	AGL2025 AGL2025 AGL2025	Al Fabric Fabric Al Fabric Al (exposed)	2.3	C: 43.8 R: 106.5	C: 145.5 R: Not reached	C: >60 R: > 60	C: 84.2 R: 92.3

(Continued)

TABLE 3 | Continued

Assembly no.	Layered fabrics	Alignment	Thickness[a] (mm)	Time to $T_b = 300°C$ C: Conv. R: Rad. (s)	Time to $q = 13$ kW/m^2 C: Conv. R: Rad. (s)	TPP rating[b] C: Conv. R: Rad. (cal/cm^2)	HBE[d] C: Conv. R: Rad. (%)
D6	1299-074 1299-074	Al Fabric Fabric Al (exposed)	0.28	C: 9.8 R: N/A	C: 8.3 R: N/A	C: 17.7 R: N/A	C: 75.7 R: N/A
E5	FS-OLD FS-OLD	Fabric Al Fabric Al (exposed)		C: N/A R: 236.2	C: N/A R: Not reached	C: N/A R: 59.8	C: N/A R: 92.4
E6	FS-OLD FS-OLD	Al Fabric Fabric Al (exposed)	0.33	C: 8.8 R: 93.0	C: 29.3 R: Not reached	C: 24.9 R: > 60	C: 68.2 R: 95.4
F5	SW-HD SW-HD	Fabric Al Fabric Al (exposed)	0.8	C: 18.7 R: N/A	C: 21.8 R: N/A	C: 40.2 R: N/A	C: 78.0 R: N/A
F6	SW-HD SW-HD	Al Fabric Fabric Al (exposed)	0.8	C: 13.3 R: 121.3	C: N/A R: Not reached [c]	C: 50.0 R: > 60	C: 89.5 R: 96.2
F7	SW-HD SW-HD SW-HD	Fabric Al Fabric Al Fabric Al (exposed)		C: N/A R: 210.3[e] 155.9[f]	C: N/A R: Not reached[e] 165.5[f]	C: N/A R: > 60	C: N/A R: 88.6[e] 84.1[f]
F8	SW-HD SW-HD SW-HD	Al Fabric Fabric Al Fabric Al (exposed)		C: N/A R: 84.2	C: N/A R: 260.0	C: N/A R: > 60	C: N/A R: 87.3
Amorphous Silica/Fiberglass Fabrics							
G6	FS-NEW-I FS-NEW-O	Al Fabric Fabric Al (exposed)	0.38	C: 10.7 R: 78.9	C: 52.5 R: Not reached	C: 41.9 R: > 60	C: 85.6 R: 92.6

[a] *Measured.*

[b] *Thermal Protective Performance (TPP). Measured with the Meker burner (incident heat flux: 83±2 kW/m^2) and a calorimeter with a 6.4 mm-thick air gap.*

[c] *Radiative Protective Performance (RPP). Measured with the cone heater (incident radiative heat flux: ≈83.5 kW/m^2) and a water-cooled heat flux transducer with a 6.4 mm-thick air gap.*

[d] *Heat Blocking Efficiency (HBE) = 1—[(transmitted heat flux)/(incident heat flux)]. Convective: Meker burner, radiative: cone heater.*

[e] *The adhesive did not ignite in the cone heater experiment.*

[f] *The adhesive ignited in the cone heater experiment.*

at 200–300°C (390–570°F), occurred (see **Figure 2C**). The temperature of the wood inner surface increased gradually to the maximum of ≈200°C at 400 s.

For the metalic amorphous silica blanket, the trend was similar to the pre-oxidized carbon case, but the fabric outer surface and wood outer surface temperatures were somewhat lower and reached ≈750°C and ≈650°C, respectively. The fabric outer surface temperature exceeded the melting point of aluminum (660°C), and the surface was severely damaged (see **Figure 2C**). However, the continuous operating temperature of base material (amorphous silica) was 980°C, and there was no significant damage on the fabric except discoloring. The wood inner surface temperature went up to the maximum of ≈400°C at 400 s. This result was consistent with the visual observation that the inner surface of the wood was more pyrolized for the silica fabric case. It was difficult to speculate the differences between the two different fabrics because the heat exposure conditions may be different. Note that, even though the fabric was damaged and the pyrolizing wood outer surface temperature exceeded 300°C and reached ≈750°C for both cases, flaming ignition was prevented because the fabric was in contact with the charring wood surface to block the oxygen penetration. By definition, the both fire blankets are judged as a "pass/minimum success."

An additional burn-room experiment was conducted using the same fire blanket materials in a two-story house, which was burned down after the experiment and firefighter training. The

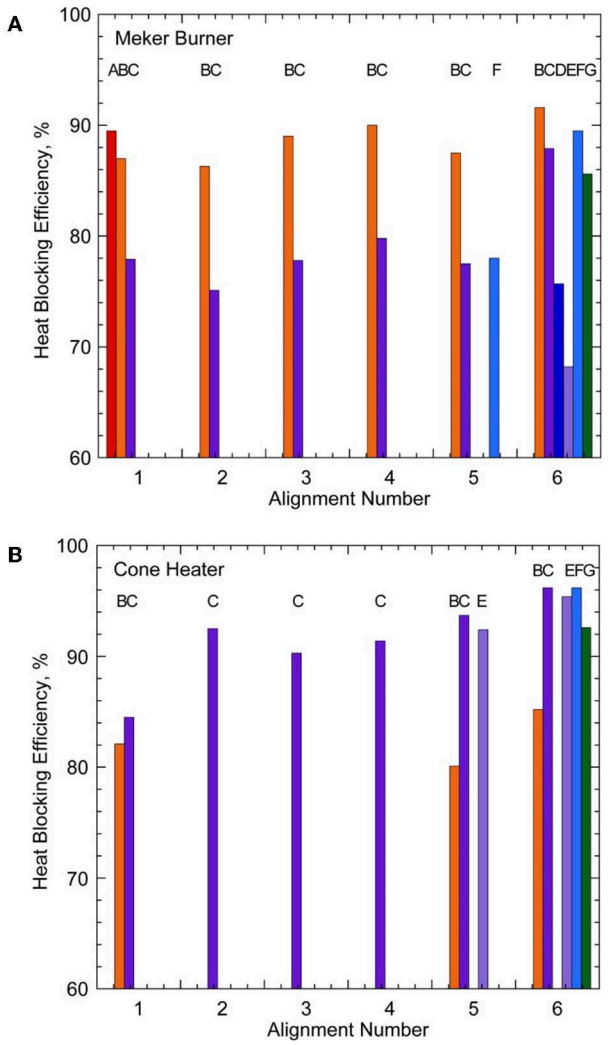

FIGURE 1 | Effects of the layer alignment on the heat-blocking efficiency of double-layered aluminized materials in the **(A)** Meker burner and **(B)** cone heater. Assembly number (see **Table 3**), A-aramid/fiberglass, B-aramid/carbon/fiberglass, C, D, E, F-fiberglass, G-fiberglass (inner) and amorphous silica (outer); 1-fabric+fabric (exposed), 2-fabric+fabric/Al (exposed), 3-fabric/Al+fabric (exposed), 4-al/fabric+fabric, 5-fabric/Al+fabric/Al (exposed), 6-Al/fabric+fabric/Al (exposed).

FIGURE 2 | The burn-room experiment in Avon Lake, Ohio experiment. **(A)** The fire gushes through the window toward a temperature and heat-flux sensor stand (left), **(B)** the blanketed wooden model structures surrounded by palettes before ignition. Left: metallic polyester coated amorphous silica (AAS1800) and right: pre-oxidized carbon fiber (CK-3), and **(C)** the structures after fire exposure (left: CK-3 and right: AAS1800).

effects of heat exposure and high temperature on the structures were very similar to the previous fire experiment. Again, the fire blankets were damaged and the wood charred, but ignition of the structures was prevented. This result suggested that it is critically important to secure the fire blanket in contact with the wood structure to keep oxygen in air from contacting with the high-temperature wood surface and thus to prevent flaming ignition.

Prescribed Burn Experiments in California

Experimental Approach

The field-fire experiments of fire blankets were conducted in prescribed wildland fires in Castaic, Los Angeles County, California, as a part of the live-burn testing operation for bull-douser operator protection and fire shelter testing hosted by the USDA Forest Service San Dimas Technology Development Center (FS SDTDC). The prescribed burn was administered by the Los Angeles County Fire Department. A satellite map of the live burn sites is presented as **Supplementary Figure 1**. The burn areas are on slopes facing north (darker shades) and the observation viewpoint areas are located on the south-facing

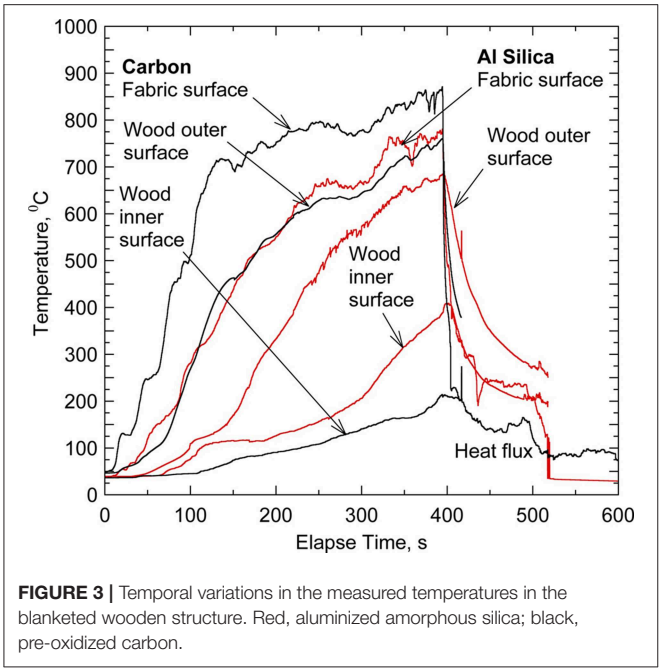

FIGURE 3 | Temporal variations in the measured temperatures in the blanketed wooden structure. Red, aluminized amorphous silica; black, pre-oxidized carbon.

slopes across the valley. The distances between the test structures and the view areas are ≈229 m (≈750 ft) for Burn #1 and ≈153 m (≈500 ft) for Burn #2. The fuel is chaparral, a special plant community characterized by drought-hardy, woody shrubs, shaped by a Mediterranean-type climate (summer drought, winter rain) and intense, infrequent wildfires (Anon, 2012).

For each burn, four instrumented wall-and-roof wooden structures are used. A sketch of the wall-and-eave wooden structure is included as **Supplementary Figure 2**. The wall (1.22 m [4 ft] width × 1.83 m [6 ft] height) and roof (1.22 m [4 ft] width × 0.61 m [2 ft] length) are made of plywood sheathing (Lowe's, 12242, 19/32" thickness, pine rated) with cedar siding (Star Lumber, Winlock, WA; CSS3484, ¾" × 8' × 4') and plywood sheathing with cedar shingle roof panels (Star Lumber, 6C-RFP), respectively. The cedar siding and roof panel materials are the same kind with those for a full-size shed (see section Prescribed Burn Experiments in New Jersey).

Each structure is instrumented for heat-flux and temperature measurements. Two incident heat flux transducers (ITI Model HT-50, T-type thermocouple) are placed on the wall (near the edges of Panels #1/#2 and #3/#4 at 1.22 m [48"] height). A water-cooled through-the-fabric heat flux transducer (Medtherm 64 Series) and three K-type thermocouples (for the fabric's front surface, back surface, and the sheathing back surface temperatures at 1.22 m [48"] height) on each panel. The cooling water is circulated using two sets of a pump and a buried 18.9 L (5 gallon)-reservoir to the heat-flux transducers on Panels #1/#2 and #3/#4. The signals from the sensors are recorded at 10 Hz using a field data-acquisition system (National Instruments, CompactRIO, cRIO-9014) covered by an insulated stainless steel box. Photographic and video observations are made using a digital camera (Nikon D300s) at a distant viewing area across the valley. Two fire-box-protected video cameras are also installed nearby the structures by the USDA FS Missoula Technology Development Center (MTDC).

TABLE 4 | Fire blanket materials tested in prescribed burns.

Panel #[a] or location[b,c]	Code name	Fabric description
Castaic, California		
Burn #1		
1[a]	FS-NEW-I and FS-NEW-O	Fiberglass (USFS new fire shelter, inner shell), aluminized coating inside + amorphous silica (outer shell), aluminized coating outside
2	SW-HD	Fiberglass (structure wrap, heavy duty), aluminized coating
3	1299-074 double	Fiberglass, aluminized polyester coating inside and outside
4	AFLPN1500	Aramid-carbonized acrylic blend (non-woven)/aramid outer layer (woven)/fiberglass core (woven), aluminized PET coating
Burn #2		
1	FS-NEW-O	Amorphous silica (USFS new fire shelter, outer shell), aluminized coating
2	SW-STD	Fiberglass (structure wrap, standard duty), aluminized coating
3	AGL2025	100% fiberglass, aluminum foil coating
4	1025	Fiberglass, aluminized polyester coating
Warren Grove, New Jersey		
Burn #2		
A/B[b] (S/W)[c]	AGL2025	100% fiberglass, aluminum foil coating
B/C (N/W)	SW-HD	Fiberglass (structure wrap, heavy duty), aluminized coating
C/D (N/E)	FS-NEW-O	Amorphous silica (USFS new fire shelter, outer shell), aluminized coating
D/A (S/E)	1025	Fiberglass, aluminized polyester coating

[a] *From left to right on the back side.*
[b] *A-B-C-D (wall identifier): clockwise A (entrance), B, C, and D. Wall A faces south.*
[c] *N-E-S-W (geographic directions): north (N), east (E), south (S), and west (W).*

Materials

Each structure is wrapped with a different aluminized fire blanket material as shown in **Table 4**. The blankets are secured with staples using a manual staple gun. The materials of the base fabrics are fiberglass, amorphous silica, and aramid/fiberglass/pre-oxidized carbon composite as shown in **Table 1**. The laboratory performance test results for single and double-layer fire blankets are included in **Tables 2**, **3**, respectively. The fire blankets, which exhibited relatively high performance (mainly HBE values) among the 50 single-layer fabrics reported previously (Takahashi et al., 2014), are selected for the fire exposure tests. All fire blanket tested (**Table 4**) are single-layer, except for the USFS new fire shelter (assembly #G6 in **Table 3**) used for Panel #1 in Burn #1 and the double fiberglass with aluminized polyester for Panel #3 (assembly #D6 in **Table 3**) in California. Since the single fabrics performed well in Burn #1 as described below, double-layer blankets are not used in proceeding fire exposure experiments.

Results and Discussion

Burn #1

Figure 4A shows four wall-and-eave structures covered with fire blankets standing ≈1.8 m (6 ft) away from the edge of the vegetation on a steep slope before Burn #1. Two heat-shielded video camera boxes are also seen besides the structures. There is a fire break line (no vegetation) of 3 m to 6 m (10 to 20 ft) width on the slope on the right hand side (west) of the structures. The fire, started at the east end along the bottom of the valley, climbed up the slope and spread westward. **Figure 4B** shows the fire front approaching the wall-and-eave structures. **Figures 4C,D** show the wall-and-eave structures after Burn #1. Both the fire blankets and the wood parts (not shown) exhibited no sign of damage. Therefore, by definition, the all four fire blankets are judged as a "pass/complete success."

Figure 5A shows the measured incident heat flux (and the transducer temperature) on the wall (near the edges of Panels #1/#2 and #3/#4) in Burn #1. For Panels #1/#2 and #3/#4, the incident heat flux peak at ≈10 kW/m^2 and ≈15 kW/m^2, respectively, and the exposure duration was ≈150 s for both locations. **Figure 5B** shows the measured incident and through-the-fabric heat fluxes, fabric front-side (T_{front}) and back-side (T_{back}) surface temperatures, and the plywood sheathing back-side temperature (T_{inside}) for Panel #1. The fabric front and back surface temperatures varied in response to the incident heat-flux peaks (when a flare approached occasionally). The fabric front surface temperature peak only up to 120°C, and the wood back surface (and inside) temperature were kept <80°C. The measured heat-flux and surface temperature values were lower than the critical heat flux and ignition temperature of wood (13 to 20 kW/m^2 and ≈300°C). The intensity and duration of heat exposure on the structures were weaker than expectation. A plausible explanation for this result was due to the relatively scarce vegetation on the slope, the bare (no-fuel) fire line along the slope, the cleaned front gap in Burn #1 (see **Figure 4C**) as well as the steep slope, which caused fast flame spread and short fire exposure. Thus, more intense and longer heat exposure was desired to test the fire blankets' performance.

Burn #2

Because the Burn #1 did not leave any obvious damage to the blankets and wood panels, additional tree branches and bushes were piled up in front of the structures in Burn #2 to increase the fire exposure. **Figure 6A** shows four wall-and-eave structures covered with different fire blankets before Burn #2, standing on a slope shallower than that of Burn #1. The fire was ignited on the bottom of the valley and reached the structure location in several minutes. **Figures 6B,C** show the wall-and-eave structures being exposed to a blaze for a few minutes. **Figure 6D** shows four undamaged protected structures (right) in contrast to an nearly unprotected (covered with coarse "chicken" wire mesh) wooden structure ≈6 m (≈20 ft) away (left), which was burning for a relatively long period (≈20 min) after the fire front has passed. Video footages that cover the times corresponding to **Figures 6C,D** are presented as **Supplementary Videos 1**, **2**, respectively.

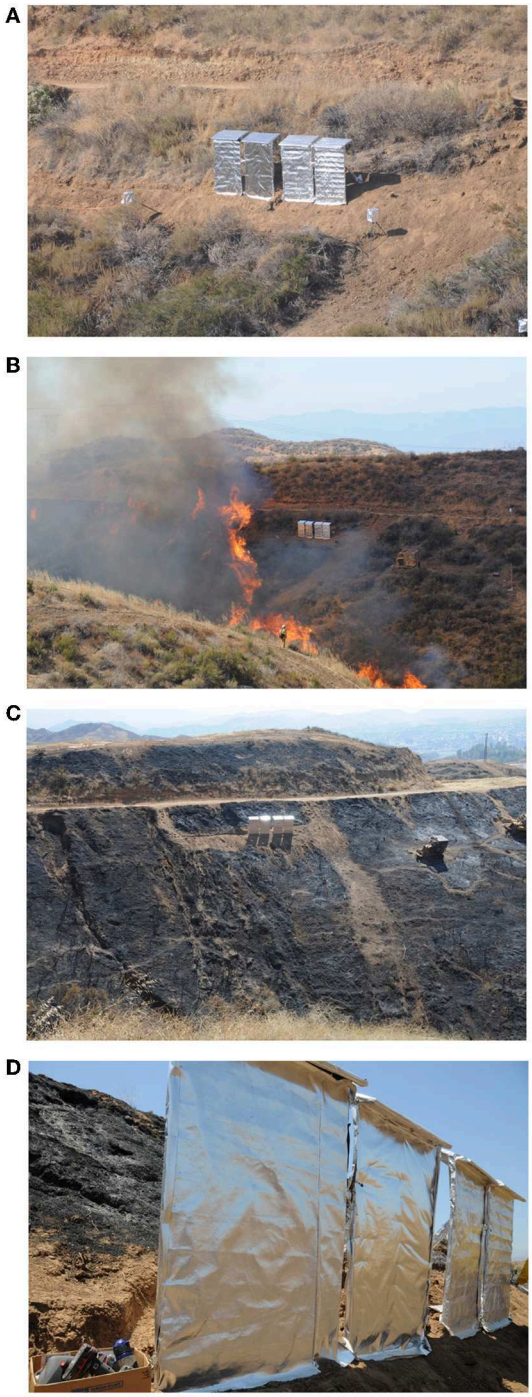

FIGURE 4 | Photographs of Burn #1. **(A)** Four wall-and-eave wood structures covered with different fire blankets (see **Table 4**) standing on the slope and two protected camera box stands on both sides, **(B)** the fire front is climbing up the slope and approaching the structures, and **(C,D)** the undamaged wood structures with fire blankets after the prescribed burn.

This Burn #2 result demonstrated the impressive performance of fire blankets in a real wildland fire scenario. **Figures 7A,B** show all four undamaged fire blankets and the wood panels before and

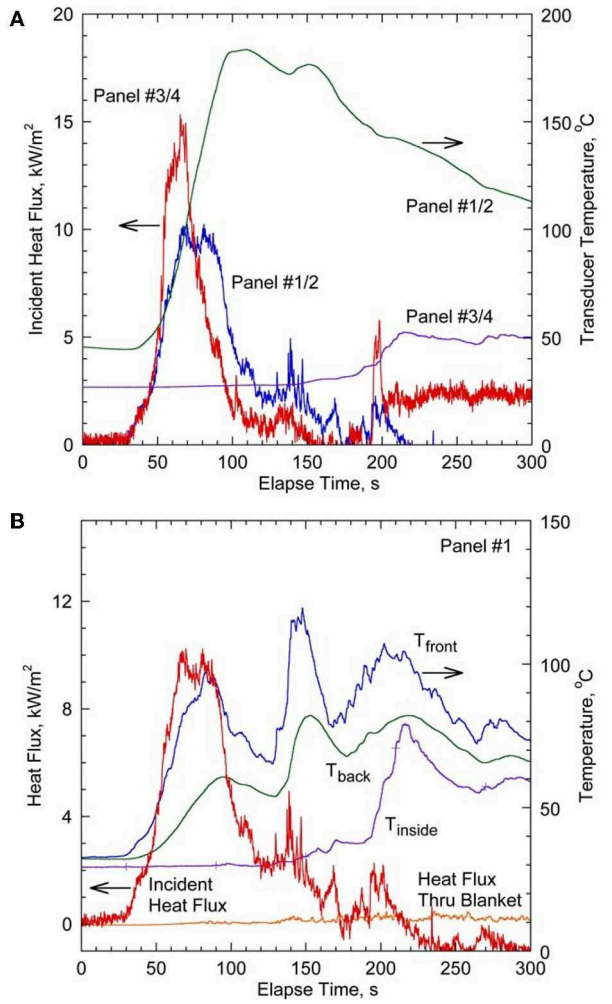

FIGURE 5 | Measurements in Burn #1. **(A)** The incident heat flux and transducer temperature at the wall locations between the edges of Panels #1/#2 and #3/#4, and **(B)** incident and through-the-fabric heat fluxes and temperatures at the fabric front and back surfaces and the back (inside) of the wood sheath of Panel #1.

after removing the blankets after the burn. **Figure 7C** shows a coin-size scorched spot on the bottom left corner of the leftmost Panel #4. This burn mark seemed to happen as a result of hot-gas penetration through a small gap between two fire blankets, which were secured with staples. This incidence suggests that although the aluminized fire blankets are impermeable, it is crucially important to seal gaps between fire blankets to avoid hot-gas or firebrand penetration. Nonetheless, by definition, all four fire blankets are judged as a "pass/complete success."

Figure 8A shows the measured heat fluxes and temperatures in the wooden wall structure (Panel #3). The plots include the incident heat flux, incident heat flux transducer temperature ($T_{\text{inc.HFT}}$), through-the-blanket heat flux, fabric front-side (T_{front}) and back-side (T_{back}) surface temperatures, and the plywood sheathing back-side temperature (T_{inside}). The heat exposure on the blanketed structures (Panels #3 and #4) lasted

FIGURE 6 | Photographs of Burn #2. **(A)** Four wall-and-eave wood structures covered with different fire blankets (center; see **Table 4**) and another wood structure covered with wire mesh screen (left) standing on the slope **(B,C)**, the fire front is approaching and engulfing the structures, and **(D)** the undamaged four wood structures (right) and the burning wire mesh-covered structure (left) after the prescribed burn (see **Supplementary Videos 1**, **2**).

≈5 min with a peak incident heat flux of ≈20 kW/m^2 and $T_{\text{inc.HFT}}$ peaked at 300°C. The heat exposure (level and duration) was greater than those in Burn #1 (**Figure 5A**) and comparable to the threshold for ignition of woods (13 to 20 kW/m^2 and ≈300°C). T_{front} rose up to peaks of 200°C, while T_{back} and T_{inside} remained low (<80°C), thereby protecting the wood structure. The heat exposure for Panels #1 and #2 (not shown) was much smaller. This observation was consistent with video observations showing more fire attack on Panels #3/#4 compared to #1/#2 (see **Figure 6C** and **Supplementary Video 1**).

Figure 8B shows the numerical results based on the method previously used (Hsu et al., 2011) for Panel #3 as well (dashed). Note that the applied heat source as a function of time is prescribed according to the measured incident heat flux, and the simulated through-the-blanket heat flux and T_{back} are respectively obtained at $x = L_f$ and $x = L_s$ in the model. It is found that using 70% of incident heat flux from radiation (30% from convection) has a good comparison with the experimental data. The numerical model based on the laboratory experiment successfully captured the general trend in the thermal response of the structure in a real wildland fire scenario.

Prescribed Burn Experiments in New Jersey

Experimental Approach

The large-scale proof-of-concept fire exposure experiments for fire blankets were conducted in the Pine Barrens in Warren Grove, New Jersey, as a part of the controlled-burn fuel management operation regularly performed by the New Jersey Forest Fire Service (NJFFS) during late fall through early spring to reduce accumulated fuels. Although two burns were conducted over the 2 year period, the post-rain wet vegetation conditions prevented the development of a full-fledged surface-to-crown fire in Burn #1. Therefore, the only results of Burn #2 are presented here. The prescribed burn activities were based on the NJFFS Coyle Field, where a test shed was built. The shed was airlifted by a helicopter from the Coyle Field to the burn site 15 km (9.3 mi) prior to the test day. The shed was placed in a 9 m × 9 m (30 ft × 30 ft) cutout area in the Pitch Pine forest.

A satellite map of the live burn sites in Warren Grove, New Jersey is presented as **Supplementary Figure 3**. The map illustrates the prescribed burn strategy in the experiment. Two blocks directly east of the block where the shed was place were burned earlier to contain the fire within the shed block. Two other blocks east were burned the year before. The prescribed burn was planned as a west wind driven "head fire," and keep sending the head fire into the flanks to eliminate any chance of escape. The total area burned for the day was 890 m^2 (220 acres). The fuel is Pitch Pine (4.5 to 9 m height) and underbrush (scrub oak). To make intense heat exposure more evenly distributed around the shed, additional fuels (pine branches) are placed 1.5 m to 3.3 m (5 ft to 10 ft) away from the shed.

An instrumented wooden shed (Home Depot, Star Select Cedar Shed, Model 100659823, 3.1 m W × 2.4 m D × 3.3 m H [10 ft × 8 ft × 11 ft], with cedar bevel siding, cedar roof shingles and additional solid pine sheathing) was used as the test structure. The shed structure is instrumented for heat-flux and temperature measurements. Six incident heat flux transducers (ITI Model HT-50, T-type thermocouple), eight water-cooled through-the-fabric heat flux transducers (Medtherm 64 Series), and forty K-type/T-type thermocouples are placed on the walls and the roof. The cooling water is circulated through the heat

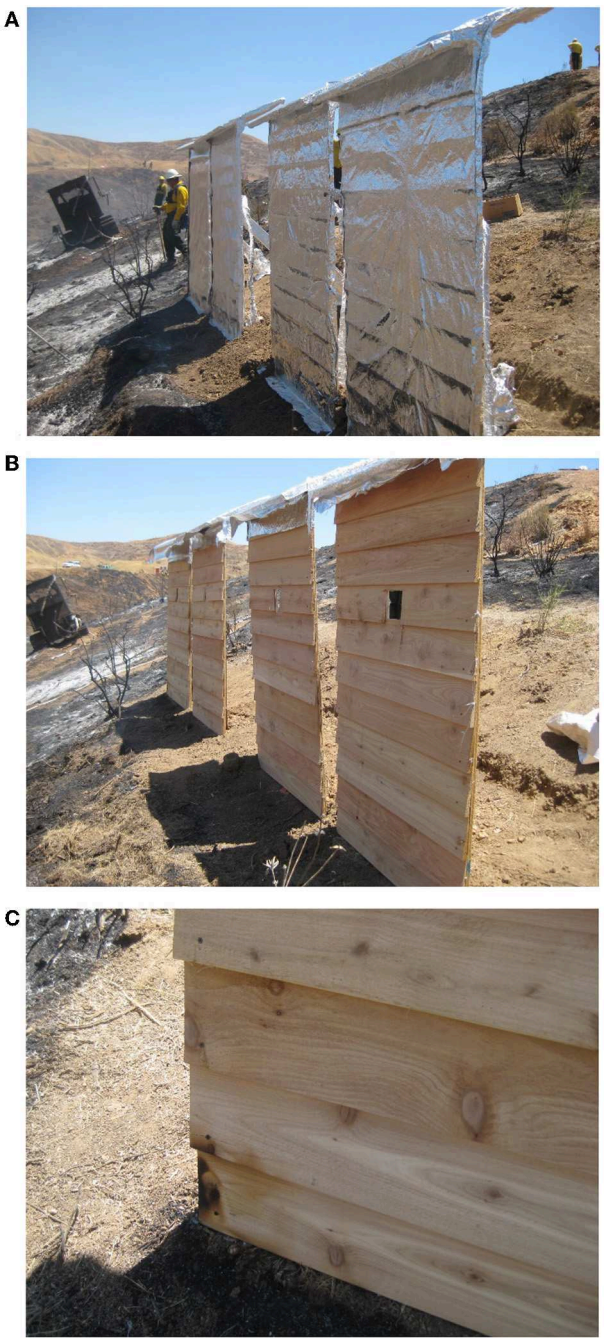

FIGURE 7 | Photographs of the structures after Burn #2. **(A)** All four different fire blankets were undamaged and **(B)** the wood panels are also undamaged, except for **(C)** a coin-size scorching area on the bottom left corner of the leftmost Panel #4.

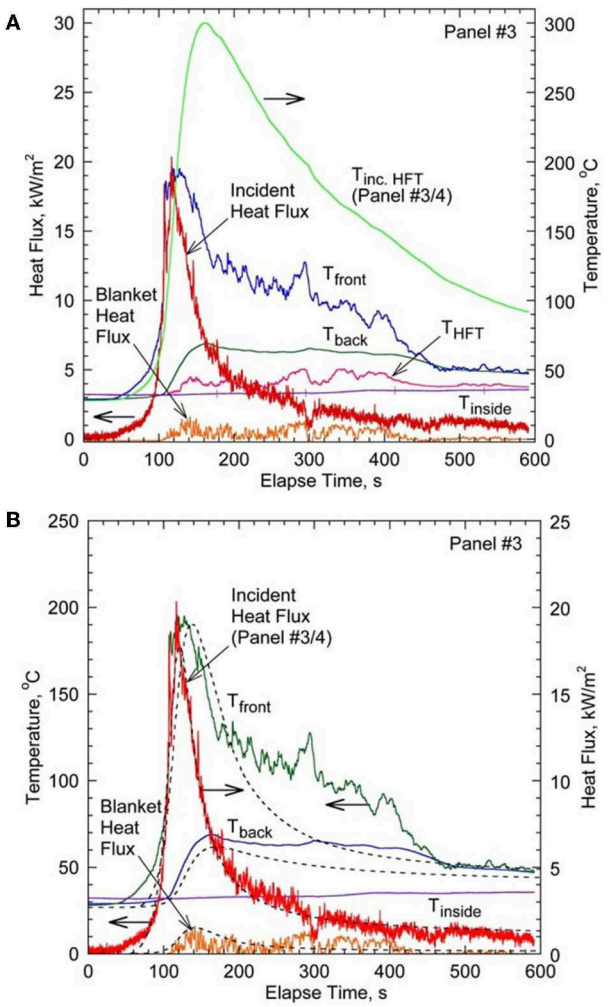

FIGURE 8 | Measurements and calculations in Burn #2. **(A)** Measured incident and through-the-fabric heat fluxes, and temperatures at the fabric front and back surfaces and the back (inside) of the wood sheath of Panel #3, and **(B)** calculated (dashed curves) fabric front and back surfaces and through-the-fabric heat flux based on the prescribed incident heat flux from the experiment.

flux transducers using two pumps from two 18.9 L (5 gallon)-reservoirs. A hemispherical cup anemometer (Met One 034B) and a weather tracker (Kestrel 4000) are placed on a pole 3.3 m (10.8 ft) and 2 m (6.6 ft), respectively, above the ground. The signals from the sensors are recorded at 10 Hz using a field data-acquisition system (National Instruments, CompactRIO, cRIO-9014 and two notebook computers) in a steel box buried outside the shed. Two digital HD video cameras (Sony HDR-CX110) located in the northeast and southwest of the shed are set in heat-shielded steel boxes. The sensors and data system were tested in the prior experiments.

Materials

The structure (shed) is wrapped with four different aluminized fire blanket materials listed in **Table 4**. The blankets are secured with staples using a manual staple gun. From a top view perspective, each blanket covers a quarter section of the shed around the corner of the walls and a quarter part of the roof. All fire blankets are selected from ones used in the fire-exposure experiments in California, except that only single outer layer of the USFS new fire shelter (FS-NEW-O) is used instead of the original double-layer ensemble. The materials of the base fabrics are fiberglass or amorphous silica as listed in **Table 1**. The laboratory performance test results for single-layer fire blankets are included in **Table 2**.

Results and Discussion

The underbrush was ignited by drip torches over 91 m (300 ft) along the west fire line (see **Supplementary Figure 3**) to gain the best possible chance of success yet limit the amount of head fire ignited at one time. The incipient fire after ignition quickly developed into ground-to-crown fire (see **Supplementary Figure 4**). The fire front spread at ∼9 to 12 m/min to reach the east fire line in ≈20 min. One of two high-definition video cameras, facing the incoming fire front, captured successfully the sequence of event while the fire front was approaching, engulfing, and passing the shed. A 4 min video footage (2 min before and after the fire front arrival) is presented as **Supplementary Video 3** and the selected video images are shown in **Figure 9**.

The video camera was located ≈6 m (≈20 ft) northeast of the shed, thus viewing walls "C" and "D" (see **Table 4**). Another video camera located ≈10 m (≈30 ft) southwest of the shed could not capture the event because the quartz window of the box was covered with soot and firebrand debris soon after the fire front arrival. A plastic iris inside the lens (of both cameras) locked open after radiant heat exposure fused vanes together, even it was protected by the quartz window. A scene when the fire front was still ≈20 m away (**Figure 9A**), the shiny blanketed shed and trees with green leaves are seen under ordinary sunshine. As the fire front approached from the west side (wall "B"), bright flame became visible (**Figure 9B**). A shower of firebrands and spotting ignition of surface vegetation were observed on the ground. As the fire front reached the shed (**Figure 9C**), the westerly wind became stronger as evident from the fast rotating cup anemometer. **Figure 9D** shows the fire engulfing the shed and the burning branches moving around. The camera box supporting pole flexed backward by the wind so that the shed disappeared from the field of view temporarily. As the fire front moved away from the shed (**Figure 9E**), the camera pole returned to the original position and the branches piled around the shed remained burning (**Figure 9F**). The video camera also recorded the audio signal from the firebrands hitting the camera box supporting pole during the fire front passing.

Figure 10 shows post-fire photographs revealing damage to the fire blankets and wall surfaces of the wooden structure. A left half of the entrance wall "A" (**Figures 10A,B**) and a right half of the wall "B" (**Figures 10C,D**) and a quarter of the roof were covered with aluminum foil laminated fiberglass fabric (see **Table 4**). The aluminum foil was partially peeled and broken away on wall "A," but there was no damage on the wood. The blanket might have been damaged partially when firefighters

FIGURE 9 | Video images from the northeast side captured the fire front approaching from the east side and passing over the blanketed wood structure in a few minutes (see **Supplementary Video 3**). **(A)** The fire front is still ∼20 m away, **(B)** approaching, **(C)** arriving, **(D)** engulfing, **(E)** passing the shed, and **(F)** additional fuels continue to burn.

broke in through the door after the burn. A left half of the wall "B" (**Figures 10C,D**) and a right half of the wall "C" (**Figures 10E,F**) were covered with a heavy-duty structure wrap fabric. There was no apparent damage on both the blanket and wood. A left half of the wall "C" (**Figures 10E,F**) and a right half of the wall "D" (**Figures 10G,H**) were covered with aluminum foil laminated amorphous silica. For wall "C," there was no apparent damage on both the blanket and wood, except that the blanket wrinkled. However, for wall "D," the aluminum foil burned away and the wood was charred. A left half of the wall "D" (**Figures 10G,H**) and a right half of the wall "A" (**Figures 10A,B**) were covered with aluminized polyester laminated fiberglass fabric. The fire blanket burned away, and a part of the wooden wall burned through. Firefighters extinguished the fire on wall "D" by entering the shed and gently spraying water shortly after the controlled burn. The fire blankets and the wood shingle surfaces of the roof were completely intact despite the hot-gas and firebrand exposure.

Based on the success criteria (see section Limitations and Success Criteria) and the observations above, the performance of the fire blankets tested are categorized as: AGL2025 (on walls "A"/"B"), pass/complete success; SW-HD (on walls "B"/"C"), pass/complete success; FS-NEW-O (on walls "C"/"D"), pass/minimum success; and 1,025 (on walls "D"/"A"), fail. Note that the success criteria do not include the nature of fire exposure. Although all blankets were exposed to the same fire, the severity of fire exposure was different, depending on the location in the shed, which affected the incident heat flux, heat transfer modes—radiation, convection, and conduction, gas temperature, wind speed/direction, firebrand, and fuel loading; and most importantly, the exposure duration. For example, wall "D" was located behind the approaching fire front, which caused the wake of the wind direction and relatively low-speed area with a long residence time. The fire lasted a longer time behind the shed, compared to the front side, as evident from the video (**Supplementary Video 3**) and images (**Figures 9E,F**). Moreover, the fire blanket 1025 performed well in the laboratory experiment (see **Table 2**) but failed in the fire exposure probably due to the burn out loss of the combustible reflective layer and the long lasted direct flame contact. The experiment including both pass and fail results is valuable to demonstrate the potential and limitation of the present approach for the structure protection by fire blankets.

FIGURE 10 | Fire blanket and wood structure damage after the prescribed burn (see **Table 4** for the blanket materials). **(A,B)** Wall "A" facing south, **(C,D)** Wall "B" facing west, **(E,F)** Wall "C" facing north, and **(G,H)** Wall "D" facing east.

The data acquisition systems started to record data before the ignition along the west fire line (**Supplementary Figure 3**). However, one of the data acquisition systems stopped prematurely and the incident and through-the-fabric heat flux, blanket temperature, and cup anemometer data were not recorded during the fire exposure. Fortunately, the weather tracker data were acquired successfully. **Figure 11A** shows the air temperature, pressure, relative humidity, and wind speed at 2 m (6.6 ft) above the ground near the shed entrance. **Figure 11B** shows the data collected 1.4 m (4.6 ft) above the ground at the

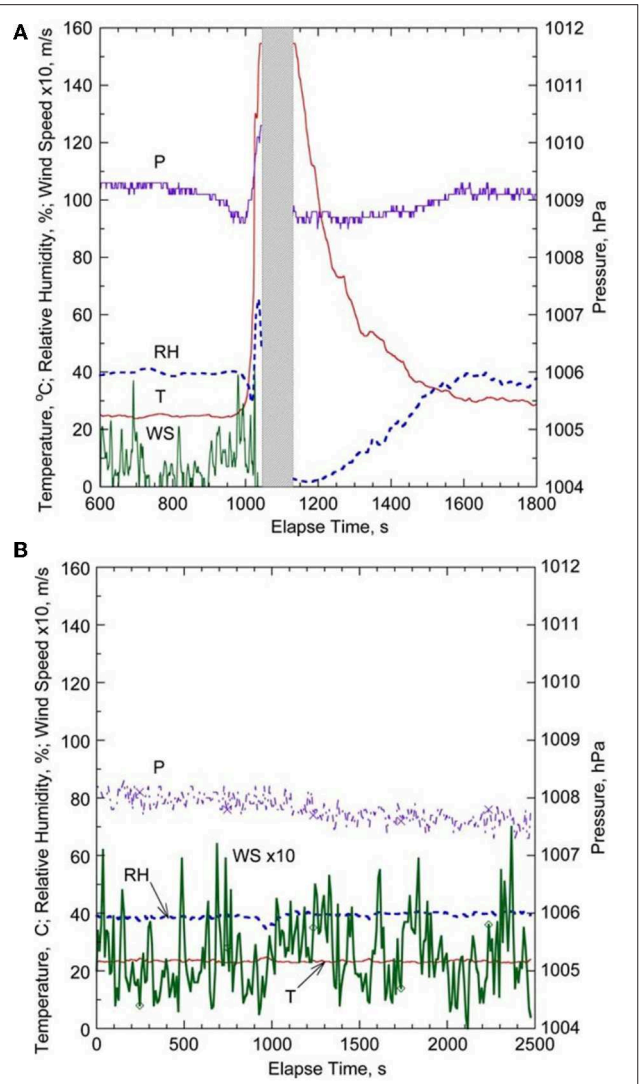

FIGURE 11 | Measured air temperature, pressure, relative humidity, and wind speed. **(A)** At 2 m (6.6 ft) above the ground near the structure entrance (see a cup anemometer in **Figure 9A**) and **(B)** at 1.4 m (4.6 ft) above the ground at the roadside of the west fire line.

road side near the ignition point. The weather condition at the shed before the fire front arrival were sunny/partly cloudy, 22°C (71.6°F), relative humidity of 40%, pressure of 1,009 hPa (14.6 psi), generally westerly wind: 1 to 2 m/s (2.2 to 4.4 mph). As the fire front arrived at the shed (arbitrary elapse time: 1,000 s), the air temperature rose rapidly above the upper measurement limit (clipped at 155°C [311°F]; blackout), the pressure slightly decreased, and the relative humidity dropped. The wind speed vanes meted and quit working as soon as the fire front arrived. As the fire front moved away from the shed, these values except the wind speed recovered gradually toward the initial values in approximately 10 min. The high-temperature blackout period (>155°C) was approximately 50 s. It is consistent with the time period required for the fire front with a spread rate of 9 to 12 m/min to advance 7.5 to 10 m.

Summary

The proof-of-concept experiments, conducted by exposing various fire-blanket-protected wooden structures to realistic fires from burn room to full-scale prescribed burns, have demonstrated both remarkable performance and limitations of the structure protection method using fire blankets. In real fires, the level of heat exposure intensity and duration can vary widely depending on actual WUI fire scenarios and the situation of the structure surroundings. The present field fire experiments have provided valuable information on different cases where the heat exposure vary from relatively low intensity and short duration to severe conditions, thus causing no damage to complete destruction on the fire blankets and structures. In addition, a simple theoretical model is proved to be useful in capturing the trend of the transient response of the blanketed structures to a prescribed incident heat flux input.

The present field fire test results suggest that it is more likely that relatively thin (<1 mm) aluminized fire blankets can protect wooden structures if the heat exposure (heat-flux intensity, air temperature, etc.) does not destroy the aluminized layer and the duration is relatively short (<10 min). The aluminized polyester (PET) film is likely to burn and the aluminum foil laminate tends to peel (due to burning of the adhesive with low temperature resistance, i.e., 148°C) and burn under high heat exposure. If a higher-temperature resistant reflective layer is developed, the performance of fire protective blankets can be improved significantly. Although amorphous silica has a high continuous operating temperature (980°C, see **Table 1**), fiberglass (540°C) may perform properly if the reflective layer keeps the base material temperature sufficiently low. Additional experiments are needed for longer heat exposure period, which plays a critical role in the structure-to-structure ignition in high housing density areas.

CONCLUSIONS

The performance of fire blankets to block heat has been investigated experimentally in the laboratory and prescribed wildfires. Two-layer thin fabric assemblies blocked up to 92% of the convective heat and up to 96% of the radiation (with an aluminized surface). Multiple layers (or thicker single fabric) increase the heat-blocking efficiency by enhanced insulation against the convective heat exposure. On the other hand, multiple layers do not improve the performance against the radiation because the reflection and emission heat loss from the high-temperature front surface dominate the heat transfer mechanism. The series of proof-of-concept experiments provided valuable insight into the capabilities of fire blankets. The experiments demonstrated both successful performance and limitations of thin fire blanket materials by covering the conditions of all success criteria: "pass/complete success," "pass/minimum success," and "fail." The best performed fire blankets may be able to protect building structures if the heat exposure is relatively short (<10 min). This conditions would happen when a wildfire front passes an isolated structure, e.g., a historic cabin. If the heat exposure continues, the fire blanket may more likely to be deteriorated or destroyed, while the building materials are

being pyrolyzed and failed eventually. This situation would be the case for the structure-to-structure ignition. Therefore, for longer exposures (10 s of minutes to more than an hour), better fire blankets (materials, layer assemblies, etc.) would be needed. The key success factors in protecting the WUI structure are (1) the fire blanket's heat-blocking capability, (2) endurance under severe heat-exposure and high-wind conditions, and (3) proper installation to prevent hot-gas and firebrand penetration. Therefore, additional studies are needed in the future in the areas of advanced material/layer developments, blanket deployment methods, and multi-structure protection strategies.

DATA AVAILABILITY STATEMENT

The datasets generated for this study are available on request to the corresponding author.

AUTHOR CONTRIBUTIONS

The author confirms being the sole contributor of this article and has approved it for publication.

FUNDING

This work was supported by the U.S. Department of Homeland Security, Federal Emergency Management Agency, Assistance to Firefighters Grant Program, Fire Prevention and Safety Grant No. EMW-2007-FP-02677.

ACKNOWLEDGMENTS

The author would like to thank valuable contributions to the project by Prof. James S. T'ien, Dr. Sheng-Yen Hsu (CWRU), Dr. Sandra L. Olson (NASA Glenn Research Center), Ted Huffman (Cuyahoga Community College, Fire Academy), Ralph Gonzales, Sam Wu, Ian Grob, Anthony Petrilli (USDA Forest Service, SDTDC and MTDC), and James Dusha (New Jersey Forest Fire Service). Assistance in conducting the experiment by undergraduate co-op students: Amber Abbott, Timothy Murray, Mallory Miller, Jason Williams, Jacob Teets, Brian Guzek, Margaret Rybach (CWRU), and Wyatt Ratliff (Stanford University) was acknowledged. Fire shelter materials and **Supplementary Video 1** were provided by USDA FS MTDC. Some fabric samples were provided by Auburn Manufacturing, Inc.

SUPPLEMENTARY MATERIAL

The Supplementary Material for this article can be found online at: https://www.frontiersin.org/articles/10.3389/fmech.2019.00060/full#supplementary-material

REFERENCES

Ahrens, M. (2010). *Brush, Grass, and Forest Fires*. National Fire Protection Association, NFPA No. USS89.

Albini, F. A. (1986). Wildland fire spread by radiation – a model including fuel cooling by natural convection. *Combust. Sci. Technol.* 45, 101–113. doi: 10.1080/00102208608923844

Anderson, W. R., Catchpole, E. A., and Butler, B. W. (2010). Convective heat transfer in fire spread through fine fuel beds. *Int. J. Wildland Fire* 19, 1–15. doi: 10.1071/WF09021

Anon (2006). *Building and Fire Research Laboratory Activities, Accomplishments and Recognitions*. NIST SP 838-19, National Institute of Standards and Technology, p. 23.

Anon (2009). *Wildland Fire Shelter: History and Development of the New Generation Fire Shelter*, presented by the Interagency Fire Shelter Task Group. Available online at: http://www.fs.fed.us/td/programs/fire/documents/shelhist.pdf (accessed May 29, 2019).

Anon (2012). *The Chaparral*. The California Chaparral Institute. Available online at: http://www.californiachaparral.com/

Anon (2018). *It's a Wrap! How the Forest Service Protects Historic Structures from Fires*. Active NorCal. Available online at: https://activenorcal.com/its-a-wrap-how-the-forest-service-protects-historic-structures-from-fires/ (accessed May 29, 2019).

Anon (2019). *Protecting Homes, Cabins, and Historic Landmarks From Wildfires-With No Water*. Firezat Inc. Available online at: https://www.firezat.com/ (accessed May 29, 2019).

ANSI/FM 4950 (2007). *American National Standard for Evaluating Welding Pads, Welding Blankets and Welding Curtains for Hot Work Operations*. FM Approvals LLC.

ASTM D 4108 (1982). *Standard Test Method for Thermal Protective Performance of Materials for Clothing by Open-Flame Method*. American Society for Testing and Materials.

ASTM D 4151 (2001). *Standard Test Method for Flammability of Blankets*. American Society for Testing and Materials.

ASTM E 1354 (2002). *Standard test Method for Heat and Visible Smoke Release Rates for Materials and Products Using an Oxygen Consumption Calorimeter*. American Society for Testing and Materials.

ASTM F 1939 (2007). *Standard Test Method for Radiant Heat Resistance of Flame Resistant Clothing Materials*. American Society for Testing and Materials.

ASTM F 1989 (2005). *Standard Specification for Cooking Fire Suppression Blankets,* 2005 Edn. American Society for Testing and Materials.

Babrauskas, V. (2001). *Ignition of Wood: A Review of the State of the Art, in Interflam 2001*. Interscience Communications Ltd, London, pp. 71–88.

Backus, P. (2013, May 19). U.S. Forest Service Trains Group on how to protect historic buildings from wildfire. *Missoulian*. Available online at: https://missoulian.com/news/state-and-regional/u-s-forest-service-trains-group-on-how-to-protect/article_e267603c-c0f1-11e2-9ce6-0019bb2963f4.html (accessed May 29, 2019).

Ballinger, V. R. (1973). *Fire Protection Apparatus for a Building*. U.S. Patent, No. 3715843. Alexandria, VA: U.S. Patent and Trademark Office.

Brent, K. M. (2012). *Optimization of fire blanket performance by varying radiative properties* (M.S. thesis). Cleveland, OH: Department of Mechanical and Aerospace Engineering, Case Western Reserve University.

British Standards BS 7944 (1999). *Type 1 Heavy Duty Fire Blankets and Type 2 Heavy Duty Heat Protective Blankets* (superseded withdrawn BS 6575:1985).

British Standards BS EN 1869 (1997). *Fire Blankets* (superseded withdrawn BS 6575:1985).

Butler, B. W. (2010). "Characterization of convective heating in full scale wildland fires," in *VI International Conference on Forest Fire Research,* ed D. X. Viegas (Coimbra).

Cal Fire (2006). *General Guidelines for Creating Defensible Space*. State Board of Forestry and Fire Protection (BOF), California Department of Forestry and Fire Protection. Available online at: http://www.highsierrameadows.com/wp-content/uploads/2016/01/CalFire-Defensible-Space-1.pdf (accessed May 29, 2019).

Cal Fire (2018). *List of California Wildfires*. Available online at: https://en.wikipedia.org/wiki/List_of_California_wildfires (accessed May 29, 2019).

Calderwood, P. L., Brock, J. R., and Chattaway, A. (2006). *Fire Blanket*. U.S. Patent Application, Publication No. WO/2006/008514. Alexandria, VA: U.S. Patent and Trademark Office.

Chitrphiromsri, P., and Kuznetsov, A. V. (2005). Modeling heat and moisture transport in firefighter protective clothing during flash fire exposure. *Heat Mass Transfer* 41, 206–215. doi: 10.1007/s00231-004-0504-x

Chitrphiromsri, P., and Kuznetsov, A. V., Song, G., Barker, R. L. (2006). Investigation of feasibility of developing intelligent firefighter-protective garments based on the utilization of a water-injection system. *Numer. Heat Transfer* A49, 427–450. doi: 10.1080/10407780500359869

Cohen, J. D. (1999). *Reducing the Wildland Fire Threat to Homes: Where and How Much*? USDA Forest Service, General Technical Report No. PSW-GTR-173. Available online at: http://www.fs.fed.us/rm/pubs_other/rmrs_1999_cohen_j001.pdf (accessed November 26, 2018).

Cohen, J. D., and Stratton, R. D. (2008). *Home Destruction Examination: Grass Valley Fire, Lake Arrowhead, California*. USDA Forest Service, Technical Paper, R5-TP-026b (Vallejo, CA). Available online at: http://www.fs.fed.us/rm/pubs_other/rmrs_2008_cohen_j001.pdf [accessed May 29, 2019).

Cohen, J. P. (1991). *A Site-Specific Approach for Assessing the Fire Risk to Structures a the Wildland/Urbanin Interface*. GTR SE-69. USDA Forest Service, Ashville, NC, 252–256.

Davis, W. D., Donnelly, M. K., and Selepak, M. J. (2006). *Testing of Portable Radios in a Fire Fighting Environment*, NIST Technical Note 14774, National Institute of Standards and Technology.

Donnelly, M. K., Davis, W. D., Lawson, J. R., and Selepak, M. J. (2006). *Thermal Environment for Electronic Equipment Used by First Responders,* NIST Technical Note 1474, National Institute of Standards and Technology.

Evans, D. D., Rehm, R. G., and Baker E. S. (2004). *Physics-Based Modeling for WUI Fire Spread – Simplified Model*. Algorithm for ignition of structures by burning vegetation, NISTIR 7179. Available online at: https://www.gpo.gov/fdsys/pkg/GOVPUB-C13-9b91be4e9e8024979f4c8e766261d6f5/pdf/GOVPUB-C13-9b91be4e9e8024979f4c8e766261d6f5.pdf (accessed May 29, 2019).

Evarts, B. (2019). *Fire Loss in the United States During 2018*. NFPA J. 113, 76–83.

Finney, M. A., Cohen, J. D., Grenfell, I. C., and Yedinak, K. M. (2010). An examination of fire spread thresholds in discontinuous fuel beds. *Int. J. Wildland Fire* 19, 163–170. doi: 10.1071/WF07177

Floyd, A. (1997). *Fire Resistant House Cover*. U.S. Patent, No. 5608992. Alexandria, VA: U.S. Patent and Trademark Office.

Frankman, D., Webb, B. W., and Butler, B. W. (2010). Time-resolved radiation and convection heat transfer in combusting discontinuous fuel beds. *Combust. Sci. Technol.* 182, 1–22. doi: 10.1080/00102202.2010.486388

Gabbert, B. (2013, May 20). Cabin wrap: 15,000 staples in, and 15,000 staples out. *Wildfire Today*. Available online at: https://wildfiretoday.com/2013/05/20/cabin-wrap-15000-staples-in-and-15000-staples-out/ (accessed May 29, 2019).

Gainer, W. C. Jr. (1992). *Apparatus and Method for Thrusting a Cover Over a Target Area*. U.S. Patent, No. 5146996. Alexandria, VA: U.S. Patent and Trademark Office.

General Services Administration A-A-50230 (1987). *Blanket, Fire* (Wool, With Case).

General Services Administration A-A-54409 (1991). *Blanket, Burn, (Water-Gel Type, 6 by 5* feet).

General Services Administration A-A-54629 (1992). *Blanket, Burn Relief*.

Gleich, J. (1999). *Rapidly Deployable Fire-Protection Apparatus*. U.S. Patent, No. 5860251. Alexandria, VA: U.S. Patent and Trademark Office.

Goldberg, S. (2006). *Fire Blanket*. U.S. Patent Application, Publication No. WO/2006/122876. Alexandria, VA: U.S. Patent and Trademark Office.

Grant, C. (2018). Modern scourge. *NFPA J.* 112:52.

Hammer, R. B., Radeloff, V. C., Fried, J. S., and Stewart, S. I. (2007). Wildland-urban interface housing growth during the 1990s in California, Oregon, and Washington. *Int. J. Wildland Fire* 16, 255–265. doi: 10.1071/WF05077

Hansen, J. G. R., and Frame, B. J. (2008). Flame penetration and burn testing of fire blanket materials. *Fire Mater.* 32, 457–483. doi: 10.1002/fam.979

Hirschler, M. M. (1997). Analysis of thermal performance of two fabrics intended for use as protective clothing. *Fire Mater.* 21, 115–121.

Hitchcock, D.J. (1997). *Automated Exterior Fire Protection System for Building Structure*. U.S. Patent, No. 5423150. Alexandria, VA: U.S. Patent and Trademark Office.

Hsu, S.-Y., T'ien, J. S., Takahashi, F., and Olson, S. L. (2011). "Modeling heat transfer in thin fire blanket materials under high external heat fluxes, fire safety science," in *Proceedings of the Seventh International Symposium on Fire Safety Science* (Bethesda, MD: International Association for Fire Safety Science).

ICC (2018). *International Wildland-Urban Interface Code*. International Code Council, Club Hills, IL. Available online at: https://codes.iccsafe.org/content/IWUIC2018/toc (accessed May 29, 2019).

Jones, D. N., and Smith, M. C. (1998). *Fire Protection Apparatus for a Building Structure*. U.S. Patent, No. 5829200. Alexandria, VA: U.S. Patent and Trademark Office.

Kilduff, P., and Oswald, T. (2003). *Portable Fire Curtain System*. U.S. Patent, No. 6658801 B2. Alexandria, VA: U.S. Patent and Trademark Office.

Kramer, H. A., Mockrin, M. H., Alexandre, P. M., Stewart, S. I., and Radeloff, V. C. (2018). Where wildfires destroy buildings in the US relative to the wildland–urban interface and national fire outreach programs. *Int. J. Wildland Fire* 27, 329–341. doi: 10.1071/WF17135

Kuruvila, M. (2008). *Tassajara Monks Practice Zen of Firefighting*. The Budhist Channel. Available online at: http://www.buddhistchannel.tv/index.php?id=65,6792,0,0,1,0#.XPA5WfZFw2w (accessed May 29, 2019).

Leonard, J. (2009). *Building Performance in Bushfires*. Report to the 2009 Victorian Bushfires Royal Commission. Commonwealth Scientific and Industrial Research Organisation (CSIRO).

Madrzykowski, D. (2007). "Fatal training fires: fire analysis for the fire service," in *Proceedings of the 11th International Interflam Conference* (Interflam '07) (London), 1–12.

Maranghides, A., and Mell, W. E. (2009). *A Case Study of a Community Affected by the Witch and Guejito Fires*. NIST Technical Note 1635. Available online at: https://ws680.nist.gov/publication/get_pdf.cfm?pub_id=902864 (accessed May 29, 2019).

McQuirk, K. (1989). *Fire Protection for Structures*. U.S. Patent, No. 4858395. Alexandria, VA: U.S. Patent and Trademark Office.

Mell, W. E., and Lawson, J. R. (1999). *A Heat Transfer Model for Fire Fighter's Protective Clothing*. National Institute of Standards and Technology, NISTIR 6299. Available online at: https://nvlpubs.nist.gov/nistpubs/Legacy/IR/nistir6299.pdf (accessed May 29, 2019).

Mell, W. E., Manzello, S. L., Maranghides, A., Butry, D., and Rehm, R. G. (2010). The wildland-urban interface fire problem – current approaches and research needs. *Int. J. Wildland Fire* 19, 238–251. doi: 10.1071/WF07131

Meyer, T. I., and Kessler, H. F. (2004). *Fire Protection Device for Building Structure*. U.S. Patent, No. 6810626 B2. Alexandria, VA: U.S. Patent and Trademark Office.

Miller-Carl, M. (2008). *Fire Spares Historic Structure Thanks to Protective Wrap*. Gold Country Media, Auburn Journal. Available online at: https://goldcountrymedia.com/news/1029/fire-spares-historic-structure-thanks-to-protective-wrap/ (accessed May 29, 2019).

Montanez, R. (2014). *Protective Wrap Covers Historical Structures Near French Fire*. Available online at: https://abc30.com/news/protective-wrap-covers-historical-structures-near-french-fire-/238207/ (accessed May 29, 2019).

Morandini, F., Silvani, X., and Cannac, M. (2007). "Measurement device for data collection during fire spread experiments in the field," in *4th International Wildland Fire Conference* (Sevilla).

Morgan, G., and Leonard, M. (2010). "Australia's most deadly wildfire disaster and its aftermath," in *VI International Conference on Forest Fire Research*, ed D. X. Viegas (Coimbra).

National Wildfire Coordinating Group (2019). *Frequently Asked Questions about Fire Shelters*. Available online at: https://www.nwcg.gov/sites/default/files/memos/eb-m-19-001b.pdf (accessed May 29, 2019).

NFPA (2018). *Wildfire. National Fire Protection Association.* Quincy, MA. Available online at: https://www.nfpa.org/Public-Education/By-topic/Wildfire (accessed May 29, 2019).

NFPA 1144 (2004). *Standard Methods of Fire Tests for Flame Propagation of Textiles and Films,* 2004 Edn. National Fire Protection Association.

NFPA 701 (2018). *Standard for Reducing Structure Ignition Hazards From Wildland Fire*, 2008 Edn. National Fire Protection Association, Quincy, MA.

Petrilli, T. (2006) *What's New With the New Generation Fire Shelter? Fire Tech Tips*, 0651-2322-MTDC, USDA Forest Service.

Putnam, T., and Butler, B. W. (2004). Evaluating fire shelter performance in experimental crown fires. *Can. J. For. Res.* 34, 1600–1615. doi: 10.1139/x04-091

Quarles, S. L., Valachovic, Y., Nakamura, G. M., Nader, G. A., and De Lasaux, M. J. (2010). *Home Survival in Wildfire-Prone Areas: Building Materials and Design Considerations*. University of California, Agriculture and Natural Resources, Publication 8393. Available online at: https://anrcatalog.ucanr.edu/pdf/8393.pdf (accessed May 29, 2019).

Radeloff, V. C., Hammer, R. B., Stewart, S. I., Fried, J. S., Holcomb, S. S., and Mckeefry, J. F. (2005). The wildland–urban interface in the United States. *Ecol. Appl.* 15, 799–805. doi: 10.1890/04-1413

Radeloff, V. C., Helmers, D. P., Kramer, H. A., Mockrin, M. H., Alexandre, P. M., Bar-Massada, A., et al. (2018). Rapid growth of the US wildland-urban interface raises wildfire risk. *Proc. Natl. Acad. Sci. U.S.A.* 115, 3314–3319. doi: 10.1073/pnas.1718850115

Romaine, J.W. (1986). *Fire Blanket*. U.S. Patent 4624320. Alexandria, VA: U.S. Patent and Trademark Office.

Song, G., Barker, R. L. Hamouda, H., Kuznetsov, A. V., Chitrphiromsri, P., and Grimes, R. V. (2004). Modeling the thermal protective performance of heat resistant garments in flash fire exposures. *Textile Res. J.* 74, 1033–1040. doi: 10.1177/004051750407401201

Stein, S. M., Menakis, J., Carr, M. A., Comas, S. J., Stewart, S. I., Cleveland, H., et al. (2013). *Wildfire, Wildlands, and People: Understanding and Preparing for Wildfire in the Wildland-Urban Interface—A Forests on the Edge Report*. Gen. Tech. Rep. RMRS-GTR-299. Fort Collins, CO: U.S. Department of Agriculture, Forest Service, Rocky Mountain Research Station.

Stephen, B. (2014). *Firefighters Wrap Historic Buildings to Protect Them From Forest Fires*. Available online at: http://time.com/3096340/forest-fires-buildings/ (accessed May 29, 2019).

Stewart, S. I., Radeloff, V. C., Hammer, R. B., and Hawbaker, T. J. (2007). Defining the wildland urban interface. *J. For.* 105, 201–207. doi: 10.1093/jof/105.4.201

Stoll, A. M., and Chianta, M. A. (1968). Method and rating system for evaluation of thermal protection, *Aerosp. Med.* 40, 1232–1238.

Takahashi, F., Abbott, A., Murray, T. M., T'ien, J. S., Olson, S. L. (2014). Thermal response characteristics of fire blanket materials. *Fire Mater.* 38, 609–638. doi: 10.1002/fam.2202

Tewarson, A., Wu, P. K., Chin, W. K., and Shuford, R. (2001). *Fire Blankets for Munition Protection: Flame and Heat Blocking Properties of Advanced Materials*. Army Research Laboratory, ARL-TR-2398.

Torvi, D. A., and Dale, J. D. (1999a). Influence of air gaps on bench-top test results of flame resistant fabrics. *J. Fire Protect. Eng.* 10, 1–12. doi: 10.1177/104239159901000101

Torvi, D. A., and Dale, J. D. (1999b). Heat transfer in thin fibrous materials under high heat flux. *Fire Technol.* 35, 210–231. doi: 10.1023/A:1015484426361

Torvi, D. A., and Threlfall, T. G. (2006). Heat transfer model of flame resistant fabrics during cooling after exposure. *Fire Technol.* 42, 27–48. doi: 10.1007/s10694-005-3733-8

U.S. Fire Administration (2002). *Fires in the Wildland/Urban Interface*. Topical Fire Research Series, Vol. 2, .

USDA Forest Service (2003). *The New Generation Fire Shelter*. National Wildfire Coordinating Group, PMS 411, NFES 2710. Available online at: https://www.fs.fed.us/t-d/pubs/pdfpubs/pdf03512803/pdf03512803dpi300.pdf (accessed May 29, 2019).

USDA Forest Service (2007). *Specifications for Water Enhancers (gels) for Wildland Firefighting*. Specification 5100-306a. Available online at: http://www.fs.fed.us/rm/fire/wfcs/documents/306a.pdf (accessed May 29, 2019).

USDA Forest Service (2008a). *Specification, Shelter, Fire, M-2002, 5100-505B*.

USDA Forest Service (2008b). *Specification, Cloths, Laminated, Fire Shelter, Fire, M-2002, 5100-607D*.

USDA Forest Service (2009). *Wildland Fire Shelter: History and Development of the New Generation Fire Shelter*, presented by the Interagency Fire Shelter Task Group. Available online at: http://www.fs.fed.us/t-d/programs/fire/documents/shelhist.pdf (accessed May 29, 2019).

Verzoni, A. (2019). Old and in harm's way: how demographics and topography collided to make the Camp fire California's deadliest and most destructive wildfire ever. *NAPA J.* 113, 10–13.

Wagner, P.R. (1944). *Conflagration-Retardative Curtain*. U.S. Patent, No. 2365127. Alexandria, VA: U.S. Patent and Trademark Office.

Conflict of Interest: The author declares that the research was conducted in the absence of any commercial or financial relationships that could be construed as a potential conflict of interest.

frontiers in Mechanical Engineering

ORIGINAL RESEARCH
published: 22 January 2020
doi: 10.3389/fmech.2019.00069

Modeling Vorticity-Driven Wildfire Behavior Using Near-Field Techniques

Jason J. Sharples[1,2]* *and James E. Hilton*[2,3]

[1] School of Science, UNSW, Canberra, ACT, Australia, [2] Bushfire and Natural Hazards Cooperative Research Centre, East Melbourne, VIC, Australia, [3] CSIRO Data61, Clayton, VIC, Australia

Dynamic modes of fire propagation present a significant challenge for operational fire spread simulation. Current two-dimensional operational fire simulation platforms are not generally able to account for the complex interactions that drive such behaviors, and while fully coupled fire-atmosphere models are able to account for dynamic effects to an extent, their computational demands are prohibitive in an operational context. In this paper we consider techniques for extending two-dimensional fire spread simulators so that they are able to simulate certain dynamic fire behaviors. In particular, we consider modeling vorticity-driven lateral spread (VLS), which is characterized by rapid lateral fire propagation across steep, leeward slopes. Specifically, we consider modeling the influence of the fire on the local surface airflow via a "pyrogenic potential" model, which allows for vertical vorticity effects (in a near-field sense) using the Helmholtz decomposition. The ability of the resulting model to emulate fire propagation associated with VLS is demonstrated using a number of examples.

Keywords: wildfire simulation, dynamic fire propagation, near-field modeling, vorticity-driven lateral spread, pyrogenic potential, Spark

OPEN ACCESS

Edited by:
Dipankar Chatterjee, Central Mechanical Engineering Research Institute (CSIR), India

Reviewed by:
Wei Tang, National Institute of Standards and Technology (NIST), United States
Sandip Sarkar, Jadavpur University, India

***Correspondence:**
Jason J. Sharples
j.sharples@unsw.edu.au

Specialty section:
This article was submitted to Thermal and Mass Transport, a section of the journal Frontiers in Mechanical Engineering

Received: *22 March 2019*
Accepted: *06 December 2019*
Published: *22 January 2020*

Citation:
Sharples JJ and Hilton JE (2020) Modeling Vorticity-Driven Wildfire Behavior Using Near-Field Techniques. Front. Mech. Eng. 5:69. doi: 10.3389/fmech.2019.00069

1. INTRODUCTION

Fire spread simulators are an essential component in the assessment of wildfire risk. Given the requisite information on weather, topography and fuels, they provide fire management end-users with a way to map the likely evolution of an active wildfire across a landscape. Fire spread simulators can also be used to evaluate the effectiveness of different suppression options, as part of a technical assessment of individual fires, or they can be used to inform hazard reduction programs (e.g., prescribed burning or mechanical thinning) as part of broader strategic objectives. The effectiveness of a fire spread simulator, however, is critically dependent on: (i) the accuracy of the information that is used as its input; and (ii) the ability of the underpinning fire spread models and propagation algorithms to faithfully represent the main processes driving fire propagation. This second dependence becomes critical when a fire exhibits dynamic behaviors, which arise in response to multi-scale interactions between the fire and the local fire environment, namely the fuel, weather and topography.

In fact, the current suite of operational fire spread simulators (e.g., Phoenix Rapidfire, FARSITE) are poorly suited to modeling dynamic fire propagation. This is mainly due to their reliance on the assumption that a fire will spread at a quasi-steady rate uniquely determined by environmental conditions, and the assumption that different parts of a fire line propagate independently. This latter assumption, for example, is implicit in propagation algorithms such as those based on Huygens'

Principle, which is often used in operational fire spread simulators (Finney, 2004; Tolhurst et al., 2008). Given that several modes of dynamic fire propagation are now known to influence the development of a fire, the limitations of current operational fire spread simulators constitute a significant gap in operational capability.

Documented examples of dynamic fire propagation include that exhibited by junction fires (Viegas et al., 2012; Thomas et al., 2017; Raposo et al., 2018), eruptive fires (Viegas and Pita, 2004; Viegas, 2006), and vorticity-driven lateral spread (VLS) (Sharples et al., 2012; Simpson et al., 2013, 2014, 2016). These modes of dynamic fire propagation are driven by complex interactions between the fire and the atmosphere, or between different parts of the fire itself. For example, VLS arises due to wind-terrain-fire interactions that produce vertical vorticity, which rapidly propagates a fire across steep, leeward slopes in a direction nearly perpendicular to the ambient wind direction (Simpson et al., 2013). **Figure 1** provides a clear illustration of how a fire burning on a leeward slope can produce pyrogenic vertical vorticity.

At present it is only possible to accurately model phenomena like VLS using three-dimensional coupled fire-atmosphere models. While such an approach is useful for providing insights into the physical processes that drive such behaviors, their computational cost makes them impractical for operational use. Sharples et al. (2017) modified a two-dimensional fire spread simulator using a specific parameterization that forced the model to emulate the dynamic fire behavior observed in connection with VLS. While this approach permitted faster than real time simulations that captured the main characteristics of VLS and improved the overall accuracy of simulations, the lack of a physical basis for the modifications raises questions about the applicability of such an approach in general.

In this paper we consider a recently developed approach to modeling fire spread (Hilton et al., 2018a), which relaxes the assumptions that rate of spread is quasi-steady and that different parts of a fire burn independently. Although this approach is still manifestly two-dimensional, it has been used to successfully model a number of different modes of dynamic fire spread such as the behavior of junction fires. The two-dimensional nature of the model means that it is able to run much faster than real time, yet is still able to reproduce fire spread features that have previously required fully coupled fire-atmosphere models to resolve. Specifically, we demonstrate how this two-dimensional approach can be extended to accommodate vorticity effects, and use it to model the VLS phenomenon.

We begin by giving a more detailed account of the VLS phenomenon in the next section, before outlining the model extension and its application in a number of specific examples.

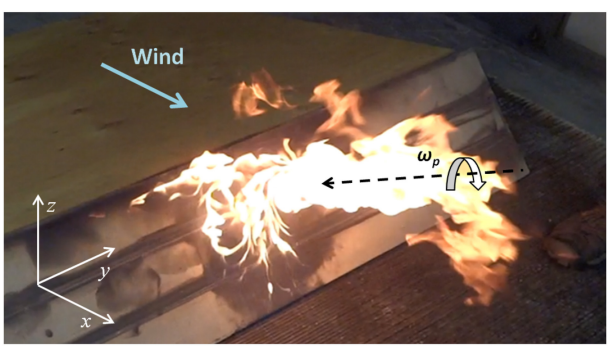

FIGURE 1 | Experimental fire in a wind tunnel showing a fire whirl (vortex) on the leeward slope of an idealized ridge. Note that the vortex is on the left flank of the fire and has components $\omega_x, \omega_z < 0$. The pyrogenic vorticity $\boldsymbol{\omega}_p$ and its orientation are indicated in the figure. The figure has been adapted from Sharples et al. (2015).

2. VORTICITY-DRIVEN LATERAL SPREAD

McRae (2004) first noted the presence of atypical modes of fire propagation in multispectral line-scan data from the 2003 Canberra bushfires. These instances, initially referred to as "lee-slope channeling," are characterized by rapid lateral fire spread across the top of a steep leeward slope in a direction approximately perpendicular to the synoptic wind direction. The upwind edge of the region of lateral spread is constrained by a major break in topographic slope, such as a mountain ridge line. It is also common for the active flaming zone to extend hundreds of meters downwind of the lateral spread region, most likely due to enhanced spotting. Additional features include distinctively darker smoke and vigorous convection associated with the laterally advancing flank of the fire. The rapidity of the lateral spread in a direction that is at odds with the direction a fire would normally be expected to spread, means that this atypical mode of fire propagation can pose a significant danger to firefighter and civilian safety. Indeed, this mode of fire spread has since been implicated in the development of violent pyroconvection (McRae et al., 2015) and in firefighter entrapments (Lahaye et al., 2017).

Subsequent investigation of the phenomenon by Simpson et al. (2013, 2014) using a coupled fire-atmosphere model, indicated that the atypical lateral spread was driven by a three-way interaction between the synoptic winds, the terrain and an active fire. Specifically, it was found that the ambient horizontal vorticity created by flow separation over steep leeward slopes, could be titled and stretched by the rising plume of a fire on the leeward slope to produce strong vertical vorticity, which could then carry the fire laterally across the slope (Sharples et al., 2015). It is of interest to note that the propensity for strong vertical vorticity to form over leeward slopes had been noted much earlier by Countryman (1971). The critical role of pyrogenic vorticity in driving the lateral spread prompted a change in terminology, with the phenomenon subsequently referred to as "vorticity-driven lateral spread" or VLS.

Sharples et al. (2012) identified a number of environmental conditions that were necessary for VLS occurrence. Specifically, they noted that VLS occurrence typically required: a leeward slope angle in excess of about 20–25°; a leeward aspect that aligns to within 30–40° of the wind direction; and wind speeds in excess of about 20 km h^{-1}. In addition, VLS has been observed to occur almost exclusively in heavier fuels (e.g., forest fuels of the order of 15–20 t ha^{-1}). The conditions relating to topography and wind direction can be combined in a simple filter model that identifies

parts of the landscape prone to VLS occurrence under a specified wind direction. The VLS filter takes the form of a binary variable, χ, which assumes a value of 1 in regions prone to VLS occurrence and 0 elsewhere. Mathematically, this can be expressed as follows:

$$\chi(\sigma,\delta) = \begin{cases} 1, & \text{if } \dfrac{180^\circ}{\pi}\tan^{-1}(\|\nabla h\|) > \sigma \text{ and } \theta < \delta; \\ 0, & \text{otherwise.} \end{cases} \quad (1)$$

Here h is the ground elevation and θ is the angle between the downslope direction and the normalized local wind vector $\hat{\mathbf{w}}$, defined by:

$$\theta = \begin{cases} \dfrac{180^\circ}{\pi}\cos^{-1}\left(-\dfrac{\nabla h\cdot\hat{\mathbf{w}}}{\|\nabla h\|}\right), & \text{if } \|\nabla h\| > 0; \\ 180^\circ, & \text{otherwise.} \end{cases} \quad (2)$$

The parameters σ and δ, which define the VLS filter, represent threshold values for the topographic slope and θ, respectively. Only parts of the landscape with slopes greater than σ and with θ less than δ are prone to VLS. The values $\sigma = 16^\circ$ and $\delta = 40^\circ$ were found to be appropriate for a digital elevation model of 90 m resolution, but may not be optimal for digital elevation models of different spatial resolution. While this is an important issue, which is currently the focus of ongoing research, it will not affect the results presented in the following sections.

While the VLS filter is useful for identifying slopes that are prone to VLS occurrence, laboratory experiments, wildfire observations and numerical simulations have revealed that the rapid lateral spread associated with VLS really only occurs in a relatively narrow portion of the leeward slope near the top of the hill (Quill and Sharples, 2015; Raposo et al., 2015; Simpson et al., 2016). This region could be better identified using a second-order VLS filter, based on the second-derivative of elevation, but for the idealized cases considered in sections 3 and 4, a crude approximation will suffice. We therefore use a refined version of the first-order filter χ to define VLS prone regions. Specifically, we consider parts of the landscape VLS-prone only if $\chi = 1$ and they are within 100 meters of the ridge line.

Unfortunately, the fact that VLS arises due to a strong coupling between the fire and the atmosphere, means that it is not possible to model VLS using existing two-dimensional fire spread simulators. These simulators, which are based on the notion of a quasi-steady rate of spread and the assumption that different points along a fire line can be treated essentially as independent source fires, are fundamentally unable to account for the dynamic interactions that drive VLS. While it is possible to model the VLS phenomenon using coupled fire-atmosphere models, their computational demand means that they are not feasible as operational tools. Hence, from the operational perspective, the possible effects of VLS on the overall propagation of a wildfire remain unresolved. Indeed, until computational resources evolve to the point that fully coupled fire-atmosphere simulations can be conducted in the order of minutes (rather than hours or days), there appears to be only two possible approaches to incorporating dynamic effects such as VLS in operational fire spread prediction:

(i) Develop parameterizations of the dynamic behaviors, which then facilitate the use of specially tailored sub-models to emulate the observed behaviors; or
(ii) Develop reduced models that capture the main processes governing the dynamic behaviors, but which can be implemented in a highly computationally efficient manner.

Sharples et al. (2017) presented an example of the first of these approaches, using the VLS filter (1) to switch between a standard fire propagation model and one that specifically includes an additional lateral spread component. This model essentially forces the fire to spread laterally in regions identified as prone to VLS, and while this approach was able to improve the accuracy of the fire spread simulator, the lack of a physical basis remains somewhat dissatisfying.

In the remainder of this manuscript we follow the second approach, and discuss a reduced model that accounts for pyroconvective coupling between the fire and the atmosphere in a very straightforward manner.

3. INCORPORATING NEAR-FIELD EFFECTS IN FIRE SPREAD MODELING

3.1. Mathematical Model for Local Vorticity Effects

Hilton et al. (2018a) detailed a two-dimensional fire spread model that uses a potential flow formulation to account for local air flows induced by the fire. The so-called "pyrogenic potential" model simulates the pyrogenic air flow close to the ground (mid-flame height), which is assumed to flow horizontally until it reaches the fire, whereupon it moves vertically upwards with the fire's plume. Essentially the model treats the fire as a sink to the induced horizontal flow, the strength of which is related to the intensity of the fire. Once determined, the pyrogenic flow $\mathbf{u}_p$ can be added to the ambient wind field, and this net wind field can be used to model the evolution of the fire. In the present work we use a level-set method to simulate the evolution of the fire perimeter, as implemented in the Spark fire simulation framework (Miller et al., 2015).

To determine the pyrogenic flow $\mathbf{u}_p$, we invoke the Helmholtz Decomposition, which states that a twice continuously differentiable vector field with compact support can be expressed as the sum of an irrotational (curl-free) vector field and a solenoidal (divergence-free) vector field (Arfken and Weber, 1999). That is, if a vector field is sufficiently smooth and vanishes as distance $r \to \infty$, then we may write it as the sum of an irrotational vector field $\nabla\psi$ and a solenoidal vector field $\nabla \times \boldsymbol{\eta}$. We refer to ψ as the scalar potential and $\boldsymbol{\eta}$ as the vector potential.

Considering the flow $\mathbf{u}_p$ induced by a fire, it is reasonable to assume that $\mathbf{u}_p \to 0$ sufficiently far away from the fire. Hence if we make the assumption that $\mathbf{u}_p$ is sufficiently smooth, we can then write:

$$\mathbf{u}_p = \nabla\psi + \nabla\times\boldsymbol{\eta}, \quad (3)$$

for some scalar ψ and some vector $\boldsymbol{\eta}$. Hilton et al. (2018a) discuss how ψ and $\boldsymbol{\eta}$ can be determined as

solutions of the Poisson equations:

$$\nabla^2\psi = \nu, \quad \nabla^2\boldsymbol{\eta} = \boldsymbol{\omega}, \tag{4}$$

where $\nu = -\partial_z u_z$, which represents the derivative of the plume updraft, and $\boldsymbol{\omega}$ represents sources of vertical, z, vorticity. Once ψ and $\boldsymbol{\eta}$ are known, the pyrogenic flow $\mathbf{u}_p$ can be determined to account for the effects of the fire on the local atmosphere – we refer to these as *near-field effects*.

In particular, the model can be used to account for potential sources of vertical vorticity via the solenoidal term in (3), reducing the vector Poisson Equation (4) to:

$$\nabla^2\eta_z = \omega_z, \tag{5}$$

and the resulting flow in the ground plane to:

$$u_{px} = \frac{\partial\psi}{\partial x} + \frac{\partial\eta_z}{\partial y}, \quad u_{py} = \frac{\partial\psi}{\partial y} - \frac{\partial\eta_z}{\partial x}, \tag{6}$$

3.2. Numerical Implementation of Fire Spread

The spread of a fire over a landscape can be modeled using a two-dimensional approach where the fire is represented as an interface between burnt and unburnt regions (Miller et al., 2015). The growth of this interface, or fire perimeter, can be calibrated to data gathered from experimental fires giving an empirical fire spread rate as a function of variables such as fuel type, wind speed and local topography (Sullivan, 2009). The computational representation for the perimeter can be implemented in several forms. Here we use the level set approach to represent the perimeter (Sethian, 1999), in which the signed distance from the perimeter ϕ is updated over time using the level set equation:

$$\frac{\partial\phi}{\partial t} + s|\nabla\phi| = 0 \tag{7}$$

where s is the speed normal to the fire perimeter. The perimeter is identified by finding the contour for which $\phi = 0$. For the applications in this study a simple first-order rate-of-spread model (Hilton et al., 2016) consisting of a constant outward spread rate, s_c, plus a term depending on the wind field, $\mathbf{u}$ was used:

$$s = s_c + \max(\mathbf{u}\cdot\hat{\mathbf{n}}, 0) \tag{8}$$

where $\hat{\mathbf{n}}$ is the outward normal vector at the perimeter. To couple the pyrogenic and fire spread models we used $\mathbf{u} = \mathbf{u}_a + s_w\mathbf{u}_p$, where $\mathbf{u}_a$ is an ambient wind vector, $\mathbf{u}_w$ is the wind vector created by vorticity sources, given in Equation (6), and s_w is an arbitrary constant governing the effect of the vortex-generated wind speed on the fire.

An example simulation using the pyrogenic vector potential coupled to a wildfire spread simulation is shown in **Figure 2** with $s_c = 0.5$ and $s_w = 0.5$ in Equation (8). These constants were chosen arbitrarily for illustration. The fire was started from a single start point of radius 4 m located 200 m in the horizontal and vertical directions away from a pyrogenic source term. This source term was a single point with $\omega_z = 5$ at the indicated location. No ambient wind speed was used in the simulation with $\mathbf{u}_a = 0$. The resolution was set to 1 m and run for 200 s. The solid black lines show the position of the fire perimeter every 20 s time and the local wind vectors resulting from the pyrogenic model are shown as grayscale arrows. The effect of the vortex point source is to draw the fire perimeter in a circular path due to the resultant circulating flow around the source in the ground plane. The simulation took approximately 15 s to run on a NVidia GTX 1060 graphics processing unit.

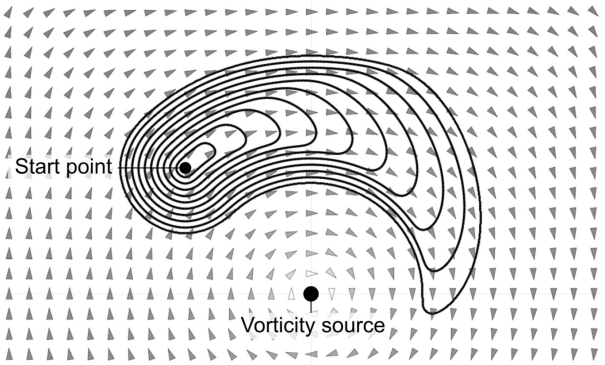

FIGURE 2 | Example application of the pyrogenic potential model with vortex source term to a dynamic wildfire simulation. The black lines show isochrones of a fire perimeter and the arrows show the resultant wind field from the vorticity source.

3.3. Analytical Solution for Vortex Roll Interaction

The key challenge in modeling VLS is to determine a way of translating the ambient horizontal vorticity that forms over a leeward slope due to flow separation, into vertical (pyrogenic) vorticity, ω_z. Specifically, we seek a closed-form solution for the components of the ambient horizontal vortex roll lofted by a buoyant fire plume.

The set-up under consideration is shown in **Figure 3**, where separation of the flow creates horizontal vorticity over the leeward slope. We require the vortex components $\boldsymbol{\omega}$ for the pyrogenic model:

$$\mathbf{u} = \nabla\psi + \nabla\times\boldsymbol{\eta}, \tag{9}$$

where

$$\nabla^2\boldsymbol{\eta} = \boldsymbol{\omega}. \tag{10}$$

We make the following assumptions for the flow dynamics on the lee slope:

(a) The flow can be approximated as steady state using the general steady-state inviscid vorticity equation as the outward spread of the fire is much slower than the wind flow. This is given by (Vallis, 2017):

$$(\mathbf{u}\cdot\nabla)\boldsymbol{\omega} = (\boldsymbol{\omega}\cdot\nabla)\mathbf{u} + \mathbf{s}, \tag{11}$$

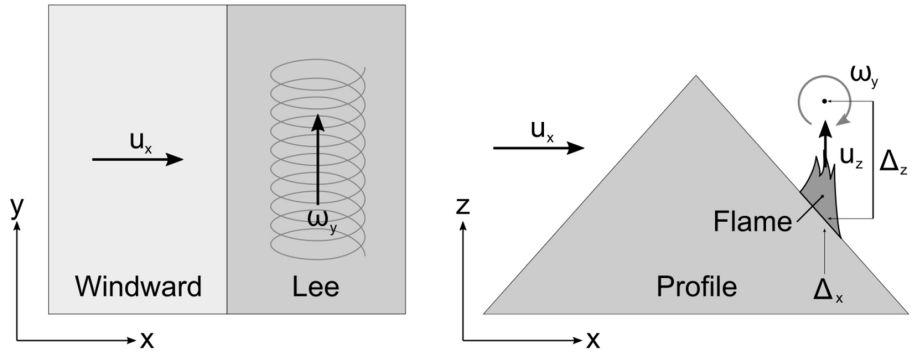

FIGURE 3 | Schematic set-up of model.

where **u** is the flow field, $\boldsymbol{\omega}$ is the vorticity vector and **s** is a source term.

(b) The dominant flow is the vertical lofting flow created by the fire plume; that is, $u_z \gg u_x, u_y$. This allows the u_x and u_y components to be neglected in Equation (11).

(c) The flow over the ridge results in a vortex that can be modeled as a prescribed source term. With no loss of generality, this can be aligned with the y-axis so $\omega_x = 0$. The source term is assumed to be a localized line source of the form:

$$s_y = a\delta(x - \Delta_x)\delta(z - \Delta_z),$$

where a is a constant and Δ_x and Δ_z are the x and z coordinates of the vortex line source.

(d) The assumption in the scalar model (Hilton et al., 2018a), $\nu = -\partial_z u_z$, is carried over so that $u_z = \nu z$ with the standard no-flow boundary condition at ground level, $u_z = 0$ at $z = 0$.

With these assumptions, Equation (11) reduces to:

$$u_z \frac{\partial \omega_y}{\partial z} = s_y \tag{12}$$

and

$$\omega_y \frac{\partial u_z}{\partial y} + \omega_z \frac{\partial u_z}{\partial z} = u_z \frac{\partial \omega_z}{\partial z}. \tag{13}$$

Rewriting Equation (12) using assumptions (c) and (d) gives:

$$\frac{\partial \omega_y}{\partial z} = \frac{a}{\nu z}\delta(x - \Delta_x)\delta(z - \Delta_z). \tag{14}$$

Equation (14) can now be solved for ω_y using Laplace transforms. The solution so obtained is:

$$\omega_y(z) = \frac{a}{\nu \Delta_z}\delta(x - \Delta_x)H(z - \Delta_z) + b, \tag{15}$$

where $H(z)$ is the Heaviside unit step function and b is some constant. This function is sketched in **Figure 4**—the solution simply has an optional constant vorticity at ground level of magnitude b, undergoes a step change at the line source and is constant thereafter.

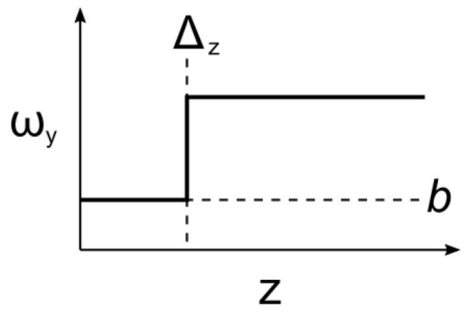

FIGURE 4 | Vorticity ω_y as a function of height z.

Rearranging Equation (13) gives:

$$z\frac{\partial \omega_z}{\partial z} - \omega_z = \frac{\omega_y}{\nu}\frac{\partial u_z}{\partial y}, \tag{16}$$

and substitution of Equation (15) yields

$$z\frac{\partial \omega_z}{\partial z} - \omega_z = \frac{1}{\nu}\frac{\partial u_z}{\partial y}\left(\frac{a}{\nu \Delta_z}\delta(x - \Delta_x)H(z - \Delta_z) + b\right). \tag{17}$$

This equation has an analytic solution of the form:

$$\omega_z(z) = A\delta(x - \Delta_x)H(z - \Delta_z)\left(\frac{z}{\Delta_z} - 1\right) - B + Cz, \tag{18}$$

where C is some constant and

$$A = \frac{a}{\nu^2 \Delta_z}\frac{\partial u_z}{\partial y}, B = \frac{b}{\nu}\frac{\partial u_z}{\partial y}. \tag{19}$$

Equation (18) has the form of a ramp function starting at Δ_z. The solution supports a linear term Cz representing the vertical advection of any non-zero ω_z source terms at $z = 0$. For $C = 0$ the function is constant for $b \neq 0$ and $\partial_y u_z \neq 0$. In the simplest

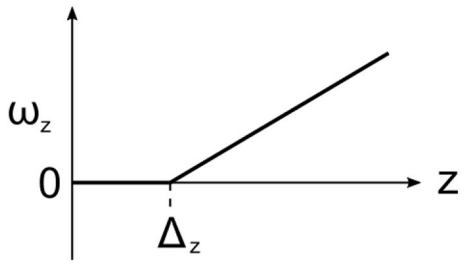

FIGURE 5 | Vorticity ω_z as a function of height z for $B = 0$ and $C = 0$.

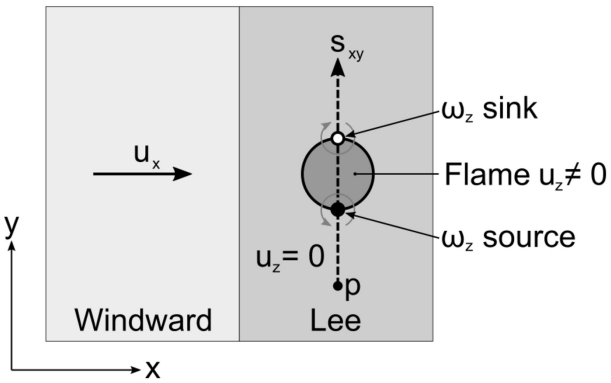

FIGURE 6 | Resultant vorticity in the z direction and circulation in the x-y plane from an idealized plume.

possible case of $B = 0$ and $C = 0$ the z component of the vorticity will be generated above the line source and linearly scale with height, as shown in **Figure 5**. Both the ramp function and Cz terms are linearly proportional to z, which is unphysical since $\omega_z \to \infty$ as $z \to \infty$. However, these unbounded terms arise from the assumption in the scalar model of $\nu = -\partial_z u_z$ and realistically Equation (18) only applies to regions below the free stream and above the flame source where the plume is accelerating.

The pyrogenic model is applied at a nominal mid flame height z_0. At $z = z_0 + \Delta_z$ and with $b = 0$ and $C = 0$, Equation (18) reduces to:

$$\omega_{z0} = k\delta(x - \Delta_x)\frac{\partial u_z}{\partial y}, \tag{20}$$

where:

$$k = \frac{az_0}{\nu^2 \Delta_z^2} \tag{21}$$

This result can be generalized to the case of a line source given by a vector equation of the form $\mathbf{p} + \mathbf{s}_{xy}$:

$$\omega_{z0} = k\delta(|\mathbf{x} - \mathbf{x}'|)(\nabla u_z \cdot \mathbf{s}_{xy}), \tag{22}$$

where $\mathbf{x}'$ is the nearest point on the line source to $\mathbf{x}$. In the case of a plume with constant u_z within a localized region and $u_z = 0$ outside the region ω_z will only be produced at the intersection of the line source $\mathbf{s}_{xy}$ and the edges of the region. This will give rise to a source term where $\nabla u_z \cdot \mathbf{s}_{xy} > 0$ and a sink where $\nabla u_z \cdot \mathbf{s}_{xy} < 0$ resulting in two counter-rotating vortices, as illustrated in **Figure 6**.

In this case the expression for the vertical vorticity can undergo a final simplification:

$$\omega_{z0} = k'\delta(|\mathbf{x} - \mathbf{x}'|)\delta(\phi)(\hat{\mathbf{n}} \cdot \mathbf{s}_{xy}), \tag{23}$$

where $k' = u_z k$, ϕ is the distance from the fire perimeter and $\hat{\mathbf{n}}$ is the outward normal of the perimeter.

4. TWO-DIMENSIONAL SIMULATION OF VLS

In this section we implement the two-dimensional model described in the previous section and evaluate its ability to capture the patterns of dynamic fire propagation associated with VLS. Moreover, we compare the performance of the two-dimensional model with output from a more sophisticated coupled fire-atmosphere model. To this end, we begin by giving a brief overview of the coupled modeling results.

4.1. Coupled Fire-Atmosphere Model

Simpson et al. (2013) conducted idealized large eddy simulations of the VLS phenomenon using the WRF-Fire coupled fire-atmosphere model (Skamarock et al., 2008). The basic configuration considered was an idealized hill with a triangular profile and a height of $\sim$ 1 km. The ridge line at the top of the hill was aligned in a north-south direction. A westerly wind of 20 ms^{-1} (at the surface) was allowed to flow over the hill, which had a windward slope angle of 20° and a leeward slope angles of 35°. A fire was initiated as a line ignition near the bottom of the leeward slope and allowed to spread. Full details of the simulations are provided by Simpson et al. (2013). It is also of interest to note that Simpson et al. (2015) used similar methods to model a real case, in which VLS had influenced the propagation of the fire, with good agreement between the observed and simulated fire progression.

The idealized simulations were conducted with the fire-atmosphere feedback turned off or turned on. When the fire-atmosphere feedback was turned off, the fire simply propagated back up the leeward slope toward the ridge line and spread laterally at a roughly uniform rate. An example of an uncoupled simulation can be seen in **Figures 7A–C**. By contrast, when the fire-atmosphere coupling was turned on, the fire spread up the slope until it neared the ridge, at which point it exhibited distinct and rapid lateral growth in a relatively narrow band in the immediate lee of the ridge line. This situation is depicted in **Figures 7D–F**. These simulations clearly indicate that the rapid lateral spread in the lee of the ridge line associated with VLS is a form of dynamic fire propagation driven by fire-atmosphere coupling.

It is also important to note that the simulations conducted by Simpson et al. (2013) were computationally intensive, with each 2 h simulation taking around 8–10 h to run on a HPC platform.

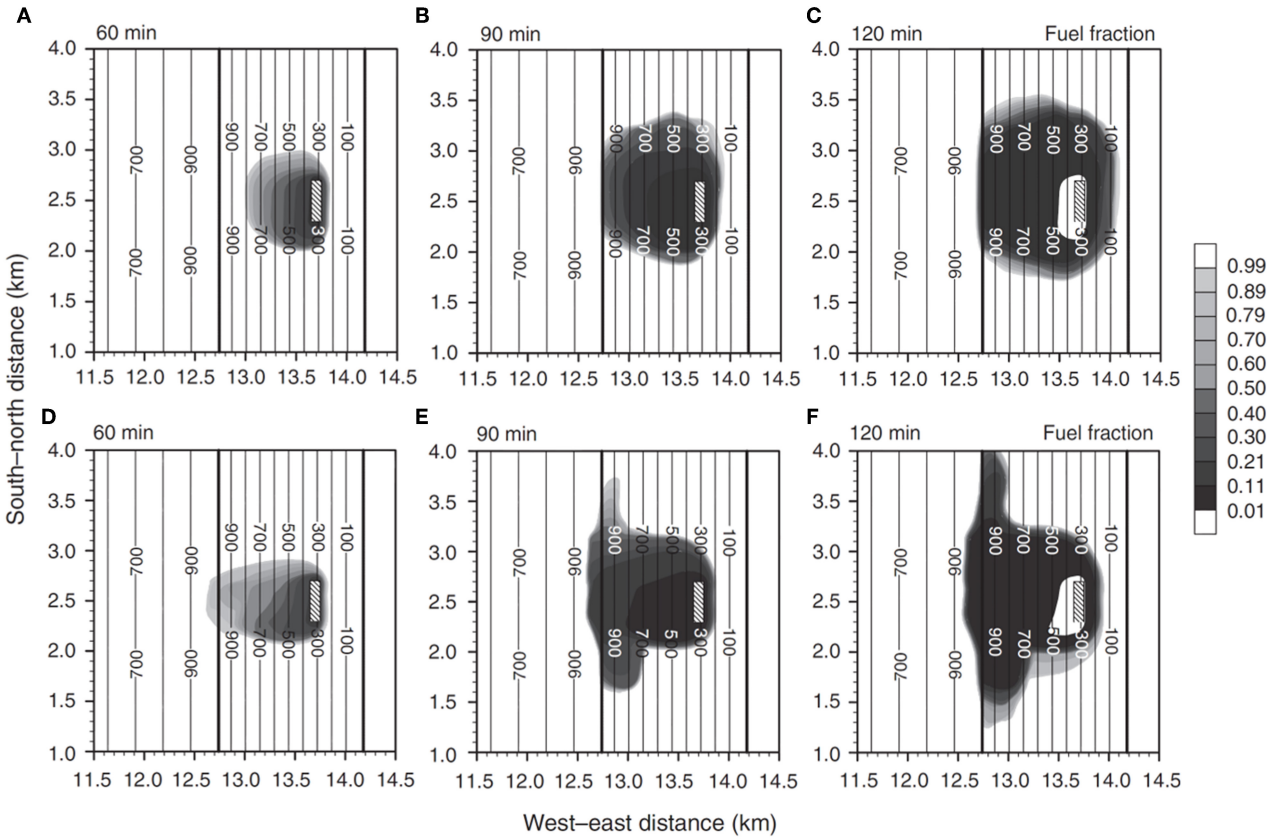

FIGURE 7 | Coupled fire-atmosphere model output of a fire burning on a leeward slope at times of 60, 90, and 120 min into the simulation. Panels **(A–C)** show model output when the fire-atmosphere coupling is turned off, while panels **(D–F)** show model output when the fire-atmosphere coupling is turned on. The gray shading indicates the instantaneous fuel fraction remaining. White shading is applied to regions where the fuel fraction remaining is over 99% or under 1%. Terrain contour lines are given at 100-m intervals and the solid black lines represent the ridge line of the hill and the base of the leeward slope. The fire ignition region is indicated by the dash-filled region. The figure has been adapted from Simpson et al. (2013).

4.2. Pyrogenic Potential Model

The pyrogenic potential model was implemented in the Spark framework, a software system for simulating wildfires (Hilton et al., 2018b). Spark consists of a core computational module for simulating the spread of fire over a landscape based the a level set method along with a set of additional modules for simulating additional types of fire behavior, such as terrain effects, firebrand dynamics and near-field effects of the fire on the local atmosphere. The use of a scalar potential to simulate the near-field effect of the plume on the local air flow was presented in Hilton et al. (2018a). As described in section 3 the extension to a vector potential is straightforward, resulting in a vector Poisson equation.

For the purposes of the two-dimensional simulations the horizontal vorticity generated by the flow over the hill was assumed to be static and steady state. This is not a requirement of the model, but simplifies calculations as the assumption of a steady state vortex allows the backwards flow in the lee side of a hill to be imposed as a steady wind condition. The vertical vorticity is assumed to be the dominant component affecting the lateral spread of the fire in the ground plane and is dynamically calculated. The assumption reduced the vector Poisson equation (4) to the scalar Poisson Equation (5). The vertical vorticity in Equation (5) is calculated from Equation (23). The equation is numerically solved using a multigrid method (Hilton et al., 2018b).

A dynamic simulation under the idealized conditions given above is shown in **Figure 8**. The domain consisted of a ridge 1 km high with a slope of 20° on the windward side and 35° on the lee slope – the same configuration as used by Simpson et al. (2013). The ignition was initiated as a line 400 m in length and 50 m in width perpendicular to the ridge at a distance of 750 m down the leeward slope. The domain size was 5 × 5 km with a simulation resolution of 10 m, and the simulation was run for a period of 2 h. The wind direction was perpendicular to the ridge with a speed was 10 ms^{-1} on the windward slope. The re-circulation was prescribed by setting the wind speed to -1 ms^{-1} on the lee slope. The fire rate-of-spread, R, used the Rothermel equation (Rothermel, 1972) with fuel type 13 (Anderson, 1982) with a fuel moisture content of 8%, a fuel load of 13.024 tons $acre^{-1}$ and a surface to volume ratio of 1159 ft^{-1}. The vorticity was prescribed as a line source with $\mathbf{p} = (-100, 0)$, $\mathbf{s}_{xy} = (0, 1)$ and $k' = 2000$.

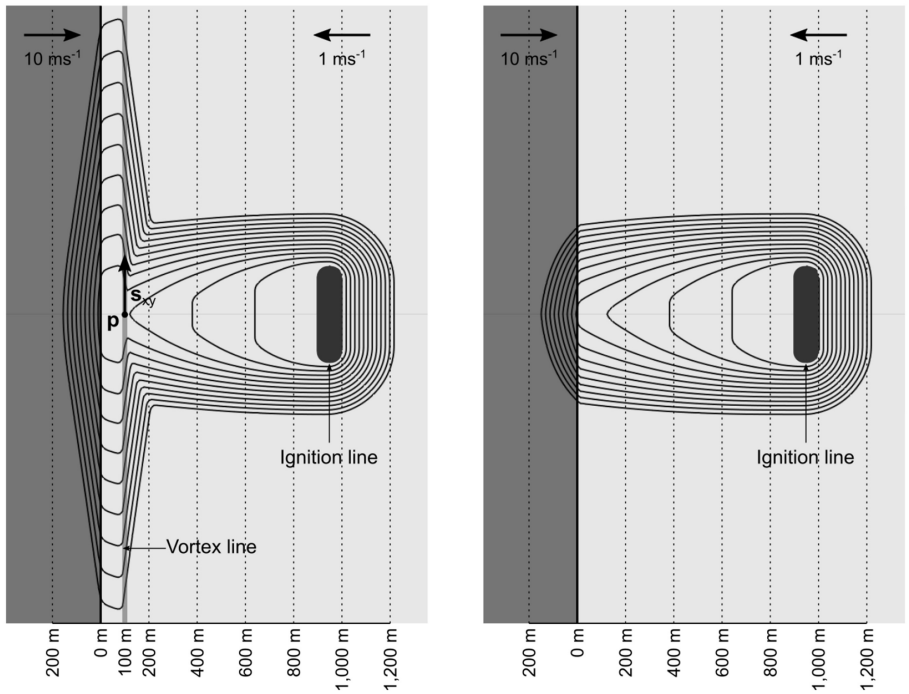

FIGURE 8 | Dynamic calculation in Spark using idealized conditions of $B = 0$ and $C = 0$, using the pyrogenic potential model (left) and without (right). The solid lines are fire isochrones at ten minute intervals.

Note that the position of the vortex line is consistent with the definition of VLS prone parts of the landscape, as discussed in section 2.

The Dirac function was represented using a smoothed function:

$$\delta(\phi) = \frac{2\epsilon}{(e^{\epsilon\phi} + e^{-\epsilon\phi})^2} \tag{24}$$

where $\epsilon = 0.15$ is a smoothing length scale, chosen to numerically smooth the Dirac function (Hilton et al., 2018a).

For the case with pyrogenic vorticity, left-hand side of **Figure 8**, the fire moves up the ridge under the effect of the imposed lee slope wind before spreading laterally along the ridge. The lateral spread occurs along the imposed vortex line. The degree of lateral spread is proportional to the term k', and the value used in this simulation was manually chosen to match to the physics-based simulations. In the case of no pyrogenic vorticity, right-hand side of **Figure 8**, the fire moves up the lee slope and stops at the ridge line.

The pyrogenic potential model output compares favorably to the coupled fire-atmosphere model output. In particular, when the effects of pyrogenic vorticity are included, the two-dimensional model is able to produce patterns of fire propagation that are qualitatively similar to that produced by the coupled fire-atmosphere model (compare the left panel of **Figure 8** with **Figure 7F**). Specifically, the two-dimensional model is able to reproduce the rapid lateral spread across the top of the hill in the immediate lee of the ridge line. Likewise, when the effects of pyrogenic vorticity are not included in the two-dimensional model, the model produces results that are qualitatively similar to the uncoupled simulations depicted in **Figure 6C**.

There are some notable differences between the two-dimensional model output and that of the fully coupled model. In particular, the lateral extent of the fire spread across the lower parts of the leeward slope, which are not prone to vorticity effects, is much less in the two-dimensional model output compared to that of the fully coupled model (even when the coupling is turned off). These differences are likely due to the influence of turbulence, which are not accounted for in the highly idealized two-dimensional pyrogenic potential model simulations.

Using the pyrogenic model imposed a modest computational overhead on the calculation. Using a NVidia GTX 1060 graphics processing unit the 2 h simulation took around 6 s to run with the pyrogenic vortex model and around 1 s without the model.

5. DISCUSSION AND CONCLUSIONS

Dynamic modes of fire propagation arising from coupling between a fire and the atmosphere pose a significant challenge to two-dimensional fire spread simulators. Currently, such models are not able to accurately account for such behaviors. Here we have presented a new two-dimensional model based on a pyrogenic vector potential formulation that is able to reproduce a specific mode of fire-atmosphere interaction, namely, rapid lateral spread associated with VLS. The model accomplishes this by incorporating near-field effects driven by pyrogenic indrafts and local interaction of the fire with ambient horizontal vorticity.

As such, the model can be seen as a "reduced physics" model, in which fire-atmosphere coupling has been greatly simplified. Despite these simplifications, however, the model is able to capture many of the key features observed in connection with VLS and other forms of dynamic fire spread (Hilton et al., 2018a).

The pyrogenic potential model has a significant computational advantage over the fully coupled fire-atmosphere models that have previously been required to accurately model VLS. The pyrogenic potential model took only about 10 s on a standard desktop computer to simulate 2 h of the spread associated with VLS, whereas the fully coupled model required around 8–10 h of to run on a current state-of-the-art high performance computing platform. This increase in computational efficiency could allow the model to be used in scenarios where computational speed is crucial, such as operational fire spread predictions.

Use of the pyrogenic model in operational prediction systems could provide fire managers with the ability to better appreciate the full range of fire behaviors that could be expected, especially under extreme conditions. For example, the VLS phenomenon has been associated with the generation of mass spotting events and the formation of deep flaming zones, which pose a serious threat to firefighter safety and can enhance the likelihood of pyrocumulonimbus development (McRae et al., 2015). This type of modeling capability would therefore provide fire managers with an unprecedented ability to identify regions most at risk to extreme bushfire development and contribute to improvements in firefighter safety.

Although the model presented here constitutes significant progress in our ability to efficiently model dynamic fire propagation, there are still further modeling scenarios that need to be considered, and a number of improvements that could be implemented. For example, the model has been shown to perform reasonably for only a single wind-terrain configuration. Other configurations such as those considered by Raposo et al. (2015) and Simpson et al. (2016) must be considered. It would also be valuable to assess how the model performs against real cases where the effects of VLS were implicated, such as those presented by Quill and Sharples (2015), Simpson et al. (2015), and Sharples et al. (2017). These avenues of inquiry will be pursued in future work.

DATA AVAILABILITY STATEMENT

The raw data supporting the conclusions of this article will be made available by the authors, without undue reservation, to any qualified researcher.

AUTHOR CONTRIBUTIONS

The study was conceived and designed by both authors. JH conducted the numerical simulations and prepared the figures, with contributions from JS. The paper was written and reviewed by JS and JH.

FUNDING

This work was supported by funding from the Bushfire and Natural Hazards Cooperative Research Centre for the project Fire coalescence and mass spotfire dynamics: experimentation, modeling and simulation. Part of this work was also performed in the framework of Project Firewhirl, with reference PTDC/EMS-ENE/2530/2014, supported by the Portuguese Foundation for Science and Technology, with National Funds.

ACKNOWLEDGMENTS

The authors acknowledge the support of the Bushfire and Natural Hazards Cooperative Research Centre. Parts of the research presented was also undertaken with the assistance of resources and services from the National Computational Infrastructure (NCI), which is supported by the Australian Government.

REFERENCES

Anderson, H. (1982). *Aids to Determining Fuel Models for Estimating Fire Behaviour*. General Technical Report INT-122, USDA Forest Service, Intermountain Forest and Range Experiment Station.

Arfken, G. B., and Weber, H. J. (1999). *Mathematical Methods for Physicists*. San Diego, CA: AAPT.

Countryman, C. (1971). *Fire Whirls... Why, When, and Where*. General technical report, USDA Forest Service, Pacific Southwest Forest and Range Experiment Station, Berkeley, CA.

Finney, M. A. (2004). *Farsite: Fire Area Simulator: Model Development and Evaluation*. Research paper RMRS-RP-4 Revised, USDA Forest Service, Rocky Mountain Research Station.

Hilton, J. E., Miller, C., and Sullivan, A. L. (2016). A power series formulation for two-dimensional wildfire shapes. *Int. J. Wildland Fire* 25, 970–979. doi: 10.1071/WF15191

Hilton, J. E., Sullivan, A., Swedosh, W., Sharples, J., and Thomas, C. (2018a). Incorporating convective feedback in wildfire simulations using pyrogenic potential. *Environ. Modell. Softw.* 107, 12–24. doi: 10.1016/j.envsoft.2018.05.009

Hilton, J. E., Sullivan, A. L., Swedosh, W., Cruz, M. G., Plucinski, M. P., Hurley, R. J., et al. (2018b). *The Spark Wildfire Prediction System*. Coimbra: Imprensa da Universidade de Coimbra.

Lahaye, S., Sharples, J., Matthews, S., Heemstra, S., and Price, O. (2017). "What are the safety implications of dynamic fire behaviours?" in *MODSIM2017, 22nd International Congress on Modelling and Simulation*, eds G. Syme, D. Hatton MacDonald, B. Fulton, and J. Piantadosi (Modelling and Simulation Society of Australia and New Zealand), 1125–1130.

McRae, R. (2004). "The breath of the dragon – observations of the January 2003 ACT bushfires," in *Proceedings of Bushfire 2004 – Earth, Wind & Fire: Fusing the Elements* (Adelaide, SA).

McRae, R., Sharples, J., and Fromm, M. (2015). Linking local wildfire dynamics to pyroCb development. *Nat. Hazards Earth Syst. Sci.* 15, 417–428. doi: 10.5194/nhess-15-417-2015

Miller, C., Hilton, J., Sullivan, A., and Prakash, M. (2015). "Spark–a bushfire spread prediction tool," in *Environmental Software Systems. Infrastructures, Services and Applications. Vol. 448 of IFIP Advances in Information and Communication Technology*, eds R. Denzer, R. Argent, G. Schimak, and J. Hřebíček (Springer International Publishing), 262–271.

Quill, R. and Sharples, J. (2015). "Dynamic development of the 2013 aberfeldy fire," in *MODSIM2015, 21st International Congress on Modelling and Simulation*, eds T. Weber, M. McPhee, and R. Anderssen (Modelling and Simulation Society of Australia and New Zealand), 284–290.

Raposo, J., Cabiddu, S., Viegas, D., Salis, M., and Sharples, J. (2015). Experimental analysis of fire spread across a two-dimensional ridge under wind conditions. *Int. J. Wildland Fire* 24, 1008–1022. doi: 10.1071/WF14150

Raposo, J., Viegas, D., Xie, X., Almeida, M., Figueiredo, A., Porto, L., et al. (2018). Analysis of the physical processes associated with junction fires at laboratory and field scales. *Int. J. Wildland Fire* 27, 52–68. doi: 10.1071/WF16173

Rothermel, R. (1972). "A mathematical model for predicting fire spread in wildland fuels," *Research Paper INT-115* (Ogden, UT: U.S. Department of Agriculture, Intermountain Forest and Range).

Sethian, J. A. (1999). *Level Set Methods and Fast Marching Methods: Evolving Interfaces in Computational Geometry, Fluid Mechanics, Computer Vision, and Materials Science*. Cambridge: Cambridge University Press.

Sharples, J., Kiss, A., Raposo, J., Viegas, D., and Simpson, C. (2015). "Pyrogenic vorticity from windward and lee slope fires," in *MODSIM2015, 21st International Congress on Modelling and Simulation*, eds T. Weber, M. McPhee, and R. Anderssen (Gold Coast, QLD: Modelling and Simulation Society of Australia and New Zealand), 291–297.

Sharples, J., McRae, R., and Wilkes, S. (2012). Wind–terrain effects on the propagation of wildfires in rugged terrain: fire channelling. *Int. J. Wildland Fire* 21, 282–296. doi: 10.1071/WF10055

Sharples, J., Richards, R., Hilton, J., Ferguson, S., Cohen, R., and Thatcher, M. (2017). "Dynamic simulation of the Cape Barren Island fire using the Spark framework," in *MODSIM2017, 22nd International Congress on Modelling and Simulation*, eds G. Syme, D. Hatton MacDonald, B. Fulton, and J. Piantadosi (Hobart, TAS: Modelling and Simulation Society of Australia and New Zealand), 1111–1117.

Simpson, C., Sharples, J., and Evans, J. (2014). Resolving vorticity-driven lateral fire spread using the WRF-fire coupled atmosphere–fire numerical model. *Nat. Hazards Earth Syst. Sci.* 14, 2359–2371. doi: 10.5194/nhess-14-2359-2014

Simpson, C., Sharples, J., and Evans, J. (2015). "WRF-fire simulation of lateral fire spread in the Bendora Fire on 18 January 2003," in *MODSIM2015, 21st International Congress on Modelling and Simulation*, eds T. Weber, M. McPhee, and R. Anderssen (Gold Coast, QLD: Modelling and Simulation Society of Australia and New Zealand), 305–311.

Simpson, C., Sharples, J., and Evans, J. (2016). Sensitivity of atypical lateral fire spread to wind and slope. *Geophys. Res. Lett.* 43, 1744–1751. doi: 10.1002/2015GL067343

Simpson, C., Sharples, J., Evans, J., and McCabe, M. (2013). Large eddy simulation of atypical wildland fire spread on leeward slopes. *Int. J. Wildland Fire* 22, 599–614. doi: 10.1071/WF12072

Skamarock, W., Klemp, J., Dudhia, J., Gill, D., Barker, D., Duda, M., et al. (2008). *A Description of the Advanced Research WRF Version*. NCAR Technical Note 475, National Center for Atmospheric Research, Boulder, CO.

Sullivan, A. L. (2009). Wildland surface fire spread modelling, 1990–2007. 3: Simulation and mathematical analogue models. *Int. J. Wildland Fire* 18, 387–403. doi: 10.1071/WF06144

Thomas, C., Sharples, J., and Evans, J. (2017). Modelling the dynamic behaviour of junction fires with a coupled atmosphere–fire model. *Int. J. Wildland Fire* 26, 331–344. doi: 10.1071/WF16079

Tolhurst, K., Shields, B., and Chong, D. (2008). Phoenix: development and application of a bushfire risk management tool. *Austral. J. Emerg. Manage.* 23:47.

Vallis, G. K. (2017). *Atmospheric and Oceanic Fluid Dynamics*. Cambridge: Cambridge University Press.

Viegas, D. X. (2006). Parametric study of an eruptive fire behaviour model. *Int. J. Wildland Fire* 15, 169–177. doi: 10.1071/WF05050

Viegas, D. X. and Pita, L. P. (2004). Fire spread in canyons. *Int. J. Wildland Fire* 13, 253–274. doi: 10.1071/WF03050

Viegas, D. X., Raposo, J. R., Davim, D. A., and Rossa, C. G. (2012). Study of the jump fire produced by the interaction of two oblique fire fronts. part 1. analytical model and validation with no-slope laboratory experiments. *Int. J. Wildland Fire* 21, 843–856. doi: 10.1071/WF10155

Conflict of Interest: The authors declare that the research was conducted in the absence of any commercial or financial relationships that could be construed as a potential conflict of interest.

Advantages of publishing in Frontiers

OPEN ACCESS
Articles are free to read for greatest visibility and readership

FAST PUBLICATION
Around 90 days from submission to decision

HIGH QUALITY PEER-REVIEW
Rigorous, collaborative, and constructive peer-review

TRANSPARENT PEER-REVIEW
Editors and reviewers acknowledged by name on published articles

Frontiers
Avenue du Tribunal-Fédéral 34
1005 Lausanne | Switzerland

Visit us: www.frontiersin.org
Contact us: info@frontiersin.org | +41 21 510 17 00

REPRODUCIBILITY OF RESEARCH
Support open data and methods to enhance research reproducibility

DIGITAL PUBLISHING
Articles designed for optimal readership across devices

FOLLOW US
@frontiersin

IMPACT METRICS
Advanced article metrics track visibility across digital media

EXTENSIVE PROMOTION
Marketing and promotion of impactful research

LOOP RESEARCH NETWORK
Our network increases your article's readership